

Some pages of this thesis may have been removed for copyright restrictions.

If you have discovered material in Aston Research Explorer which is unlawful e.g. breaches copyright, (either yours or that of a third party) or any other law, including but not limited to those relating to patent, trademark, confidentiality, data protection, obscenity, defamation, libel, then please read our [Takedown policy](#) and contact the service immediately (openaccess@aston.ac.uk)

FLEXIBILITY AND STRESS INTENSIFICATION FACTORS
OF GLASS REINFORCED PLASTIC PIPE BENDS

by

Maan Abdul Karim KANONA

A thesis submitted for the degree
of Doctor of Philosophy

February 1985

The University of Aston in Birmingham
Department of Mechanical and Production Engineering

Internal Supervisor: Dr I.M. Cole
External Supervisor: Dr D.C. Wright

SUMMARY

"The University of Aston in Birmingham"

FLEXIBILITY AND STRESS INTENSIFICATION FACTORS OF GLASS REINFORCED PLASTIC PIPE BENDS

Maan Abdul Karim KANONA

A thesis submitted for the degree of Doctor of Philosophy

1985

Straight pipes and bends made from Glass Reinforced Plastics (GRP) were investigated under different types of short term loading under laboratory conditions. The test components were made by five different manufacturers, using a combination of Chopped Strand Mat (CSM), Woven Rovings (WR), Unidirectional (UD), and Filament Wound (FW) reinforcements.

Test results for 33 bend components obtained by in-plane bending (closing and opening) and out-of-plane bending are presented as flexibility factors (K) and stress intensification factors (SIF). The results are discussed and compared with various pipe standards and bend theories.

Isotropic bend theory was modified to accommodate bends having different circumferential and longitudinal moduli and to include the effect of such anisotropies on K and SIF. Both isotropic and orthotropic bend theories have been represented by computer programmes to generate theoretical results.

A few pressure tests were carried out on bends, and the results are presented as Pressure Stress Multiplier (PSM) and are compared with theory of thin shells.

Straight pipes manufactured similarly to the bends, were tested under flexural, torsional and internal pressure loadings. The test results are presented and compared with the predictions of thin shell theory.

From failure tests, it could be shown that considerations should be given to the interlaminar shear strength of composites in the design of GRP bends. Local variability in the laminate thickness is shown to induce local bending stresses when the pipe components are pressurised.

Reasonable agreement is found between experimentally determined values of K and SIF of GRP bends and those predicted theoretically, providing the average wall thickness is used.

Key words:

Glass reinforced plastics
Piping
Stress analysis
Chemical plant

NOTATION

| | |
|--------------------------|---|
| A_1, A_2 | cross-section areas |
| B_1, B_2 | constants |
| $[C]$ | stiffness matrix |
| C_{ij} | stiffness tensor |
| $c_1 \dots c_n$ | constants |
| \bar{C} | Tsia contiguity factor |
| $d_1 \dots d_n$ | constants |
| Ext. | Extensibility |
| E_1, E_2 | moduli of material (1) and (2) |
| E_{cp} | modulus of composite |
| E | in-plane isotropic modulus |
| E_{CSM} | modulus of CSM laminate |
| E_{WR} | modulus of WR laminate |
| E_{UD} | modulus of UD laminate |
| E_f | modulus in the direction of the fibres |
| E_t | modulus transverse to the fibres |
| E_L | modulus in the longitudinal direction of the pipe |
| E_C | modulus in the circumferential direction of the pipe |
| E_i | modulus of layer (i) |
| E_{11}, E_{22}, E_{33} | moduli in the directions of x_1, x_2, x_3 axes |
| E_{33} | through thickness modulus |
| EI | flexural rigidity |
| $\sum EI_{(B)}$ | total flexural rigidity of multilayer structure |
| $\sum EI_{(B)_e}$ | average effective rigidity of the mitred bend |
| $\sum EI_{(B.C)_e}$ | average rigidity of bend centre and straight tangent of mitred bend |

| | |
|----------------------|---|
| $\Sigma EI_{(Bj)_e}$ | average rigidity of segment-edge and straight tangent of mitred bend |
| ΣEI_n | nominal flexural rigidity |
| ΣEI_{st} | straight pipe flexural rigidity |
| ΣEI_f | flange joint flexural rigidity |
| F | function |
| F_x, F_y, F_z | anchor loads in the direction of x, y, z axes respectively |
| f | inward component of mid-layer bend |
| | longitudinal stress |
| G | in-plane isotropic shear modulus |
| G_{CSM} | in-plane shear modulus of CSM laminate |
| G_{WR} | in-plane shear modulus of WR laminate, $0^\circ + 90^\circ$ from fibres |
| G_{UD} | in-plane shear modulus of UD laminates, 0° from fibres |
| G_{lt} | in-plane shear modulus lying along the longitudinal and the transverse directions to the fibre |
| G_{LC} | in-plane shear modulus lying along the longitudinal and the circumferential directions of the pipes |
| G' | interlaminar shear modulus |
| G_{ij} | shear moduli of cubical element |
| GJ | torsional rigidity |
| ΣGJ | torsional rigidity of multi-layer structure |
| I | second moment of area, $\pi r_m^3 t$ (pipe) |
| ISS | interlaminar shear strength |
| J | polar moment of area, $2\pi r_m^3 t$ (pipe) |

| | |
|-----------------|--|
| K | flexibility factor |
| K_i | in-plane flexibility factor |
| K_o | out-of-plane flexibility factor |
| $K_{\bar{m}}$ | flexibility factor for bends of orthotropic laminate |
| $K_1 \quad K_6$ | safety factor of BS4994 |
| K_{av} | average flexibility of bend |
| K_{ψ_o} | flexibility factor of bend section at angle |
| k | constant of decay length on pipes |
| $[\bar{K}]$ | stiffness matrix (Torsion) |
| k_{ij} | elements of $[K]$ |
| L | length of a beam |
| \bar{l} | length of segment on mitred bend |
| $\Delta l / l$ | change of bend length per unit length |
| l, l_1, l_2 | tangent length |
| \bar{m} | E_c / E_L of pipe wall laminate |
| M | bending moment |
| M_i | in-plane bending moment |
| M_o | out-of-plane bending moment |
| M_g | glass mass content (kg/m^2) or % |
| M_r | resin glass content |
| M_b | local bending moment |
| M_{CSM} | glass mass content for CSM laminate |
| M_{WR} | glass mass content for WR laminate |
| M_{UD} | glass mass content for UD laminate |
| N | number of terms |
| n | integer |
| P_i | internal pressure |
| PSM | pressure stress multiplier for bends |
| P | load |

| | |
|----------------------|--|
| P_V | in-plane end-load |
| P_H | out-of-plane end-load |
| R | bend radius |
| R_E | equivalent bend radius of mitred bend |
| r | pipe cross-sectional radius |
| r_m | mean pipe cross-sectional radius |
| r_i | inside pipe cross-sectional radius |
| r_o | outside pipe cross-sectional radius |
| r_n | cross-sectional radius of dual-layer laminate pipe |
| $[S]$ | compliance matrix |
| S_{ij} | compliance tensor |
| $\Delta S, \delta S$ | increment of length |
| SIF | stress intensification factor |
| SIF_i | in-plane stress intensification factor |
| SIF_o | out-of-plane stress intensification factor |
| SIF_L, SIF_C | longitudinal and circumferential stress intensification factors respectively |
| T | torque |
| t | thickness |
| t' | laminate thickness per unit glass mass per unit area |
| t_n | nominal thickness, usually as specified by BS4994 (Mg.t') |
| t_{st} | average laminate thickness of a straight pipe |
| t_j | average laminate thickness of a joint |
| t_B | average laminate thickness of a bend fitting |
| t_{BC} | average laminate thickness of a mitred bend-centre (segment-centre) |

| | |
|-----------------|---|
| t_{Bj} | average laminate thickness of a mitred bend at the edge-segment |
| $t_{(B.C)_e}$ | $(t_{st} + t_{B.C.})/2$ |
| $t_{(BJ)_e}$ | $(t_{st} + t_{B.j})/2$ |
| $t_{(B)_e}$ | $t_{st}/2 + (t_{B.C.} + t_{B.j})/4$ |
| t_f | average laminate thickness at the flange joint |
| U_1, U_2, U_3 | energy |
| U_s | strain energy |
| U_p | pressure energy |
| U_T | total energy |
| U_L | longitudinal strain energy |
| U_C | circumferential strain energy |
| UTS | ultimate tensile strength |
| UTUS | ultimate tensile unit strength |
| V_1 | volume of element (1) |
| V_2 | volume of element (2) |
| V_g | glass content (%) by volume |
| V_r | resin content (%) by volume |
| V | shear force |
| W | width of a strip |
| x | axis along pipe |
| x_1, x_2, x_3 | space axes |
| \bar{y} | position of neutral axis |
| y_i | distance from neutral axis |
| Z_1 | constant representing bend restraint |

| | |
|-----------------------|--|
| α | mitre angle |
| α_1, α_2 | decay lengths |
| β_m | efficiency factor for modulus prediction |
| β_s | efficiency factor for strength prediction |
| $\Delta \beta$ | increment of twist |
| β_1 | angular direction of principal strain |
| $\bar{\beta}$ | torsional rotation |
| γ | shear strain |
| γ_{12} | in-plane shear strain |
| γ_{ij} | shear strains of cubical element, $i \neq j = 1, 2, 3$ |
| Δ | deflection |
| $\Delta_{xy, xz, yz}$ | deflections in the xy, xz, yz planes |
| ϵ | strain |
| ϵ_{ij} | strains in the directions of space axes x_{11}, x_{22}, x_{33} , $i = j = 1, 2, 3$ |
| ϵ_{nl} | non-linearity strain |
| ϵ_f | failure strain |
| ϵ_b | local bending strain |
| ϵ_i | strain at distance y_i from neutral axis |
| η | $\Delta\psi_0 / \psi_0$ for in-plane bending, R/ρ for out-of-plane bending |
| λ | pipe factor = tR/r_m^2 |
| λ_1 | $\lambda / \sqrt{1 - \nu^2}$ |
| $\lambda_{\bar{m}}$ | $\sqrt{\bar{m}} \lambda_1$ |
| Λ | $\{3(1 - \nu^2)\}^{1/4} (r_m/t)^{1/2}$ |
| λ_E | equivalent pipe factor of mitred bend |
| ν | Poisson's ratio |
| ν_{LC} | circumferential to longitudinal Poisson's ratio |

| | |
|-----------------|--|
| V_{CL} | longitudinal to circumferential Poisson's ratio |
| ρ | bend curvature due to out-of-plane bending |
| ρ_g | glass density |
| ρ_r | resin density |
| σ | stress |
| (σ_B) | stress around the bend |
| (σ_B) | maximum bend stress |
| σ_{ij} | stresses in the direction of space axes x_{11} , x_{22} , x_{33} , $i=j=1,2,3$ |
| σ_{nl} | non-linearity stress |
| σ_f | failure stress |
| σ_b | local bending stress |
| σ_i | stress at distance y_i from neutral axis |
| σ_{cp}^* | strength of composite |
| σ_g^* | strength of glass fibre |
| σ_r^* | strength of resin |
| σ_n | maximum simple bending stress |
| σ_{nn} | maximum simple bending stress for dual laminate |
| τ | in-plane shear stress |
| $\bar{\tau}$ | interlaminar shear stress |
| τ_f | shear strength |
| θ | angle around bend cross-section perimeter |
| ϕ | angle around bend cross-section perimeter |
| Φ | slope |

| | |
|-----------------|---|
| $\bar{\psi}$ | bend pressure parameter |
| ψ_0 | bend angle |
| $\Delta \psi_0$ | change of bend angle |
| ω | displacement of bend wall (ω_r radial, ω_t tangential) |

LIST OF TABLES

| | Page | |
|------|--|-----|
| 2.1 | Comparative properties of CSM reinforced thermoset resins | 9 |
| 2.2 | Effect of mixture components on end properties of polyester resin | 10 |
| 2.3 | Laminate cure time of Atlac 382-05 resin mix | 10 |
| 2.4 | Typical properties of reinforcing fibres | 13 |
| 3.1 | Thickness and glass content of flat GRP sheets | 52 |
| 3.2 | Average test results obtained from tensile testing of GRP flat sheets | 52 |
| 3.3 | Theoretical and experimental comparison of tensile test results of GRP flat sheets | 57 |
| 3.4 | Flexural test results obtained from 3-pt bending of GRP flat sheets | 60 |
| 3.5 | 3-pt and 4-pt bending of GRP specimens | 60 |
| 3.6 | Theoretical and experimental results of 4-pt flexural loading | 64 |
| 3.7 | Shear strength of GRP | 64 |
| 3.8 | Specifications of GRP straight pipes tested under pressure loading | 67 |
| 3.9 | Specifications of GRP bends tested under pressure loading | 68 |
| 3.10 | Pressure stress multiplier of GRP bends | 98 |
| 4.1 | Flexibility factors and SIF of smooth bends | 111 |
| 5.1 | Raw materials, Manufacturing Process and Manufacturer's Names for the pipe samples tested in the programme | 129 |
| 6.1 | Description of CSM pipe components | 153 |
| 6.2 | Burn-off test results | 155 |

| | | |
|--------|---|-----|
| 6.3 | Mechanical properties obtained from CSM strips | 156 |
| 6.4 | Mechanical properties obtained from CSM rings | 159 |
| 6.5 | Young's moduli and Poisson's ratios results | 161 |
| 6.6 | Decay lengths of straight CSM pipes | 164 |
| 6.7 | In-plane shear strains test results | 173 |
| 6.8a,b | Thickness and glass content measurements of CSM pipe components | 178 |
| 6.9 | Dimensions and mechanical properties of CSM Pipe components | 180 |
| 6.10 | In-plane flexibility factors of smooth CSM bends | 186 |
| 6.11 | In-plane longitudinal SIF of smooth CSM bends | 197 |
| 6.12 | In-plane circumferential SIF of smooth CSM bends | 198 |
| 6.13 | Out-of-plane flexibility factors of CSM smooth bends | 204 |
| 6.14 | In-plane longitudinal SIF of smooth CSM bends | 215 |
| 6.15 | In-plane circumferential SIF of smooth CSM bends | 216 |
| 6.16 | In-plane and out-of-plane SIF/K ratios | 219 |
| 6.17 | In-plane bending moments to failure of three smooth CSM Bends | 223 |
| 7.1 | Description of smooth CSM/PVC lined pipe components | 226 |
| 7.2 | Description of mitred CSM/PVC lined mitred pipe components | 227 |
| 7.3 | Flexural behaviour of CSM/PVC rings | 229 |
| 7.4 | Dimensions and mechanical properties of CSM/PVC lined pipe components | 231 |
| 7.5 | In-plane shear strains test results | 234 |
| 7.6 | In-plane and out-of-plane flexibility factors of smooth CSM/PVC lined bends | 237 |
| 7.7a,b | In-plane and out-of-plane SIF of smooth CSM/PVC lined bends | 247 |

| | | |
|---------|---|-----|
| 7.8 | Comparison of K and SIF results of smooth CSM and CSM/PVC lined bends | 248 |
| 7.9 | In-plane bending moments to failure of bend S016 | 256 |
| 7.10 | Probable mechanisms of bend failure | 257 |
| 7.11 | In-plane ovality measurements of mitred bend | 268 |
| 7.12 | Out-of-plane ovality measurements of mitred bend | 268 |
| 7.13 | In-plane and out-of-plane flexibility factors of mitred CSM/PVC lined bends | 273 |
| 7.14 | In-plane SIF of mitred CSM/PVC lined bends | 286 |
| 7.15 | Out-of-plane SIF of mitred CSM/PVC lined bends | 298 |
| 7.16 | Measured strain distribution of mitred bend S060 under combined in-plane/out-of-plane loading | 303 |
| 7.17 | In-plane end loads to failure of bend S034 | 314 |
| 8.1 | Description of orthotropic pipe components | 316 |
| 8.2 | Burn-off test results of CSM/WR/UD pipe component | 317 |
| 8.3a,b | Mechanical properties obtained from longitudinal strips and rings | 320 |
| 8.4 | Dimensions and mechanical properties of CSM/WR/UD pipe components | 324 |
| 8.5 | In-plane shear strains results of CSM/WR/UD pipe tested under torsion | 326 |
| 8.6 | In-plane and out-of-plane flexibility factors of smooth CSM/WR/UD bends | 330 |
| 8.7 | In-plane SIF of smooth CSM/WR/UD bends | 338 |
| 8.8 | Out-of-plane SIF of smooth CSM/WR/UD bends | 344 |
| 8.9 | Measured strain distribution of bend S045 under combined in-plane/out-of-plane loading | 346 |
| 8.10a,b | Burn-off test results of CSM/WR and FW pipe components | 350 |

| | | |
|---------|---|-----|
| 8.11a,b | Mechanical properties of CSM/WR pipe components obtained from longitudinal strips and rings | 352 |
| 8.12 | Mechanical properties of WR Pipe components obtained rings | 353 |
| 8.13 | Dimensions and mechanical properties of CSM/WR pipe components | 354 |
| 8.14 | Dimensions and mechanical properties of WR Pipe components | 355 |
| 8.15a,b | In-plane and out-of-plane SIF of smooth CSM/WR bends | 364 |
| 8.16a,b | In-plane and out-of-plane SIF of smooth WR/FW (bend/tangent) | 365 |
| 9.1 | Bending moment, strain and interlaminar shear strength of three bends taken to failure under in-plane bending | 394 |
| V.1 | Elastic constants of UD laminate | 453 |

LIST OF FIGURES

| | Page | |
|-----------------|---|----|
| 2.1 | Optimization of cure for thermosets | 6 |
| 2.2 | Glass fibre products for reinforcement | 14 |
| 2.3 | Hand lay-up process | 16 |
| 2.4 | Entrapped air voids in GRP laminate | 18 |
| 2.5 | Drawing of a typical hand lay-up laminate | 20 |
| 2.6 | Laminate composition of Vera pipe | 20 |
| 2.7 | Two component composite material | 23 |
| 2.8a,b | Comparison of rule of mixture prediction with experimental data | 26 |
| 2.9a,b,c | In-plane shear properties of GRP | 27 |
| 2.10 | Laminate thickness versus glass content | 29 |
| 2.11 | Stresses in a cubical element | 29 |
| 2.12a,b,c | Time-temperature superposition and creep of GRP | 37 |
| 2.13a,b,c | Fatigue of GRP | 40 |
| 2.14a,b | Environmental stress cracking of GRP | 43 |
| 2.15a,b | Block diagram of BS4994 design procedure | 45 |
| 2.16a,b, c,d | Comparison of rule of mixture prediction and BS4994 specifications mechanical properties | 48 |
| 3.1a,b | Tensile specimen | 51 |
| 3.2a,b | Load/strain tensile curves of CSM laminate | 54 |
| 3.3 | Load/strain tensile curve of CSM/PVC laminate | 55 |
| 3.4 | GRP young's modulus for different reinforcements | 58 |
| 3.5 | 4-pt. bending of CSM/PVC laminate | 62 |
| 3.6 | 4-pt. bending of CSM/WR laminate | 62 |
| 3.7a,b | Pressure loading versus strain for pipe components | 70 |
| 3.8a,b | Measured strains on pipe S004 under 4 bar pressure | 72 |
| 3.9a,b | Measured stresses on pipe S004 under 4 bar pressure | 73 |
| 3.10a,b | Measured stresses on pipe S027 under 9 bar pressure | 74 |

| | | |
|----------------|---|-----|
| 3.11a,b | Measured stresses on pipe S00A under 3.5 bar pressure | 76 |
| 3.12a,b | Measured stresses on pipe S00B under 3.5 bar pressure | 77 |
| 3.13 | Strain gauge locations on pipe S00C | 80 |
| 3.14 | Measured stresses on pipe S00C under 5 bar pressure | 80 |
| 3.15a,b | Measured strains and stresses on pipe S032 under 6 bar pressure | 81 |
| 3.16a,b | Measured strains on bend S021 under 4 bar pressure | 83 |
| 3.17a,b | Measured stresses on bend S024 under 6 bar pressure | 84 |
| 3.18 | Local bending stresses due to pipe pressure loading | 86 |
| 3.19 | Strain gauge locations on mitred bends | 86 |
| 3.20a,b,c | Measured strains on bend S034 under 6 bar pressure | 87 |
| 3.21a,b,c | Measured strains on bend S060 under 2 bar pressure | 89 |
| 3.22 | Pressure failure of pipe S004 | 92 |
| 3.23a,b,c | Pressure failure of bend S021 | 93 |
| 4.1 | Bend ovality under external load | 100 |
| 4.2 | Deformation of a bend under in-plane bending | 102 |
| 4.3 | Effect of laminate anisotropy on bend behaviour | 115 |
| 4.4 | Mitred bend deformation under in-plane bending | 117 |
| 4.5 | Block diagram of mitred bend analysis under in-plane bending | 122 |
| 4.6 | Flexibility factor of mitre bends | 123 |
| 4.7 | SIF of mitre bends | 124 |
| 5.1a,b, c,d | General construction lay out of GRP Pipe | 132 |
| 5.2a,b, c,d | General construction lay out of GRP bend | 135 |
| 5.3 | Dough moulding compound lip flange | 138 |

| | | |
|----------|--|-----|
| 5.4 | Cantilever testing of pipes | 140 |
| 5.5 | Pressure testing of pipes | 140 |
| 5.6 | Torsional testing of pipes | 141 |
| 5.7a,b | Bend test rig | 142 |
| 5.8a,b,c | Locations of strain gauges on bend | 146 |
| 5.9 | Picture showing outside strain gauges | 149 |
| 5.10 | Picture showing inside strain gauges | 149 |
| 6.1 | Flexural loading of pipe ring by opposite point loading | 158 |
| 6.2 | Instrumented ring under opposite point loading | 158 |
| 6.3 | Stress distribution around a ring under flexural loading | 158 |
| 6.4 | Four point bending of a straight pipe | 165 |
| 6.5 | Strains measured on pipes S007, S008, S009 under 4-pt bending | 166 |
| 6.6a,b | Strains measured on pipes S003, S004, S005 under 4-pt bending | 167 |
| 6.7a,b | Strains measured on pipe S027 under 4-pt bending | 168 |
| 6.8a,b,c | Cantilever bending of a straight pipe | 170 |
| 6.9 | Stresses measured on pipe S026 under cantilever bending | 172 |
| 6.10 | In-plane shear strains measured on pipe S027 under torsion | 172 |
| 6.11 | Locations of strain gauges on bends | 176 |
| 6.12 | End loading of bends | 176 |
| 6.13a,b | Ovality measurements on bend S006 under in-plane bending | 181 |
| 6.14 | In-plane flexibility factors as a function of laminate thicknesses | 187 |

| | | |
|---------|---|-----|
| 6.15 | In-plane flexibility factors of smooth CSM bends | 187 |
| 6.16a,b | Longitudinal strains measured on bends S001, S002, S006 under in-plane bending | 190 |
| 6.17a,b | Circumferential strains measured on bends S001, S002, S006 under in-plane bending | 191 |
| 6.18 | Stress distributions measured on bend S001 under in-plane bending | 192 |
| 6.19 | Stress distributions measured on bend S002 under in-plane bending | 192 |
| 6.20 | Stress distributions measured on bend S019 under in-plane bending | 193 |
| 6.21 | Stress distributions measured on bend S024 under in-plane bending | 194 |
| 6.22 | Stress distributions measured on bend S025 under in-plane bending | 194 |
| 6.23 | Stress distributions measured on bend S021 under in-plane bending | 195 |
| 6.24 | Stress distributions measured on bend S022 under in-plane bending | 195 |
| 6.25 | In-plane longitudinal SIF as a function of laminate thicknesses | 199 |
| 6.26 | In-plane circumferential SIF as a function of laminate thicknesses | 199 |
| 6.27 | In-plane longitudinal SIF of smooth CSM bends | 200 |
| 6.28 | In-plane circumferential SIF of smooth CSM bends | 200 |
| 6.29 | Ovality measurements on bend S006 under out-of-plane bending | 203 |
| 6.30 | Out-of-plane flexibility factors as a function of laminate thickness | 205 |

| | | |
|---------|--|------|
| 6.31 | Out-of-plane flexibility factor of smooth CSM bends | 2 05 |
| 6.32a,b | Longitudinal strains measured on bends S001, S002, S006 under out-of-plane bending | 2 09 |
| 6.33a,b | Circumferential strains measured on bends S001, S002, S006 under out-of-plane bending | 2 10 |
| 6.34 | Stress distributions measured on bend S001 under out-of-plane bending | 2 11 |
| 6.35 | Stress distributions measured on bend S002 under out-of-plane bending | 2 11 |
| 6.36 | Stress distributions measured on bend S019 under out-of-plane bending | 2 12 |
| 6.37 | Stress distributions measured on bend S024 under out-of-plane bending | 2 13 |
| 6.38 | Stress distributions measured on bend S025 under out-of-plane bending | 2 13 |
| 6.39 | Stress distributions measured on bend S021 under out-of-plane bending | 2 14 |
| 6.40 | Stress distributions measured on bend S022 under out-of-plane bending | 2 14 |
| 6.41 | Out-of-plane longitudinal SIF as a function of laminate thicknesses | 2 17 |
| 6.42 | Out-of-plane circumferential SIF as a function of laminate thicknesses | 2 17 |
| 6.43 | Out-of-plane longitudinal SIF of smooth CSM Bends | 2 18 |
| 6.44 | Out-of-plane circumferential SIF of smooth CSM bends | 2 18 |
| 6.45a,b | In-plane SIF/K ratio | 2 20 |
| 6.46a,b | Out-of-plane SIF/K ratio | 2 21 |
| 6.47 | Picture showing failure of CSM Bend under in-plane bending (opening) | 2 24 |

| | | |
|-----------|---|-----|
| 7.1a,b | Strains and stresses measured on pipe S011 under 4-pt bending | 232 |
| 7.2 | Stresses measured on pipe S010 under 4-pt bending | 232 |
| 7.3 | Strains measured on pipe S038 under cantilever bending | 232 |
| 7.4 | Strains measured on pipe S035 under cantilever bending | 233 |
| 7.5 | Shear strains measured on pipe S038 under torsion | 233 |
| 7.6 | Stress distribution in curved dual laminate | 239 |
| 7.7a,b | Longitudinal stress distribution of bends S012, S014, S016 under in-plane bending | 243 |
| 7.8 | Circumferential stress distribution of bends S012, S014, S016 under in-plane bending | 243 |
| 7.9a,b | Longitudinal stress distribution of bends S012, S014, S016 under out-of-plane bending | 244 |
| 7.10 | Circumferential stress distribution of bends S012, S014, S016 under out-of-plane bending | 245 |
| 7.11 | Strain distribution through dual laminate thickness | 246 |
| 7.12 | End-deflection versus end-load to failure of bend S016 under in-plane (opening) | 250 |
| 7.13a,b | Pictures showing failure on bend S016 | 251 |
| 7.14a,b | Inside cracks on bend S016 | 253 |
| 7.15 | Measured strains versus end-load to failure of bend S016 under in-plane bending (opening) | 255 |
| 7.16 | Strain gauge locations on mitred bends | 259 |
| 7.17a,b,c | Pictures showing features of mitred bends | 260 |
| 7.18 | Device for measuring bend ovality | 265 |
| 7.19 | In-plane ovality measurements of bend S060 | 266 |
| 7.20 | Out-of-plane ovality measurements of bend S060 | 266 |

| | | |
|---------|---|-----|
| 7.21 | In-plane ovality measurements of bend S061 | 267 |
| 7.22 | Out-of-plane ovality measurements of bend S061 | 267 |
| 7.23 | In-plane ovality measurements on tangent and bend fitting of bend S060 | 269 |
| 7.24 | In-plane and out-of-plane flexibility factors of mitred bends | 274 |
| 7.25 | Strain distributions measured on bend S033 under in-plane bending (closing) | 277 |
| 7.26 | Stress distributions measured on bend S033 under in-plane bending (closing) | 277 |
| 7.27 | Strain distributions measured on bend S034 under in-plane bending (closing) | 278 |
| 7.28 | Stress distributions measured on bend S034 under in-plane bending (closing) | 278 |
| 7.29 | Strain distributions measured on bend S036 under in-plane bending (closing) | 279 |
| 7.30 | Stress distributions measured on bend S036 under in-plane bending (closing) | 279 |
| 7.31 | Strain distributions measured on bend S037 under in-plane bending (closing) | 280 |
| 7.32 | Stress distributions measured on bend S037 under in-plane bending (closing) | 280 |
| 7.33 | Strain distributions measured on bend S060 under in-plane bending (closing) | 281 |
| 7.34a,b | Stress distributions measured on bend S060 under in-plane bending (closing) | 282 |
| 7.35 | Strain distributions measured on bend S061 under in-plane bending (closing) | 283 |

| | | |
|---------|--|------------|
| 7.36a,b | Stress distributions measured on bend S061 under in-plane bending (closing) | 284 284 |
| 7.37 | In-plane longitudinal SIF of CSM/PVC mitred bends | 285 |
| 7.38 | In-plane circumferential SIF of CSM/PVC mitred bends | 285 |
| 7.39 | Strain distributions measured on bend S033 under out-of-plane bending | 289 |
| 7.40 | Stress distributions measured on bend S033 under out-of-plane bending | 289 |
| 7.41 | Strain distributions measured on bend S034 under out-of-plane bending | 290 |
| 7.42 | Stress distributions measured on bend S034 under out-of-plane bending | 290 |
| 7.43 | Strain distributions measured on bend S036 under out-of-plane bending | 291 |
| 7.44 | Stress distributions measured on bend S036 under out-of-plane bending | 291 |
| 7.45 | Strain distributions measured on bend S037 under out-of-plane bending | 292 |
| 7.46 | Stress distributions measured on bend S037 under out-of-plane bending | 292 |
| 7.47 | Strain distributions measured on bend S060 under out-of-plane bending | 293 |
| 7.48a,b | Stress distributions measured on bend S060 under out-of-plane bending | 294 |
| 7.49 | Strain distributions measured on bend S061 under out-of-plane bending | 295 |
| 7.50a,b | Stress distributions measured on bend S061 under out-of-plane bending | 296 |

| | | |
|-----------|---|-----|
| 7.51 | Out-of-plane longitudinal SIF of CSM/PVC mitred bends | 297 |
| 7.52 | Out-of-plane circumferential SIF of CSM/PVC mitred bends | 297 |
| 7.53a,b,c | Strains measured on bend S060 under combined in-plane and out-of-plane bending | 300 |
| 7.54 | End-deflection versus end-load to failure of bend S034 under in-plane bending (opening) | 306 |
| 7.55 | Picture showing outside cracks on bend S034 | 307 |
| 7.56 | Stress distributions measured on bend S034 under in-plane bending (opening) | 308 |
| 7.57 | Picture showing outside cracks on the joint of bend S034 | 309 |
| 7.58 | Picture showing laminate local buckling of bend S034 on the outside | 310 |
| 7.59 | Section on bend S034 showing inside cracks | 311 |
| 7.60 | Magnification of inside cracks on bend S034 | 312 |
| 7.61 | Measured strains versus end-load of failure on bend S034 under in-plane bending (opening) | 313 |
| 8.1 | Strains measured on pipe S041 under cantilever bending | 325 |
| 8.2 | In-plane shear strains measured on pipe S041 under torsion | 325 |
| 8.3 | In-plane and out-of-plane flexibility factors of smooth CSM/WR/UD bends | 331 |
| 8.4 | Strain distributions measured on bends S039 and S040 under in-plane bending (closing) | 334 |
| 8.5 | Stress distributions measured on bends S039 and S040 under in-plane bending (closing) | 334 |

| | | |
|---------|---|-----|
| 8.6 | Strain distributions measured on bends S045 and S046 under in-plane bending (closing) | 335 |
| 8.7a,b | Stress distributions measured on bends S045 and S046 under in-plane bending (closing) | 336 |
| 8.8a,b | In-plane longitudinal and circumferential SIF of smooth CSM/WR/UD bends | 337 |
| 8.9 | Strain distributions measured on bends S039 and S040 under out-of-plane bending | 340 |
| 8.10 | Stress distributions measured on bends S038 and S040 under out-of-plane bending | 340 |
| 8.11 | Strain distributions measured on bends S045 and S046 under out-of-plane bending | 341 |
| 8.12a,b | Stress distributions measured on bends S045 and S046 under out-of-plane bending | 342 |
| 8.13a,b | Out-of-plane longitudinal and circumferential SIF of smooth CSM/WR/UD bends | 343 |
| 8.14 | End-load versus end-deflection of bend S045 under combined in-plane/out-of-plane bending | 347 |
| 8.15 | Strains measured on pipe S044 under cantilever loading | 356 |
| 8.16 | Strains measured on pipe S032 under cantilever loading | 356 |
| 8.17 | In-plane shear strains measured on pipe S044 under torsion | 357 |
| 8.18 | In-plane shear strains measured on pipe S031 under torsion | 357 |
| 8.19 | In-plane and out-of-plane flexibility factors of smooth CSM/WR bends | 359 |
| 8.20 | In-plane ovality measurements on bend S050 | 360 |

| | | |
|---------|--|-----|
| 8.21 | Out-of-plane ovality measurements on bend S050 | 360 |
| 8.22a,b | Stress distributions measured on bends S048 and S049 under in-plane bending (closing) | 362 |
| 8.23a,b | Stress distributions measured on bends S048 and S049 under out-of-plane bending | 363 |
| 8.24a,b | In-plane longitudinal and circumferential SIF of smooth CSM/WR bends | 367 |
| 8.25a,b | Out-of-plane longitudinal and circumferential SIF of smooth CSM/WR bends | 368 |
| 9.1 | In-plane flexibility factors | 377 |
| 9.2 | Out-of-plane flexibility factors | 378 |
| 9.3 | Maximum in-plane SIF | 386 |
| 9.4 | Maximum out-of-plane SIF | 387 |
| I.1 | In-plane flexure of a bend | 403 |
| I.2 | Out-of-plane flexure of a bend | 407 |
| I.3 | Flexure and torsion of variable cross-section beam | 411 |
| I.4 | Overlap joints on bend | 419 |
| II.1 | Smooth bend under in-plane bending | 423 |
| II.2 | Correction for extensibility | 428 |
| IV.1a,b | Axes on torus shell and mitre joint | 445 |
| V.1 | UD composite model | 447 |
| V.2 | Off axis stress/strain relationship | 447 |
| V.3 | Forces and strains on multi-layer laminate | 450 |
| V.4 | Nomenclature for laminate with even plies | 450 |
| VI.5 | Edge loading of a thin cylinder | 458 |

ACKNOWLEDGEMENTS

I am indebted to the Rubber and Plastics Research Association for the opportunity they have afforded me to submit this work for a Ph.D. degree.

I should like to thank my supervisors, Dr I. Cole and Dr D.C. Wright for their valuable advice and guidance throughout the project. In addition I am grateful to my colleagues for useful discussions.

I also like to express my thanks to Mrs Lyn Whalley for her patience combined with professional excellence in typing this thesis.

Finally, I would like to thank my wife Rafel, whose support and understanding over the years, has sustained my interest in this study.

TABLE OF CONTENTS

| | Page |
|---|-------|
| Title page | i |
| Summary | ii |
| Notations | iii |
| List of Tables | x i |
| List of Figures | x v |
| Acknowledgements | x xvi |
| Table of Contents | xxvii |
| Chapter 1 | |
| INTRODUCTION | 1 |
| 1.1 Objectives | 1 |
| 1.2 General introduction | 1 |
| 1.3 Outline of the thesis | 3 |
| Chapter 2 | |
| COMPOSITE REVIEW | 5 |
| 2.1 Introduction | 5 |
| 2.2 Resins of interest | 7 |
| 2.2.1 Polyester resin | 7 |
| 2.2.2 Epoxy resin | 8 |
| 2.3 Cure and post cure | 8 |
| 2.4 Fibrous reinforcements | 11 |
| 2.5 Manufacturing processes | 15 |
| 2.5.1 Low pressure contact moulding | 15 |
| 2.5.2 Filament winding | 19 |
| 2.5.3 Centrifugal casting | 21 |
| 2.6 Mechanical properties of GRP | 22 |
| 2.6.1 Modelling of composite element | 22 |
| 2.6.2 Rule of mixture | 24 |
| 2.6.3 Shear properties of GRP | 25 |
| 2.6.4 Thickness prediction | 28 |
| 2.7 Elastic stress-strain relationship of composites | 28 |

| | | |
|-----------|--|----|
| | 2.8 Modes of failure | 32 |
| | 2.9 Viscoelastic Behaviour | 35 |
| | 2.10 Fatigue of GRP | 38 |
| | 2.11 Environmental stress cracking (ESC) | 41 |
| | 2.12 Design procedures and standards for GRP components | 44 |
| Chapter 3 | FLAT SHEET AND PRESSURE TEST RESULTS | 49 |
| | 3.1 General introduction | 49 |
| | 3.2 Flat sheet test results | 49 |
| | 3.2.1 Introduction | 49 |
| | 3.2.2 Test methods | 50 |
| | 3.2.3 Tensile test results | 50 |
| | 3.2.4 Flexural test results | 59 |
| | 3.2.5 Shear test results | 63 |
| | 3.3 Pressure test results of GRP straight pipes and bends | 66 |
| | 3.3.1 Introduction | 66 |
| | 3.3.2 Pressure test results of straight pipes | 71 |
| | 3.3.2.1 Hand lay-up straight pipes | 71 |
| | 3.3.2.2 Specially made hand lay-up straight pipes | 75 |
| | 3.3.2.3 Machine made straight pipes | 78 |
| | 3.3.3 Pressure test results of bends | 82 |
| | 3.3.3.1 Hand lay-up smooth bends | 82 |
| | 3.3.3.2 Hand lay-up mitred bends | 85 |
| | 3.3.4 Failure of hand lay-up straight pipe and bend | 91 |
| | 3.3.5 Pressure stress multiplier (PSM) | 96 |

| | | |
|-----------|---|-----|
| Chapter 4 | REVIEW OF BEND THEORY | 99 |
| | 4.1 Simple beam theory | 99 |
| | 4.2 Loading of bends | 99 |
| | 4.2.1 Smooth bends | 104 |
| | 4.2.1.1 External loading of smooth metallic bends | 104 |
| | 4.2.1.2 External loading of smooth GRP bends | 112 |
| | 4.2.1.3 Pressure loading of smooth bends | 114 |
| | 4.2.2 Mitre Bends | 116 |
| | 4.2.2.1 External loading of mitred bends | 116 |
| | 4.2.2.2 Pressure loading of mitred bends | 126 |
| Chapter 5 | SAMPLE DESCRIPTION, EXPERIMENTAL PROCEDURE AND INSTRUMENTATION | 128 |
| | 5.1 Straight pipes and bend components | 128 |
| | 5.1.1 Pipe components made by the hand lay-up process | 131 |
| | 5.1.2 Pipe components made by the filament winding process | 134 |
| | 5.2 Testing rig | 137 |
| | 5.2.1 Testing of straight pipes | 137 |
| | 5.2.2 Testing of bends | 139 |
| | 5.3 Instrumentation | 145 |

| | | |
|-----------|--|-----|
| Chapter 6 | FLEXURAL TESTING OF CSM STRAIGHT PIPES AND | |
| | SMOOTH BEND COMPONENTS | 152 |
| 6.1 | Introduction | 152 |
| 6.2 | Coupon testing | 154 |
| 6.2.1 | Burn-off tests | 154 |
| 6.2.2 | Longitudinal strip tests | 154 |
| 6.2.3 | Ring tests | 157 |
| 6.3 | Testing of straight pipes | 162 |
| 6.3.1 | Flexural testing of pipes | 162 |
| 6.3.1.1 | Four point bending | 162 |
| 6.3.1.2 | Cantilever loading | 169 |
| 6.3.2 | Torsional testing | 171 |
| 6.4 | Flexural behaviour of smooth CSM bends | 174 |
| 6.4.1 | Introduction | 174 |
| 6.4.2 | Bend geometrical variations | 177 |
| 6.4.3 | In-plane bending | 179 |
| 6.4.3.1 | In-plane flexibility factor | |
| | (K_i) | 179 |
| 6.4.3.2 | In-plane stress ratio | |
| | distribution and stress | |
| | intensification factors | |
| | (SIF_i) | 188 |
| 6.4.4 | Out-of-plane bending | 201 |
| 6.4.4.1 | Out-of-plane flexibility | |
| | factor (K_o) | 201 |
| 6.4.4.2 | Out-of-plane stress ratio | |
| | distribution and stress | |
| | intensification factors | |
| | (SIF_o) | 206 |

| | | |
|-----------|--|-----|
| | 6.4.5 SIF to K ratios | 208 |
| | 6.4.6 Strength of smooth CSM bends | 222 |
| Chapter 7 | FLEXURAL TESTING OF CSM/PVC LINED STRAIGHT PIPES, SMOOTH AND MITRED BEND COMPONENTS | 225 |
| | 7.1 Introduction | 225 |
| | 7.2 Coupon testing | 225 |
| | 7.3 Flexural and torsional testing of straight pipes | 228 |
| | 7.3.1 Four point bending test results | 230 |
| | 7.3.2 Cantilever test results | 235 |
| | 7.3.3 Torsional test results | 235 |
| | 7.4 Flexural behaviours of smooth CSM/PVC lined bends | 235 |
| | 7.4.1 In-plane and out-of-plane flexibility factors | 236 |
| | 7.4.2 Stress ratio distribution and stress intensification factors (SIF) | 240 |
| | 7.4.3 Failure test results of smooth bend S016 | 249 |
| | 7.5 Flexural behaviour of mitred CSM/PVC lined bends | 258 |
| | 7.5.1 Introductory remarks | 258 |
| | 7.5.2 Ovality measurements | 263 |
| | 7.5.3 In-plane and out-of-plane flexibility factors | 270 |
| | 7.5.4 In-plane and out-of-plane bend strains and stresses | 275 |

| | | |
|-----------|---|-----|
| | 7.5.4.1 In-plane stress ratio distribution and stress intensification factors (SIF _i) | 276 |
| | 7.5.4.2 Out-of-plane stress ratio distribution and stress intensification factors (SIF _o) | 287 |
| | 7.5.4.3 Combined in-plane (closing)/out-of-plane bending of bend S060 | 299 |
| | 7.5.5 Failure test results of mitred bend S034 | 299 |
| Chapter 8 | FLEXURAL TESTING OF CSM/WR/UD CONSTRUCTED STRAIGHT PIPES AND BENDS | 315 |
| | 8.1 Introduction | 315 |
| | 8.2 Orthotropic CSM/WR/UD straight pipes and smooth bends of 2:1 circumferential to longitudinal extensibility ratio, Set I | 315 |
| | 8.2.1 Glass content, dimensions and mechanical properties | 315 |
| | 8.2.2 Straight pipes test results | 323 |
| | 8.2.2.1 Cantilever test results | 323 |
| | 8.2.2.2.Torsion test results | 323 |
| | 8.2.3 Flexural behaviour of smooth bends | 328 |
| | 8.2.3.1 In-plane and out-of-plane flexibility factors | 329 |

| | |
|---|-----|
| 8.2.3.2 In-plane and out-of-plane stress ratio distribution and stress intensification factors (SIF) | 332 |
| 8.2.3.3 Combined in-plane (closing)/out-of-plane bending of bend S045 | 345 |
| 8.3 Orthotropic CSM/WR straight pipes and smooth bends of 1:1 circum- ferential to longitudinal extensi- bility ratio, Sets II, III and IV | 348 |
| 8.3.1 Glass content, dimensions and mechanical properties | 348 |
| 8.3.2 Straight pipes test results | 349 |
| 8.3.2.1 Cantilever test results | 349 |
| 8.3.2.2 Torsion test results | 349 |
| 8.3.3 Flexural behaviour of smooth bends | 358 |
| 8.3.3.1 In-plane and out-of- plane flexibility factors | 358 |
| 8.3.3.2 In-plane and out-of- plane stress ratio distribution and stress intensifica- tion factors (SIF) | 361 |

| | | |
|-----------|--|-----|
| Chapter 9 | DISCUSSION OF RESULTS | 369 |
| | 9.1 Discussion of bend theoretical analysis | 369 |
| | 9.2 Discussion of mechanical properties and geometrical variations | 370 |
| | 9.2.1 Mechanical properties | |
| | 9.2.2 Pipes and bends geometrical variations | 372 |
| | 9.3 Discussion of straight pipes and bends pressure test results | 373 |
| | 9.4 Discussion of flexural and torsional deformations of straight pipes test results | 375 |
| | 9.5 Discussion of bend's flexibility factors test results | 375 |
| | 9.5.1 Flexibility factors of smooth CSM bends | 381 |
| | 9.5.2 Flexibility factors of mitred CSM/PVC Lined bends | 381 |
| | 9.5.3 Flexibility factors of smooth orthotropic bends | 382 |
| | 9.6 Discussion of bend stress ratio distribution and stress intensification factors (SIF) test results | 384 |
| | 9.6.1 Stress test result of smooth CSM bends | 389 |
| | 9.6.2 Stress test results of mitred CSM/PVC lined bends | 389 |
| | 9.6.3 Stress test results of smooth orthotropic bends | 390 |

| | | |
|------------|---|-----|
| | 9.7 Discussion of bend failure test results | 392 |
| | under in-plane bending | |
| | 9.8 Design of GRP bends | 395 |
| Chapter 10 | CONCLUSIONS AND FUTURE WORK | 397 |
| | 10.1 Conclusions | 397 |
| | 10.2 Future work | 399 |
| Appendix I | BEND/TANGENT DEFORMATION UNDER EXTERNAL | |
| | LOADING | 402 |
| | I.1 Uniform thickness throughout the bend/ tangent structure | 402 |
| | I.1.1 In-plane bending | 402 |
| | I.1.1.1 Determination of in-plane flexibility factor | 402 |
| | I.1.1.2 In-plane stress intensification factor | 405 |
| | I.1.2 Out-of-plane bending | 406 |
| | I.1.2.1 Determination of out-of- plane flexibility factor | 406 |
| | I.1.2.2 Out-of-plane stress inten- sification factor | 409 |
| | I.2 Non-Uniform thickness of the Bend/Tangent structure | 410 |
| | I.2.1 Joint effect on straight pipe behaviour | 410 |
| | I.2.1.1 Under bending moment | 410 |
| | I.2.1.2 Under end load | 413 |
| | I.2.1.3 Torsional deformation | 416 |

| | | |
|--------------|--|-----|
| | I.2.2 Joint effects on bend/tangent structure under in-plane mode of bending | 418 |
| | I.2.3 Joint effects on bend/tangent structure under out-of-plane mode of bending | 420 |
| Appendix II | THEORY OF ISOTROPIC SMOOTH BEND | 422 |
| | II.1 In-plane bending analysis | 422 |
| | II.2 Out-of-plane bending analysis | 429 |
| | II.3 Generalized solution | 430 |
| | II.4 Computer programme | 433 |
| Appendix III | THEORY OF ORTHOTROPIC SMOOTH BEND | 436 |
| | III.1 Theoretical derivation | 436 |
| | III.2 Generalized solution | 437 |
| | III.3 Computer programme | 440 |
| Appendix IV | PREDICTION OF STRAINS AND STRESSES IN THIN WALL STRAIGHT PIPES AND BENDS LOADED BY INTERNAL PRESSURE | 443 |
| | IV.1 Straight pipes | 443 |
| | IV.2 Smooth bends | 443 |
| | IV.3 Mitre bends | 444 |
| Appendix V | THEORETICAL DETERMINATION OF THE ELASTIC CONSTANTS OF A LAMINATE | 446 |
| | V.1 Elastic constants properties of unidirectional laminate | 446 |
| | V.2 Off-axis stress/strain relationship | 448 |

| | | |
|-------------|--|-----|
| | V.3 Stress/strain relationship for multi- | |
| | layer laminated plate | 449 |
| | V.3.1 General considerations | 449 |
| | V.3.2 Stress/strain relationship for \pm | |
| | 55° FW straight pipe (12 layers) | 451 |
| Appendix VI | RADIAL DEFORMATIONS IN A THIN CYLINDRICAL | |
| | SHELL AT THE EDGE | 457 |
| | REFERENCES | 459 |

CHAPTER ONE

INTRODUCTION

1.1 Objectives

- (a) To examine the performance of GRP pipe bends under conditions of external loading.
- (b) To analyse and express the performance in terms of generalised flexibility and stress intensification factors.

1.2 General Introduction

Design, procurement and installation of pipework in materials such as steel is based on codes which define; the materials, pipework components, operating conditions for which they are suitable, methods of designing the system, fabrication and inspection standards. Examples are BS806 and ANSI B31.3. These codes are used directly and are also the bases of computer systems for design, procurement and construction purposes.

No comparable basis exists for GRP pipe systems. These systems have however been used in process pipe systems for a number of years, the rate of use having increased progressively as confidence in the material has been gained. Most of this experience has been where the material has technical advantages that justify design effort proportionately greater than is needed for conventional materials and make uncertainties in the integrity of the design acceptable. The absence of a recognised design code however, has limited its application in such areas.

Work within industry has led to the development of documents that cover some design aspects, but this work has shown significant gaps exist in the knowledge needed for a comprehensive design code. Very

little information is available on the distribution of stress and strain in areas of complex geometry, which is essential for design of pipework components such as bends, junctions or flanges and other joints, and on the effect of complex loadings applied to pipe systems including these components and straight pipes. Moreover, while there is a considerable body of knowledge on material properties, most relates to simple uniaxial stress conditions and relatively little of the existing information can be used to assess the effect of complex stress or strain situations on the behaviour and integrity of the material. Knowledge of the distribution of stress and strain in a pipe system and of its implications is a fundamental requirement for design of the system. The experimental programme was designed to cover this aspect of the problem and has taken into account existing information derived from the relevant parts of other research programme.

Design methods for GRP vessels are covered in documents such as BS4994 and these provide a basis for some pipework problems. Knowledge of the strain distribution and its implications in complex situations in equipment other than that is however inadequate, and this experimental programme is relevant to the more general problem.

RAPRA as a research laboratory, provides a vital link in conveying research work into viable industrial means and it has served the plastics industry since the mid-fifties and the rubber industry since its foundation in 1919. The facilities available within the Association together with the considerable design experience in the polymer industry were the main reasons that in the late seventies, RAPRA was requested by a consortium of users, manufacturers, and raw material suppliers of glass reinforced plastics, to carry out the pipe bend project. The results of this project are to be incorporated in a future British Standard Code of Practice for the GRP processing industry. The project

was executed under the terms and supervision of a design committee representing the pipe consortium.

In carrying out a project of such nature, there are strong commercial pressures which tend to limit the depth and rigour of any investigation, resulting mainly from the competitive requirements of the different companies.

It is thought that one detrimental effect of such commercial pressures in the present program, was in the means used to reach the required objectives in the form of a parametrical study, where a large number of bends constructed by several fabricators were tested within the elastic limit (0.2% strain) rather than using the highly detailed analysis of fewer bends of standard construction.

In structures where the nature of the stress distribution is of a complex nature such as bends, a design criterion would be considered arbitrary if the cause of failure is pre-assumed or unknown. Therefore the author found it necessary, within the limited time scale and budget to test and analyse a limited number of pipe bend samples to failure under different types of loading.

All experimental results are compared with prediction of the existing isotropic bend theories and the specifications of the different codes used for metallic bends. For bends having in-plane anisotropy, the relevant theory has been modified from first principle of strain energy formulation accommodating such in-plane anisotropies in the analysis. The analytical work is reported in the Appendices.

1.3 Outline of the Thesis

Due to the fact that the samples tested are composite bends, it is considered desirable to review the background and literature separately for composites and bends. These are presented in Chapter 2 and Chapter 4 respectively.

Mechanical properties obtained from tests carried out on flat sheets manufactured at the same time as the bend fittings are reported in Chapter 3, together with test results obtained by pressurising the straight pipes and bends.

The experimental procedures, bend manufacture and instrumentation are essentially common for all bends, and are reported in Chapter 5.

Due to the different types of bend wall construction of the tested samples, the results in the form of flexibility factors and stress intensification factors are reported in Chapter 6 for smooth CSM bends, Chapter 7 for smooth and mitred CSM/PVC lined bends, and Chapter 8 for smooth bends of orthotropic laminate properties, where the bends walls are constructed from CSM, WR, UD, and FW reinforcements.

Discussion of the experimental results is presented in Chapter 9. Conclusions and future work are presented in Chapter 10.

CHAPTER TWO

COMPOSITE REVIEW

2.1 Introduction

For structural purposes, plastics are most commonly utilised as composites. Of these, the reinforced plastics of fibrous composites are the most widespread. In these composites, the plastic is strengthened and stiffened by being combined with high-strength fibres, most commonly glass. Fibres may range from extremely short to continuous filaments of indefinite length. Because of the wide range of fibres and plastics, numerous types of composites are reported in the literature⁽¹⁶⁾.

This technology is applied extensively to both thermoplastics and thermosetting materials. However, although fibre reinforced thermoplastics have important applications, these are not generally regarded as 'structural materials' and are rarely used to sustain moderate loads. Thermoplastics exhibit relatively high melt viscosities and therefore long fibres, or more precisely fibres of high aspect ratio can not be effectively added to the polymer without damage. Short fibre reinforced thermoplastics offer increased stiffness and heat distortion temperature (HDT), but because of the stress concentration at the fibres ends, impact and fatigue resistance can actually be reduced by their presence.

This restriction does not apply to the reinforcement of thermosetting resins. Such resins prior to cure are available as low-viscosity syrups, and therefore moulding compounds with high content of long fibres can be prepared. For thermosett resins, viscosity, reactivity (degree of unsaturation), shrinkage and gel time are important factors to be considered for ease of fabrication. End product requirements including chemical resistance, rigidity, impact strength, fire resistance, HDT and resistance to ultra violet light are optimized when the product has been formed by the process of cure (Fig. 2.1).

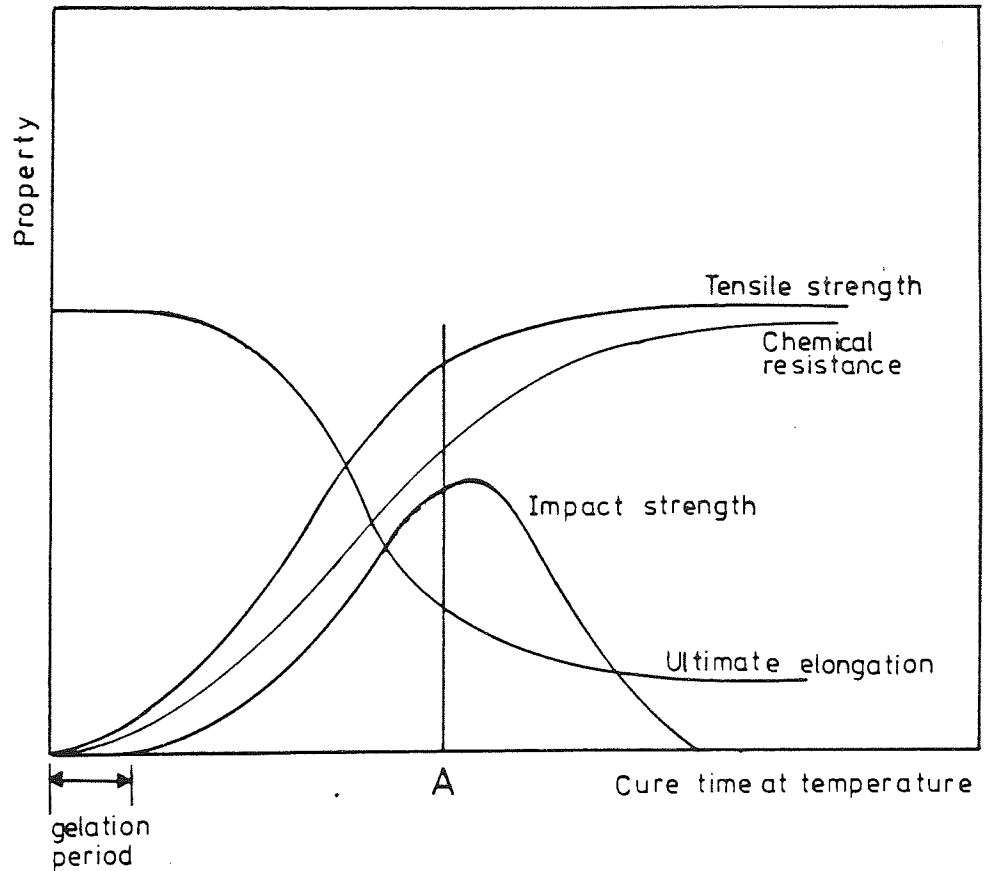


Figure (2.1) Optimization of cure schedule for thermosetting plastics. Optimum properties occur at point A.

Thermoplastic pipes covering amorphous materials such as ABS, PVC, Polysulfone and semi-crystalline materials such as Acetals, Polybutylene, PE, PP and Nylons are usually extruded with no reinforcements, do account for a high fraction of the total consumption. Their resistance to a wide variety of chemicals and corrosive environmental conditions make them favourable for long term services⁽¹⁾. Nevertheless, their comparatively low strength and rigidity especially at elevated temperatures make their use restricted and limited in the process industry.

Although GRP is less resistant to aqueous salts, weak or strong minerals, alkalis and oxidizing agents when compared to thermoplastics, their superior strength and stiffness are balanced carefully. GRP has been successfully used in severe environments such as the chemical and the oil industries⁽²⁾ with a high level of cost effectiveness on long term basis.

2.2 Resins of Interest

Four thermosetting resins are mainly used for the manufacture of fibre reinforced plastic pipes. These are listed in Table 2.1 together with their general properties as composites reinforced with randomly oriented glass fibres. The selection of one resin or the other is mainly dependent on the environmental service conditions. Only the polyesters and the epoxies are reviewed below:

2.2.1 Polyester resin

Polyesters are formed by the reaction of saturated acid with a dihydric alcohol glycol and unsaturated acid, forming a solid thermosetting polymer resin which will only have a commercial value when dissolved in a polymerisable monomer (styrene is usually used) to form

a useful low viscosity liquid resin. The properties of a cured unsaturated resin can be varied widely by changing the ratio of its constituents as shown for example in Table 2.2. Glass reinforced polyester resins are widely used for structures other than pipes and tanks, and their general properties as composites are obtainable from the different sources in the literature^(2,6,36,49,61).

2.2.2 Epoxy resin

Like polyesters, except they exhibit a lower shrinkage (1-2%) on curing compared to polyesters (5-7%); they are more expensive; have a better chemical resistance; and have a better bonding characteristic to fibres and metals. They exhibit higher viscosity than polyesters and hence, for ease of fibre wetting during the lamination process, heat (150°C) is applied to reduce viscosity.

2.3 Cure and Post Cure

Cure is the cross-linking of the monomer (solvent) with the unsaturation of the resin, and is initiated by the addition of an organic peroxide and in order to effect a rapid cure at an ambient temperature; an accelerator is used, and the time to cure is dependent on the ratios used as demonstrated for example in Table 2.3 for curing polyester resin.

Resin manufacturers recommend that laminates should be cured for at least 24 h at room temperature (23°C) and then post cured for 3 h at 80°C or 15 h at 50°C⁽⁶⁾. Post cure is advantageous in that a lower safety factor is used, e.g., BS4994⁽³⁾ recommends a safety factor of 1.1 for post-cured laminates compared with 1.5 for other curing methods. One of the disadvantages that can be associated with post-curing is the reduction of the strain to failure due to styrene evaporation or further

TABLE 2.1 - Comparative Properties of glass reinforced CSM Thermoset Resins

| Resin | Relative * Cost (mass) | Specific * Gravity | Operating Temperature °C | Tensile Strength N/mm ² | Tensile Modulus kN/mm ² | | Chemical Resistance | Pipe Application |
|-----------|------------------------------|--------------------------|--------------------------------|--|--|------|------------------------|---------------------|
| | | | | | R.T. | O.T. | | |
| Polyester | 1.5 | 1.3 | 60 - 110 | 100 | 7.0 | 5.5 | Good | Wide |
| Epoxy | 2.5 | 1.3 | 110 - 140 | 100 | 14 | 11 | Very good | Wide |
| Furane | 3.6 | 1.5 | 140 - 170 | 100 | 7.0 | 3.5 | Excellent | Wide |
| Phenolic | 1.0 | 1.5 | 200 - 250 | 100 | 7.0 | 7.0 | Fair | Limited |

* = unreinforced resin

R.T. = room temperature

O.T. = operating temperature

TABLE 2.2 - Effect of Mixture Components on End Properties of Polyester Resin

| <u>Glycol</u> <u>Propylene</u> | <u>Unsat. acid</u> <u>Maleic</u> <u>Anhydride</u> | <u>Sat. acid</u> <u>Phthalic</u> <u>Anhydride</u> | <u>Reactivity</u> | <u>Chemical</u> <u>Resistance</u> | <u>HDT</u> | <u>Flexibility</u> <u>% ϵ_f</u> |
|-----------------------------------|---|---|-------------------|--------------------------------------|------------|--|
| 3 | 1 | 2 | High | High | 95°C | Low (1%) |
| 3 | 1.5 | 1.5 | Medium | | 75°C | |
| 3 | 2 | 1 | Low | Low | 60°C | High (> 2.5) |

TABLE 2.3 - Laminate Cure Time of Atlac 382-05A Resin Mixes (40)

| <u>Room Temperature</u> <u>(C°)</u> | <u>6% cobalt</u> <u>napthenate</u> <u>cm³/kg</u> | <u>5% active MEKP</u> <u>catalyst</u> <u>cm³/kg</u> | <u>Curing time</u> <u>(mins)</u> |
|--|---|--|-------------------------------------|
| 15 | 10.0 | 12.0 | 40 - 50 |
| | 8.0 | 12.0 | 60 - 70 |
| | 6.0 | 12.0 | 120 - 130 |
| | 4.0 | 12.0 | ≥ 5 hrs |
| 21 | 10.0 | 12.0 | 30 - 40 |
| | 8.0 | 12.0 | 40 - 50 |
| | 6.0 | 12.0 | 60 - 70 |
| | 4.0 | 12.0 | 120 - 150 |
| 27 | 10.0 | 12.0 | 20 - 25 |
| | 8.0 | 12.0 | 30 - 35 |
| | 6.0 | 12.0 | 40 - 50 |
| | 4.0 | 12.0 | 60 - 70 |

cross-linking or both⁽¹⁰⁾. Experimental results discussing the effects of immediate and late post-cure are found in several references^(2,6,10, 11-16, 49).

2.4 Fibrous Reinforcements

In general, the type of fibres used will dictate the mechanical properties of the laminate. These could be natural or synthetic, organic or inorganic as for example demonstrated in Table 2.4⁽²⁰⁾. All are used as reinforcements, but by far the most important in structural application and in pipe manufacture in particular is fibrous glass, and two types are commonly employed, E and C. Glass fibres such as S and R types are used in very specialised structures⁽¹⁶⁾.

The wide variety of reinforcement products as shown in Fig. 2.2⁽⁷⁾ are only available with E glass grade. They are usually supplied to the users as strands of numerous filaments, usually 204 of 8 ~ 15 μm diameter. Virgin glass fibre has about 3.5 kN/mm² tensile strength, however, this value will drop to about 1.0 kN/mm² because of the microcracks damage being formed on the surface of the fibre during their passage through processing equipment.

Out of the types of reinforcements shown in Fig. 2.2, only four types are used in the manufacture of all the pipe components investigated in the present programme. They are also widely used in most GRP structural applications. These are summarised as the following:

(i) Unidirectional rovings (UD): This type of reinforcement is used for the filament winding process, as chopped rovings for spray deposition and for the centrifugal casting process for pipes. Their use in the hand lay-up process is limited except when directional stiffening is required. For the latter process, the glass content tolerance and laminate mechanical properties should meet BS3691⁽¹⁷⁾ specifications.

(ii) Woven roving (WR): These are cloth made from UD reinforcements. The end product in the form of a laminate could have different uniaxial strengths and stiffness by incorporating different amount of glass rovings in the warp and the weft directions. Laminate made by the hand lay-up process should have their mechanical properties and glass content to comply with BS4749⁽¹⁸⁾ specifications.

(iii) Chopped Strand Mat (CSM): This form of glass reinforcements is most widely used in the GRP production using the hand lay-up process. It is made from strands 25-50 mm in length randomly distributed on a moving belt to form a mat which is held together with a binder⁽¹⁶⁾. Such a method of production may induce a slight bias orientation in the machine direction.⁽⁴⁹⁾ A finished laminate using CSM reinforcements is assumed to exhibit in-plane isotropy, although similar to all other reinforcements; it exhibits through-thickness anisotropy. CSM is usually recommended to be used as an interlay when WR and UD reinforcements are employed in the lamination process to improve the overall laminate resistance to delamination^(3,11,61). CSM laminates are inspected for quality requirements by using BS3496⁽¹⁹⁾ specifications.

(iv) 'C' Glass Veil: This is the only end product of glass reinforcements that uses single filament. It is usually used to cover the finished laminate; enclosing any protruded glass fibres, hence preventing wicking⁽⁶⁾. It does not enhance the stiffness of the laminate, but it would have the additional advantage of reducing the shrinkage of the gel coat to that of the main laminate. In severe corrosive environments such as hydrofluoric acid (HF) a synthetic veil (thermoplastic polyester) is usually used.

TABLE 2.4 - Typical Properties of Reinforcing Fibres

| Generic Type | Fibre | Tensile Strength N/mm ² | Tensile Modulus kN/mm ² | Specific Gravity | Polymer Matrix |
|---------------------|-----------------|---------------------------------------|---------------------------------------|------------------|------------------------------------|
| Natural organic | Cotton | 0.3-0.7 | - | 1.6 | - |
| Synthetic organic | Aramid (Kevlar) | 2.94-3.45 | 59-124 | 1.45 | Polyester, epoxy |
| Natural inorganic | Asbestos | 0.7-1.4 | 135-170 | 2.5 | Phenolic |
| Synthetic inorganic | Glass | 2.4-3.6 | 69- 76 | 2.56 | Polyester, epoxy, furane, phenolic |
| | Carbon | 2.1-2.6 | 235-330 | 1.75 | Polyester, epoxy, furane |

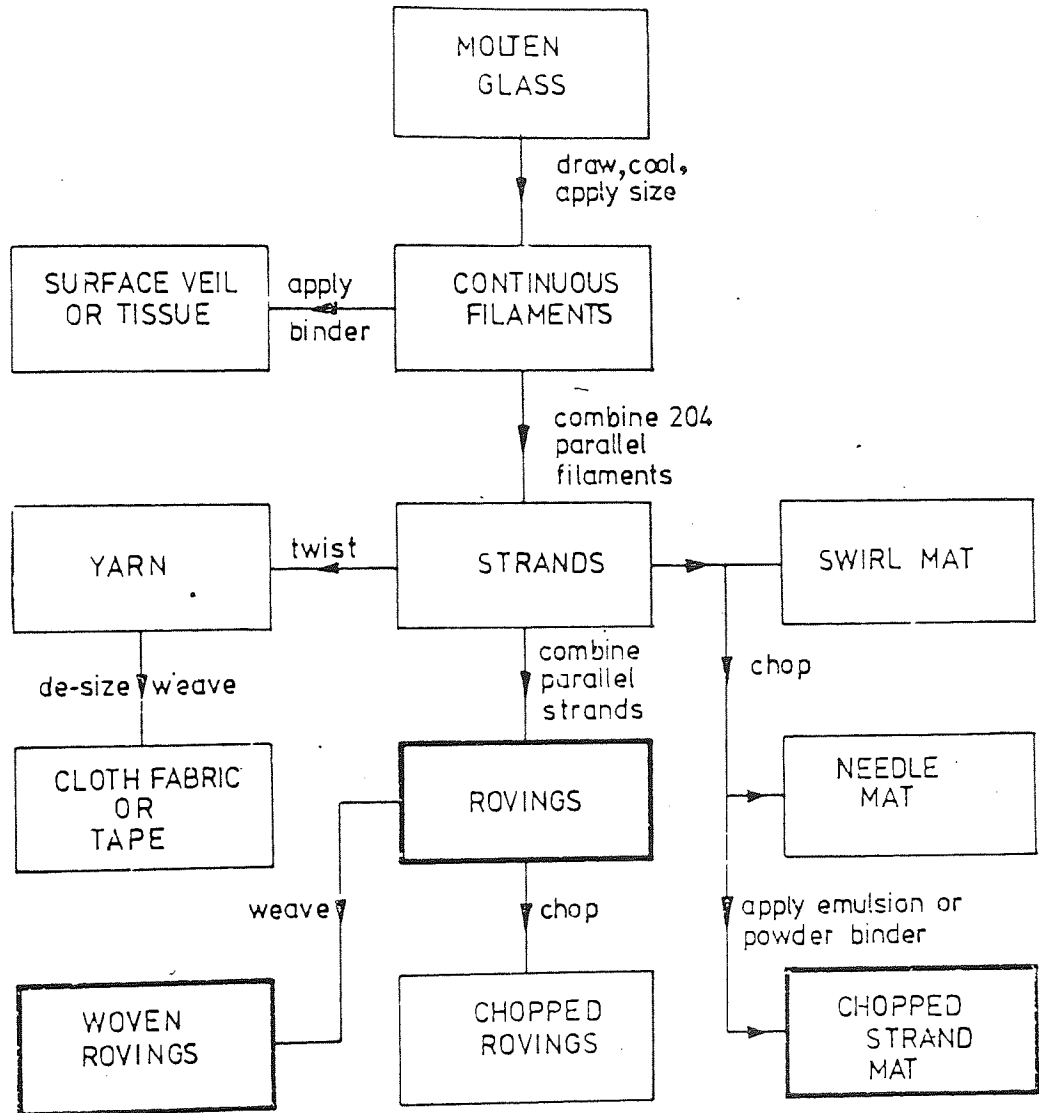


Figure (2.2) Glass fibre products for reinforcement.

2.5 Manufacturing Processes

There are many different methods for producing GRP components. The following listed processes are the principle manufacturing methods used for GRP pipes and vessels.

2.5.1 Low pressure contact moulding

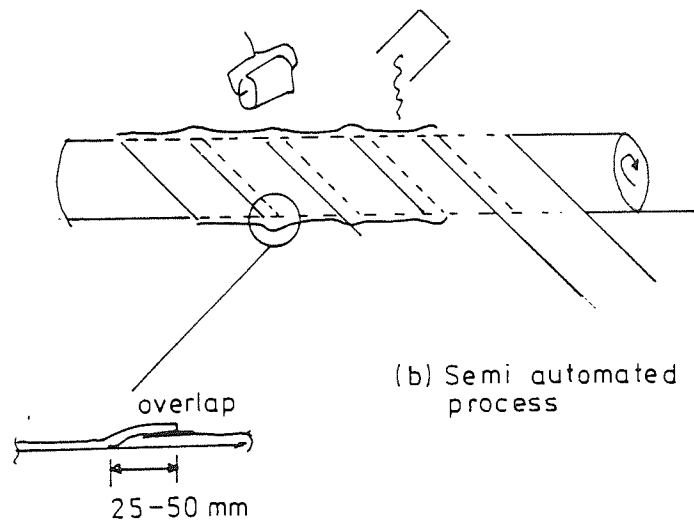
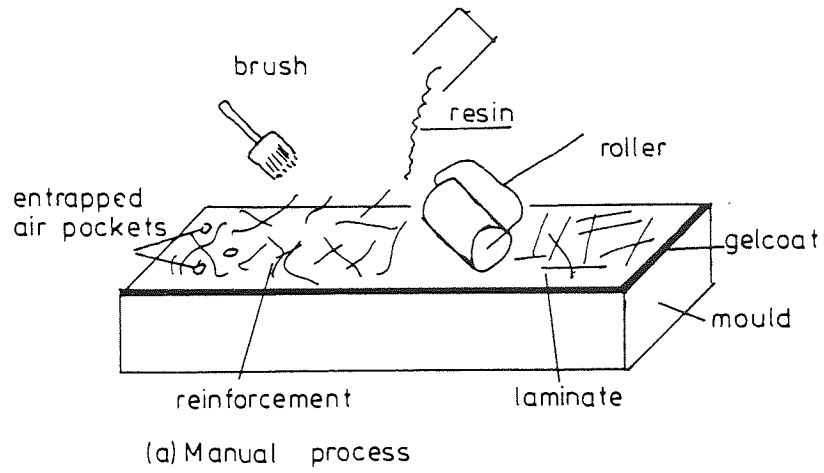
It is a labour intensive process, requiring low capital investment and suitable for low rate of production.

2.5.1.1. Hand lay-up process

For the manufacture of pipes, it could be 100% manual process as shown in Fig. 2.3a or could be semi-automated for straight pipes production by feeding 100 mm wide CSM tapes on the rotating mandrel whilst pouring the required amount of resin as shown schematically in Fig. 2.3b. Pipes investigated under the present programme were manufactured using that presented in Fig. 2.3a.

It is a low pressure process and hence suitable for low volume production of large and small complicated shapes. CSM, WR and sometimes UD rovings are added if required. The process starts by applying the corrosion barrier onto a clean mandrel which has been already coated or covered by a release agent, such as, wax, PVA or Melinex film of 0.1 mm minimum thickness⁽⁵⁾. When the gel coat starts to gel, the required amount of glass and resin is applied successively. It is usually recommended^(3,4,5) to lay two layers of 600 g/m² CSM straight after the gel coat, to act as a backing layer. For pipe components tested in the present programme, wax was used for some, and Melinex film was used for others with accordance to the manufacturer's practice.

Effective brushing and rolling is essential to remove any entrapped air between the layers of the reinforcements. Entrapped air bubbles would cause blistering of the gel coat if they happen to occur nearer to



Figure(2.3)The low pressure contact laminating process
Hand lay-up

the surface⁽⁶⁾, apart from being a stress raiser. Fig. 2.4 shows entrapped air bubbles in a specimen obtained from well laminated flat sheet tested in the present project. No air voids are allowed on the gelcoat surface (pits), and void sizes vary between 1.5-3.0 mm dia. from the inside to the outside surface of the pipe laminate^(5,9). Void content by volume was found to vary between 0.1-0.6% in well laminated flat sheets using the hand lay-up process^(21,22).

A typical construction, using hand lay-up process, incorporating the different reinforcements is shown in Fig. 2.5. It should be emphasised that the gel coat should be always backed up by CSM reinforcement. Using WR instead, proved to reduce the gel coat strain to failure considerably⁽¹¹⁾.

The low pressure employed by the process enables high ratios of resin to be incorporated into the reinforcements. CSM reinforcements which are associated with high resin content, are usually considered (in comparison with WR and UD) to exhibit relatively higher chemical resistant characteristics. However, due to the manual nature employed, repeatability of the finished product is often very low. Such low repeatability is mainly associated with thickness variation of the laminate.

In highly corrosive environments, a thermoplastic liner is used. Unplasticised polyvinyl chloride (uPVC) and polypropylene (PP) are recommended to be used^(3,4). The liner in effect would replace the gel coat, and also is used as the mandrel to build up the wall of the pipe.

The thickness of the uPVC liner is specified to be between 2 to 4.5 mm⁽⁴⁾. No method of inspection is suggested, however, a specimen failing under 70-80% of the failure pressure of the seamless tube would be rejected. To ensure adequate bonding between the uPVC liner and the main GRP laminates, the lap shear strength between the two should be at least 5 N/mm²^(3,4).



Figure (2.4) Entrapped air voids in a Hand laid - up laminate

No particular mention in any of the standards used for uPVC lined pipes and vessels^(3,4) of the problem of embrittlement of the uPVC by the presence of the polyester resin^(24,25,26,27). Short term testing to failure of flat sheets and bend samples showed that such liners could fail in a brittle manner.

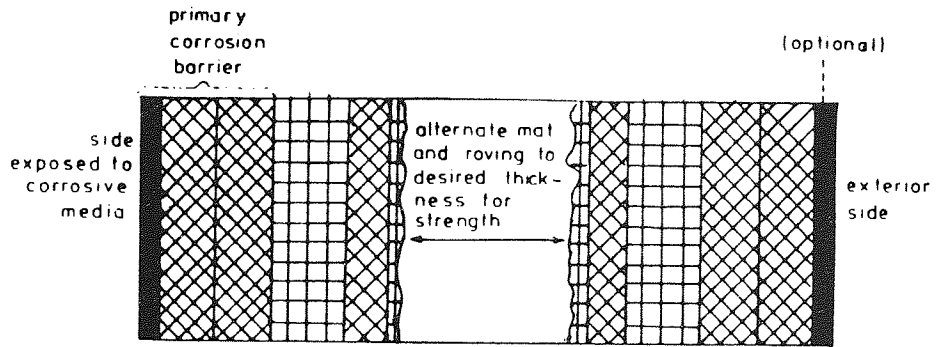
2.5.1.2 Spray-up process

This method offers an alternative to hand lay-up technique, when higher rates of production are desired. Catalyst, pre-accelerated resins and chopped glass rovings are simultaneously sprayed on the mould surface until a layer of the required thickness is built up. As with hand lay-up mouldings, thickness variations are expected. In this process, a resin with low styrene emission is used because of the larger areas exposed to the air, thus ensuring an efficient curing of the laminate⁽⁶⁾. Pipe ducting, boats, large surface mouldings, etc., are usually the common product produced by such process.

2.5.2 Filament winding

This technique is based on the idea of Ulrik Poulson from Denmark, and was developed mechanically by Dorostholm Products⁽³⁴⁾. Pipes up to 3500 mm in diameter and vessels up to a capacity of 150 m³ can be manufactured by this method using epoxy resins, as well as polyesters. It is a fully automated process, with high capital cost and suitable for high rate of production.

The laminate is made on a rotating mandrel. First a release film (usually thermoplastic polyester film) is wound onto the mandrel. This is followed by a dry C-glass surface veil, then continuous rovings passing through a bath of resin are wound on to the mandrel to the required winding angle suitable for the service requirements. The






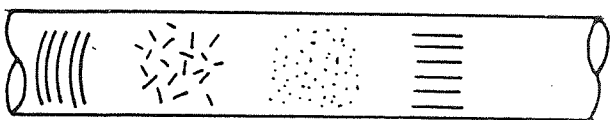
-  C glass surfacing veil, 0.25 to 0.5 thick, 10-12% glass mass content
-  Bark up wall, 2 x 450 g/m² (pipe) or 2 x 600 g/m² (vessel) CSM, 30% glass mass content
-  Woven glass roving, 50% glass mass content

Figure (2.5) Drawing of a typical Hand lay-up laminate

| Type of material Type of pipe |  | | | | |
|----------------------------------|--|-------------------------|-----------------------|-------------------------------|-------------------------|
| | % By mass F.W filament | % By mass Chopped glass | % By mass Filler sand | % By mass Axial reinforcement | % By mass Resin content |
| Gravity | 2.5 | 10 | 50 | 0 | 37.5 |
| 6 Bars | 25 | 15 | 20 | 0 | 40 |
| 10 to 16 Bars | 45 | 15 | 0 | 0 | 40 |

Figure(2.6) Laminate composition of Vera pipe⁽³⁴⁾

filaments are usually loosely wound to increase the resin content (40% by mass), whilst 15% by mass of chopped rovings are added intermittently to increase longitudinal stiffness. Fig. 2.6 shows the laminate composition used for Vera pipes⁽³⁴⁾.

Fittings such as flanges are usually made using compression moulding process where long fibres - epoxy paste (dough moulding compound, DMC) is being compressed under temperature. Any bonding process of fittings to the main pipe line should be carried out using a compatible resin usually epoxy⁽³⁶⁾. Filament wound (FW) pipes have minimal thickness variation, with smooth inside and outside surface.

2.5.3 Centrifugal casting

This method was developed by Hobas in Switzerland. The pipe wall is built up by dropping chopped rovings, resin and sand (when required) from the inside. The process is fully automated, using high capital investment and having high rate of production. The ability of these pipes to accommodate different loading conditions (e.g. flexural and pressure) can be designed into them by rearranging the layers of glass rovings, and sand about the pipe wall centrodial axis.

Longitudinal and circumferential moduli are varied by altering the orientation of the chopped glass rovings. This is done by controlling the mass rate of two air jets directing compressed air into the circumferential and the longitudinal direction. Minimal air voids and thickness variation are found in these pipes due to the centrifugal force which condense the fibre into the resin in a uniform manner. The corrosion barrier (on the inside) consists of a flexible, high chemical resistant vinyl ester resin⁽²⁸⁾.

2.6 Mechanical Properties of GRP

2.6.1 Modelling of a composite element

This considers the composite as being equivalent to a combination of elementary blocks of the component materials. The two blocks representing the matrix and the fibre are assumed to be in a parallel loaded arrangement under an applied force (P_{cp}) as shown in Fig. 2.7. Assuming constant strain throughout the whole cross-section, then it could be shown that⁽³⁵⁾:

$$E_{cp} = E_1 \frac{A_1}{A} + E_2 \frac{A_2}{A} \quad (2.1)$$

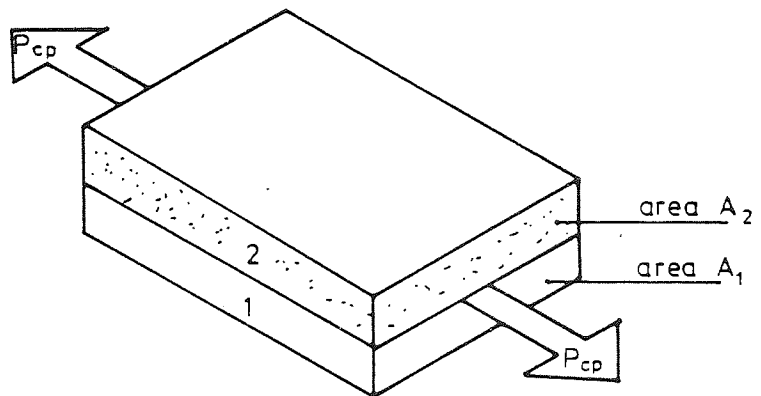
Because the blocks are parallel sided, their cross-sectional areas A_1 and A_2 are proportional to their volumes V_1 and V_2 . Therefore the area fractions in Eq. (2.1) above must be equal to the volume fractions V_1 and V_2 , i.e.

$$E_{cp} = E_1 V_1 + E_2 (1 - V_1) \quad (2.2)$$

experimental results^(29,31,45) on UD laminates have shown to be comparable to the prediction of Eq. (2.2). The transverse young's modulus could be predicted with less accuracy, by using the block model in series rather than in parallel⁽³⁵⁾ incorporating a lower and an upper limit^(29,31), where experimental results shown to be comparable with the lower limit^(31,45).

For WR laminates, the modulus could be predicted by using Eq. (2.2) and assuming alternate plies lying perpendicular to each other^(47,48).

For the tensile modulus of CSM laminates, the model is further modified to consider a quasi-isotropic orientation of the fibres together with the effect of the fibre aspect ratio^(35,39,54,55).



Figure(2.7) Homogeneous strain model for two component composite material

Predicting the strength of UD laminates, a similar model is used to that of Eq. (2.2), but with less accuracy, since strain compatibility is invalidated once debonding takes place. Also, the model does not take into consideration factors relating to fibre/resin bonding, stress concentrations, presence of voids, and the difference of strain to failure of both the resin and the fibre. For GRP, where the polyester resin and the glass fibre have similar strain to failure, the theoretical model is reasonably adequate^(42,43,56,57,58).

The dominating factor that assesses the strength level of the composite is the volume of the fibres employed. The minimum of such volume is determined such that the composite will have a higher strength than the matrix on its own, i.e.

$$\sigma_{cp}^* = [\sigma_g^* V_g + \sigma_r (1-V_g)] > \sigma_r^* \quad (2.3)$$

here, σ_r is the stress in the resin when the stress in the fibres equals to σ_r^* , and for high volume percentage of the fibres, then $\sigma_{cp}^* \cong \sigma_g^*$.

2.6.2 Rule of mixture

The short term strength and modulus of glass/epoxy and glass/polyester composites could be predicted with reasonable accuracy via the rule of mixture. That is

$$\text{strength } \sigma_{cp}^* = \beta_s \sigma_g^* V_g + \sigma_r^* (1-V_g) \quad (2.4a)$$

$$\text{modulus } E_{cp} = \beta_m E_g V_g + E_r (1-V_g) \quad (2.4b)$$

$\beta_s, \beta_m \equiv$ efficiency factors

= 1.0 for UD reinforced laminates

= 0.5 for WR reinforced laminates

= 0.33-0.375 for CSM reinforced laminates

= 0.20 for 3D randomly distributed fibres

The comparison of collected experimental data⁽⁴⁹⁾ and the prediction of the rule of mixture is shown in Fig. 2.8a and b for both modulus and strength prediction respectively.

2.6.3 Shear properties of GRP

2.6.3.1 In-plane shear of GRP (Fig 2.9)

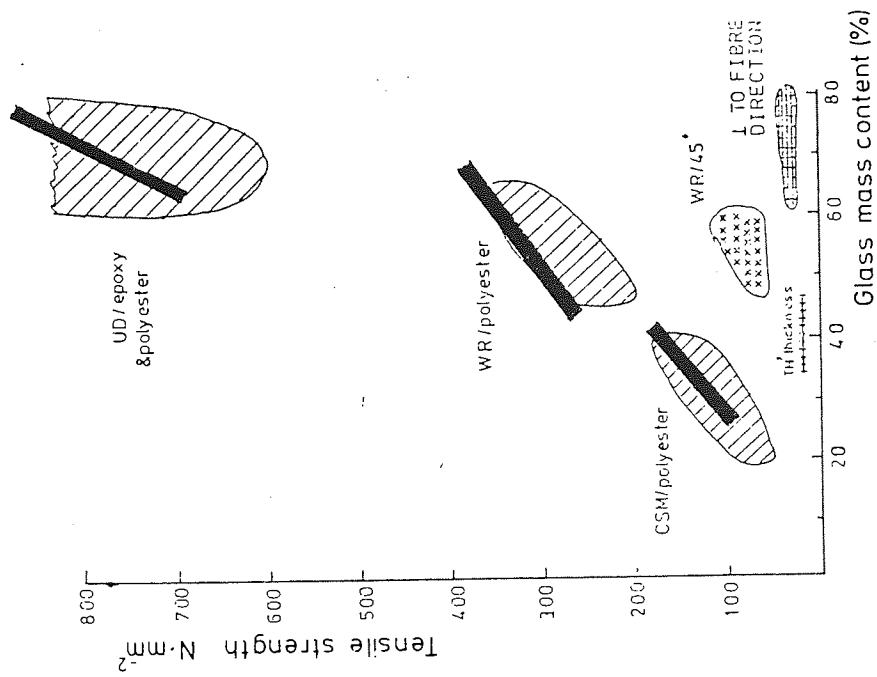
In-plane shear properties of GRP are seldom available in the literature. In-plane shear stiffness and strength are dependent on both the type of reinforcement and the direction of loading. For example, the weakest in-plane shear strength for UD laminate (Fig. 2.9a) is when the shear stress produce a sliding deformation of the fibres. While for CSM (Fig. 2.9c), the strength properties display in-plane isotropy because of the approximate in-plane isotropy of the randomly oriented fibres.

Prediction of the in-plane shear stiffness using theoretical models is well documented in the literature^(29,31,32,47,48). Experimental results for CSM and FW pipes are also reported in the literature^(38,40,41,51).

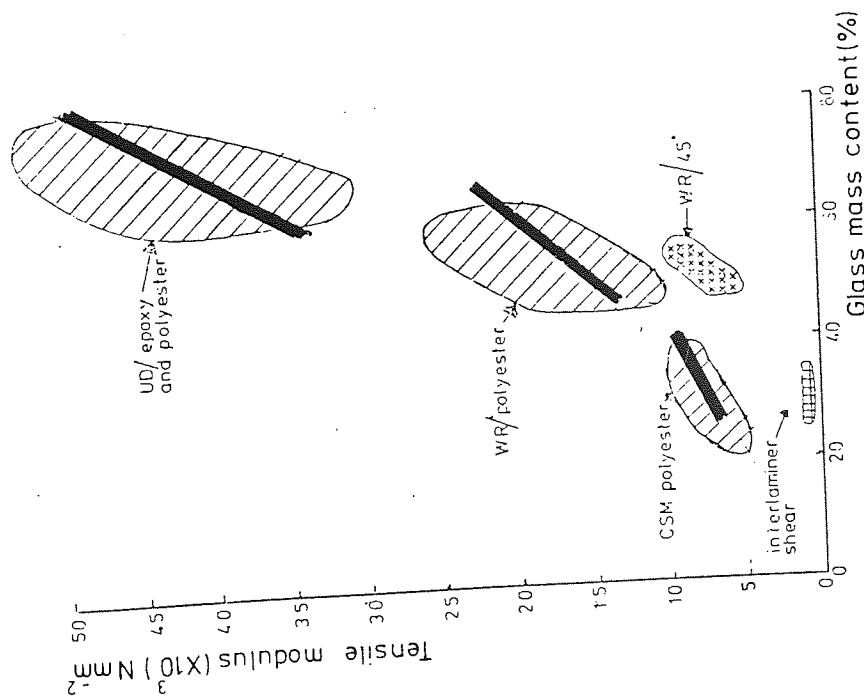
2.6.3.2 Interlaminar shear properties of GRP

Interlaminar shear strength and similarly through thickness tensile strength are the weakest among any reinforced composite due to the absence of reinforcements in the direction of the thickness. Their measured values are quoted^(3,49,68) to be in the region of 7-25 N/mm², and shear strength magnitude could be also influenced by the stacking sequence of the constituent layers of reinforcements⁽⁶⁴⁾.

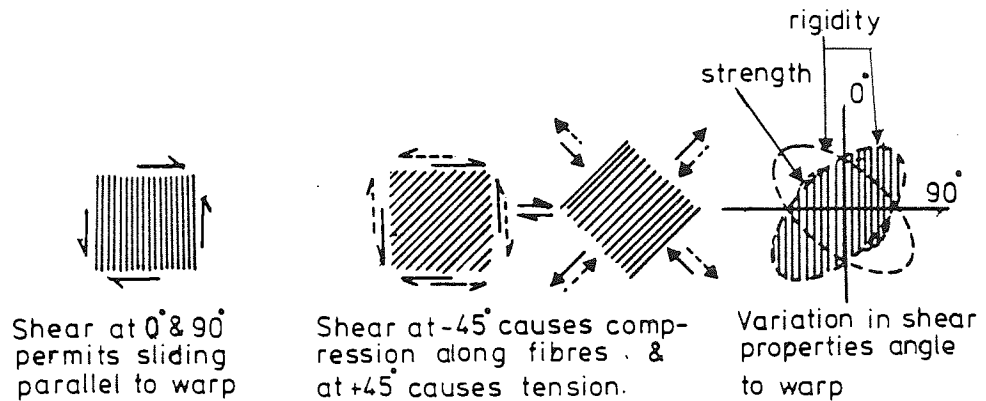
The interlaminar shear modulus (G') for GRP is quoted in the literature⁽⁴⁵⁾ to be of similar value to that of the resin, and experimental results obtained for CSM confirm it⁽³⁷⁾. Limited



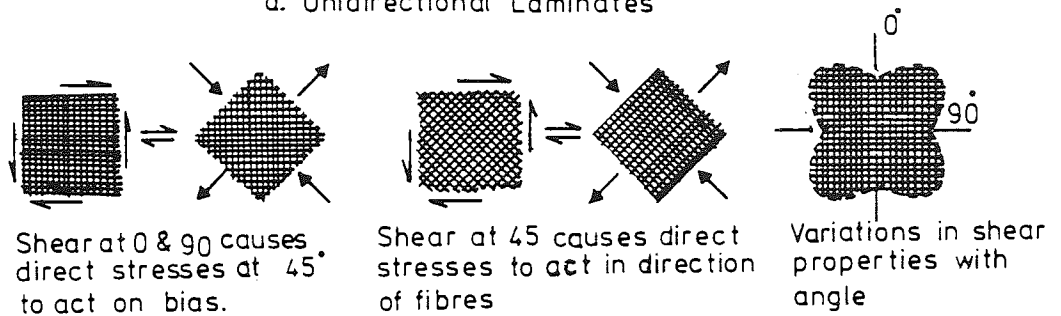
— Predicted via the rule of mixture
 Figure(2.8b) Tensile strength of GRP as a function of glass content



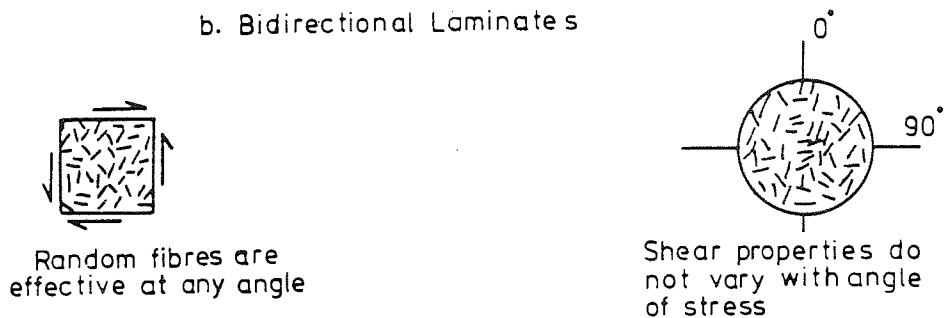
— Predicted via the rule of mixture
 Figure(2.8a) Tensile modulus of GRP as a function of glass content



a. Unidirectional Laminates



b. Bidirectional Laminates



c. Planar-Isotropic (Mat) Laminates

Figure (2.9) Directional characteristics of typical laminates under in-plane shear stress

experiments by Kirk⁽⁴⁰⁾ showed that G' could be in the range of 0.1-1.0 kN/mm² based on flexural loading of CSM strips.

2.6.4 Thickness Prediction

Thickness prediction of a laminate could be achieved with the knowledge of the physical properties of the resin and the glass used together with their mass content, i.e.

$$t = \frac{M_g}{\rho_g} + \frac{M_r}{\rho_r} \quad (2.5a)$$

or as thickness per unit glass mass per unit area (t')

$$t' = \frac{t}{M_g} = \frac{1}{\rho_g} + \frac{M_r/M_g}{\rho_r} \quad (2.5b)$$

t/M_g as predicted by Eq. (2.5b) is plotted versus BS4994 specification in Fig. 2.10. It is often that glass content is given by volume rather than mass percentage, and the relation between the two quantities is as follows:

$$\frac{M_g}{M_g + M_r} = \frac{V_g \rho_g}{V_g \rho_g + (1 - V_g) \rho_r} \quad (2.6)$$

2.7 Elastic Stress-Strain Relationship of Composites

Composite laminate behaviour under load, up to the stage of irreversible damage, could be predicted based on the principles of the Generalised Hooke's law for orthotropic materials^(29,31,32,66). The stress-strain relationship with reference to the element shown in Fig. 2.11 in matrix form is as follows:

$$\begin{bmatrix} \sigma_{11} \\ \sigma_{22} \\ \sigma_{33} \\ \tau_{13} \\ \tau_{23} \\ \tau_{12} \end{bmatrix} = \begin{bmatrix} C_{11} & C_{12} & C_{13} & 0 & 0 & 0 \\ & C_{22} & C_{23} & 0 & 0 & 0 \\ & & C_{33} & 0 & 0 & 0 \\ & \text{SYMM} & & C_{44} & 0 & 0 \\ & & & & C_{55} & 0 \\ & & & & & C_{66} \end{bmatrix} \begin{bmatrix} \epsilon_{11} \\ \epsilon_{22} \\ \epsilon_{33} \\ \gamma_{13} \\ \gamma_{23} \\ \gamma_{12} \end{bmatrix} \quad (2.7a)$$

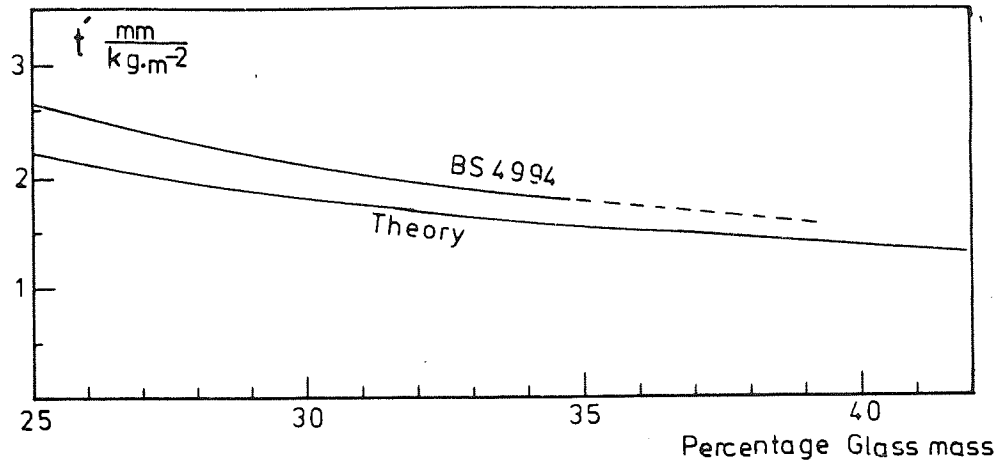
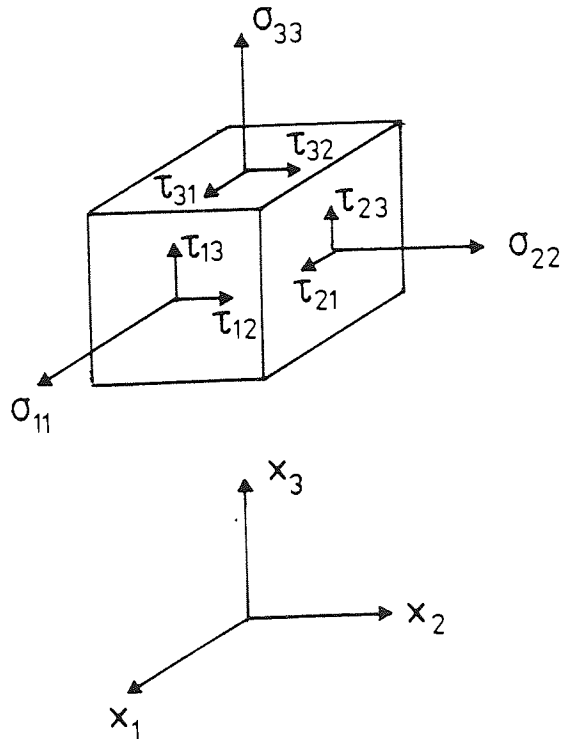


Figure (2.10) Thickness as a function of glass content for CSM



Figure(2.11) The tensile (σ) and shear (τ) stresses on a cubical element

where [C] is the stiffness matrix. The stress-strain relationship could be also defined in terms of the compliance matrix, i.e.

$$\begin{aligned} \epsilon_i &= S_{ij} \sigma_j \\ \text{where } [S] &= [C]^{-1} \end{aligned} \quad (2.7b)$$

the constants of the compliance matrix are defined in terms of the mechanical constants of the composite to be:

$$[S] = \begin{bmatrix} 1/E_{11} & -\nu_{12}/E_{11} & -\nu_{13}/E_{11} & 0 & 0 & 0 \\ -\nu_{21}/E_{22} & 1/E_{22} & -\nu_{23}/E_{22} & 0 & 0 & 0 \\ -\nu_{31}/E_{33} & -\nu_{32}/E_{33} & 1/E_{33} & 0 & 0 & 0 \\ 0 & 0 & 0 & 1/G_{23} & 0 & 0 \\ 0 & 0 & 0 & 0 & 1/G_{13} & 0 \\ 0 & 0 & 0 & 0 & 0 & 1/G_{12} \end{bmatrix} \quad (2.7c)$$

For UD type of composites, assuming axis X_1 in Fig. 2.11 to be in the fibre direction, then for the purpose of stress analysis; E_1 ; E_2 ; E_3 ; $G_{12} = G_{23}$; G_{13} and ν_{ij} for $i, j = 1, 2, 3$ should be either theoretically predicted or experimentally determined or both^(50,66).

For WR type of composites, $E_{11} = E_{22}$; E_{33} ; $G_{13} = G_{23}$; G_{12} ; $\nu_{21} = \nu_{12}$; ν_{13} ; ν_{23} ; ν_{31} should be similarly obtained.

For CSM type of composites, where in-plane isotropy is assumed, then: $E = E_{11} = E_{22}$; E_{33} (through thickness modulus); $G_{13} = G_{23} = G'$ (interlaminar shear modulus); $\nu = \nu_{12} = \nu_{21}$; $\nu_{23} = \nu_{32}$; $\nu_{31} = \nu_{13}$, and $G_{12} = E/2(1 + \nu)$ should be similarly obtained.

For thin plates and cylinders, 'plane stress' condition is assumed⁽⁴⁴⁾, i.e. the stress components acting perpendicular to the plane of the laminate is assumed to be negligible ($\sigma_{33} \cong 0$). This assumption will decouple⁽⁶⁶⁾ the compliance matrix of Eq. (2.7c) to:

$$\begin{bmatrix} \epsilon_{11} \\ \epsilon_{22} \\ \gamma_{12} \end{bmatrix} = \begin{bmatrix} 1/E_{11} & -\nu_{12}/E_{11} & 0 \\ -\nu_{21}/E_{22} & 1/E_{22} & 0 \\ 0 & 0 & 1/G_{12} \end{bmatrix} \begin{bmatrix} \sigma_{11} \\ \sigma_{22} \\ \tau_{12} \end{bmatrix}$$

and

$$\begin{bmatrix} \gamma_{13} \\ \gamma_{23} \end{bmatrix} = \begin{bmatrix} 1/G_{13} & 0 \\ 0 & 1/G_{23} \end{bmatrix} \begin{bmatrix} \tau_{13} \\ \tau_{23} \end{bmatrix} \quad (2.7d)$$

The prediction of the mechanical constants for UD reinforced composite is based on the knowledge of the physical properties of both the resin and the fibres. Mechanical constants predicted for other types of reinforcements, e.g. CSM, WR, are based on the UD Model. Theories encountered in the literature are generally based on the following assumptions:

- a - the matrix and the reinforcements conform to the Hooke's law;
- b - the fibres have a constant cross-section and are regularly spaced;
- c - the laminate is free of voids;
- d - the two components are homogeneous, isotropic and are perfectly bonded.

Micromechanical analytical procedure for the prediction of elastic constants are well documented in the literature^(29,31,32,45,48). For FW pipes the network analysis is also employed. In this case the presence of the matrix is ignored for the purpose of analysis, where under closed end pressure loading, the direction of the fibres are predicted to be oriented by $\pm 55^\circ$ from the longitudinal direction, but such an analysis could prove to be misleading when loading other than closed-end pressure are applied⁽⁸⁰⁾.

The applicability of plane stress condition for design purposes can not be considered justified for thick GRP structures under loading. In this instance, curved laminates of thick sections undergoing constant or variable gradient of bending moment, will experience through thickness tensile loading. Since the through tensile strength of GRP is about 7-10 N/mm², then the corresponding stress should be checked.

Similarly, under variable bending moment loading, such laminates can experience high level of interlaminar shear deformation, and failure can be fully attributed to interlaminar shear stress^(40,158), e.g., three-point bending of short beam.⁽³³⁾

2.8 Modes of Failure

Although fibre reinforcements when combined with resin matrix formulate a stiff and strong composite, they will have a diverse effect on the level of the strains causing both damage and failure of the composite. This is mainly attributed to the fibres acting as stress raisers^(42,43). Also, the structural integrity can largely depend on the bonding strength between the fibres and the resin⁽⁷⁵⁾. In design, these facts are reflected on the magnitude of design strains recommended for GRP structures, e.g. ASTM 3299⁽⁷²⁾ recommends a design strain of $\leq 0.1\%$ for FW vessels, while a design strain of $\leq 0.2\%$ is specified for GRP tanks and vessels by BS4994⁽³⁾.

Test results reported^(60,76,82,89,92,93,95) of experiments carried out on large number of GRP samples in the form of plates and cylinders suggested that, first damage of an irreversible nature occurred at about 0.3% strain ($\sim 20-30\%$ UTS). For CSM laminates for example, this was observed to commence by debonding fibres lying perpendicular to the applied load. On increasing the load further; fibres lying at smaller angles to the load started to debond with

progressive resin cracking. At about 60-70% UTS complete debonding was nearly achieved with resin cracking continued in an intensive manner, and no load was carried by the resin at that stage. Finally localised fibre breakage occurred, leading to complete failure of the laminate with the fracture surface showing broken and pulled out fibres. Part or all stages to failure have been also reported to be influenced by factors such as glass mass percentage⁽⁸⁴⁾, type of resin^(60,76), fibre surface treatment⁽⁷³⁾, and waviness of fibres such as cross-overs in WR⁽⁷⁶⁾.

Failures induced under compressive type of loading parallel to the fibres may occur by one form of buckling or shearing between the matrix and the fibres. Buckling failures may be due to individual fibre buckling, with and without matrix failure or debonding, or due to buckling of plies often accompanied by transverse splitting. Under transverse compression, failure may occur by either matrix compressive failure or matrix shear failure, possibly with fibre debonding^(40,45,66,87,128). Compressive failure test results reported by Owen et al⁽⁸⁹⁾ for CSM laminates, suggested the absence of debonding; with resin cracking taking place at about 80-90% UTS.

Similar forms of failures have been observed and suggested under flexural and torsional type of loadings^(40,83,85).

GRP pipes and pipe fittings often experience biaxial state of stress if not multiaxial. The prediction of failure envelopes under such type of loading is considered important in understanding the loading capabilities of such components. These failure envelopes will enable the identification of the load-carrying capacity of a material under multiaxial state, by employing the material strengths obtained from simple type of loading.

Failure theories used for traditional materials have been considered by the different researchers for the development of failure envelopes for GRP. Theories that are usually used for a brittle material such as, the maximum principal stress theory and the maximum principal strain theory, were considered. Also theories such as, the maximum shear stress theory (Tresca) and the maximum shear strain energy theory (von Mises), usually used for ductile materials were equally considered. Utilization of all the theories was based on a semi-empirical approach, where, the inhomogeneity and strength anisotropies of GRP were considered.

For a number of amorphous and semi-crystalline polymers, a modified version of von Mises theory has reasonably described the biaxial state of failure by taking the ratio of the compressive strength to the tensile strength to be 1.3⁽⁹²⁾.

Owen and Found⁽⁸⁹⁾ investigated experimentally half of the failure envelope using CSM tubes, and varying ratios of the principal stresses from $-\infty$ to $+\infty$. The envelope was constructed for the debonding stage, resin cracking stage and on complete failure. The biaxial rupture strength fell well inside the maximum stress theory with debonding stress being approximately 1/5th of the ultimate values. The tension - tension biaxial state of stress was found in general more damaging than the compressive - tension state of stress. The experimental results were reasonably described by complex form of failure models which require complex set of strength data.

For fabric reinforced tubes⁽⁷⁶⁾, half of the failure envelope was similarly constructed, with compression - tension state of stress shown to be more damaging than the tension - tension quarter. Pure compressive strengths being lower than pure tensile strengths. Experimental results indicated that only those theories modified from

von Mises version, which allow for the interaction between direct and shear stresses and require complex stress data, provided a reasonable fit^(93,95).

Earlier work by Hull^(77,78) confirmed the dependence of the biaxial strength of FW pipes on the winding angle⁽⁸⁷⁾. The failure was developed in two stages, firstly; the initiation of damage in the form of streaks running parallel to the fibres already debonded from the resin due to shear failure of the latter, and secondly; final failure of the pipe in a bursting mode having the pipe relined with a rubber liner to prevent weepage. Streaks started on the inside plies and occurred successively up to the outside surface⁽⁸⁸⁾.

Eckold⁽⁷⁹⁾ reported that biaxial test results obtained from FW pipes were in reasonable correlation with the prediction of a modified version of the maximum stress failure criterion. Biaxial test results reported by Soden⁽⁸⁰⁾ for similar pipes were shown to be favourably described using a semi-empirical criterion based on Puppo-Everson⁽⁹⁴⁾ modified version of von Mises model. He also confirmed the dependence of the biaxial strength on the winding angle, and reported that failure strengths could vary by a factor of ten in magnitude accordingly.

Inherent defects such as voids and flaws could greatly influence the failure of GRP structures. In this instance, a fracture mechanics approach is relevant to investigate for example crack propagation under relatively low level of stress^(93,95).

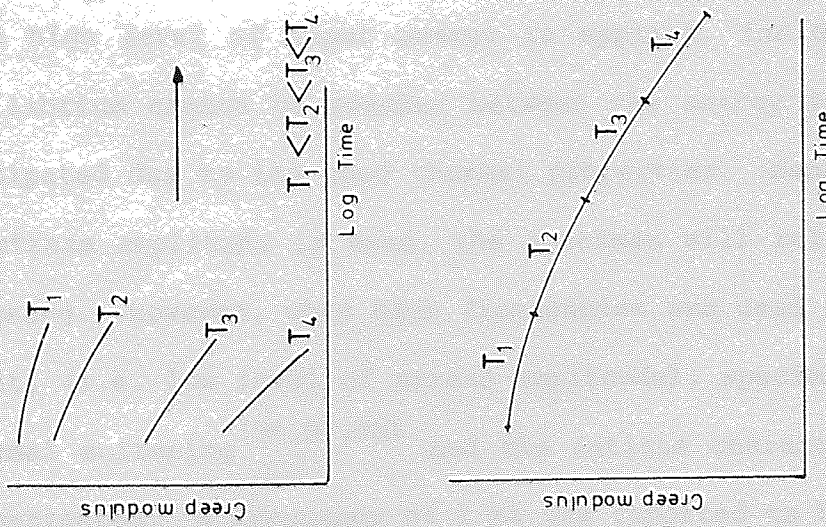
2.9 Viscoelastic Behaviour

All plastics exhibit an attenuation of strength with time under an applied load. Creep and relaxation effects are less obvious in GRP than in thermoplastics, but the effect is very significant and has a major influence in determining the acceptable design stress for a laminated

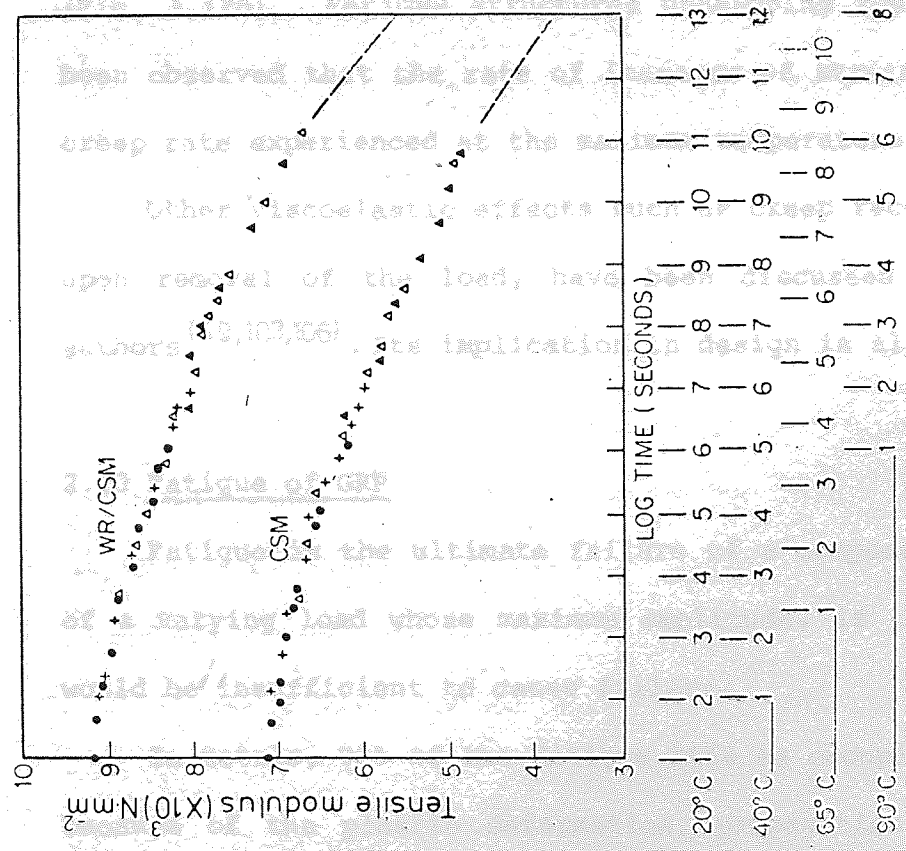
structure. Mathematical models describing such viscoelastic behaviour represented in the form of spring-dashpot systems is documented in the literature^(46,103).

During the determination of the short term mechanical properties of plastics, the creep effect is minimised by adjusting the rate of deformation or specifying the time of testing. For GRP as an example, specimens are usually tested in the range of 1-10 mm/min⁽³³⁾. Tensile and flexural test results obtained under strain rates of 10^{-3} - 10^3 s⁻¹ and cross-head speeds of 10^{-6} - 10 m/s respectively, have shown that tensile and flexural strengths doubled in magnitude. Minimal change of strength was reported under low ranges of strain rates indicating a minimal effect of creep^(104,105).

Under long term static loading service conditions, design stress for GRP pipes is usually taken to be half of the creep rupture strength at 30 or 50 years^(115,116). Strength under such durations are estimated by extrapolating strength data measured over few months or years plotted versus time (log scale). Obtaining such data could prove expensive, and in this case time-temperature superposition technique is usually used as an alternative. This is achieved by plotting short term modulus or strength measured under different levels of temperatures. By shifting and overlapping the high temperature curves along the time axis as shown in Fig. 2.12a, the long term creep curve at ambient temperature is approximated. Tensile modulus versus time predicted using such a technique is shown in Fig. 2.12b for CSM and WR laminates. The data of Fig. 2.12b were originally developed by creep tests for about two weeks. Creep test results reported elsewhere⁽¹⁰⁸⁾, have shown that percentage reduction of in-plane shear modulus for CSM laminates with time, was equal to that of the young's modulus. At the same time, Poisson's ratios experienced negligible effects.



Figure(212a)Time - Temperature superposition



Figure(212b)Tensile creep modulus of CSM & CSM/WR polyester laminates at four temperature
 ●: 20°C, ▲: 40°C, △: 65°C, ▲: 90°C, (ref. 7)

Creep rate of GRP is increased when the temperature is increased (Fig. 2.12b). For GRP structures undergoing thermal cycling, it has been observed that the rate of increase of strain was dominated by the creep rate experienced at the maximum temperature⁽¹⁰⁸⁾.

Other viscoelastic effects such as creep recovery, which will occur upon removal of the load, have been discussed by the different authors^(49,103,106). Its implication in design is also considered.

2.10 Fatigue of GRP

Fatigue is the ultimate failure of a component by the application of a varying load whose maximum amplitude, if continuously applied, would be insufficient to cause failure.

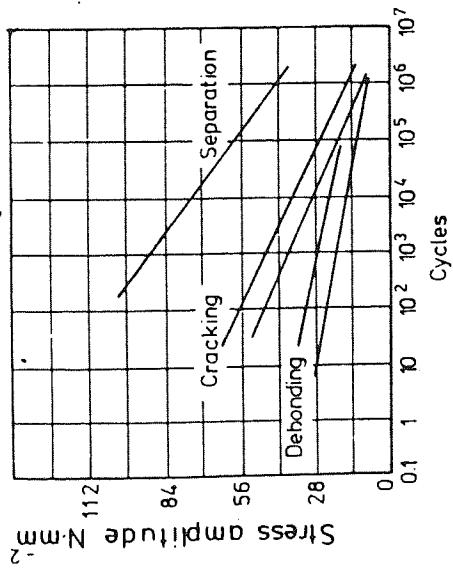
In metals, 90% of the fatigue life is occupied by crack initiation because of the plastic deformation, propagation of a single crack consumes the remaining period before catastrophic failure occurs. For GRP, fatigue cracks occur throughout the stressed material and are often well developed at an early stage of fatigue life^(81,95).

The energy absorbed by a GRP fatigue specimen is dependent upon the level of the stress amplitude and the frequency used. Unlike metals, when high level of input energy is applied, for GRP the state of equilibrium cannot be reached between the energy input and the heat dissipated due to its good thermal properties. Hence, when high level of stress amplitude is used, the specimen will relieve the energy by cracking. However, when high frequencies are used for the same energy input, (i.e. low level of stress amplitude), specimens usually fail by thermal softening^(96,97,98) and the fatigue characteristics cannot be investigated. A frequency of 2 Hz was reported to be suitable to reach the state of equilibrium⁽⁹⁵⁾, whilst for metals up to 30 Hz is usually used⁽⁹⁶⁾.

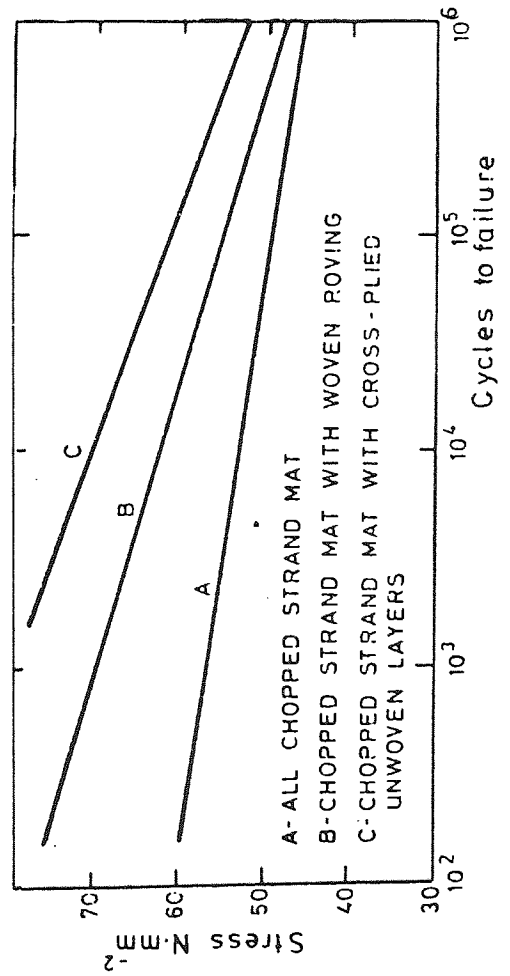
Stages of damage to failure of CSM specimens up to 10^6 cycles starts by debonding of the transverse fibres up to 0.5 cycle ratio with relatively low level of resin cracking. This becomes more progressive after 0,5 cycle ratio accompanied with debonding of the aligned fibres, leading to sharp reduction of strength, followed by complete rupture of the specimen and fibre pull out^(82,98,99,100). Similar stages were observed for WR laminates, and cross-plyed non-woven laminates^(76,101). The failure curve for CSM of failure stress versus number of cycle could be described as a straight line in the range of 10^3 to 10^7 cycles, appearing to extrapolate to zero stress (i.e. no endurance limit) somewhere between 10^9 and 10^{11} ⁽⁹⁵⁾.

In GRP piping systems especially those used to carry corrosive environments, the design is based upon the prevention of debonding⁽³⁾ or gel coat cracking^(115,116). During the service life of the pipe, once a crack is initiated, the pipe's structural integrity will deteriorate due to the glass fibre being attacked by the environment. Hence, fatigue effect has been correlated on the basis of strain debonding occurring at about 0.14% after 10^6 cycles^(3,95). The different level of fatigue damage occurring in a CSM laminate is shown in Fig. 2.13a⁽⁸²⁾. Different glass fibre reinforcements would have different strength reduction under fatigue as shown in Fig. 2.13b where the higher the anisotropy, the higher the strength reduction⁽¹¹⁹⁾.

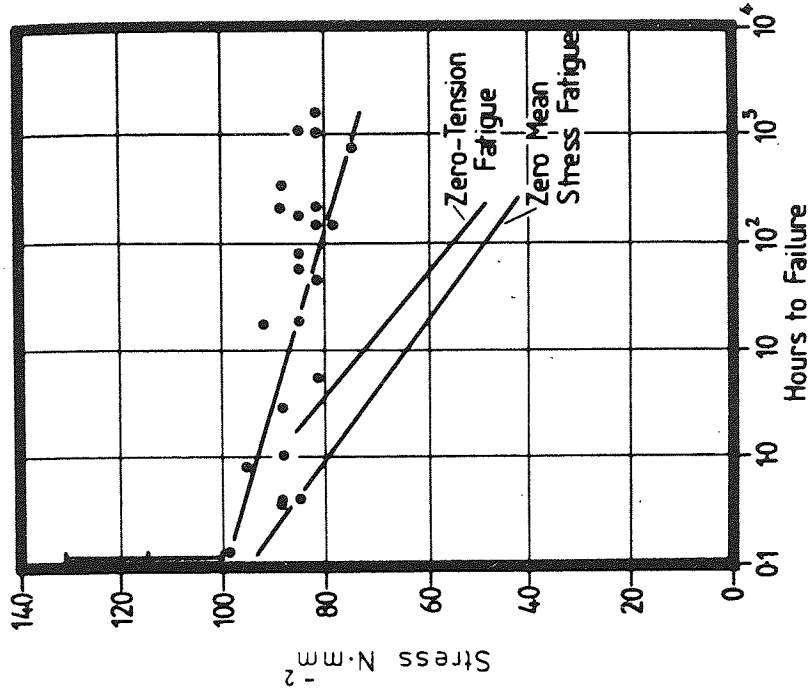
Fatigue performance of GRP could be influenced by many factors such as type of loading, reinforcements and manufacture. Using flexible resins lead to a delay in debonding⁽⁶⁰⁾. Using fillers reduced the fatigue performance and resin cracking appeared to start earlier⁽⁸²⁾. Glass percentage variation might have an effect on the static strength but has no influence on the fatigue performance⁽⁸²⁾. Chopped strand mat (CSM) samples having a butt-joint, experienced a higher level of



Figure(2.13a) S-N diagram for CSM/polyester laminate at various failure conditions⁽⁴⁹⁾



Figure(2.13b) S-N diagram for GRP laminates of different types of glass reinforcements⁽¹¹⁹⁾



Figure(2.13c) Stress rupture data compared with fatigue curves for CSM/polyester laminates⁽¹⁸⁷⁾

strength reduction under fatigue compared with sample having no joint. While with fabric reinforcements samples having lap-joint, the strength reduction under fatigue was comparable with samples having no over-lap joints⁽¹¹⁷⁾. Cyclic flexural loading caused 'gel coat' cracking strain to be reduced by 65% at 10^6 cycles and first damage was believed to have started by debonding the gel coat from the main body laminate⁽⁸³⁾.

Under biaxial mode of fatigue loading on chopped strand mat (CSM) and fabric reinforcement samples, the tension -tension (I quadrant) type of loading was found to be more damaging than under tension - compression (IV quadrant) mode of load^(67,89). Fatigue strength at 10^6 cycles of cylinders under uniaxial circumferential stress was found to be approximately half of that of corresponding flat coupons⁽⁶⁷⁾.

Experimental results obtained by Owen⁽¹⁸⁷⁾ have shown that GRP would experience larger reduction of strength under fatigue loading in comparison to creep loading. This is shown in Fig. 2.13c, where the fatigue duration has been obtained by knowing the frequency and the number of cycles to failure. This is expected of a brittle material such as GRP, and it is thought that similar magnitudes of strength reduction may well be found for example for concrete and clay components. The work reported by Gotham⁽⁷¹⁾ for uPVC pipes has shown a dramatic reduction in strength under fatigue loading in comparison to creep loading.

2.11 Environmental Stress Cracking (ESC)

Effect of chemical attack on GRP usually takes the form of deterioration of mechanical properties when in contact with a corrosive environment. Chemical attack has been well documented by the resin manufacturers using test methods, such as ASTM C581⁽¹²⁰⁾, to determine the loss in laminate modulus and strength with immersion. However, the

combination of load and exposure to corrosive environment has been observed to displace creep rupture curves for GRP to a lower stress level in comparison to that in air, and failure is attributed to environmental stress failure mechanism, as illustrated by the diagram shown in Fig. 2.14a^(109,110).

The mechanism by which ESC has been observed^(109,110) is of two stages, firstly debonding of the laminate due to pure mechanical stress and secondly, the initiation of a crack which would allow direct attack of the glass by the environment, followed shortly by failure of the laminate. It is envisaged that the second stage where ECS has the major influence. Such failure procedure has been also reported elsewhere^(111,112). ESC cracking is believed to be more aggressive under fatigue than creep (Fig. 2.14a, b) due to the progressive nature of resin cracking in the former. There is experimental evidence although limited, that debonding strain could be also effected due to increased rate of diffusion of environment through the gel coat⁽¹¹³⁾.

Present methods of detecting environmental strain corrosion are provided by ASTM 3262⁽¹¹⁵⁾ and BS5480⁽¹¹⁶⁾ by which a pipe ring immersed in one normality sulphuric acid is of acceptable quality if no obvious signs of damage, that is, pitting or stress cracking are apparent under the following combination of strain and time.

ASTM 3262 0.7% after 100 hour

0.6% after 1000 hour

BS5480 0.70% after 100 hour

0.64% after 1000 hour

These conditions are of equal severity and are equivalent to 0.53% strain imposed for 100,000 hours or to 0.49% to 40 years⁽²⁴⁾. No tests have been suggested to determine the environmental effect under constant load which is believed to be of severer nature due to increased strain with time (creep).

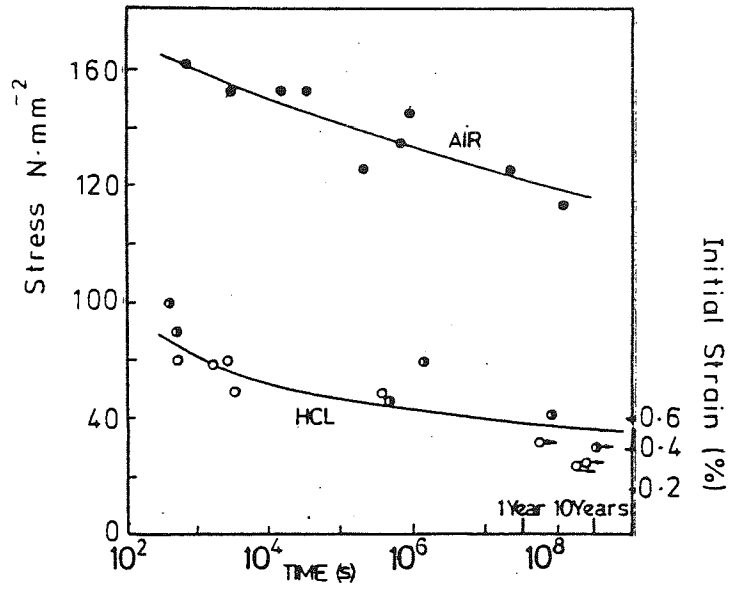


Figure (2.14 a) Creep rupture of CSM laminate ⁽¹⁰⁹⁾

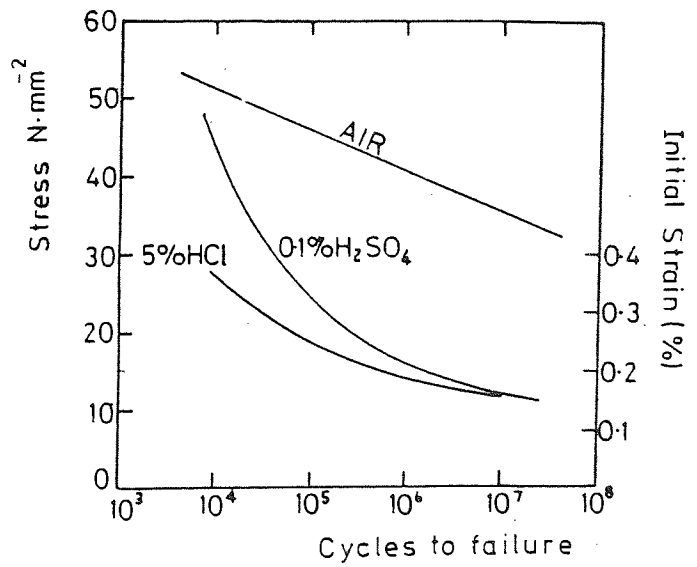


Figure (2.14 b) Environmental fatigue of CSM laminate ⁽¹¹⁰⁾

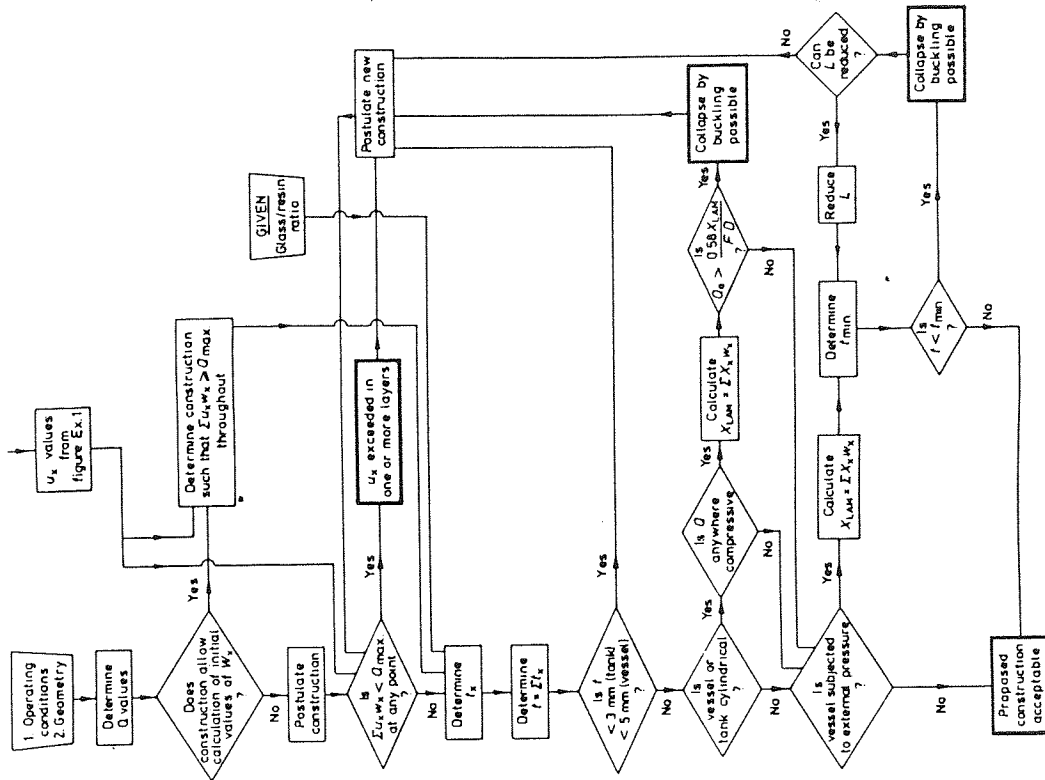
2.12 Design Procedures and Standards for GRP Components

Although many standards such as ASTM 3262⁽¹¹⁵⁾, BS5840⁽¹¹⁶⁾, S3299⁽⁷²⁾, BS4994⁽³⁾ and PS15-69⁽⁹⁾ are specified for GRP straight pipes and vessels made by different processes and used for the different loading conditions, no comparable standards are available for GRP fittings such as bends and tees.

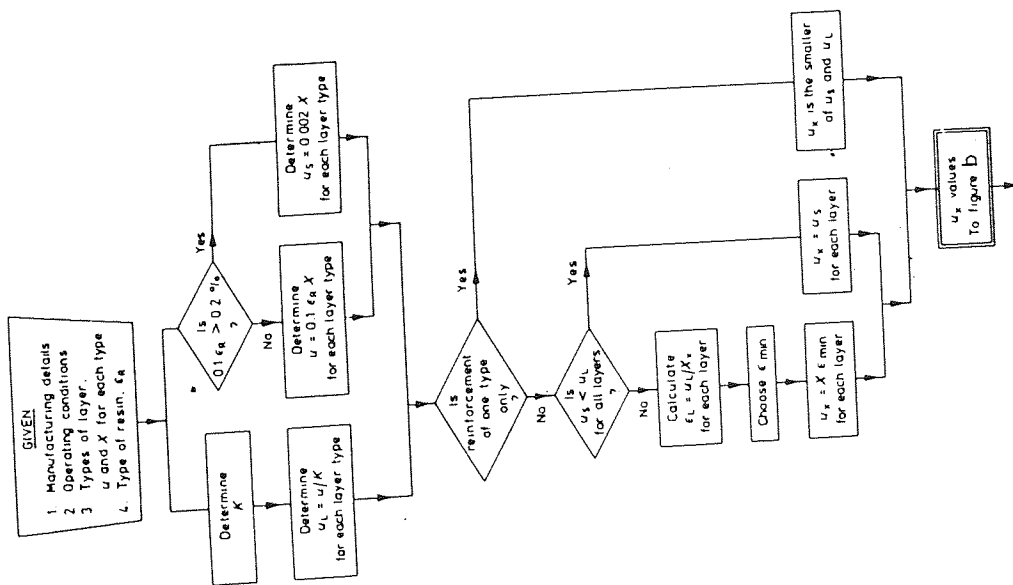
Large sector of the chemical industry in the UK, uses pipes and pipe fittings designed with accordance to few available in-house standards such as B202B⁽⁴⁾, B201B⁽⁵⁾ and B220⁽¹²²⁾. These standards are mainly based on design procedures for GRP vessels and tanks (BS4994)⁽³⁾ and those of metallic fittings such as BS806⁽¹²³⁾. Manufacturers tend to use these standards as guidelines, and their in-house code of practice is based upon past experience such as failures, case histories and limited research data. Similarly, procedures for quality inspection of the finished product do not exist. Destructive tests prove to be expensive, thus, non-destructive testing procedures such as acoustic emission⁽¹²⁵⁾ has been suggested, but not yet established as an inspection procedure, certainly not in the UK.

PS15-69⁽⁹⁾ was the first voluntary code of practice developed for the chemically-resistant hand lay-up reinforced polyester process equipment. It specifies pressure rating of pipes and vessels using a safety factor of 10 on tensile strength of the laminate up to 82°C service temperature, with minimum laminate thickness of 1/8 inch. Dimensional tolerances of flanges and butt joints are also specified.

Design procedure of BS4994⁽³⁾ is summarised as presented by PD6430⁽⁶⁹⁾ in Fig. 2.15a,b. That of Fig. 2.15a summarises the derivation of design procedures used to determine design stress based on strength or strain to failure, hence: 'load limited' or 'strain limited' respectively. The smaller value out of the two is used as the design



Figure(2.15b) Determination of laminate construction with accordance to BS 4994 (3) (69)



Figure(2.15a) Determination of design unit loadings with accordance to BS 4994 (3) (6)

stress. That in Fig. 2.15b outlines design calculations for vessels and tanks experiencing membrane type of loading.

Short term mechanical properties of GRP laminate are expressed as extensibility (Ext.) and ultimate tensile unit strength (UTUS)⁽³⁾.

These are defined as the following:

$$\text{UTUS} = \frac{\text{Failure load per unit width}}{\text{Glass mass per unit area}} \quad \frac{\text{N mm}^{-1}}{\text{kg m}^{-2}} \quad (2.7a)$$

$$\text{EXT.} = \frac{\text{Load per unit width at 0.2\% strain}}{\text{Glass content per unit area}} \quad \frac{\text{N mm}^{-1}}{\text{kg m}^{-2}} \quad (2.7b)$$

In normal engineering terms, UTUS replaces the strength and extensibility replaces modulus. This approach is being adopted to overcome the manufacturing problems of thickness variation in particular for hand lay-up laminates⁽⁷⁰⁾.

Service conditions in BS4994 are represented via safety factors coping for each service condition individually. They are all then presented as a design factor. These are related as the following:

$$\text{D.F.} = 3 \times K_1 \times K_2 \times K_3 \times K_4 \times K_5$$

where:

D.F. = Design factor

3 = Standard safety factor

K_1 = Factor relating to method of manufacture, $K_1 = 1.6$ for hand lay-up against 1.1 for filament winding

K_2 = Factor relating to long term behaviour (1.2 \approx 2.00). May prove to be underestimated when compared with creep rupture test results reported by Wright⁽⁷⁾.

K_3 = Factor relating to service temperature, where a minimum of 20°C is recommended to be sustained between HDT of resin and service temperature⁽³⁾.

K_4 = Factor relating to cyclic loading. It is of minimum value of 1.1 for normal service conditions such as filling and emptying up to 1000 cycles, thereafter it increases to 2.0 for 10^6 cycles on a liner-log scale. The factor could be reviewed based on Robert's work⁽¹¹⁰⁾.

K_5 = Factor relating to curing procedure. The importance of post curing is declared by using a lower safety factor.

Mechanical properties specified by BS4994 are lower than what can actually be obtained in practice. This is shown in Fig. 2.16a,b,c for CSM laminates in comparison with the rule of mixture. In this instance a conservative value of the design stress is obtained using BS4994 specification. But for piping systems, using a lower value of the modulus will lead to an underestimation of anchor loads, which may cause over-stressing either of the pipes or any attached vessel or both. In general, the design procedures outlined by BS4994 could be considered for the purpose of future GRP piping standards, with further modifications.

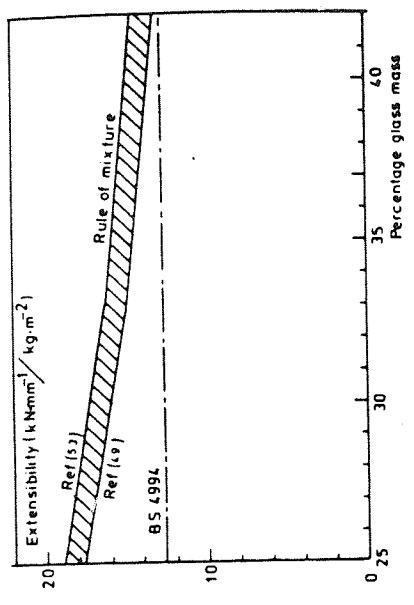


Figure (2.16 b)
Extensibility as a function of glass content for CSM laminates

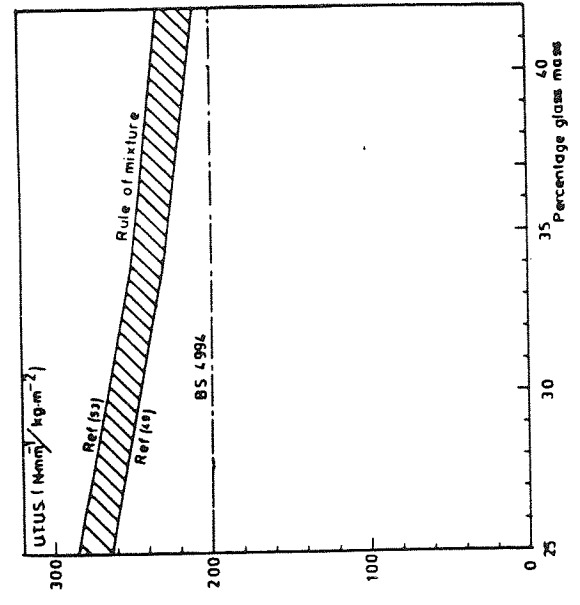


Figure (2.16 d) Ultimate tensile unit strength as a function of glass content for CSM laminates

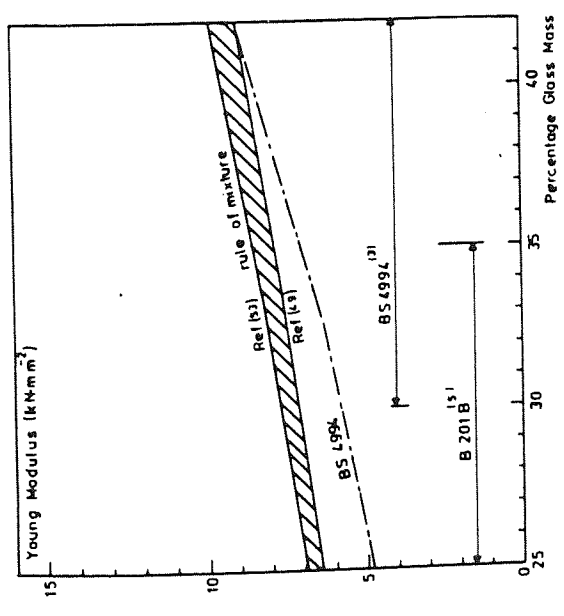


Figure (2.16 a)
Young Modulus as a function of glass content for CSM laminates

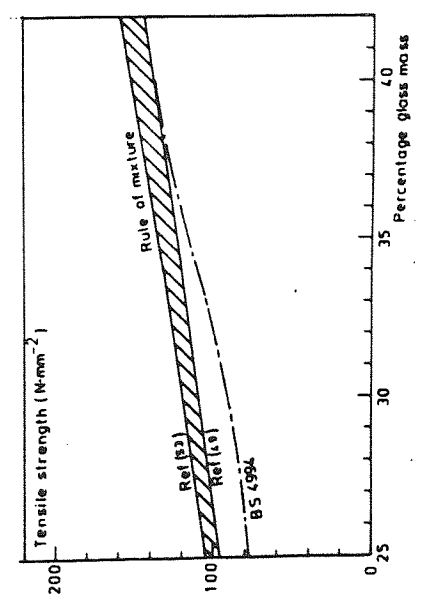


Figure (2.16 c)
Tensile strength as a function of glass content for CSM laminates

CHAPTER THREE

FLAT SHEET

AND

PRESSURE TEST RESULTS

CHAPTER THREE

FLAT SHEET AND PRESSURE TEST RESULTS

3.1 General Introduction

This chapter presents experimental test results obtained from flat sheet laminates having similar nominal glass content to the straight pipes and bends samples, and , experimental results obtained from pressurising such pipes and bends.

A reasonable understanding of the material mechanical behaviour could be obtained from testing simple shapes, e.g.: flat specimens; under simple type of loading, e.g.: tensile testing. The mechanical behaviour of dual composite laminates could be similarly investigated and compared with theory of composite strips.

Straight pipes and fittings used in the chemical industry are usually designed to sustain a certain level of service pressure. Thus, they are often identified by their pressure ratings. Straight pipes and bends have been tested under incremental pressure loading and results in the form of measured strains and stresses are presented and discussed.

3.2 Flat Sheet Test Results

3.2.1 Introduction

Testing of coupons constructed similar to the finished product is a common practice in the chemical industry to ensure both the manufacturer and the user of the quality of the product in question. Such procedure is laid down in standards such as BS4994⁽³⁾. The test samples are preferably chosen from waste areas on the finished product where they could represent exactly the main laminate. Where this procedure is impractical, then test samples should be laid by the same operator at the same time, with the same material and in the same manner as the item they represent, and under the same conditions as the main laminates.

The main differences found between flat GRP sheets and curved GRP structure such as pipes, is that the pipe laminate will have overlaps^(4,5), residual strains⁽¹¹⁹⁾, and will have less controlled dispersion of resin and glass leading to wider thickness variability. Test results obtained from pipe strips shown to have 60-70% of the strength measured on flat sheet strips.

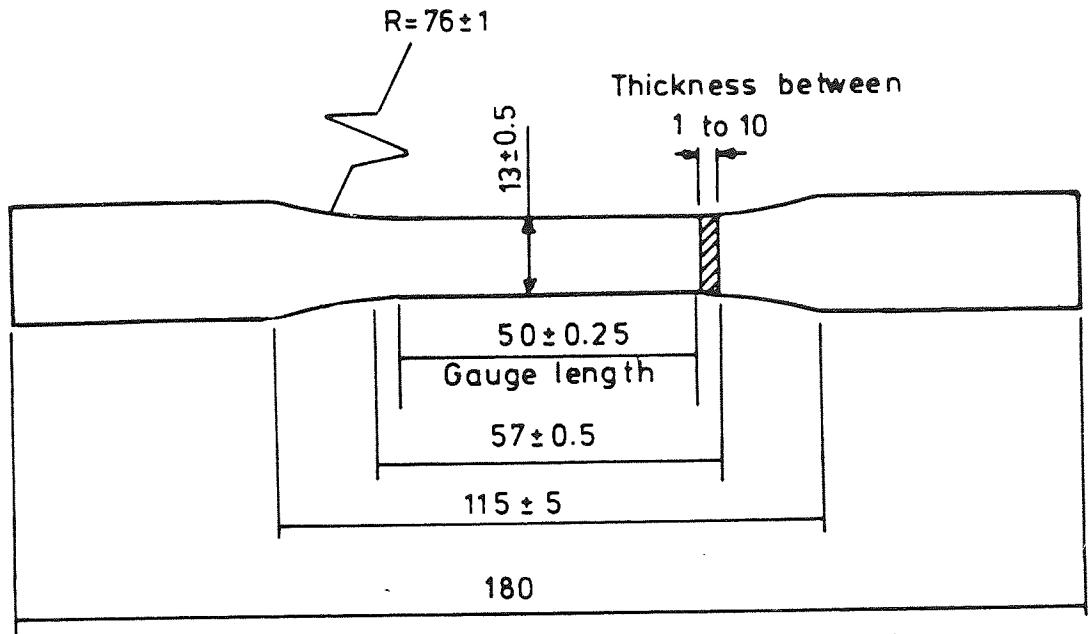
The test results of four types of GRP flat sheet construction are reported in comparison with BS4994 specifications and the rule of mixture prediction. The average thickness and glass content for four constructions are presented in Table 3.1.

3.2.2 Test methods

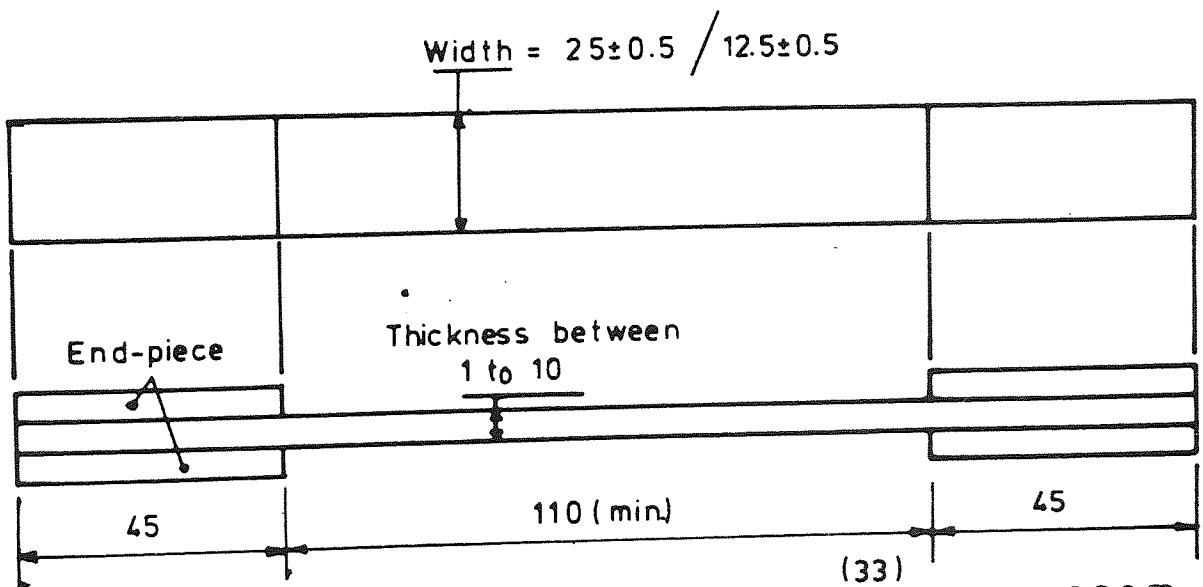
Tensile, flexural and shear tests were carried out with accordance to BS2782⁽³³⁾. The shape of the tensile specimen was chosen of that specified by BS4994⁽³⁾ for cast resin as shown in Fig. 3.1. The main reasons for such preference, is the relative ease of routing specimen in Fig. 3.1a, and more importantly is the occurrence of failure near to the grips on testing the sample of Fig. 3.1b apart from adhesion problems of the end pieces. Limited number of test specimens were strain gauged for the determination of Poisson's ratio, and to monitor the strain versus force applied. All tests have been carried out on 10 Tons tensile testing machine (INSTRON) using an optical extensometers for tensile testing.

3.2.3 Tensile test results

The experimentally determined mechanical properties of the four types of GRP flat sheet laminates are presented in Table 3.2. The level of variability of the measured properties is almost equal in severity among the four types. The average values of the test results are reasonable compared with those reported in the literature^(21,22,49,127).



(a) Specimen type of BS.4994⁽³⁾



(b) Specimen type of BS 2782, method 320E

Figure(3.1) Tensile test specimen

↔ All dimensions are in (mm)

TABLE 3.1 - Thickness and glass content of flat GRP sheets used for mechanical testing

| | | t (mm) | | glass content | | | |
|------------|-----|------------------------|----------|------------------------|-----------------------|-----------------------|------------------------|
| | | nominal ⁽³⁾ | measured | nominal ⁽³⁾ | | measured | |
| | | | | Mg % | Mg ₋₂ kg.m | Mg % | Mg ₋₂ kg.m |
| CSM | | 3.96 | 4.41 | 30 | 1.8 | 29 | 1.75 ± 0.3 |
| | | 7.92 | 8.5 | 30 | 3.6 | 30 | 3.53 ± 0.11 |
| PVC * /CSM | PVC | 4 | - | - | - | - | - |
| | CSM | 3.96 | 3.26 | 30 | 1.8 | 30 | 1.57 ± 0.15 |
| WR/CSM | WR | 2.50 | 2.51 | - | - | 1.8 (fw) 21.4 (cw) | 0.92 (fw) 1.59 (cw) |
| | CSM | - | 2.50 | - | - | 15.8 | 1.17 |

* PVC = rigid, fw = fine weave, cw = coarse weave

TABLE 3.2 - Average test results obtained from tensile testing of flat sheets

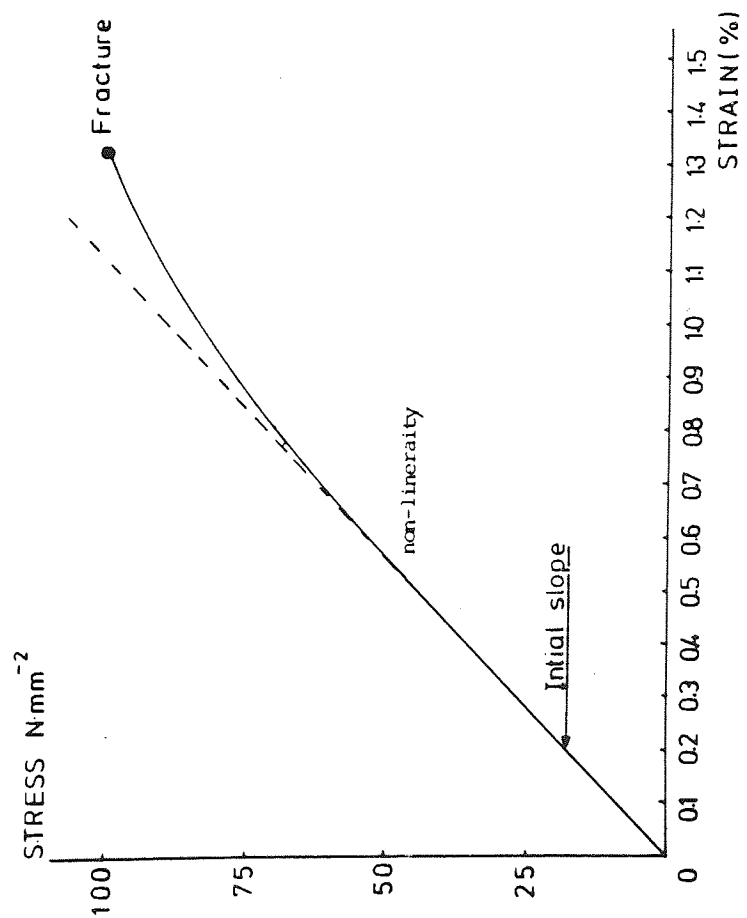
| Mech. Properties | laminate | CSM | | | | CSM/PVC (10 sp.) | | CSM/WR* (6 sp.) | |
|---|----------|---------------------------------|--------------|---------------------------------|--------------|------------------|--------------|-----------------|--------------|
| | | 1.8 kg.m ⁻² (12 sp.) | | 3.6 kg.m ⁻² (11 sp.) | | av. | min. max. | av. | min. max. |
| | | av. | min. max. | av. | min. max. | | | | |
| E_{nl} (%) | | 0.37 | 0.30 0.54 | 0.31 | 0.26 0.40 | 0.25 | - | 0.28 | 0.17 0.44 |
| σ_{nl} (N.mm ⁻²) | | 28 | 20 39 | 28 | 21 31 | 16 | - | 40 | 30 60 |
| E_f (%) | | 1.62 | 1.31 1.82 | 1.96 | 1.75 2.03 | 1.86 | 1.65 2.10 | 1.81 | 1.3 2.43 |
| σ_f (N.mm ⁻²) | | 97 | 87 108 | 114 | 102 133 | 74 | 65 87 | 162 | 134 182 |
| E (kN.mm ⁻²) | | 7.9 | 6.51 10.3 | 8.18 | 7.56 8.84 | 4.64 | 4.14 5.14 | 12.8 | 9.81 15.9 |
| E_{xt} (kN.mm ⁻¹ /kg.m ⁻²) | | 19.8 | 16.3 29.8 | 19.8 | 17.2 21.5 | 21 | 18.4 24 | 17.7 | 13.4 22 |
| E_{TUS} (N.mm ⁻¹ /kg.m ⁻²) | | 242 | 202 267 | 271 | 200 310 | 345 | 296 402 | 229 | 192 249 |

* WR fibres deviate 13° from direction of loading.

A typical stress-strain relation measured during loading are shown in Fig. 3.2a,b for CSM laminate, and in Fig. 3.3 for dual CSM/PVC laminate. For the CSM laminate, failure was observed to start with audible resin cracking followed by the appearance of visual transverse cracks on the gel coat at the non-linearity region, and complete failure occurred with fibre pull out and fibre breakage similar to those reported by Owen⁽⁸¹⁾. The CSM/PVC laminates followed a similar path to failure with the PVC showing a brittle fracture surface and no yielding in the form of whitening has been detected. This embrittlement of the PVC is believed to be caused when in contact with the polyester resin.

As for the CSM/WR dual laminate, failure started with intensive resin cracking of the CSM layer at the non-linearity region leading to fibre breakage and fibre pull-out, leaving the WR layer to carry out the total load. At this stage, delamination of the CSM from the WR has taken place before complete failure of the WR has occurred.

The debonding strains of the fibres from the resin matrix could not be evaluated from the above described tests due to the microscopic nature of damage^(81,93,95). It was reported to occur at about 0.3% strain for CSM laminates and as low as 0.19% for fabric reinforcements⁽⁷⁶⁾. The debonding strain was also reported to occur below the resin cracking stage (0.6-0.7% strain) for the different laminates. The average non-linearity strains observed from the present tests is around $\sim 0.3^+$ % which is half the resin-cracking strains reported before. Comparison of the level of strain to failure of the different laminates reported in Table 3.2 suggest no significant difference. Experimentally measured strain to failure reported in the literature⁽⁹³⁾ for CSM laminates is 1.72%. Strain to failure as interpreted from BS4994 are 1.57% for CSM laminates and 1.88% for WR.



Figure(3.2a) Stress strain curve for CSM laminate specimen under tension

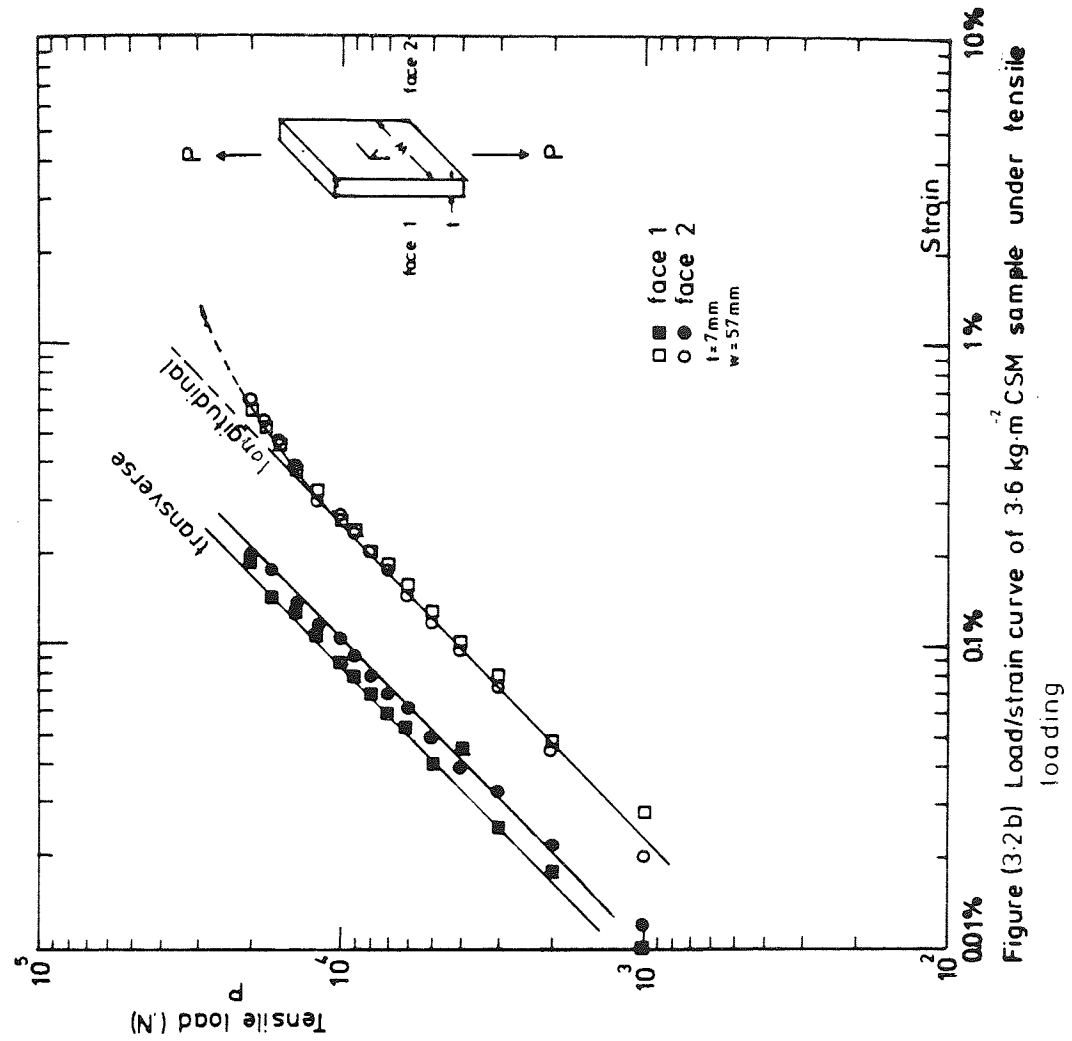
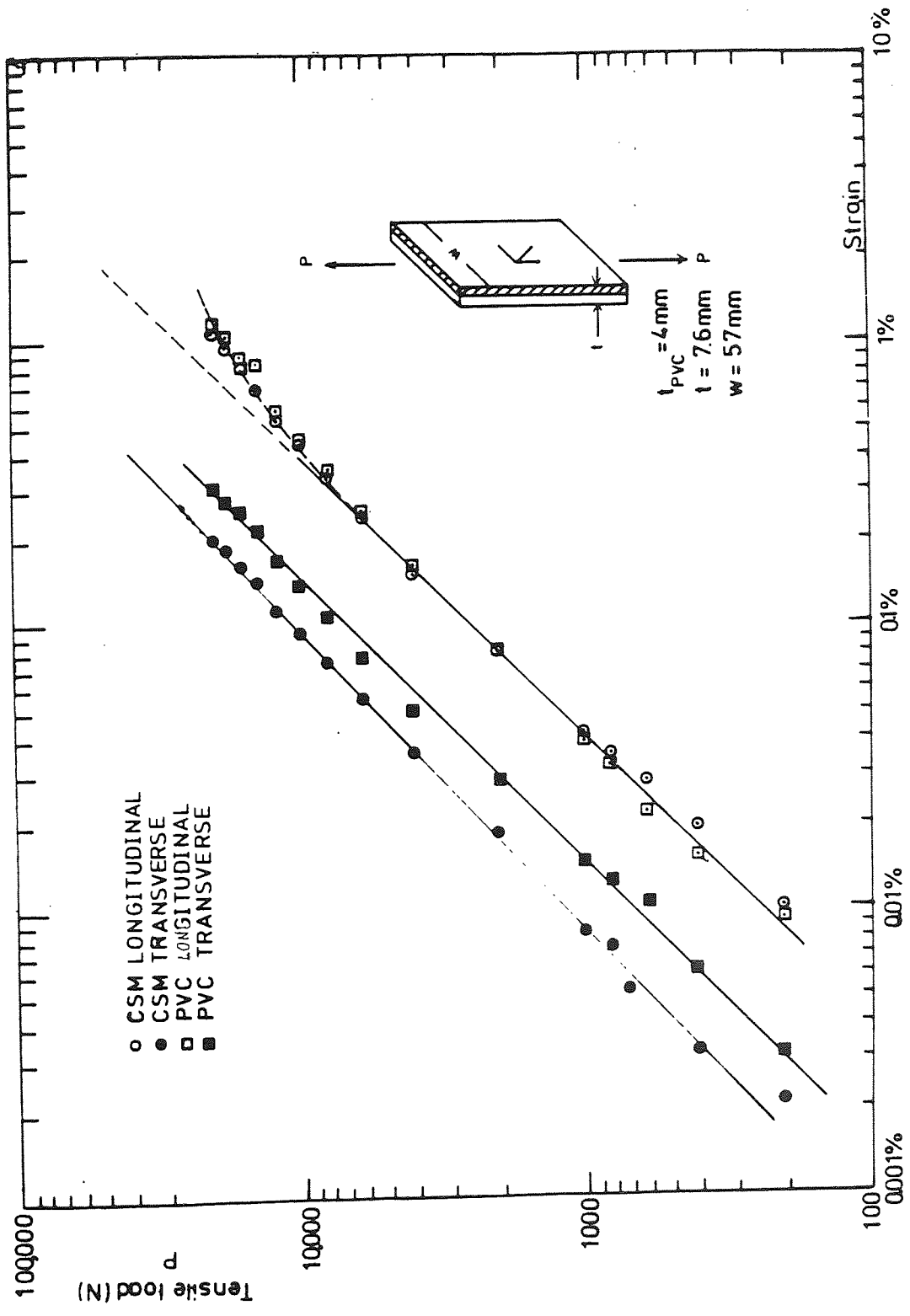


Figure (3.2b) Load/strain curve of 3.6 kg-m CSM sample under tensile loading



Figure(3.3) Load/strain curve of CSM/PVC dual laminate specimen under tensile loading

Table 3.3 presents the comparison between the average experimental results and theoretical prediction using the rule of mixture and those specified by BS4994. The modulus and extensibility were calculated using Eqs. (3.1) and (3.2) respectively.

$$E = \frac{1}{t} \sum_{i=1}^N E_i t_i \quad (3.1)$$

$$\text{Ext.} = \frac{1}{\text{Mg}} \sum (\text{Ext.})_i (\text{Mg})_i \quad (3.2)$$

and the strength and UTUS were similarly calculated using Eqs. (3.3) and (3.4):

$$\sigma_f = \frac{1}{t} [\sigma_1 t_1 + \sigma_2 \frac{\epsilon_1}{\epsilon_2} t_2] \quad (3.3)$$

$$\text{UTUS} = \frac{1}{\text{Mg}} [(\text{UTUS})_1 (\text{Mg})_1 + (\text{UTUS})_2 \frac{\epsilon_1}{\epsilon_2} (\text{Mg})_2] \quad (3.4)$$

where

E = modulus of laminate; Ext. = Extensibility of laminate

t_i = thickness of individual layer; t = thickness of laminate

$(\text{Mg})_i$ = glass mass of individual layer; Mg = glass mass of laminate

σ_f = strength of laminate;

σ_1 = strength of layer 1; σ_2 = strength of layer 2;

ϵ_1 = failure strain of layer 1

ϵ_2 = failure strain of layer 2

σ_f and UTUS of Eqs. (3.3) and (3.4) were calculated assuming $\epsilon_1 = \epsilon_2$.

If however $\epsilon_1 \neq \epsilon_2$ then for the purpose of design, the thickness of the two layers should be balanced to produce a dual laminate which will have a strength value greater than the strength of the weaker constituent⁽³⁵⁾.

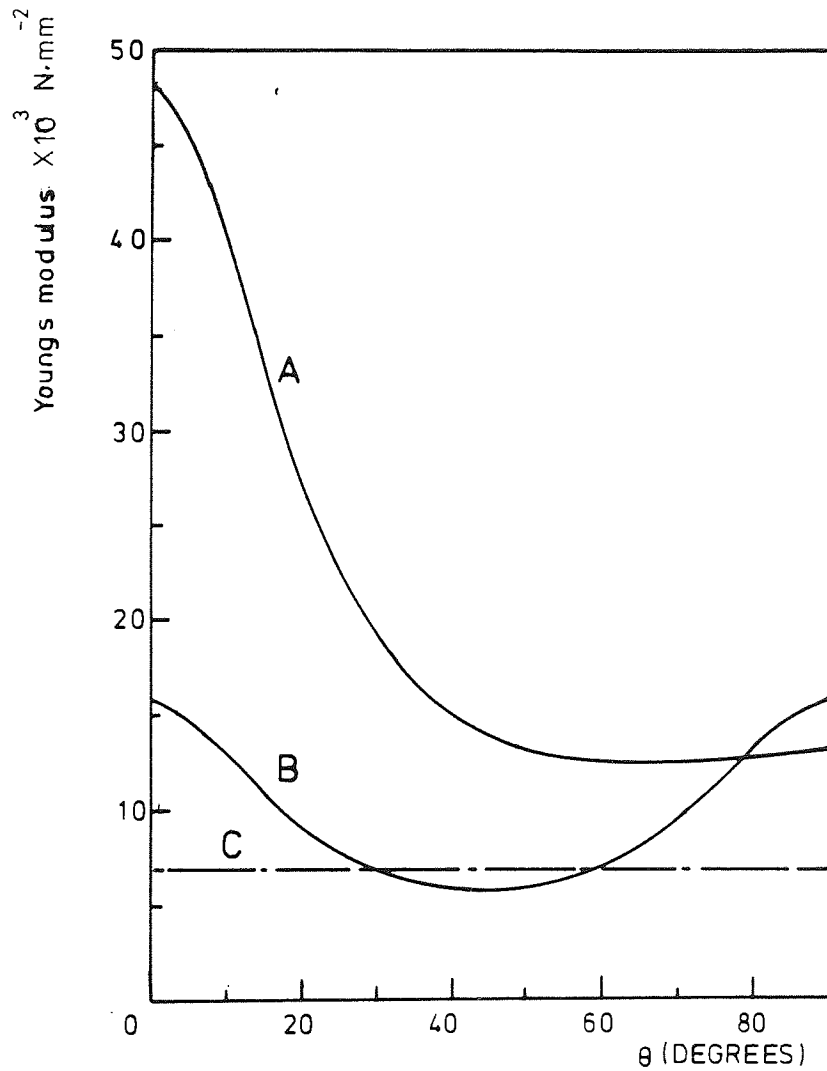
Poisson's ratios measured, were on average to be 0.32 for CSM (average of four specimens), and 0.39 for the PVC (average of three specimens). For the CSM laminates, modulus and strength values measured

TABLE 3.3 - Theoretical and experimental comparison of tensile test results of flat sheet

| Property | Reference | CSM | CSM/PVC | CSM/WR [*] |
|---|---|----------------------------|---------------------------|----------------------|
| t (mm) | BS4994 ⁺ Rule of mix. Exp. | 3.87/7.77 - 4.41/8.5 | 3.45/+ 4 - 3.26/+ 4 | 5.34 - 5.1 |
| E (kN.mm ⁻²) | BS4994 Rule of mix. Exp. | 5.7 7.4 7.96 | 5.7 5.2 4.64 | 9.4 11.5 12.8 |
| Ext. ₁ (kN.mm ⁻¹ / kg.m ⁻²) | BS4994 Rule of mix. Exp. | 12.7 16.8 19.8 | 12.7 - 21 | 13.7 16.0 17.7 |
| σ_f (n.mm ⁻²) | BS4994 Rule of mix. Exp. | 90 115 105 | 90 69 74 | 167 180 162 |
| UTUS (N.mm ⁻¹ / kg.m ⁻²) | BS4994 Rule of mix. Exp. | 200 282 256 | 200 - 345 | 242 260 229 |

* WR fibres deviate 13° from direction of loading, theoretical prediction was modified with accordance to Fig. 3.4.

+ Ref (3)



Figure(3.4) Variation of tensile Young modulus with angle between fibre and force direction⁽⁴⁹⁾ for different composites

- A UD/epoxy (75% glass by mass)
- B WR/polyester (50% glass by mass)
- C CSM/polyester (25% glass by mass)

in directions other than the longitudinal and the transverse directions gives justification of the in-plane isotropy assumption.

3.2.4 Flexural test results

The mechanical properties measured under three point bending are presented in Table 3.4. The force-deflection relation ⁽¹³¹⁾ for small deflection is represented by Eq. (3.5).

$$\Delta_{\text{centre}} = \Delta_{\text{bending}} + \Delta_{\text{shear}} \quad (3.5a)$$

$$= \frac{PL^3}{48EI} + \frac{1.2}{AG'} \frac{PL}{4} \quad (3.5b)$$

$$\cong \frac{PL^3}{48EI} \quad (\text{for the present test}) \quad (3.5c)$$

For CSM laminates, the average flexural modulus of 5.5 kN.mm^{-2} is 32% lower than the tensile modulus of 7.96 kN.mm^{-2} . Such difference is attributed to the contribution of the interlaminar shear deflection (Δ_{shear} of Eq. (3.5)) which is ignored in the calculation for the modulus. This shear deformation is usually ignored for long homogeneous isotropic beams, but for GRP it could have some influence on deformation due to the low value of G' . This is expressed mathematically as in Eq. (3.6).

$$\frac{\Delta_{\text{shear}}}{\Delta_{\text{bending}}} = 1.2 \frac{E}{G'} \left(\frac{t}{L}\right)^2 \quad (3.6)$$

The value of G' for CSM laminates has been reported to be similar to that of the resin matrix ⁽³⁷⁾, i.e. for polyester resin then $G' \cong 1.0 \text{ kN.mm}^{-2}$. It was also reported by Kirk ⁽⁴⁰⁾ to be as low as 0.1 kN.mm^{-2} . By decreasing the ratio of t/L (Eq. (3.6)), it can be seen that the effect of E/G' will be of a second order, and the shear deflection contribution is reduced, i.e. the flexural modulus will approach that of the tensile modulus. The flexural modulus obtained from four point bending tests listed in Table 3.5 are of similar values to the tensile modulus. In this case, the shear deformation is negligible.

TABLE 3.4 - Flexural test results obtained from three point bending of flat sheets

| | CSM ⁻² 1.8 kg.m ⁻² (12 sp.) | | CSM ⁻² 3.6 kg.m ⁻² (9 sp.) | | CSM/PVC (7 sp.) | | CSM/WR (6 sp.) | |
|--|---|--------------|--|--------------|--------------------|-----------------|-------------------|--------------|
| | av. | min. max. | av. | min. max. | av. | min. max. | av. | min. max. |
| L/t | 16 | - | 16 | - | 20 | - | 16 | - |
| E (kN.mm ⁻²) | 5.51 | 4.46 6.34 | 5.49 | 4.84 6.30 | 4.34 | 3.94 4.92 | 8.35 | 7.66 8.77 |
| σ_f (N.mm ⁻²) | 149 | 122 177 | 145 | 130 167 | 126* 91 | 122 130 - | 235 170* | |
| Ext. ₋₁ (kN.mm ⁻² / kg.m ⁻²) | 12.7 | 10.8 15.0 | 13.3 | 11.7 15.6 | 21 | 20 25 | 11.5 | 10.7 12.0 |
| UTUS ₋₁ (N.mm ⁻² / kg.m ⁻²) | 344 | 278 401 | 313 | 304 416 | 569* 428 | 484 613 | 240* 310 | |
| ΣEI (MN mm ²) | - | - | - | - | 1.77 | 1.5 1.89 | 1.12 | 0.91 1.42 |

* CSM layer is under tension

TABLE 3.5 - Flexural Test Results of Mono-CSM Laminates under three point and four point bending using the same specimen

| t (mm) | W (mm) | 3-pt | 4-pt | | E (N.mm ²) | |
|-----------|-----------|-----------|------|-------------|---------------------------|------|
| | | L (mm) | L | L/3 (mm) | 3-pt | 4-pt |
| 8.04 | 16.51 | 152 | 180 | 60 | 7080 | 8060 |
| 7.88 | 18.49 | 240 | 240 | 80 | 7360 | 7230 |
| 8.19 | 19.86 | 330 | 330 | 110 | 7130 | 2150 |
| 4.85 | 13.42 | 152 | 180 | 60 | 6300 | 7400 |
| 5.28 | 10.5 | 102 | 102 | 34 | 5780 | 7190 |
| 5.18 | 10.38 | 102 | 102 | 34 | 5080 | 7320 |
| 5.38 | 10.53 | 102 | 102 | 34 | 5760 | 7370 |

The average experimental flexural strength for CSM is 150 N.mm^{-2} , which is 30% higher than the tensile strength of 105 N.mm^{-2} . The difference is attributed to the stress pattern induced under each type of loading. Under flexural type of loading, the maximum stresses and strains lie at the outer most surface of the laminate, thus, less susceptible to laminate imperfections and stress raisers.

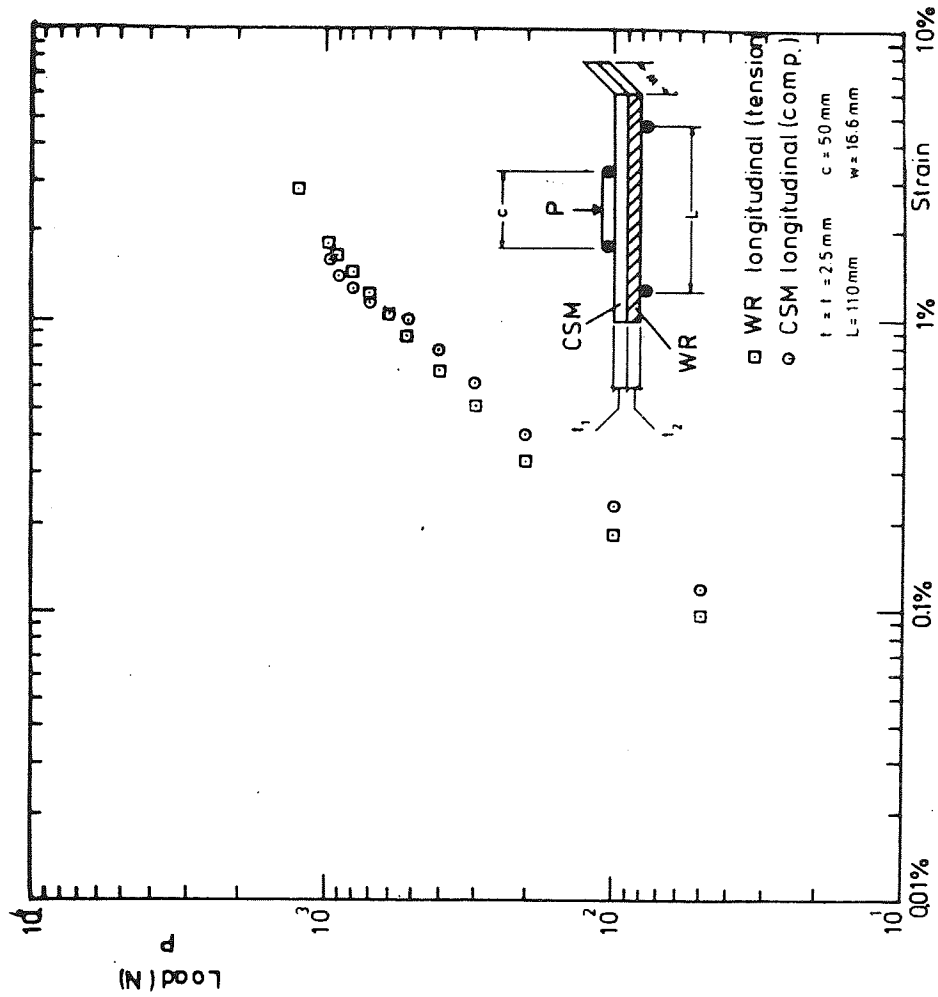
Average flexural extensibility experimentally determined for CSM is $13 \text{ kN.mm}^{-1}/\text{kg.m}^{-2}$, which is comparable with BS4994⁽³⁾ specification, and less than the tensile extensibility of $19.8 \text{ k.mm}^{-1}/\text{kg.m}^{-2}$. This difference is directly related to the relatively lower value of the flexural modulus. The experimentally measured flexural UTUS of $350 \text{ N.mm}^{-1}/\text{kg.m}^{-2}$ for CSM, is higher than the tensile UTUS of $260 \text{ N.mm}^{-1}/\text{kg.m}^{-2}$ due to the higher flexural strength. Failure always started by the formation of a crack of the gel coat on the tension surface, propagating through the laminate thickness to complete failure by fibre breakage and fibre pull-out, similar to the failure patterns reported by Raymond^(20,21).

Typical load versus strain to failure for CSM/PVC and CSM/WR dual laminates under four point bending are shown in Figs. 3.5 and 3.6 respectively. For both laminates, strain to failure is measured to be 2%. Table 3.6 summarises the experimental results of Figs. 3.5 and 3.6 compared with theoretical results using the concept of composite strip⁽¹¹⁸⁾, i.e.

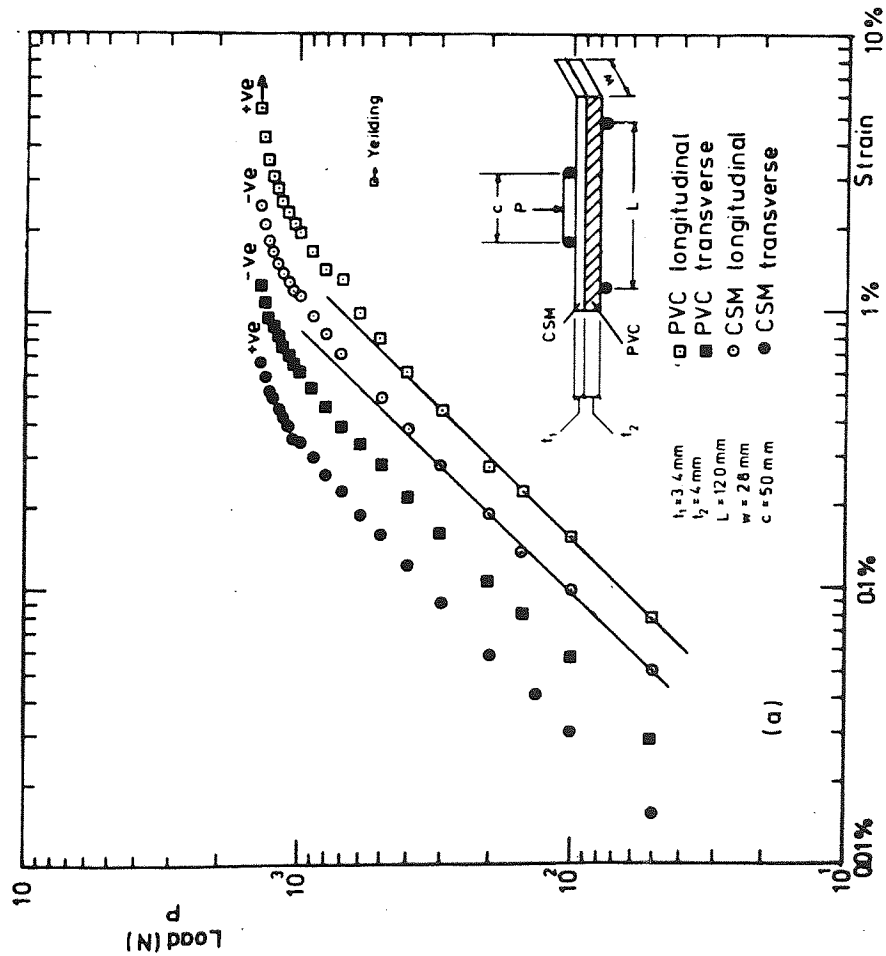
$$EI_{\text{dual laminate}} = \sum_{i=1}^N E_i I_i \quad (3.7a)$$

and

$$\bar{y} \text{ (neutral axis)} = \frac{\sum_{i=1}^N y_i A_i E_i}{\sum_{i=1}^N A_i E_i} \quad (3.7b)$$



Figure(3.6) Load strain curve of CSM/WR dual laminate specimen under four point bending.



Figure(3.5) Load/strain curve of CSM/PVC dual laminate specimen under four point bending.

Poisson's ratios interpreted from Fig. 3.5 are 0.31 for the CSM layer and 0.36 for the PVC. These are comparable with those obtained from tensile tests.

Unlike the mono-CSM flexural modulus results, the flexural modulus of the CSM/PVC dual laminate of 4.34 kN.mm^{-2} is comparable with that measured under tension of 4.64 kN.mm^{-2} . In this case, the interlaminar shear deflection could be considered negligible due to the high (L/t) ratio when just the CSM is considered. Whilst for the CSM/WR dual laminate, the flexural modulus of 8.4 kN.mm^{-2} is 30% lower than that measured under tension because of the interlaminar shear deformations experienced by both the CSM and the WR layers.

The flexural strengths of both the CSM/PVC and the CSM/WR dual laminates, could be considerably different dependent on which layer constituent is experiencing tension as presented in Table 3.5. On average the flexural strength and the flexural UTUS are 30% lower when the weakest layer constituent is undergoing tension in comparison.

When the PVC experienced tension (Fig. 3.5), it failed in a ductile manner being identified by whitening and the permanent deformation upon reloading, with the CSM layer being crushed and delaminated by the compressive stress component. But, when the loading was reversed, the PVC failed in a brittle manner similar to that observed under tension.

The WR layer of the CSM/WR dual laminate was observed to have experienced some form of buckling at the fibre cross-overs under both flexural tension and compression.

3.2.5 Shear test results

The shear strengths of the four types of laminates have been obtained experimentally and are presented in Table 3.7.

TABLE 3.6 - Theoretical and experimental mechanical behaviour of dual GRP laminates under flexural loading.

(The results correspond the Fig. 3.5 and 3.6)

| | | \bar{y} (mm) | ΣEI MN mm ² | Ratio of surface strains |
|---------|------------------|--------------------|-----------------------------------|-----------------------------|
| CSM/PVC | Th. ⁺ | 2.87 [*] | 4.5 | 1.63 (PVC ÷ CSM) |
| | Exp. | 2.81 | 5.15 | 1.58 |
| CSM/WR | Th. ⁺ | 2.04 ^{**} | 1.95 | 1.43 (CSM ÷ WR) |
| | Exp. | 2.22 | 1.79 | 1.25 |

* neutral axis measured from CSM outer surface.

** neutral axis measured from WR outer surface.

+ theory of composite strips ⁽¹¹⁸⁾

TABLE 3.7 - Shear strength of GRP measured by different methods

| | | CSM laminate | CSM/PVC laminate | CSM/WR laminate |
|--|------------------------------|-------------------|---------------------|--------------------|
| In-plane shear strength, ⁽³³⁾ Punch test (N.mm ⁻²) | | 83 (20 sp.) | 69 (2 sp.) | - |
| Interlaminar shear strength (N.mm ⁻²) | lap shear ⁽³⁾ | 8.65 (15 sp.) | - | 12.4 (6 sp.) |
| | 3-pt bending ⁽³³⁾ | > 14.2 (9 sp.) | - | - |

For CSM laminates, the in-plane shear strength obtained by the Punch test⁽³³⁾ was measured to be 83 N.mm^{-2} . This is higher than shear strength reported⁽⁹²⁾ for cast polyester resin of 50 N.mm^{-2} and lie in the range of $68\text{-}92 \text{ N.mm}^{-2}$ in-plane shear strength of CSM reported by Johnson. Kirk⁽⁴⁰⁾ obtained a value of 70 N.mm^{-2} by testing CSM pipe under torsion to failure, and Owen⁽⁸⁹⁾ reported a value of 64 N.mm^{-2} by testing CSM plates under twisting moment. The in-plane shear strengths measured for laminates of 1.8 kg.m^{-2} and 3.6 kg.m^{-2} nominal glass content were of similar magnitude.

For the dual CSM/PVC laminate, the in-plane shear strength obtained by the punch test was measured to be 69 N.mm^{-2} regardless whether the laminate is punched on the PVC surface or the CSM surface. Such a drop in the shear strength in comparison to the mono-CSM laminate value, is due to the weaker shear strength of the PVC which is approximately 40 N.mm^{-2} .

The interlaminar shear strength (ISS) of the CSM laminates of 8.65 N.mm^{-2} obtained by the lap shear test⁽³⁾ is 40% lower than that of $> 14 \text{ N.mm}^{-2}$ obtained by the three point bending testing of short beam⁽³³⁾. The value of the ISS obtained by the lap shear test is believed to be under-estimated because of the stress concentration and peeling^(129,130) effects taking place at the saw-cut edges. ASTM D3846⁽⁶²⁾ does suggest a method to minimise the peeling effect for UD laminates being tested by the lap shear test.

The ISS obtained by the three point bending test method would be considered more acceptable due to the absence of peeling and stress concentration effect except for that imposed by the central anvil. All the test specimens had a ratio of $L/t = 5$, and failure always started as a flexural failure followed later by either delamination or crushing under the central anvil. In this instance it is believed that (L/t)

ratio should be reduced below 5, thus ensuring a delamination failure to occur before the flexural failure does. This could be explained mathematically as follows, taking CSM as an example.

$$\sigma_f \text{ (flex. strength)}_{3\text{-pt}} = \frac{3}{2} \frac{PL}{wt^2} = 150 \text{ N.mm}^{-2} \quad (3.8a)$$

$$(\text{ISS})_{3\text{-pt}} = \frac{3}{4} \frac{PL}{wt} = 25 \text{ N.mm}^{-2} \text{ (Ref. 49)} \quad (3.8b)$$

$\therefore \frac{L}{t} \approx 3$ to satisfy the shear failure requirement.

The interlaminar shear strength of the CSM/WR laminate was measured to be on average of 12.4 N.mm^{-2} as obtained by the lap shear test. It is higher than that obtained for CSM, probably due to the relatively higher stiffness of the WR which would resist peeling.

3.3 Pressure Test Results of Straight Pipes and Bends

3.3.1 Introduction

Pressure test results within the elastic region of GRP straights and bends are presented and discussed in this article. Only two failure cases were investigated, one for a straight pipe and one for a bend. For the rest of the pipe components, the incremental pressure load applied was limited by 0.2% maximum strain. The dimensions and the mechanical properties of the pipe components and their identification are listed in Tables 3.8 and 3.9 for straight pipes and bends respectively.

All the pressure tests were of closed-ended type of test, i.e. for a straight pipe the circumferential stress is twice the longitudinal stress. The tests were carried out using water as the pressurising medium having the inside strain gauges waterproofed using silicon rubber (RS) with the exception of few components having the inside strain gauges embedded in the inside gel coat of the pipe.

TABLE 3.8 - Specifications of GRP Straight Pipes tested under Pressure Loading

| Pipe Number | Previous Reference | Nominal Specification | | | | Measured Specification | | | | Mechanical Properties | | Type of Pipe Wall Construction |
|-------------|--------------------|-----------------------|---------|----------------------|------|------------------------|---------|----------------------|------|--------------------------|---------------------------|--------------------------------|
| | | t (mm) | 2r (mm) | Mg kg/m ² | Mg % | t (mm) | 2r (mm) | Mg kg/m ² | Mg % | E (kN/mm ²) | v | |
| S004 | Ch. 6 | 3.92 | 100 | 1.8 | 30 | 4.6 | 102 | 1.89 | 31 | 7.45 | 0.3 | CSM |
| S005 | Ch. 6 | 3.92 | 100 | 1.8 | 30 | 4.8 | 102 | 1.89 | 31 | 7.45 | 0.3 | CSM |
| S027 | Ch. 6 | 5.28 | 200 | 2.4 | 30 | 6.3 | 203 | 2.52 | 30 | 7.45 | 0.3 | CSM |
| S00A | - | 3.92 | 100 | 1.8 | 30 | 5.5 | 102 | - | - | 7.0 | 0.3 | CSM |
| S00B | - | 3.92 | 100 | 1.8 | 30 | 5.5 | 102 | - | - | 7.0 | 0.3 | CSM |
| S011* | Ch. 7 | 3.92+ | 100 | 1.8 | 30 | 9.45 | 106 | - | - |) E _{PVC} = 3.0 |) v _{PVC} = 0.35 |) |
| S038** | Ch. 7 | 3.92+ | 250 | 1.8 | 30 | 11.0 | 244 | - | - |) E _L = 6.2 |) v _{LC} = 0.17 |) CSM/PVC |
| S062* | Ch. 7 | 5.24+ | 600 | 2.4 | 30 | 11.08 | 589 | - | - |) CSM = 7.0 |) v _{CL} = 0.30 |) |
| S041 | Ch. 8 | 4.8 | 200 | 4.8 | - | 10.5 | 202 | 6.25 | 47 | E _C = 11.3 | v _{CL} = 0.30 | CSM/WR/VD |
| S044 | Ch. 8 | 4.8 | 200 | 4.8 | - | 11.1 | 202 | 6.79 | 45 | E _L = 6.2 | v _{LC} = 0.17 | CSM/WR |
| S032 | Ch. 8 | 5.0 | 250 | - | - | 5.2 | 250 | 6.6 | 70 | E _{C,L} = 9.1 | v = 0.25 |) |
| S00C | Ch. 6 | 7.0 | 250 | - | - | 7.0 | 250 | 4.3 | 41 | E _C = 22 | v _{CL} = 0.513 |) F.W. |
| | | | | | | | | | | E _L = 13.7 | v _{LC} = 0.318 |) |
| | | | | | | | | | | E _C = 13.0 | v _{CL} = 0.3 |) Centrifugally |
| | | | | | | | | | | E _L = 7.4 | v _{LC} = 0.17 |) cast chopped |
| | | | | | | | | | | | |) rovings |

+ Nominal thickness of the CSM only

* Measured thickness includes 4 mm of PVC Liner

** Measured thickness includes 3 mm of PVC Liner



TABLE 3.9 - Specifications of GRP Bends tested under Pressure Loading

| Bend Number | Type of Bend | Previous Reference | Nominal Specification | | | | Measured Specification | | | | Mechanical Properties | | Type of Bend Wall Construction | |
|-------------|----------------------|--------------------|-----------------------|----------------------|------------------|----------------------|------------------------|--|----------------------|----------------------|-----------------------|---|--|-----------|
| | | | t (mm) | 2r _i (mm) | R/r _i | Mg kg/m ² | Mg % | t (mm) | 2r _i (mm) | Mg kg/m ² | Mg % | E (kN/mm ²) | | v |
| S021 | Smooth | Ch. 6 | 3.92 | 250 | 2 | 1.8 | 30 | 6.3 | 250 | 1.85/3.50 | 27.58 | 7.45 | 0.3 | CSM |
| S024 | Smooth | Ch. 6 | 5.28 | 200 | 3 | 2.4 | 30 | 7.57 | 204 | 2.19/4.54 | 31.28 | 7.45 | 0.3 | CSM |
| S002 | Smooth | Ch. 6 | 3.92 | 100 | 6 | 1.8 | 30 | 5.84 | 102 | - | - | 7.45 | 0.3 | CSM |
| S014* | Smooth | Ch. 7 | 3.92+ | 100 | 6 | 1.8 | 30 | 8.7 | 106 | - | - | - | - | CSM/PVC |
| S016* | Smooth | Ch. 7 | 3.92+ | 100 | 6 | 1.8 | 30 | 8.7 | 106 | - | - | - | - | CSM/PVC |
| S034** | Mitred α = 12.85° | Ch. 7 | 5.28+ | 200 | 3 | 2.4 | 30 | 9.35 ^b 13.5 ^j | 199 | - | - | - | - | CSM/PVC |
| S037** | Mitred α = 12.85° | Ch. 7 | 3.92+ | 250 | 2 | 1.8 | 30 | 9.16 | 244 | - | - | - | - | CSM/PVC |
| S060* | Mitred α = 12.85° | Ch. 7 | 5.28+ | 600 | 2 | 2.4 | 30 | 11.87 ^b 18.56 ^j | 589 | - | - | - | - | CSM/PVC |
| S061* | Mitred α = 12.85° | Ch. 7 | 5.28+ | 600 | 2 | 2.4 | 30 | 11.87 ^b 18.56 ^j | 589 | - | - | - | - | CSM/PVC |
| S043 | Smooth | Ch. 8 | 4.8 | 200 | 3 | 4.8 | - | 12.45 | 202 | 4.2 / 9.4 | 47 | E = 9.1 | v = 0.25 | CSM/WR |
| S048 | Smooth | Ch. 8 | 5 | 100 | 2.5 | - | - | 8.9 | 102 | 6.79/12.25 | 44 | E = 9.0 | v = 0.25 | CSM/WR |
| S049 | Smooth | Ch. 8 | 5 | 100 | 2.5 | - | - | 8.9 | 102 | 6.79/12.15 | 44 | E = 9.0 | v = 0.25 | CSM/WR |
| S046 | Smooth | Ch. 8 | 4.8 | 250 | 2.0 | 4.8 | - | 12.50 | 250 | 7.65/10.24 | 48.55 | E _C = 11.3 E _L = 6.2 | v _{CL} = 0.30 v _{LC} = 0.17 | CSM/WR/UD |

+ Nominal thickness of the CSM only

* Measured thickness includes 4 mm of PVC Liner

** Measured thickness includes 3 mm of PVC Liner

b bend centre

j joint

The results are graphically presented describing the longitudinal and the circumferential strains and/or the stresses measured as a function of 180° circumferential positions. For the bends, the stress measurements starts at the intrados ($\theta = 0^\circ$) and terminates at the extrados ($\theta = 180^\circ$). Measured strains and stresses showed a reasonably defined linear relationship as a function of the pressure increments (see Fig. 3.7a,b) , upon which the present pressure results are based. Theoretical comparison is based on the prediction of thin cylinders for straight pipes. Smooth bends results are compared with the prediction of torus shells under pressure. Experimental results of mitered bends are compared with Owen & Emmerson⁽¹⁶⁷⁾ analysis ignoring the presence of the uPVC liner. The relevant equations are presented in App. IV. The strains and stresses pressure results for the filament wound pipe is compared with Tsai^(29,31) theoretical analysis presented in App. V.

The experimental results are also presented as membrane and local bending stresses both in the circumferential and the longitudinal direction by using Eq. (3.9):

$$\sigma_m \text{ (membrane)} = \frac{\sigma_{IN} + \sigma_{OUT}}{2} ; \quad \epsilon_m = \frac{\epsilon_{IN} + \epsilon_{OUT}}{2} \quad (3.9a)$$

$$\sigma_b \text{ (local bending)} = \frac{\sigma_{IN} - \sigma_{OUT}}{2} ; \quad \epsilon_b = \frac{\epsilon_{IN} - \epsilon_{OUT}}{2} \quad (3.9b)$$

Equation (3.9) indicates a positive value of σ_b and ϵ_b when the inside surface is in tension and outside surface is in compression and vice versa. Such separation or segregation of experimental results helped greatly in providing a better interpretation for relating the pipe behaviour to, firstly, the method of construction and, secondly, to theoretical prediction.

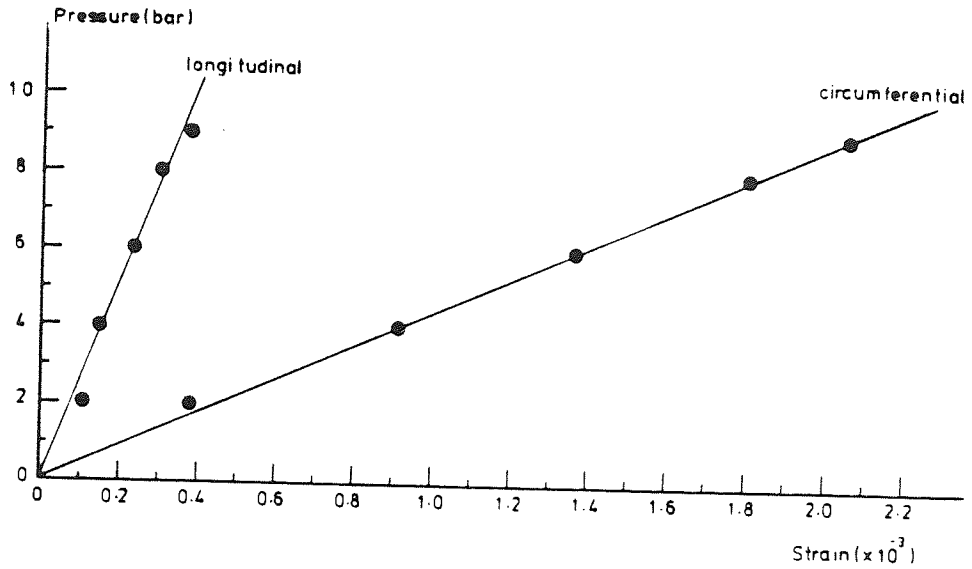


Figure (3.7a) Inside longitudinal and circumferential strains monitored on straight pipe S027 at $\theta = 100^\circ$ as a function of incremental pressure loading.

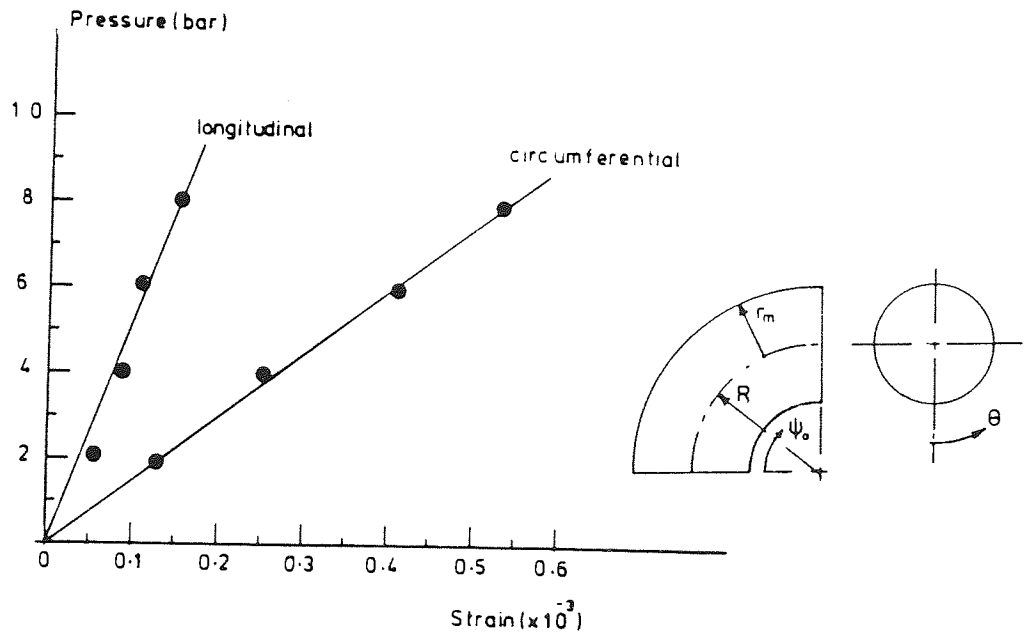


Figure (3.7b) Inside longitudinal and circumferential strains monitored on bend S048 as a function of the incremental pressure loading. $\theta = 30^\circ$

3.3.2 Pressure test results of straight pipes

The test results of the straight pipes discussed in this article, are identified in Table 3.8.

3.3.2.1 Hand lay-up straight pipes

For all the straight pipes tested, the strains measured on the inside surface were in general higher than those measured on the outside surface. Typical distribution of strains measured around half the pipe perimeter are shown in Fig. 3.8. Strains are converted to stresses by using Hooke's law for homogeneous isotropic material under plane stress conditions.

Figs. 3.9a and 3.10a show considerable scatter of stresses measured on the inside and the outside surfaces of the pipe. The scatter is more pronounced among the circumferential stresses. Such scatter is believed to be directly related to the local variability of thickness and glass content of the pipe wall laminate. As will be reported later, the thickness variability is more influential.

By representing the experimentally measured inside and outside stresses as membrane and bending stresses as shown in Figs. 3.9b and 3.10b, a better described pattern of stress distribution is achieved, where the membrane stresses are far more uniform along their circumferential position and reasonably compared with thin shell theory prediction (Fig. 3.10a).

The local bending stresses shown in Figs. 3.9b and 3.10b are of direct consequence of, firstly, thickness variation and, secondly, the rate of change of the thickness. Circumferential bending stresses as shown in Fig. 3.9b are of a severer nature than those obtained in the longitudinal direction. The severity is recognised by change of sign or sharp slopes in-between adjacent measured bending stresses.

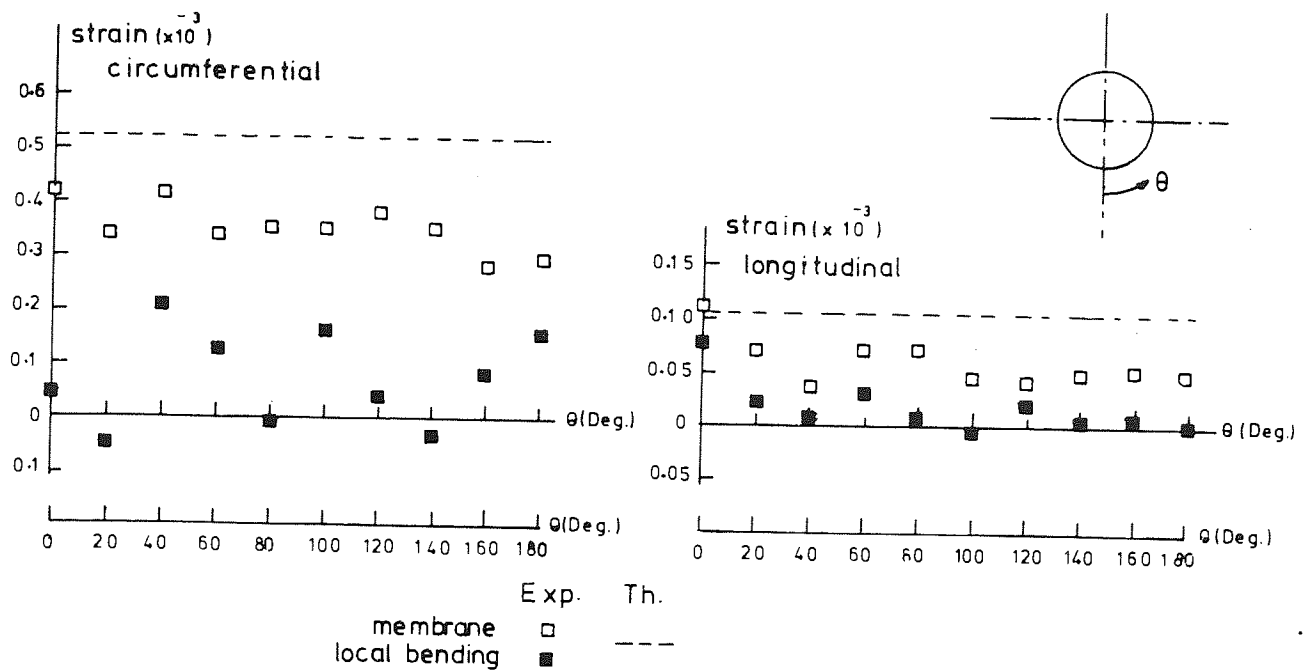


Figure (3.8b) Membrane and local bending strains measured on straight pipe S004 under 4-bar internal pressure

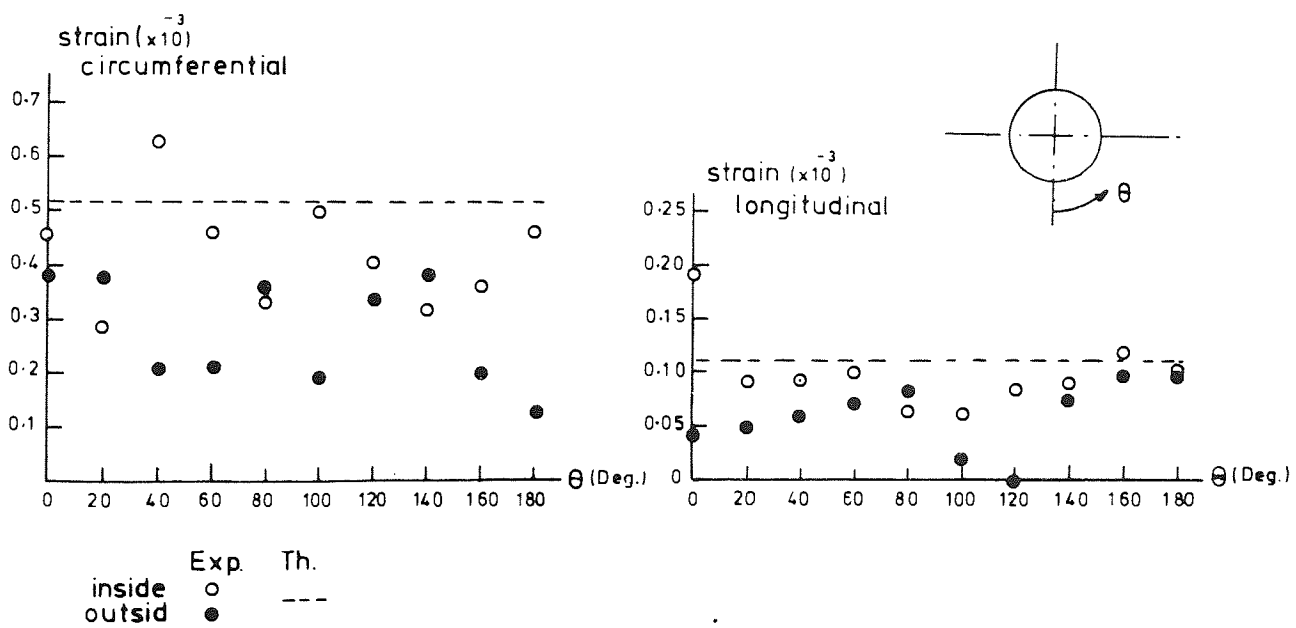


Figure (3.8a) Inside and outside strains measured on straight pipe S004 under 4-bar internal pressure

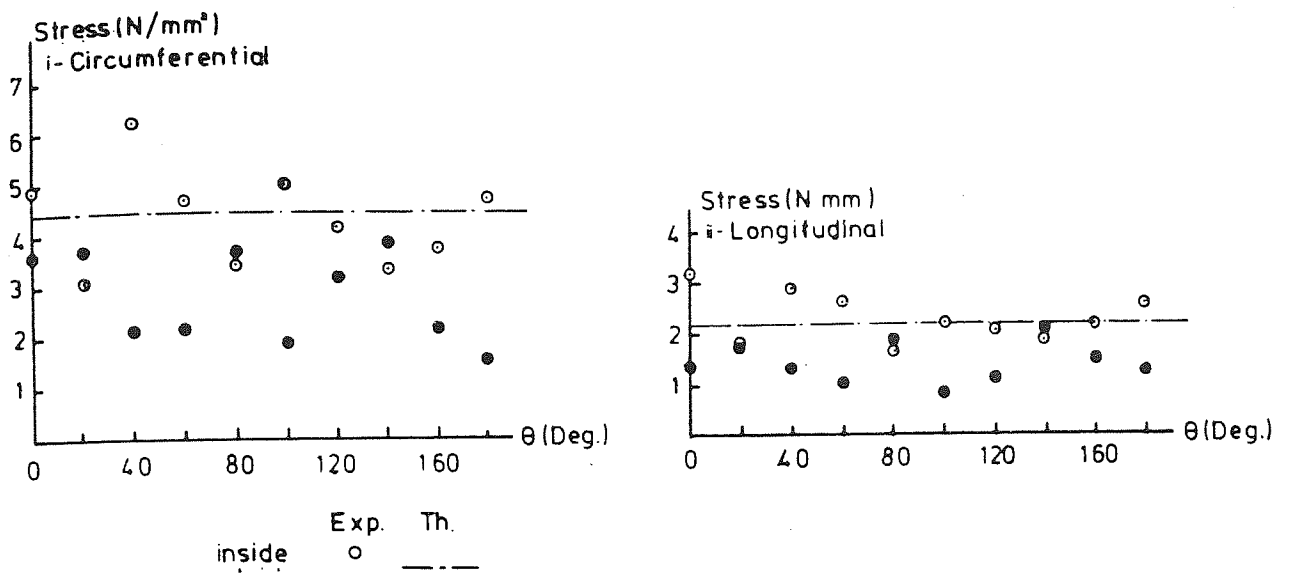


Figure (3.9a) Inside and outside stresses measured on straight pipe S004 under 4 bar internal pressure.

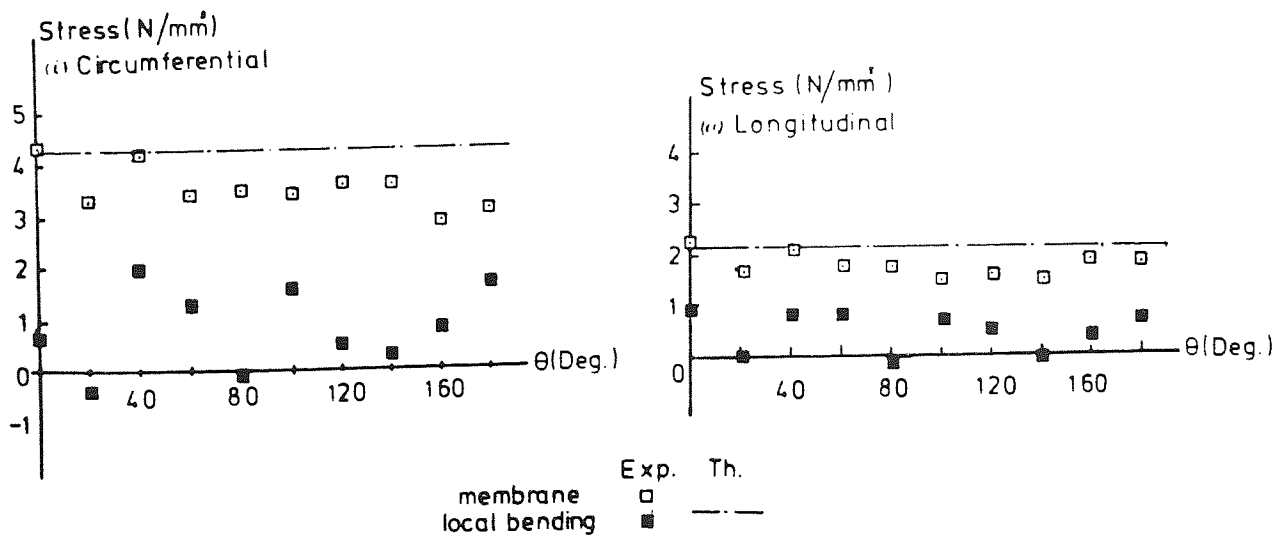


Figure (3.9b) Membrane and local bending stresses measured on straight pipe S004 under 4 bar internal pressure.

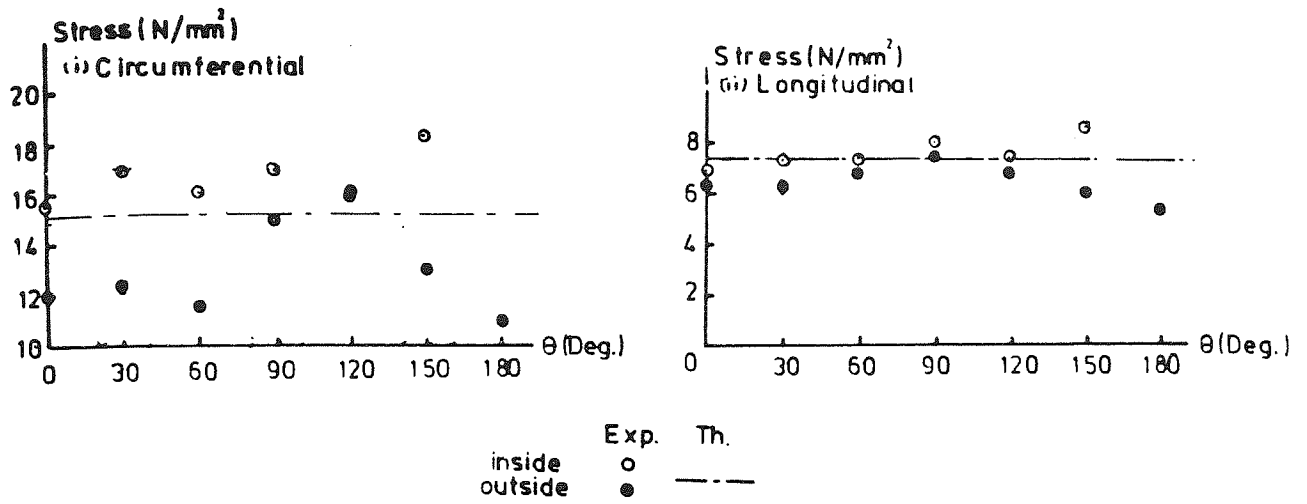


Figure (3.10a) Inside and outside stresses measured on straight pipe S027 under 9 bar internal pressure.

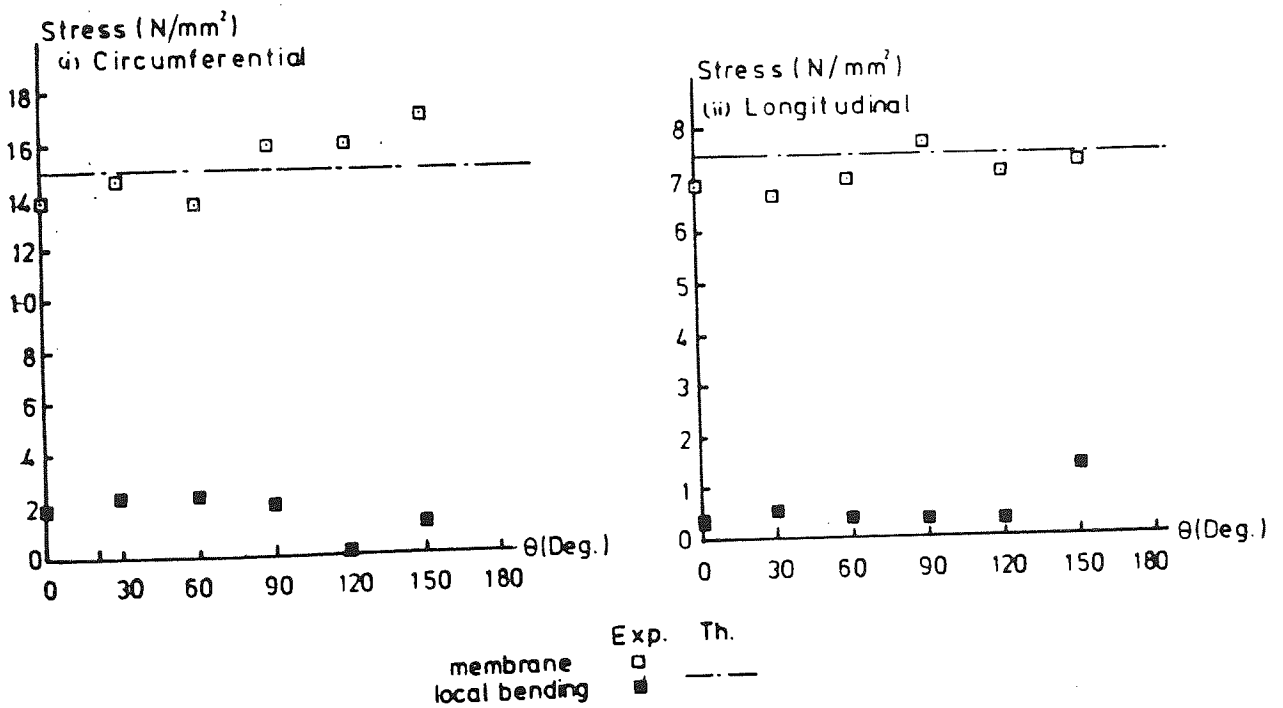


Figure (3.10b) Membrane and local bending stresses measured on straight pipe S027 under 9 bar internal pressure.

3.3.2.2 Specially made hand lay-up straight pipes

The problem of local bending accompanying pressure tests and the variability of the stresses from one angular position to the other, caused considerable concern. Attempts were made theoretically⁽¹⁸⁶⁾ to relate stress variability to thickness variability brought about by the helically induced overlapping of CSM laminates. The analysis based its mathematical model for pipes manufactured using the semi-automated hand lay-up process (see Fig. 2.3b of Ch. 2). The outcome of the theoretical analysis was not entirely justified since limited experimental data were available at the time and the restriction to the manufacturing method used. That led to the suggestion of manufacturing two specially made pipes by one of the manufacturers sponsoring the project. The first, and referred to as 'S00A'; was manufactured with no overlaps, and the second, and referred to as 'S00B'; was manufactured with the usual overlaps but later machined on the outside. Both pipes were strain gauged on the inside and the outside around 180° of the circumference with 30° intervals.

The circumferential stresses measured under 3.5 bar pressure of such pipes are shown in Fig. 3.11 for pipe S00A (no overlaps) and in Fig. 3.12 for pipe S00B (machined on the outside). The stresses were obtained using 7 kN.mm^{-2} Young's modulus and a Poisson's ratio of 0.3. The actual tests were carried out by the National Engineering Laboratory (NEL) which is the other research body concerned.

The inside and the outside circumferential stresses measured around 180° of the circumference of pipe S00A as shown in Fig. 3.11a, suggest that stress variability may still exist even though the overlaps were eliminated. This is observed experimentally by the relatively high non-uniformity shown by the bending stresses presented in Fig. 3.11b.

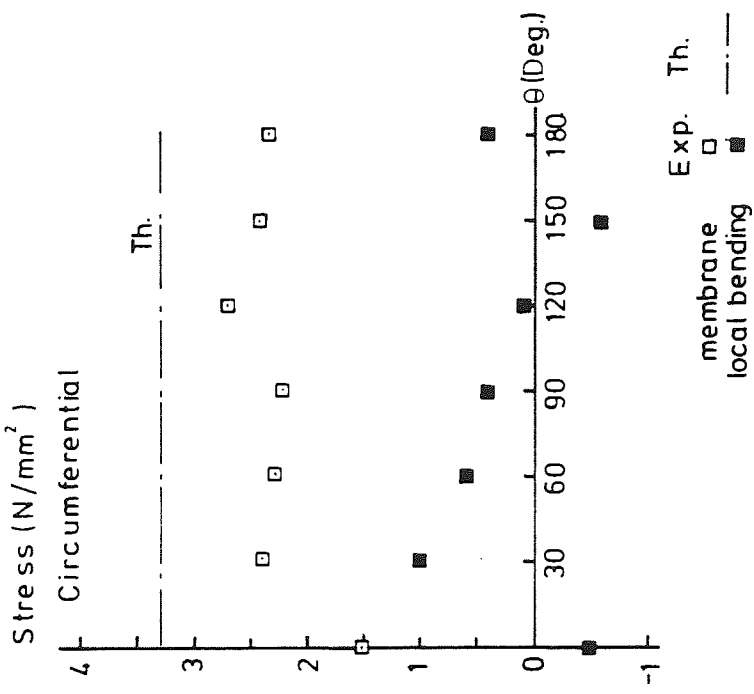


Figure (3.11a)

Inside and outside circumferential stresses measured on straight pipe S00A (no overlaps) under 3.5 bar internal pressure.

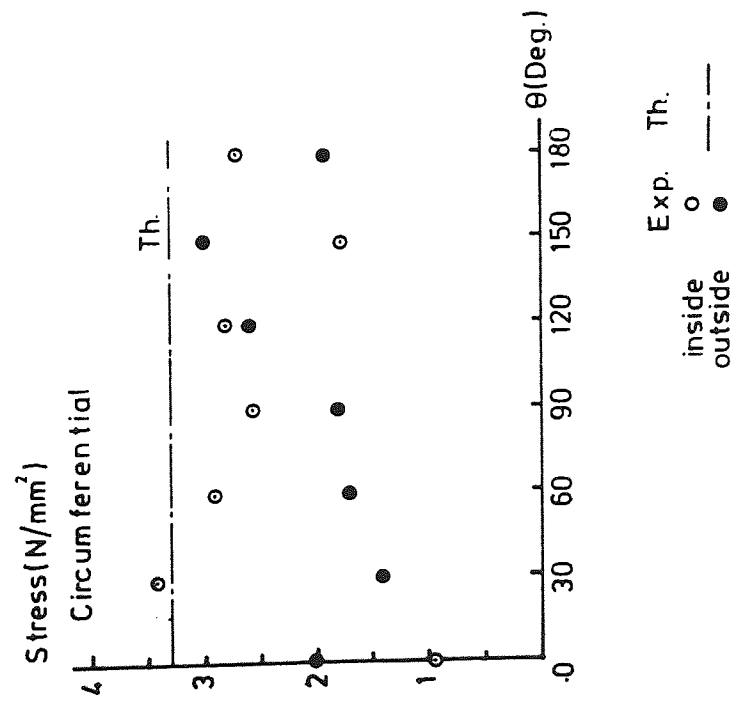


Figure (3.11b)

Membrane and local bending circumferential stresses measured on straight pipe S00A (no overlaps) under 3.5 bar internal pressure.

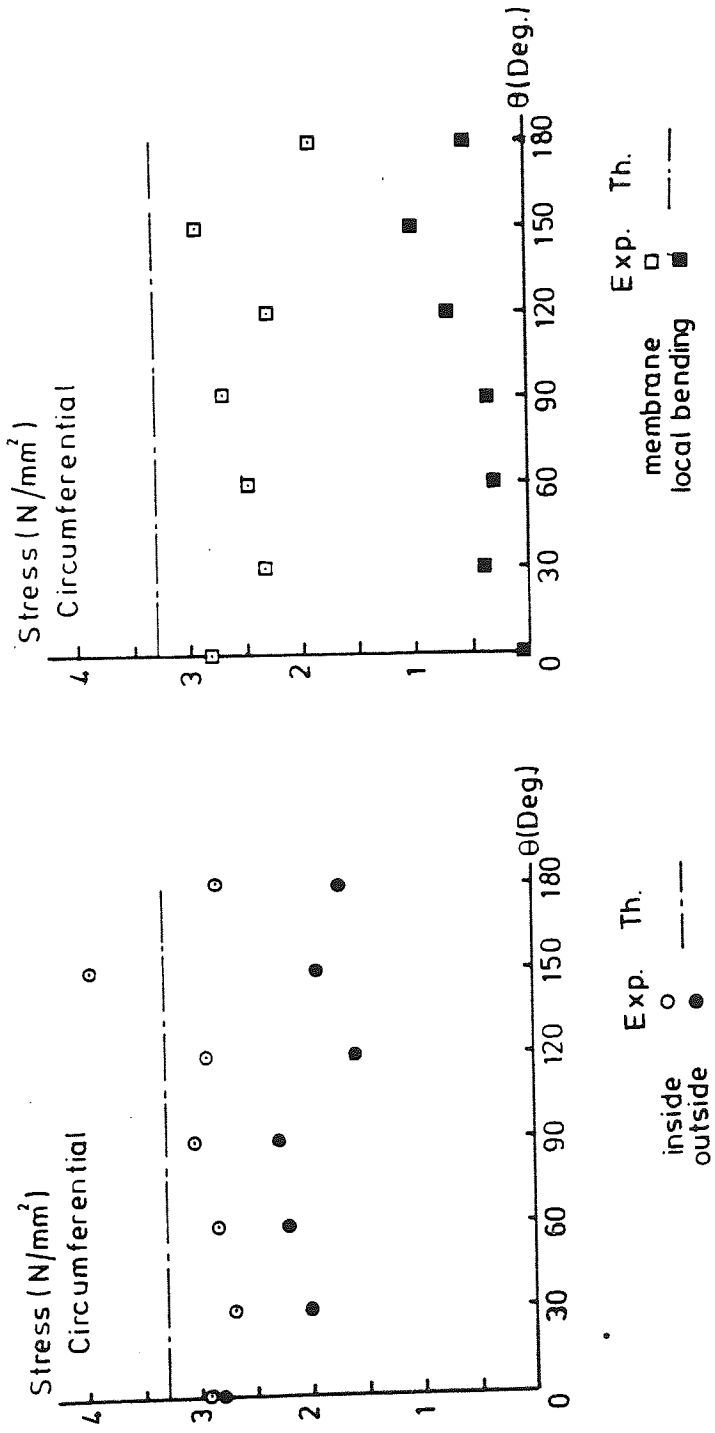


Figure (3.12a)

Inside and outside circumferential stresses measured on straight pipe S00B (machined outside surface) under 3.5 bar internal pressure.

Figure (3.12b)

Membrane and local bending stresses measured on straight pipe S00B (machined outside surface) under 3.5 bar internal pressure.

For pipe S00B (machined pipe), the level of the stress variability shown in Fig. 3.12a is relatively lower than those shown by pipe S00A. The bending stresses as shown in Fig. 3.12b are relatively uniform in comparison, suggesting that more uniform the thickness is, the less the variability or local bending stresses under pressure loading. Keeping in mind the fact that the machining process might have chopped off some of the fibre reinforcements, thus, locally affecting the mechanical properties, it could be at the least said that some improvement has been noticed by unifying the pipe wall thickness (i.e. machining the outside surfaces).

3.3.2.3 Machine made straight pipes

These are two pipes made by different automated manufacturing process. Pipe S00C made by the centrifugally casting process, and pipe S032 made by the filament winding process.

(a) Centrifugally cast pipe

Independently of the present GRP pipe program, a 250 mm nominal bore GRP straight pipe was tested. The pipe was manufactured by the centrifugal casting process and supplied by Johnston Pipes (UK). Such a method of manufacture (see article 2.5.3 of Chapter 2) produces a uniform pipe wall thickness and distribution of chopped glass content, e.g. thickness is measured was 7.02 ± 0.05 mm, and glass percentage to be 41 ± 2 .

The measured stresses in the circumferential and the longitudinal directions are determined from the measured strains and elastic constants presented in Table 3.8, using Hooke's law for orthotropic laminates as in Eq. (3.10).

$$\sigma_C = \frac{E_C}{1 - \nu_{LC}\nu_{CL}} [\nu_{LC}\epsilon_L + \epsilon_C] \quad (3.10)$$

$$\sigma_L = \frac{E_L}{1 - \nu_{LC}\nu_{CL}} [\epsilon_L + \nu_{CL}\epsilon_C]$$

and stresses were measured at different positions on the pipe as located in positions shown in Fig. 3.13. The pressure test results under 5 bar internal pressure are presented in Fig. 3.14 compared with thin shell theory prediction.

The experimentally determined stresses on the inside and the outside surfaces show minimal magnitude of local bending, and in good agreement with thin shell theory prediction. The slight stress variation shown, could be related to variation in elastic modulus, and such variation has not exceeded 10% in practical terms.

These results are of great interest because they positively isolate the thickness variability of the laminate to be the major factor contributing to local bending of a GRP pipe wall under pressure loading.

(b) Filament wound pipe

Pressure test results are presented and described for straight pipe S032 of $\pm 55^\circ$ fibre winding angle. The strains measured on both the inside and the outside surfaces are presented in Fig. 3.15a. The experimental stresses (Fig. 3.15b) were calculated using Eq. (3.10) together with the elastic constants as predicted by Tsia analysis (App. V). The results are presented as a function of the laminate contiguity factor \bar{c} suggested by Tsia⁽³¹⁾.

Experimental strains (Fig. 3.15a) are shown to be bound by theoretical predictions using $\bar{c} = 0.2$ to $\bar{c} = 1.0$, and experimental stresses (Fig. 3.15b) are closely related to thin cylinder theory using $\bar{c} = 1.0$. Similar to the results of the centrifugally cast pipe, the

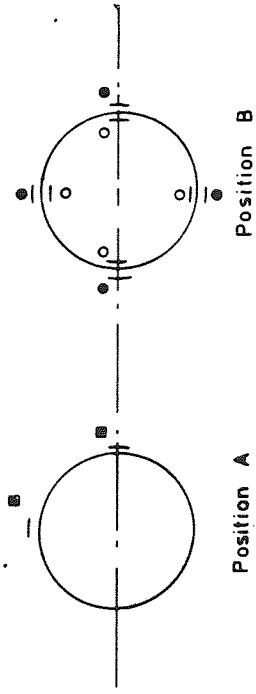
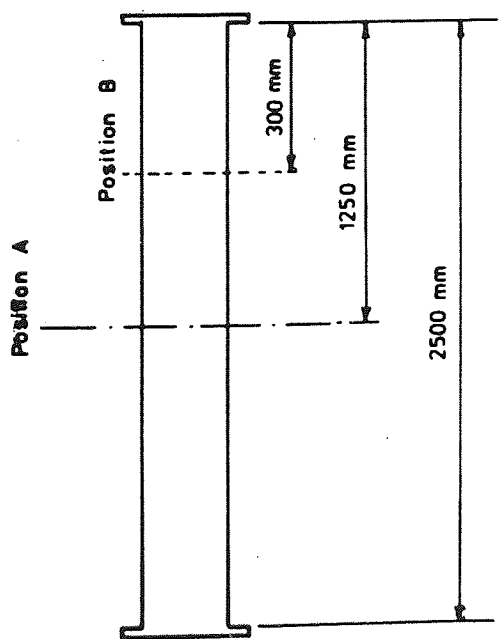


Figure (3.13)

Strain gauge positions located on centrifugally cast GRP straight pipe (SDOC).

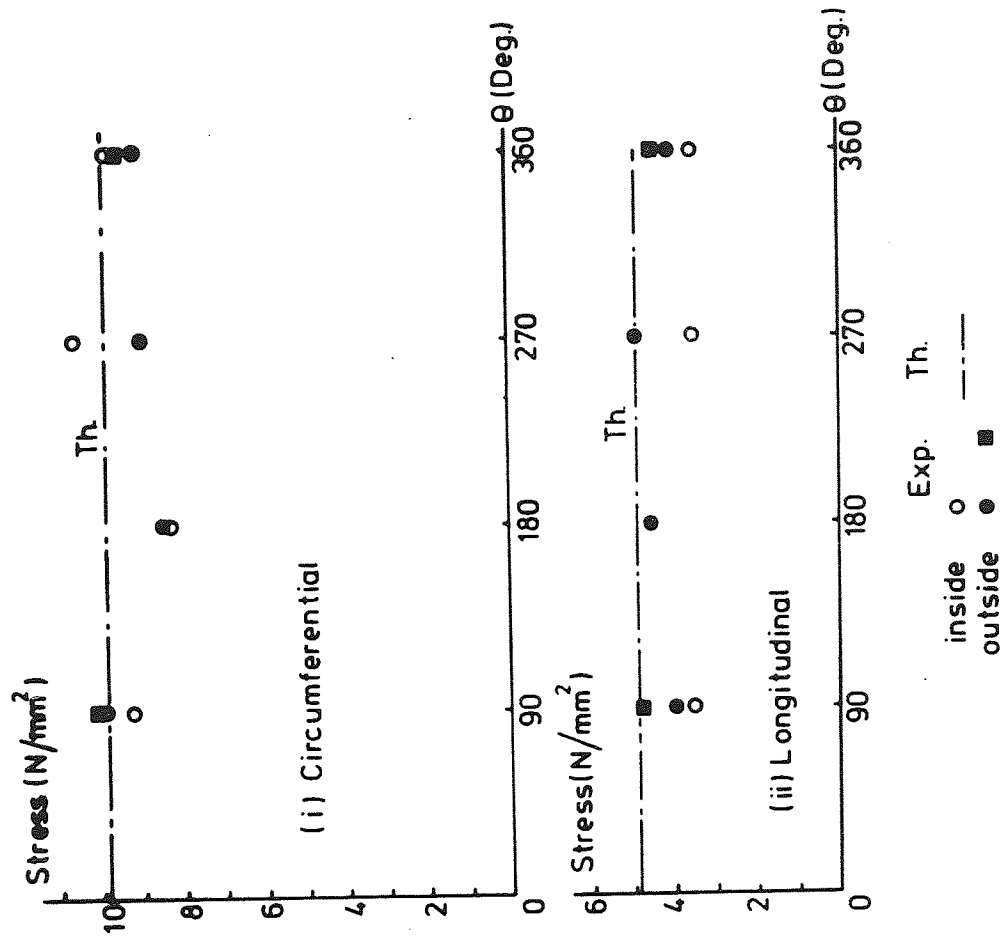


Figure (3.14)

Inside and outside stresses measured on straight pipe S00C under 5 bar internal pressure.

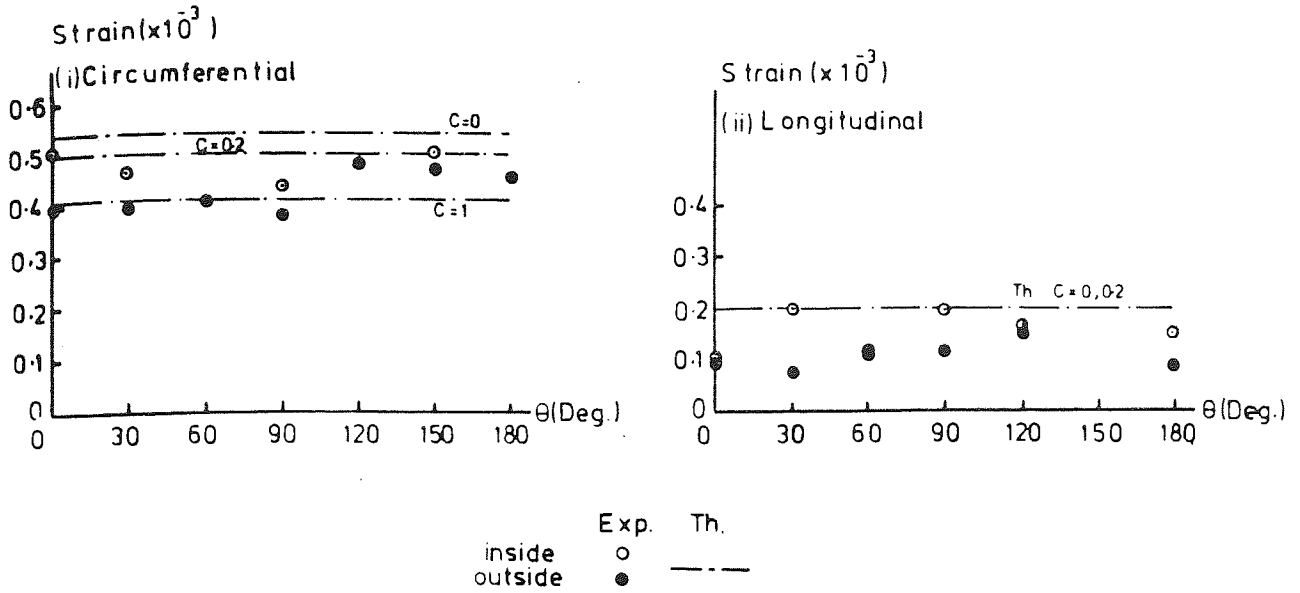


Figure (3.15a) Inside and outside strains measured on straight pipe S032 under 6 bar internal pressure.

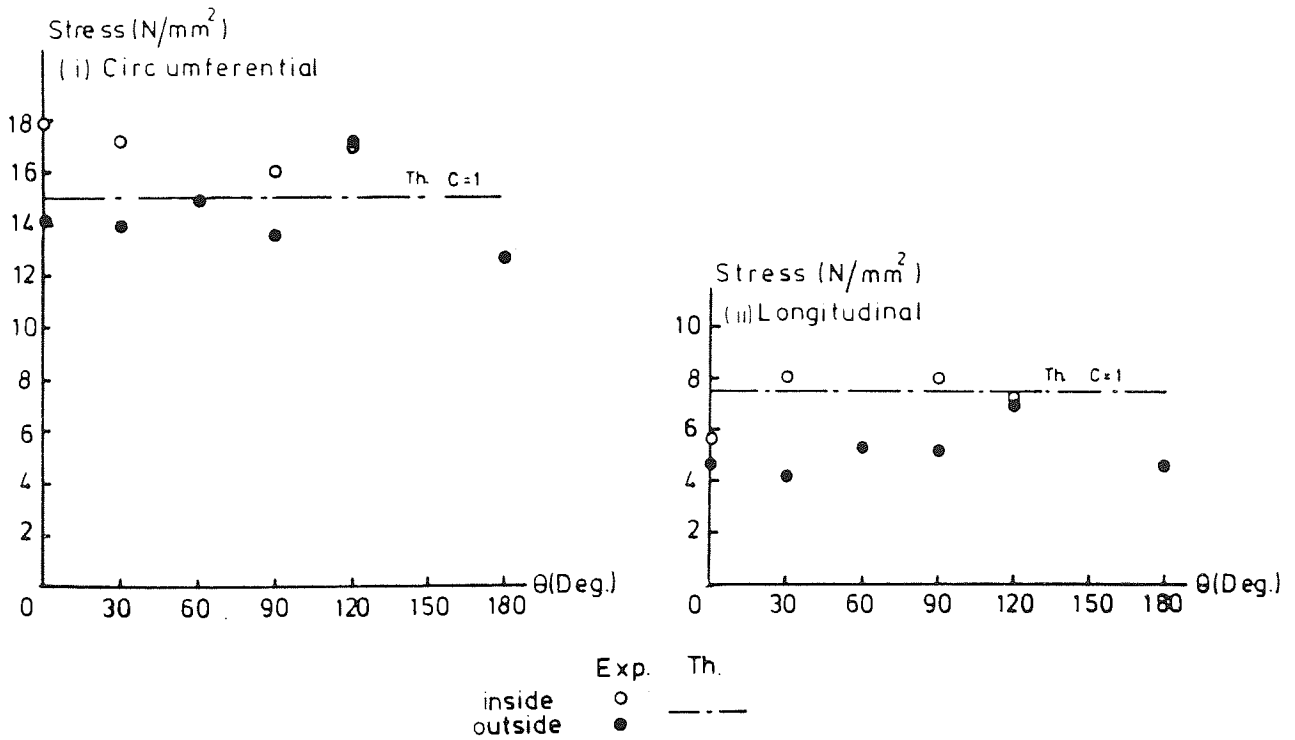


Figure (3.15 b) Inside and outside stresses measured on straight pipe S032 under 5 bar internal pressure.

uniform thickness of the FW pipe is shown to be an important factor in minimizing scatter of stresses.

3.3.3 Pressure test results of bends

Pressure test results are described and presented for smooth and mitred GRP bends. The bends as identified in Table 3.9 are of different dimensions and glass fibre reinforcements. Similar to the straight pipes test results, the experimental results are presented as measured stresses and membrane and local bending stresses using Eq. (3.9).

3.3.3.1 Hand lay-up smooth bends

Typical strains and stresses measured on such bends are shown in Fig. 3.16a,b and Fig. 3.17a,b respectively for bends S021 and S024.

Directly measured inside and outside strains (Fig. 3.16a) and stresses (Fig. 3.17a), indicate the presence of local bending strains and stresses being superimposed on top of the membrane strains and stresses induced under the pressure loading. Such observations are similar to those presented and discussed for the straight pipes made by the hand lay-up process.

By separating the measured strains and stresses into membrane and local bending strains (Fig. 3.16b) and stresses (Fig. 3.17b), a better comparability is obtained between the experimentally determined membrane component and the prediction of thin torus shell theory. The experimentally determined local bending strains and stress show random type of distribution among all the bends tested in the program. Similar results have been reported by Kitching⁽¹⁸⁵⁾ on smooth CSM bends.

The direct consequences of the presence of the local bending stresses under the pressure loading, is that, interlaminar shear stresses would develop. Their magnitude is dependent on the rate of

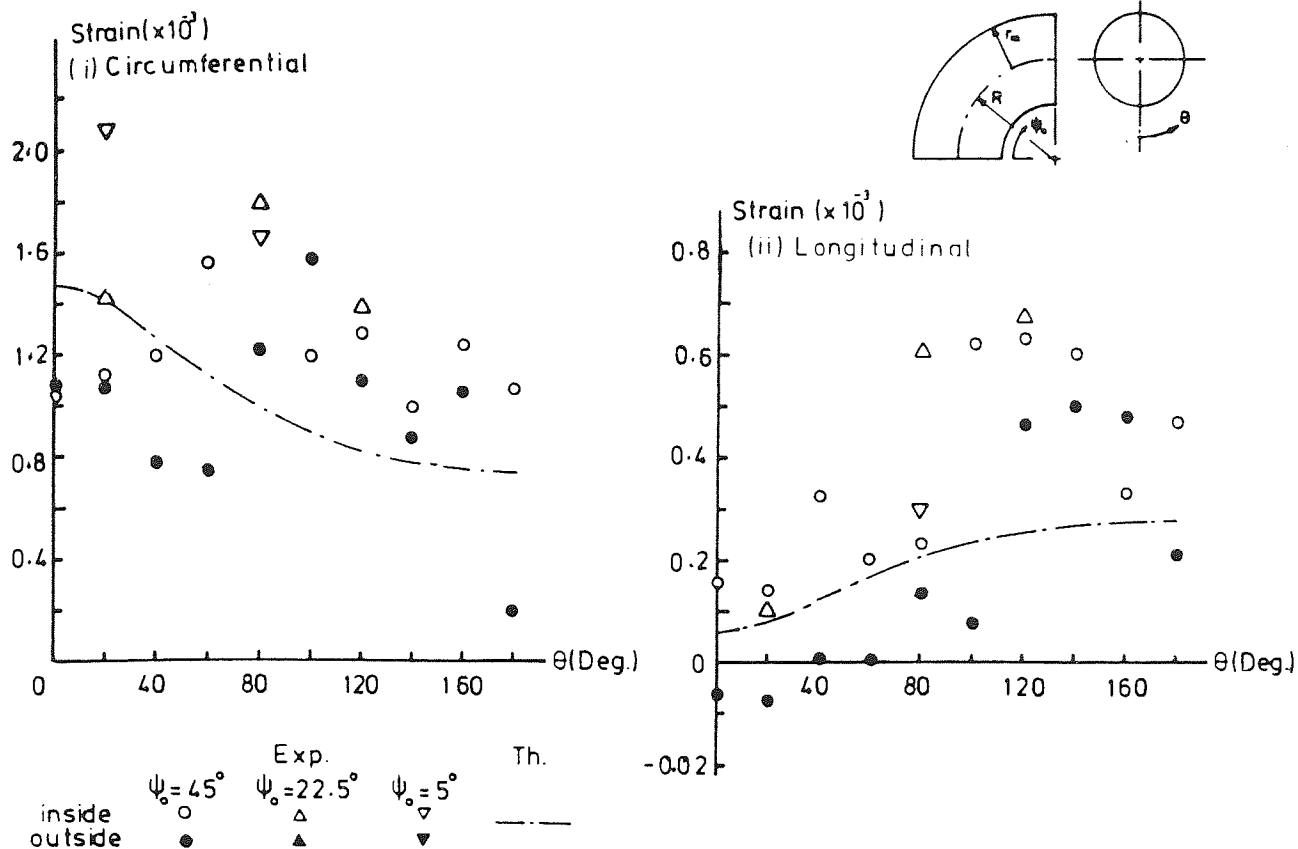


Figure (3.16a) Inside and outside strains measured on bend S021 under 4 bar internal pressure.

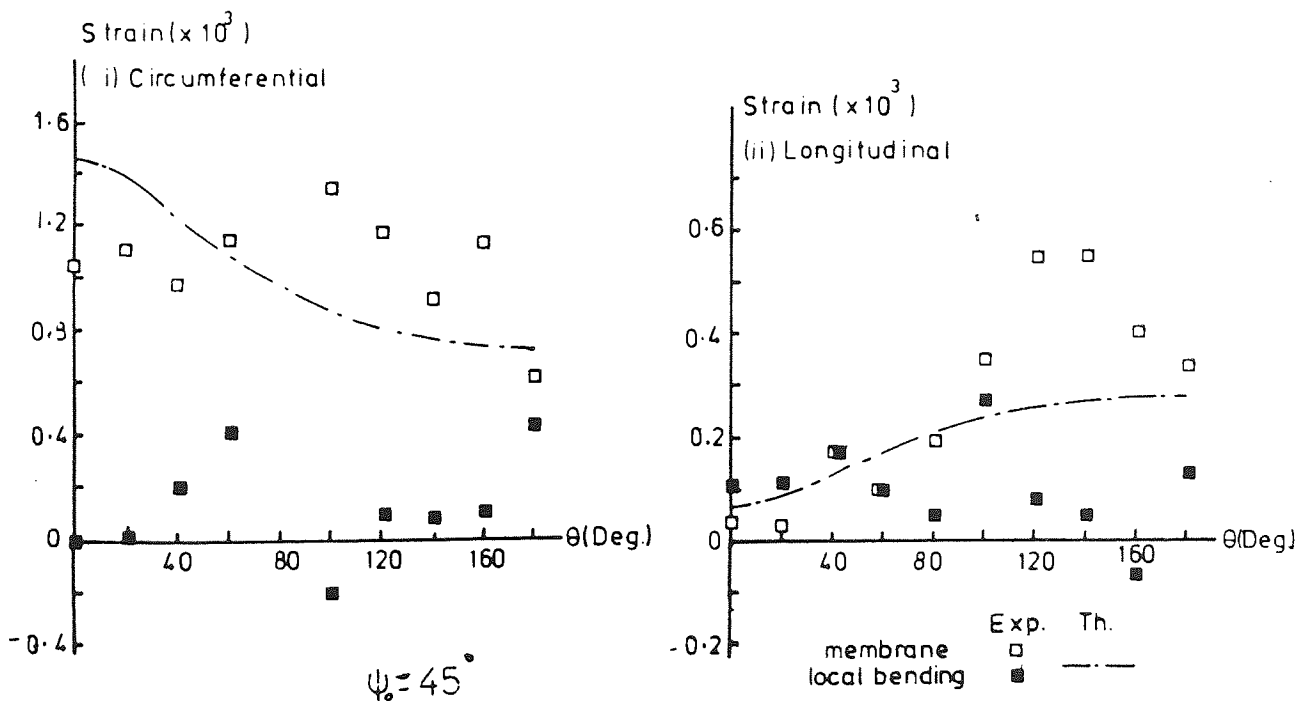


Figure (3.16b) Membrane and local bending strains measured on bend S021 under 4 bar internal pressure.

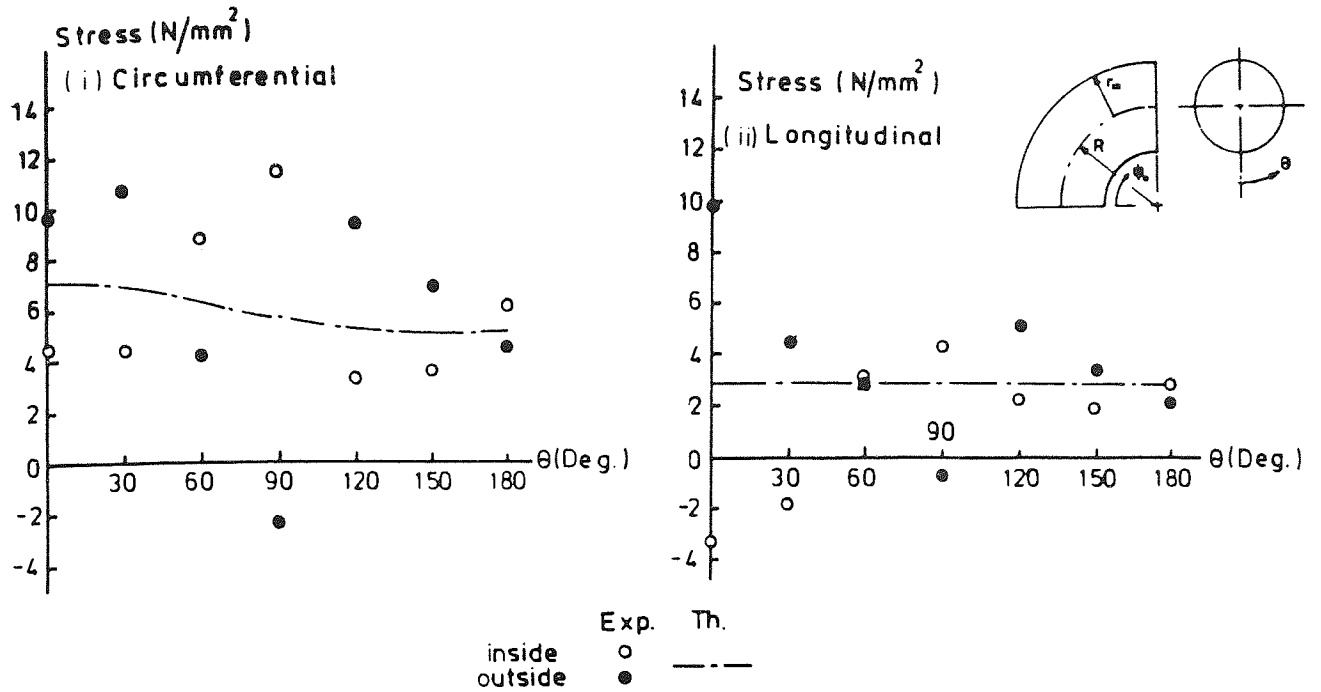


Figure (3.17a) Inside and outside stresses measured on bend S024 under 6 bar internal pressure.

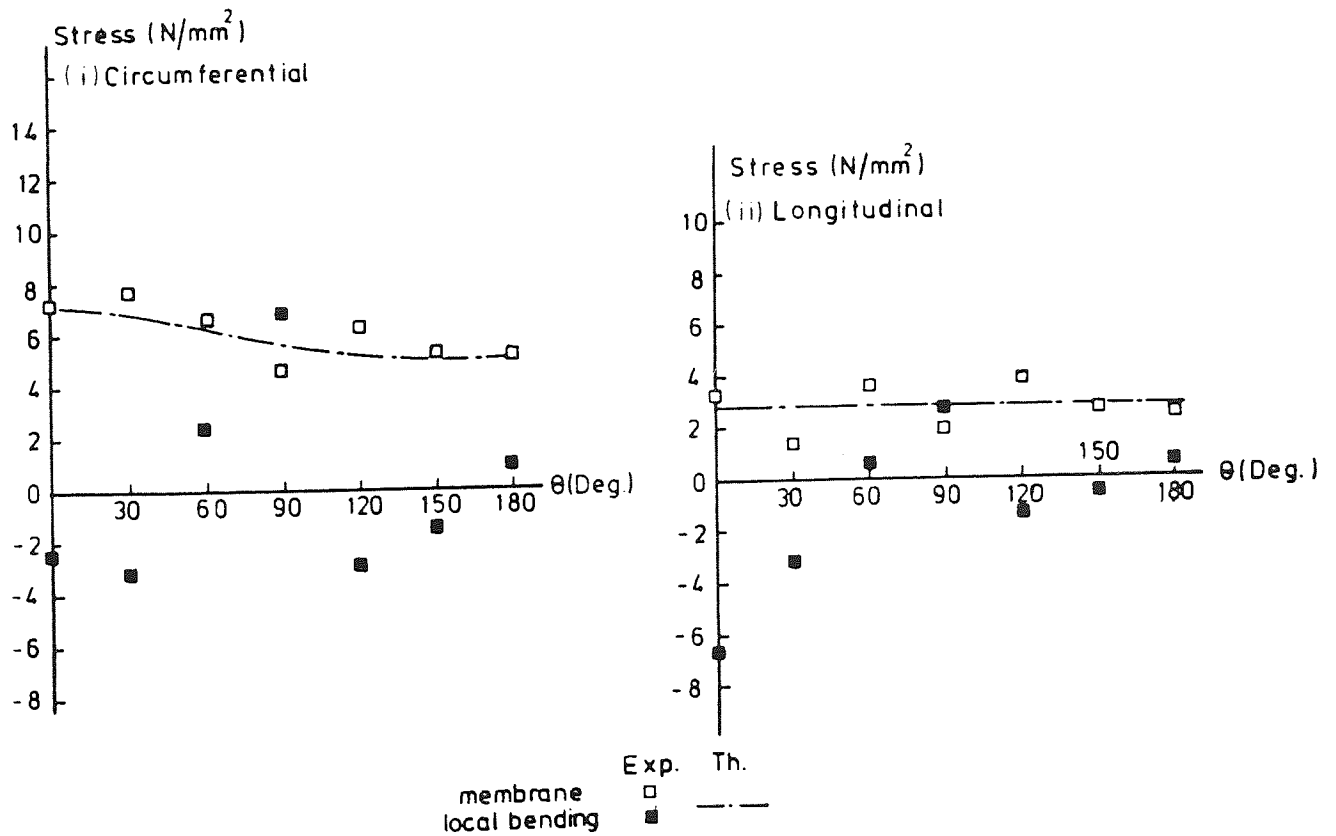


Figure (3.17b) Membrane and local bending stresses measured on bend S024 under 6 bar internal pressure.

change of the local bending stress per unit length (either the circumferential or the longitudinal). Such a relation could be described mathematically, with the aid of Fig. 3.18, as follows:

$$v = \frac{d(M_b)}{ds} ; \quad ds = rd\theta$$

now $\sigma_b = \frac{6M_b}{t^2}$ and $\tau = 1.5 \frac{v}{t}$ (3.11)

$\therefore \tau = \frac{t}{4} \frac{d\sigma_b}{ds}$

3.3.3.2 Hand lay-up mitred bends

Strain measurements were taken on mitred bends on positions indicated in Fig. 3.19. The experimental results in the form of longitudinal and circumferential strains are presented in Fig. 3.20a,b,c for bend S034 (200 mm nominal bore), and in Fig. 3.21a,b,c for bend S060 (600 mm nominal bore). Experimental results are presented in comparison with Owen and Emmerson theoretical analysis⁽¹⁶⁷⁾.

The strains measured on the inside and the outside surfaces at the segment-centre as shown in Figs. 3.20a and 3.21a, do indicate the presence of a local bending strain component similarly described before. When measured strains are presented as membrane and local bending strains as shown in Figs. 3.20b and 3.21b, then membrane strains are seen to be comparable with theoretical prediction assuming thin cylinder.

The flexural type of strains measured at the segment-edge as shown in Fig. 3.20c and 3.21c compare reasonably in pattern of distribution with Owen and Emmerson theoretical analysis⁽¹⁶⁷⁾. The negligible magnitude of the longitudinal strains measured at the intrados ($\theta = 0^\circ$), is possibly due to the extra thickening located at that position. Local thickening of the intrados has been experimentally investigated by Ingerhouze⁽¹⁷⁸⁾ with similar effects on strain levels.

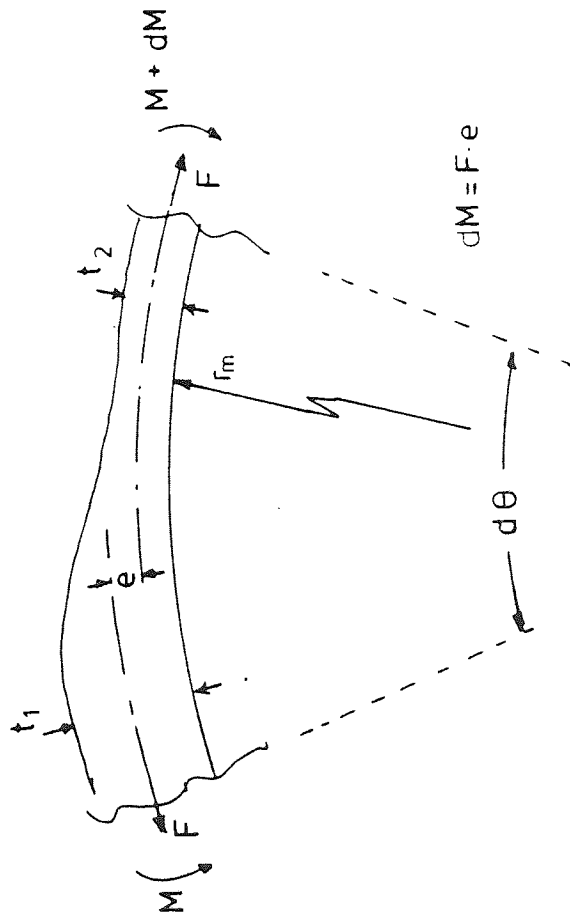
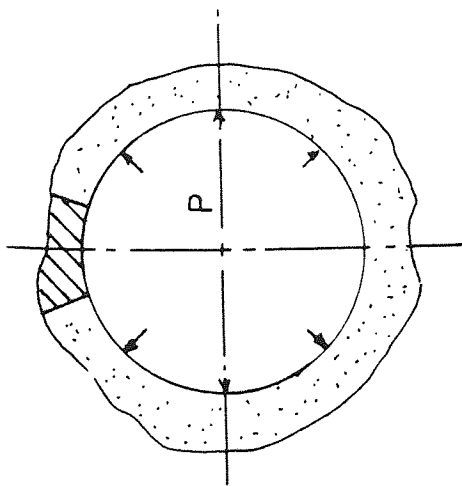


Figure (3.18) Diagrammatic representation of the effect of thickness variation and how it is related to local bending stresses induced in a pipe under pressure.

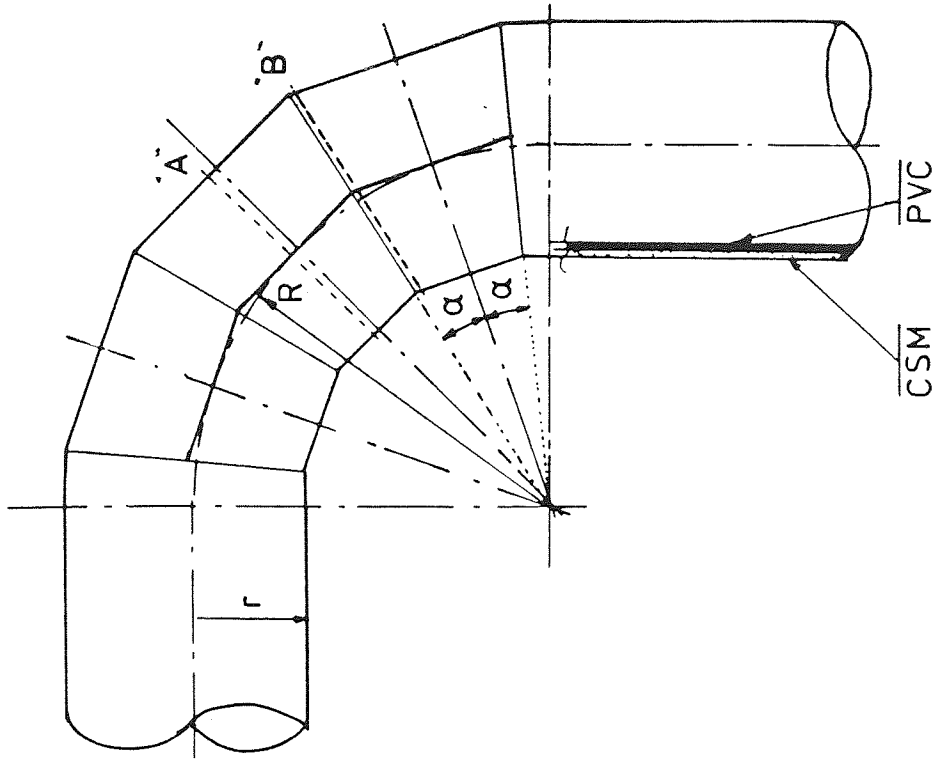


Figure (3.19) Strain gauge positions located on mitred bends.

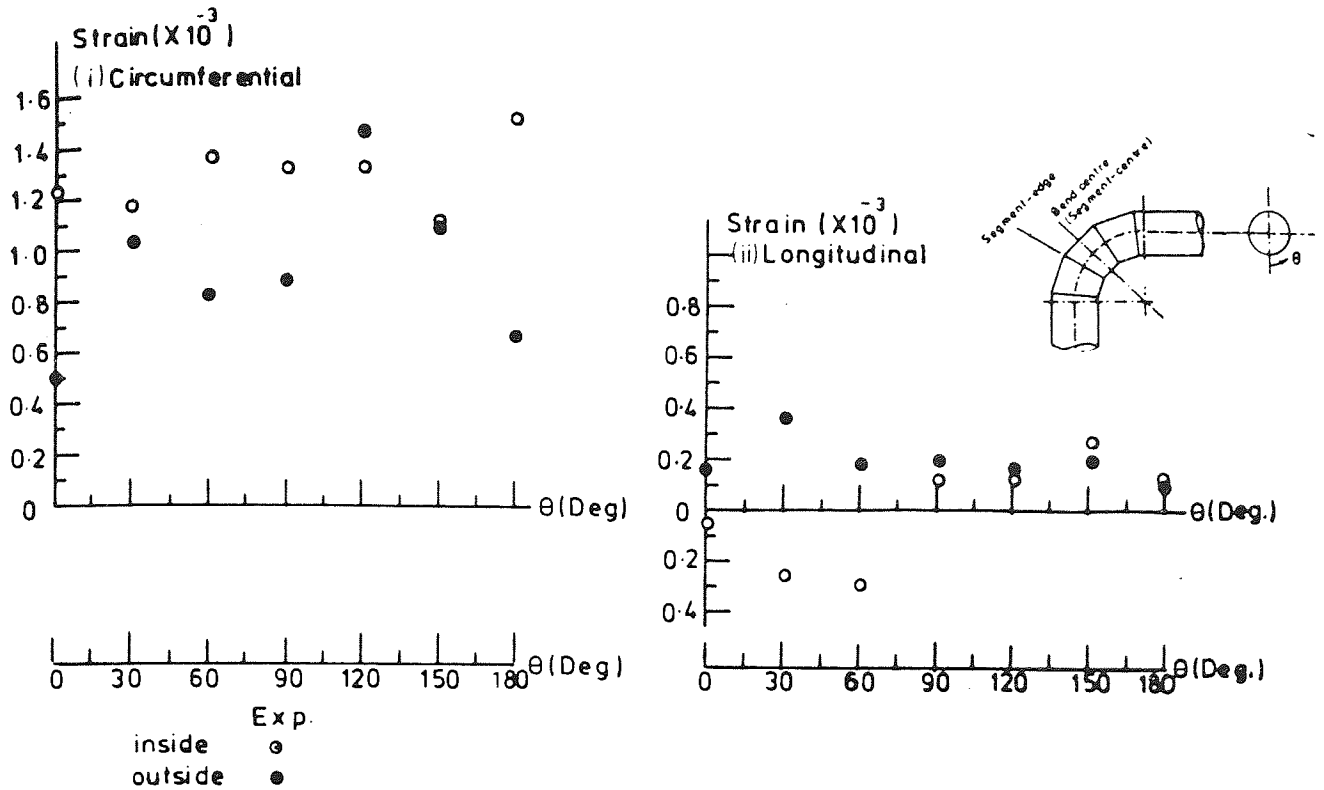


Figure (3.20a) Inside and outside strains measured on bend S034 at the segment-centre under 6 bar internal pressure.

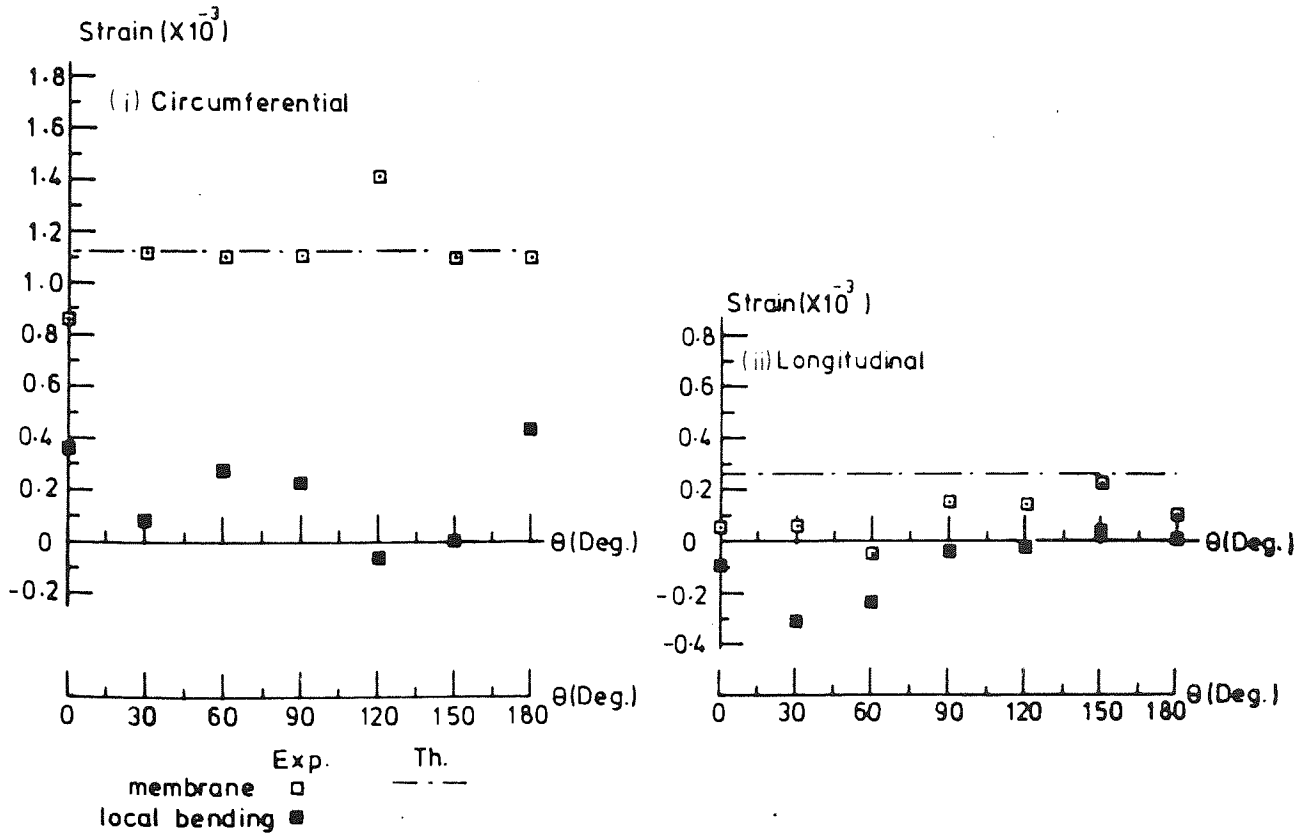


Figure (3.20b) Membrane and local bending strains measured on bend S034 at the segment-centre under 6 bar internal pressure.

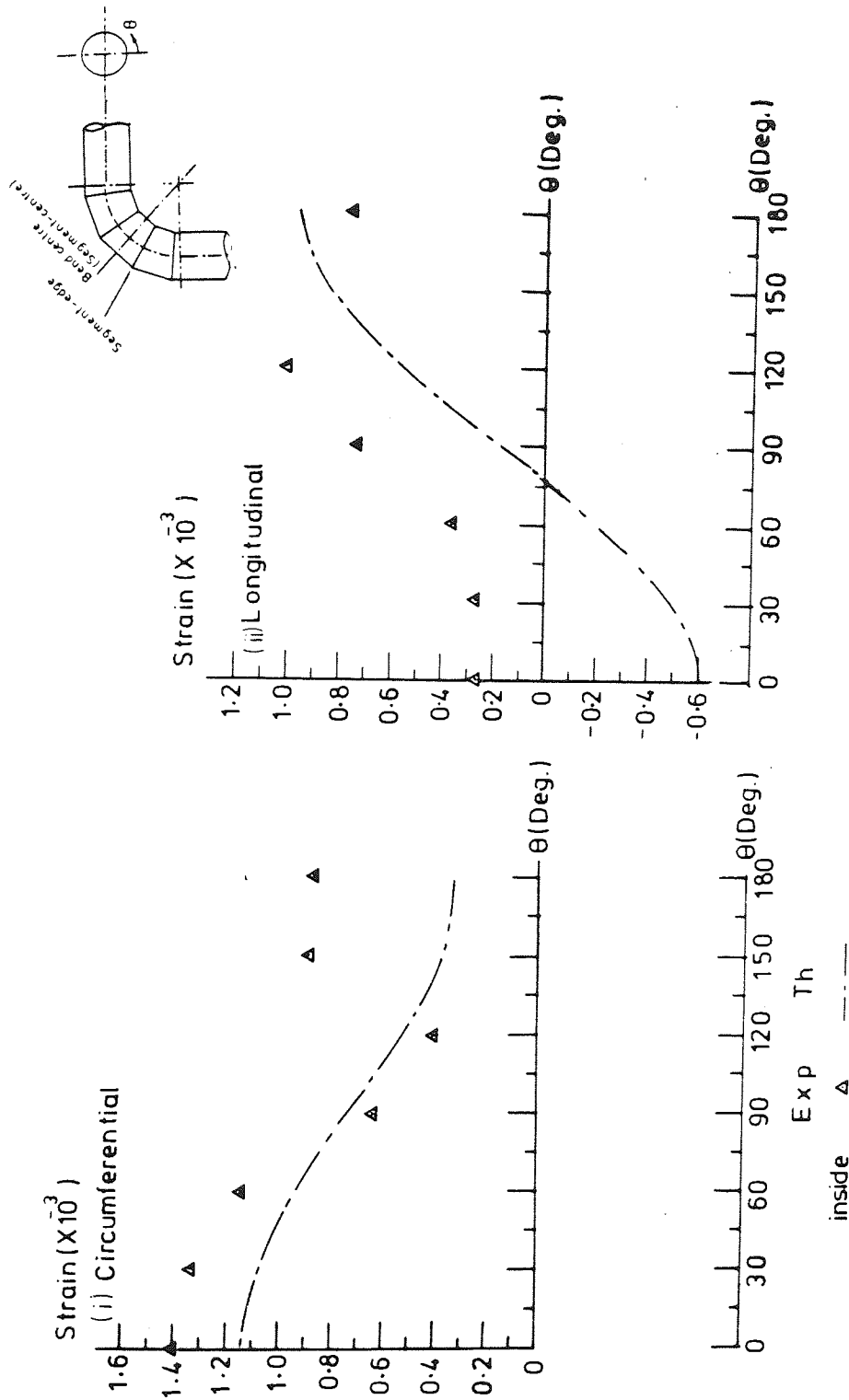


Figure (3.20c) Inside strains measured on bend S034 at the segment-edge under 6 bar internal pressure.

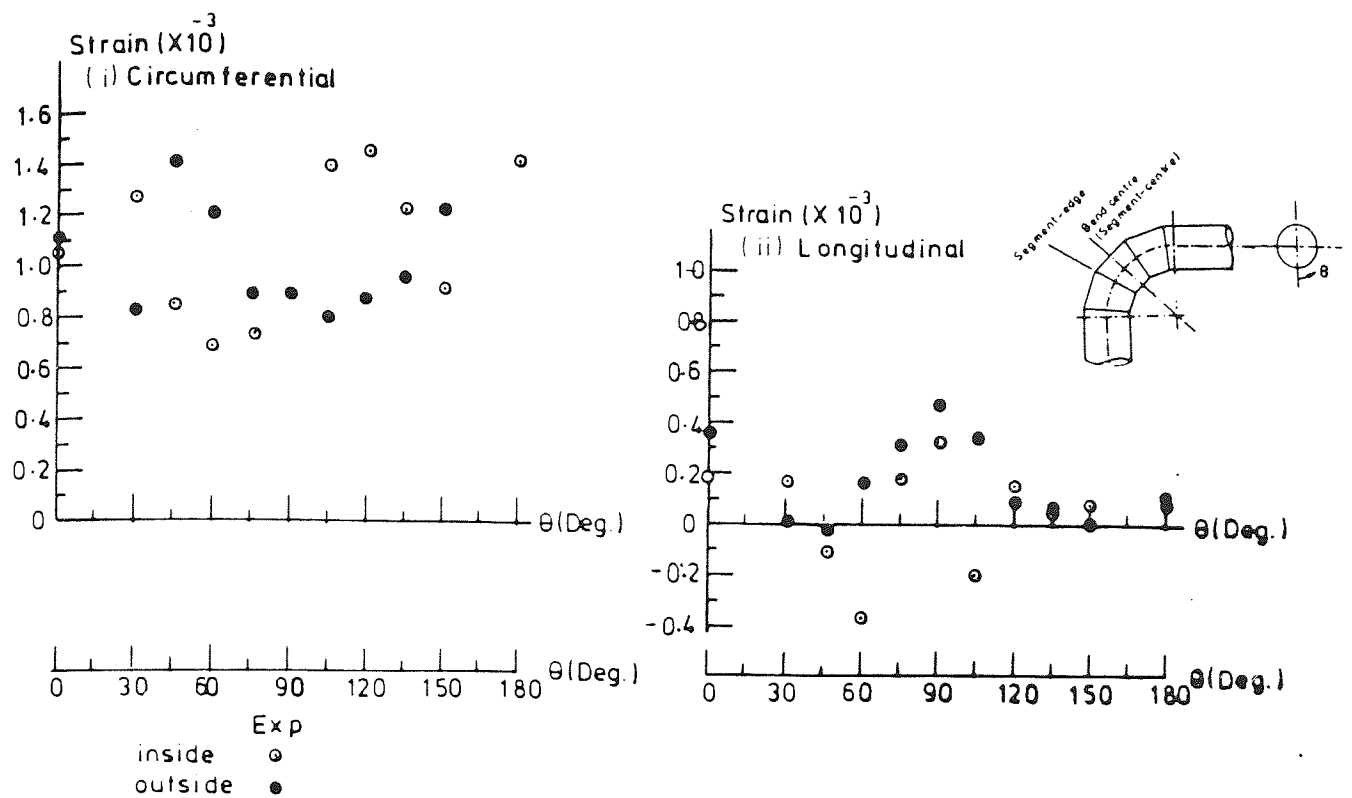


Figure (3.21a) Inside and outside strains measured on bend S060 at the segment-centre under 2 bar internal pressure.

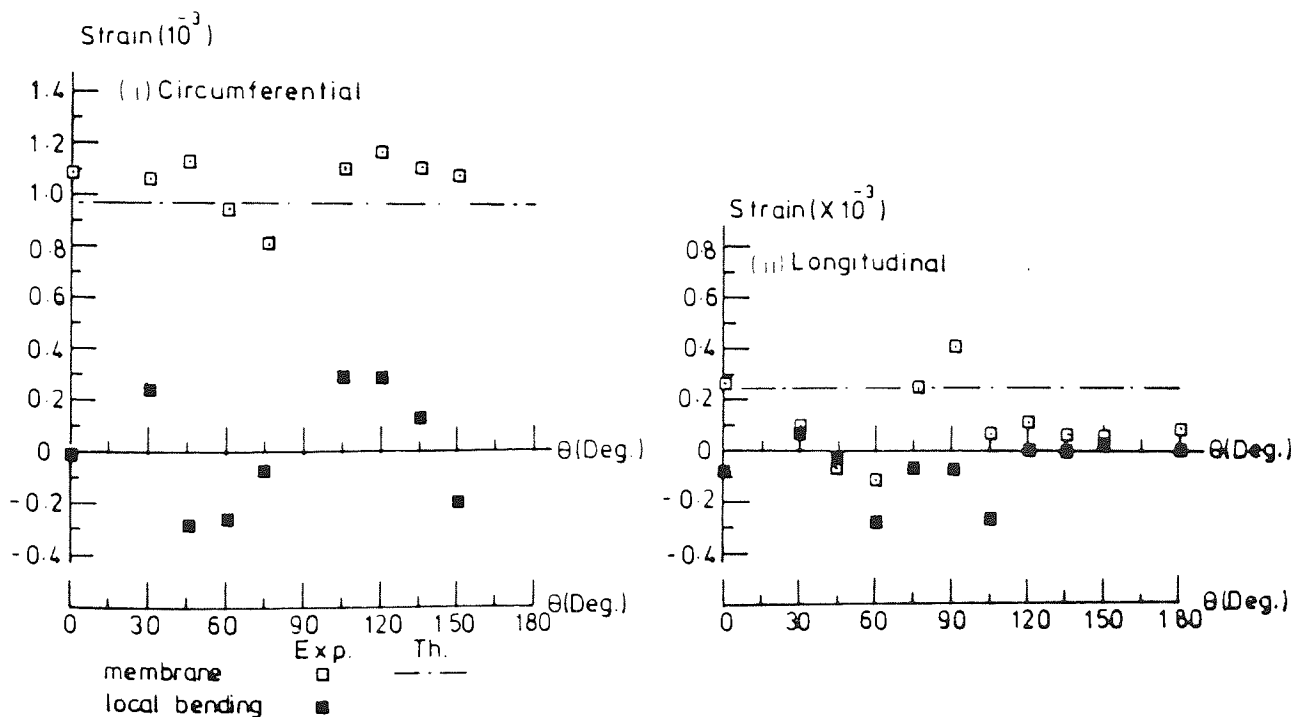


Figure (3.21b) Membrane and local bending strains measured on bend S060 at the segment-centre under 2 bar internal pressure.

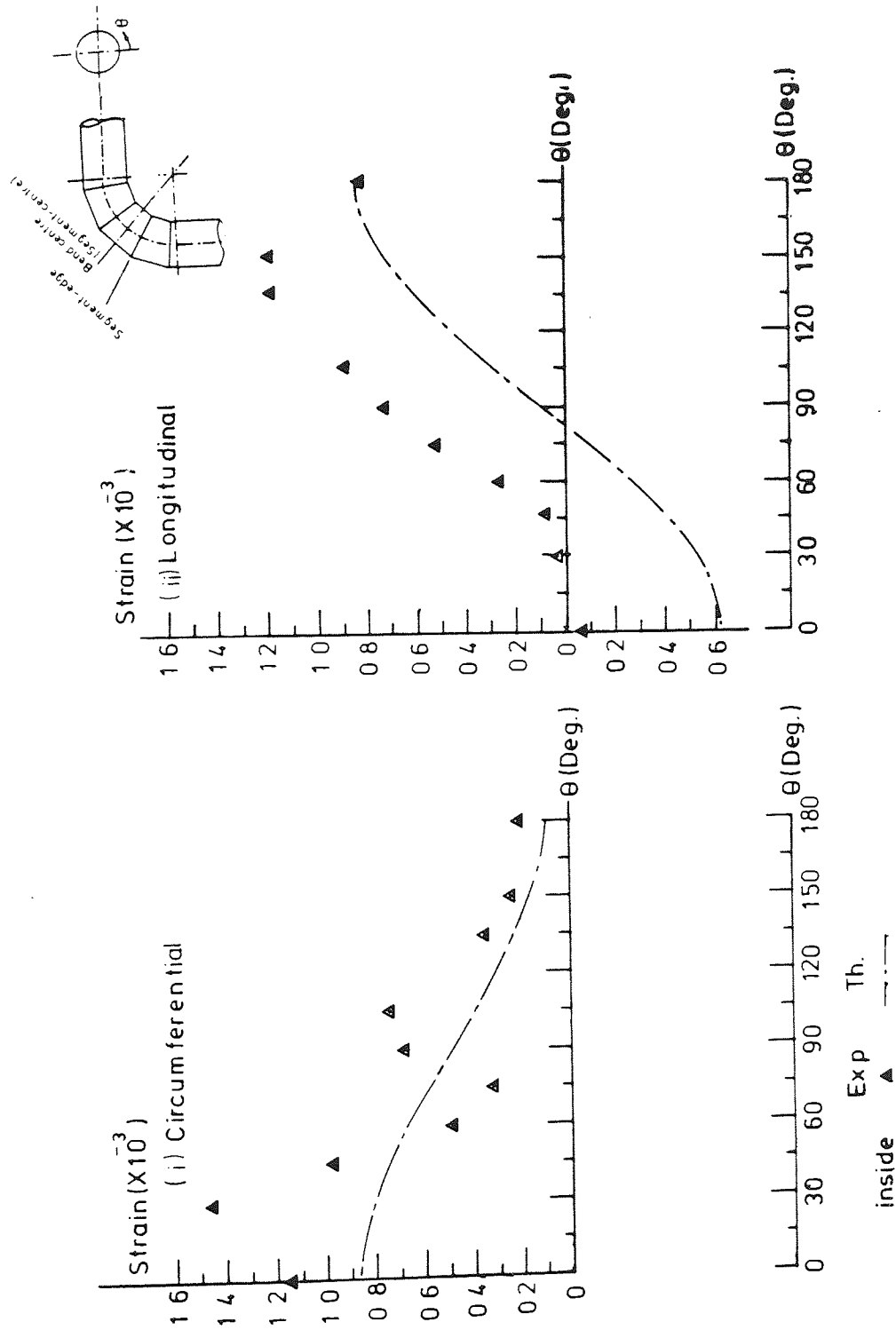


Figure (3.21c) Inside strains measured on bend S060 at the segment-edge under 2 bar internal pressure.

For bend S060, similar patterns of the inside circumferential strain distributions are observed at the segment-edge (Fig. 3.21c) and at the segment-centre (Fig. 3.21a). This is particularly identified by the peak strains located at positions $\theta = 30^\circ$ and $\theta = 105^\circ$. What is believed to be a decay of strains from the segment-edge to the segment centre, is probably due to the relatively short length of the segment in comparison to the pipe diameter. Decay of flexural stresses induced at the segment-edge has been similarly reported for metallic mitred bends by Lane and Rose⁽¹⁶⁶⁾.

3.3.4 Failure of hand lay-up straight pipe and bend

Straight pipe S004 (100 mm nominal bore) of Table 3.8 and bend S022 (250 mm nominal bore) of Table 3.9 have been taken to failure under closed-ended pressure loading. Both pipe components showed signs of shear failures, although it is believed that failure has been initiated by inside gel coat cracking.

The shape of failure obtained by pipe S004 is shown in Fig. 3.22. Failure started in the form of water droplets at 650 psi (45 bar) and later developed into jets at 780 psi (54 bars), and the pressure could no longer be held. Maximum circumferential stress at failure was found by extrapolation to be 83 N.mm^{-2} . The shape of failure shown in Fig. 3.22 clearly indicate an interlaminar shear failure where whitening suggest that the laminate has been split into two layers. Membrane cracks were observed on the inside gel coat running in the longitudinal direction. The total area of delamination is about 30 mm wide and 200 mm long.

During pressurising bend S022, one end flange started to leak at the flange/tangent joint at 350 psi (24 bar). The joint was repaired using WR layers. On re-pressurisation, the same



Figure (3.22) Picture showing failure envelope in the form of delamination developed on straight pipe S004 under 53 bar internal pressure.

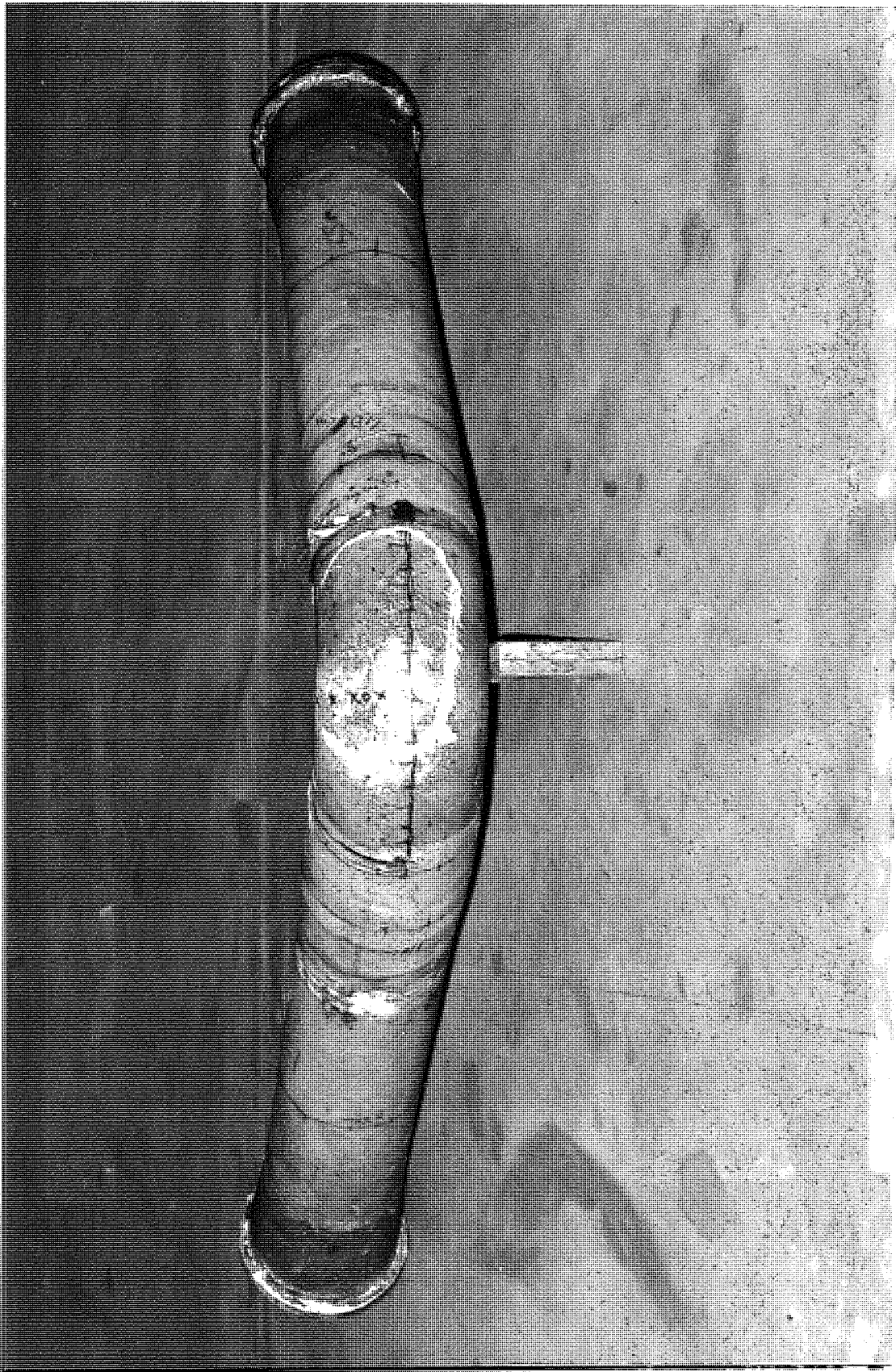


Figure (3-23a) Picture showing location of failure developed on bend S022 under 27.6 bar internal pressure.



Figure (3.23b) Picture showing the detail of intensive resin cracking and fibre breakage of bend S022.



Figure (3.23c) Picture showing wall laminate splitting of bend
S022.

flange joint started to leak this time at 400 psi, the bend was de-pressurised and both end flanges were similarly reinforced. Third time pressurisation, a flap envelope failure was developed at the centre of the bend at 400 psi (28 bar), and failure is shown in Fig. 3.23a. On inspection the failure area, cracks were shown to be induced on the inside gel coat running approximately in the circumferential direction as shown in Fig. 3.23b, and an interlaminar split of the laminate as shown in Fig. 3.23c. The laminate split seems to be running through an area of rich resin, probably of different degree of cure to the rest of the wall laminate. The maximum circumferential stress at failure is estimated to be 85 N.mm^{-2} .

Final failure configuration observed on both the straight pipe (Fig. 3.22) and bend component (Fig. 3.23c) suggest a dominant role of the interlaminar shear stresses in either initiating failure or accelerating failures already initiated by membrane cracks. It is important, at this stage, to perhaps link the observed local bending stresses already described and discussed in the previous articles with the present shear failures. Such a relation could be associated with the fact that the occurrence of a variable bending moment, imposed on a structure would lead to shear forces.

3.3.5 Pressure stress multiplier (PSM)

The bends pressure test results could be summarised in the form of PSM, where the maximum membrane stresses induced in the bend is taken as a ratio to the circumferential stress calculated for a straight pipe using similar dimensions, i.e.

$$\text{PSM} = \frac{\text{max. membrane stress measured on the bend}}{pr_m/t} \quad (3.12)$$

the bends' PSM are presented in Table 3.10 as a function of their angular positions. They are compared with theoretical PSM as calculated from pressure theories in App. IV. The PSM for the mitred bends are based on the average thickness measured at the segment-edge and at the straight tangent.

TABLE 3.10 - Pressure stress multiplier of GRP bends

| Bend Number | Pressure stress multiplier (PSM) | | | |
|-------------|--------------------------------------|------------------------------------|--------------------------------------|----------------------------------|
| | Exp. | | Th. | |
| | PSM | θ (Deg.) | PSM | θ (Deg.) |
| S021 | 1.48 | 90 | 1.51 | 0 |
| S024 | 1.42 | 30 | 1.27 | 0 |
| S002 | 1.51 | 60 | 1.11 | 0 |
| S014 | 1.40 | 40 | 1.15 | 0 |
| S016 | 0.90 | 0 | 1.15 | 0 |
| S034 | 1.88 ^c /1.37 ^L | 0 ^c /150 ^L | 1.21 ^c /1.34 ^L | 0 ^c /180 ^L |
| S060 | 2.86 ^c /2.55 ^L | 30 ^c /135 ^L | 1.31 ^c /1.72 ^L | 0 ^c /180 ^L |
| S061 | 2.62 ^c /3.00 ^L | 105 ^c /150 ^L | 1.31 ^c /1.72 ^L | 0 ^c /180 ^L |
| S043 | 1.90 | 120 | 1.30 | 0 |
| S048 | 1.08 | 60 | 1.38 | 0 |
| S049 | 1.32 | 30 | 1.38 | 0 |
| S046 | 0.77 | 120 | 1.62 | 0 |

L = longitudinal measured at the joint
c = circumferential measured at the joint

CHAPTER FOUR

REVIEW OF BEND THEORY

4.1 Simple Beam Theory

When a straight pipe is subjected to a flexural bending moment, then the relative change of slope per unit length $\frac{\Delta\psi_0}{\Delta s}$ is

$$\frac{\Delta\psi_0}{\Delta s} = \frac{M}{EI} \quad (4.1a)$$

and the maximum longitudinal stress is

$$\sigma = \frac{Mr_m}{I} \quad (4.1b)$$

where EI is the flexural rigidity, M is the bending moment; and r_m is the mean radius of the pipe, and I is the second moment of area.

When the pipe is subjected to torsional moment, then the relative change of twist angle per unit length $\frac{\Delta\bar{\beta}}{\Delta s}$ is

$$\frac{\Delta\bar{\beta}}{\Delta s} = \frac{T}{GJ} \quad (4.2a)$$

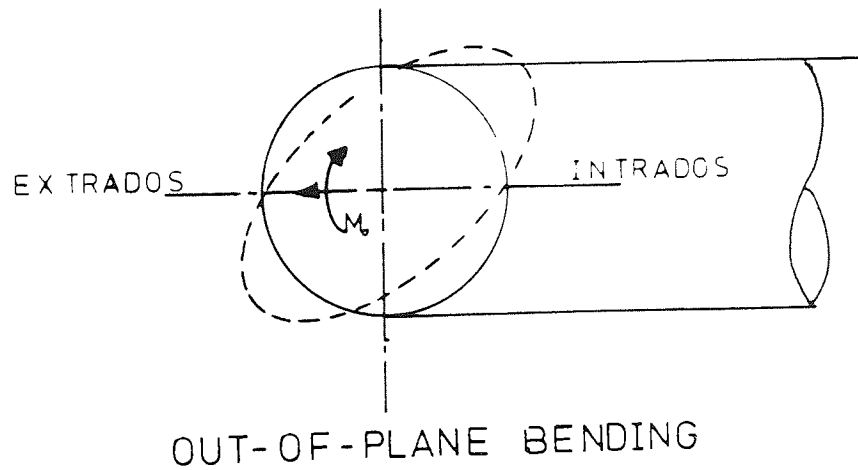
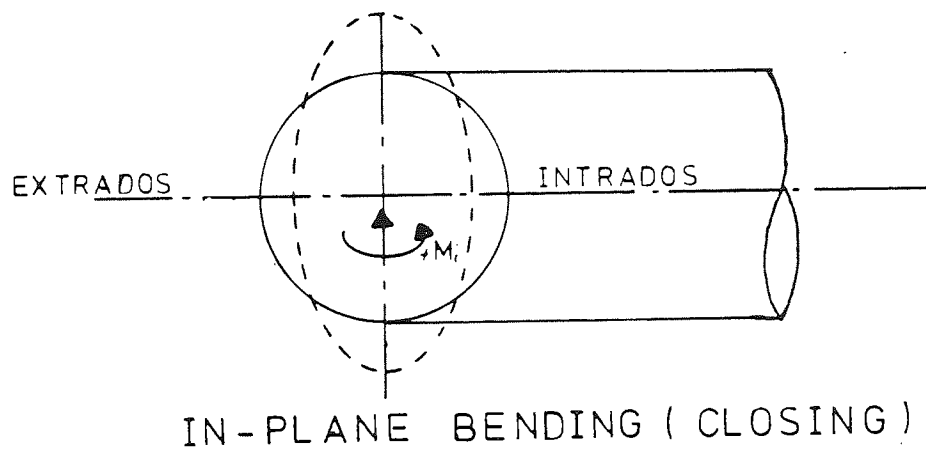
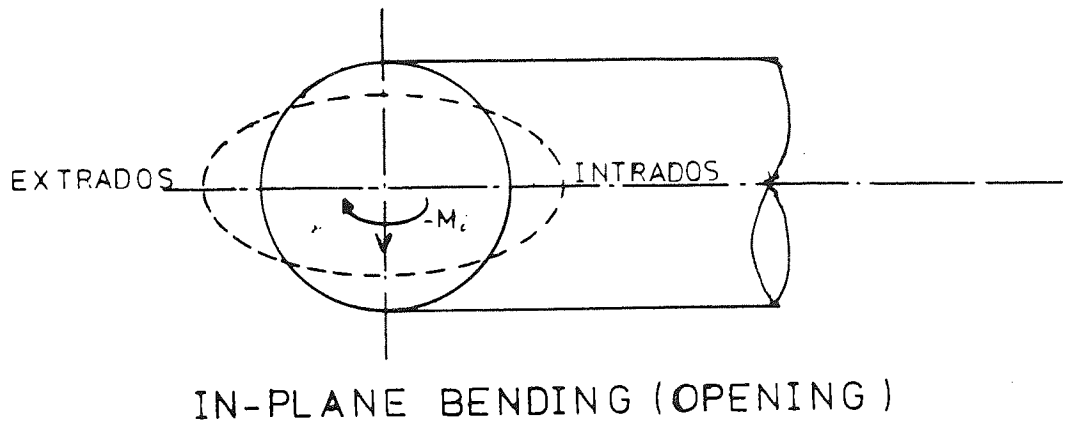
where T is the torsional moment, and GJ is the torsional rigidity.

The maximum shear stress τ occurring at the outer surface of the pipe is given by:

$$\tau = \frac{Tr_o}{J} \quad (4.2b)$$

4.2 Loading of Bends

Bends tend to behave differently from straight pipes whereby they ovalize when loaded with different modes of bending moments as demonstrated diagrammatically in Fig. 4.1. Such ovalization tends to increase the angular rotation $\frac{\Delta\psi_0}{\Delta s}$ of the bend compared with a straight of the same construction and under the same bending moment. This brings about added flexibility but also gives rise to a complication of the stress system, where, the maximum stress is greater than that predicted by simple bending theory. The longitudinal direct stresses



Figure(4.1) Diagrammatic representation of bend cross-sectional distortion under In-plane & Out-of-plane bending moments.

are not distributed linearly across the section and since the maximum does not occur at the intrados or the extrados, it is different from that for simple bending. Circumferential stresses will be induced due to the bending of the shell when the section is flattened. The overall maximum stress may be either longitudinal or circumferential, depending on the dimensions of the pipe bend. Typical bend deformation and stress distribution are shown in Fig. 4.2.

When pipe bends are being discussed and compared, two useful quantities arise as a result of these physical facts. They are the flexibility factor (K) of a bend and the stress intensification factor (SIF), defined as follows:

$$K = \frac{\text{Flexural rigidity of straight length of pipe calculated by simple bending theory (EI)}}{\text{Flexural rigidity of similar length of pipe forming pipe bend}} \quad (4.3)$$

$$\text{SIF} = \frac{\text{Maximum stress in pipe bend due to applied moment}}{\text{Maximum stress in similar straight pipe calculated by simple bending theory}} \quad (4.4)$$

or

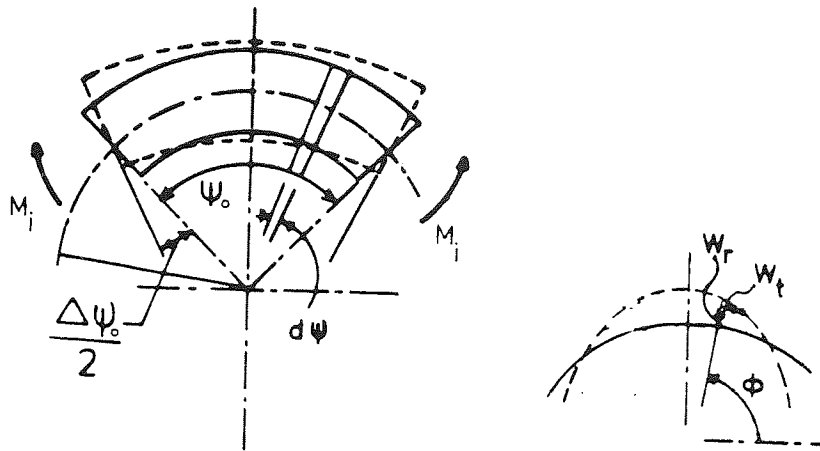
$$\frac{\Delta\psi_0}{dS} = \frac{KM}{EI} \quad K > 1 \quad (4.4a)$$

$$\sigma_{\text{longitudinal}} = (\text{SIF})_L \frac{Mr_m}{I} \quad (4.4b)$$

$$\sigma_{\text{circumferential}} = (\text{SIF})_C \frac{Mr_m}{I} \quad (4.4c)$$

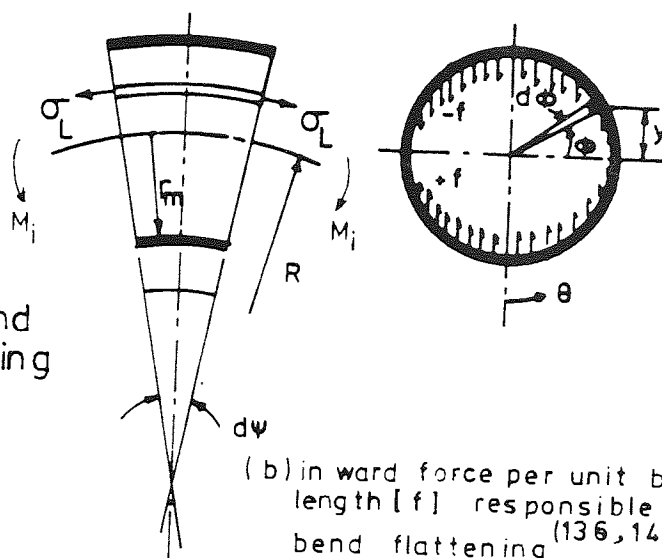
where $(\text{SIF})_C$, and $(\text{SIF})_L$ are the circumferential SIF and the longitudinal SIF respectively. All three factors depend considerably on a non-dimensional quantity ($\lambda = Rt/r_m^2$) known as the pipe factor.

Though more complex in detail, the overall behaviour of a multi-mitred bend is similar to that of a smooth bend, since flattening of a pipe section forming the bend again occurs under flexural bending moment. The definitions of K and SIF are, therefore, applicable to multi-mitred bends where maximum stresses occur near the junctions between the segments of a mitre.

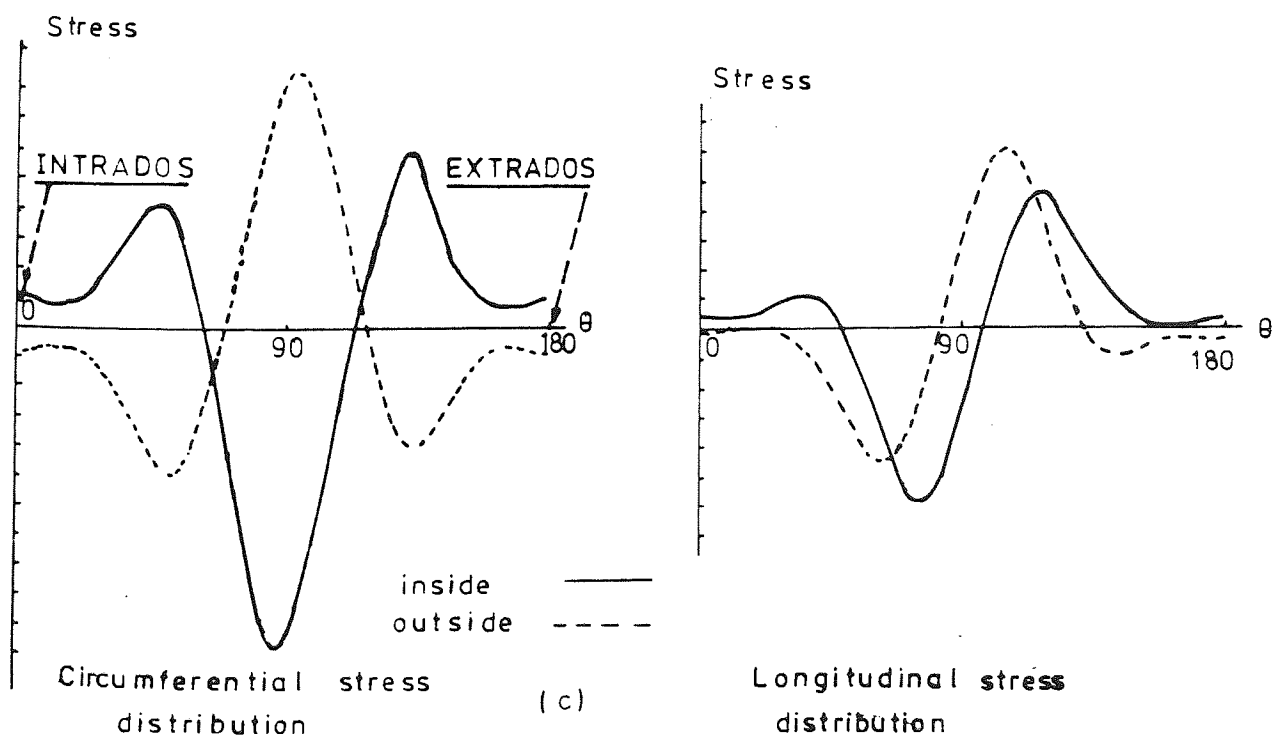


(a) Bend cross sectional distortion

Figure (4.2)
Deformation of a bend under in plane Bending moment



(b) in ward force per unit bend length [f] responsible for bend flattening (136,145)



Under the effect of changes in temperature of the pipeline, or of movement of support reaction (either translation or rotation), or both, the determination of the stresses distribution in a pipe becomes a statically undeterminate problem. In general the problem may be solved by the modification of the standard arch theory.

$$\begin{bmatrix} \Delta_x \\ \Delta_y \\ \Delta_z \end{bmatrix} = \begin{bmatrix} \text{Function of the dimensional, the mechanical properties of the piping components and flexibility factors} \end{bmatrix} \quad \& \quad \begin{bmatrix} F_x \\ F_y \\ F_z \\ M_{xy} \\ M_{xz} \\ M_{yz} \end{bmatrix} \text{ anchor loads} \quad (4.5)$$

Δ_x , Δ_y and Δ_z are elongations computed on the basis of the overall linear expansion of the piping system, and depending on the boundary conditions⁽¹³⁴⁾, the anchor loads (F_x , F_y and F_z) and the anchor moments (M_x , M_y and M_z) are determined. Then the stresses at any point on the piping system could be predicted.

Thermal expansion or contraction in piping systems is accommodated by different methods:

- (i) Expansion joints, slip joints and/or swivel points⁽¹³²⁾;
- (ii) Inherent flexibility of the pipe itself, utilized through pipe bends, loops, right angle turns offset in the line--- etc.

Although method (i) has its own advantage in certain types of long straight piping systems, it could be associated with practical problems⁽¹³³⁾ apart from additional cost. Method (ii) is considered more convenient and is widely used since it relies on the inherent properties of the components used. No standard is available for GRP piping systems, and carbon steel pipe lines are commonly analysed using one of three piping codes, namely, ANSI B31-3⁽¹²⁴⁾, BS3351⁽¹³⁵⁾ and BS806⁽¹²³⁾.

The first two standards are intended for highly dynamical conditions (e.g. Petroleum industry), whilst the last is specifically a high temperature code (e.g. Power Plant) where the creep of component is of interest⁽¹³³⁾.

4.2.1 Smooth Bends

4.2.1.1 External loading of smooth metallic bends

The stress analysis of elbows and curved pipe has been the subject of numerous theoretical and experimental studies since Bantlin⁽¹³⁸⁾ first demonstrated experimentally that a curved pipe responds differently under load than predicted by simple beam theory, and von Karman⁽¹³⁹⁾ later presented the first rational explanation of this discrepancy.

von Karman's analysis was based on formulating the total strain energy⁽¹³⁹⁾ associated with the two principal longitudinal and circumferential deformations. The flattening of the bend, brought about by the inward components (vector f in Fig. 4.2b) of the longitudinal stress, was represented by a trigonometric function describing the tangential component of deformation assuming symmetrical radial deformation about the polar axes of the bend cross-section, i.e.

$$\omega_t = \sum_{n=1}^N C_n \sin 2n\phi \quad (4.6a)$$

using inextensibility assumption⁽¹⁴⁰⁾, the radial component of deformation is obtained

$$\omega_r = - \frac{d\omega_t}{d\phi} \quad (4.6b)$$

upon that, the longitudinal strain assuming no shifting of the bend centre-line under deformation was predicted to be

$$\epsilon_{\text{longitudinal}} = \frac{(\Delta l)}{l} \underset{\substack{\text{outermost} \\ \text{fibres}}}{=} = \frac{1}{R} \left(\frac{\Delta \psi_0}{\psi_0} r_m \sin \phi + \omega_t \cos \phi \frac{d\omega_t}{d\phi} \sin \phi \right) \quad (4.6c)$$

Similarly the circumferential strain components were formulated assuming only flexural bending to be taking place within the bend wall.

$$\epsilon_{\text{circumferential}} = -\left(\omega_r + \frac{d^2\omega_r}{d\phi^2}\right) \frac{z}{r_m^2}, \quad -\frac{t}{2} \leq z \leq \frac{t}{2} \quad (4.6d)$$

The total strain energy was formulated ignoring the Poisson's ratio effect, ⁽¹³⁹⁾ i.e.

$$U_T = U_L + U_C$$

where $U_L = \frac{r_m t E}{2} \int_0^{2\pi} \epsilon_L^2 d\phi$, $U_C = \frac{t^3 E}{24 r_m^3} \int_0^{2\pi} \left(\frac{d\omega_r}{d\phi} + \frac{d^3\omega_r}{d\phi^3} \right)^2 d\phi$ (4.7)

and minimizing U_T , $\frac{dU_T}{dc_n} = 0$, for values of $c_1 \dots c_n$

thus the results for in-plane bending using one term ⁽¹³⁹⁾, are:

$$K = \frac{12\lambda^2 + 10}{12\lambda^2 + 1} \quad (4.8a)$$

$$\sigma_L / \sigma_n = \frac{K}{1-\nu^2} \left\{ \sin \phi - \frac{6}{5+6\lambda^2} \sin^3 \phi + \nu \frac{18zR}{r_m^2} \cos 2\phi \right\} \quad (4.8b)$$

$$\sigma_c / \sigma_n = \frac{K}{1-\nu^2} \left\{ \nu \sin \phi - \nu \frac{6}{5+6\lambda^2} + \frac{18zR}{r_m^2} \cos 2\phi \right\} \quad (4.8c)$$

The accuracy of the analysis is dependent on the number of terms (c_n) required for a range of bend parameter (λ).

von Karman's main assumptions were:

- (1) the thickness of the pipe is very much smaller than the bend cross section radius, i.e. $\frac{r_m}{t} > 10$, hence it is reasonable to assume a state of plane stress, $\sigma_z = 0$.
- (2) the bend cross-sectional radius could be neglected in comparison to the bend radius, $R \gg r_m$, which implies that: ⁽¹³⁶⁾

$$\text{membrane circumferential stress} = \frac{r}{R} \int \sigma_L d\phi. \cos \phi \approx 0$$

$$\text{through thickness shear stress} = \frac{r}{R} \int \sigma_L d\phi. \sin \phi \approx 0$$

- (3) the applied bending moment is uniform throughout the bend, and the bend experiences constant flattening.
- (4) the longitudinal and circumferential directions are the principal axes for the stresses.

The implications of the above assumptions in conjunction with the flexibility and stress results are discussed in the literature^(136,137,148).

Vigness⁽¹⁴³⁾ using the potential strain energy method of analysis predicted the out-of-plane flexibility factor and the SIF. The flexibility factor was exactly the same function of λ as for the in-plane case, and the SIF were differently presented due to the rotation of the principal bend cross-sectional axes⁽¹⁴⁸⁾ of deformation, by 45° from that under in-plane bending, (see Fig. 4.1). Experiments⁽¹⁴³⁾ carried out on 90° and 180° metallic bends were accomplished by loading the free-tangent end in three different space axes and measuring the corresponding end deflections. The experimentally determined in-plane flexibility factor and in-plane and out-of-plane SIFs were in good comparison with theory, whilst the out-of-plane K were 60% higher than predicted due to probable experimental error or incompleteness of the model⁽¹⁴³⁾. The effect of the straight tangents and attached flanges acting as a restraint on the bend fitting were also experimentally investigated⁽¹⁴⁴⁾, indicating a sharp reduction in both flexibility and the SIF with flanges being welded directly to the bend. The effect of the tangent was not significant, probably due to its extra flexibility brought about by the decaying ovalization of the bend. In the same work⁽¹⁴⁴⁾, end torsional

moments were used instead of end loadings producing comparable theoretical and experimental out-of-plane flexibility factors. The torsional component of moment was assumed to have no contribution to the bend ovalization⁽¹⁴³⁾.

Hovguard^(141,142) approached the problem from a Mechanics of Material basis by satisfying the equilibrium of forces acting on an element of a bend. Using von Karman's assumption, he achieved similar theoretical results to von Karman which were in agreement with experimental results obtained for in-plane bending of 180° bends having $\lambda > 0.5$; and $R/r_m > 5$.

Beskin⁽¹⁴⁵⁾ adopted the minimization of the complementary strain energy method of analysis by assuming a trigonometric series for the longitudinal stress. He used six terms in the analysis (using von Karman's assumptions), and his results were suitable for small bend factor ($\lambda < 0.33$). Beskin results for the in-plane and out-of-plane bending were presented in a numerical format by Markl⁽¹⁴⁶⁾ who compared them with experimental results obtained from fatigue loads on bends. Markl's empirical results were half of Beskin's predictions for the SIF and are used by Standards such as in ANSI B3.31⁽¹²⁴⁾ and BS 3351⁽¹³⁵⁾.

In 1951, Clarke and Reissner⁽¹⁵⁰⁾ obtained similar results to those predicted by Beskin for in-plane bending. The problem was considered from a differential equation point of view considering the curved tube as part of a thin shell of revolution. The normal stresses and moments in the bend were represented by a stress function satisfying equilibrium for elements of the shell, and also as a function of the assumed strain model representing the circumferential displacement. Two differential equations were obtained and simplified by the use of von Karman's original assumptions. The solution was carried out by a special

mathematical technique which was later used for the analysis of elliptical cross-sectional bends.

Ford and Gross^(151,152) carried out an intensive experimental programme testing short radius bends (i.e. $\frac{r_m}{R} < \frac{1}{3}$) of small pipe factors (λ) under in-plane bending combined with internal pressure. Their experimental findings indicated that the assumption used by von Karman⁽¹³⁹⁾, Vigness^(143,144), Beskin⁽¹⁴⁵⁾ and Clarke⁽¹⁵⁰⁾, of pure flexural circumferential strains occurring in the wall of the bend, would undermine the actual maximum peak strain and stress usually measured on the inside of the bend. The higher value of the inside circumferential SIF is brought about by the addition of a membrane circumferential stress. This stress component was theoretically predicted by Gross by balancing the inward stress component of the longitudinal membrane stresses, the transverse shear stress and the circumferential membrane stress.

The theory was accordingly modified by superimposing such membrane circumferential stress on the flexural ones already predicted theoretically⁽¹⁵²⁾. Although such a stress component should have been included in the potential strain energy formulation, however, the superposition technique used by Gross⁽¹⁵²⁾ gives a good approximation ($\sim 2\%$) of the value obtained by considering r_m/R ratio in the strain energy formulation in the first place⁽¹³⁶⁾. The consequences of incorporating the circumferential membrane stress was argued to cause a shift of the neutral axis from the bend centre line, and such shift was later considered in the analysis^(147,149,156).

Gross⁽¹⁵²⁾ modification of the theory lead to a good comparison with experimental results obtained previously⁽¹⁵¹⁾. No theoretical analysis was incorporated for internal pressure effects, but, experimental results showed that such superimposed internal pressure was

to reduce the peak stresses arising from the externally applied moment. It was suggested that the dimensional variability of the metallic bends lead to a variation of the determined flexibility factor, e.g. a change of $\pm 1^\circ$ of the angle of a 90° bend would lead to a 10% change of flexibility factor, and thickness variations of the bend wall suggested the opinion that the resistance to bending was dependent on an effective section modulus which may not be the average value measured, and may lead to 15% variations on the flexibility factor. Those observations should be considered with respect to GRP bends where high degree of thickness variation is expected due to the processing technique (i.e. hand lay-up), and also possible bend angle variation due to resin shrinkage on curing.

In 1957, Turner and Ford⁽¹⁴⁹⁾ re-derived bend theory in a generalized form taking the (r_m/R) ratio into consideration, and using minimization of the complementary strain energy. An interesting pattern of end results was presented in the form of the equivalent stresses using von Mises mathematical equation of plasticity, describing the stress condition of a bend by one SIF rather than the traditional longitudinal and the circumferential SIF. Later Smith⁽¹⁴⁷⁾ followed a similar procedure and presented a generalized form of the bend problem under out-of-plane bending.

In 1955, Kafka and Dunn⁽¹⁵³⁾ incorporated the influence of the internal pressure into Von Karman's strain energy analysis in a form of work acting against the ovalization of the bend cross-section. Their theoretical predictions agreed with experimental results by Ford and Gross^(151,152).

In the following year, Rodabaugh, George and Louisville⁽¹⁷⁹⁾ generalized the von Karman-Vigness analysis of a bend deformation under in-plane and out-of-plane bending, including the influence of pressure.

When internal pressure is included, the flexibility factor and the SIF were dependent on a second dimensionless parameter $\bar{\psi}$, e.g. for flexibility using one term -

$$K = \frac{12\lambda^2 + 10 + 24\bar{\psi}}{12\lambda^2 + 1 + 24\bar{\psi}} \text{ where } \bar{\psi} = \frac{PR^2}{Ert} \quad (4.9)$$

The complete analysis was presented in terms of infinite series which were solved to obtain expressions for the flexibility factor and the in-plane and out-of-plane stress intensification factors. They emphasized on the importance of using the right number of terms in the trigonometric function to get a reasonably accurate result. They suggested that the following ranges should be used:

| <u>value of λ</u> | <u>Approx. order required (c_n)</u> |
|--------------------------------------|--|
| 0.5 and larger | 1st |
| 0.4 to 0.16 | 2nd |
| 0.12 to 0.08 | 3rd |
| 0.06 to 0.04 | 4th |

In the course of their literature review, they summarized Beskin and Clarke's work for non-pressurized bends in simple expressions incorporating the Poisson's ratio effect as listed in Table 4.1.

TABLE (4.1) Flexibility factors and SIF of smooth bend

| | Ref ⁽¹⁷⁹⁾ | $\nu = 0.2$ | $\nu = 0.3$ | $\nu = 0.35$ | ANSI ⁽¹²⁴⁾ Code |
|--------------------|--------------------------------|-------------------------------|-------------------------------|-------------------------------|----------------------------|
| Flexibility factor | $\frac{1.73}{\lambda_1}$ | $\frac{1.695}{\lambda}$ | $\frac{1.65}{\lambda}$ | $\frac{1.62}{\lambda}$ | $\frac{1.65}{\lambda}$ |
| In-plane SIF | $\frac{1.95}{\lambda_1^{2/3}}$ | $\frac{1.924}{\lambda^{2/3}}$ | $\frac{1.89}{\lambda^{2/3}}$ | $\frac{1.867}{\lambda^{2/3}}$ | $\frac{1.80}{\lambda}$ |
| Out-of-plane SIF | $\frac{1.67}{\lambda_1^{2/3}}$ | $\frac{1.647}{\lambda^{2/3}}$ | $\frac{1.618}{\lambda^{2/3}}$ | $\frac{1.60}{\lambda^{2/3}}$ | $\frac{1.5}{\lambda}$ |

$$\lambda_1 = \frac{\lambda}{\sqrt{1-\nu^2}}, \quad \lambda = \frac{tR}{r_m^2}$$

The theoretical predictions of Table 4.1 show that up to 4% variation in flexibility factor and up to 3% variation on the outside SIF could be observed due to a change of Poisson's ratio from 0.2 to 0.35 which could be exhibited by CSM and WR laminates.

The generalized analysis of Rodabaugh et al⁽¹⁷⁹⁾ was modified by Dodge and Moore⁽¹⁵⁴⁾ taking into consideration Gross⁽¹⁵²⁾ correction for the membrane circumferential stress. This work was presented in a written computer programme format sub-contracted to the atomic energy commission of the United States⁽¹⁵⁵⁾. Experimental results obtained and investigated in the present thesis were compared with Dodge analysis represented in a computer programme written in Basic using four terms and presented in App. II and App. III.

Work carried out by Jones⁽¹⁵⁶⁾ on smooth bends incorporated $\frac{r_m}{R}$ effect, and the neutral axis shift was considered by including odd terms in Eq. (4.6a). His conclusions were that the flexibility factor is not influenced by r_m/R ratio and, although this ratio has an influence on the SIF, it is not significant.

Reducing the bend angle would tend to restrain the bend from further ovalization and accordingly flexibility factors and SIF are reduced. This has been shown experimentally⁽¹⁵⁷⁾ to be the case, whereby the in-plane flexibility factor was reduced by a factor of two when the bend angle was reduced from 90° to 40°.

4.2.1.2 External loading of smooth GRP Bends

The first work done in RAPRA was by Wright⁽⁴¹⁾ on in-house built GRP straights and bends. It was due to Wright's preliminary programme that the present large scale investigation was started in mid-1978^(159,160,161,162) preceded by work on GRP straights in early 1977.

Wright investigated the flexibility factors and stress intensification factors for a range of pipe factors, under in-plane and out-of-plane bending. The bends were originally strain gauged on the outside and later, one bend was amputated, instrumented on the inside and re-tested. His remarks and conclusions can be summarised as follows:

- (1) the Beskin prediction of flexibility factor would largely over-estimate the experimentally determined in-plane K_i and slightly under-estimate the out-of-plane K_o ;
- (2) the circumferential SIF measured on the outside surface were at least 50% lower than Beskin prediction for both type of bending, but the inside SIF were comparable;
- (3) bend failure was caused due to maximum circumferential stress under in-plane bending;
- (4) limited fatigue tests on bends under in-plane bending showed a reduction of 30% of the short UTS of the bend;
- (5) shear modulus of CSM pipes could be obtained by using $G = E/2(1+\nu)$. thus, supporting the in-plane isotropy assumed for CSM laminates.

Kirk⁽⁴⁰⁾ carried out limited tests on commercially made GRP bends strain gauged on the outside. He indicated the problems that could be associated with joints present on the bend-tangent structure, increasing its overall rigidity, and were susceptible to failure by peeling when they ovalize. Based on the tests he carried out on Tee intersections, he indicated that the through-thickness anisotropy exhibited by the GRP laminates may have an influential effect on the initiation of failure and failure progression. The tests carried out on GRP straights showed the applicability of simple shell theory under flexure, torsion and pressure. The pressure effect was later shown to cause a rise in interlaminar shear stresses^(158,185).

Failure tests carried out on smooth CSM bends under bending and pressure loading, also indicated a possible cause of failure to be due to interlaminar shear stresses⁽¹⁵⁸⁾.

Due to the wide range of reinforcements available, GRP pipes can be produced with different degrees of in-plane anisotropy to cope with working conditions such as high pressures. In this case WR or UD reinforcements are added to the main CSM laminates so that the pipe would be classified under a higher pressure rating. The added in-plane anisotropy is not usually taken into consideration insofar as bends or Tee behaviour is concerned under bending. The author investigated this⁽¹⁶¹⁾ by incorporating the in-plane anisotropy in the von Karman's strain energy⁽¹³⁹⁾ analysis as presented in App. III, and the conclusion reached is that extra added circumferential stiffness would lead the bend to exhibit a lower flexibility factor, reduce its longitudinal SIF and slightly increase the circumferential SIF. Such an effect is shown on the flexibility to be:

$$K = \frac{12\bar{m}\lambda^2 + 10}{12\bar{m}\lambda^2 + 1} \text{ where } \bar{m} = \frac{E_{\text{circumferential}}}{E_{\text{longitudinal}}} \quad (4.10)$$

and the effect on the SIF is shown in Fig. 4.3.

4.2.1.3 Pressure loading of smooth bends

In pressurised piping systems, fittings such as bends and Tees, are investigated for their pressure rating capability, in addition to their deformation under external load.

Pressure stresses for metallic bends are similarly predicted for straight pipes as specified by BS806⁽¹²³⁾. While for Tees, a pressure stress multiplier (PSM) greater than 2.5 is usually employed depending on the dimensions of the Tee. Previous experiments^(151,152) on metallic smooth bends suggest that PSM could be greater than unity.

Tests carried out by Gross on metallic bends of $\frac{R}{r_m}$ ratio of 3.0 indicated that maximum stress would be a circumferential stress situated at the inside surface and located at the intrados. The bend PSM interpreted from his numerical results would be approximately 1.4, and he reported that the stress distribution of smooth bends could be predicted using the analysis of thin torus shell subjected to pressure⁽¹⁵¹⁾.

Such an analysis is thought to be best suited for bends of large $\frac{R}{r_m}$ ratio. Its accuracy becomes less adequate as the ratio decreases below 5. However, its simplistic format and its adequate comparability with experimental results make it more convenient to use. There could be bending stresses associated with pressure loading of a torus shell⁽¹⁶³⁾, but they are considered negligible, however, those bending stresses would be magnified when an ovalized bend cross-section is pressurised⁽¹⁵¹⁾.

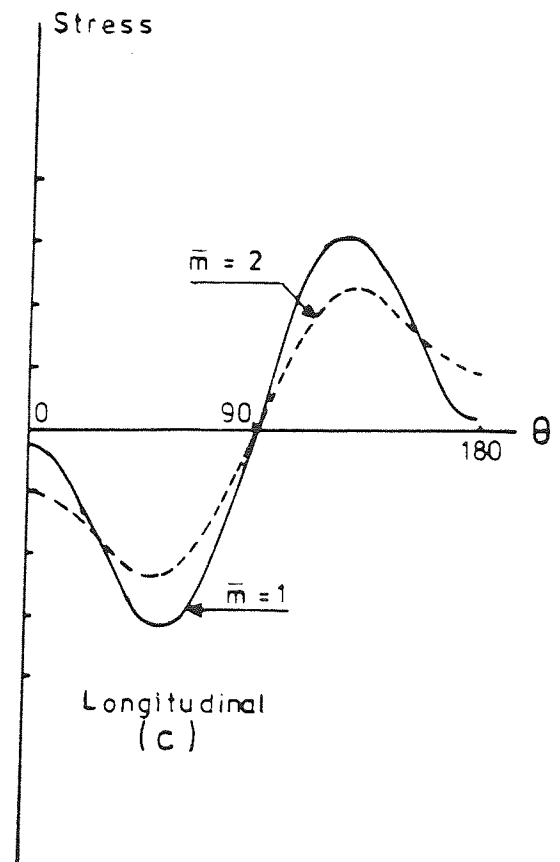
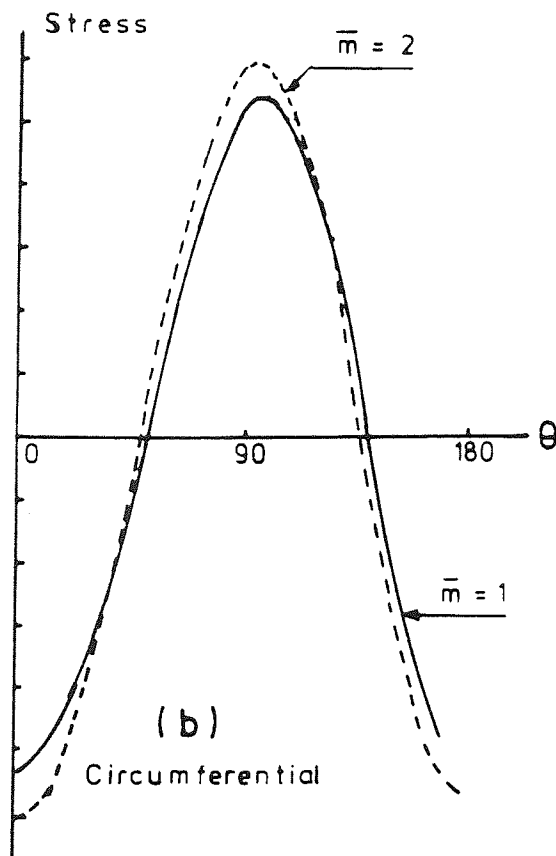
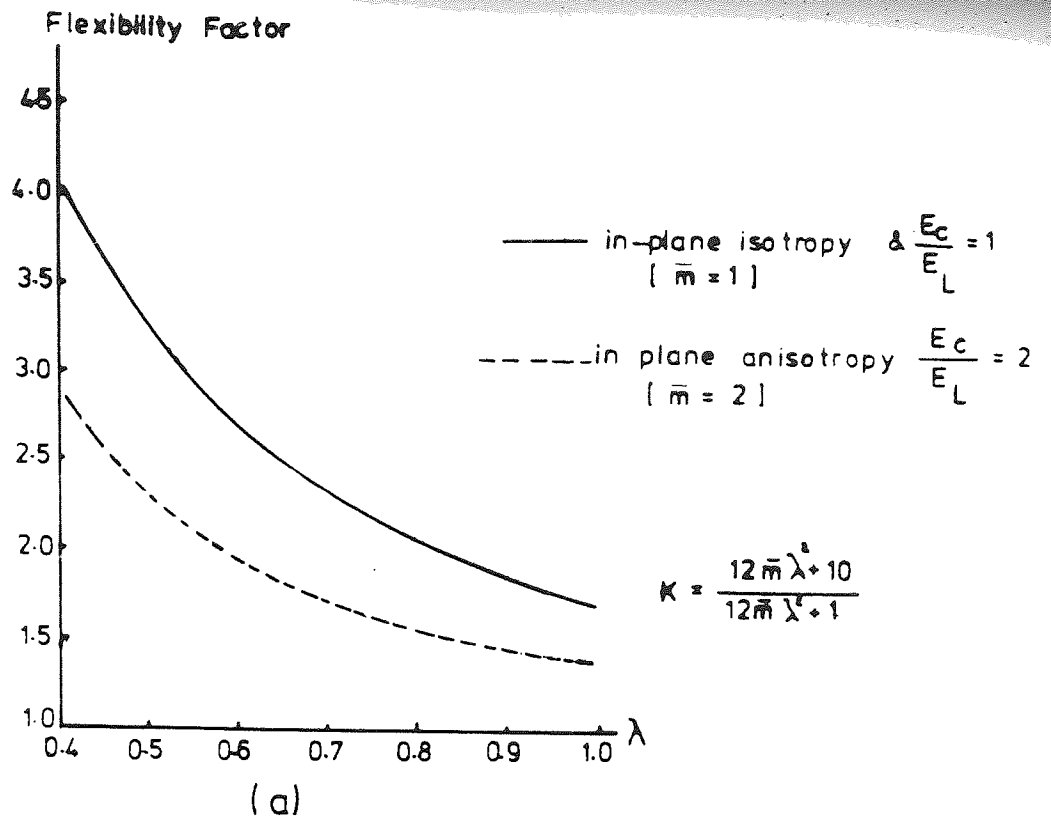


Figure (4.3)

Flexibility & Stress distribution of a bend as a function of its pipe wall anisotropy

4.2.2 Mitre Bends

These are usually used as an alternative when large cross-sectional diameter bend is required in a piping system. Particularly for GRP, for some pipe manufacturing processes (e.g. centrifugal casting), it might prove more economical to construct small diameter bends in a mitred form.

Mitre bends did not receive the same attention as smooth bends until the last 25-30 years, especially under different modes of bending moment. A comprehensive review of their deformation is presented by Kitching⁽¹⁴⁸⁾.

4.2.2.1 External loading of mitred Bends

The behaviour of multi-mitred bend under any specific loading condition is similar to that of a smooth bend, but the discontinuities arising where the segments of straight pipe are joined along oblique sections give rise to important differences. At these positions, stress levels will not be the same as for smooth bends under the types of loading already considered. Typical deformation of a mitred bend is shown in Fig. 4.4⁽¹⁴⁸⁾.

The edge discontinuityⁱⁿ was first tackled theoretically by van der Neut⁽¹⁶⁴⁾, whereby he predicted the local bending stresses in an oblique edge of a cylinder by simplifying the edge to a helical one developed upon the flat plane. He suggested that the pressure longitudinal stresses at the edge are not of a local nature and could be of the same magnitudes in sections remote from the joint, which was later contradicted theoretically and experimentally^(165,166,167).

The problem of bending of mitred bends were investigated experimentally by Ford and Gross⁽¹⁵¹⁾. They tested five welded segments mitre steel bends and found that flexibility factors did not differ much

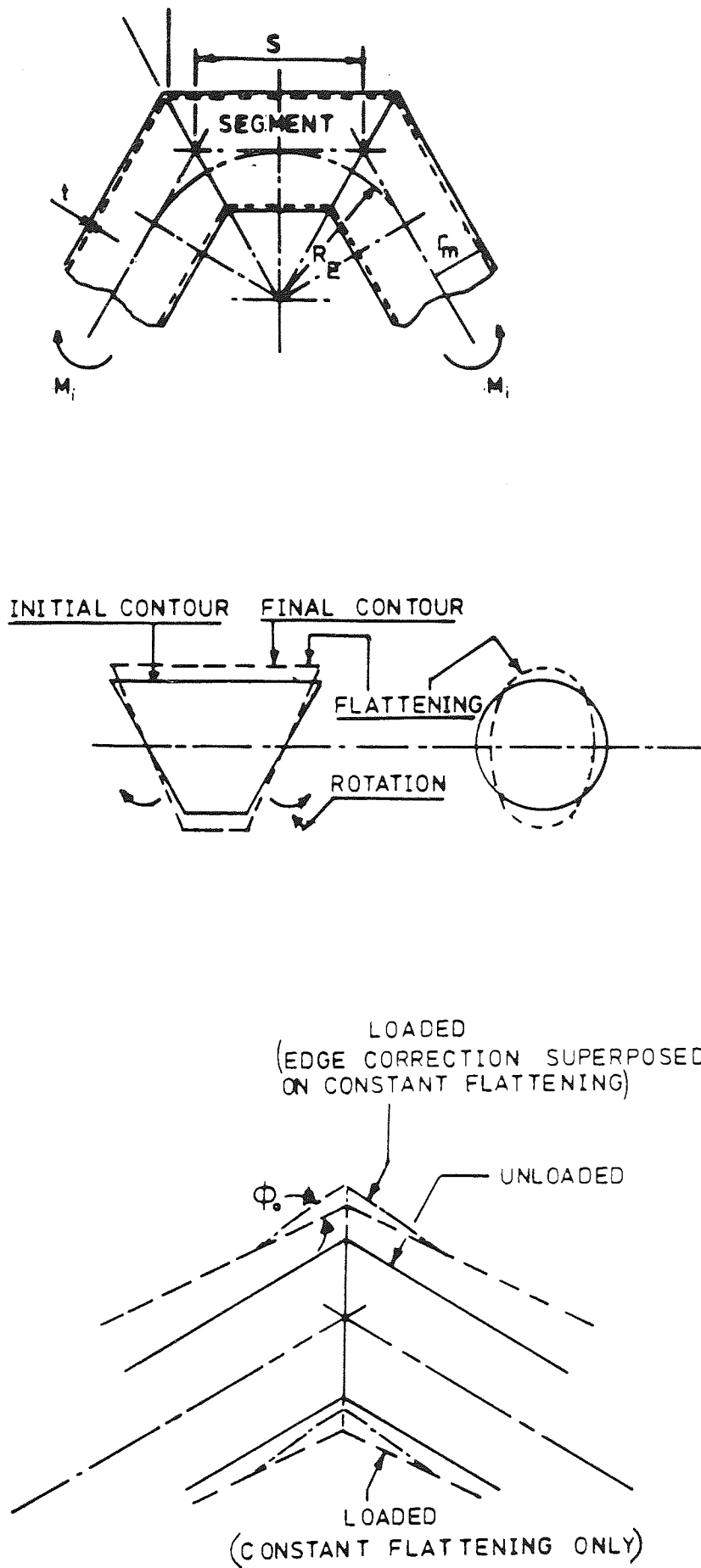


Figure (4.4)
 Mitred bend deformation under in plane
 bending moment⁽¹⁶⁸⁾

from that obtained by smooth bend theory, and the difference was about 15% lower than predicted. They attributed such a reduction in flexibility to the restraint of the straight tangents. In fact, the tangents themselves ovalize by flattening decaying from the bend so it could be proposed that what is lost by the bend flexibility, is substituted by the flexibility of the tangents (depending on the tangent length). Hence the reduction of the 15% might have been realistic difference. The stresses were measured only in the centre of the segment where the induced stresses are not as high as those induced in the segment joints. Therefore, there was not enough data to comment on the SIF's.

Lane and Ross⁽¹⁶⁶⁾ tested 12 inch diameter, 90° welded steel bends of 15° and 22½° mitre angles. Their tests were carried out under internal pressure combined with external loading. Their experimental findings can be summarised as follows:

- (1) the flexibility of 2-welded and 3-welded structures are 15-25% less than a corresponding smooth bend;
- (2) the maximum stress induced in a mitred bend under bending could be 1.4 times the maximum stress in a smooth bend;
- (3) diametral change at the mitre joint is similar to the diametral change at the segment-centre and both could be predicted by smooth bend theory;
- (4) the flexibility of mitred bends is diminished by the presence of internal pressure by an amount similar to that for smooth bends, and
- (5) additional edge stress components should be superimposed on those predicted by von Karman bend theory.

Similar observations were reported by Owen and Emmerson⁽¹⁶⁷⁾ indicating that the distortion of mitred bends was similar to that of a smooth bend and suggested that mitred bend analysis under bending should be based on a modified von Karman work.

The most comprehensive theoretical and experimental work done on multi-mitred bends under different types of bending moments was that carried out by Bond and Kitching under in-plane bending⁽¹⁶⁸⁻¹⁷¹⁾, under out-of-plane bending⁽¹⁷²⁾ and under combined external loading and internal pressure⁽¹⁷³⁾.

Kitching⁽¹⁶⁸⁾ generalised the work based on those of von Karman⁽¹³⁹⁾, Vigness⁽¹⁴³⁾, Nent⁽¹⁶⁴⁾, Den Hartog⁽¹⁴⁰⁾, Ford and Gross^(151,152), Green and Emmerson⁽¹⁶⁵⁾ and others^(166,167), and reported that an approximate analysis could be obtained by superposing two major deformation in the bend determined independently by:

- (1) carrying out the von Karman's constant flattening analysis for smooth bends, and
- (2) satisfying compatibility and equilibrium conditions at the mitre joint (defined as edge correction) in a form of sine and cosine distributed stress functions.

Such edge corrections would produce similar trigonometric edge deformations around the circumference, and those stresses (longitudinal and circumferential) would accordingly decay exponentially along the longitudinal direction of the segment of the bend. He presented this decay (based on beams on elastic foundation) to be of short and long decays which could both be represented by the following mathematical relationship for the radial deformation of the bend cross-section⁽¹⁷⁰⁾.

$$\omega_r = \omega_{n1} \exp\left(\frac{-\alpha_1 x}{r_m}\right) \cos(n\theta) + \omega_{n2} \exp\left(\frac{-\alpha_2 x}{r_m}\right) \cos(n\theta) \quad (4.11)$$

where x is the distance along the segment starting from the mitre joint, and α_1 and α_2 are the short and the long decay factors respectively. They are defined mathematically as a function of the geometry of the segment as the following:

$$\alpha_1 = (k + \Lambda)/2, \quad \alpha_2 = (k - \Lambda)/2 \quad (4.11)$$

where $\Lambda = \{3(1 - \nu^2)\}^{1/4} \left(\frac{r_m}{t}\right)^{1/2}$

and $k = \{2n^2 + (4n^4 + \Lambda^4)^{1/2}\}^{1/2}$

where n is the integer defining sinusoidal distribution (e.g. $\cos n\theta$ above). For low values of n (e.g. $n = 2$), α_1 is much greater than α_2 , and hence the α_2 part of the deformation will decay more gradually than the α_1 contribution. The portion of the deflection associated with α_1 will be negligible at a short distance from the edge of the segment. That associated with α_2 corresponds to the deflection assumed in the constant-flattening analysis. Accordingly, the stresses at the mid-segment are modified exponentially and those at the edges are superposed onto the short decay stresses. The exponential modification is dependent on the geometry of the segment and in particular on the centre-line length (Fig. 4.4, i.e. short, medium or long) together with the number of terms assumed in the radial deformation⁽¹⁶⁹⁾. The analysis is

valid for short length cylinders where $\frac{\alpha_2 x}{r_m} \ll \frac{\pi}{4}$ ($n = 2$) and

experiments⁽¹⁶⁸⁾ have indicated that no serious errors would be incurred if the validity condition is taken as $\frac{\alpha_2 x}{r_m} \ll 1$. If the ratio $\frac{\alpha_2 x}{r_m} > 1$,

then serious errors could arise especially for the circumferential bending stresses^(168,169). The analysis incorporated the r_m/R ratio in the energy formulation by expanding binominally the term:

$$\left(1 + \frac{r_m}{R} \cos \phi\right)^{-1} = 1 - \frac{r_m}{R} \cos \phi + \left(\frac{r_m}{R}\right)^2 \cos^2 \phi + \dots \quad (4.13)$$

The theory was programmed, and the results^(171,172,173) were presented in the form of the total stresses and deformations at the segment-centre and at the segment-edge including pressure effects. The programme was found to predict factors for smooth bends by inserting a very small mitre angle, typically 10^{-9} degrees⁽⁴⁰⁾. The theoretical analysis could be summarised as shown in the diagram in Fig. 4.5 for in-plane bending. A similar analytical procedure is followed for the out-of-plane bending.

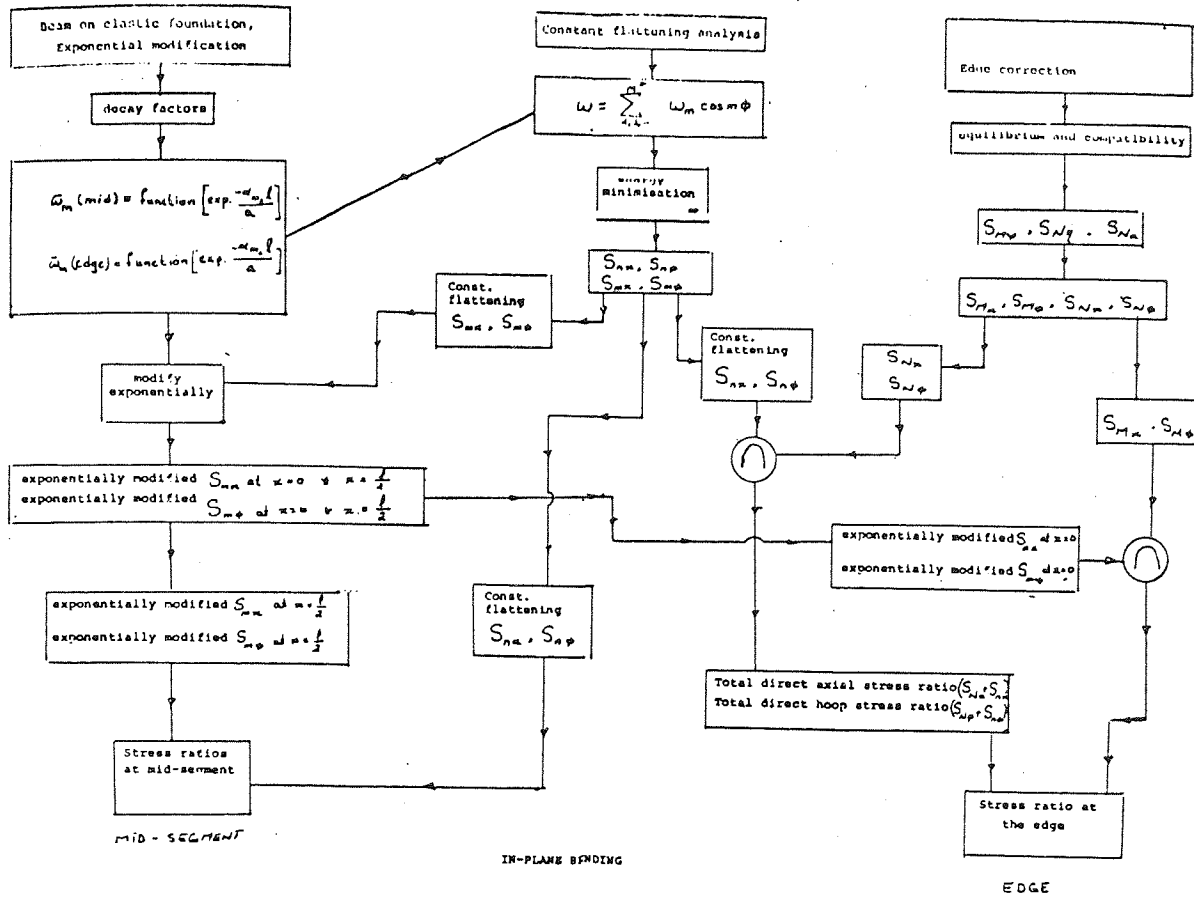
The flexibility factors and the maximum stress intensification factors predicted theoretically for a mitred bend under in-plane bending were summarised in a simple non-dimensional equations⁽¹⁷⁰⁾ as:

$$K = B/\lambda^p \quad \text{SIF} = C/\lambda^q \quad (4.14)$$

and presented graphically as shown in Figs. 4.6 and 4.7 respectively. The results are suitable for the following bend characteristics $0.0125 \leq \lambda \leq 0.25$, $0.1 \leq \frac{r_m}{R} \leq 0.5$, $9.0^\circ \leq \alpha \leq 22.5^\circ$ and $\nu = 0.3$.

The analysis⁽¹⁷⁰⁾ predicted that the maximum stress would always occur at the joint, either, on the outside surface as a longitudinal stress, or, on the inside surface as a circumferential stress, and both of these maxima would be of similar magnitude. It was later indicated⁽¹⁷²⁾ that maximum stresses obtained for a mitred bend undergoing out-of-plane bending would be comparable to those obtained under in-plane bending, i.e. corresponding to those obtained in Figs. 4.6 and 4.7.

Because of the similarity of the mitre bends and smooth bends, the ANSI⁽¹²⁴⁾ piping code adopts the procedure of assuming that a mitre bend can be replaced by an equivalent smooth bend of radius R_E for the purpose of calculating flexibilities and stresses. It should be stated



S_{nx} Direct longitudinal stress due to constant flattening

$S_{n\phi}$ Direct circumferential stress due to constant flattening

S_{mx} Bending longitudinal stress due to constant flattening

$S_{m\phi}$ Bending circumferential stress due to constant flattening

S_{Nx} Direct longitudinal stress due to edge correction

$S_{N\phi}$ Direct circumferential stress due to edge correction

S_{Mx} Bending longitudinal stress due to edge correction

$S_{M\phi}$ Bending circumferential stress due to edge correction

W radial deformation

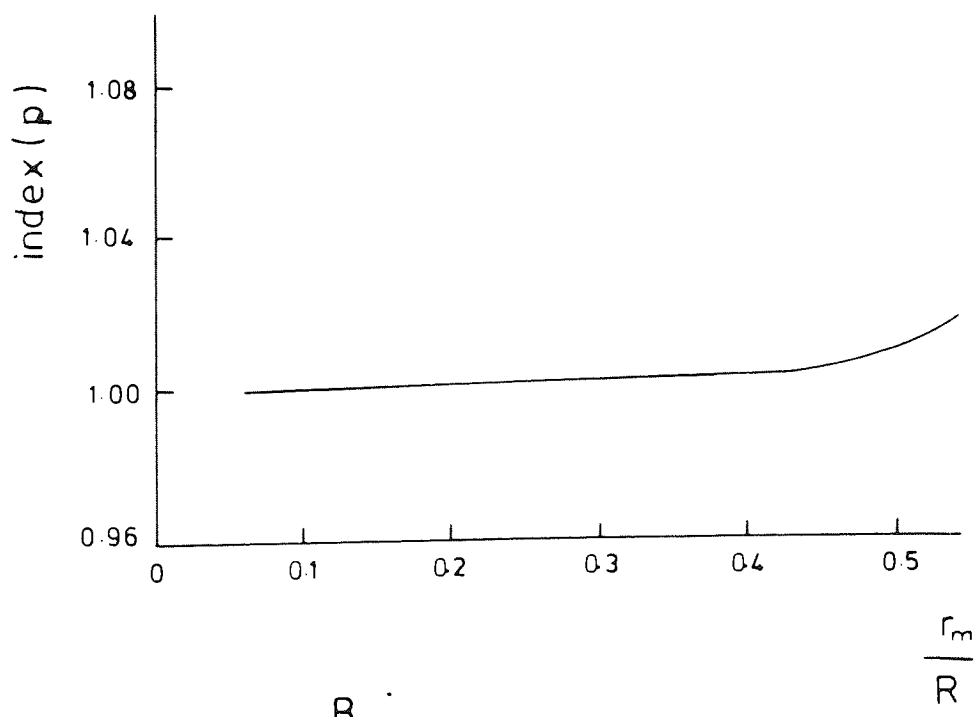
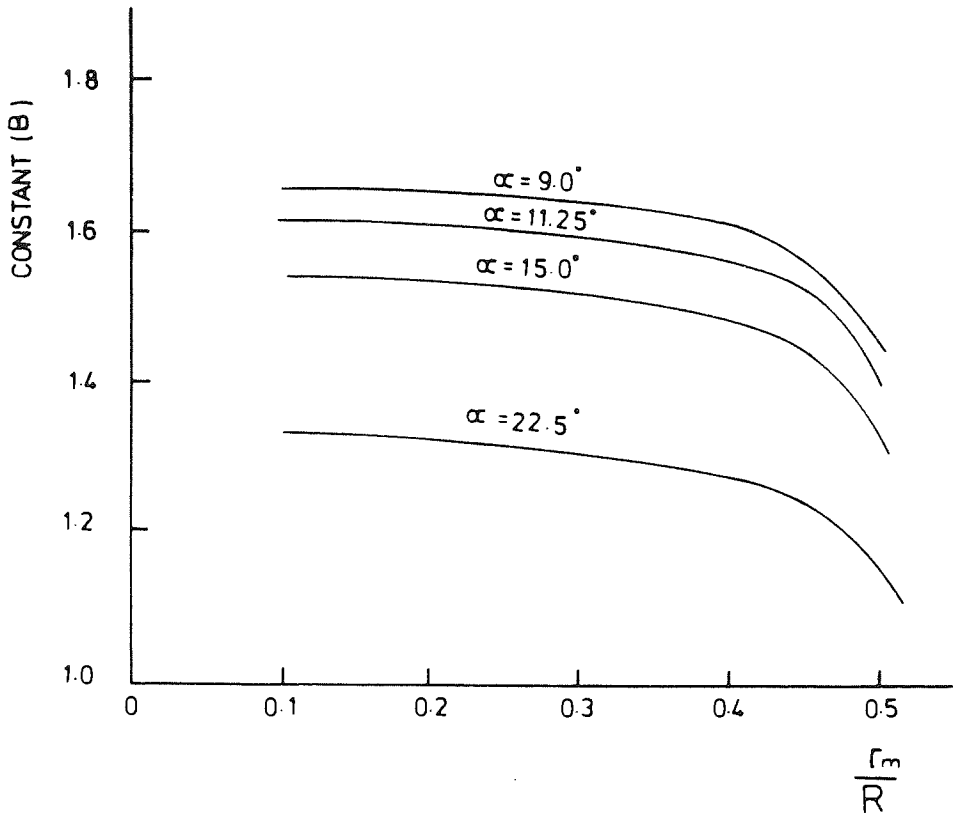
q_{m2} long decay factor

a radius of the pipe cross-section

l length of the segment

ϕ angle around the circumference

Figure(4.5) Block diagram representing theoretical analysis of mitred bend under In-plane bending



$$K = \frac{B}{\lambda^p}$$

Figure (4.6)
Flexibility factor (K) of mitred bends as a function of the bend radii ratio & mitred angle (α)⁽¹⁷⁰⁾

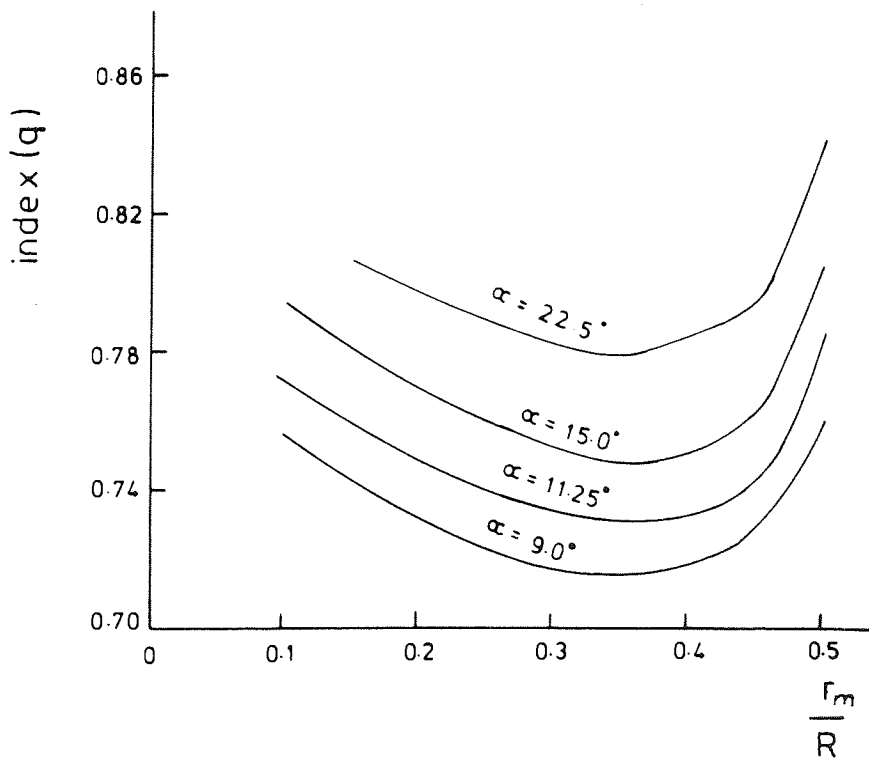
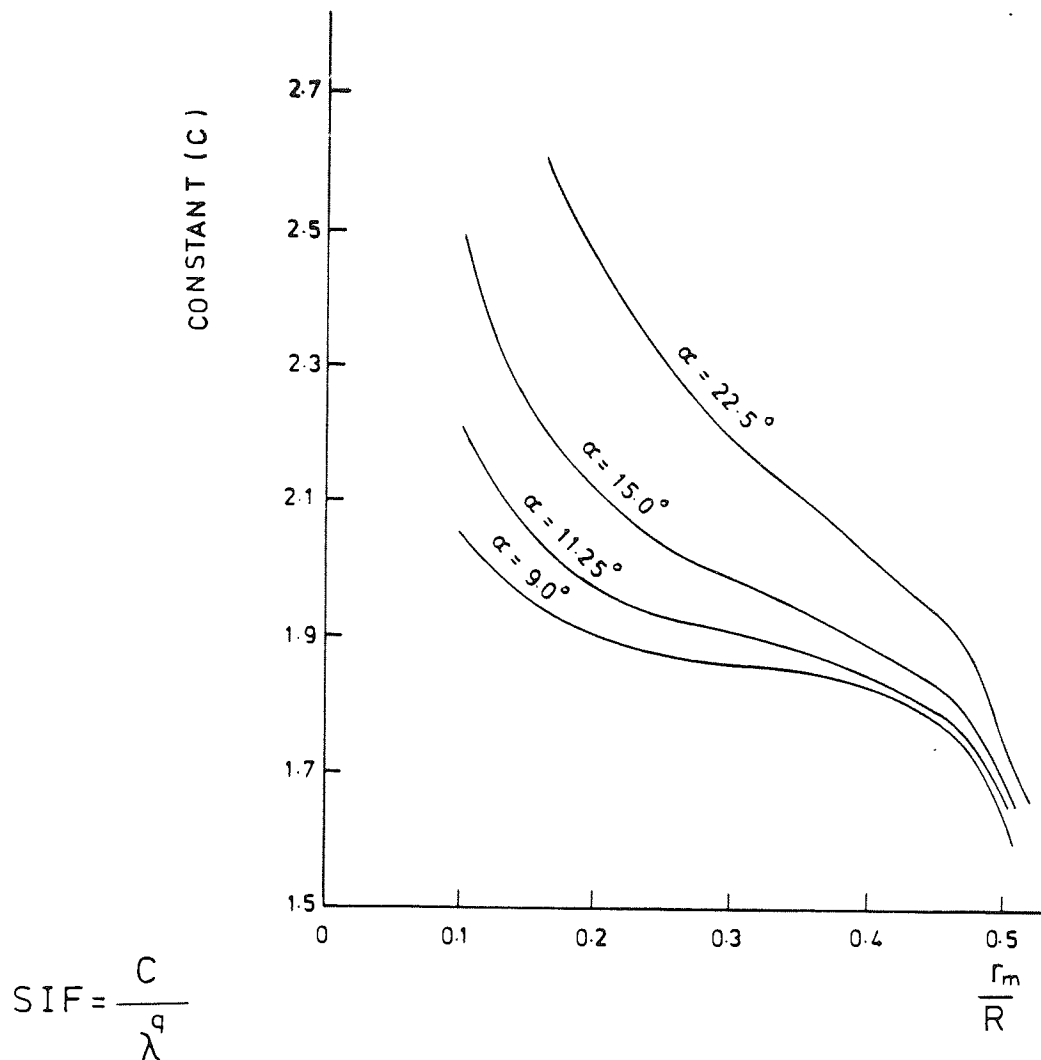


Figure (4.7)

Maximum in plane Stress Intensification Factor (SIF) of mitred bends as a function of the bend radii ratio (ρ) & mitred angle (α)⁽¹⁷⁰⁾

that the standard is based on a modification of a smooth bend formula given by Clarke and Riessner⁽¹⁵⁰⁾. The formula in the code intentionally gives stress intensification factors which are half the true elastic stress factors which were based on fatigue tests carried out by Markl⁽¹⁴⁶⁾, so the code values have been doubled here. Taking this into account the code formula become⁽¹³⁷⁾:

$$\begin{aligned} K &= 1.52/\lambda^{5/6} \\ \text{SIF} &= 1.8/\lambda^{2/3} \end{aligned} \quad \lambda = \frac{tR_E}{r_m^2} = \frac{\cot \alpha}{2} \cdot \frac{t \cdot s}{r_m^2} \quad (4.15)$$

for small mitre spacing where $s < r_m (1 + \tan \alpha)$, and

$$\begin{aligned} K &= 1.52/\lambda_E^{5/6} \\ \text{SIF} &= 1.80/\lambda_E^{2/3} \end{aligned} \quad (4.16)$$

for large mitre spacing or single mitre, where $s > r_m (1 + \tan \alpha)$,

$$\lambda_E = (1 + \cot \alpha) t/2 r_m, \text{ and } R_E = \frac{r_m(1 + \cot \alpha)}{2}.$$

Bending of single mitred bends is a special case. It has been shown experimentally⁽¹⁷⁴⁾ and theoretically⁽¹⁷⁵⁾, that Eq. (4.16) would largely over-estimate the flexibility, and slightly under-estimate the SIF under in-plane bending. A comprehensive analysis was later reported for the in-plane bending moment case⁽¹⁷⁶⁾. As for out-of-plane bending, the maximum circumferential stress was found to be almost half the corresponding maximum in-plane bending moment, although the maximum longitudinal stress ratios were of the same order of magnitude⁽¹⁷⁴⁾. Also, it was reported that the out-of-plane flexibility factor was found to be only a little greater than that using simple bending theory⁽¹⁷⁴⁾. It was suggested⁽¹⁴⁸⁾ that, where possible, out-of-plane bending moment should be avoided where single mitres are used, due to the high stresses accompanying such type of loading.

4.2.2.2 Pressure loading of mitred bends

The circumferential and the longitudinal stress distributions for a single mitred bend under pressure loading, have been predicted theoretically by Green and Emmerson⁽¹⁶⁵⁾ for bends of small mitre angle (α), using the general differential equation of elasticity. Their analysis (contrary to Neut⁽¹⁶⁴⁾) showed that the longitudinal stress at the edge would decay rapidly along the axis of the straight pipe to a $P r_m / 2t$ value of magnitude. Similar theoretical results were achieved by Owen and Emmerson⁽¹⁶⁷⁾ and others⁽¹⁷⁷⁾ using the thin shell theory equation expressed in the form of differential equations describing deformation. The theoretical results describing the membrane and bending circumferential and longitudinal stress at the joint of the single mitred bend, are presented in App. IV.

Owen and Emmerson⁽¹⁶⁷⁾ carried out pressure tests on single-mitred bends made out of hot-cured Araldite epoxy resin with various mitre angles. The stress distribution and its magnitude in comparison to a straight pipe was measured using stress-freezing technique of photo-elasticity. They obtained a pattern of experimental stress distribution comparable with that of theory up to 15° mitred angle, whereby, the maximum principal stress (membrane + bending) is the circumferential stress situated on the outside surface and located at the intrados ($\theta = 0^\circ$) at the joint. As α is increased the measured stresses diverge from those predicted by theory. The maximum principal stress continues to be a circumferential stress at the intrados but it would be located at the inside of the bend at $\alpha = 45^\circ$ due to the effect of bending stresses changing signs at approximately $\alpha = 37^\circ$. Regardless of the surface location of the maximum principal stress, its value in comparison to a maximum stress induced in a straight pipe similarly constructed (i.e. pressure stress multiplier) would increase from a

factor approximately 2 for $\alpha = 15^\circ$ up to $3\sqrt{4}$ for $\alpha = 45^\circ$. As theory predicts, the experimentally measured longitudinal and the circumferential stresses at the edge would decay to a uniform membrane pattern of stresses at a distance $2.5 r_m$ away from the joint.

Lane and Rose⁽¹⁶⁶⁾ reported that for $\alpha = 22\frac{1}{2}^\circ$ the maximum circumferential edge stress could be as high as twice as the circumferential stress calculated on a straight pipe, and for $\alpha = 15^\circ$ the bend PSM could be in the region of 1.4. For both values of α , the maximum measured stress was 30° away from the intrados and located on the inside surface.

Ingen Housz⁽¹⁷⁸⁾ carried out pressure tests on multi-mitred GRP/PVC lined bends. He presented the results in a strain format for the dual laminate construction. His experimental results showed that the strains at the joint would be maximum at the intrados located on the inside surface and positioned in the circumferential direction. Such a maximum strain is about 1.67 higher than the maximum strain induced in a straight pipe constructed similarly to the bend and loaded by the same pressure. The strains measured at the mid-segment were comparable with the maximum strain of a straight pipe with noticeable bending strains observed. No theoretical comparison was presented due to possible errors arising from the thickness variation around the bend, but based on Murthy's⁽¹⁷⁸⁾ theoretical prediction, Ingen Housz suggested that increasing the intrados thickness to 2-3 times the original thickness would decrease the strains to an 'acceptable' level.

CHAPTER FIVE

SAMPLE DESICRIPTION, EXPERIMENTAL PROCEDURE

AND

INSTRUMENTATION

CHAPTER FIVE

SAMPLE DESCRIPTION, EXPERIMENTAL PROCEDURE AND INSTRUMENTATION

5.1 Straight Pipes and Bend Components

All the pipe specimens tested are commercially manufactured by five suppliers in total.

The different pipe samples have been characterized in Chs. 6, 7 and 8, whereby they are described as a function of their glass content (burn-off tests), dimensions (tangent length, internal diameter and bend radius), thickness measured from cut pipes and bends, and mechanical properties as obtained from coupon testing. Table 5.1 lists the raw material used, manufacturing process used, strain gauges positions and manufacturers.

The dimensions of the bends were pre-selected on nominal basis to cover a wider range as possible of the pipe factor λ used in practice. Because of the absence of a recognised code of practice for GRP bends, the pipe components were constructed by the individual manufacturers with accordance to their own in-house codes of practice. These practices were supposed to follow similar recommendations to those specified by PS15-69⁽⁹⁾, BS4994⁽³⁾, B202B⁽⁴⁾ and B201B⁽⁵⁾.

The straights and bends were not post-cured due to probable damage occurring to the strain gauges already installed at the early stages of construction. Also, due to the considerable volume of those bends, it was impractical from an economical point of view to post-cure them in special ovens. The latter is true for all sizeable components used in practice.

The research bodies, NEL and RAPRA, had no direct supervision on the manufacturer's constructional procedure used to make the pipe samples. However, these samples were supposed to sustain similar features to those pipe fittings actually used in the chemical industry.

TABLE 5.1 - Raw Materials, Manufacturing Process and Manufacturer's Names for the Pipe Samples tested in the Programme

| Specimen Number | Resin Used | Glass fibre Reinforcements | Pipe Component | Process of Manufacture | Manufacturer's Name | Strain gauged Surfaces | Chapter |
|-----------------|------------|----------------------------|----------------|------------------------|---------------------|------------------------|---------|
| S001 | UP | CSM | B/S | H.L.U. | PD & E | in and out |) |
| S002 | UP | CSM | B/S | H.L.U. | PD & E | in and out |) |
| S003 | UP | CSM | St. | H.L.U. | PD & E | out |) |
| S004 | UP | CSM | St. | H.L.U. | PD & E | in and out |) |
| S005 | UP | CSM | St. | H.L.U. | PD & E | in and out |) Ch. 6 |
| S006 | UP | CSM | B/S | H.L.U. | PD & E | out |) |
| S007 | UP | CSM | St. | H.L.U. | PD & E | out |) |
| S008 | UP | CSM | St. | H.L.U. | PD & E | in and out |) |
| S009 | UP | CSM | St. | H.L.U. | PD & E | out |) |
| S010 | UP | CSM/PVC * | St. | H.L.U. | PD & E | out |) |
| S011 | UP | CSM/PVC | St. | H.L.U. | PD & E | in and out |) |
| S012 | UP | CSM/PVC | B/S | H.L.U. | PD & E | in and out |) Ch. 7 |
| S014 | UP | CSM/PVC | B/S | H.L.U. | PD & E | in and out |) |
| S016 | UP | CSM/PVC | B/S | H.L.U. | PD & E | in and out |) |
| S017 | UP | CSM | B/S | H.L.U. | PD & E | out |) |
| S018 | UP | CSM | B/S | H.L.U. | PD & E | out |) |
| S019 | UP | CSM | B/S | H.L.U. | PD & E | in and out |) |
| S020 | UP | CSM | B/S | H.L.U. | Porodrite | out |) |
| S021 | UP | CSM | B/S | H.L.U. | Porodrite | in and out |) |
| S022 | UP | CSM | B/S | H.L.U. | Porodrite | in and out |) Ch. 6 |
| S023 | UP | CSM | B/S | H.L.U. | esinform | out |) |
| S024 | UP | CSM | B/S | H.L.U. | Resinform | in and out |) |
| S025 | UP | CSM | B/S | H.L.U. | Resinform | in and out |) |
| S026 | UP | CSM | St. | H.L.U. | Resinform | out |) |
| S027 | UP | CSM | St. | H.L.U. | Resinform | in and out |) |
| S028 | Ep. | WR/FW | B/S | H.L.U./FW | Wavin | out |) |
| S029 | Ep. | WR/FW | B/S | H.L.U./FW | Wavin | out |) |
| S030 | Ep. | WR/FW | B/S | H.L.U./FW | Wavin | in and out |) Ch. 8 |
| S031 | Ep. | FW | St. | FW | Wavin | in and out |) |
| S032 | Ep. | FW | St. | FW | Wavin | out |) |
| S033 | UP | CSM/PVC | B/M | H.L.U. | PD & E | in and out |) |
| S034 | UP | CSM/PVC | B/M | H.L.U. | PD & E | in and out |) |
| S035 | UP | CSM/PVC | St. | H.L.U. | PD & E | in and out |) |
| S036 | UP | CSM/PVC | B/M | H.L.U. | PD & E | in and out |) Ch. 7 |
| S037 | UP | CSM/PVC | B/M | H.L.U. | PD & E | in and out |) |
| S038 | UP | CSM/PVC | St. | H.L.U. | PD & E | in and out |) |
| S039 | UP | CSM/WR/UD | B/S | H.L.U. | PD & E | in and out |) |
| S040 | UP | CSM/WR/UD | B/S | H.L.U. | PD & E | In and out |) |
| S041 | UP | CSM/WR/UD | St. | H.L.U. | PD & E | in and out |) |
| S042 | UP | CSM/WR | B/S | H.L.U. | PD & E | in and out |) |
| S043 | UP | CSM/WR | B/S | H.L.U. | PD & E | in and out |) |
| S044 | UP | CSM/WR | St. | H.L.U. | PD & E | in and out |) |
| S045 | UP | CSM/WR/UD | B/S | H.L.U. | PD & E | in and out |) Ch. 8 |
| S046 | UP | CSM/WR/UD | B/S | H.L.U. | PD & E | in and out |) |
| S047 | UP | CSM/WR/UD | St. | H.L.U. | PD & E | in and out |) |
| S048 | UP | CSM/WR/FW | B/S | H.L.U./FW | BCME | in and out |) |
| S049 | UP | CSM/WR/FW | B/S | H.L.U./FW | BCME | in and out |) |
| S050 | UP | CSM/WR/FW | B/S | H.L.U./FW | BCME | - |) |

| Specimen Number | Resin Used | Glass fibre Reinforcements | Pipe Component | Process of Manufacture | Manufacturer's Name | Strain gauged Surfaces | Chapter |
|-----------------|------------|----------------------------|----------------|------------------------|---------------------|------------------------|---------|
| S060 | UP | CSM/PVC | B/M | H.L.U. | PD & E | in and out |) |
| S061 | UP | CSM/PVC | B/M | H.L.U. | PD & E | in and out |) Ch. 7 |
| S062 | UP | CSM/PVC | St. | H.L.U. | PD & E | in and out |) |

PD&E = Plastic Engineering & Design
 BCME = Bristol Composite and Material Engineering
 B/S = Bend/Smooth
 B/M = Bend/Mitred
 St. = Straight
 H.L.U. = Hand lay-up
 U.P = Unsaturated polyester resin
 Ep. = Epoxy resin
 * PVC = rigid PVC

User's representatives from BP and ICI were the inspectorate in assessing the existence of such features.

5.1.1 Pipe components made by the hand lay-up process

All pipes and bend components were manufactured using ATLAC 382-05 (ICI Polyester resin), with the different types of reinforcements made out from 'E' glass fibres. MEKP was used as a catalyst, and cobalt naphthanate was used as an accelerator.

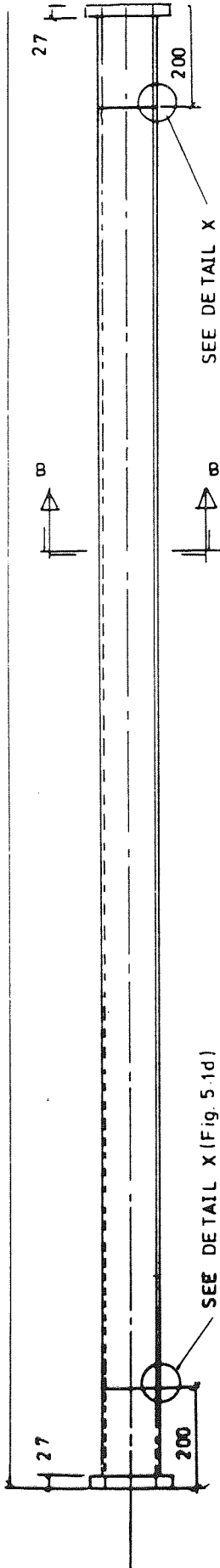
(a) Straight pipes

All the straight pipes were delivered in 3m lengths with stub flanges at each end. The construction procedure used for pipe diameters ranging from 100mm to 600mm nominal bores could be described by the drawing laid down in Fig. 5.1a. The main wall laminate of the straight was to have three over laps distributed around 120° of the circumference as shown in Fig. 5.1b. This pattern of overlap distribution was not found to be consistent with wall thickness measurements; but more likely having the reinforcements being displaced by the rolling operation.

Pre-made stub flanges with mild steel backing rings were used to clamp the ends of the pipe components (Fig. 5.1c). Such a technique is favourable for GRP pipe used in the chemical industry, since it avoids bolt hole mis-alignment and compensate for any-flange lip distortion (upon curing) by using 3 mm soft rubber seal⁽¹⁸²⁾. The stub flanges were laminated by hand with the reinforcements being carried around in line with the pipe wall. The PVC/GRP flanges are constructed in a similar manner to the GRP flange, except that the face of the stub flange is covered with PVC (Fig. 5.1c).

The ready made stub flanges were then butt-jointed to the main body of the pipe (Fig. 5.1d). The ends of the pipe are usually ground to a taper of 1 in 6 leaving intact the chemically resistive liner laminate of 1.2 kg.m⁻² CSM + gel coat. The pipe was then held firmly in position

3 000



STANDARD STUB FLANGE

SEE DETAIL X

Figure 5.1a General layout of 100 mm (4 inch) Nominal Bore GRP straight pipe

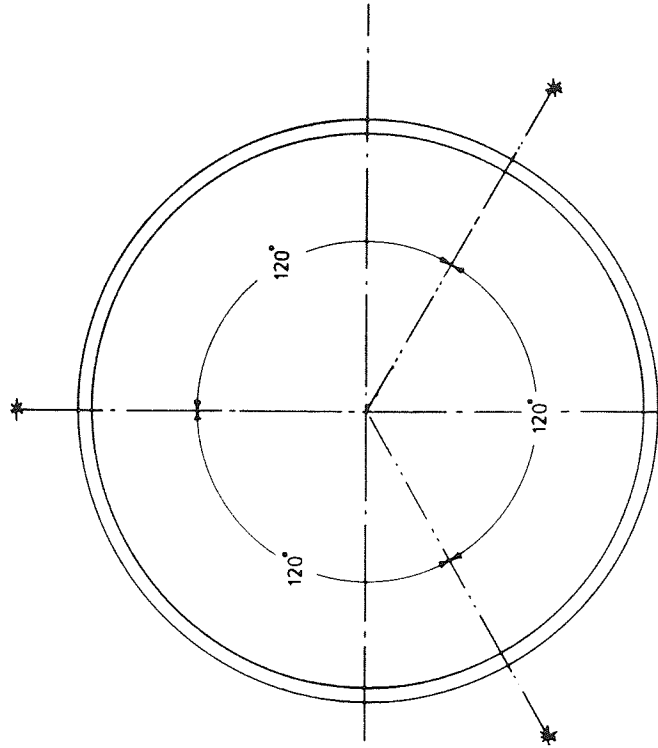
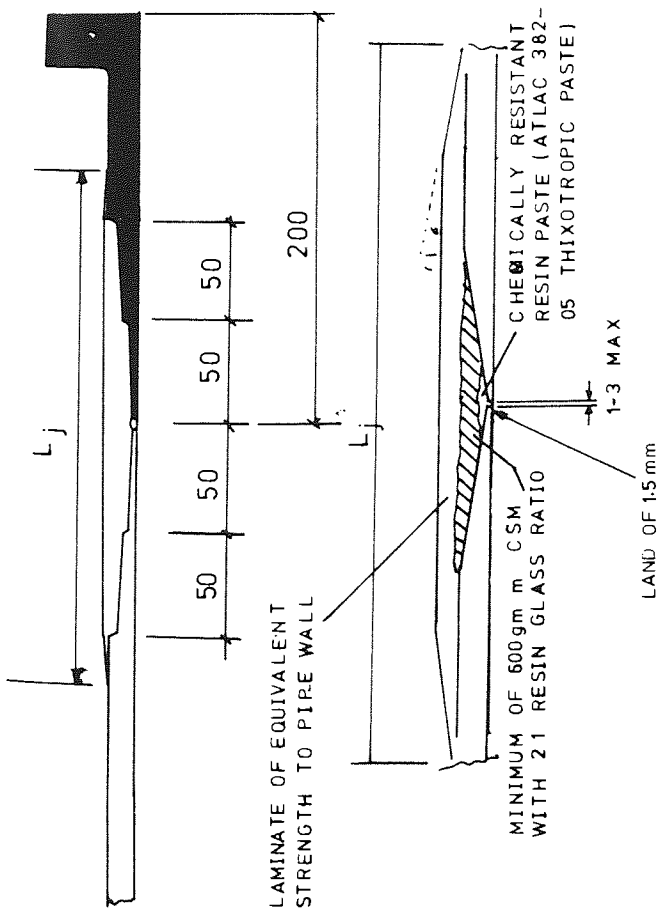
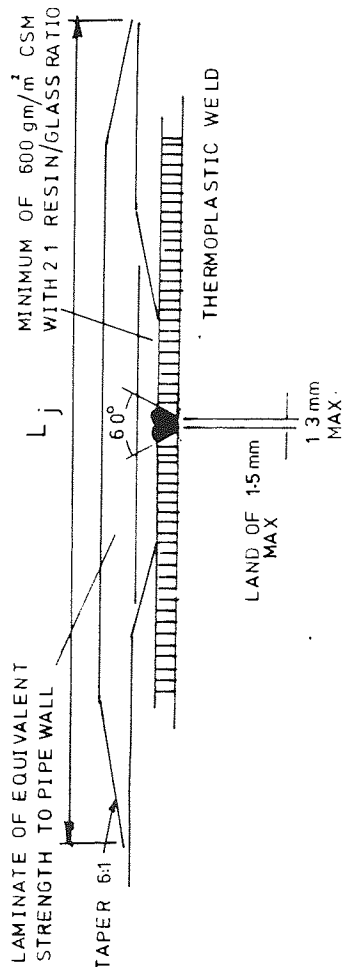


Figure (5.1b)

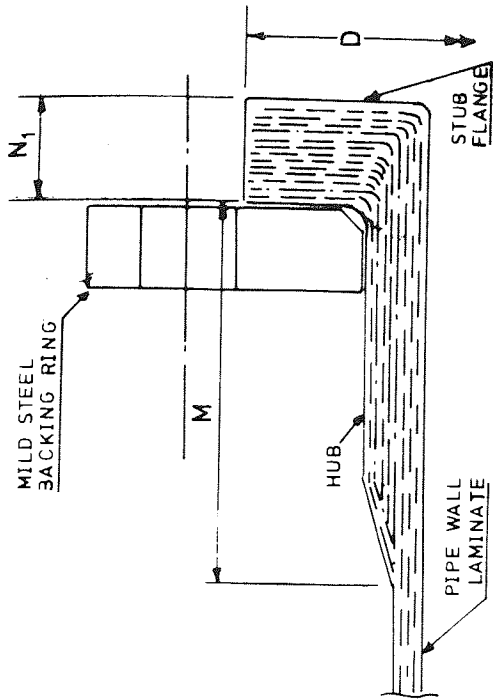
SECTION B-B
POSITION OF OVERLAPS
OVERLAP LAYER - 40 mm MAX
30 mm MAX



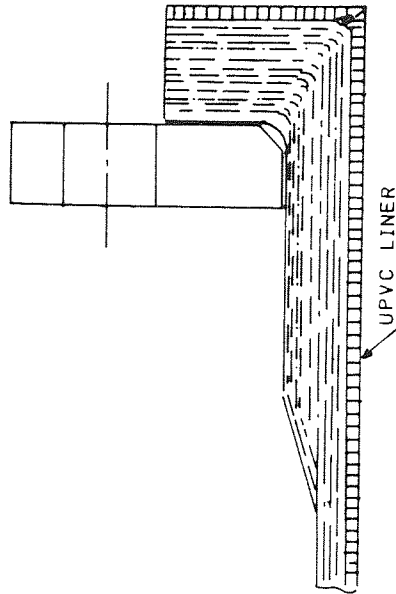
(i) BUTT JOINT BUILD UP OF UNLINED PIPE



(ii) BUTT JOINT BUILD UP : LINED PIPE (182)



GRP STUB FLANGE



PVC/GRP STUB FLANGE (182)

Figure (5.1c)

Figure (5.1d)

with gap of not more than 3 mm between them, the gap being filled with thixotropic resin paste as an initial sealant. The joint was then made with successive layer of reinforcement with the outer edges of the overlay being tapered to blend in with the pipe.

For a PVC/GRP joint, the GRP layer is ground back at a taper of 1 in 6, leaving the PVC end intact. A weld preparation was made, and runs of weld were applied using a hot gas gun and PVC filler rod. The weld was proven by a high frequency spark test before layers of reinforcement were applied in a similar way to the GRP butt joint (Fig. 5.1d).

(b) Bend Samples

The bend/tangent structure shown in Fig. 5.2a was made from the bend fitting and the tangents made separate, being butt-jointed together as shown in Fig. 5.2a.

A collapsible type of mandrel was used as the mould for the construction of the bend fitting. The gel coat and the backing reinforcements were laid on the mould, having the mat tailored as shown in Fig. 5.2b for ease of lamination. As the mandrel was removed, the bend ends had small straight extension as shown in Fig. 5.2c for ease of butt-joining with the tangents. Thereafter, the bend fitting was butt-jointed to the tangents, and the specified glass mass per unit area was laminated. In this instance, the mat overlaps were supposed to be positioned as shown in Fig. 5.2d. At the end of lamination a 'c' veil was used to cover the outside surface.

5.1.2 Pipe Components made by the Filament Winding Process

The process has been already described in Chapter 2 (see article 2.5.2). Epoxy resin + MDA curing agent was used, with fibre

STANDERED STUB
FLANGE (see Figure 5.1c)

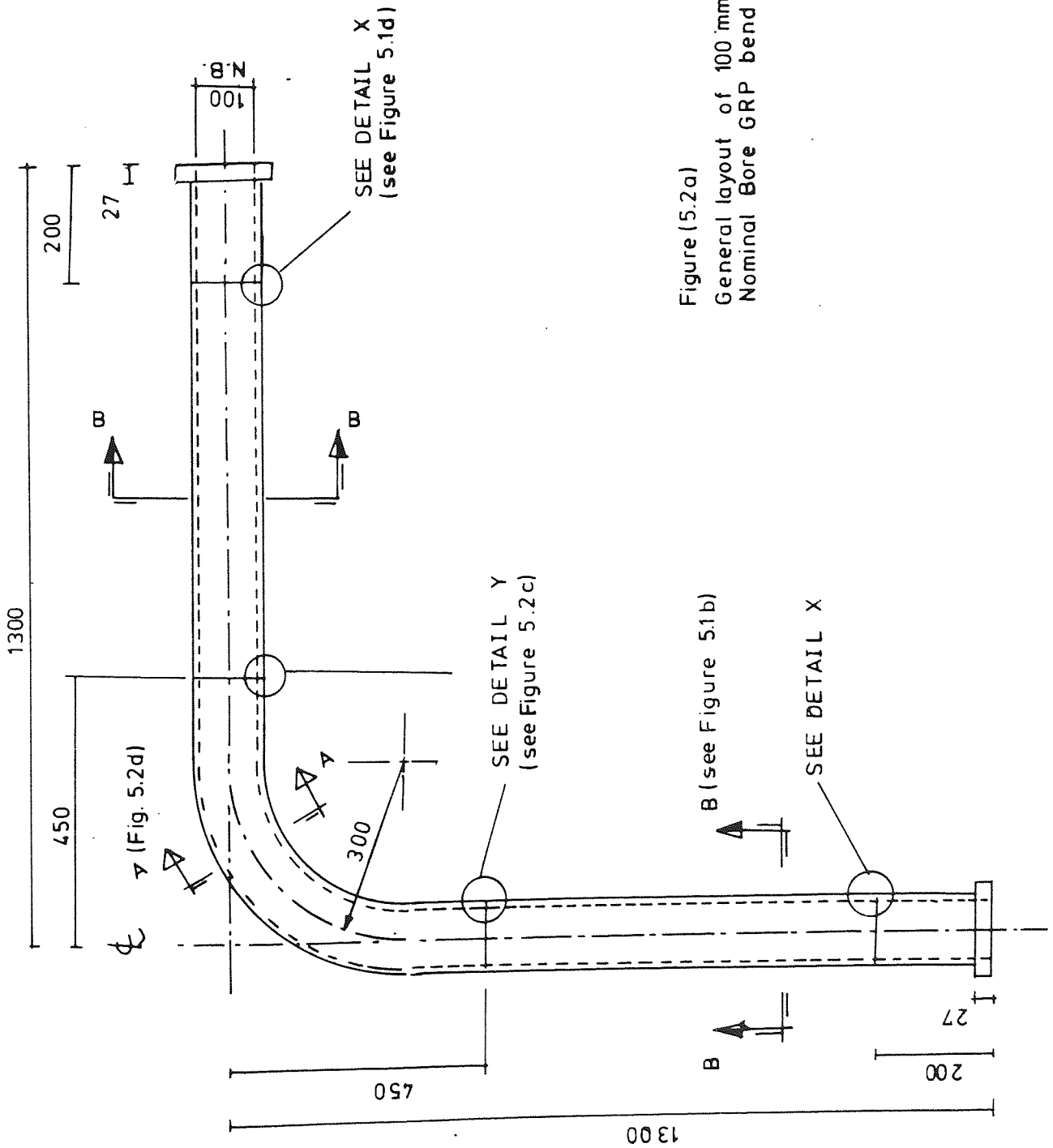
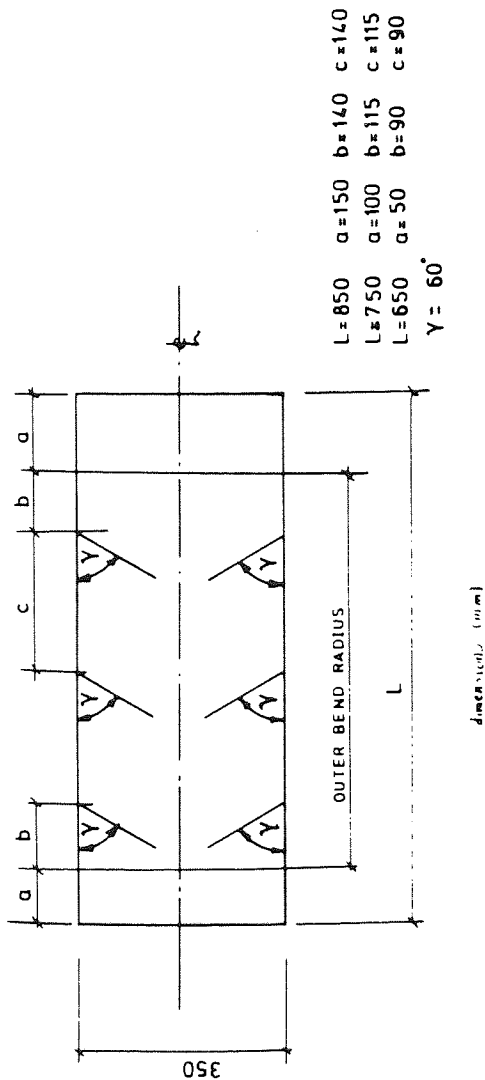


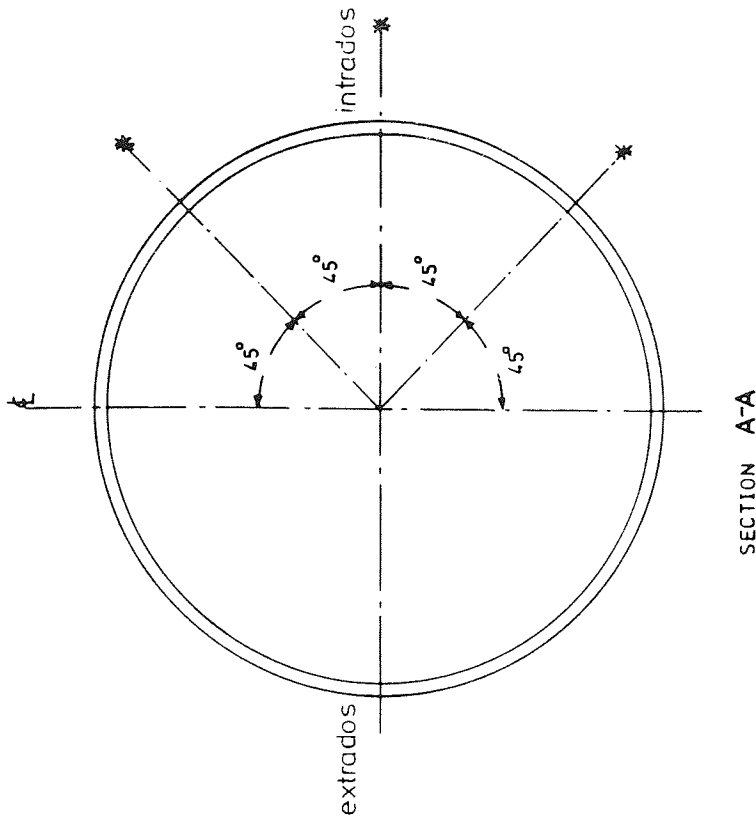
Figure (5.2a)
General layout of 100 mm (4 inch)
Nominal Bore GRP bend

B (see Figure 5.1b)

SEE DETAIL X

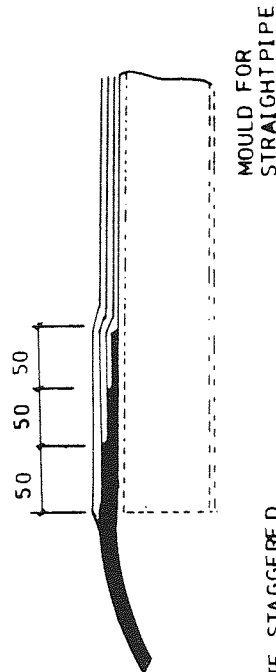


Figure(5.2b) Shape of mat reinforcement on bend



POSITION OF OVERLAPPS ON BEND *
OVERLAP LAYER 40 mm MAX
30 mm MIN

Figure(5.2d)



BASIC BEND WITH LAMINATE STAGGERED
AT END FOR CONNECTION TO MOULDING
AT STRAIGHT LENGTH

DETAIL Y

Figure(5.2c) MAKE UP OF BEND TO STRAIGHT

reinforcements being situated at $\pm 55^\circ\text{C}$ from the longitudinal axis of the pipe.

With this type of pipe, compression moulded flanges are usually used and they are of collar type with pre-drilled bolt holes (Fig. 5.3) The tangent is pushed into the collar flange by a specified distance (50 mm in this case) using a compatible adhesive (e.g. epoxy). Surface preparation and method of jointing is well provided by the different manufacturers⁽³⁶⁾. The same procedure was used to joint the bend fitting, which was hand-laminated, to the filament wound tangents.

5.2 Testing Rig

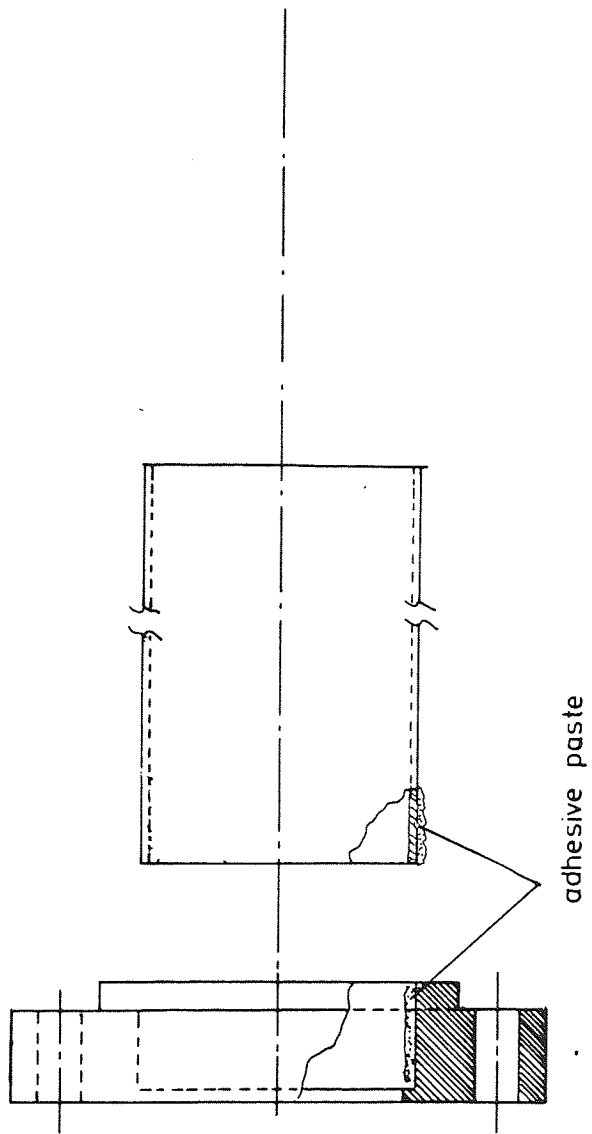
5.2.1 Testing of straight pipes

The different straights were tested under flexural, torsional, and pressure loading. All tests were carried out under relatively low load limited by a maximum strain of 2000 microstrain measured on the surfaces of the pipes.

(a) Flexural loading

Originally it was anticipated that four-point bending tests would be used to induce a pure bending moment on the pipe specimen (see background of Fig. 5.7a). However, preliminary test results discussed in Chapter 6 revealed that the cross-section of the straights would ovalize due to the anvil effect, hence, the necessity of reinforcing out that position or the use of very long pipes.

A convenient method is to test these straight pipes under cantilever loading. This is shown in Fig. 5.4 where the pipe was tested horizontally by fixing one stub flange and applying dead weights at the other. At the same time as the loads were applied, strain readings were registered from strain gauges located at the centre of the pipe.



Figure(5.3) Dough moulding compound lip flange

(b) Pressure testing

All pressure tests were carried out under closed-end condition. This type of test was agreed upon by the design committee among other tests suggested in the literature, e.g. Ref (90). The pipe ends were sealed using mild steel plates and backing rings closures, with 3 mm soft rubber full face gasket⁽¹⁸²⁾. The pipes were pressurised lying horizontally and supported on wooden saddles (120°) displaced as shown in Fig. 5.5, having the pipe being cushioned with rubber pads to minimise any restraint on deformation. The advantages of the horizontal position of loading is the easy access on installing and dismantling the heavy end plates. All pipes were subjected to incremental pressure loading, and for most of them the strains were logged on pressurizing and de-pressurizing.

(c) Torsional testing

Torsional moment is applied to the body of the straight by fixing one end of the straight and freely rotating the other end; which is restrained from flexural deflection. The rig is shown in Fig. 5.6 where the ball bearings were allowed to move axially, thus, eliminating any possibility of warpage that might occur due to the unevenness of the pipe wall thickness. The shear deformation was monitored via the measured strains. Measurement of angular rotation were extensively used by Wright⁽⁴¹⁾ on in-house-built CSM pipes.

5.2.2 Testing of Bends

All the bends were tested on the rig shown in Fig. 5.7a except for the 600mm nominal bore bends, where they were tested vertically. The stressing frame was designed and constructed in RAPRA⁽¹⁸³⁾.

The bends were tested under in-plane bending (closing and opening); using the load cell positioned at the side; and under out-of-plane

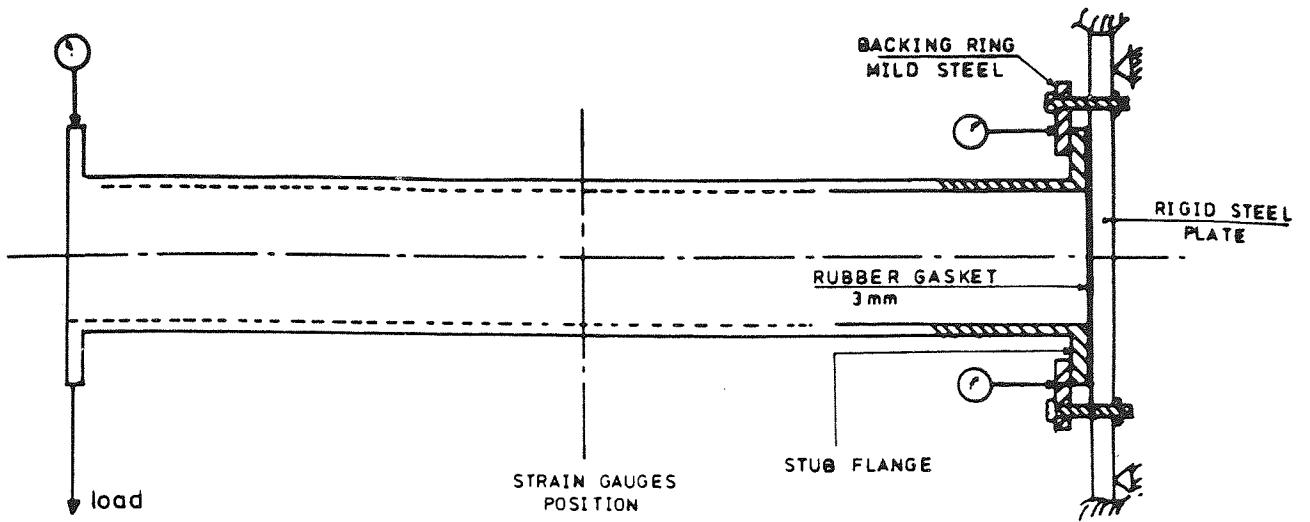


Figure (5.4) Cantilever Testing

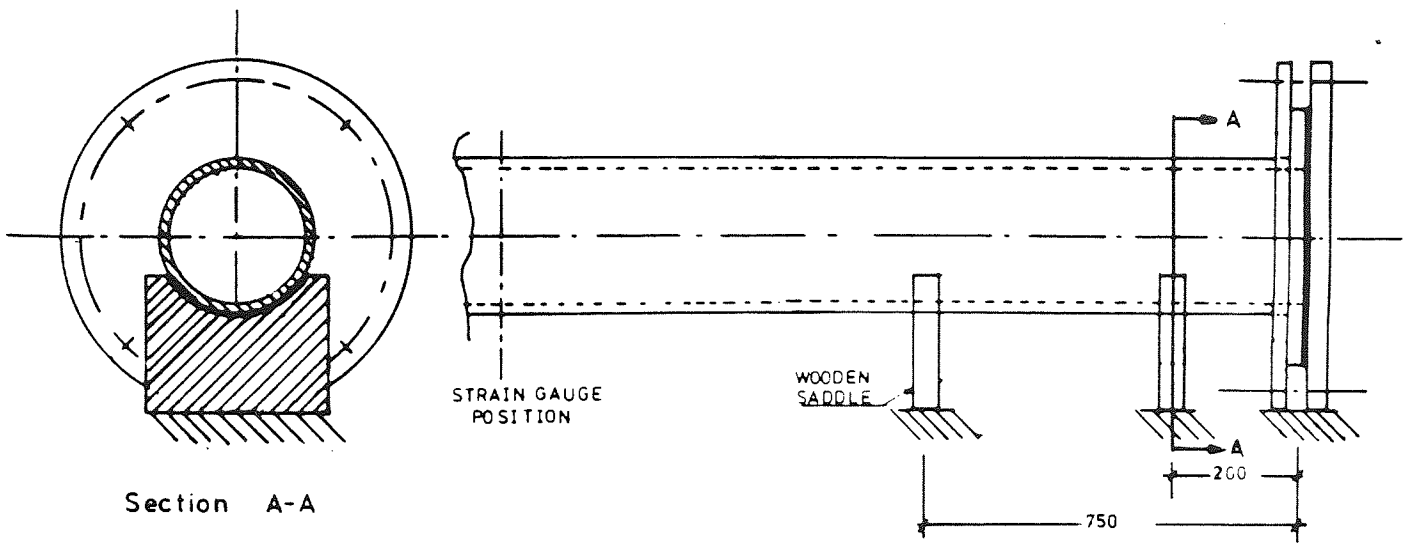


Figure (5.5) Pressure Testing

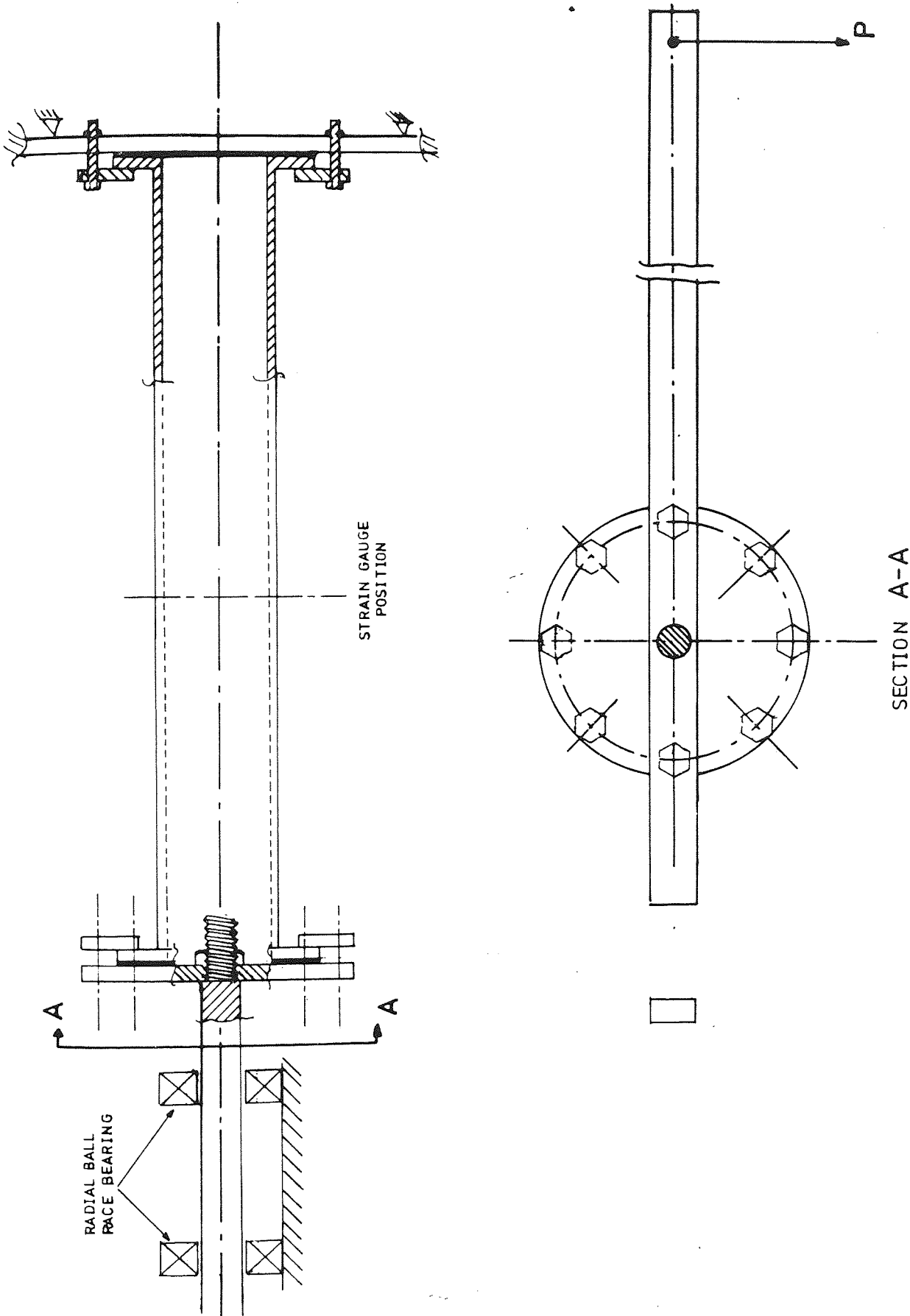
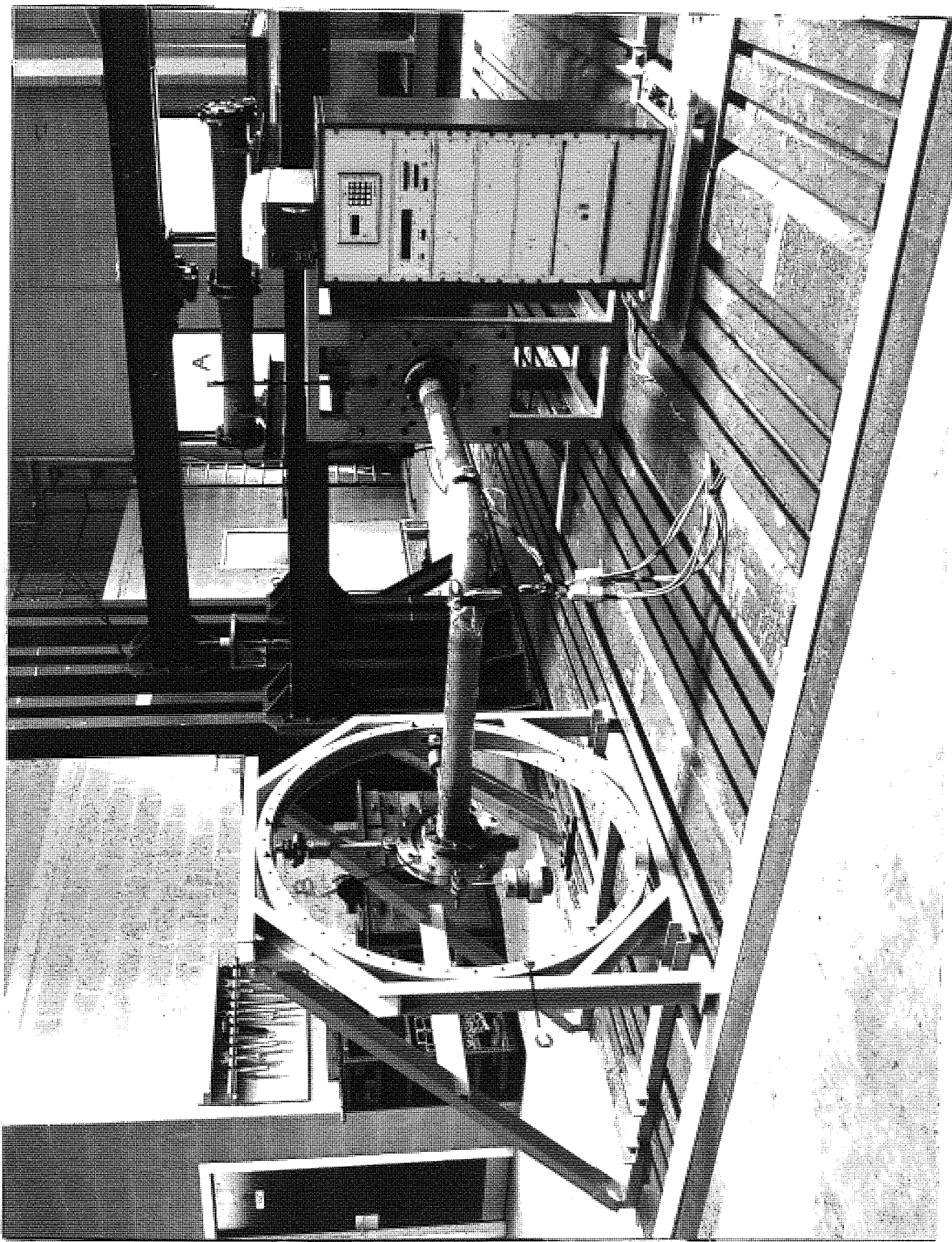
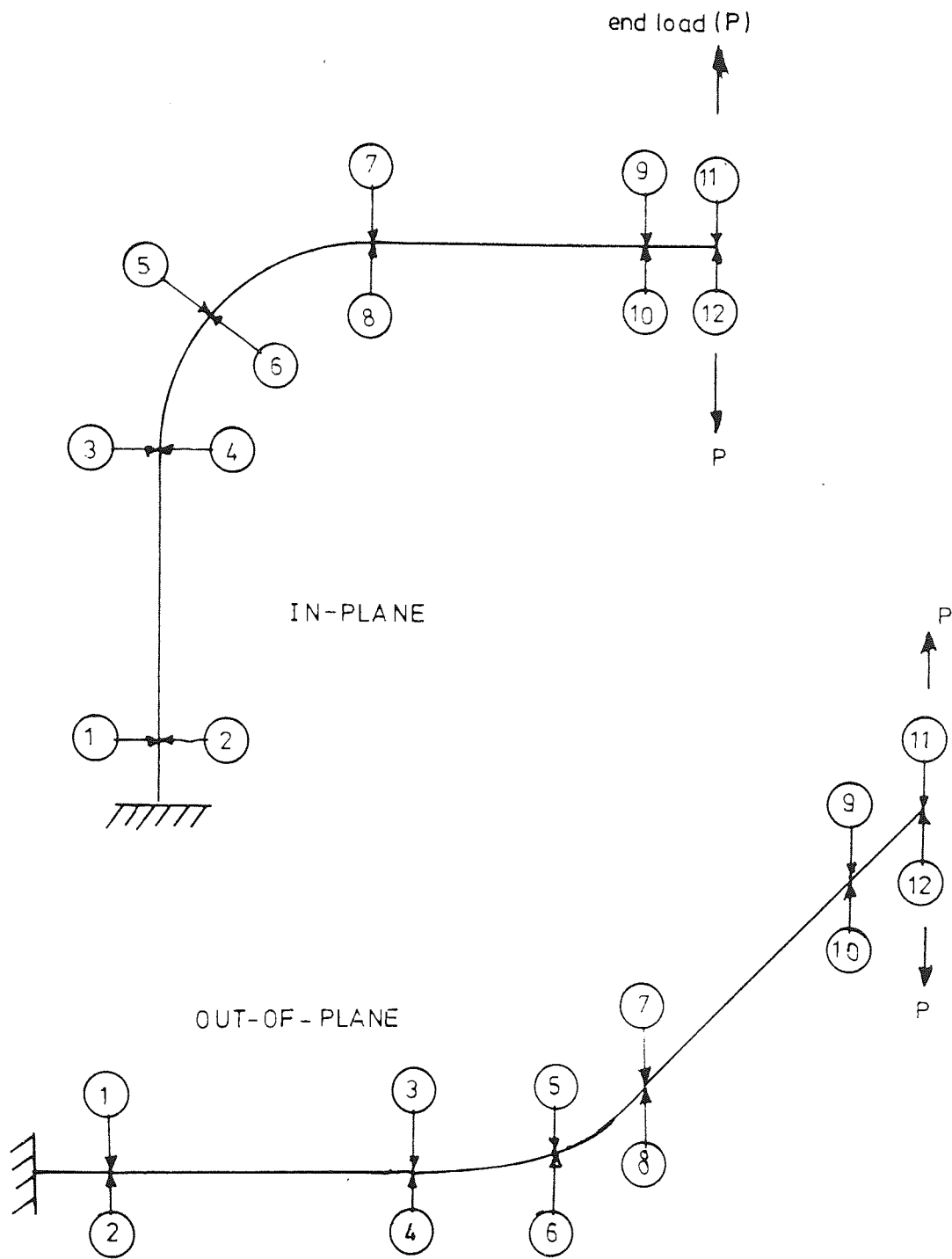


Figure (5.6) Torsional Testing



Figure(5.7a) Stressing Frame



Figure(5.7 b) Dial gauges positions on the bend

bending; using the top load cell. The tests were carried out by fixing one stub-flange and applying the force to the other. The bends could be also tested under combined internal pressure and bending loadings. In this instance, water was used as the pressurising medium, being pumped at the fixed flange anchor point.

Upon incremental loading, deflections were measured at the different parts of the bend, by using dial gauges positioned against small aluminium plates ($\sim 1.5 \times 20 \times 20$ mm) pre-bonded to the bend in the positions shown in Fig. 5.7b. For the purpose of flexibility calculations, the average free end-deflections measured by dial gauges 11 and 12 were used (App. I).

At the same time as the deflections were measured, strains were logged from strain gauges at the bend centre. These were used to calculate the SIF factors (App. I).

The bend specimen was anchored at one end to a vertical steel plate which was mounted on a rigid frame (position A in Fig. 5.7a). The other end of the bend was bolted to a circular plate (position B in Fig. 5.7a). Long nut/screws lead turn buckle system; connected in series to a load cell, acted as the link between the circular plate and the outer steel circular frame (position C in Fig. 5.7a); using universal joints. The joints were to give the end of the bend complete freedom of rotation.

The test rig is suitable for testing bends up to 250mm diameter by using compatible sizes of end plates. Maximum applied end-loads were limited by the 50mm displacement travelled by the nut/screw mechanism. Bends of different tangent lengths could also be accommodated on the rig by displacing the anchor positions.

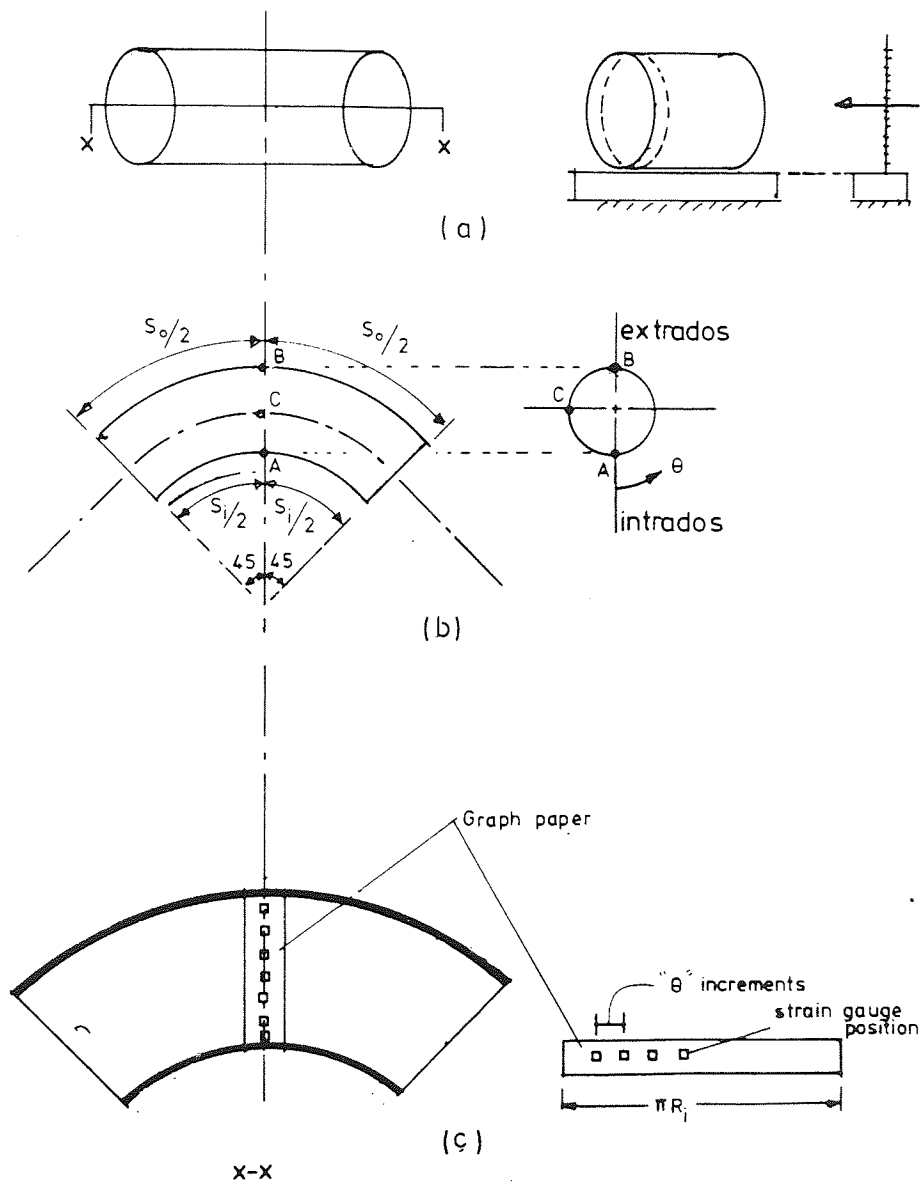
Bends taken to failure under in-plane bending, were tested standing vertically using an overhead crane connected in series to a load cell.

5.3 Instrumentation

All bends and straight pipes were strain gauged at the centre, either on the inside and at the outside surfaces or at the outside surface only as summarised in Table 5.1. The strain gauges used, were rectangular type three-element rosette.

The inside strain gauges were bonded to the bend fittings while the bends were in the factory before being joined to the tangents. The procedure could be summarised as the following (with the aid of Fig. 5.8a,b,c).

- (a) The middle plane bisecting the bend in the horizontal plane was located by height measurements on both the inner and the outer bend radii, i.e. axis x-x of Fig. 5.8a.
- (b) Point A at the intrados ($\theta = 0^\circ$) and point B at the extrados ($\theta = 180^\circ$) were located by bisecting arc lengths S_i and S_o as shown in Fig. 5.8b. Point C was then marked by locating the 45° angular position on the bend (Fig. 5.8a).
- (c) Once points A, B and C were located, a line was drawn through the points on the outside surface, and this was carefully copied on the inside surface.
- (d) The distance length joining points A and B via C on the inside surface, was determined by using a graph paper strip of 20-25 mm width, and following the contour of the inside surface of the bend fitting. The A to B distance was then divided into uniformly displaced divisions required by the number of the strain gauges that were to be used (see Fig. 5.8c).



Figure(5.8)
Location of strain gauge positions on bend

- (e) Similar surface area dimensions of that of the strain gauges elements, were cut on the graph paper, allowing an extra 1 or 2 mm at each side. The graph paper was then bonded to the inside surface of the bend by an adhesive tape, and the positions of the strain gauges were marked on the bend surface. Also, the edges of the graph paper strip were similarly marked.
- (f) The graph strip was removed, and the marked positions of the strain gauges were rubbed with fine grade of emery paper to provide a sound bonding surface. The surface was later degreased using a tissue lightly saturated with acetone. The graph strip was put back into place guided by its edge marking.
- (g) The strain gauges were bonded into positions after applying a thin layer of cyanoacrylate glue (PERMABOND C) to the surface and the gauge was pressed with the finger tip for at least 60s using a polyethylene film.
- (h) The terminals were next glued into position.
- (i) Welding the strain gauge wires onto the terminal, using a small mirror if necessary accessed through one end of the bend fitting.
- (j) The connecting wires were later welded to the terminals.
- (k) The gauges were checked for any electrical disconnections and then covered with (RS) silicone rubber covering both the strain gauge rosette and the terminal.
- (l) The leading wires were bundled together with the appropriate labels. The connecting wire were waterproof fine copper wires (RS insulated 0.2 mm copper wires).

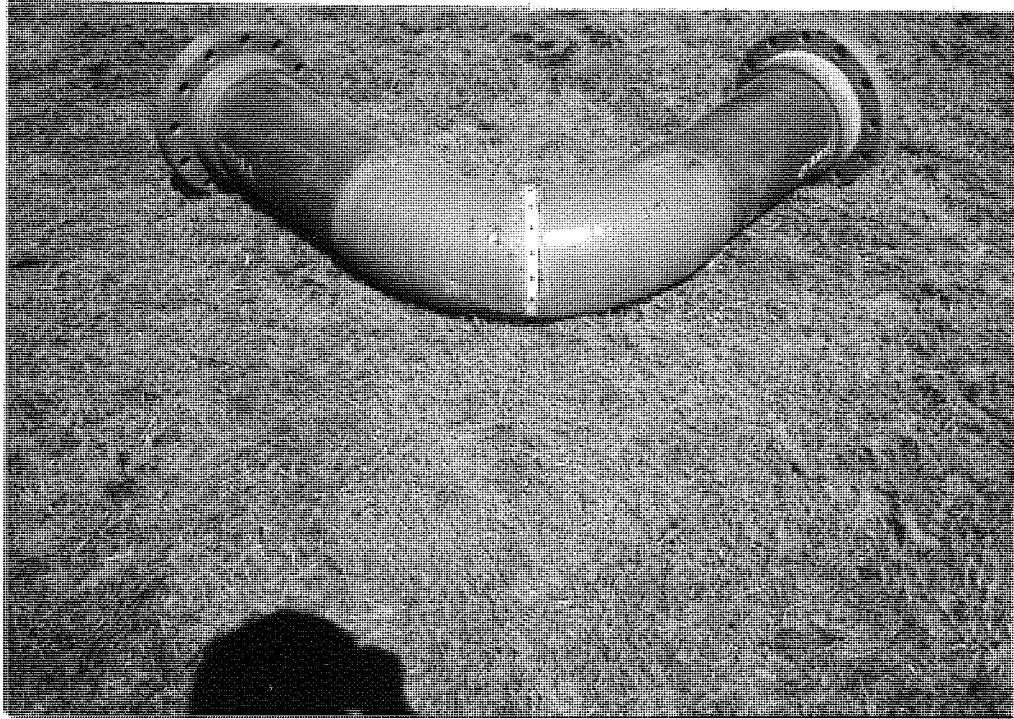
For the straight pipes, the same procedure was followed, by first making the pipe into two portions, 1.8m and 1.2m, where the strain gauges are located 300 mm from the edge of the 1.8mm long portion, and the two parts were then butt-jointed.

The outside strain gauges were positioned on the bend when the bend samples were in the finished form. They were adhered to the pipe wall using similar procedure used to those of the inside. Their positions corresponded to those of the inside strain gauges, by using a light bulb inside the pipe or the bend.

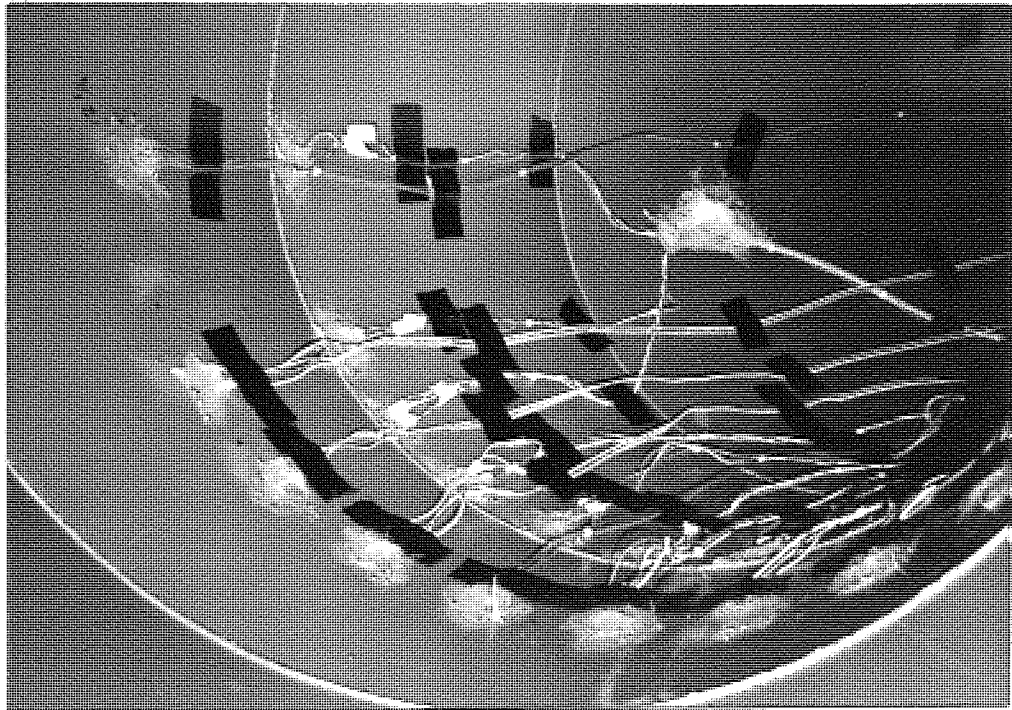
The instrumentation of the inside gauges for the PVC/mitred GRP bends was similar to those of the smooth bends. The inside gauges were adhered into position (centre of the bend and at the segment joint) when the PVC liner was partially welded. For the 600mm nominal bore pipes and bends, these were strain gauged on the inside and the outside, in their finished form. For the smooth CSM/PVC lined bends and their corresponding straight pipes, the strain gauge rosettes were first adhered into position on the outside surface of the PVC liner, before the required CSM reinforcements were laminated. The outside gauges were adhered into position after the laminate has cured. The leading wires connecting the gauges at the CSM/PVC interface surface, were laid along the same surface and emerged at the stub-flange joint. The major problem associated with the PVC lined bends was the inaccuracy of alligning or positioning the outside gauges to the inside gauges due to the opaque nature of the PVC liner.

Fig. 5.9 show a typical positioning of the strain gauge on the outside surface of a smooth GRP bend, and Fig. 5.10 shows typical strain gauge positions on the inside surface of a CSM/PVC lined mitred bend.

All the straight pipes and the bends were strain gauged over 180° of the circumference, assuming symmetry of deformation. Strain gauging throughout the 360° would have provided a reasonable base for assessing the above assumed symmetry. Perhaps the dominating factor that overruled the opportunity of 360° instrumentation is the number of strain gauges rosettes (1000) which consumed a large proportion of the capital located for the project.



Figure(5.9) Picture showing outside strain gauge rosettes on 250 mm nominal bore smooth bend



Figure(5.10) Picture showing inside strain gauge rosettes on 600 mm nominal bore mitre bend

The strain gauges were purchased from three different suppliers.

These are:

(1) Micro-measurements (M=M)

Gauge rosette type: EA-13-125RA-120

Gauge factor = $2.07 \pm 1.0\%$

Active gauge length = 0.125 inch

Gauge resistance = $120 \Omega \pm 0.2\%$

(2) Techni-measure (TML)

Gauge rosette type: NFRA-3

Gauge factor = 2.1

Active gauge length = 3 mm

Gauge resistance = $120 \pm 0.5 \Omega$

(3) Environmental equipments (Northern) Ltd (EE)

Gauge rosette type: N31-FA-2-170-11

Gauge factor = $2.1 \pm 1\%$

Active gauge length = 2 mm

Gauge resistance = 120Ω

The short active length of the strain gauges (2-3 mm) is due to the expected sharp strain gradient induced in an ovalized section of a bend.

FENSCAN-3 data logger was used to register the pipe bend strains during loading as voltage units. The logger is capable of recording up to 100 readings in 10s. The data-logger uses a three-wire connection circuit, which compensate for the electrical resistance of the connecting wires. The strain readings were recorded on a tape using a punch interface and Dataack Punch for each increment of loading.

The measured data in the form of strains (voltage), force (voltage, recorded by a Felow 7000 DVM). deflections (measured via dial gauges) were then processed on IBM computer programmes MAVIS and FLEX for the longitudinal and circumferential strains and stresses, principal strains and their orientation, deflections (mm), end force (N), bending moment (N m) and flexibility factors.

The test results presented in the present thesis are based on the best straight line fit of force versus strains and deflections. Early experiments were carried out more than once, e.g. interchanging loading positions of force and fixed tangent, and for most the tests, the measurements were taken on loading and reloading.

CHAPTER SIX

FLEXURAL TESTING OF CSM STRAIGHT PIPES

AND

SMOOTH BEND COMPONENTS

CHAPTER SIX

FLEXURAL TESTING OF CSM STRAIGHT PIPES AND SMOOTH BEND COMPONENTS

6.1 Introduction

The first four sets of CSM pipes and pipe bends recommended by the Joint Design Committee of the project for testing, are described nominally in Table 6.1. They were manufactured by three UK companies using the low pressure contact moulding process, i.e. hand lay-up. The tests carried out on the bends were in-plane and out-of-plane flexural bending. The straights were tested under flexural and torsional loadings.

The flexural and the torsional test results obtained for the straight pipes are compared with the prediction of simple beam and torsion theories respectively, presented in a graphical format. The results of the bends are presented as flexibility factors (K) and stress intensification factors (SIF) compared with BS806⁽¹²³⁾ specifications and isotropic bend theory^(154,155) (App. II)

Elastic constants of the straights and the bends pipe wall were determined from tests carried out on longitudinal strips and rings cut from the bends and straights themselves⁽¹¹⁶⁾, and used in converting the measured strain into experimental stresses, by using Hooke's law for homogeneous, isotropic material under plane stress condition.

Early investigation in the programme indicated that rigidities of such straights and bends cannot be predicted using their nominal thickness, hence a realistic description of the bends, was sought by thickness measurements and burn-off tests⁽³³⁾. The latter would not only give a better idea of the construction pattern, but also enables the prediction of extensibilities and UTUS values.

TABLE 6.1 - Description of CSM Straight and Bend Sets as supplied by the Manufacturer

| Set | Component | Description |
|-------|-----------|--|
| I | S001) | 100 mm nominal bore smooth bend, 3D bend radius construction: 1.8 kg/m ² CSM, 30% glass percentage. |
| | S002) | |
| | S006) | 3m long straight, same construction as S001/002/006. |
| | S003) | |
| | S004) | |
| S005) | | |
| II | S017) | 100 mm nominal bore smooth bend, 3D bend radius construction: 3.6 kg/m ² CSM, 30% glass percentage. |
| | S018) | |
| | S019) | 3m long straight, same construction as S017/018/019. |
| | S007) | |
| | S008) | |
| S009) | | |
| III | S023) | 200 mm nominal bore smooth bend, 1½D bend radius construction: 2.4 kg/m ² CSM, 30% glass percentage. |
| | S024) | |
| | S025) | 3m long straight, same construction as S023/024/025. |
| | S026) | |
| | S027) | |
| IV | S020) | 250 mm nominal bore smooth bend, 1D bend radius construction: 1.8 kg/m ² CSM, 30% glass percentage. |
| | S021) | |
| | S022) | |

6.2 Coupon Testing

6.2.1 Burn-off tests

Those were carried out according to BS2782⁽³³⁾, on samples selected from the different positions on the bends, i.e. the tangents, bend fitting and the joints. The results are presented in Table 6.2 compared with BS4994⁽³⁾ specifications based on the nominal glass content forwarded by the manufacturer.

The measurements of Table 6.2 show that glass mass percentage could vary from 26% to 34% on the same bend (Set IV of Table 6.2). The average thickness per unit glass mass per unit area is 2.465 mm/kg.m⁻² which is higher than the average of 2.2 mm/kg.m⁻² commonly used in industry based on BS4994⁽³⁾. The actual thickness measured on a straight tangent component could well vary by a factor of 1.5 (see Set II of Table 6.2) due to mat overlap, and could be over a factor of 2 when compared to the joints and the bend intrados. In general, the maximum thickness among the whole-tangent-bend system could be either located on the joints or/and on the bend intrados. In both cases the increase of the thickness is of direct function of the glass mass per unit area.

6.2.2 Longitudinal strip tests

These are prepared with accordance to BS5480⁽¹¹⁶⁾. The sample ends, were built to a flat parallel surfaces by adhering treated aluminium plate, using room temperature cured epoxy resin. The load and extension was monitored using an optical extensometer of 50mm gauge length.

The experimental results in the form of the modulus, extensibility, strength, UTUS, non-linear strain, failure strain and non-linear stress are presented in Table 6.3. The experimentally determined mechanical properties are compared with those obtained from flat sheets made similarly to the bends, BS4994 specification and the rule of mixture.

TABLE 6.2 - Burn-off Test Results obtained from the Different Parts
of the CSM Bend Fittings

| | Mg % | Mg kg.m ⁻² | t (mm) | Bore (mm) | t' mm/kg.m ⁻² |
|--------------------|---------|--------------------------|-----------|--------------|-----------------------------|
| <u>Set I</u> | | | | | |
| Nominal (BS4994) | 30 | 1.8 | 3.96 | - | 2.2 |
| Straight-tangents | 28.6 | 1.93 | 5.52 | 102 | 2.86 |
| | 33.3 | 1.84 | 4.14 | 102 | 2.25 |
| Bend-Int* (θ=0°) | - | - | 8.60 | 102 | - |
| Bend-Ext* (θ=180°) | - | - | 4.35 | 102 | - |
| Bend (θ=90°) | - | - | 4.20 | 102 | - |
| Joint | 31.84 | 3.81 | 8.71 | 102 | 2.29 |
| <u>Set II</u> | | | | | |
| Nominal (BS4994) | 30 | 3.6 | 7.92 | - | 2.2 |
| Straight-tangents | 34.78 | 3.56 | 7.36 | 102 | 2.07 |
| | 34.82 | 5.29 | 11.40 | 102 | 2.16 |
| Bend-Int (θ=0°) | 30.66 | 6.00 | 15.03 | 102 | 2.51 |
| Bend-Ext (θ=180°) | 28.23 | 3.28 | 8.33 | 102 | 2.54 |
| Bend (θ=90°) | 29.63 | 3.24 | 8.58 | 102 | 2.65 |
| Joint | 33.47 | 6.07 | 13.83 | 102 | 2.28 |
| <u>Set III</u> | | | | | |
| Nominal (BS4994) | 30 | 2.4 | 5.28 | - | 2.2 |
| Straight-tangents | 30.92 | 2.37 | 5.85 | 204 | 2.47 |
| | 29.86 | 2.66 | 6.82 | 204 | 2.56 |
| Bend-Int (θ=0°) | 30.73 | 4.54 | 11.03 | 204 | 2.43 |
| Bend-Ext (θ=180°) | 32.64 | 2.19 | 4.94 | 204 | 2.26 |
| Bend (θ=90°) | 30.47 | 2.75 | 6.75 | 204 | 2.46 |
| Joint | - | - | - | - | - |
| <u>Set IV</u> | | | | | |
| Nominal (BS4994) | 30 | 1.8 | 3.92 | - | 2.2 |
| Straight-tangents | 32.26 | 2.31 | 5.321 | 250 | 2.31 |
| | 27.04 | 1.75 | 4.38 | 250 | 2.48 |
| Bend-Int (θ=0°) | 28 | 3.5 | 8.40 | 250 | 2.83 |
| Bend-Ext (θ=180°) | 26.4 | 1.89 | 5.67 | 250 | 3.00 |
| Bend (θ=90°) | 28.33 | 1.85 | 5.09 | 250 | 2.75 |
| Joint | 33.99 | 5.1 | 10.92 | 250 | 2.14 |

* Int = Intrados

Ext = Extrados

TABLE 6.3 - Mechanical Properties of CSM Laminates obtained by Tensile Testing of Longitudinal Strips cut from the Pipe Components

| Set No. | t (mm) | W (mm) | E $\frac{N}{mm^2}$ | $\epsilon_{nl} \%$ | $\epsilon_f \%$ | σ_{nl} $\frac{N}{mm^2}$ | σ_f $\frac{N}{mm^2}$ | Mg % | Mg $\frac{kg}{m^2}$ | Extensibility $\frac{N \cdot mm^{-1}}{kg \cdot m^{-2}}$ | UTUS $\frac{N \cdot mm^{-1}}{kg \cdot m^{-2}}$ |
|----------------------|-----------|-----------|-----------------------|--------------------|-----------------|-----------------------------------|--------------------------------|---------|------------------------|--|---|
| I | 5.14 | 12 | 6950 | 0.22 | 1.11 | 17.5 | 76* | 28.6 | 1.93 | 18500 | 200* |
| | 4.55 | 18.9 | 7500 | - | - | - | 66 | 33.3 | 1.84 | 18600 | 160 |
| II | 6.23 | 19.1 | 6650 | 0.51 | 1.6 | 36.2 | 86 | - | - | - | - |
| | 6.55 | 17.8 | 7990 | 0.18 | 1.38 | 13.6 | 81* | - | - | - | - |
| | 10.40 | 17.7 | 6010 | 0.42 | - | 23.3 | 55 | - | - | - | - |
| III | 5.1 | 15.1 | 9940 | 0.28 | - | 28.5 | - | 32.2 | 2.31 | 21940 | - |
| | 5.12 | 14.0 | 7620 | 0.47 | 1.02 | 35.8 | 90 | - | - | - | - |
| | 5.38 | 15.3 | 7210 | 0.25 | 1.5 | 19.4 | 90 | 30.5 | 2.04 | 18660 | 230 |
| Average | | | 7840 ± 970 | 0.33 ± 0.12 | 1.32 ± 0.31 | 24.9 ± 8.2 | 85 ± 7.72 | | | 19410 | |
| Flat sheet Result | | | 7950 ± 370 | 0.34 ± 0.027 | 1.77 ± 0.1 | 27.5 ± 2.1 | 105 ± 5.3 | - | - | 19800 ± 1238 | 260 ± 13 |
| BS4994 | | | 5770 | - | - | - | 91 | 30 | | 12700 | 200 |
| Rule of Mixture | | | 7500 | | | | 115 | | | 17000 | 255 |

* sample failed near the grips

In comparison with the representative flat sheets, the modulus and extensibilities are comparable, whilst the failure strain and strength show a noticeable reduction. Such a reduction might be directly linked with the higher occurrence of stress raisers such as voids (see Fig. 2.6 of Ch. 2) brought about by the lower standard of compaction when laminating on a curved surface to that of a flat surface.

Cracks were observed visually to be initiated on both surfaces of the sample, with a higher intensity on the inside surface where a thick gel coat is usually located. The final failure occurred with glass fibres being broken and pulled-out.

6.2.3 Ring tests

This test is mainly used for the determination of the flexural modulus and strength of a pipe ring in the circumferential direction. The loading arrangement is shown in Fig. 6.1.

Rings which had strain gauges on the inside and the outside surfaces were among those tested. The experimental mechanical properties obtained are presented in Table 6.4, where the modulus has been obtained using the measured strains and the measured horizontal and vertical deflections. The modulus and strength were calculated using thin ring theory⁽¹³¹⁾ as the following:

$$M = \frac{Pr_m}{2} \left(\cos \phi - \frac{2}{\pi} \right) \quad (6.1a)$$

$$M = 0.318 Pr_m \text{ at } \phi = \pi/2$$

$$M = 0.182 Pr_m \text{ at } \phi = 0$$

$$\Delta_v = 0.149 \frac{Pr_m^3}{EI} \quad (6.1b)$$

$$\Delta_H = 0.137 \frac{Pr_m^3}{EI} \quad (6.1c)$$

$$\sigma = \frac{6M}{W.t^2} \quad (6.1d)$$

where $I = Wt^3/12$.

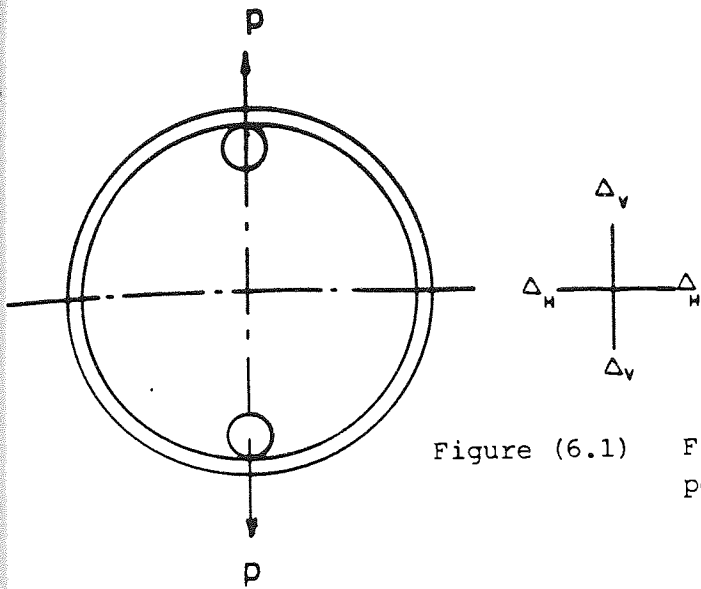


Figure (6.1) Flexural loading of a pipe ring by opposite point-loading

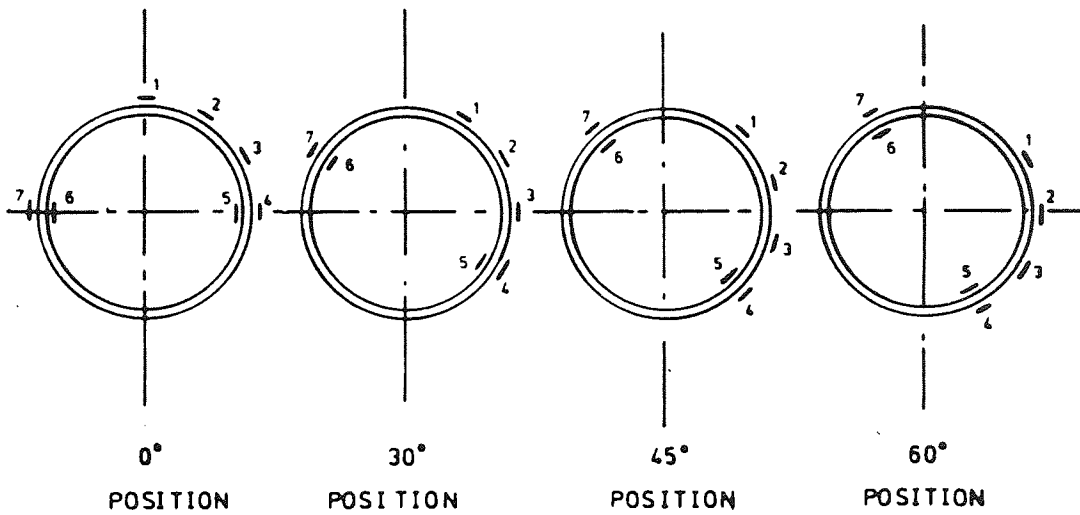


Figure (6.2) Fully instrumented 102 mm Nominal Bore CSM ring under flexural point-loading

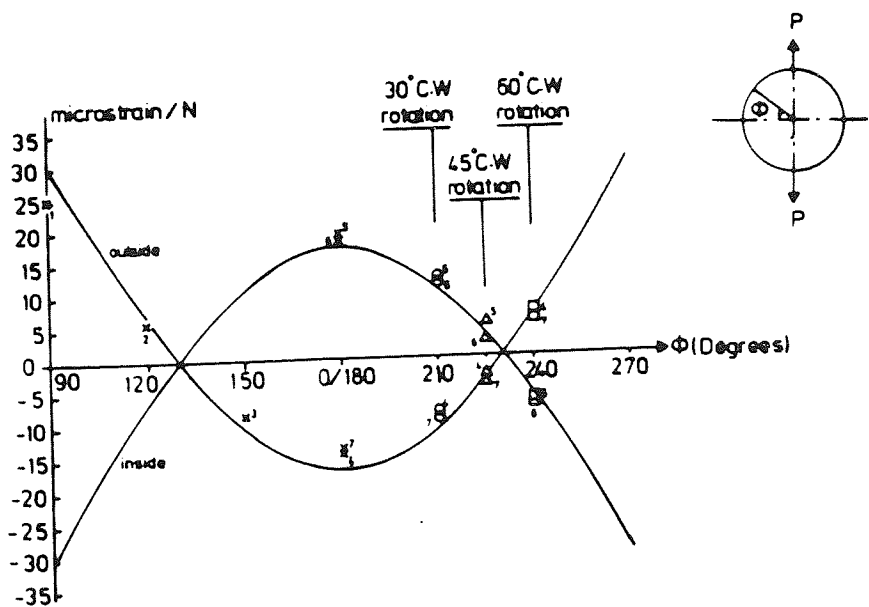


Figure (6.3) Circumferential strain distribution measured under opposite-point flexural loading of sample No. 9 of Table 6.1, $P = 50N$

TABLE 6.4 - Mechanical Properties obtained from Opposite Point Flexural Loading of CSM Pipe Rings

| Set No. of pipe components | Area Selected | t (mm) | r _m (mm) | W (mm) | P/Δ ⁻¹ N.mm | E _{def} ⁻² (N.mm ⁻²) | | E _{strain} ⁻² (N.mm ⁻²) | | | | σ _f ⁻² (N.mm ⁻²) |
|----------------------------------|------------------|-----------|------------------------|-----------|---------------------------|---|-------|--|--------|---------|--------|---|
| | | | | | | Vert | Horiz | L.H.S. | | R.H.S. | | |
| | | | | | | | | Outside | Inside | Outside | Inside | |
| I | ST. | 4.52 | 53.3 | 19 | 47.5 | 7320 | - | - | - | 9410 | 7440 | 130 |
| | ST. | 4.63 | 53.3 | 19 | 50.0 | 7180 | - | - | - | - | - | 145 |
| | ST. | 4.72 | 53.4 | 19.7 | 59.1 | 7790 | - | - | - | - | - | 160 |
| II | ST. | 10.27 | 56.1 | 25.5 | 475 | 5440 | - | - | - | - | - | 110 |
| | BEND | 9.58 | 55.8 | 12.6 | 274 | 7680 | - | - | - | - | - | 260 |
| III | ST. | 6.53 | 105.3 | 28 | 32.0 | 7800 | - | - | - | - | - | 145 |
| | ST. | 5.35 | 104.6 | 25 | 13.8 | 7410 | - | - | - | - | - | 140 |
| | ST. | 5.54 | 104.6 | 25 | 15.6 | 7540 | - | - | - | - | - | 150 |
| | ST. | 5.83 | 104.9 | 26.8 | 18.4 | 7420 | 8600 | 6360 | 8920 | 6440 | - | 160 |
| | BEND | 7.75 | 104.7 | 25 | 15.6 | 7520 | - | - | - | - | - | 160 |
| IV | ST. | 5.04 | 127.5 | 26 | 6.5 | 7210 | 7421 | - | - | - | - | 150 |
| Average | | | | | | 7300 | 7660 | | | | | 160 |

Ring sample No. 9 whose test results are encircled in Table 6.4 was strain gauged as shown in Fig. 6.2. The ring has been loaded up to 100N maximum load with 10N load increments, and at each load strain measurements were taken. Then the ring was rotated C.W. by 30°, 45° and 60° angular displacement, and at each angular position the strains were measured at 50N. A linear relationship was observed between the measured strains and the applied load, and the corresponding experimental prediction of the modulus and the measured Poisson's ratios are tabulated in Table 6.5.

A comparison of the theoretical stress distribution using Eq. (6.1) with the measured experimental stress around the circumference is shown in Fig. 6.3. The experimental stresses were obtained using a modulus of 7450 N.mm^{-2} and Poisson's ratio of 0.3.

A general consideration of the modulus results presented in Tables 6.4 and 6.5 show that the predicted modulus based on the inside strain measurements is about 20% lower than that based on the outside strain measurements. In other words, at any angular position on the ring, the inside strains are higher than the outside ones. This is attributed to the presence of a thick gel coat on the inside surfaces. Microscopic measurements showed that the inside gel coat thickness is about twice the outside, and could vary between 1 to 2 mm. On the bases of 5.8mm total thickness of the laminate, together with the assumption that the gel coat modulus is 40% of the main laminate modulus, and by using simple mathematical derivation of the first moment of area of the thickness cross-section, it could be predicted that the neutral axis would be shifted by 0.3mm from the centroidal axis towards the outside surface, resulting in a strain ratio of the inside to the outside to be:

$$\frac{(5.8/2 + 0.3)}{(5.8/2 - 0.3)} = 1.23$$

TABLE 6.5 - Experimental Tensile Modulus and Poisson's Ratio
obtained from Fully Instrumented Ring shown
in Figure (6.2)

| <u>Gauge No. 1</u> | E_{strain} | Zero Position |
|--------------------|----------------------------|------------------------|
| | <u>(N.mm⁻²)</u> | <u>Poisson's ratio</u> |
| 1 | 8530 | 0.25 |
| 2 | - | 0.24 |
| 3 | - | 0.30 |
| 4 | 8570 | 0.26 |
| 5 | 6360 | 0.29 |
| 6 | 6340 | 0.31 |
| 7 | 8920 | 0.29 |

$$(E_{\text{def}}) = 6660 \text{ N.mm}^{-2}$$

or the inside strain would be 23% higher than the outside, which is comparable with the 20% difference of inside to outside modulus experimentally calculated.

The failure strengths listed in Table 6.4 are flexural strengths. Failure usually starts with a crack initiated on the outside surface at the point of the applied load, and final failures occur at the same place. Before final failure, cracks were initiated on the inside gel coat at an angular position 90° from the applied load and then propagating along the mid-layer on the ring splitting the laminate.

6.3 Testing of Straight Pipes

6.3.1 Flexural testing of pipes

These tests examine the applicability of the simple beam theoretical prediction to the present tested pipes, comparing their flexural rigidity and stress distribution around the circumference.

6.3.1.1 Four point bending

This test is based on the recommendation of BS5480⁽¹¹⁶⁾ for the determination of the longitudinal strength of GRP pipes, and was utilised in the present work to examine both the flexural rigidity and stress distribution around the circumference.

Predictions for the decay lengths of deformation for pipes undergoing local type of loading could be calculated from the work reported by Kitching⁽¹⁶⁸⁾, based on the mathematical model of a beam on an elastic foundation. Such spacing length is dependent on the geometry of the pipe as explained in App. VI.

The pipes were supported and loaded onto to wooden supports of 50mm thick and 120° saddle angle with a total span length of 2 m. The load was applied dividing the span into three equi-distances of 667mm, having

the strain gauges situated at the centre of the pipe undergoing pure bending moment, as shown in Fig. 6.4. The decay length of each straight pipe is calculated based on its dimensions and compared against the distance of the strain gauge positions to the nearest support (i.e. 333mm), as presented in Table 6.6.

The comparison in Table 6.6 indicates that for pipes S007, S008 and S009 of 102mm bore and 9mm thickness, the centre position of the pipe would not experience ovalization due to the effect of the applied load, whilst for pipes S003, S004, S005 of 102mm bore and 4.6mm thickness, the mid-section would almost be on the verge of the decay length (i.e. decay length ~ 3 diameter). On the other hand, pipes S026 and S027 of 204mm bore and 5.8mm thickness, decay length of 855mm would overlap the spacing length of 333mm. All the pipes were loaded as shown in Fig. 6.4 and the strain gauge readings were monitored under increments of applied load. The experimentally measured strains are shown in Fig. 6.5 for pipes S007; S008 and S009, Fig. 6.6a,b for pipes S003; S004 and S005, and in Fig. 6.7 for pipe S027.

It could be clearly seen from Fig. 6.5 for pipe S007, S008 and S009 that such pipes would follow a comparable pattern as predicted by simple beam theory. It is important to observe that circumferential strains are due to a Poisson's ratio effect and comparable with theoretical prediction based on $\nu = 0.3$. Furthermore, the experimentally measured angular deviation of the principal stresses did not exceed 3° from the longitudinal direction and the longitudinal experimental strains reasonably fit the sine wave distribution.

As for pipes S003, S004 and S005, the experimentally measured strains as shown in Fig. 6.6 indicate that the squashing induced by the applied load at 333mm from the mid-section, is picked up by the circumferential strains as they tend to form a cosine wave maximising at

TABLE 6.6 - Decay Length for Straight Pipes tested under Four-Point Bending as shown in Figure (6.4)

| <u>Set No.</u> | <u>$\frac{2r_i}{(mm)}$</u> | <u>$\frac{t}{(mm)}$</u> | <u>Decay Factor</u> [*] <u>(α_{22})</u> | <u>Decay Length</u> <u>(mm)</u> | <u>Actual Spacing</u> <u>(mm)</u> |
|----------------|---------------------------------------|------------------------------------|---|------------------------------------|--------------------------------------|
| I | 102 | 4.6 | 0.495 | 338 | 333 |
| II | 102 | 9.00 | 0.695 | 250 | 333 |
| III | 204 | 5.80 | 0.385 | 855 | 333 |

* App.(VI)

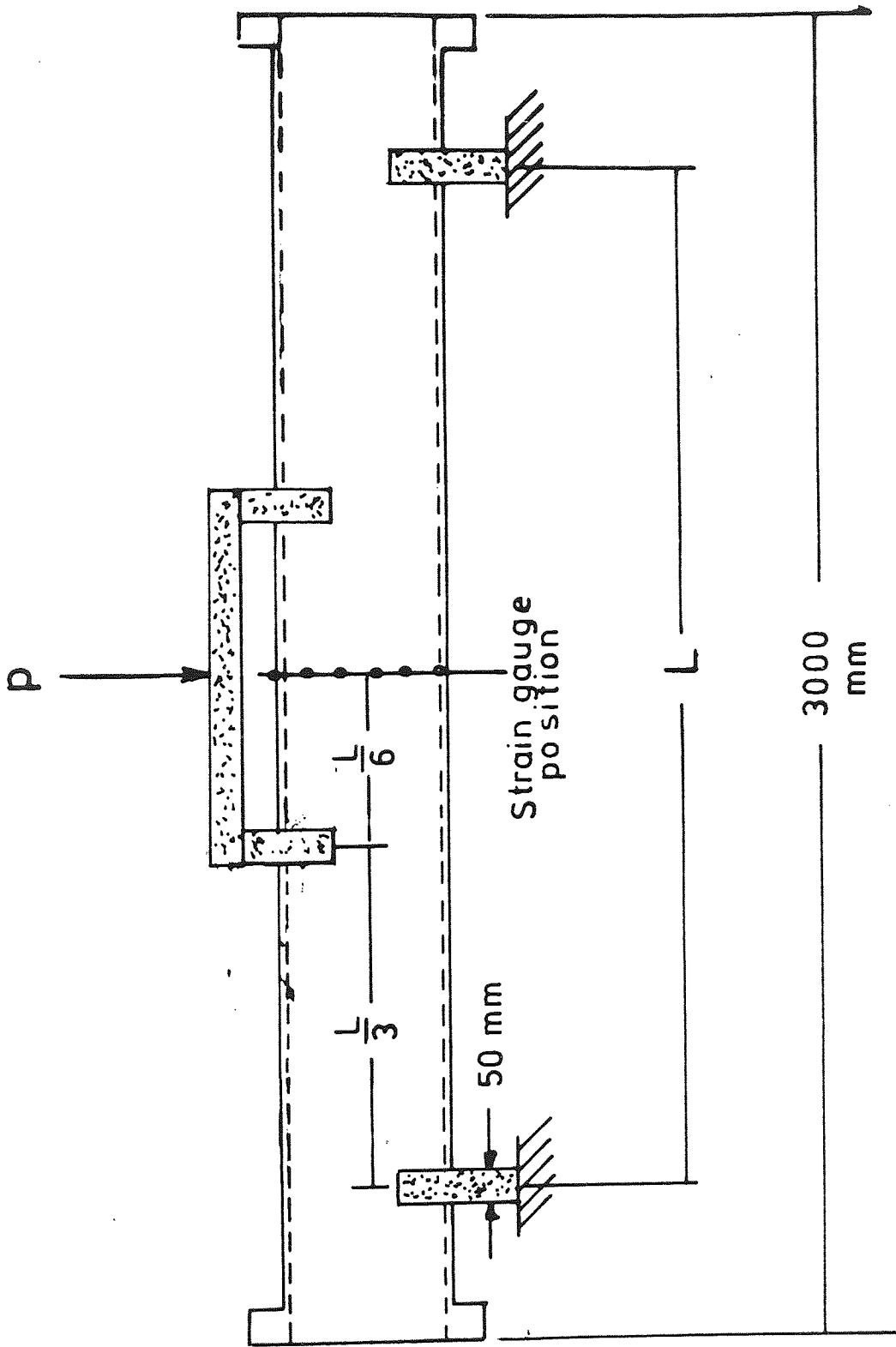


Figure (6.4) Four point bend of a straight pipe

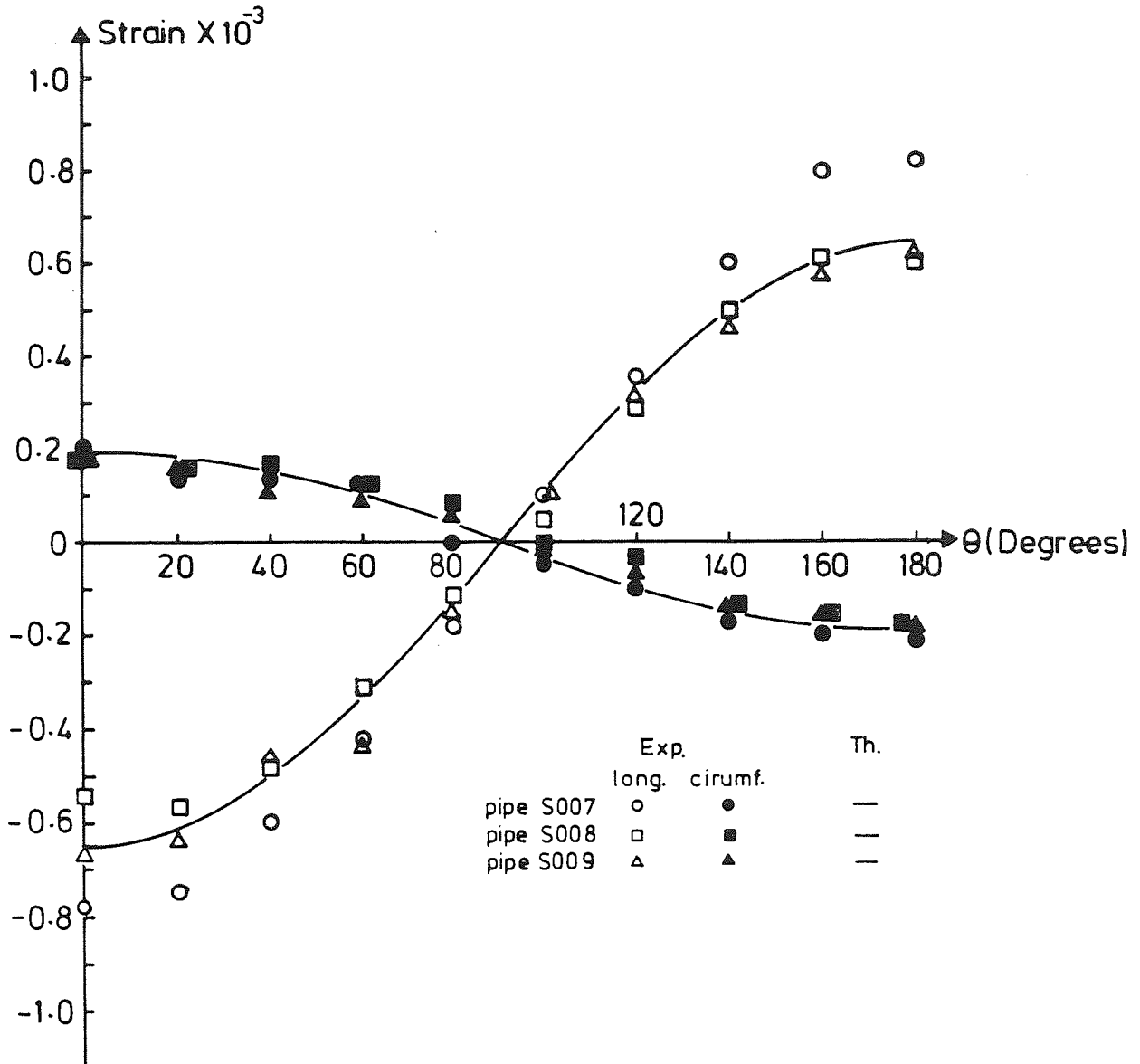


Figure (6.5) Outside longitudinal and circumferential strains measured on pipes S007, S008 and S009 under four-point bending moment of 4.25×10^5 N mm

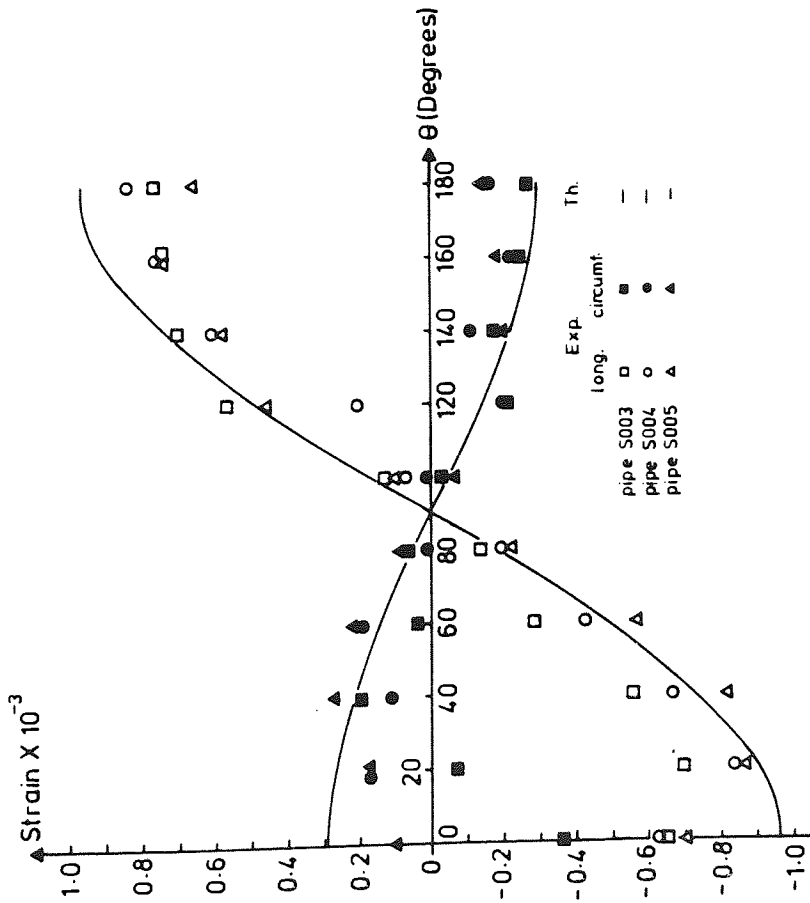


Figure (6.6a) Outside longitudinal and circumferential strains measured on pipes S003, S004 and S005 under four-point bending moment of 2.94×10^5 N mm

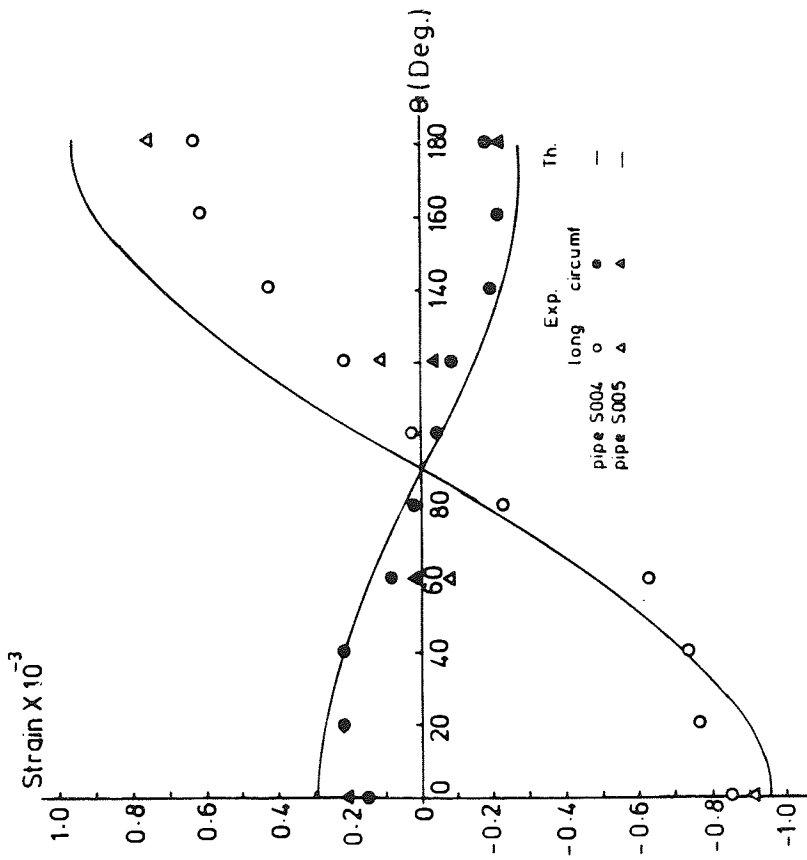


Figure (6.6b) Inside longitudinal and circumferential strains measured on pipes S003, S004 and S005 under four-point bending moment of 2.94×10^5 N mm

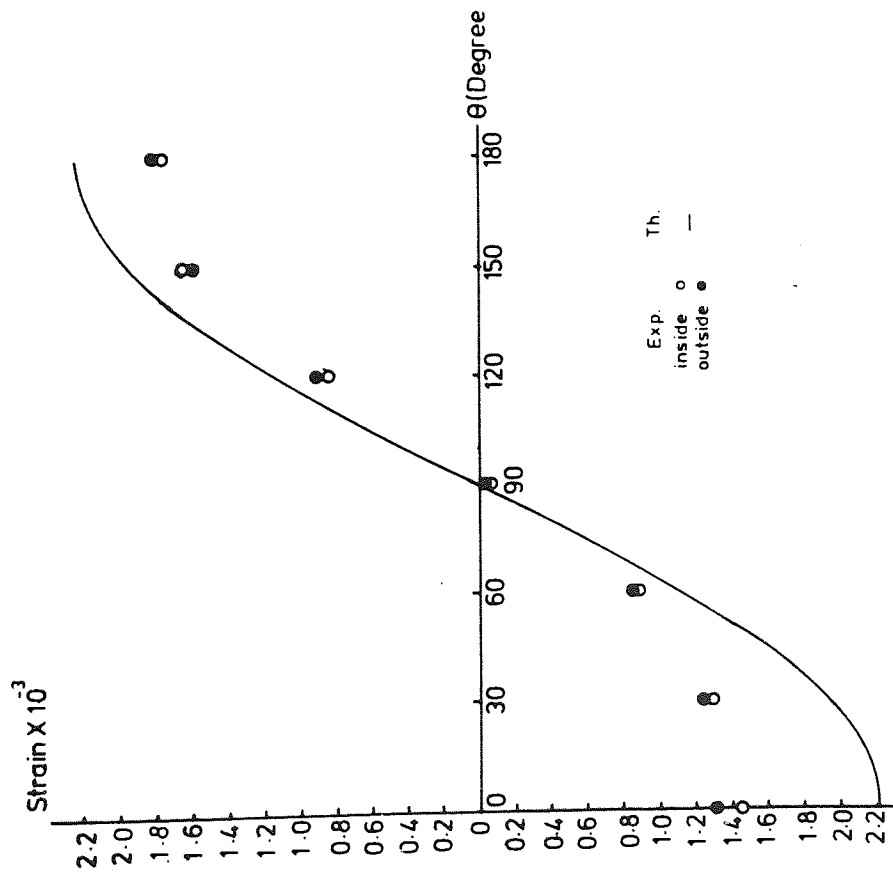


Figure (6.7a) Inside and outside longitudinal strains of pipe S027 under four-point bending moment of 3.33×10^6 N.mm

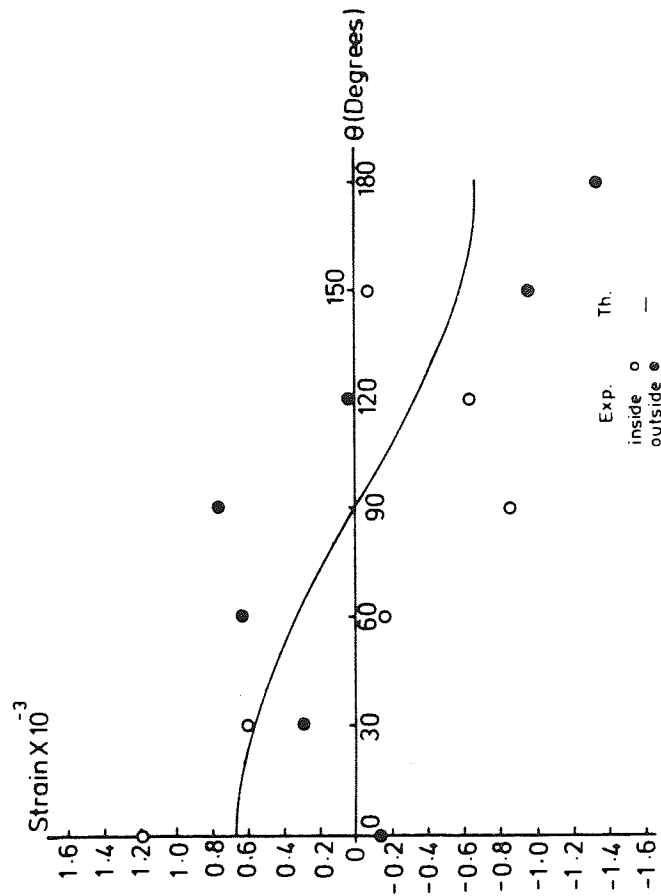


Figure (6.7b) Inside and outside circumferential strains of pipe S027 under four-point bending moment of 3.33×10^6 N.mm

$\theta = 30-50^\circ$ position. Such effect on the circumferential strains could be clearly shown in Fig. 6.7 when the larger diameter pipes (204mm) are tested.

The effect of local loading is of importance to the problem of pipe lines installed on saddles, where the problem of the circumferential ovalization⁽⁹³⁾ should be investigated beside the maximum longitudinal stress and/or strain.

6.3.1.2 Cantilever loading

Two pipes of 102mm and 204mm bores were tested as cantilevers.

(a) Pipe S005

A length of 1340mm was cut from pipe S005 (Set I of Table 6.1) and tested as a cantilever fixed at the flange. Top and bottom dial gauges were mounted along the length of the pipe as shown in Fig. 6.8a and the pipe was loaded at the free end using a 4" x 4" wooden cylinder fitted to the inside of the pipe preventing any local effects. Displacements were measured under incremental end-loading. The main objective of the test was to investigate the flange-joint effect on the overall rigidity and deformation of the pipe under flexure, where such joints are usually constructed at twice the thickness of the main body of the pipe. The average (top and bottom) measured deflections versus incremental loading are shown in Fig. 6.8c where a reasonably linear relationship could be observed. The deflection corresponding to 150N end load was plotted against the length of the pipe is shown in Fig. 6.8b. The experimental results are compared with cantilever deflection ignoring the presence of the joint via simple beam theory⁽¹³¹⁾, i.e.

$$\Delta = \frac{P}{EI} \left(L \frac{x^2}{2} - \frac{x^3}{6} \right) \quad (6.2)$$

The experimental deflections are also compared with theoretical prediction taking into account the longitudinal rigidity of the joint

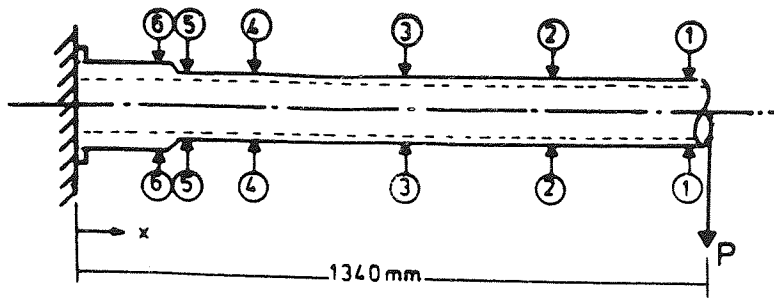


Figure (6.8a) Dial gauge arrangement for a cantilever test of 102 mm diameter pipe (S005)

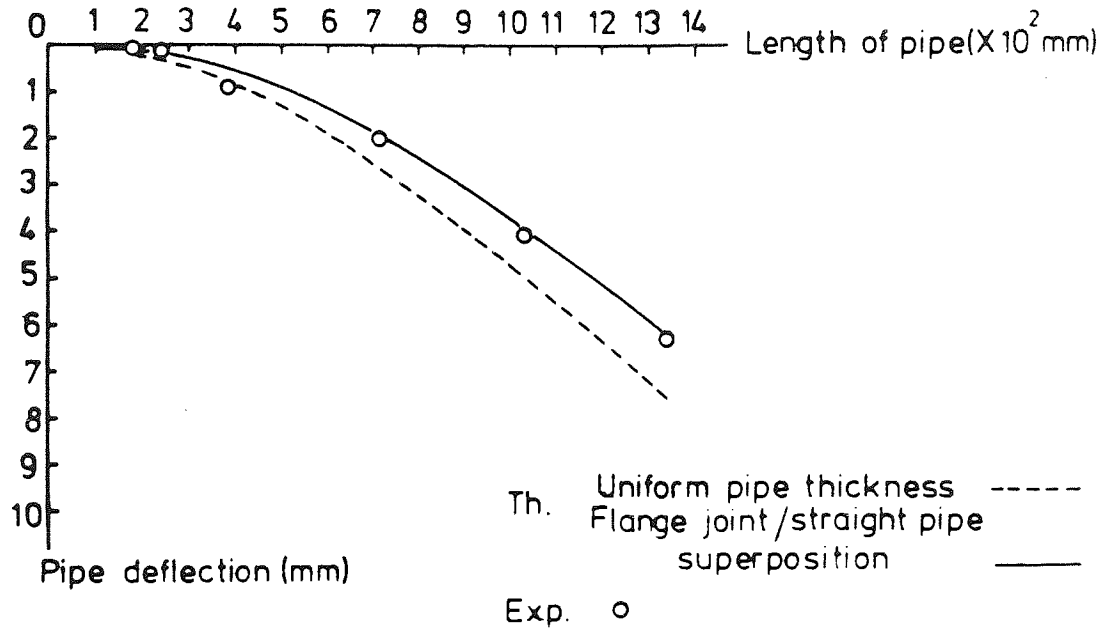


Figure (6.8b) Deflection measured along the pipe length under 150N end force in cantilever loading

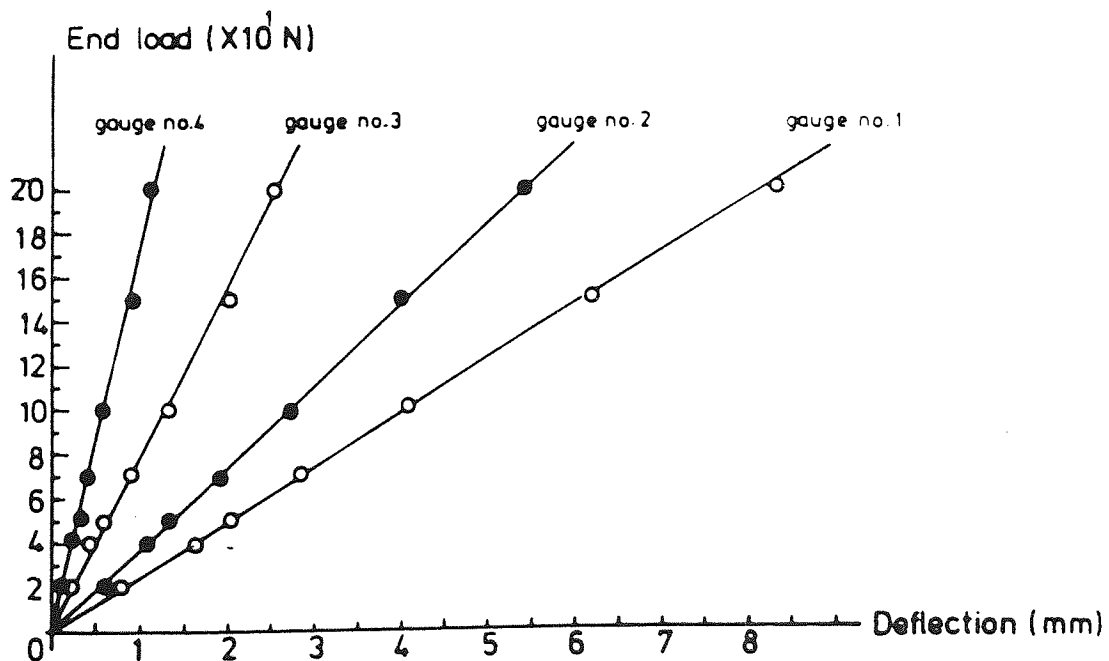


Figure (6.8c) Measured deflections along the pipe length versus applied end force in cantilever loading

into consideration as described in App. I. It is seen from Fig. 6.8b that the joint-straight superposition analysis fits better with the experimentally measured deflections. The same technique was later used to include the joint rigidities into the bend analysis.

(b) Pipe S026

Pipe S026 of Set III (Table 6.1) of 204mm bore was tested as a cantilever. The strains at the centre of the pipe were monitored under a low magnitude of end load to avoid any damage to the flange. The experimentally measured longitudinal stresses under 900 kN mm bending moment; distributed around 180° of the circumference are shown in Fig. 6.9, compared with simple beam prediction.

6.3.2 Torsional testing

Under out-of-plane bending, pipes and bend fittings experience torsional bending. Torsional rigidity of steel pipes is predicted using Hooke's law, based on the isotropy of the material, i.e.

$$G = \frac{E}{2(1 + \nu)} \quad (6.3)$$

Little experimental data has been published on the torsional rigidity of GRP pipes. Wright⁽⁴¹⁾ carried out limited tests on in-house built CSM pipes. He obtained the shear modulus by measuring the angular displacement per unit length by optical means using mirrors fixed at two positions on the pipe. He also carried out tests on rectangular strips cut from the longitudinal direction and tested on the ICI/RAPRA extensometry using Moire fringe technique. In both cases, the shear modulus of CSM pipes and laminates are comparable with the prediction of Eq. (6.3).

Kirk⁽⁴⁰⁾ did similar work on in-house and commercially built CSM pipes using strain gauges and similarly assessed the validity of Eq. (6.3) for CSM straight pipes.

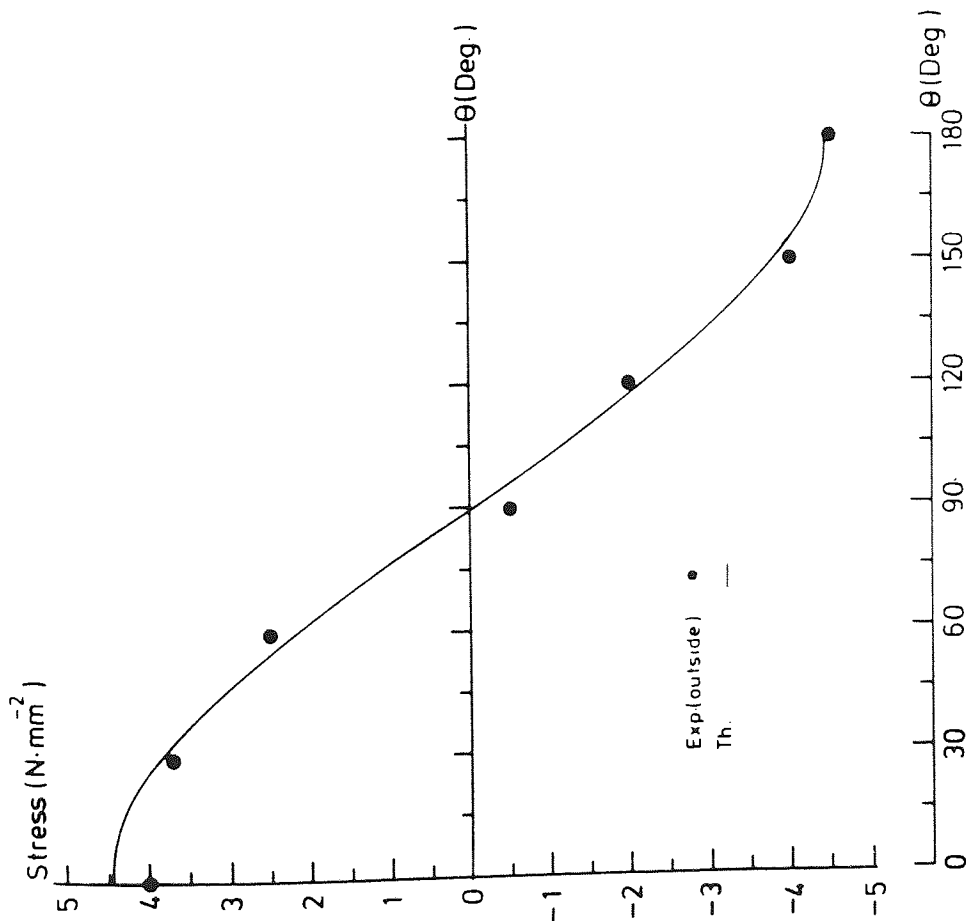


Figure (6.9)

Outside longitudinal stresses measured on pipe S026 under 9×10^5 N mm cantilever bending moment

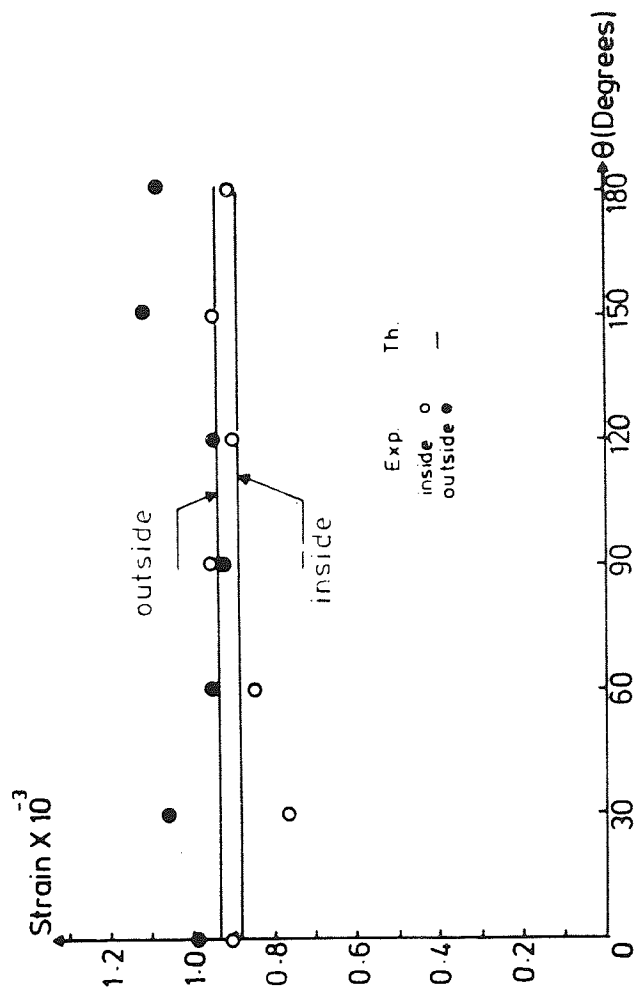


Figure (6.10)

Inside and outside in-plane shear strains measured on pipe S027 under 1.04×10^6 N mm torsional moment

TABLE 6.7 - Experimental Shear Modulus of CSM Laminate obtained from Torsional Testing of Pipe S027

| Gauge Position (Deg.) | Experimental Shear Moduli | | | | Hook's Law Prediction* (N.mm ⁻²) | Rule of Mixture Prediction (N.mm ⁻²) |
|-----------------------|--|--------------------------|--|--------------------------|---|---|
| | Inside | | Outside | | 2870 | 2830 |
| | G ₋₂ (N.mm ⁻²) | β ₁ (Deg.) | G ₋₂ (N.mm ⁻²) | β ₁ (Deg.) | | |
| 0 | 2780 | - 45.7 | 2720 | +44.4) |) | |
| 30 | 3300 | + 42.9 | 2510 | 43.8) |) | |
| 60 | 2980 | + 45 | 2790 | -44.1) |) | |
| 90 | 2670 | 43.9 | 2980 | -43.5) |) | |
| 120 | 2800 | - 42.4 | 2810 | 43.3) |) | |
| 150 | 2680 | 45 | 2390 | -38.6) |) | |
| 180 | 2790 | - 43 | 2480 | -42.3) |) | |

(G)
average = 2770 ± 160 N.mm⁻²

* Based on E = 7450 N.mm⁻², ν = 0.3

β₁ = direction of the principal measured from the longitudinal direction of the pipe

In the present programme, pipe S027 of 204 mm bore, 58 mm thickness, 3m long (Set III of Table 6.1), was loaded under a torque of 1040 kN mm applied at one end-flange whilst the other was fixed. Strain gauges were monitored at the mid-span of the pipe in the longitudinal, skew and circumferential direction. The inside/outside measured shear strain are shown in Fig. 6.10 compared with theoretical shear strain based on shear modulus obtained from $E = 7450 \text{ N.mm}^{-2}$, and $\nu = 0.3$.

Using the experimentally measured shear strains in Fig. 6.10, the experimental shear modulus could be obtained at each strain gauge position using Eq. (6.4).

$$G_{\text{exp}} = \frac{T \cdot r_m}{\gamma_{\text{exp}} \cdot J} \quad (6.4)$$

and these are listed in Table 6.7. They are compared with that using Hooke's law for isotropic material, and with that similarly predicted by the rule of mixture, i.e.

$$G_{\text{composite, CSM}} = (0.33) V_g \cdot G_g + (1 - V_g) G_r \quad (6.5)$$

where:

$$V_g = 30\% \text{ by mass} = 21\% \text{ by volume}$$

$$G_g = \frac{E_g}{2(1+\nu_g)} = \frac{73 \times 10^3}{2(1+0.21)} \text{ (N.mm}^{-2}\text{)}$$

$$G_r = \frac{E_r}{2(1+\nu_r)} = \frac{2450}{2(1+0.35)} \text{ (N.mm}^{-2}\text{)}$$

The angular position of the measured principal strains are also listed in Table 6.7, and they are reasonably compared with the theoretical position of $\pm 45^\circ$.

6.4 Flexural Behaviour of Smooth CSM Bends

6.4.1 Introduction

The bends nominally presented in Table 6.1 have been tested under in-plane and out-of-plane flexural loading. The loads applied in each case were limited by a maximum strain of 2×10^{-3} measured on the bends

via electrical strain gauges in the form of rosettes, distributed around half the circumference starting from the intrados ($\theta = 0^\circ$) and terminating at the extrados ($\theta = 180^\circ$) as shown in Fig. 6.11. The test results are presented in the form of flexibility factors (K) and stress intensification factors (SIF). These terms have already been defined in Ch. 4.

The in-plane and the out-of-plane bending moments were introduced to the bend by a force acting at the end of the free tangent as shown diagrammatically in Fig. 6.12. The free end-deflection reading was used to calculate the flexibility factor of the bend. Such a method was reported in the literature to have been used with reasonable success for metallic⁽¹⁶⁸⁻¹⁷⁰⁾ and GRP^(40,41) bends, though it may not be for small diameter bends⁽⁴⁰⁾.

The welds on the metallic bend-tangent systems were reported to provide a local stiffening effect against ovalization^(151,152). For GRP pipe bend-tangent systems, the weld is not a circumferential line as in the metallic structures, but it rather occupies a sizeable length^(9,188) (100-200mm) and is at least twice the thickness of the laminate due to the overlap-joint techniques recommended for GRP joints^(3,4,5). Thus, such GRP joints provide both circumferential and longitudinal stiffness.

The degree of the longitudinal stiffening could be modelled by considering the actual variation of the thickness along the length of the pipe as already shown in Fig. 6.8 for straight pipe S005. It is much more difficult to investigate the circumferential stiffening of the joints in the tangent-bend systems analysis.

It is further envisaged that such circumferential stiffening, would be of great significance for small diameter pipes than for large diameter pipe due to the t/r_m ratio. The reported results show that flexibilities of the small diameter bends (100mm nominal bore) suffer a

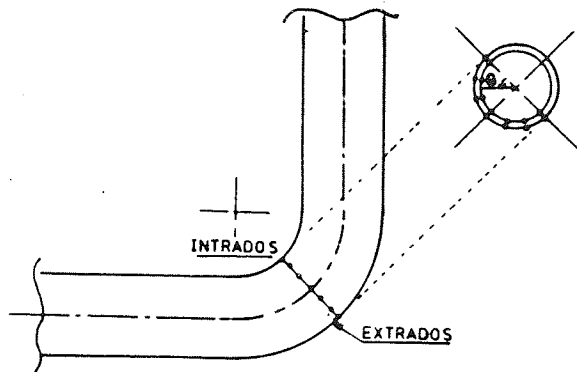


Figure (6.11) Strain gauge positions on GRP bends

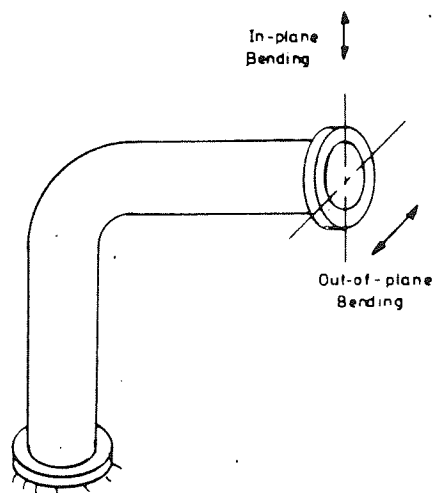


Figure (6.12) Direction of end loads

considerable variability when the actual thickness is not taken into consideration.

Stress intensification factors are obtained by the direct division of the maximum experimental measured stress on the bend by the maximum stress predicted using simple beam theory (App. I).

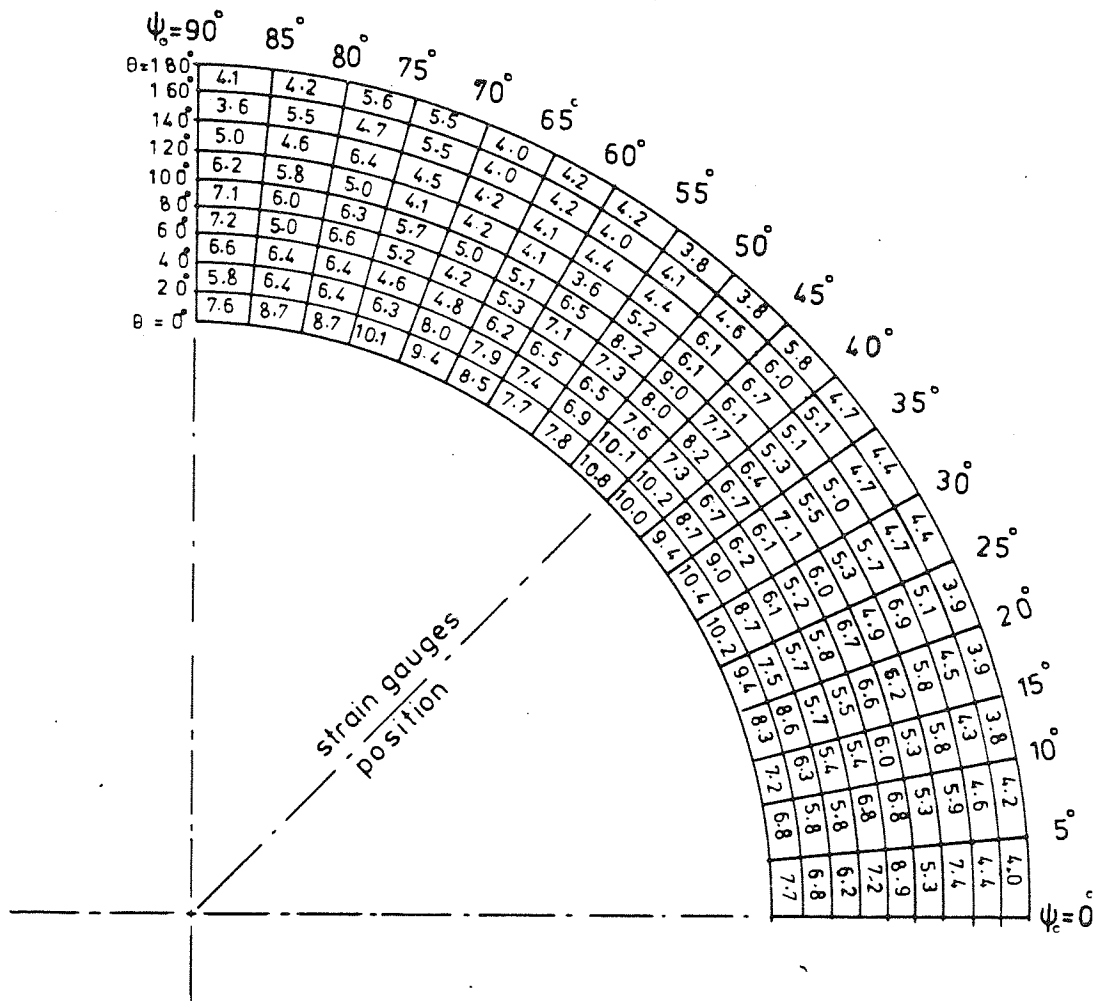
6.4.2 Bend geometrical variation

The bends are essentially constructed from two tangents and a bend fitting, which are joined together using an overlap joint. The tangents are terminated by flanges using a similar joint construction. Such by-part construction using the manual process of hand lay-up technique, leads to large variations of glass content and bend wall thickness. Extensive thickness and glass content measurements have been carried out on the different parts of the bends, e.g. Tables 6.8a,b.

It was originally decided to use an ultrasonic 'GRP thickness measurement' device to avoid cutting the bends. Such a device was found to predict accurately for flat GRP surfaces, but the accuracy diminished as measurements were taken on curved surfaces, and it was extremely poor on areas such as the intrados, where an acute double curvature is present. Hence, it was decided that the majority of the bends were to be cut and actual thickness to be measured by hand. For those which have not been cut, the average thickness was estimated by measuring the outside circumference and the bore of the bend.

A summary of thickness glass mass per unit area and glass mass percentage have been already presented in Table 6.2 for the different parts of the bend. The main features observed from such thickness/glass distribution of Table 6.2 could be summarised as the following:

Table(6.8a) Wall thickness (mm) of Bend S001



Table(6.8b) Glass mass percentage measured at the centre of Bend S022

| Angular Position | Glass Mass Percentage |
|------------------|-----------------------|
| 0 (Intrados) | 30.4 |
| 20 | 29.1 |
| 40 | 31.7 |
| 60 | 31.4 |
| 80 | 28.2 |
| 100 | 29.3 |
| 120 | 26.0 |
| 140 | 21.8 |
| 160 | 23.8 |
| 180 (Extrados) | 24.8 |

- (a) Thickness on the intrados is 1.5-2.0 times greater than the thickness of the straight tangent. The thickness decreases towards the extrados to a value similar to that of the straight.
- (b) Thickness of the joint is equal or higher (up to 20%) than thickness measured on the intrados.
- (c) The increase in measured thickness is directly related to the glass mass per unit area rather than to the resin mass percentage, although the latter is believed to be the main contributor to a thick gel coat. Direct thickness measurement would fairly indicate the amount of glass mass per unit area.

6.4.3 In-plane bending

6.4.3.1 In-plane flexibility factor (K_i)

The in-plane flexibility factor is determined by using Eq. (I.6) of App. I, where the second moment of area (I_e) is calculated using the average effective thickness t_e (see Table 6.9). For reasons of further investigations, Eq. (I.7) and (I.33) are also used in the text.

The above analysis assumes that an average uniformly distributed flexibility factor is obtained for the bend, with the tangents having unity flexibility factor. However, with reference to Fig. 6.13, it is shown from ovality measurements that flattening continues from the bend to the tangents. Such observation suggests that the straight should have a flexibility factor higher than unity, which may compensate for that lost on the bend flexibility due to the tangent/joint restraints.

Table 6.9 summarises the dimensions and the mechanical properties of all the CSM bends tested. Measured joint lengths vary from 100-180mm for 102mm bore bends and 150-200mm for 250mm bore bend. It could be also noticed that such joints are of similar thickness for all the bends tested regardless ^{of} the pipe diameter. This is due to the fact that a

TABLE 6.9 - Dimensions and mechanical properties of tested CSM smooth Bends

| | Set I | | | Set II | | | Set III | | | Set IV | | |
|--|---------|---------|---------|---------|---------|---------|---------|---------|---------|---------|---------|---------|
| | S001 | S002 | S006 | S017 | S018 | S019 | S023 | S024 | S025 | S020 | S021 | S022 |
| Nominal bore $2r_i$ (mm) | 100 | 100 | 100 | 100 | 100 | 100 | 200 | 200 | 200 | 250 | 250 | 250 |
| Bend radius to pipe radius (R/r_i) | 6 | 6 | 6 | 6 | 6 | 6 | 3 | 3 | 3 | 2 | 2 | 2 |
| Nominal glass content $(kg.m^{-2})$ | 1.8 | 1.8 | 1.8 | 3.6 | 3.6 | 3.6 | 2.4 | 2.4 | 2.4 | 1.8 | 1.8 | 1.8 |
| Nominal glass percentage $\%$ | 30 | 30 | 30 | 30 | 30 | 30 | 30 | 30 | 30 | 30 | 30 | 30 |
| Young modulus E, kN.mm $^{-2}$ | 7.45 | 7.45 | 7.45 | 7.45 | 7.45 | 7.45 | 7.45 | 7.45 | 7.45 | 7.45 | 7.45 | 7.45 |
| Poisson's ratio, ν | 0.3 | 0.3 | 0.3 | 0.3 | 0.3 | 0.3 | 0.3 | 0.3 | 0.3 | 0.3 | 0.3 | 0.3 |
| Tangent length (mm) | 1000 | 1000 | 1000 | 1000 | 1000 | 1000 | 710 | 710 | 710 | 1300 | 1300 | 1300 |
| Joint length (mm) | 120-180 | 120-180 | 120-180 | 120-180 | 120-180 | 120-180 | 100-160 | 100-160 | 100-160 | 150-200 | 150-200 | 150-200 |
| Bend radius (mm) | 306 | 306 | 306 | 306 | 306 | 306 | 305 | 305 | 305 | 250 | 250 | 250 |
| Thickness: | | | | | | | | | | | | |
| nominal t_n (mm) | 3.96 | 3.96 | 3.96 | 7.92 | 7.92 | 7.92 | 5.28 | 5.28 | 5.28 | 3.96 | 3.96 | 3.96 |
| straight t_{st} (mm) | 4.62 | 4.60 | 4.60 | 9.29 | 9.71 | 8.86 | 6.20 | 6.50 | 5.90 | 5.20 | 5.20 | 5.20 |
| bend t_B (mm) | 6.91 | 5.84 | 6.10 | 9.20 | 8.59 | 9.80 | 7.53 | 7.57 | 7.48 | 6.10 | 6.30 | 6.00 |
| joint t_{jI} (mm) | 8.90 | 10.30 | 9.60 | 11.85 | 11.70 | 12.00 | 8.55 | 7.74 | 9.35 | 7.18 | 7.84 | 7.75 |
| effective t_e (mm) | 5.77 | 5.22 | 5.35 | 9.25 | 9.15 | 9.33 | 6.87 | 7.04 | 6.69 | 5.65 | 5.75 | 5.60 |
| Pipe factor | | | | | | | | | | | | |
| nominal, λ_n | 0.43 | 0.43 | 0.43 | 0.80 | 0.80 | 0.80 | 0.15 | 0.15 | 0.15 | 0.06 | 0.06 | 0.06 |
| straight, λ_{st} | 0.51 | 0.51 | 0.51 | 0.90 | 0.95 | 0.88 | 0.17 | 0.18 | 0.16 | 0.08 | 0.08 | 0.08 |
| bend, λ_B | 0.71 | 0.61 | 0.64 | 0.90 | 0.86 | 0.96 | 0.21 | 0.21 | 0.20 | 0.093 | 0.10 | 0.09 |
| effective, λ_e | 0.6 | 0.56 | 0.58 | 0.90 | 0.90 | 0.92 | 0.19 | 0.195 | 0.18 | 0.087 | 0.09 | 0.085 |
| Second moment of area: | | | | | | | | | | | | |
| nominal I_n ($\times 10^6 mm^4$) | 1.85 | 1.25 | 1.85 | 4.13 | 4.13 | 4.13 | 19.1 | 19.1 | 19.1 | 25.4 | 25.4 | 25.4 |
| straight I_{st} ($\times 10^6 mm^4$) | 2.19 | 2.19 | 2.19 | 5.03 | 5.32 | 4.74 | 22.6 | 23.3 | 21.4 | 33.9 | 33.9 | 33.9 |
| bend I_B ($\times 10^6 mm^4$) | 3.51 | 2.57 | 3.13 | 4.96 | 4.56 | 5.38 | 28.0 | 28.2 | 27.8 | 40.2 | 45.7 | 39.5 |
| effective I_e ($\times 10^6 mm^4$) | 2.84 | 2.53 | 2.60 | 5.00 | 4.93 | 5.06 | 25.3 | 26.0 | 24.6 | 37.0 | 37.8 | 36.7 |

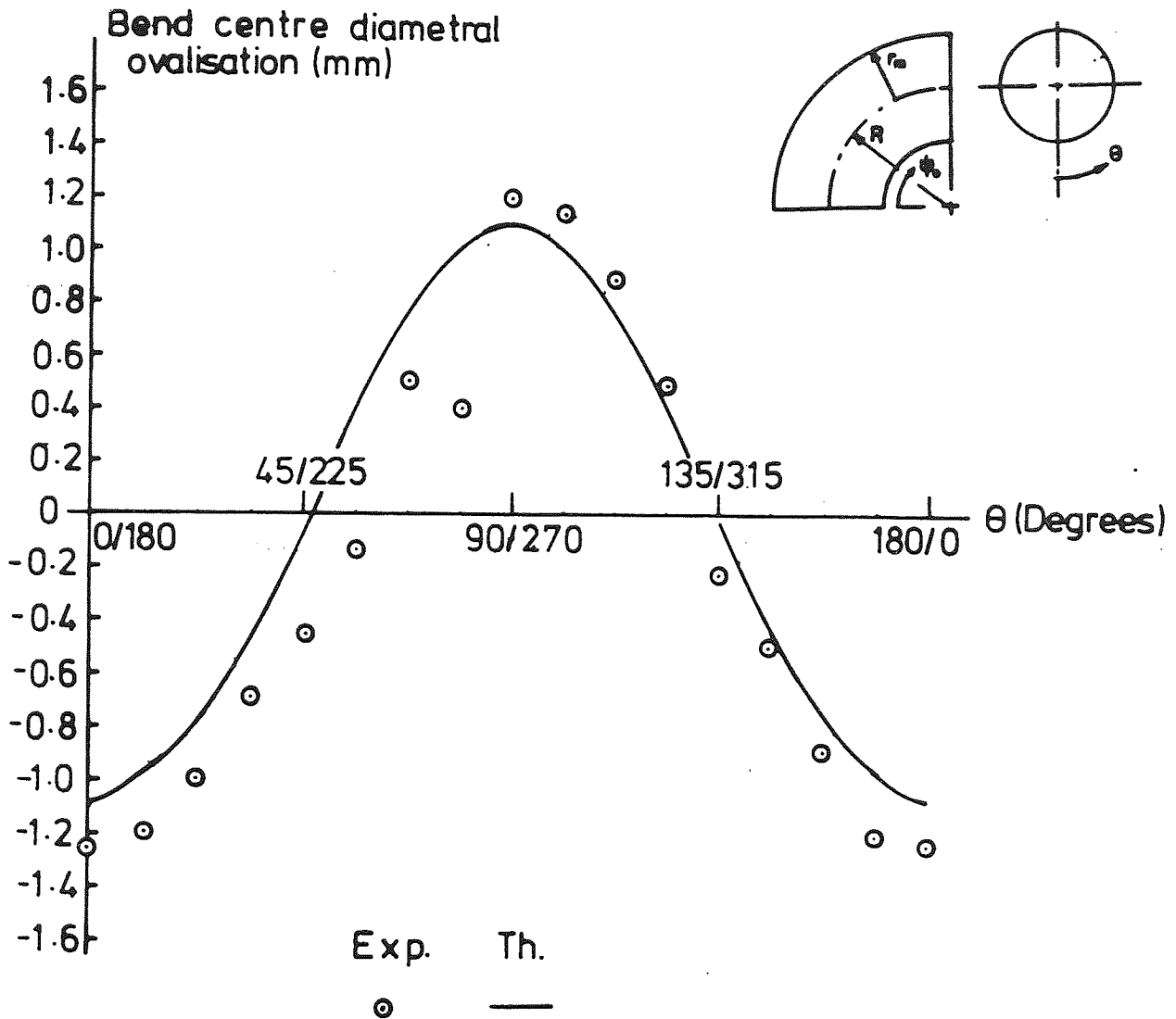


Figure (6.13a) Bend-centre diametral ovalization of bend S006 under 2.981×10^5 N mm in-plane bending moment (closing)

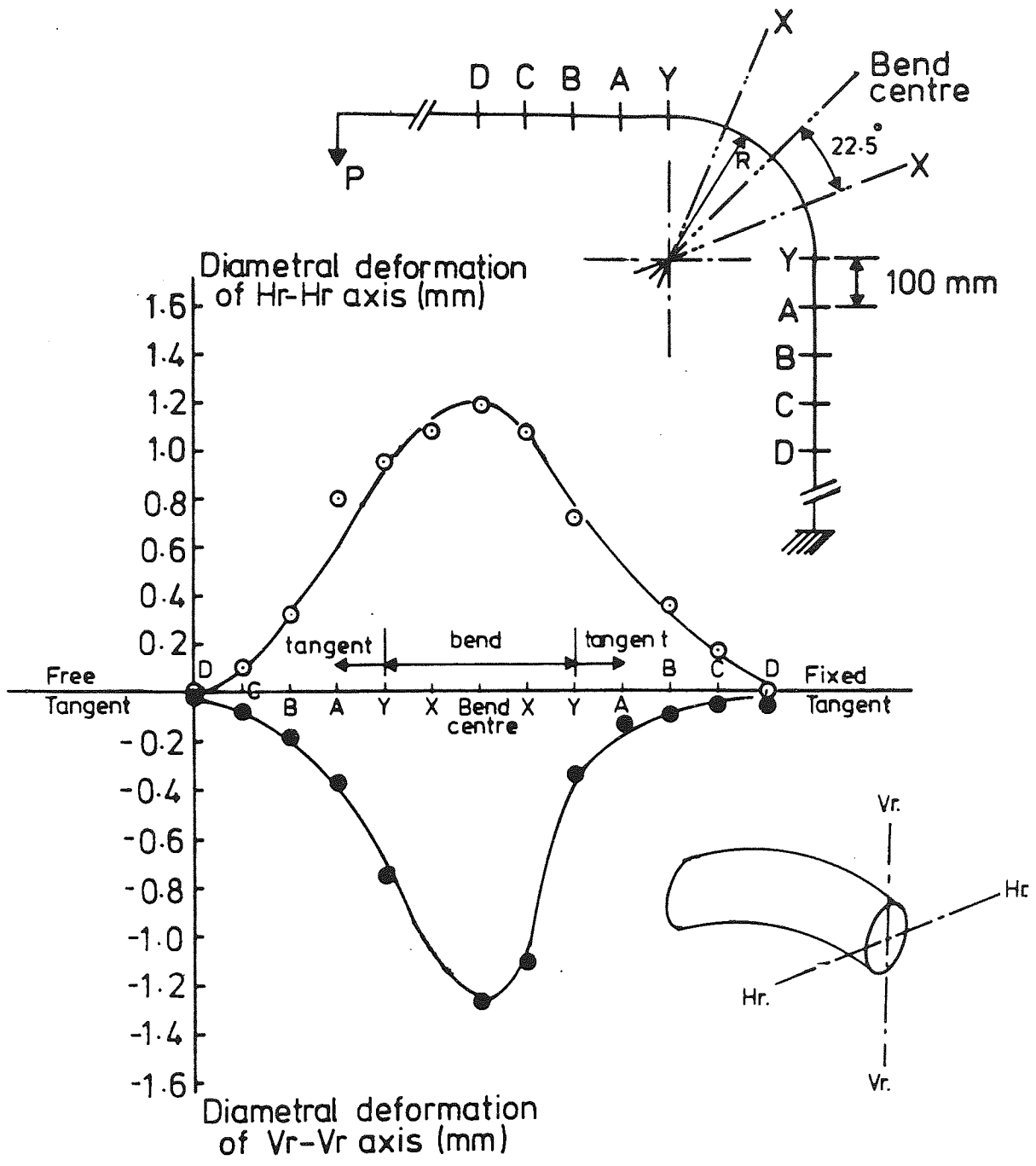


Figure (6.13b) Horizontal and vertical diametral ovalization along bend fitting and tangents of bend S006 under 245.3N end loading, closing the bend

joint should be at least twice the laminate thickness regardless of the pipe diameter. Naturally the sensitivity of such thickness would be magnified on the circumferential stiffening for the small diameter bends due to $\frac{Et^3}{D^3}$ ⁽¹¹⁶⁾.

The experimental errors that are considered when formulating the mathematical analysis for the in-plane flexibility factor are the deflection measurements and the average rigidity used. An additional factor of error is the deviation of the bend angle from 90°. The difficulty associated with checking the bend angle arises from the irregular surface finish exhibited by the bend, however, angles measured between the two faces of the end flanges, suggest 3-6° deviation from 90° bend angle.

Thus, the main error introduced into the results of the experimentally determined flexibility factor, is stemmed from the fact that the calculation is dependent on quantities which are experimentally measured, where some of which could widely vary in value. This could be summarised by inspecting the mathematical equation used for the derivation of the flexibility factor as follows:

$$K_i = \frac{\Delta/P - F(\ell, R, E, r_m^3, t)}{H(\ell, R, E, r_m^3, t)} \quad (6.6)$$

where Δ/P is the measured free end-deflection per unit load, and F and H are functions dependent on dimensions and modulus. For the small diameter bends in particular, ill-conditioning of the results is brought about by Δ/P being almost equal to F , and H being of a small value of magnitude.

The experimental in-plane flexibility factors are determined using the dimensions in Table 6.9 and the measured end-deflection in the analysis presented in App. I. The results are presented showing the influence of the different thicknesses used in the calculations. Then

the results are brought up to a conclusive format by representing the bend, using an average effective thickness (t_e).

Table 6.10 presents the in-plane flexibility factor compared with theory as a function of:

- (i) Nominal thickness specified by BS4994⁽³⁾, using Eq. (I.6) of App. I, and using t_n of Table 6.9.
- (ii) Average thickness measured by hand of the straights, using Eq. (I.6) of App. I, and using t_{st} of Table 6.9.
- (iii) Average straight thickness used for the deformation of the tangents, and average bend thickness for the bend deformation, using Eq. (I.7) of App. I, and using t_{st} and t_B of Table 6.9.
- (iv) Same as (iii), with the introduction of the joint effect, using Eq. (I.33) of App. I, and using t_{st} , t_B , t_j of Table 6.9.
- (v) The average effective thickness of the whole bend-tangent structure, using Eq. (I.6) of App. I, and using t_e of Table 6.9.

Results of columns i, ii and iv of Table 6.10 are presented diagrammatically against BS806⁽¹²⁵⁾ prediction in Fig. 6.14, and could be summarised as follows:

- (a) The experimentally determined in-plane flexibility factors, could be largely under-estimated when using the nominal thickness specified by BS4994 (col. i of Table 6.10). For the small diameter bends, the flexibility factors are shown to be not only smaller than unity, but they can be negative in value due to ill-conditioning, e.g. bend S019 in Table 6.10.
- (b) Improvement could be noticed in comparison with theory when the average straight thickness (column ii of Table 6.10) is used in the analysis. This improvement is visible for the small pipe factors, i.e. $\lambda = 0.09-0.19$

- (c) The overall results are greatly improved when the actual thicknesses of the straights, bends and joints are used in the analysis (column iv of Table 6.10). The experimental results, although limited in the region $\lambda = 0.7-1$, indicate the absence of an asymptote. It rather suggests a continuous straight line on the log-log graph, intersecting the unity flexibility factor axis.
- (d) The ill-conditioning of the flexibility test results for the small diameter bends (100mm nominal bore) can be clearly identified by the fact that, although the end deflections per unit load measured on identical bends may only vary by 16%, the calculated flexibility factor can vary by almost 100% among the same bends. It is believed that such bends will be better investigated by using longer tangents, especially for the free end, which will enhance the bend fitting flexural deformation on the end deflections, and at the same time minimise joints effects.
- (e) The end-deflection measurements are linearly related to the end load, suggesting that any variation of the flexibility factor due to incremental ovalization could be neglected.

The finalised results presented in column v of Table 6.10, show that without going into the complex analysis of incorporating the different tangent, bend and joint thicknesses into the superposition technique (Eq. (I.33) of App. I), the experimental flexibility factors could be reasonably predicted by using the average effective section modulus (I_e) based on the average of the thickness measured on the straight tangent and on the bend (t_e). Such results, when presented with 95% upper and lower confidence limits⁽¹²¹⁾, and compared diagrammatically against BS806⁽¹²³⁾ prediction as in Fig. 6.15, would converge the wide variability associated in Fig. 6.14. They are reasonably compared with theoretical results as shown in column v of

TABLE 6.10 - In-plane Flexibility Factors experimentally determined for Smooth CSM Bends

| Bend Number | End deflection per unit end load ⁻² (mm/N) x 10 ⁻² | In-plane Flexibility Factor | | | | | | | | | |
|-------------|--|-----------------------------|-------|-----------------------------|-------|-----------------------------|-------------|---------------------------------------|-------|--|--|
| | | Col. (i) | | Col. (ii) | | Col. (iii) | | Col. (iv) | | Col. (v) | |
| | | Based on nominal thickness | | Based on straight thickness | | Based on ST, Bend thickness | | Based on ST, Bend and joint thickness | | Based on effective thickness (t _e) | |
| | | λ _e | | λ _e | | λ _e | | λ _e | | λ _e | |
| Set I | S001 | 0.416 | 1.04 | 1.66 | 2.21 | 2.23 | 2.23 | 2.23 | 2.60 | 2.79 | |
| | S002 | 0.374 | 0.98 | 1.29 | 1.81 | 1.60 | 1.60 | 1.60 | 2.60 | 2.79 | |
| | S006 | 0.360 | 0.97 | 1.34 | 1.86 | 1.72 | 1.72 | 1.72 | 2.60 | 2.79 | |
| | | | | | | Average | 1.85 ± 0.9 | | | | |
| Set II | S017 | 0.245 | 0.93 | 0.92 | 1.09 | 0.91 | 0.91 | 0.91 | 1.80 | 1.84 | |
| | S018 | 0.446 | 1.42 | 0.88 | 1.33 | 1.10 | 1.10 | 1.10 | 1.80 | 1.84 | |
| | S019 | -0.072 | 0.35 | 0.40 | 0.63 | 0.54 | 0.54 | 0.54 | 1.80 | 1.84 | |
| | | | | | | Average | 0.85 ± 0.7 | | | | |
| Set III | S023 | 5.18 | 6.54 | 8.09 | 8.08 | 7.57 | 7.57 | 7.57 | 8.50 | 8.68 | |
| | S024 | 5.64 | 7.55 | 8.95 | 8.79 | 8.45 | 8.45 | 8.45 | 8.50 | 8.68 | |
| | S025 | 5.62 | 6.58 | 8.33 | 8.62 | 7.87 | 7.87 | 7.87 | 8.50 | 8.68 | |
| | | | | | | Average | 7.96 ± 1.1 | | | | |
| Set IV | S020 | 11.01 | 16.19 | 19.2 | 20.05 | 18.10 | 18.10 | 18.10 | 17.50 | 18.33 | |
| | S021 | 10.06 | 14.91 | 20.04 | 19.17 | 18.26 | 18.26 | 18.26 | 17.50 | 18.33 | |
| | S022 | 8.57 | 12.93 | 15.05 | 15.83 | 14.36 | 14.36 | 14.36 | 17.50 | 18.33 | |
| | | | | | | Average | 16.91 ± 5.4 | | | | |

* See App (II)

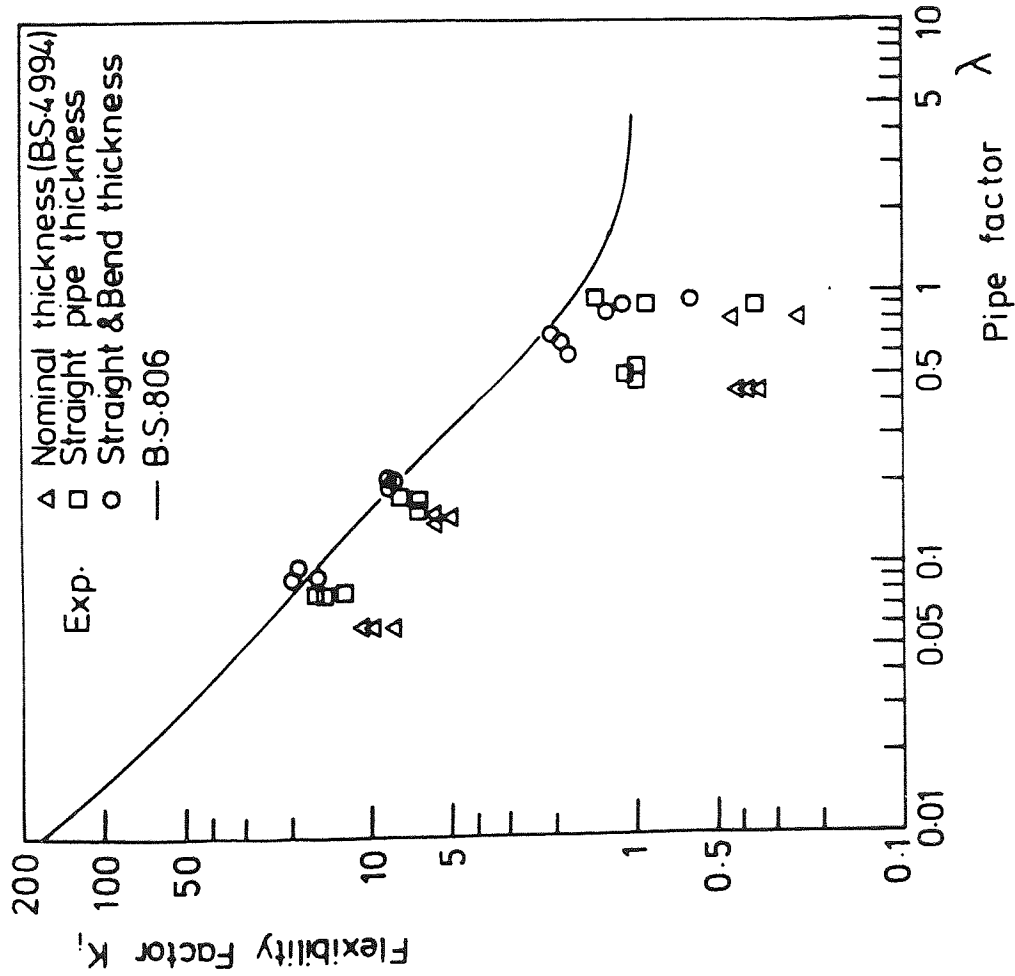


Figure (6.14)

In-plane flexibility factors (K_i) for smooth CSM bends presented as a function of the different thicknesses employed in Table 6.10, columns i, ii and iv

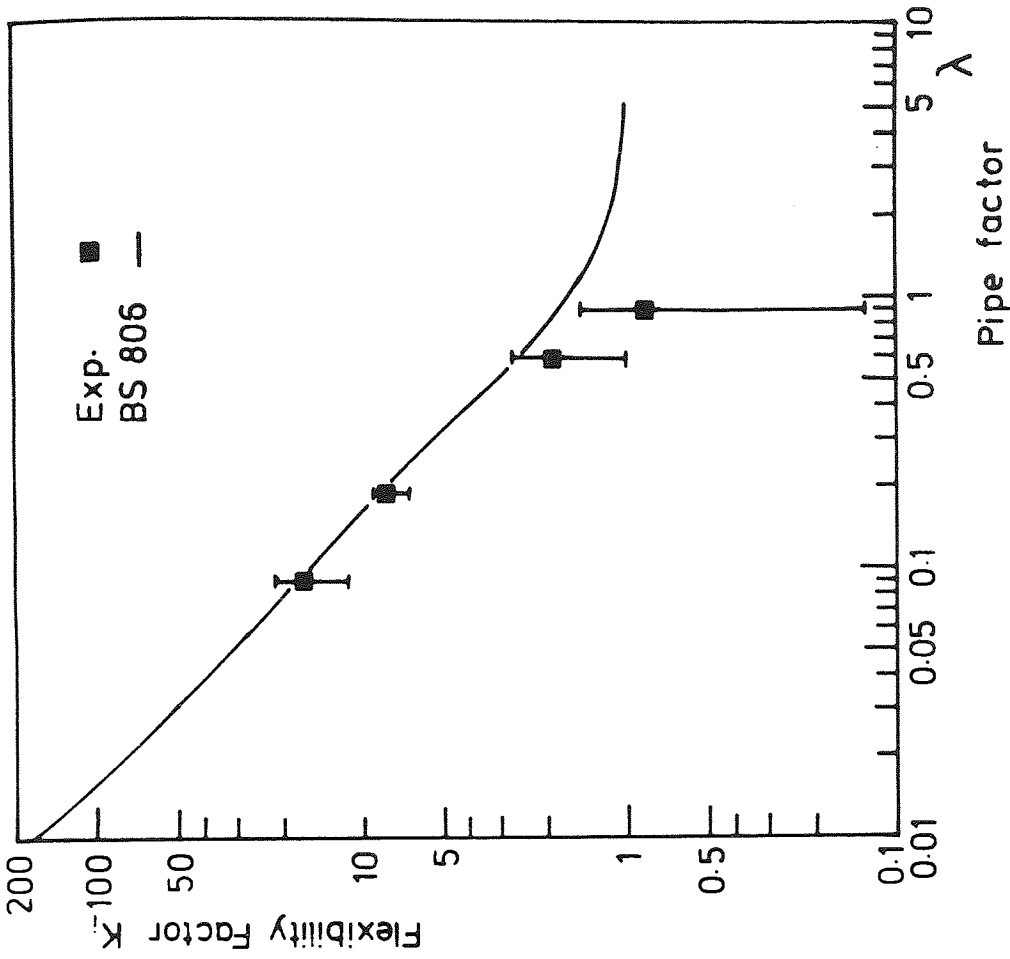


Figure (6.15)

In-plane flexibility factor (K_i) results for smooth CSM bends using the effective thickness (t_e) as in column (v) of Table 6.10. Experimental results are presented with 95% upper and lower confidence limit

Table 6.10, indicating on average a slight reduction of the experimental in-plane flexibility factors.

The importance of using the average effective thickness (t_e) method enables the experimental results of K and SIF to be directly compared with bend theory using a unique effective pipe factor λ_e .

6.4.3.2 In-plane stress ratio distribution and stress intensification factors (SIF)

Strains in the longitudinal; skew and circumferential directions, were measured from strain gauge rosettes located at the centre of the bend at the same time as the deflections were measured under the application of the load. Since maximum bend flattening occurs at the centre as shown in Fig. 6.13, then this would indicate that the maximum measured strains are also located at the bend-centre. Unlike flexibility factor results, the strains at the centre of the bend are directly measured, and hence independent of deformations taking place at the tangents.

A straight line relationship was found to reasonably fit the measured strains versus the applied load. The experimentally measured in-plane longitudinal and circumferential strain distributions of bends S001, S002, and S006 (Set I of Table 6.1) are collectively presented in Figs. 6.16a,b and 6.17a,b respectively. The strain distribution patterns among the three bends are shown to be similar, but with some scatter in magnitude, probably due to thickness differences (see Table 6.9). The maximum longitudinal strain is shown to be on the outside surface at $\theta = 120^\circ$ position (see Fig. 6.16a), and the maximum circumferential strain is shown to be on the inside surface at $\theta = 80^\circ$ - 100° position.

The experimental strains were converted to experimental stresses using Hooke's law for isotropic, homogeneous material; assuming plane stress condition. Young's modulus of 7.45 kN.mm^{-2} and Poisson's ratio of 0.3 were used in the calculations.

The experimentally measured stresses are presented as stress ratio distribution (σ_B/σ_n), where the average effective thickness (t_e) was used to calculate the maximum simple beam stress σ_n (Eq. (I.9) of App. I).

The experimental stress results measured under in-plane bending are compared with theoretical stress ratio distribution predicted by isotropic bend theory (App. II). These results are presented in Figs. 6.18 and 6.19 for bends S001 and S002 (of Set I). Fig. 6.20 for bend S019 (of Set II), Figs. 6.21 and 6.22 for bends S024 and S025 (of Set III), and Figs. 6.23 and 6.24 for bends S021 and S022 (of Set IV). The comparability of the experimental and the theoretical stress ratio distribution could be described as follows:

- (a) Despite the considerable thickness variation around and along the bend, the experimental results follow a similar pattern of stress distribution to that described by theory.
- (b) The circumferential stress ratio maximises on the inside, where it is the maximum experimental stress induced throughout the bend, and is located at $\theta = 80\text{-}100^\circ$ position similar to theoretical peaks.
- (c) The comparability of the circumferential stress ratios is less at $\theta = 0^\circ\text{-}40^\circ$ (intrados) and $\theta = 140^\circ\text{-}180^\circ$ (extrados) in particular for small diameter bends as shown in Figs. 6.18b, 6.19b and 6.20b, where less local bending is experienced by the bend than predicted by the theoretical distribution. These areas are the thickest and the thinnest parts measured around the bend respectively.

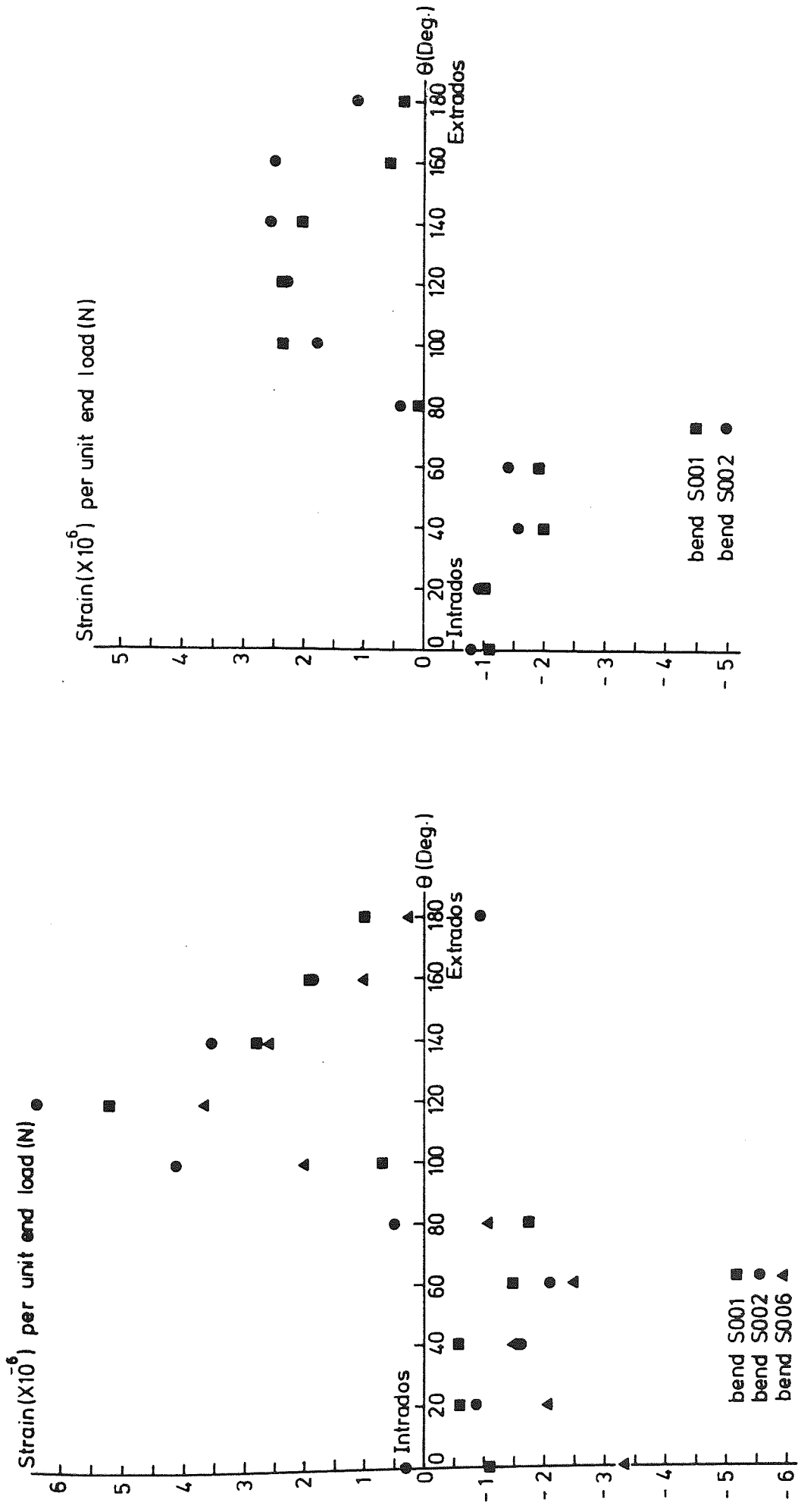


Figure (6.16a) Inside longitudinal strain distribution per unit end load measured on smooth CSM S001, S002 bends under in-plane loading (closing)

Figure (6.16b) Outside longitudinal strain distribution per unit end load measured on smooth CSM S001, S002, and S006 bends under in-plane loading (closing)

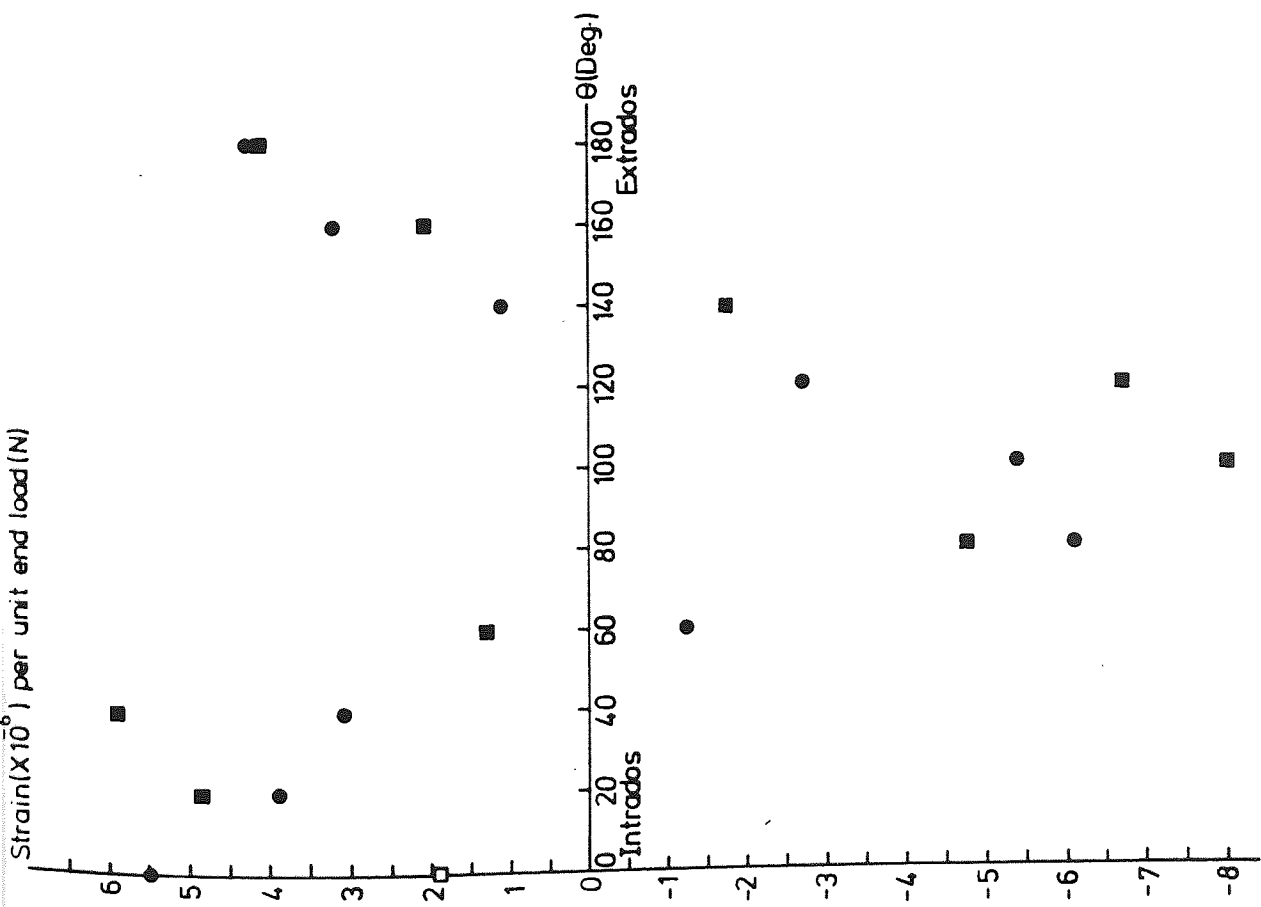


Figure (6.17a) Inside circumferential strains per unit end load measured on smooth CSM S001, S002, bends under in-plane loading (closing)

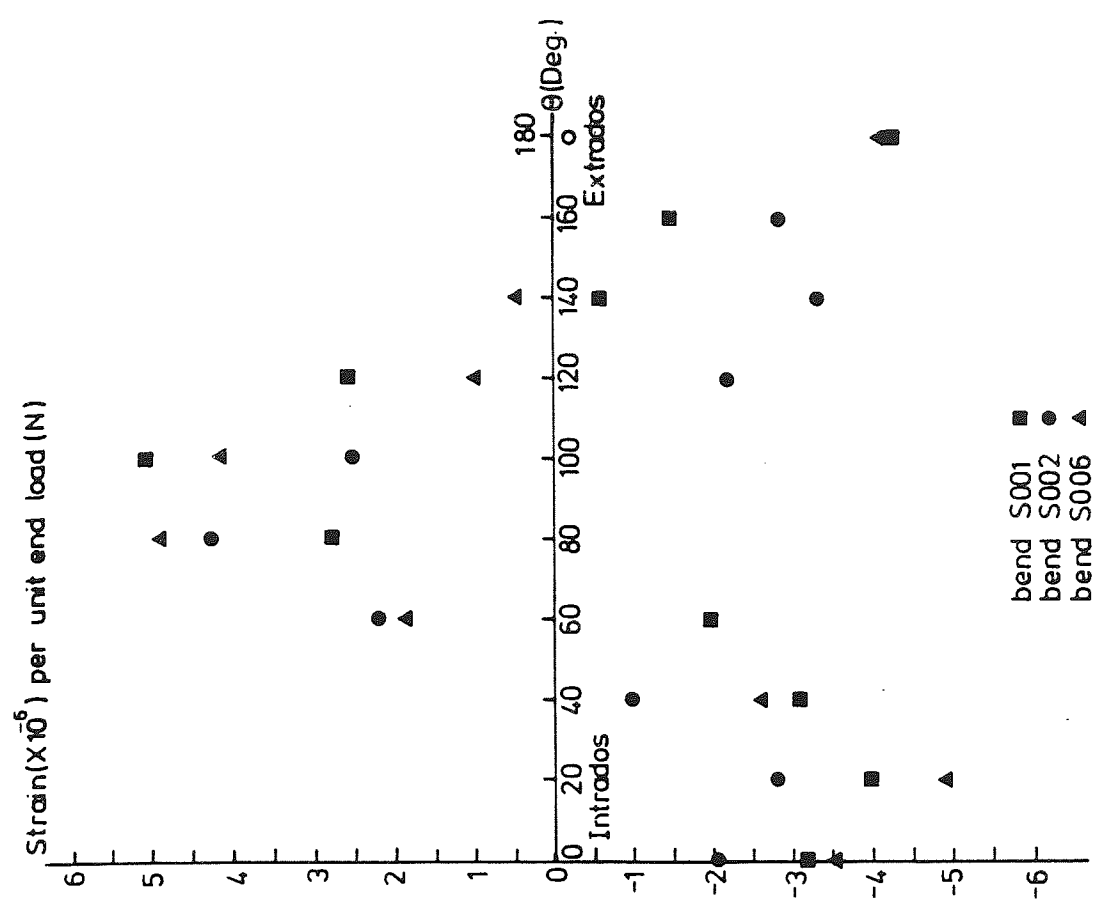
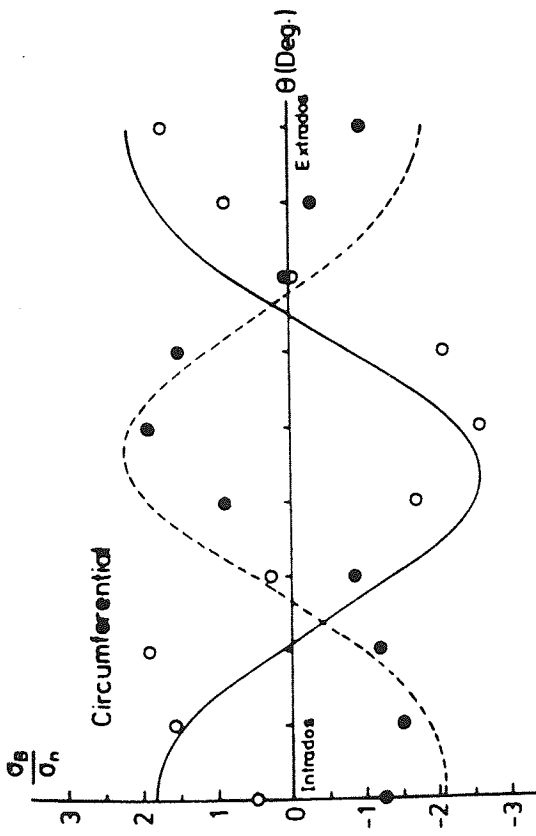


Figure (6.17b) Outside circumferential strains per unit end load of CSM smooth S001, S002, and S006 bends under in-plane bending



0 20 40 60 80 100 120 140 160 180 θ (Deg.)

Exp. Th.
inside \circ
outside \bullet

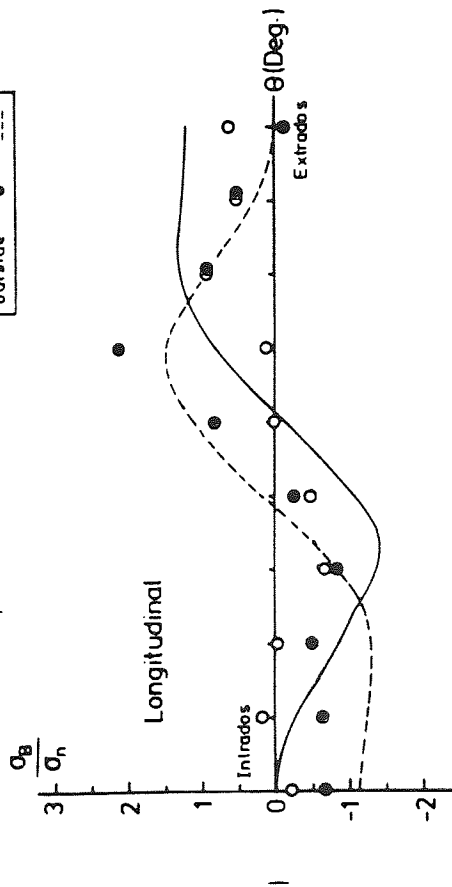
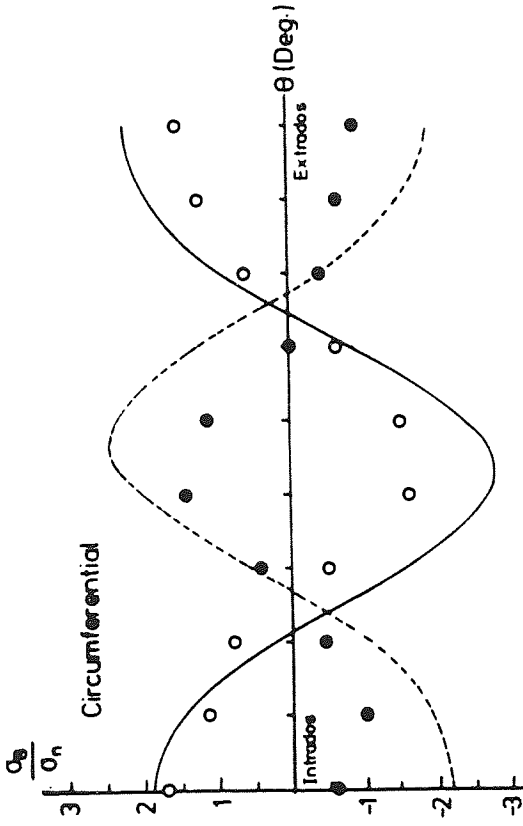


Figure (6.18) 'a' longitudinal and 'b' circumferential stress distribution measured on bend S001 under 2.72×10^5 N.mm in-plane bending moment (closing)



0 20 40 60 80 100 120 140 160 180 θ (Deg.)

Exp. Th.
inside \circ
outside \bullet

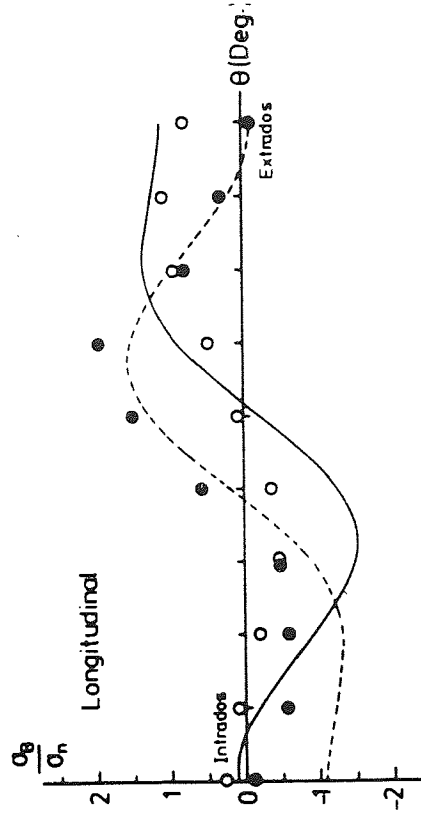


Figure (6.19) 'a' longitudinal and 'b' circumferential stress distribution measured on bend S002 under 1.91×10^5 N.mm in-plane bending moment (closing)

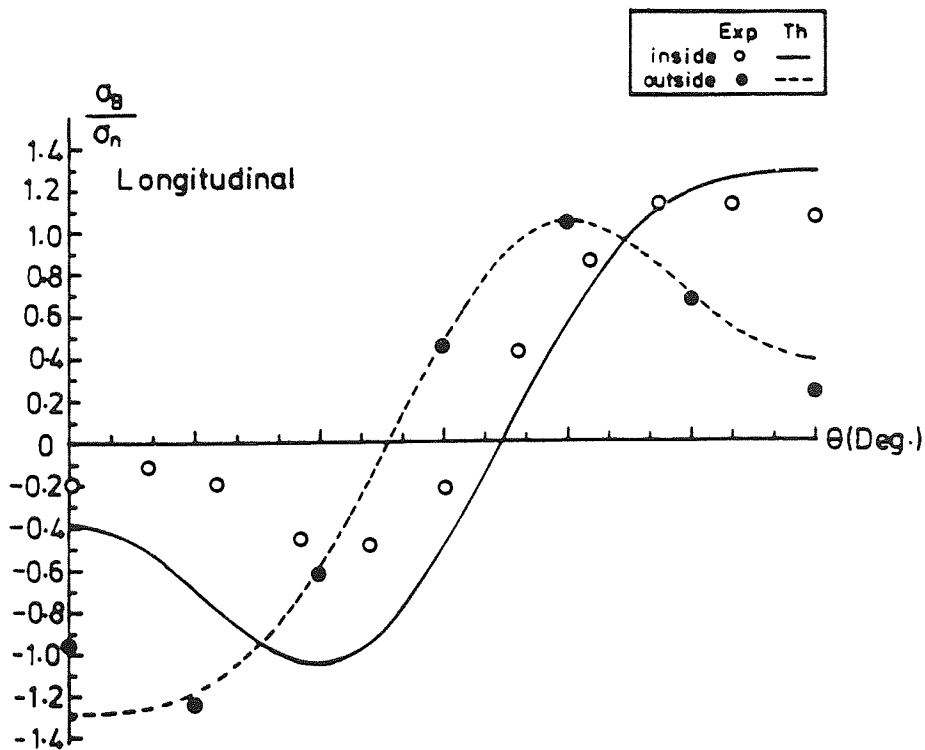
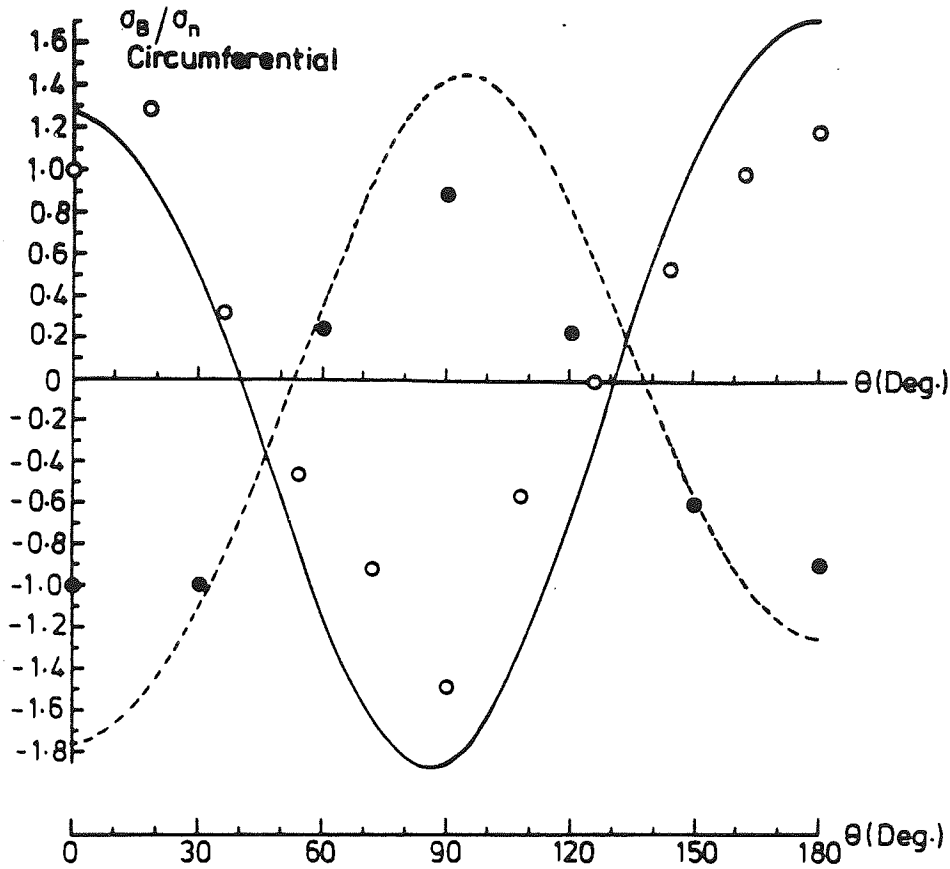


Figure (6.20) 'a' longitudinal and 'b' circumferential stress distribution measured on bend S019 under 9.03×10^5 N.mm in-plane bending moment (closing)

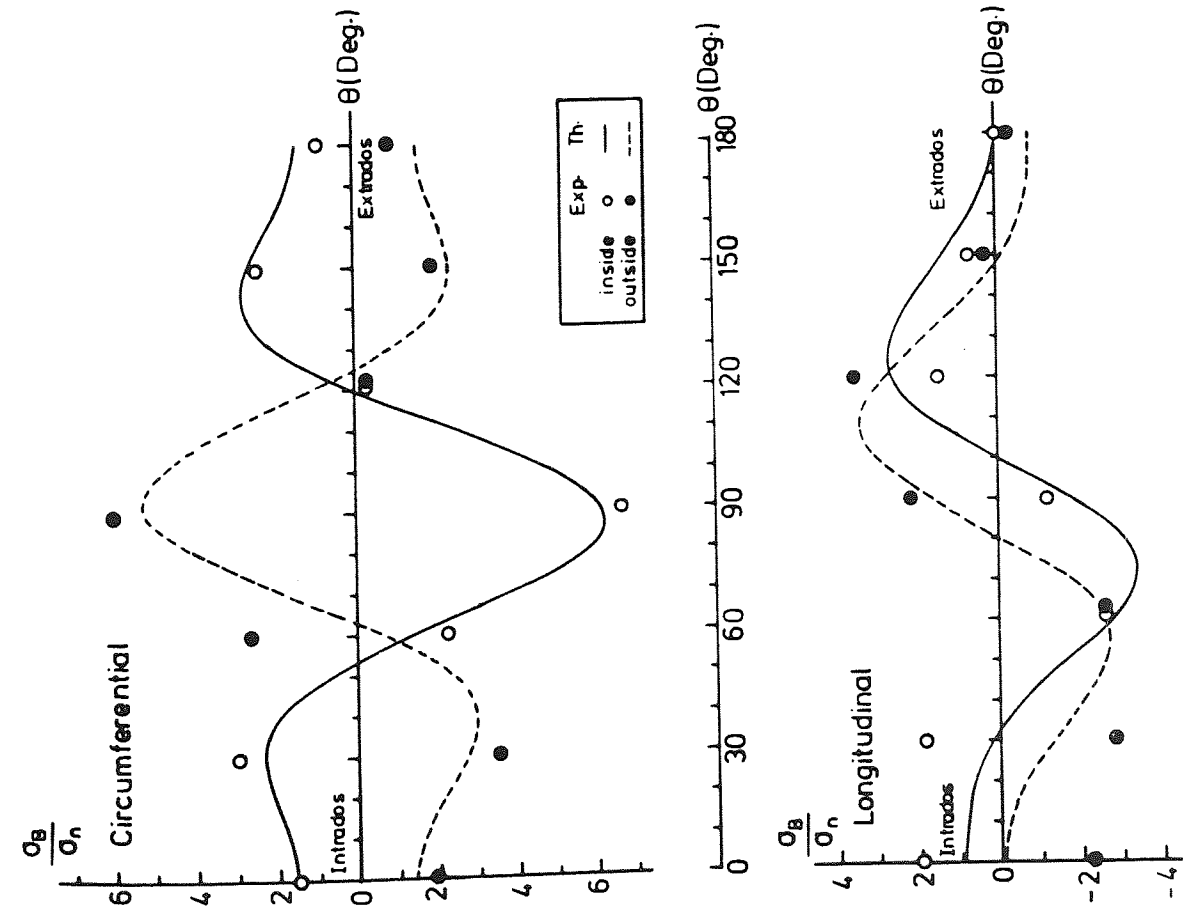


Figure (6.21) 'a' longitudinal and 'b' circumferential stress distribution measured on bend S024 under 6.25×10^5 N mm in-plane bending (closing)

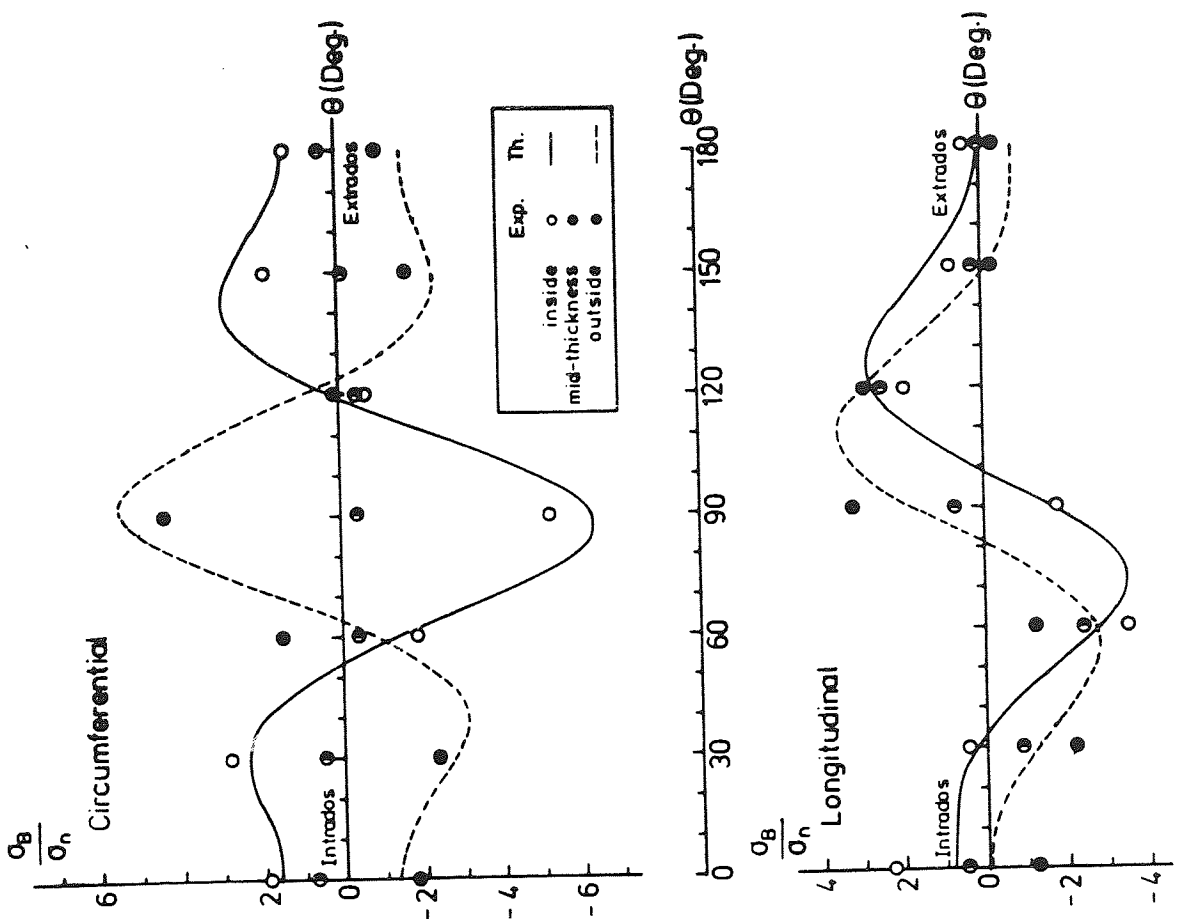


Figure (6.22) 'a' longitudinal and 'b' circumferential stress distribution measured on bend S025 under 6.25×10^5 N mm in-plane bending moment (closing)

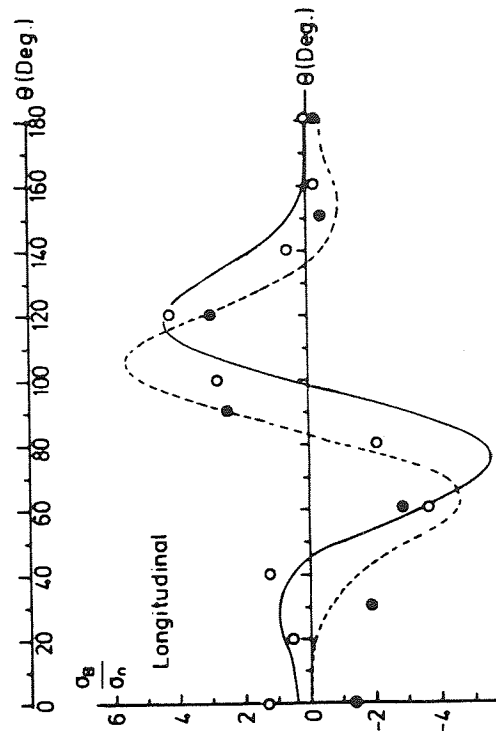
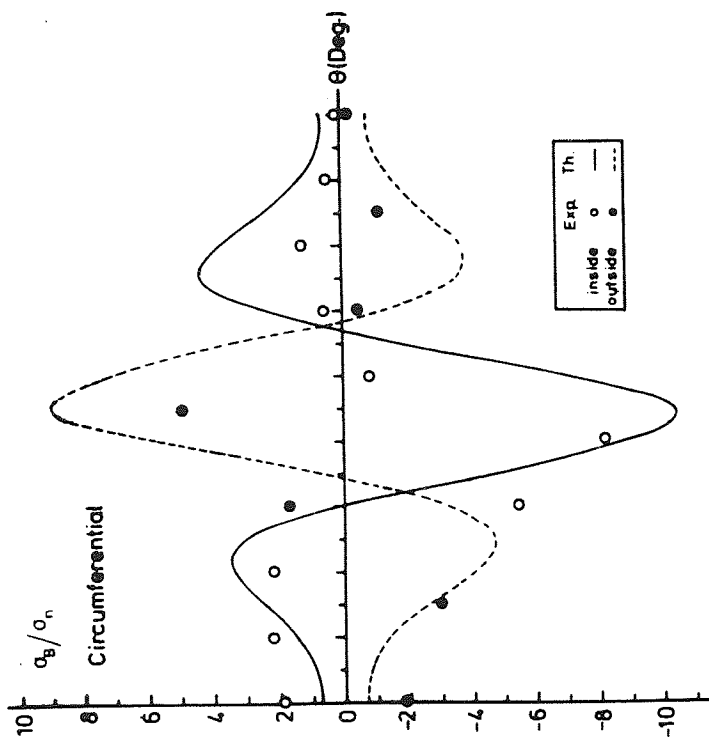


Figure (6.24) 'a' longitudinal and 'b' circumferential stress distribution measured on bend S022 under 9.97×10^5 N mm in-plane bending moment (closing)

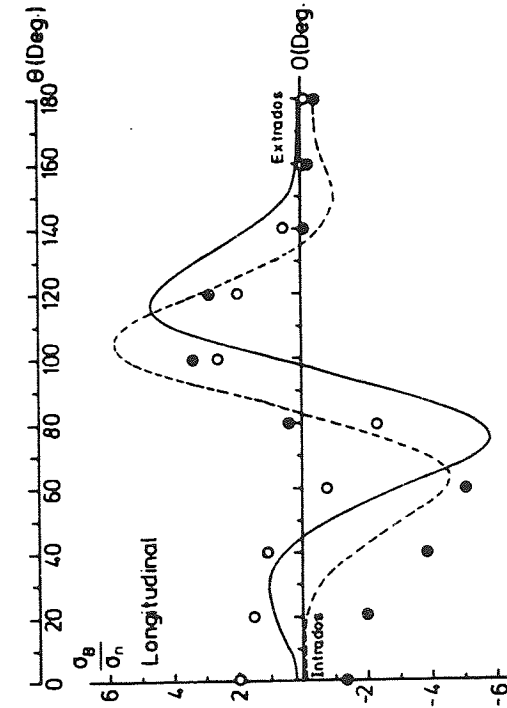
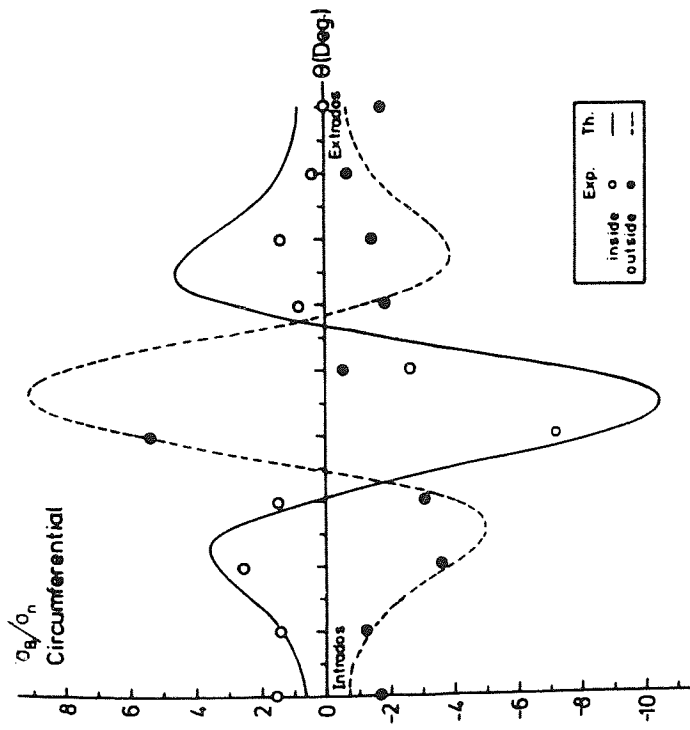


Figure (6.23) 'a' longitudinal and 'b' circumferential stress distribution measured on bend S021 under 9.97×10^5 N mm in-plane bending moment (closing)

- (d) The experimental longitudinal stress ratio distribution form a similar pattern with theory, except at $\theta = 0^\circ-60^\circ$ for large diameter bends as shown in Figs. 6.21a, 6.22a, 6.23a and 6.24a where experimental results show a higher magnitude of local bending.
- (e) The maximum longitudinal experimental stress ratio is always located on the outside surface at $\theta = 100^\circ-140^\circ$. Theory predicts that such a maximum is located not only at $\theta = 100^\circ-140^\circ$ on the outside but also at $\theta = 40^\circ-80^\circ$ on the inside. Thickness measurements show that at $\theta = 40^\circ-80^\circ$, the bends has a higher thickness than $\theta = 100^\circ-140^\circ$ which might explain the discrepancy.

The experimentally measured stress intensification factors (SIF_i) are the maximum stress ratios presented for the bends. The SIF_i experimental results are presented in a similar pattern to the flexibility factors, by incorporating the different thickness to formulate the maximum stress predicted by the simple bend theory (σ_n Eq. (I.9) of App. I), as follows:

- (i) nominal thickness as specified by BS4994, t_n ;
- (ii) average measured thickness on the straight, t_{st} ;
- (iii) average measured thickness on the bend, t_B ;
- (iv) average measured effective thickness, t_e .

The maximum experimental longitudinal and circumferential SIFs are presented and compared with their theoretical values in Tables 6.11 and 6.12 where the influence of the thickness parameter is considered. the graphical comparison of columns i, ii and iii of Tables 6.11 and 6.12 with BS806⁽¹²³⁾ prediction would further assess the prominent role of the thickness parameter having on formulating the final results of the tested bends. Such graphical presentation is shown in Figs. 6.25 and 6.26.

TABLE 6.11 - Maximum In-plane Longitudinal Stress Intensification

Factors experimentally determined for Smooth CSM Bends

| Bend No. | | In-plane longitudinal SIF | | | | | | |
|------------------------|------|----------------------------|-----------------------------|-------------------------|--|------|--------|------|
| | | Col. (i) | Col. (ii) | Col. (iii) | Col. (iv) | | | |
| | | Based on nominal thickness | Based on straight thickness | Based on bend thickness | Based on effective thickness (t_e) | | | |
| | | | | | λ_e | Exp. | Theory | |
| BS806 ⁽¹²³⁾ | | Bend Theory | | | | | | |
| Set I | S001 | 1.32 | 1.55 | 2.44 | 0.58 | 2.0 | 1.60 | 1.50 |
| | S002 | 1.48 | 1.74 | 2.25 | | 2.0 | | |
| | S006 | 0.87 | 1.03 | 1.41 | | 1.22 | | |
| | | | | | Average 1.74 ± 1.11 | | | |
| Set II | S017 | 0.91 | 1.09 | 0.99 | 0.90 | 1.09 | 1.40 | 1.30 |
| | S018 | 1.72 | 2.19 | 1.89 | | 2.04 | | |
| | S019 | 1.03 | 1.17 | 1.05 | | 1.25 | | |
| | | | | | Average 1.46 ± 1.26 | | | |
| Set III | S023 | 2.55 | 3.03 | 3.73 | 0.19 | 3.38 | 3.80 | 3.45 |
| | S024 | 2.95 | 3.67 | 4.32 | | 4.00 | | |
| | S025 | 3.34 | 3.76 | 4.83 | | 4.30 | | |
| | | | | | Average 3.893 ± 1.17 | | | |
| Set IV | S020 | 4.23 | 5.60 | 6.63 | 0.09 | 6.12 | 6.30 | 5.60 |
| | S021 | 3.22 | 4.26 | 5.73 | | 5.00 | | |
| | S022 | 3.34 | 4.43 | 5.15 | | 4.8 | | |
| | | | | | Average 5.31 ± 1.76 | | | |

TABLE 6.12 - Maximum In-plane Circumferential Stress

Intensification Factors experimentally determined for
Smooth CSM Bends

| Bend No. | | In-plane circumferential SIF | | | | | | |
|----------|-------|------------------------------|-----------------------------|-------------------------|--|------|--------|-------|
| | | Col. (i) | Col. (ii) | Col. (iii) | Col. (iv) | | | |
| | | Based on nominal thickness | Based on straight thickness | Based on bend thickness | Based on effective thickness (t_e) | | | |
| | | | | | λ_e | Exp. | Theory | |
| | | | | BS806 ⁽¹²³⁾ | Bend Theory ^{**} | | | |
| Set I | S001 | 1.73 | 2.04 | 3.20 | 0.58 | 2.62 | 2.50 | 2.80 |
| | S002* | 1.37 | 1.61 | 2.08 | | 1.85 | | |
| | S006 | 1.54 | 1.81 | 2.47 | | 2.14 | | |
| | | | | | Average 2.206 ± 1 | | | |
| Set II | S017* | 1.39 | 1.67 | 1.65 | 0.90 | 1.66 | 1.80 | 1.84 |
| | S018* | 1.88 | 2.39 | 2.07 | | 2.23 | | |
| | S019 | 1.24 | 1.41 | 1.59 | | 1.50 | | |
| | | | | | Average 1.80 ± 1 | | | |
| Set III | S023 | 3.85 | 4.56 | 5.61 | 0.19 | 5.09 | 6.00 | 6.25 |
| | S024* | 4.80 | 5.97 | 7.02 | | 6.50 | | |
| | S025 | 4.20 | 4.72 | 6.07 | | 5.40 | | |
| | | | | | Average 5.66 ± 1.84 | | | |
| Set IV | S020* | 6.20 | 8.20 | 9.71 | 0.09 | 8.96 | 10.50 | 10.35 |
| | S021 | 5.80 | 7.68 | 10.30 | | 9.00 | | |
| | S022 | 5.29 | 7.01 | 8.15 | | 7.60 | | |
| | | | | | Average 8.52 ± 2.0 | | | |

* Inside circumferential stress was estimated by using the average value of the membrane stress of the inside strain gauged bends.

** See (App. II).

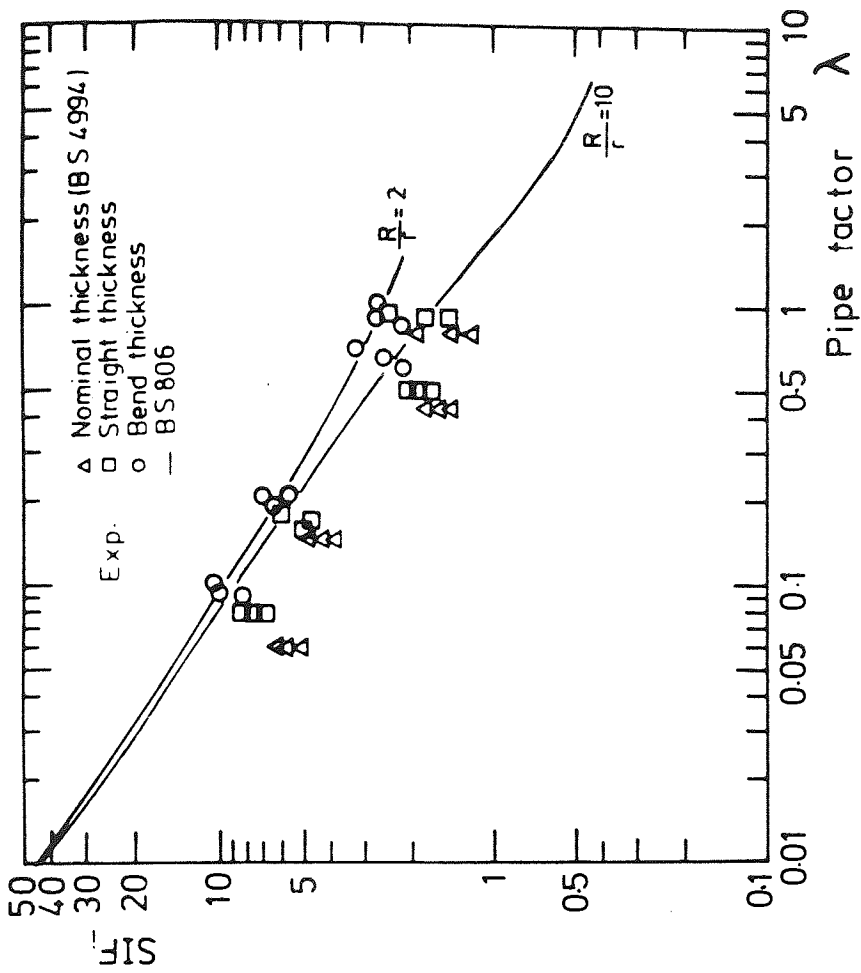


Figure (6.25)

Maximum in-plane longitudinal stress intensification factor (SIF_L) for smooth CSM bends presented as a function of the different thicknesses employed in Table (6.11), columns i, ii and iii

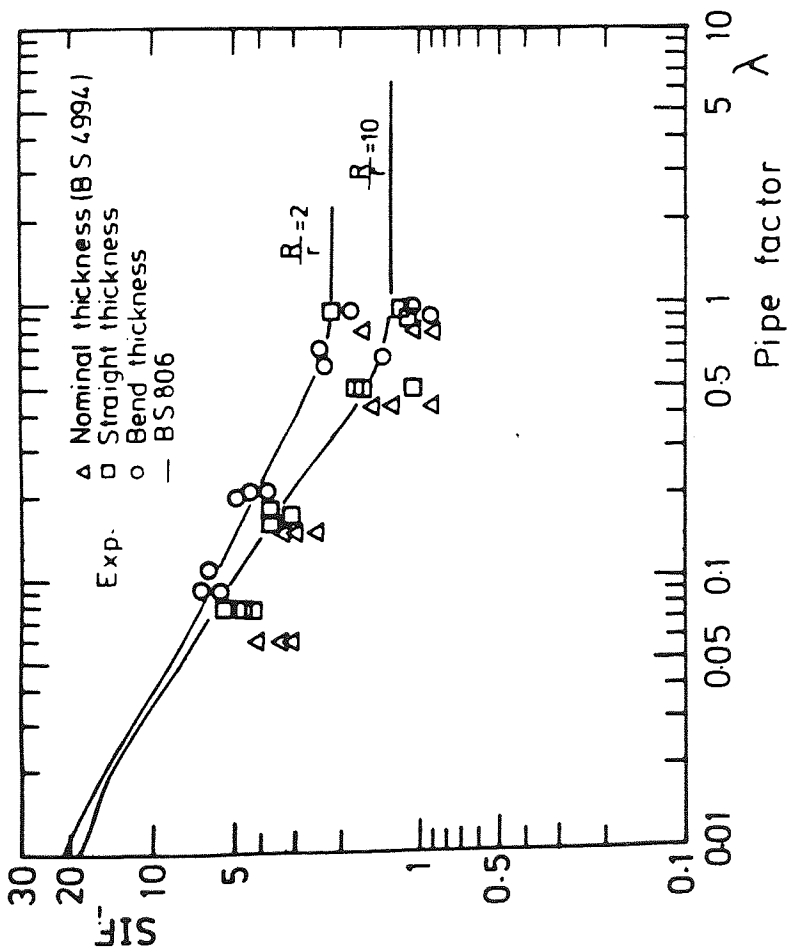


Figure (6.26)

Maximum in-plane circumferential stress intensification factors (SIF_C) for smooth CSM bends presented as a function of the different thicknesses employed in Table (6.12), columns i, ii and iii

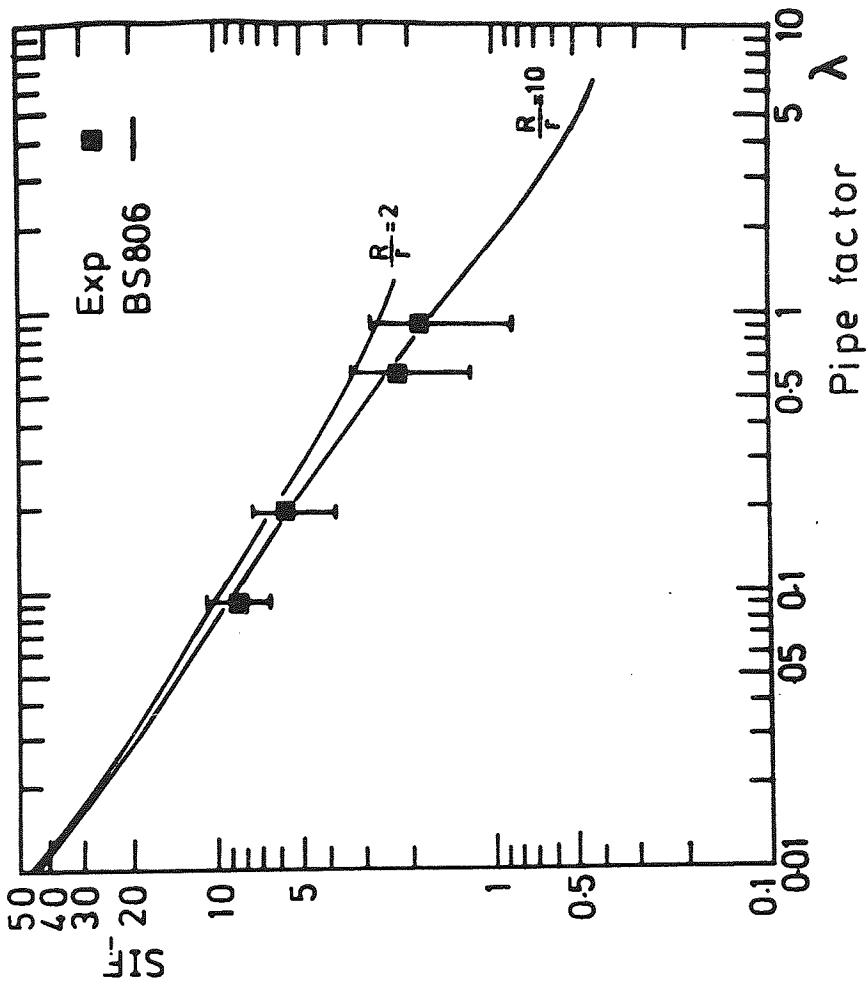


Figure (6.28)

Maximum in-plane circumferential stress intensification factors ($SIF_{i,C}$) for smooth CSM bends using the effective thickness (t_e) as in column (iv) of Table (6.12). Experimental results are presented with 95% upper and lower confidence limit

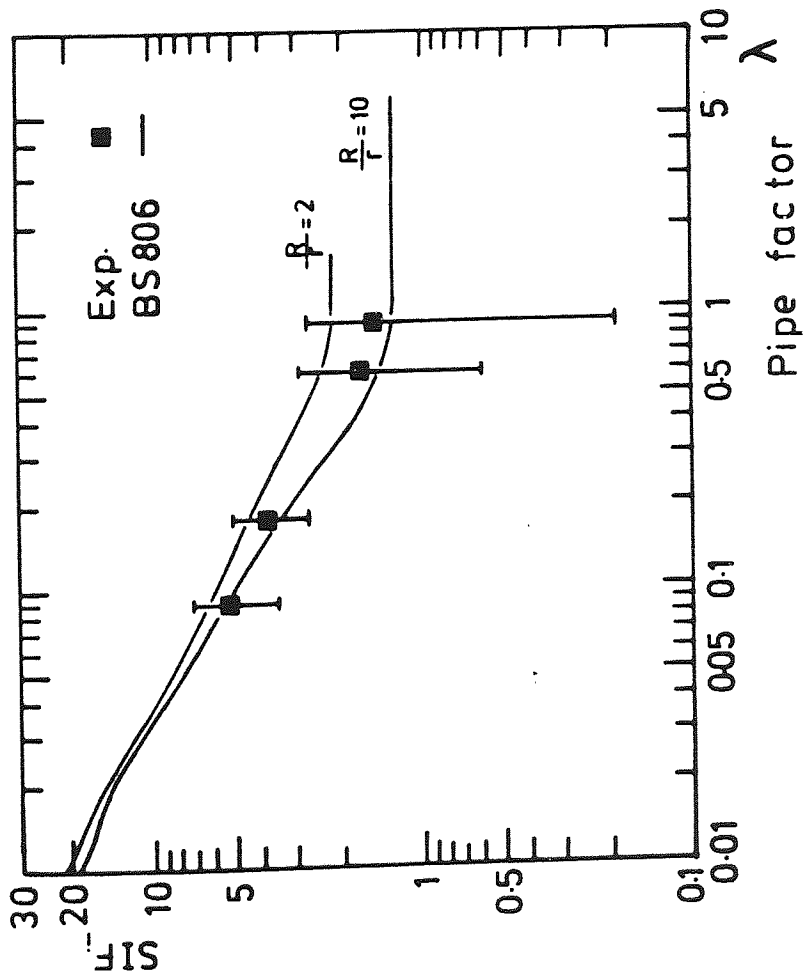


Figure (6.27)

Maximum in-plane longitudinal stress intensification factors ($SIF_{i,L}$) for smooth CSM bends using the effective thickness (t_e) as in column (iv) of Table 6.11. Experimental results are presented with 95% upper and lower confidence limit

As clearly shown from Fig. 6.25 and/or Fig. 6.26 that the variability of the experimental SIFs for small diameter bends (or large pipe factor λ) as a function of λ is not as severe as for their corresponding in-plane flexibility factors (see Fig. 6.14).

The final formulations of the results could be brought up to a conclusion by using the average effective thickness (t_e) for the bend, and basing the SIF results accordingly as listed in column iv of Tables 6.11 and 6.12. Such final formulation is presented graphically by taking the 95% upper and lower confidence limits, compared with BS806⁽¹²³⁾ predictions as in Figs. 6.27 and 6.28. The average values of the SIFs presented with the upper and lower limits could be described as follows:

- (a) Experimentally measured longitudinal SIFs are comparable with BS806 specification.
- (b) The circumferential SIFs for the tested bends are slightly over-estimated by BS806⁽¹²³⁾, by about 10-15%.
- (c) Taking the upper limit of the experimental results would necessitate a higher safety factor to be incorporated in design.
- (d) No distinctive pattern has been noticed in the experimental results due to the different bend radius to pipe radius ratio

(i.e. $\frac{R}{r_m} = 2$ to $\frac{R}{r_m} = 6$).

6.4.4 Out-of-plane bending

6.4.4.1 Out-of-plane flexibility factor (K_o)

The experimentally determined out-of-plane flexibility factor is obtained using Eq. (I.18) of App. I, where the average effective thickness (t_e) is used to calculate the second moment of area (I_e). Young modulus of 7.45 kN.mm^{-2} and shear modulus of 2.77 kN.mm^{-2} are used in the calculations. For reasons of comparison, Eq.s (I.19) and (I.34) of App. I, are also used.

The analysis in App. I, assumes that the tangents are of unity flexibility factor and the average out-of-plane flexibility factor is uniformly distributed along the bend. Similar to metallic bends^(143,144,172), it is also assumed that ovalization of the bend is a consequence of the flexural component of the applied moment, where the torsional component is assumed to have no contribution to such ovalization and accordingly none to the bend flexibility. The out-of-plane diametral measurements presented in Fig. 6.29 show that ovalization maximises at the centre of the bend decaying towards the tangents. This indicates that the central section of the bend would provide the maximum flexibility.

Similar to the presentation of the in-plane flexibility factors, the experimentally determined out-of-plane flexibility factors are calculated based on:

- (i) nominal thickness specified by BS4994; t_n , and using Eq. (I.18) of App. I.
- (ii) average thickness measured on the straight; t_{si} , and using Eq. (I.18) of App. I.
- (iii) average thickness measured on the straights used for the tangents, and average thickness measured on the the bend (t_B) and using Eq. (I.19) of App. I.
- (iv) same as (iii), with the introduction of the joints effects (t_j), and using Eq. (I.34) of App. I.
- (v) average effective thickness, t_e , and using Eq. (I.18) of App. I.

These results are listed in Table 6.13, where pronounced variability is shown for the flexibility factors of the small diameter bends, especially when the actual thickness is not considered in the derivations. The results of columns i, ii and iv are plotted in Fig.

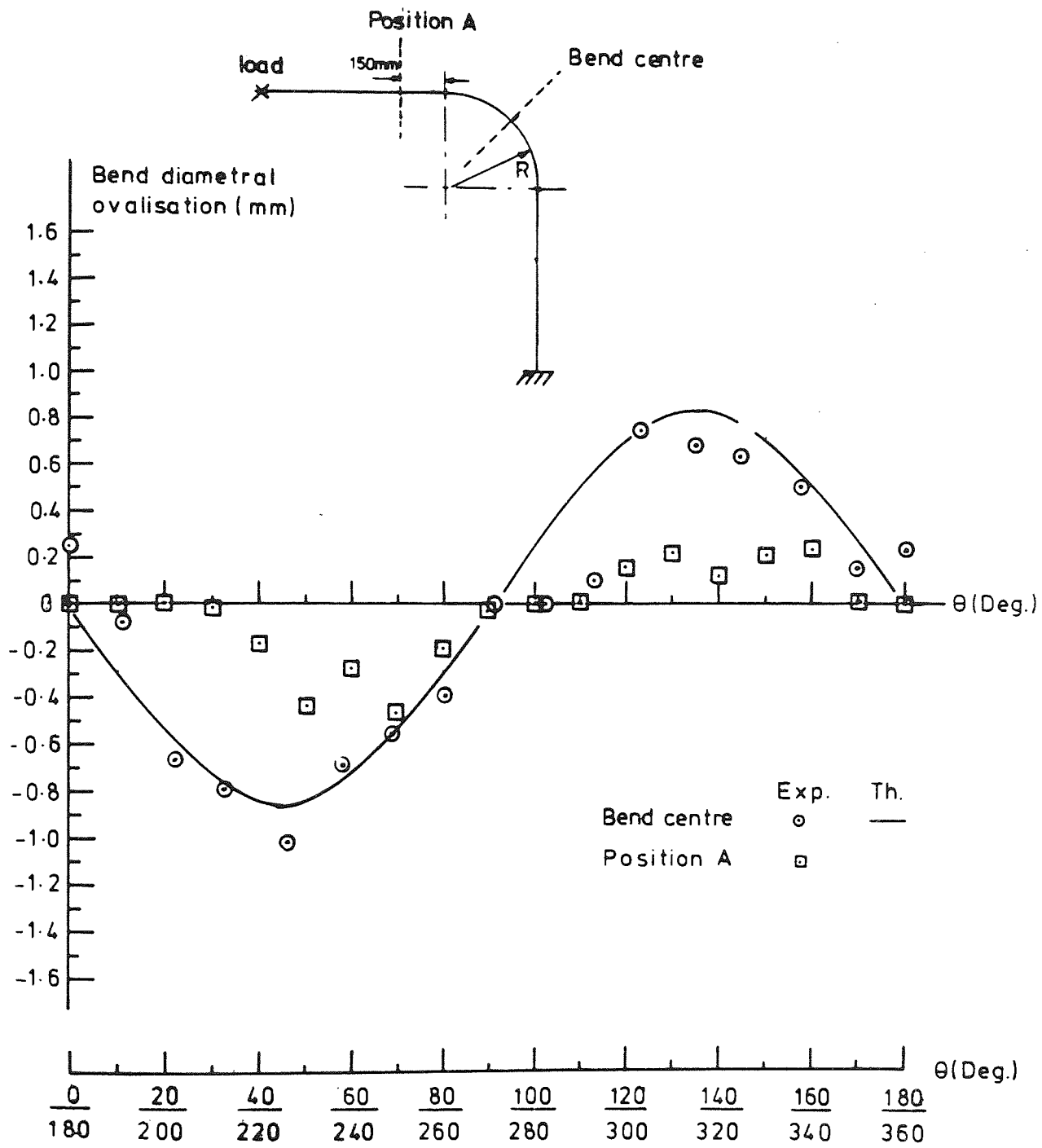


Figure (6.29) Bend-centre diametral ovalization of bend S006 under 2.25×10^5 N mm out-of-plane bending moment

TABLE 6.13 - Out-of-plane Flexibility Factors experimentally determined for Smooth CSM Bends

| Bend Number | End deflection per unit and load $\times 10^2$ (mm/N) | Out-plane Flexibility Factor | | | | | Flexibility Factor | | | |
|---------------------------------|---|------------------------------|-----------------------------|-----------------------------|---------------------------------------|--------------------------|--|--------------|-------------|-----------------------|
| | | Col. (i) | Col. (ii) | Col. (iii) | Col. (iv) | λ_e | Based on effective thickness (t_e) | Theoretical | | |
| | | Based on nominal thickness | Based on straight thickness | Based on SI, Bend thickness | Based on SI, Bend and joint thickness | | | Experimental | BS806 (123) | Bend Theory (App. II) |
| Set I S001 S002 S006 | 24.13 | - 1.14 | 0.56 | 0.90 | 3.89 | 0.58 | 3.88 | 2.60 | 2.79 | |
| | 23.23 | - 1.49 | 0.16 | 0.20 | 2.56 | | | | | 2.39 |
| | 25.7 | - 0.52 | 1.29 | 1.79 | 4.27 | | | | | 3.54 |
| | | | | | | Average 3.27 \pm 1.94 | | | | |
| Set II S017 S018 S019 | 10.62 | - 1.29 | 0.68 | 0.017 | 1.64 | 0.90 | 0.60 | 1.80 | 1.84 | |
| | 10.91 | - 1.04 | 1.65 | 1.42 | 2.02 | | | | | 0.78 |
| | 10.75 | - 1.18 | 0.18 | 0.20 | 1.57 | | | | | 0.90 |
| | | | | | | Average 0.76 \pm 0.38 | | | | |
| Set III S023 S024 S025 | 1.74 | 4.38 | 6.66 | 8.24 | 9.39 | 0.19 | 8.38 | 8.50 | 8.68 | |
| | 1.85 | 5.13 | 8.33 | 9.87 | 10.64 | | | | | 9.82 |
| | 1.78 | 4.64 | 6.19 | 8.02 | 9.57 | | | | | 8.27 |
| | | | | | | Average 8.82 \pm 2.16 | | | | |
| Set IV S020 S021 S022 | 5.92 | 10.66 | 19.28 | 22.84 | 25.97 | 0.09 | 22.47 | 17.50 | 18.33 | |
| | 5.62 | 9.34 | 17.53 | 23.56 | 24.74 | | | | | 23.16 |
| | 5.00 | 6.63 | 13.91 | 16.20 | 19.1 | | | | | 16.30 |
| | | | | | | Average 20.64 \pm 9.39 | | | | |

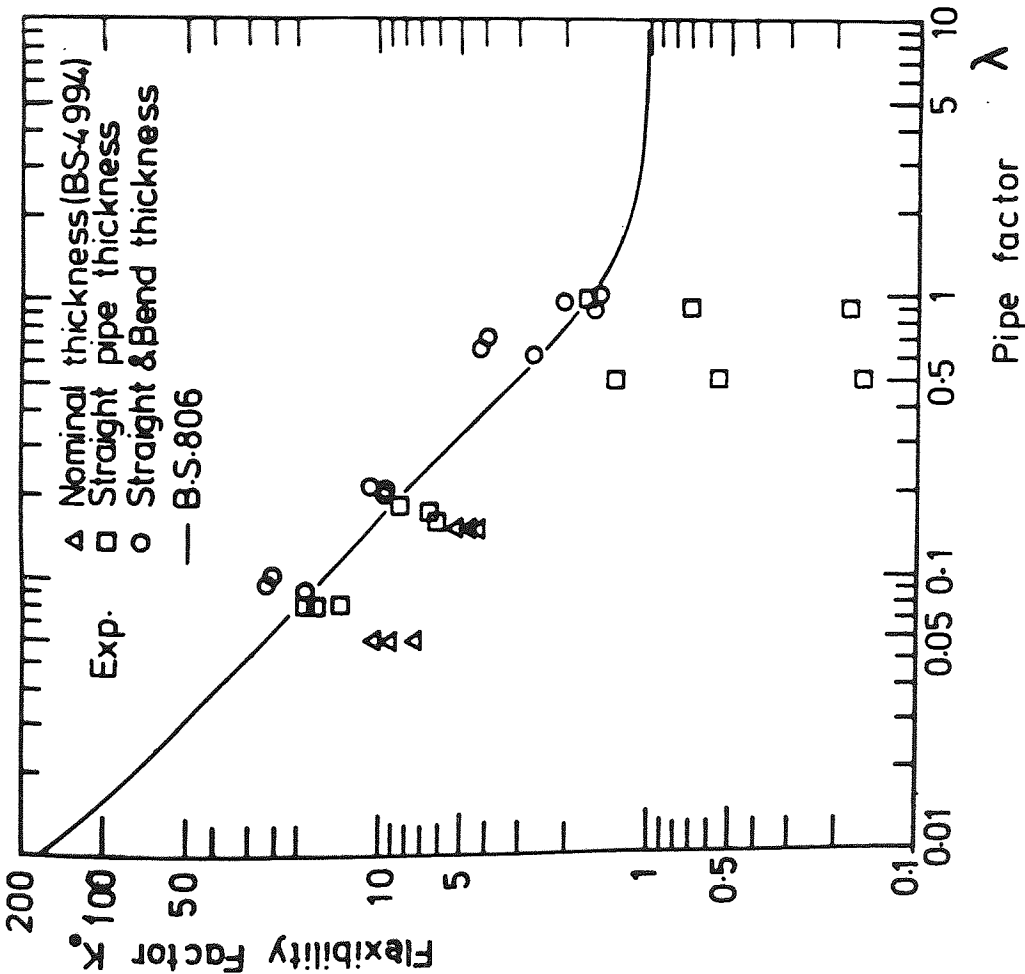


Figure (6.30)

Out-of-plane flexibility factor (K_0) for smooth CSM bends presented as a function of the different thicknesses employed in Table (6.13), columns i, ii and iv

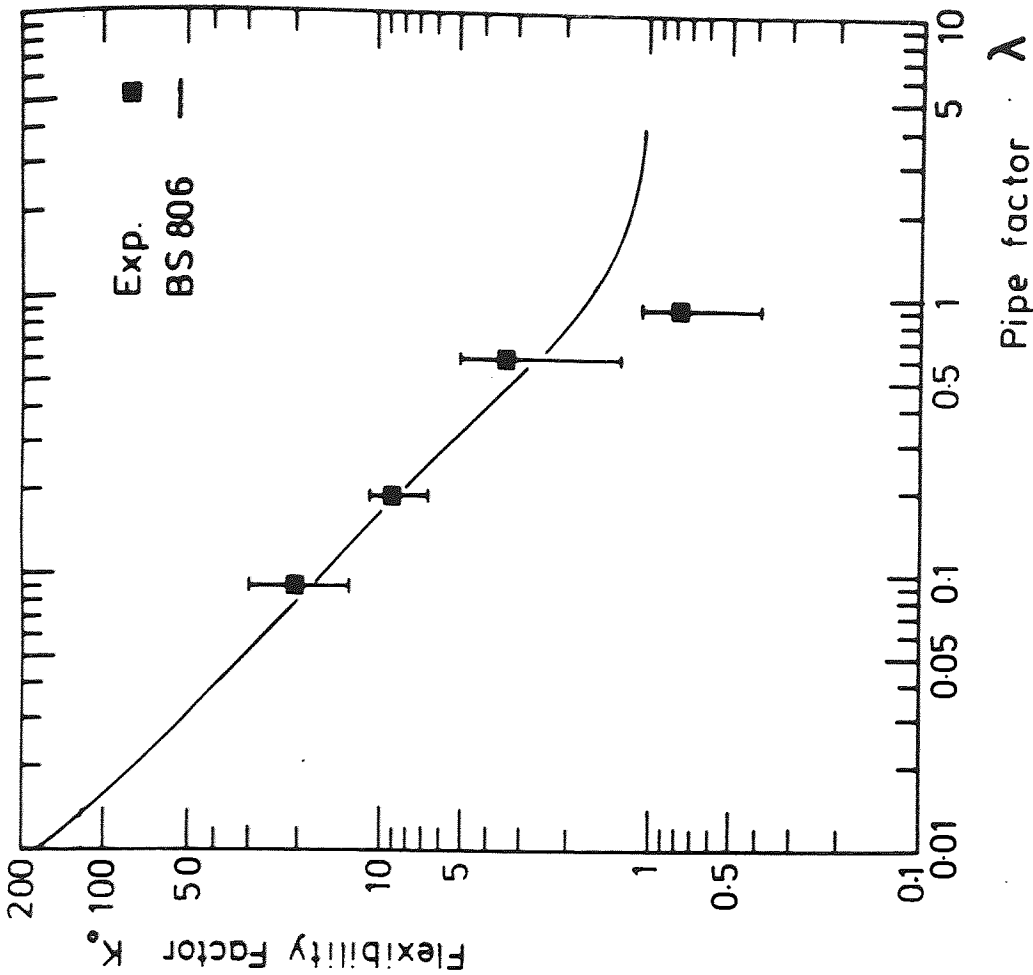


Figure (6.31)

Out-of-plane flexibility factor (K_0) results for smooth CSM bends using the effective thickness (t_e) as in column (v) of Table (6.13). Experimental results are presented with 95% upper and lower confidence limit

6.30 in comparison with BS806 specification for the purpose of describing the different results using the different thicknesses.

The conclusive experimental results for K_o listed in column v of Table 6.13 are graphically presented in Fig. 6.31. These results show that out-of-plane flexibility factors are higher than BS806 prediction and in turn, higher than the in-plane flexibility factors for the same bends, possibly indicating that the bend-tangent structure is weaker than anticipated under the application of torsional moments. In this instance, it is thought that this weakness is attributed to the joints construction.

6.4.4.2 Out-of-plane stress ratio distribution and stress intensification factors (SIF_o)

Typical strain distributions measured under out-of-plane bending are shown in Figs. 6.32 and 6.33 for the longitudinal and the circumferential strain distribution respectively, for bends S001, S002 and S006. The measurements are of three similarly constructed bends of 1.8 kg.m^{-2} , 30% nominal glass content and 100mm nominal bore (Set I of Table 6.1). All bends exhibit similar pattern of deformation, but with different levels of magnitude particularly for the circumferential strains as shown in Figs. 6.33a,b, with a narrower range of variability for the longitudinal strains (Figs. 6.32a and b).

Similar to the presentation of the in-plane stress ratio distribution, the experimentally determined out-of-plane stress ratio distribution are compared with isotropic bend theory prediction (App. II), using the average effective thickness (t_e) to calculate σ_n . The theoretical and the experimental stress ratios are presented in Figs. 6.34 and 6.35 for bends S001 and S002 (of Set I), Fig. 6.36 for bend S019 (of Set II), Figs. 6.37 and 6.38 for bends S024 and S025 (of Set

II), and in Figs. 6.39 and 6.40 for bends S021 and S022 (of Set IV). The experimentally determined out-of-plane SIF_o are then presented using Eq. (I.20) and (I.21) of App. I, and similar to the SIF_i presentation the different thickness of the bend wall are incorporated for the purpose of comparison.

The comparison of the experimental and the theoretical stress ratio distributions of Figs. 6.34-6.40, could be summarized as follows:

- (a) Experimental results follow a similar pattern of stress distribution as predicted by theory.
- (b) The experimentally measured circumferential stress ratios show a lower peak value than predicted by theory, except for bend S001 as shown in Fig. 6.34.
- (c) The experimentally measured longitudinal stress ratios are of comparable peak values with theoretical predictions and sometimes exceeds them, as shown in Fig. 6.36a and 6.40a.
- (d) The maximum experimental stress ratio measured on the bend is the circumferential stress, and it is always located on the inside surface except for bend S021 where the longitudinal stress is the maximum as in Fig. 6.39.
- (e) Unlike in-plane bending, the principal stresses measured under out-of-plane bending deviate from the principle circumferential and the longitudinal axes of deformation, due to the in-plane shear stresses induced by the torsional component of the applied moment. The average value of the in-plane shear stresses measured around the circumference is comparable with that predicted by the simple theory of torsion.
- (f) Negligible magnitude of longitudinal and circumferential stress ratios occur at both the intrados ($\theta = 0^\circ$) and at the extrados ($\theta = 180^\circ$).

The maximum experimentally measured longitudinal and circumferential SIF_{\circ} are listed in Tables 6.14 and 6.15 respectively in comparison with theoretical prediction. The effect of using the different thicknesses are incorporated into the results to emphasize the important role of the thickness on the end results. The results listed in columns i, ii and iii of Tables 6.14 and 6.15 are presented graphically with BS806⁽¹²³⁾ specification as shown in Figs. 6.41 and 6.42.

The conclusive results where the average effective thickness (t_e) is used, are presented in column iv of Tables 6.14 and 6.15 and graphically presented in Figs. 6.43 and 6.44, compared with BS806 specifications, using 95% upper and lower confidence limits.

The results presented in Figs. 6.43 and 6.44 indicate that the average of the maximum longitudinal and circumferential SIF_{\circ} would be slightly overestimated using BS806 prediction.

6.4.5 SIF to K ratios

For the bends' test results in articles 6.43 and 6.44, a further step could be taken by combining the flexibilities and the SIF in a form of a parametrical ratio of SIF/K as a function of the pipe factor (λ_e). The experimental results in Table 6.16 are compared with theoretical predictions as presented by Kellogg piping Handbook⁽¹³⁷⁾ and shown graphically in Fig. 6.45a,b for in-plane bending and in Fig. 6.46a,b for out-of-plane bending. This type of presentation, apart from its overall examination of the bend behaviour, would be of practical value for the on-site piping engineer or perhaps could be incorporated as part of the quality control procedure by the manufacturer. This could be achieved by reasonable knowledge of the bend thickness; by

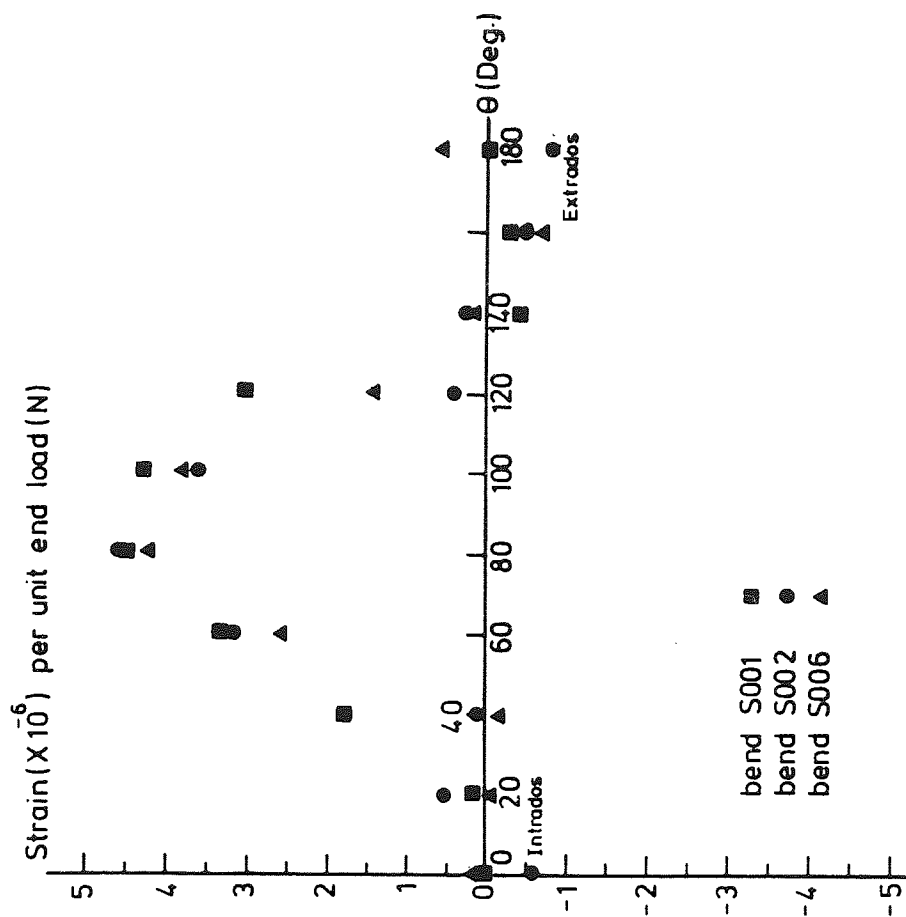


Figure (6.32b) Outside longitudinal strain distribution per unit end load measured on smooth CSM S001, S002 and S006 bends under out-of-plane bending

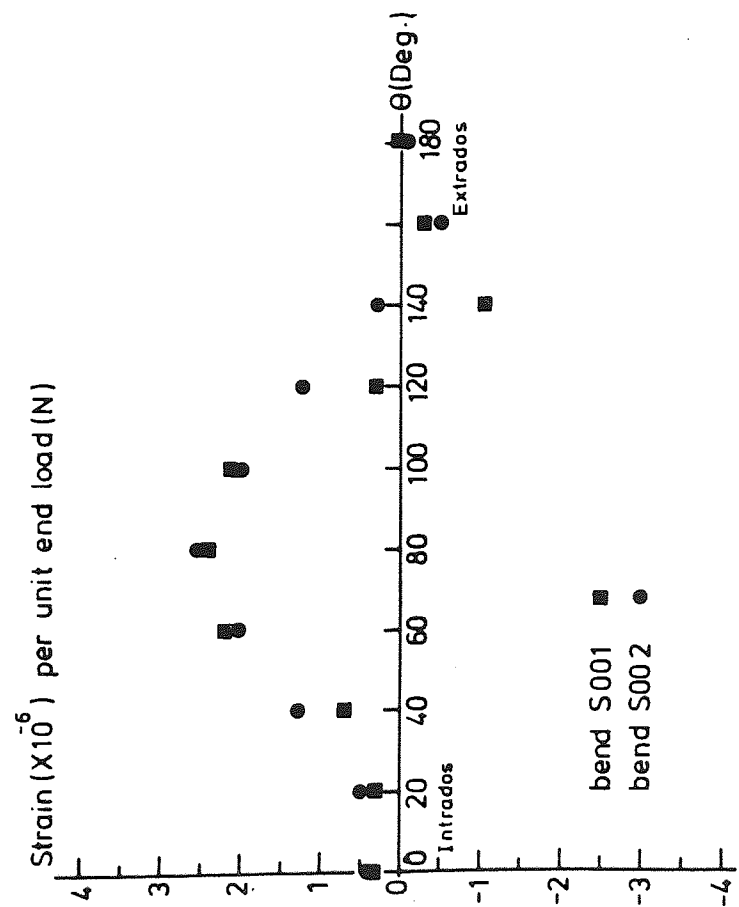


Figure (6.32a) Inside longitudinal strain distribution per unit end load measured on smooth CSM S001, S002 bends under out-of-plane bending

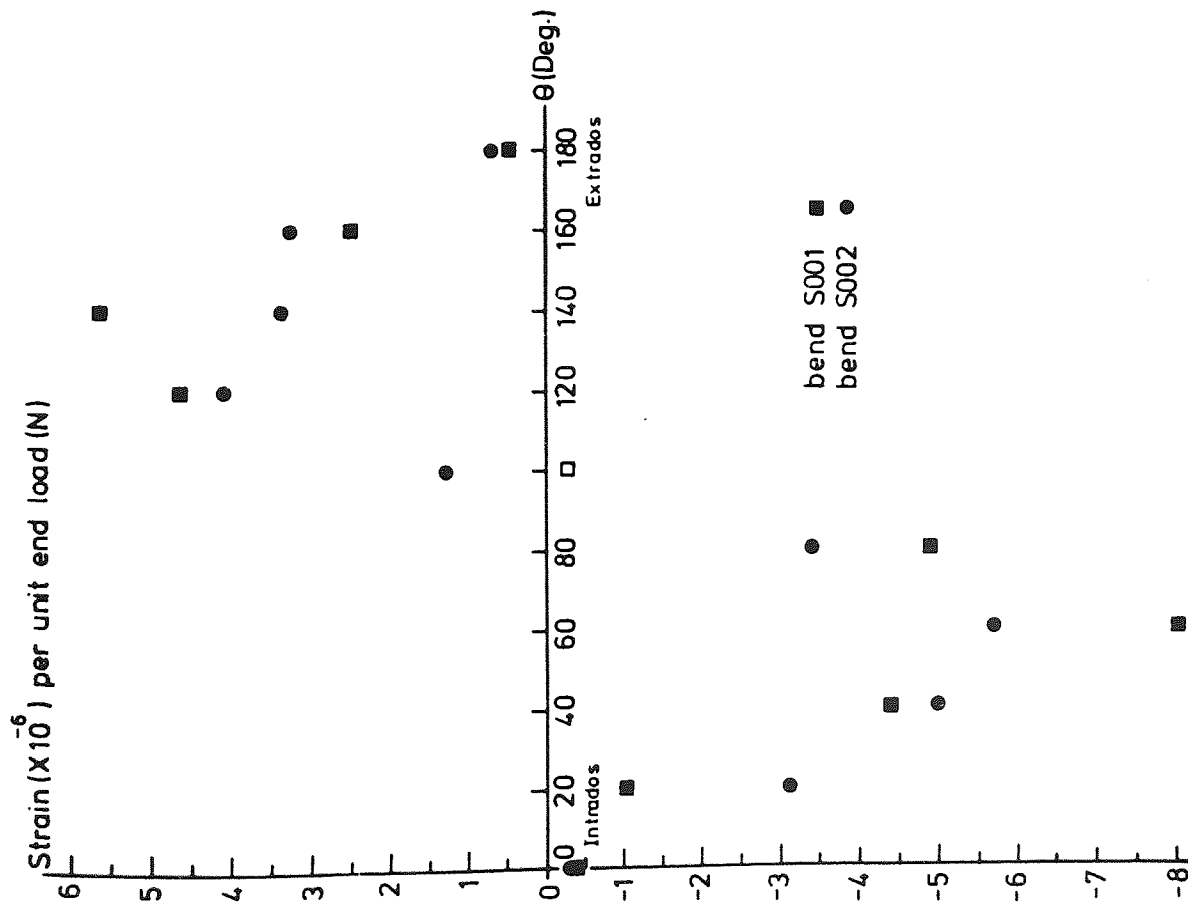


Figure (6.33a) Inside circumferential strain distribution per unit end load measured on smooth CSM S001, S002 bends under out-of-plane bending

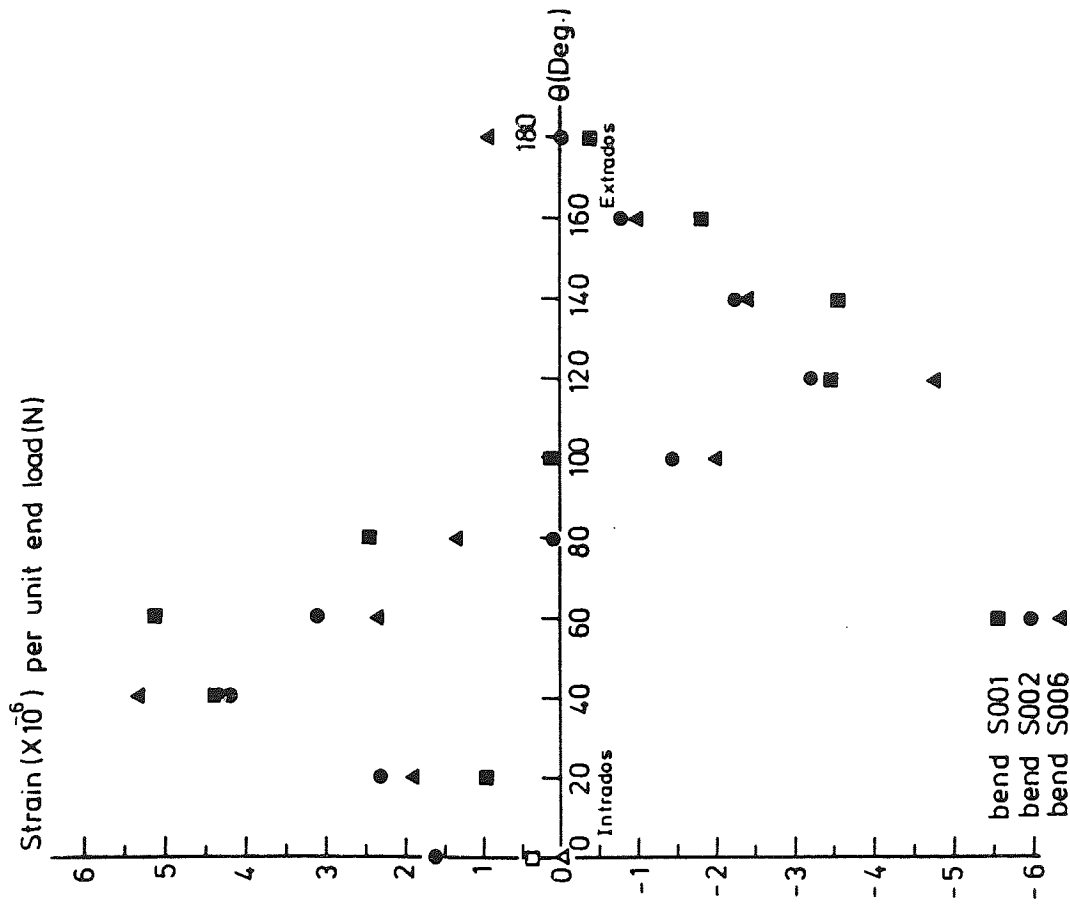


Figure (6.33b) Outside circumferential strain distribution per unit end load measured on smooth CSM S001, S002 and S006 bends under out-of-plane bending

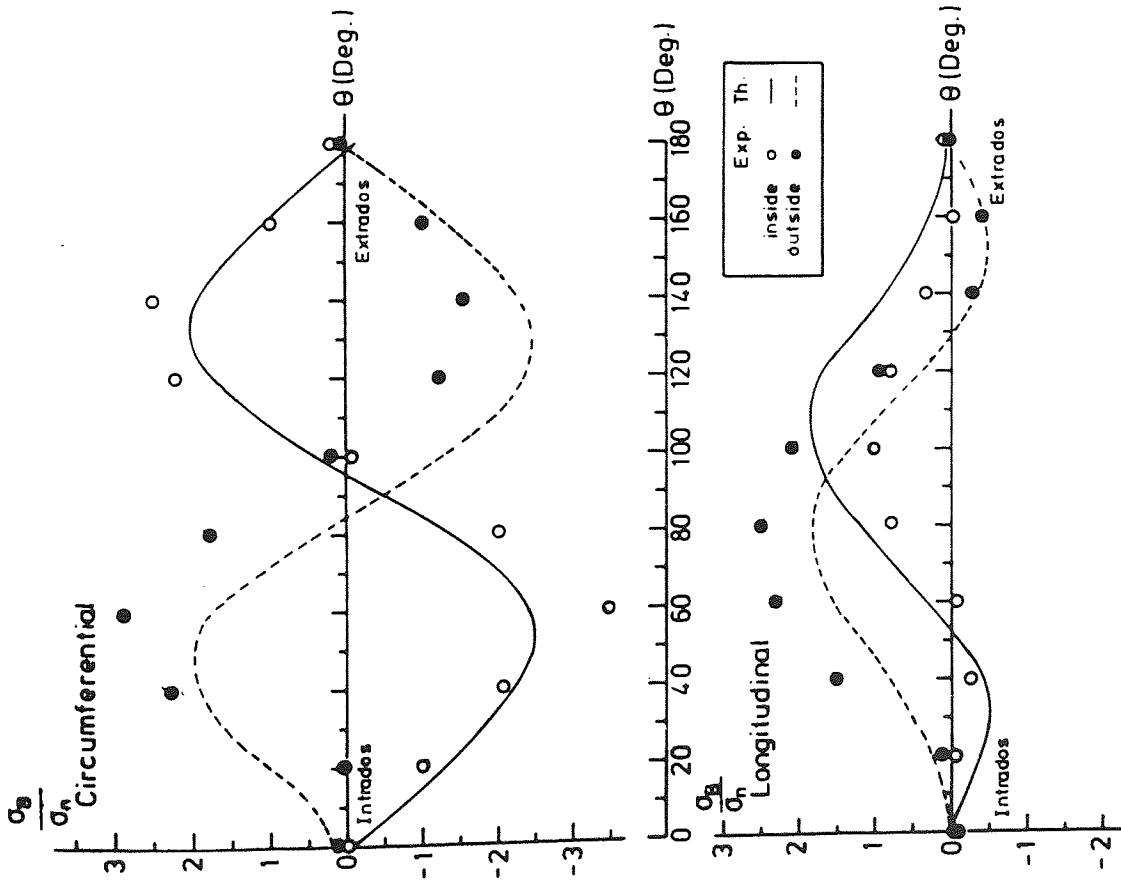


Figure (6.34) 'a' longitudinal and 'b' circumferential stress distribution measured on bend S001 under 1.52×10^5 N mm out-of-plane bending moment

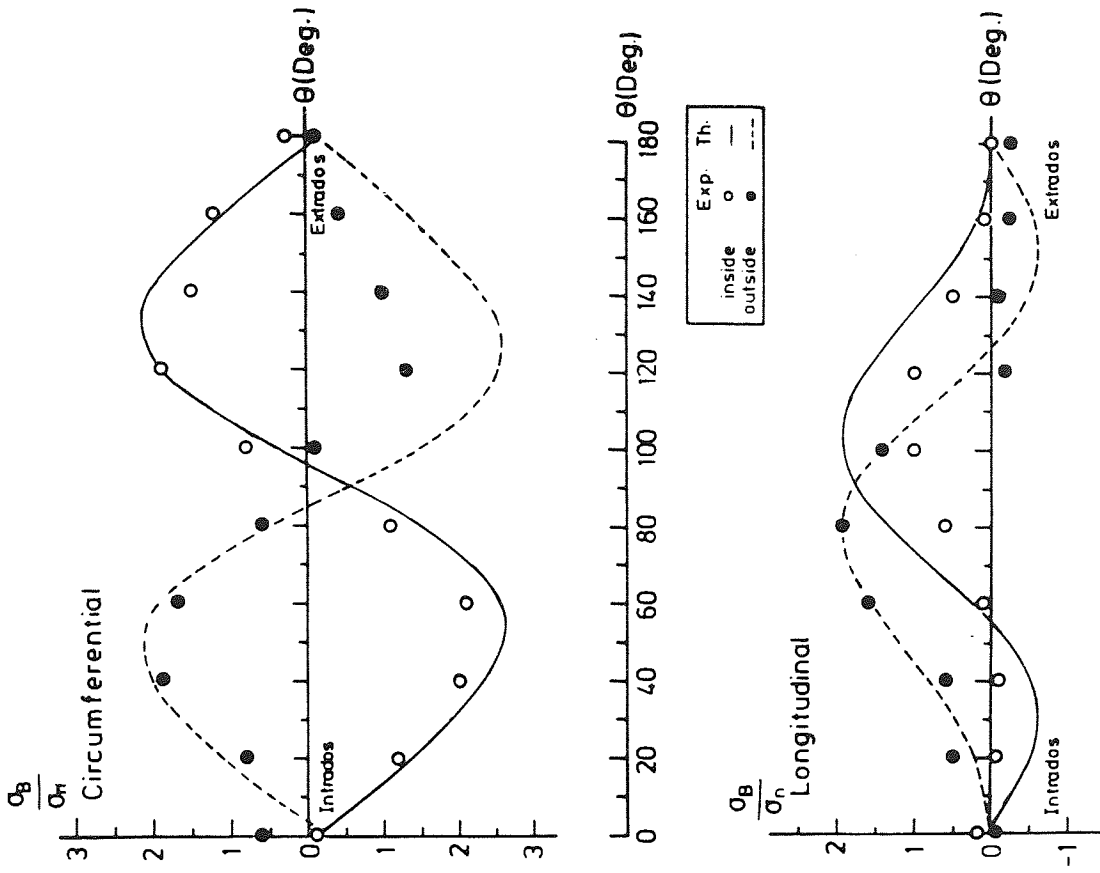


Figure (6.35) 'a' longitudinal and 'b' circumferential stress distribution measured on bend S002 under 1.48×10^5 N mm out-of-plane bending moment

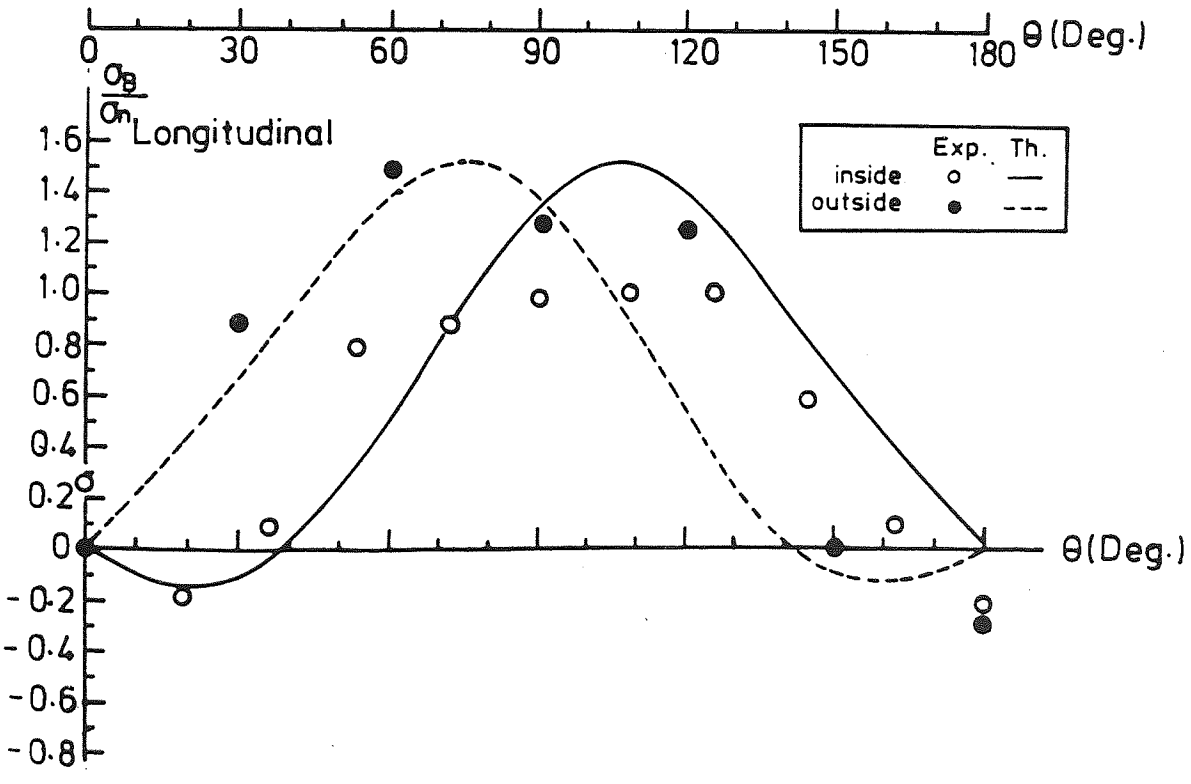
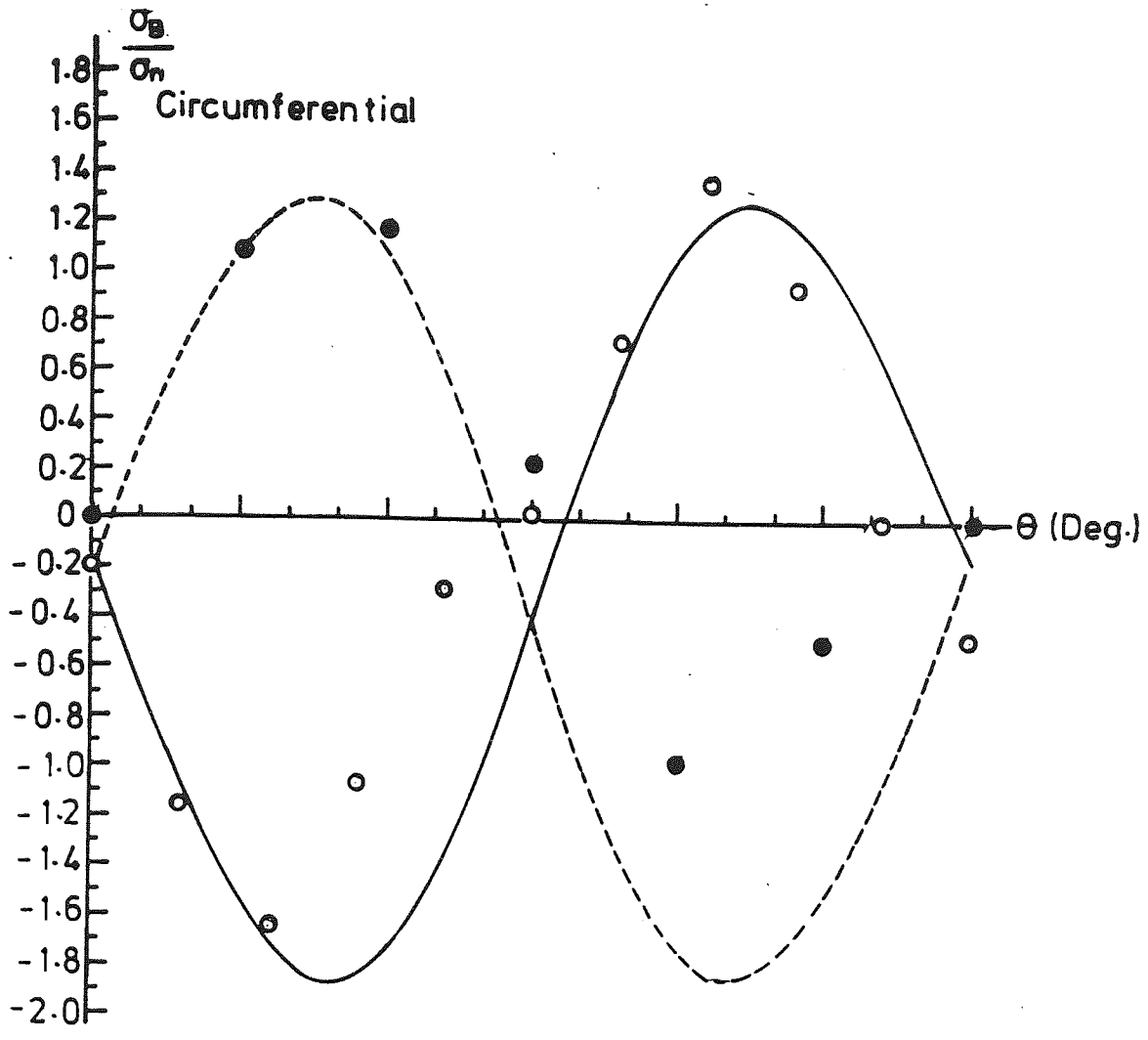


Figure (6.36) 'a' longitudinal and 'b' circumferential stress distribution measured on bend S019 under 5.75×10^5 N.mm out-of-plane bending moment

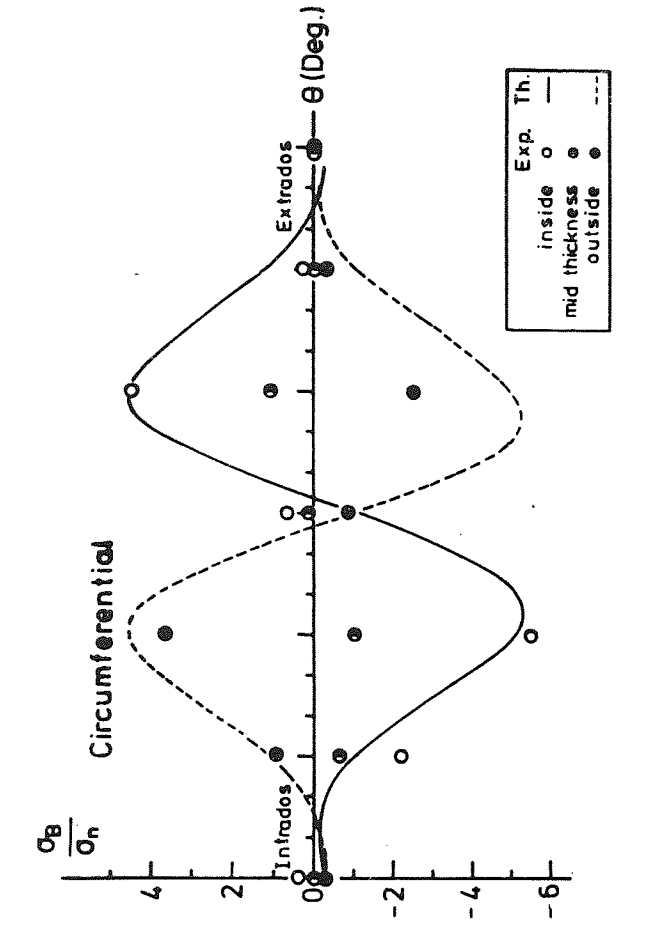


Figure (6.37) 'a' longitudinal and 'b' circumferential stress distribution measured on bend S024 under 8.07×10^5 N mm out-of-plane bending moment

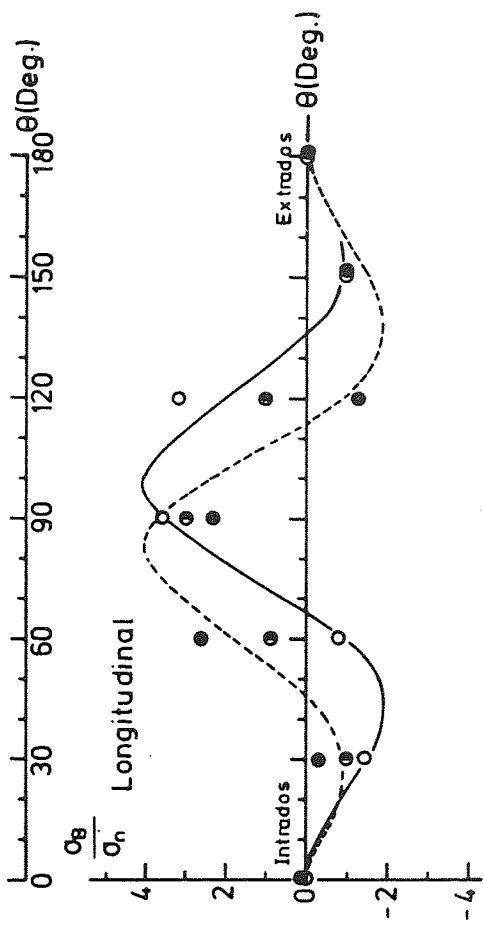


Figure (6.38) 'a' longitudinal and 'b' circumferential stress distribution measured on bend S025 under 8.07×10^5 N mm out-of-plane bending moment

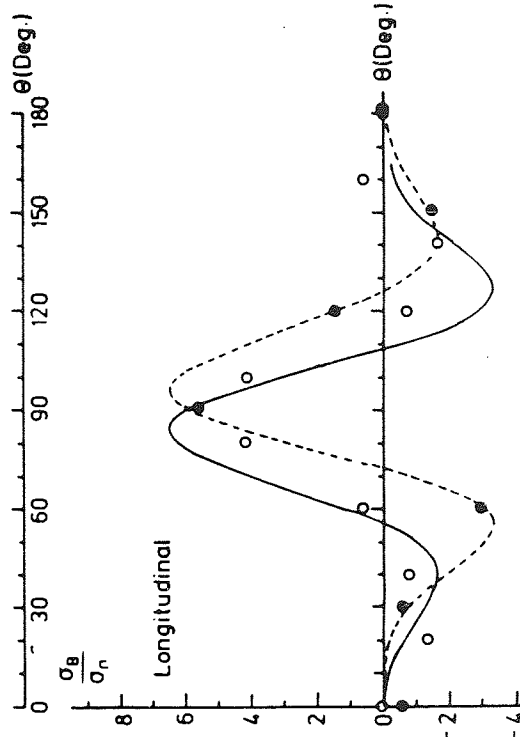
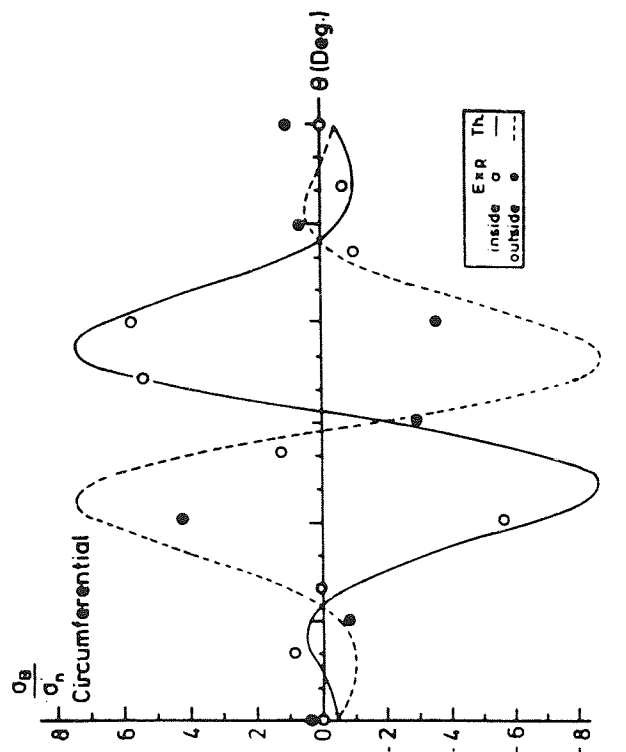


Figure (6.39) 'a' longitudinal and 'b' circumferential stress distribution measured on bend S021 under 6.9×10^5 N mm out-of-plane bending moment

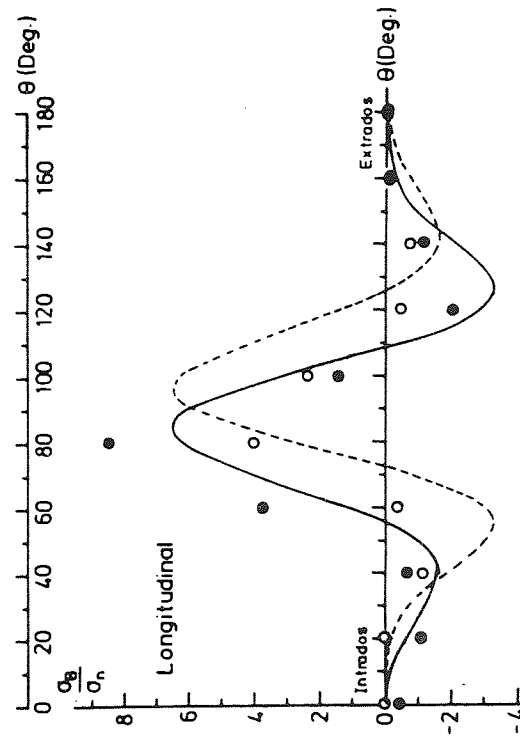
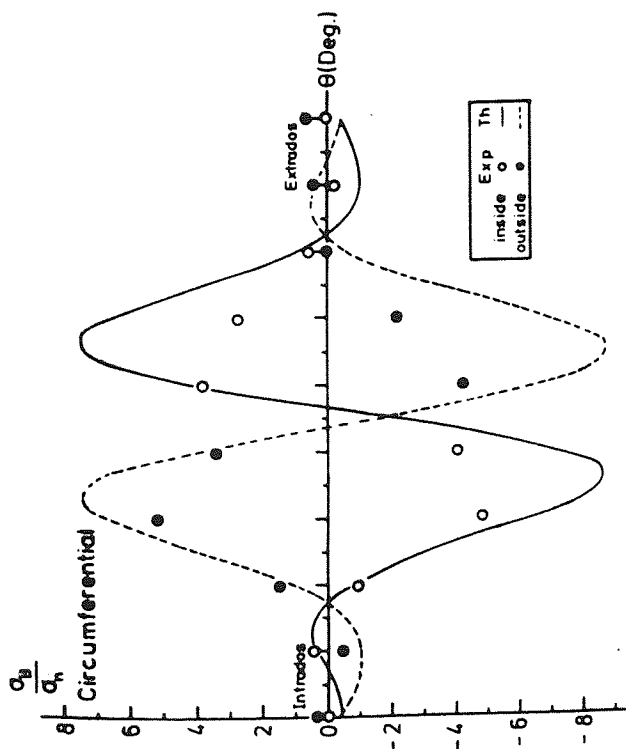


Figure (6.40) 'a' longitudinal and 'b' circumferential stress distribution of bend S022 under 6.9×10^5 N mm out-of-plane bending moment

TABLE 6.14 - Maximum Out-of-plane Longitudinal Stress
 Intensification Factors experimentally determined for
 Smooth CSM Bends

| Bend No. | | Out-of-plane longitudinal SIF | | | | | | |
|------------------------|-----------------------|-------------------------------|-----------------------------|-------------------------|--|------|--------|------|
| | | Col. (i) | Col. (ii) | Col. (iii) | Col. (iv) | | | |
| | | Based on nominal thickness | Based on straight thickness | Based on bend thickness | Based on effective thickness (t_e) | | | |
| | | | | | λ_e | Exp. | Theory | |
| BS806 ⁽¹²³⁾ | Bend Theory (App. II) | | | | | | | |
| Set I | S001 | 1.65 | 1.95 | 3.05 | 0.58 | 2.50 | 2.0 | 1.85 |
| | S002 | 1.41 | 1.66 | 2.14 | | 1.90 | | |
| | S006 | 1.45 | 1.70 | 2.32 | | 2.01 | | |
| | | | | | Average 2.14 ± 0.79 | | | |
| Set II | S017 | 1.21 | 1.46 | 1.44 | 0.90 | 1.45 | 1.6 | 1.50 |
| | S018 | 1.67 | 2.11 | 1.83 | | 1.97 | | |
| | S019 | 1.31 | 1.49 | 1.67 | | 1.58 | | |
| | | | | | Average 1.67 ± 0.67 | | | |
| Set III | S023 | 3.77 | 4.47 | 5.50 | 0.19 | 4.98 | 4.8 | 4.0 |
| | S024 | 3.39 | 4.14 | 4.87 | | 4.50 | | |
| | S025 | 2.72 | 3.06 | 3.94 | | 3.50 | | |
| | | | | | Average 4.31 ± 1.88 | | | |
| Set IV | S020 | 3.11 | 4.12 | 4.88 | 0.09 | 4.50 | 8.0 | 6.5 |
| | S021 | 5.48 | 7.26 | 9.74 | | 8.50 | | |
| | S022 | 3.51 | 4.64 | 5.40 | | 5.03 | | |
| | | | | | Average 6.0 ± 5.39 | | | |

TABLE 6.15 - Maximum Out-of-plane Circumferential Stress
Intensification Factors experimentally determined for
Smooth CSM Bends

| Bend No. | | Out-of-plane circumferential SIF | | | | | | |
|-------------|-----------------------|----------------------------------|-----------------------------|-------------------------|--|------|--------|------|
| | | Col. (i) | Col. (ii) | Col. (iii) | Col. (iv) | | | |
| | | Based on nominal thickness | Based on straight thickness | Based on bend thickness | Based on effective thickness (t_e) | | | |
| | | | | | λ_e | Exp. | Theory | |
| BS806 (123) | Bend Theory (App. II) | | | | | | | |
| Set I | S001 | 2.32 | 2.73 | 4.27 | 0.58 | 3.5 | 2.50 | 2.65 |
| | S002* | 1.63 | 1.92 | 2.48 | | 2.2 | | |
| | S006 | 1.91 | 2.24 | 3.06 | | 2.65 | | |
| | | | | | Average 2.78 ± 1.64 | | | |
| Set II | S017* | 1.42 | 1.70 | 1.68 | 0.90 | 1.69 | 1.90 | 1.88 |
| | S018* | 1.64 | 2.08 | 1.80 | | 1.94 | | |
| | S019 | 1.37 | 1.56 | 1.76 | | 1.66 | | |
| | | | | | Average 1.76 ± 0.38 | | | |
| Set III | S023* | 3.76 | 4.46 | 5.48 | 0.19 | 4.97 | 5.70 | 5.20 |
| | S024 | 3.54 | 4.41 | 5.19 | | 4.80 | | |
| | S025 | 3.36 | 4.90 | 6.30 | | 5.61 | | |
| | | | | | Average 5.12 ± 1.05 | | | |
| Set IV | S020* | 4.95 | 6.55 | 7.75 | 0.09 | 7.15 | 9.50 | 8.70 |
| | S021 | 3.80 | 5.04 | 6.76 | | 5.90 | | |
| | S022 | 4.46 | 5.91 | 6.87 | | 6.40 | | |
| | | | | | Average 6.48 ± 1.56 | | | |

* Inside circumferential stress was estimated by using the average value of the membrane stress of the inside strain gauged bends.

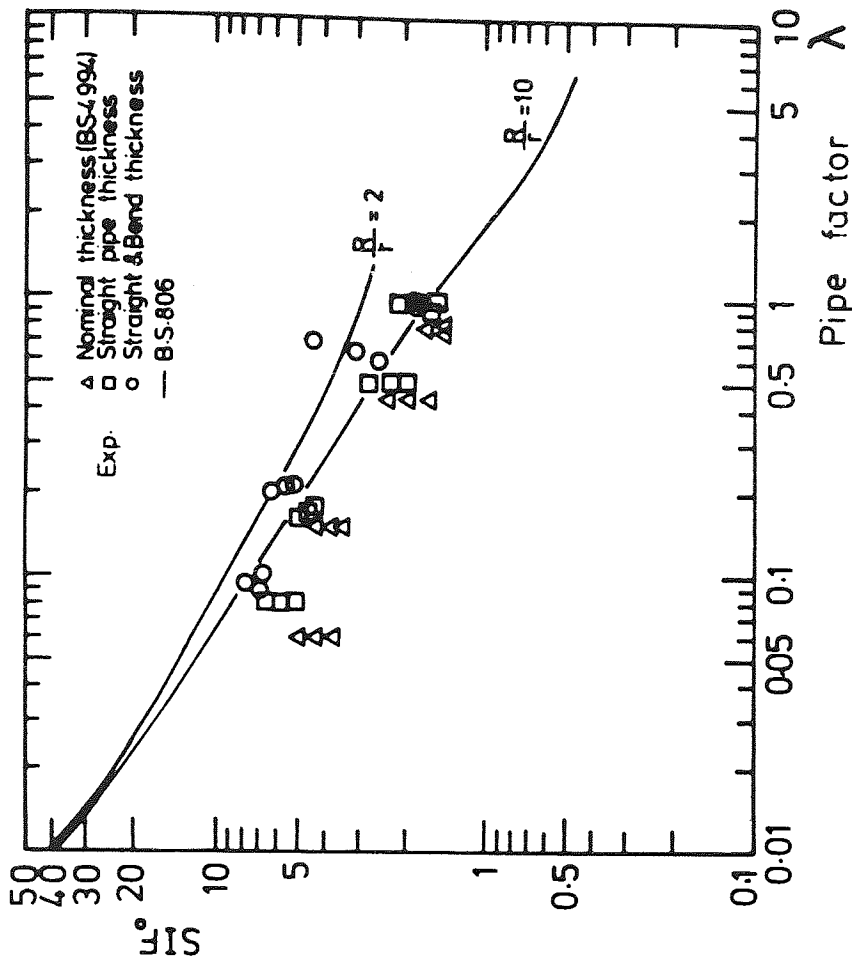


Figure (6.41)

Maximum out-of-plane longitudinal stress intensification factor (SIF_{OL}) for smooth CSM bends presented as a function of the different thicknesses employed in Table (6.14) columns i, ii and iii

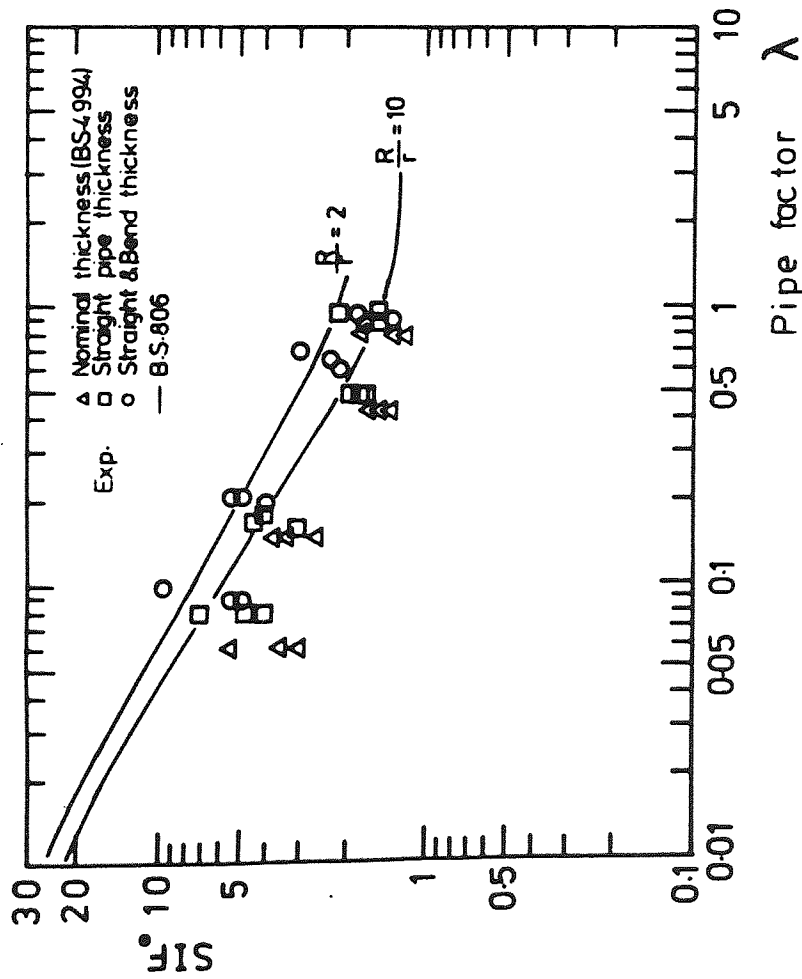


Figure (6.42)

Maximum out-of-plane circumferential stress intensification factors (SIF_C) for smooth CSM bends presented as a function of the different thicknesses employed in Table (6.15), columns i, ii and iii

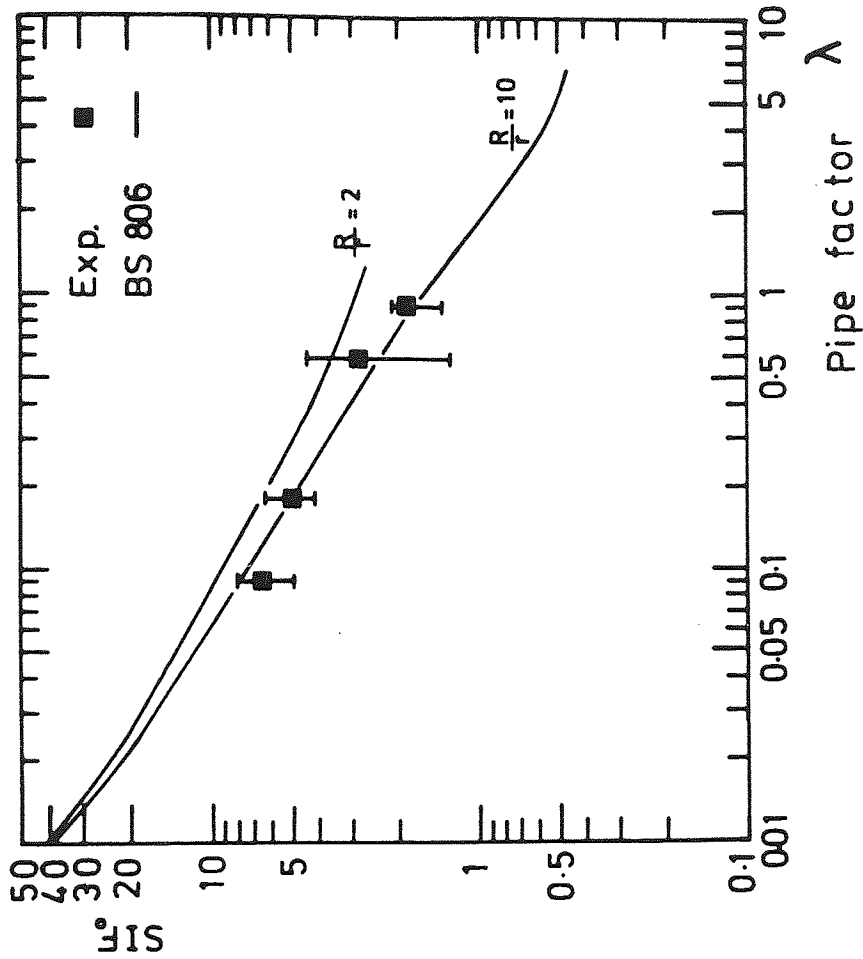
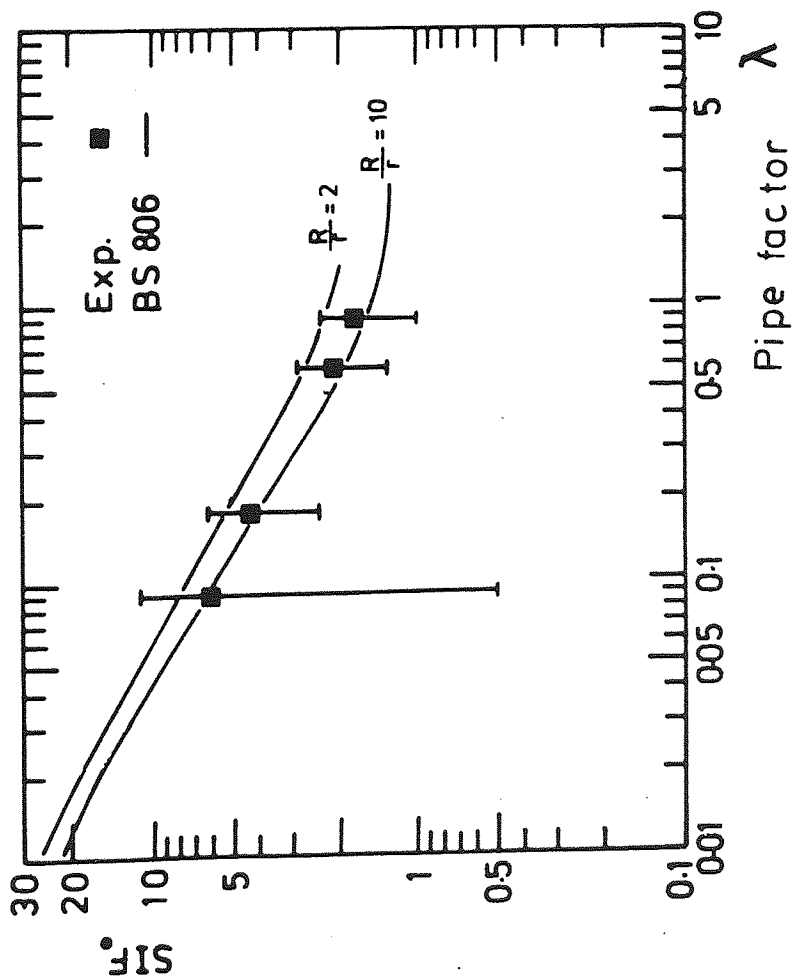


Figure (6.43)

Maximum out-of-plane longitudinal stress intensification factors (SIF_{OL}) for smooth CSM bends using the effective thickness (t_e) as in column (iv) of Table (6.14)



Figure(6.44)

Maximum out-of-plane circumferential stress intensification factors (SIF_{OC}) for smooth CSM bends using the effective thickness (t_e) as in column (iv) of Table (6.14)

TABLE 6.16 - Bend Analytical Specification in the form of
Parametrical Ratio of (SIF/K) against pipe factor λ_e

| Bend No. | λ_e | $\frac{SIF^*}{K^+}$ | | | | | | | |
|----------------------|-------------|----------------------|---------------------|----------------------|---------------------|----------------------|---------------------|----------------------|---------------------|
| | | In-plane | | | | Out-of-plane | | | |
| | | CI | | LI | | C ϕ | | L ϕ | |
| | | Exp [*] | Th ⁽¹³⁷⁾ | Exp [*] | Th ⁽¹³⁷⁾ | Exp [*] | Th ⁽¹³⁷⁾ | Exp [*] | Th ⁽¹³⁷⁾ |
| S001 S002 S006 | 0.58 | 1.17 1.16 0.99 | 0.90 | 0.89 1.25 0.69 | 0.42 | 0.77 0.92 0.74 | 0.75 | 0.64 0.79 0.56 | 0.55 |
| S017 S018 S019 | 0.90 | 1.83 2.02 2.77 | 1.0 | 1.20 1.85 2.33 | 0.50 | 2.81 2.17 1.84 | 0.90 | 2.41 2.52 1.75 | 0.62 |
| S023 S024 S025 | 0.19 | 0.67 0.77 0.68 | 0.63 | 0.44 0.47 0.54 | 0.29 | 0.59 0.48 0.67 | 0.52 | 0.59 0.45 0.42 | 0.37 |
| S020 S021 S022 | 0.09 | 0.49 0.49 0.52 | 0.50 | 0.33 0.27 0.33 | 0.23 | 0.31 0.25 0.39 | 0.41 | 0.20 0.36 0.30 | 0.38 |

+ experimental results are based on column (v) of Table (6.10) for in-plane bending and of Table (6.13) for out-of-plane bending.

* experimental results are based on column (iv) of Tables (6.11 and 6.12) for in-plane bending and of Tables (6.14 and 6.15) for out-of-plane bending.

$$CI = SIF_{i,C}/K_i$$

$$LI = SIF_{i,L}/K_i$$

$$C\phi = SIF_{o,C}/K_o$$

$$L\phi = SIF_{o,L}/K_o$$

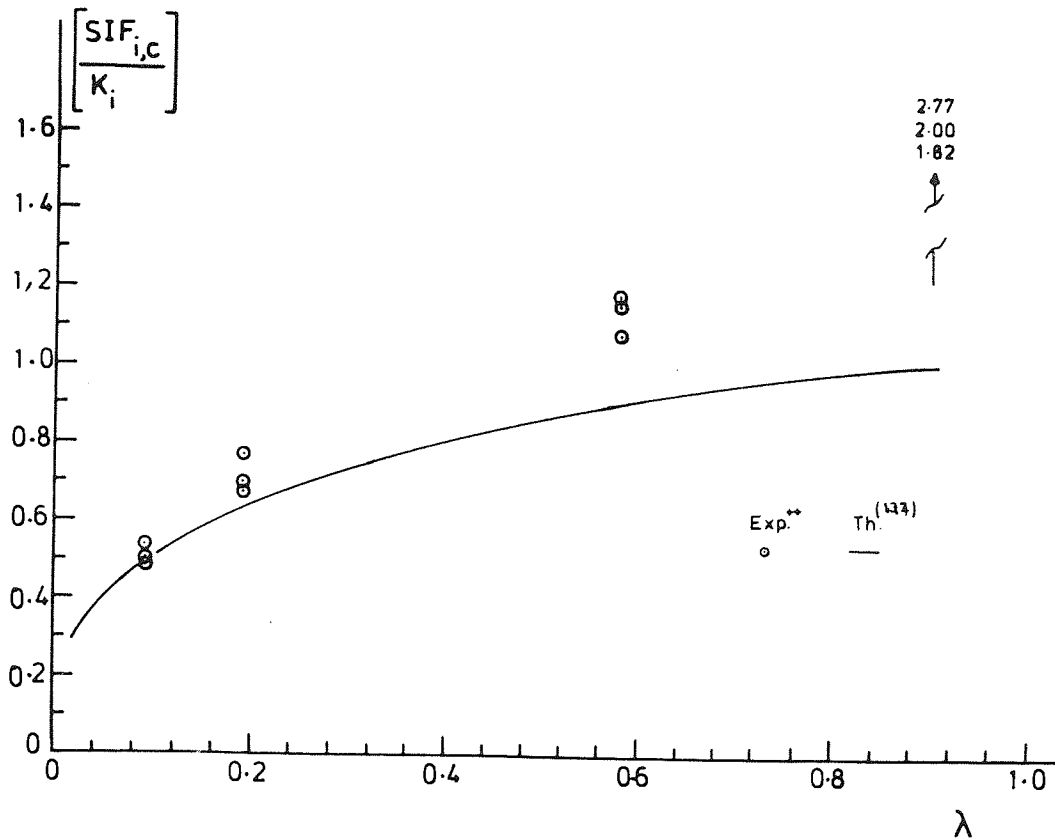


Figure (6.45b) Ratio of maximum circumferential in-plane stress intensification factors ($SIF_{i,C}$) to in-plane flexibility factor (K_i)

** refer to Tables (6.10, 6.12, & 6.17)

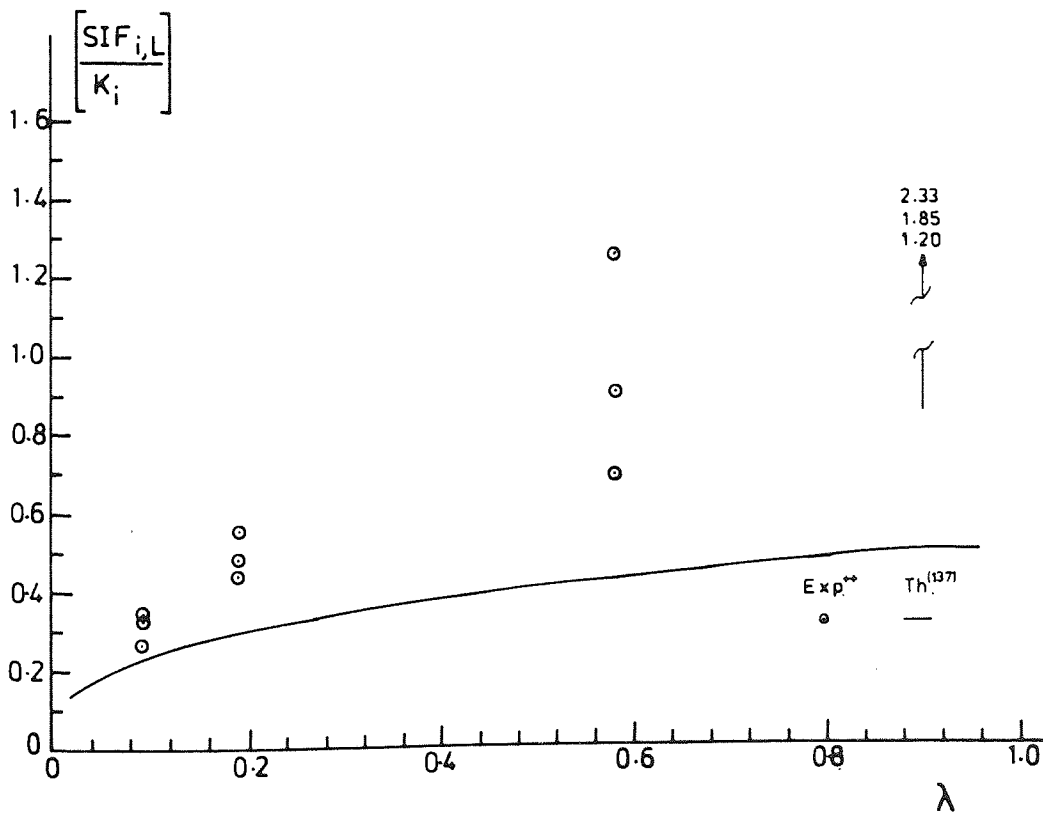


Figure (6.45a) Ratio of maximum longitudinal in-plane stress intensification factors ($SIF_{i,L}$) to in-plane flexibility factor (K_i)

** refer to Tables (6.10, 6.12, & 6.17)

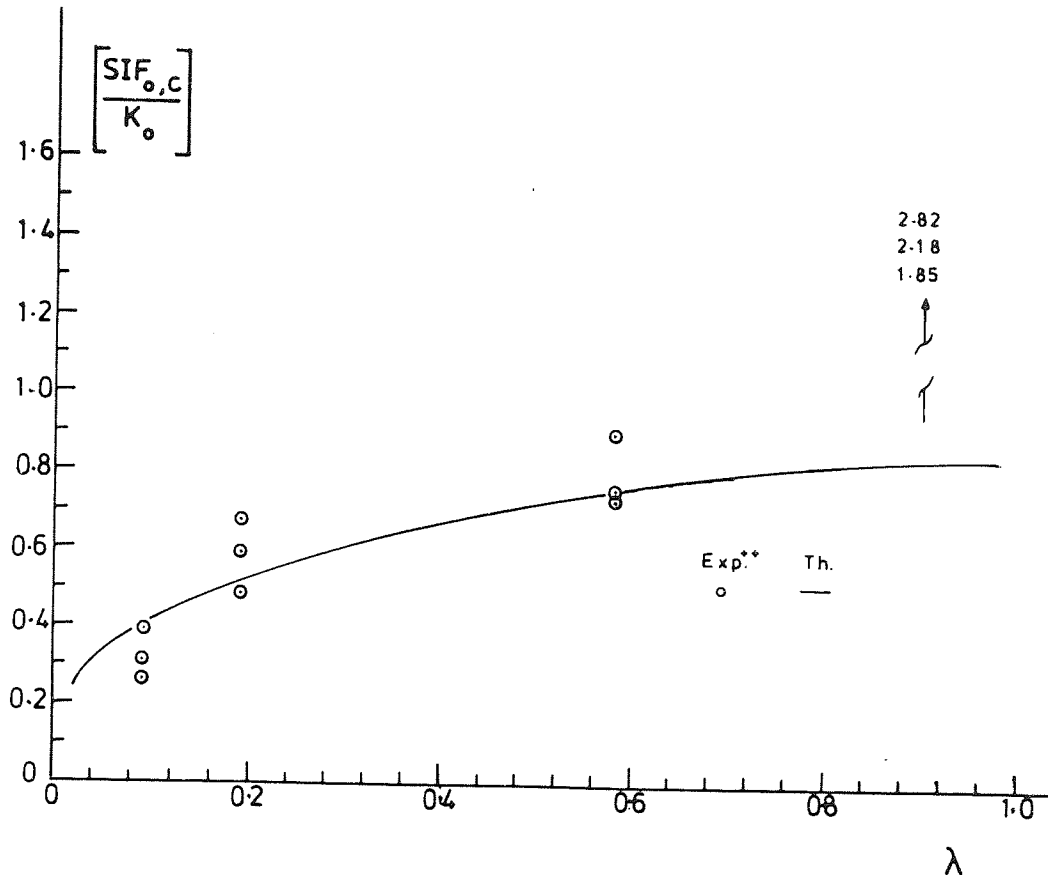


Figure (6.46b) Ratio of maximum circumferential out-of-plane stress intensification factors ($SIF_{o,c}$) to out-of-plane flexibility factor (K_o)

** refer to Tables (6.13, 6.15 & 6.17)

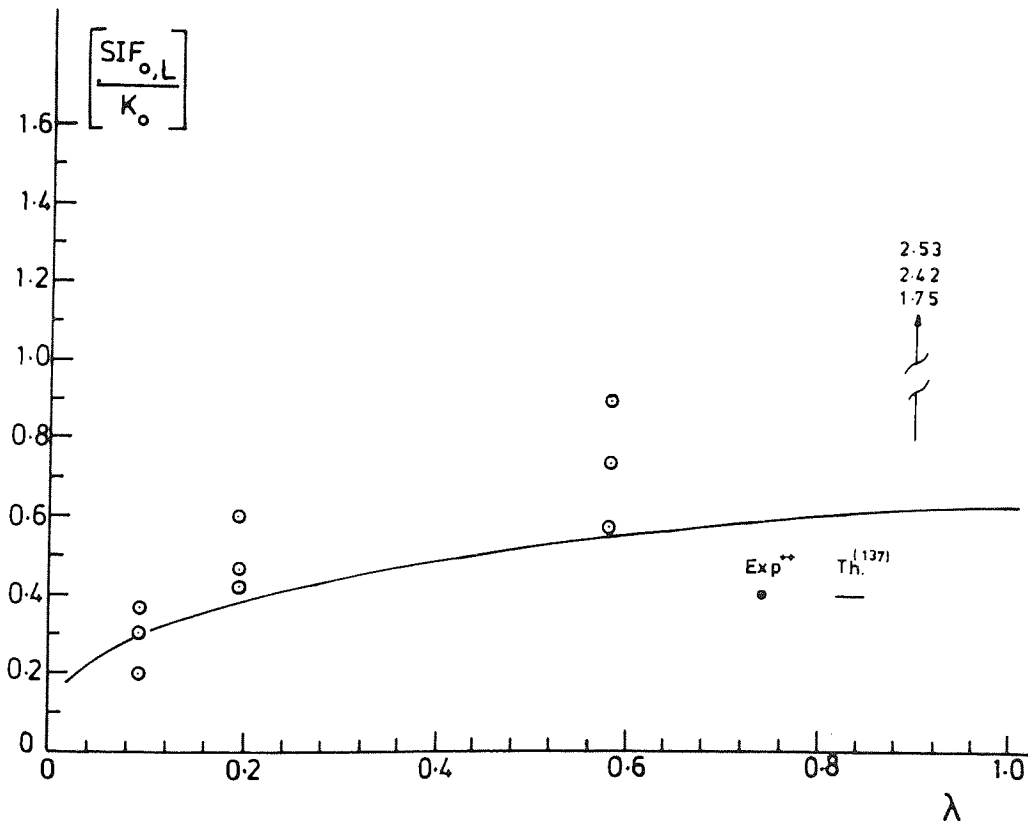


Figure (6.46a) Ratio of maximum longitudinal out-of-plane stress intensification factors ($SIF_{o,L}$) to out-of-plane flexibility factor (K_o)

** refer to Tables (6.13, 6.14 & 6.17)

measuring bore and outside diameter at different sections of the bend and thereafter formulating the pipe factor λ . The flexibility of the bend could be obtained by employing end deflection test. Finally, substituting λ and K into Figs. 6.45 and 6.46, a reasonable idea of the maximum stress induced in the bend whilst in service could be estimated.

6.4.6 Strength of smooth CSM bends

Previous work by Wright⁽⁴¹⁾ was carried out on in-house manufactured smooth CSM bends tested under in-plane bending and out-of-plane bending. Three bend samples were taken to failure under in-plane bending in the opening mode. The dimensions of the bends along with the measured bending moments at 1/10th to failure, at failure, and at 0.2% measured strain, are presented in Table 6.17. The values of the interlaminar shear stresses in Table 6.17 correspond to the bending moment at failure, and are calculated using Eq. (II.20) of App. II, using two constants⁽¹⁵²⁾.

F.g 6.47 shows a typical bend failure, where failure started by a longitudinal crack initiated at $\theta = 90^\circ$ from the intrados and followed by a circumferential one propagated from the intrados⁽⁴¹⁾.

The thick bend in particular ($\lambda = 0.35$) shows a high level of magnitude of the interlaminar shear stress at failure, which is 30% higher than the lap shear strength specified by BS4994,⁽³⁾ and comparable with the experimentally measured lap shear strengths presented in Ch. 3. This could indicate that the bend might have developed initial failure due to interlaminar shear stress rather than due to a circumferential flexural stress as indicated by the longitudinal crack shown in Fig. 6.47. In these circumstances, the pipe designer should be aware of the fact that although such levels of shear stresses are negligible for

metallic bends, but they could be of dangerous consequences when composites such as GRP are used, due to the low level of magnitude of their interlaminar shear strengths.

Bending moments measured at 1/10th of failure are approximately half of that measured at 0.2% strain. Although such an observation is not conclusive, since for two bends in Table 6.17, the maximum strain was measured on the outside surface. Nevertheless, it could be suggested that design strains of 0.2% which are usually accepted in industry as SAFE, may not reflect the complex nature of the stresses in bends, and thus design stresses should be also based on the pipe or bend strength.

TABLE 6.17 Measured in-plane bending moments (opening) to failure of smooth CSM bends

| | λ | B.M. at 0.2% strain (N.mm) x 10 ⁵ | B.M. at failure (N.mm) x 10 ⁵ | 1/10 of B.M. failure (N.mm) x 10 ⁵ | t (mm) | r _i (mm) | R (mm) | $\bar{\sigma}$ (N/mm ²) |
|--------------|-----------|--|--|---|--------|---------------------|--------|-------------------------------------|
| Thin bend+ | 0.187 | 5.33 | 28.6 | 2.86 | 5 | 75 | 225 | 4.9 |
| Medium bend* | 0.222 | 7.8 | 39.3 | 3.93 | 7 | 75 | 225 | 4.8 |
| Thick bend+ | 0.350 | 24.38 | 115.5 | 11.55 | 10 | 75 | 225 | 10 |

* 0.2% strain is based on inside strain measurements.

+ 0.2% strain is based on outside strain measurements.

B.M \equiv Bending Moment

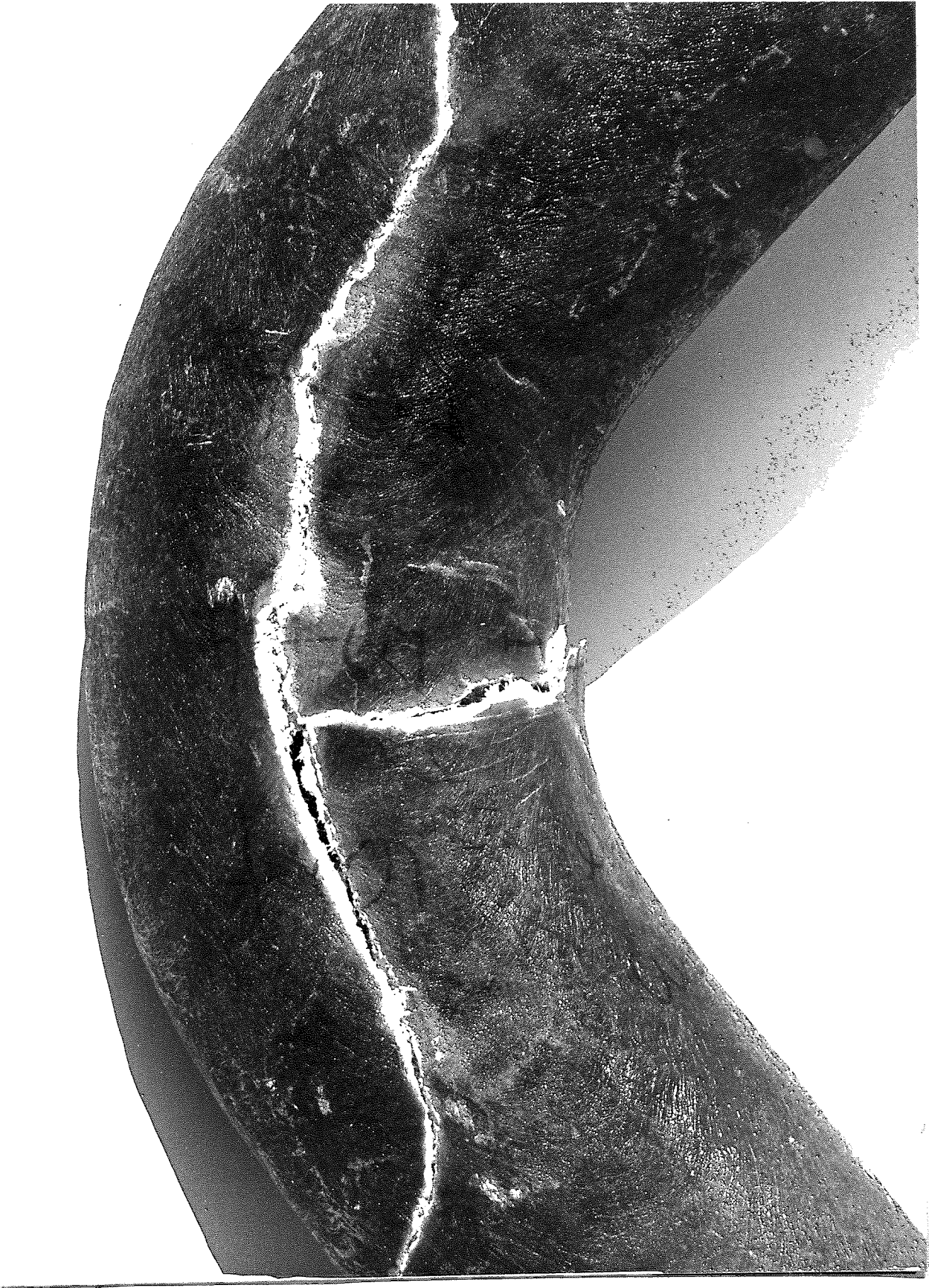


Figure (6.47) Failure of CSM bend under in-plane bending moment (opening) of 11.5 MN mm, $R = 225$ mm, $t = 10$ mm, $r_i = 75$ mm, ref(41)

CHAPTER SEVEN

FLEXURAL TESTING OF CSM/PVC LINED STRAIGHT PIPES,

SMOOTH AND MITRED BEND COMPONENTS

CHAPTER SEVEN

FLEXURAL TESTING OF CSM/PVC LINED STRAIGHT PIPES, SMOOTH AND MITRED BEND COMPONENTS

7.1 Introduction

Two groups of PVC/CSM laminate pipes were investigated in the present programme. The first group is of two 3 m long straights and three PVC/CSM smooth bends (Table 7.1). The second group consists of three sets, each set has two mitre bends and one 3 m long straight pipe (Table 7.2). Flexural tests were performed on both straights and bends similar to the procedures outlined in the previous chapter.

This chapter presents results obtained from tests carried out investigating the deformation of rings cut from the pipes using the properties of the PVC and the CSM and the deformation of the straight pipes under flexural and torsional loading.

The results for bends are presented separately; the smooth bends (Table 7.1) and mitre bends (Table 7.2), in the form of flexibility factors, stress intensification factors and failure analysis.

7.2 Coupon Testing

Rings were cut from the different pipe sizes and tested under flexure by opposite-point loading⁽¹¹⁶⁾. The experimental deformation is investigated against the theoretical prediction by using the dimensions and the mechanical properties of the PVC and the CSM. Tensile moduli used were 7450 N/mm² for the CSM and 3000 N/mm² for the PVC. The theoretical ring deflections are calculated by using the following set of equations for a dual laminate.

$$\bar{y} = \frac{\sum XEA}{\sum EA} = \frac{\frac{t^2_{CSM}}{2} E_{CSM} + E_{PVC} \left(t_{CSM} + \frac{t_{PVC}}{2} \right) t_{PVC}}{E_{CSM} t_{CSM} + E_{PVC} t_{PVC}} \quad (7.1)$$

$$\sum EI = (EI)_{PVC} + (EI)_{CSM} \text{ about the neutral axis} \quad (7.2)$$

TABLE 7.1 - Description of Group I of Smooth CSM/PVC Line Bend Components

| Component No. | General Description |
|-------------------------------------|---|
| Straights S 010) S 011) | 100 mm nominal bore, 1.8 kg/m ² CSM reinforcement, 30% glass content by mass, 3000 mm long, 4 mm PVC liner. |
| Bends S 012) S 014) S 016) | 100 mm nominal bore, 1.8 kg/m ² CSM reinforcement, 30% glass content by mass, $\bar{R} = 6$, 1000 mm straight tangents, 4 mm \bar{r}_i PVC liner. |

TABLE 7.2 - Description of Group II of Mitred CSM/PVC Lined Bend Components

| Component No. | General Description |
|---|--|
| <p><u>Set I</u></p> <p>Straight</p> <p>S 035</p> <p>Bends</p> <p>S 033)</p> <p>S 034)</p> | <p>200 mm nominal bore, 2.4 kg/m² CSM reinforcement, 30% glass content by mass, 3000 mm long, 3 mm PVC liner.</p> <p>200 mm nominal bore, 2.4 kg/m² CSM reinforcement, 30% glass content by mass, 1000 mm tangents, 3 mm PVC liner, mitred bends of 3½ segments,</p> $\frac{R}{r_i} = 3$ |
| <p><u>Set II</u></p> <p>Straight</p> <p>S 038</p> <p>Bends</p> <p>S 036)</p> <p>S 037)</p> | <p>250 mm nominal bore, 1.8 kg/m² CSM reinforcement, 30% glass content by mass, 3000 mm long, 3 mm PVC liner.</p> <p>250 mm nominal bore, 1.8 kg/m² CSM reinforcement, 30% glass content by mass, 1000 mm tangents, 3 mm PVC liner, mitred bends of 3½ segments,</p> $\frac{R}{r_i} = 2$ |
| <p><u>Set III</u></p> <p>Straight</p> <p>S 062</p> <p>Bends</p> <p>S 060)</p> <p>S 061)</p> | <p>600 mm nominal bore, 2.4 kg/m² CSM reinforcement, 30% glass content by mass, 8000 mm long, 4 mm PVC liner.</p> <p>600 mm nominal bore, 2.4 kg/m² CSM reinforcement, 30% glass content by mass, 1000 mm tangent, 4 mm PVC Liner, mitred bends of 3½ segments,</p> $\frac{R}{r_i} = 2$ |

where \bar{y} = position of the neutral axis of the thickness, starting from the outside surface, i.e. CSM, and the horizontal and the vertical diametral change per unit load are then calculated as ⁽¹³¹⁾

$$\frac{\Delta V}{P} = 0.149 \frac{r_n^3}{\Sigma EI} \quad (7.3)$$

$$\frac{\Delta V}{P} = 0.137 \frac{r_n^3}{\Sigma EI} \quad (7.4)$$

The experimental results with their corresponding theoretical counterparts are presented in Table 7.3. The results show a reasonable comparison, with theoretical deformations slightly higher than the measured values. This is an acceptable level of difference when consideration is given to the variability of modulus and thickness. It could be concluded that composite theory ⁽¹¹⁸⁾ would predict PVC/CSM dual laminate deformation to a reasonable accuracy, as already concluded for the dual composite presented in Ch. 3. The rings failed by a crack initiated and developed at the CSM where the point loads are applied. Final failure occurred by the breakage of the PVC at the same position of loading in a brittle mode. No splitting or delamination has been observed between the PVC and the CSM.

7.3 Flexural and Torsional Testing of Straight Pipes

The small diameter straight pipes of 100mm nominal bore of Group I of Table 7.1, were tested under four-point bending, and strains were measured at the outside surface and at the interface surface between the PVC liner and the CSM layer at mid-span.

Cantilever testing was carried out on straight pipes S035 and S038 of 200mm and 250mm nominal bores respectively, of Group II of Table 7.2. The strains were measured on the inside surface of the PVC liner and on the outside surface of the CSM, at mid-span.

Torsional testing as described in Ch. 5 was carried out on pipe S038.

TABLE 7.3 - Test Results obtained from Opposite Point Flexural Testing of Dual PVC/CSM Rings

$E_{CSM} = 7450 \text{ N.mm}^{-2}$; $E_{PVC} = 3000 \text{ N.mm}^{-2}$; $\nu_{CSM} = 0.3$; $\nu_{PVC} = 0.35$.

| Sp. type | t_{total} (mm) | W (mm) | \bar{y} (mm) | r_n (mm) | $\frac{\Delta V}{P}$ | | $\frac{\Delta H}{P}$ | | σ_f N/mm ² |
|----------|--|--------------------------------|-------------------------------|------------------------|--|--|--|--|------------------------------|
| | | | | | TH (mm/N) | Exp (mm/N) | TH (mm/N) | Exp (mm/N) | |
| ST. | (7.04 * (| 25.83 | 2.83 | 127 | 8.76×10^{-2} | 8.25×10^{-2} | 8.054×10^{-2} | 8.893×10^{-2} | 186 |
| | (6.86 * (| 25.58 | 2.75 | 127 | 9.08×10^{-2} | 9.25×10^{-2} | 8.35×10^{-2} | 9.00×10^{-2} | 167 |
| | (6.95 * (| 25.65 | 2.79 | 126 | 9.08×10^{-2} | 8.91×10^{-2} | 8.35×10^{-2} | 8.57×10^{-2} | 177 |
| Bend | 8.95 * 7.49 * 9.10 ** 9.02 ** | 26.2 26.5 26.84 13.98 | 3.73 3.04 3.643 3.61 | 128 102 59 58 | 4.07×10^{-2} 4.12×10^{-2} 4.00×10^{-3} 9.28×10^{-3} | 4.38×10^{-2} 3.39×10^{-2} 3.86×10^{-3} 7.89×10^{-3} | 3.74×10^{-2} 3.87×10^{-2} - - | 4.38×10^{-2} 3.85×10^{-2} - - | 134 138 138 |

* including uPVC thickness of 3 mm

** including uPVC thickness of 4 mm

In both cases of the flexural loading, the experimental stresses and strains on any surface are compared with theory using Eq. (7.4) as the following:

$$\sigma_i = \frac{M \cdot y_i \cdot E_i}{\Sigma EI} \quad (7.4a)$$

$$\epsilon_i = \frac{M \cdot y_i}{\Sigma EI} \quad (7.4b)$$

The dimensions and the mechanical properties of the straight pipes and the bend components are listed in Table 7.4.

7.3.1 Four point bending test results

The experimentally measured strain and stress distributions in the circumferential direction are shown in Fig. 7.1a,b for straight pipe S011 under a load of 1000 N which corresponds to a 333 kN mm bending moment at the mid-span section, where the strain gauges are situated. Similarly, the experimentally measured stresses for that of straight pipe S010 are shown with their theoretical stress distribution in Fig. 7.2.

The experimental and the theoretical stress distributions show a reasonable agreement for both pipes, with equal maximum stress in tension and in compression. The experimental flexural rigidity for both pipes show a slight reduction than theoretical rigidity based on measured thickness and moduli. The experimental flexural rigidity is calculated based on the measurement of the central deflection and the use of Eq. (7.5)⁽¹³¹⁾.

$$\Sigma EI = \frac{P}{\Delta} \frac{\ell}{3} \frac{1}{24} [3\ell^2 - 4 \left(\frac{\ell}{3}\right)^2] \quad (7.5)$$

These experimental rigidities are 29.4 GN mm² and 28.3 GN mm² for pipes S011 and S010 respectively, compared with theoretical rigidity of 30.8 GN mm² obtained from Table 7.4.

TABLE 7.4 - Dimensional and Mechanical Description of the CSM/PVC
Lined Smooth Bends (Group I) and the Mitred Bends
(Group II)

| | Group (I) of Table (7.1) Smooth Bends | Group (II) of Table (7.2) Mitred Bends | | |
|------------------------------------|---|---|------------------------|------------------------|
| | | Set I | Set II | Set III |
| t_{PVC} (mm) | 4 | 3 | 3 | 4 |
| t_N (CSM) | 3.96 | 5.28 | 3.96 | 5.28 |
| t_{ST} | 5.45 | 4.11/5.00* | 4.00/8.0* | 7.075 |
| $t_{B.C.}$ | 5.70 | 6.35 | 6.156 | 7.873 |
| $t_{B.J.}$ | - | 10.46 | 8.75 | 14.56 |
| t_f | 7 | 8.60 | - | - |
| $t_{(B.C.)}$ | - | 5.23 | 5.078 | 7.474 |
| $t_{(B.J.)}^e$ | - | 7.285 | 6.375 | 10.818 |
| $t_{(B)}^e$ | 5.58 | 6.258 | 5.727 | 9.146 |
| $2r_i$ (mm) | 106 | 195 | 244 | 589 |
| E_i (N/mm ²) | 7450 | 7450 | 7450 | 7450 |
| E_{CSM} | 3000 | 3000 | 3000 | 3000 |
| v_{PVC} | 0.30 | 0.30 | 0.30 | 0.30 |
| v_{CSM} | 0.35 | 0.35 | 0.35 | 0.35 |
| v_{PVC} | | | | |
| ΣEI_n (N.mm ²) | 2.342×10^{10} | 1.7×10^{11} | - | - |
| $\Sigma EI_{st.}$ | 3.081×10^{10} | 1.33×10^{11} | 2.49×10^{11} | 5.55×10^{12} |
| | | 1.55×10^{11} | 4.283×10^{11} | |
| $\Sigma EI_{B.C.}$ | 3.21×10^{10} | 1.95×10^{11} | 3.60×10^{11} | 6.08×10^{12} |
| $\Sigma EI_{B.J.}$ | - | 3.17×10^{11} | 5.0×10^{11} | 10.34×10^{12} |
| $\Sigma EI_{(B.C.)}^e$ | - | 1.64×10^{11} | 3.05×10^{11} | 5.815×10^{12} |
| $\Sigma EI_{(B.J.)}^e$ | - | 2.25×10^{11} | 3.745×10^{11} | 7.945×10^{12} |
| ΣEI_F | 3.91×10^{10} | 2.42×10^{11} | - | - |
| $\Sigma EI_{(B)}^e$ | 3.145×10^{10} | 1.945×10^{11} | 3.395×10^{11} | 6.88×10^{12} |
| λ^n | - | 0.151 | 0.061 | 0.036 |
| $\lambda_{st.}$ | - | 0.120 | 0.062 | 0.047 |
| $\lambda_{B.C.}$ | - | 0.181 | 0.094 | 0.053 |
| $\lambda_{B.J.}$ | - | 0.286 | 0.130 | 0.095 |
| λ_e | 0.509 | 0.177 | 0.088 | 0.061 |
| Tangent length | 1000 | 1000 | 1000 | 1000 |
| Bend radius (mm) | 306 | 306 | 250 | 610 |
| R/r_i | 5.8 | 3 | 2 | 2 |

* thickness measured on straight pipes

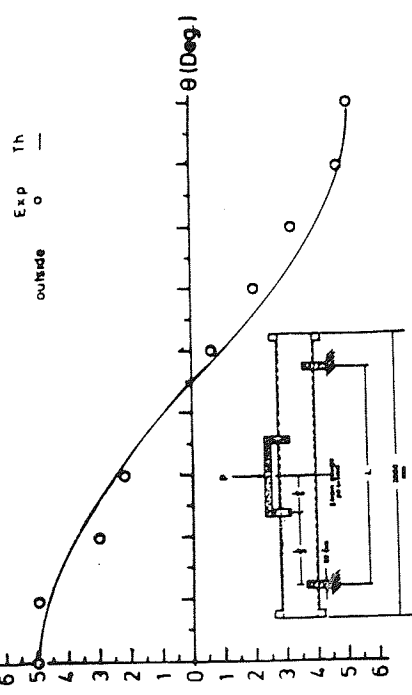


Figure (7.2) Stress distribution measured on pipe S010 under 33.33×10^4 N.mm four-point bending moment

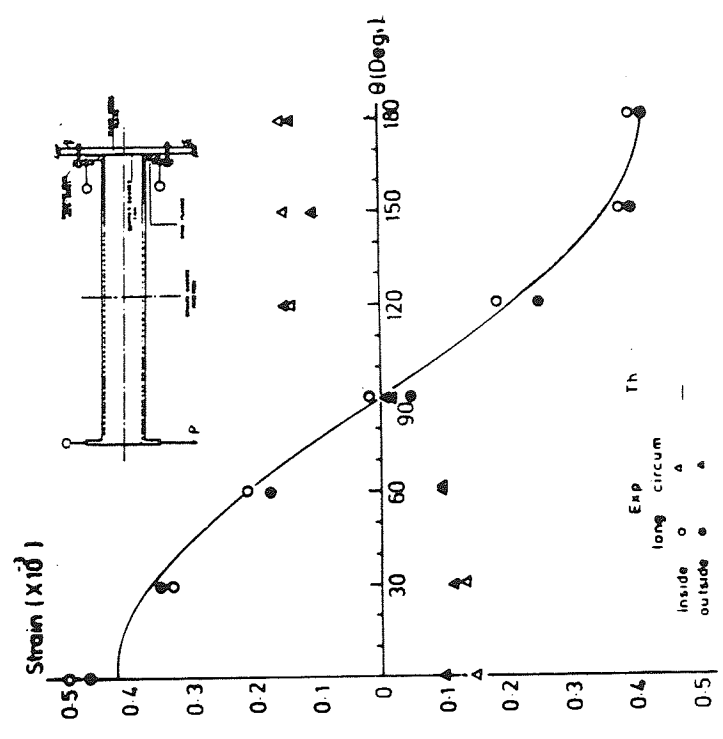
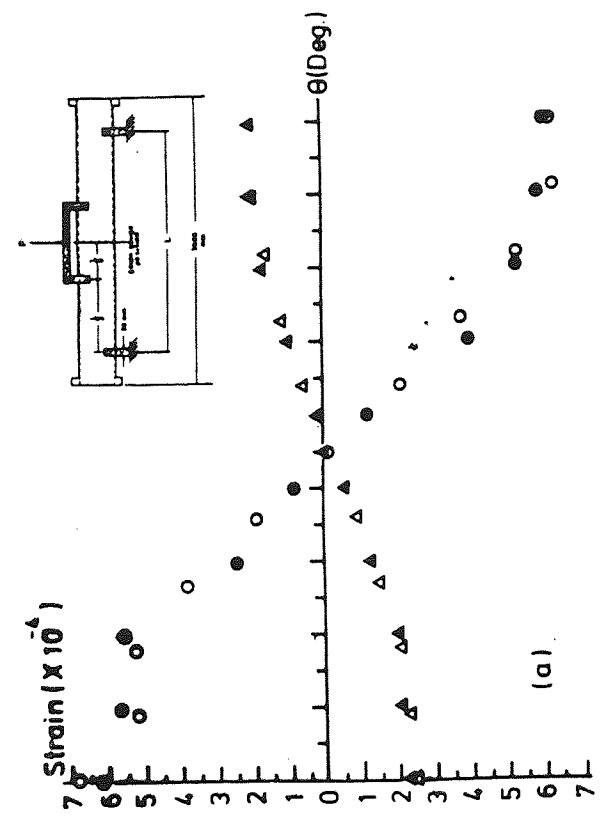
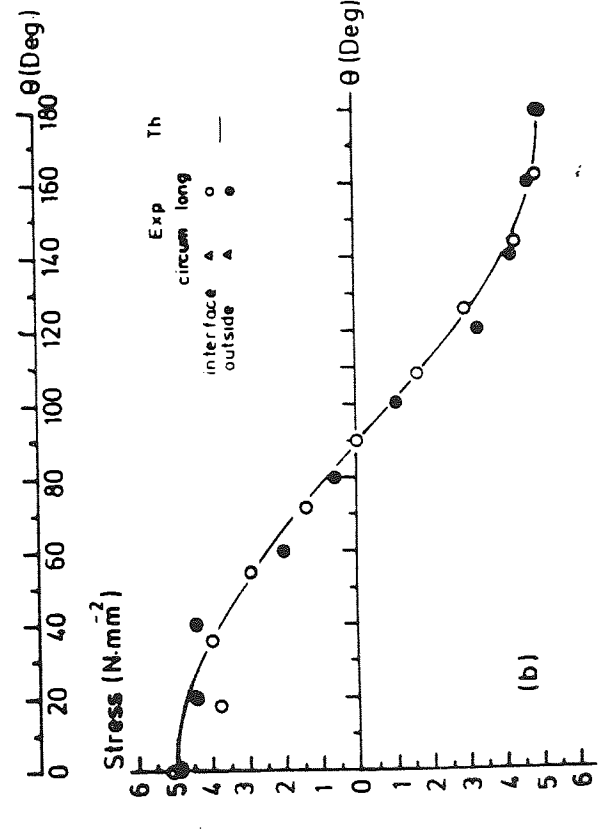


Figure (7.3) Strain distribution measured at the centre of pipe S038 under 900N cantilever end load



(a)



(b)

Figure (7.1) 'a' strain and 'b' stress distribution measured on pipe S011 under 33.33×10^4 N.mm four-point bending moment

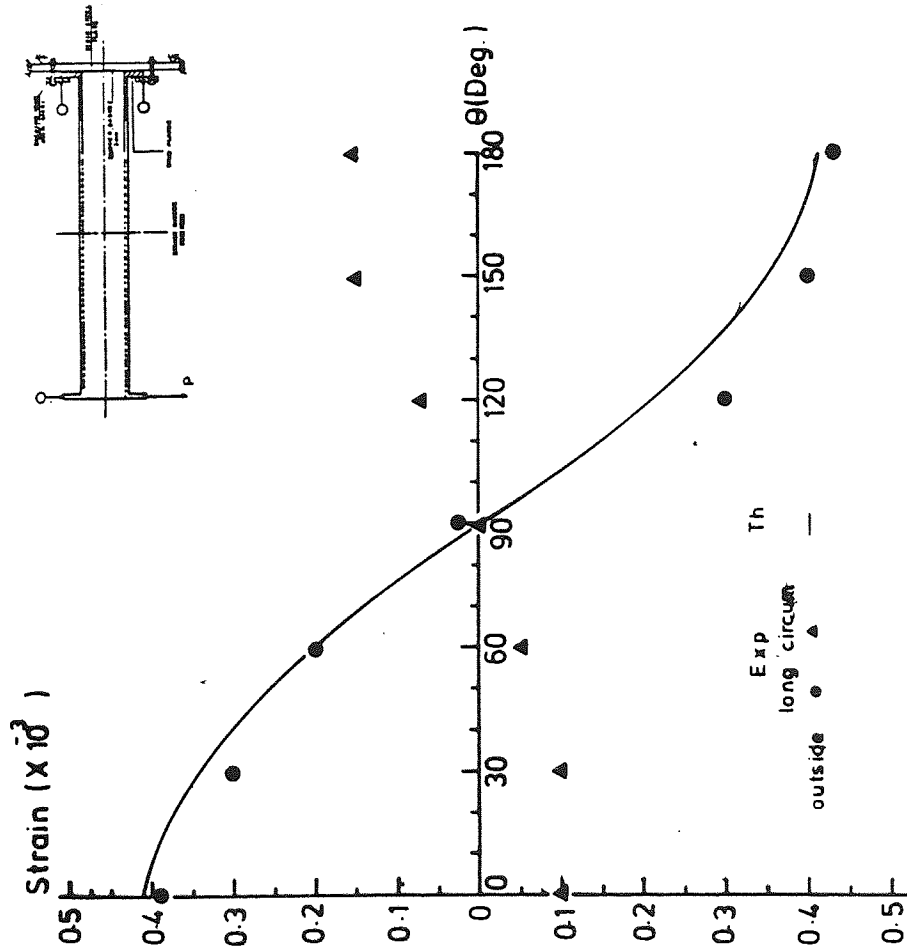


Figure (7.4) Strain distribution measured at the centre of pipe S035 under 400N cantilever end load

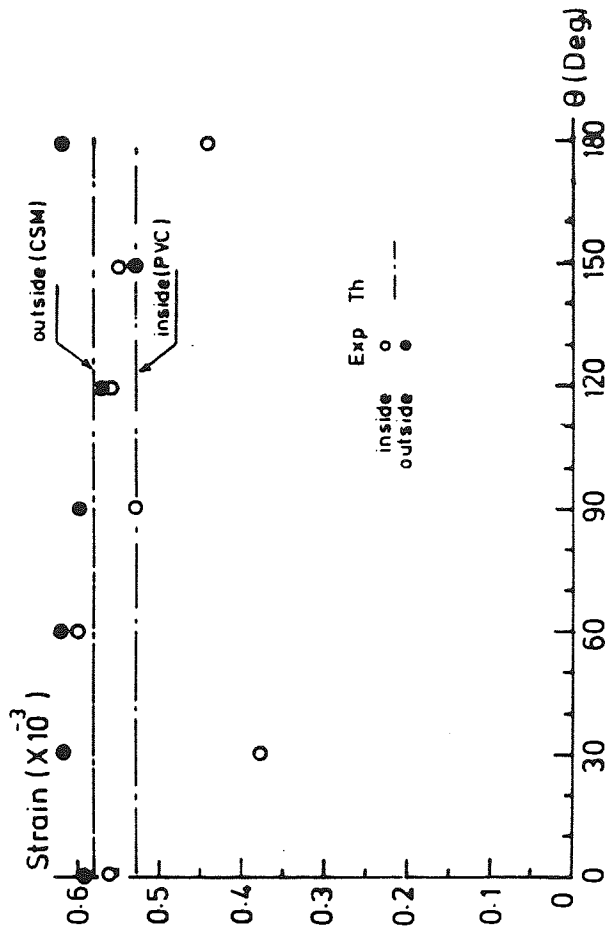


Figure (7.5) Inside and outside in-plane shear strains measured on pipe S038 under 1.42×10^6 N.mm torsional moment

TABLE 7.5 - In-plane shear strain distribution of CSM/PVC lined
Straight S038 under 1.423×10^6 N.mm Torsional Loading

| Position | Inside surface (PVC) | | | Outside surface (CSM) | | |
|----------|---------------------------------------|---------------------------------------|-----------------------|---------------------------------------|---------------------------------------|-----------------------|
| | Skew ⁽⁻⁾ x 10 strain | Skew ⁽⁺⁾ x 10 strain | β_1^* (Deg.) | Skew ⁽⁻⁾ x 10 strain | Skew ⁽⁺⁾ x 10 strain | β_1^* (Deg.) |
| 0° | -270 | 280 | - 3° | -295 | 290 | - 3° |
| 30° | -150 | 220 | 17° | -332 | 280 | - 3° |
| 60° | -270 | 330 | 3° | -323 | 295 | 2° |
| 90° | -250 | 270 | 3° | -311 | 285 | -4° |
| 120° | -270 | 285 | 1° | -285 | 280 | 5° |
| 150° | -270 | 270 | - 4° | -282 | 240 | -2° |
| 180° | -245 | 190 | - 5° | -318 | 300 | -2° |

* measured from the skew direction (i.e. 45° from the longitudinal direction of the pipe).

7.3.2 Cantilever test results

The experimentally measured strains around half the circumference, having 0° reading as the bottom gauge (tension) and 180° as the top gauge (compression) are shown in Figs. 7.3 and 7.4 for straight pipes S035 and S038 respectively.

7.3.3 Torsional test results

Torsional deformation was investigated by twisting pipe S038 as already described in Ch. 5. During loading, the inside and the outside strains were monitored in the longitudinal and the ± skew directions and those presented in Table 7.5 have been measured under 1.42 MN mm torsional moment. the directions of the principal strains are measured from the skew direction.

The experimentally measured in-plane shear strains with their theoretical prediction are presented in Fig. 7.5, where theoretical shear strains are predicted using Eq. (7.6)

$$\gamma = \frac{\tau}{G} = \frac{T y_i}{\Sigma G J} \quad (7.6a)$$

and

$$\begin{aligned} \Sigma G J &= (GJ)_{PVC} + (GJ)_{CSM} \\ &= \frac{(EI)_{PVC}}{1.35} + \frac{(\Sigma EI)_{CSM}}{1.30} \quad (\text{total torsional rigidity of the dual laminate pipe}) \end{aligned} \quad (7.6b)$$

7.4 Flexural Testing of Smooth CSM/PVC lined bends

Bend numbers S012, S014 and S016 of Group I of Table 7.1 are three similarly constructed smooth CSM/PVC lined pipe components. They were tested under in-plane and under out-of-plane modes of loading up to a maximum strain monitored at the centre of the bend of 2×10^{-3} strain. The loading was carried out by the application of an end-load in a similar procedure to the smooth CSM bends discussed in Ch. 6.

The experimental results are presented as flexibility factors and stress intensification factors. The section modulus of the bends is predicted based on the hand-measured thickness and mechanical properties

already presented in Table 7.4. The thickness measurements were obtained by cutting bend S016 after it had been taken to failure under in-plane mode of loading (opening).

7.4.1 In-plane and out-of-plane flexibility factors

Experimental flexibility factors were determined with accordance to the analysis presented in Appendix (I) using Eqs. (I.6) and (I.18) for the in-plane flexibility factor and the out-of-plane flexibility factor respectively.

The flexural rigidities of the different sections of the bend are listed in Table 7.4, where the contribution of the PVC liner (6.2 GN mm²) is included in each value. The PVC contribution to rigidity constitutes a maximum of 20% when considering the straight sections. The finalised results for flexibilities are based on the effective rigidity of 31.5 GN mm² representing the whole tangent-bend structure, i.e. $\Sigma EI_{(B)e}$. This value is based on the overall average thickness.

The comparable theoretical flexibility values are calculated based on pipe factor (λ), using the CSM thickness only.

The experimental flexibility factors of the bends compared with BS806⁽¹²³⁾ specifications, are presented in column v of Table 7.6. Experimental values presented in columns i - iv show the predicted flexibility factor as a function of the different assumed thickness for the bends. For example, if the rigidity is based on the thickness specified in BS4994, then it would predict that bend S014 is 80% stiffer than a straight pipe of the same nominal construction when loaded under in-plane bending.

Perhaps it is important, at this stage, to indicate that the bend theory (von Karman) and/or BS806 prediction is based on the assumption that the bend is constructed of isotropic and homogeneous material,

TABLE 7.6 - In-plane and out-of-plane Flexibility Factors of Smooth CSM/PVC Lined Bends, S012, S014 & S016

| Bend Number | End deflection per unit Δ Load, $P \times 10^{-1}$ (mm/N) $\times 10^{-1}$ | Flexibility factor | | | | | Based on effective thickness, $t_{(B)e}$ | |
|-----------------------------|---|----------------------------|-----------------------------|-----------------------------|---------------------------------------|------------------------|--|------------------|
| | | Col. (i) | Col. (ii) | Col. (iii) | Col. (iv) | Based on λ_e^* | Representative Flexibility Factor | Theory (App. II) |
| | | Based on nominal thickness | Based on straight thickness | Based on ST, bend thickness | Based on ST, bend and joint thickness | | | |
| <u>In-plane Bending</u> | | | | | | | | |
| S012 | 1.13 | 0.86 | 2.06 | 2.15 | 3.18 | 0.50 | 2.17 | 3.19 |
| S014 | 0.95 | 0.26 | 1.28 | 1.33 | 2.23 | | 1.37 | |
| S016 | 0.98 | 0.37 | 1.42 | 1.47 | 2.39 | | 1.51 | |
| <u>Out-of-plane Bending</u> | | | | | | | | |
| S012 | 1.42 | -1.13 | 1.80 | 1.88 | - | 0.50 | 2.06 | 3.19 |
| S014 | 1.37 | -1.46 | 1.37 | 1.43 | - | | 1.61 | |
| S016 | 1.45 | -0.94 | 2.06 | 2.15 | - | | 2.32 | |

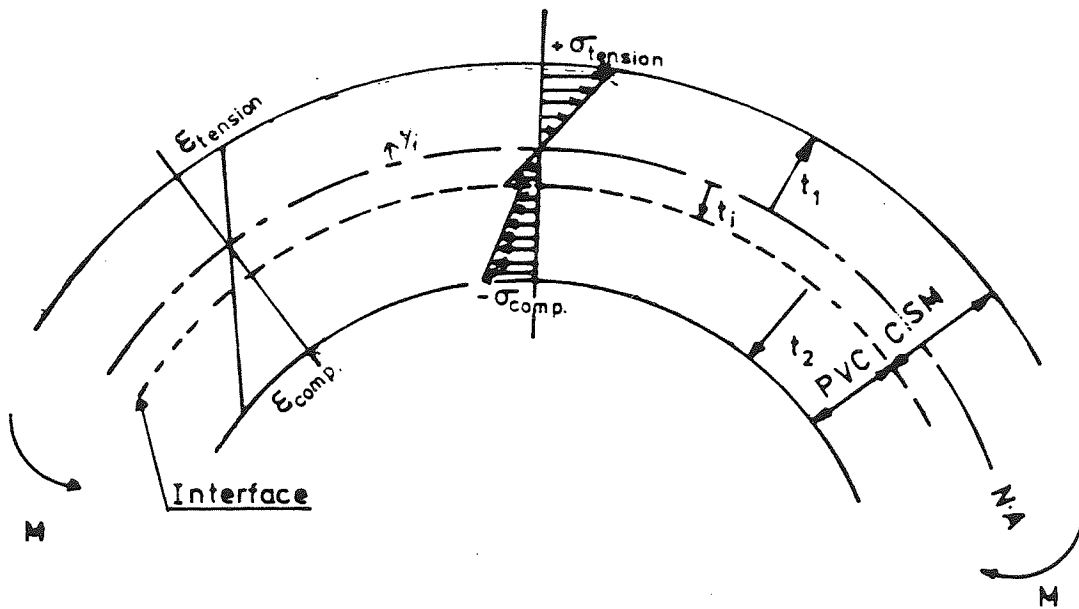
* based on thickness of the CSM only.

where the stresses induced in the circumferential and the longitudinal directions comprise a continuous-linear stress function across the thickness, whereby the derivation of the total strain energy per unit volume is based. In the present case, the presence of the PVC liner bonded to the main CSM laminate would invalidate the stress-continuity at the interface layer, although the strain compatibility assumption may still be valid within the elastic region of loading.

Under the present state of loading, the stress discontinuity occurring in the circumferential direction where the state of stress is a flexural one, the stress would be of two parts as shown diagrammatically in Fig. 7.6, where the position of the neutral axis is assumed to be a function of the thicknesses and the mechanical properties of the two materials ignoring any curvature effect.

The degree of stiffening introduced by the liner (assumed to be weaker than the main laminate) is dependent firstly on its mechanical properties and thickness, and secondly, and more importantly, on the state of stress the laminate is undergoing, i.e. whether flexural (hence $E t^3$ effect) or membrane (hence $E t$ effect). Since a flexural state of stress is present in the circumferential direction due to ovalization, the PVC Liner would probably enhance the stiffening effect in that direction. Therefore, theoretically, the presence of the PVC liner is envisaged to increase the resistance of the bend to ovalization, and, accordingly reduce the flexibility of the bend.

Returning to the comparison of experimental and theoretical flexibility factors presented in Table 7.6, it is shown that the experimental flexibility factors are 50% lower than those theoretically predicted based on pipe factor (λ) using CSM thickness only. Such difference in results could well be influenced by the ill-conditioning associated in calculating the bend flexibilities, in particular for small diameter bends as already discussed in Ch. 6.



$$\sigma_{\text{comp.}} = \frac{M \cdot E_{\text{PVC}} \cdot y_i}{\sum EI} \quad -t_2 \ll y_i \ll -t_1$$

$$= \frac{M E_{\text{CSM}} y_i}{\sum EI} \quad -t_i \ll y_i \ll 0$$

$$\sigma_{\text{tension}} = \frac{M E_{\text{CSM}} y_i}{\sum EI} \quad 0 \ll y_i \ll t_1$$

Figure (7.6) Diagrammatic presentation of stress distribution in a curved dual laminate curved beam

7.4.2 Stress ratio distribution and stress intensification factors

(SIF)

During incremental end-loading, strains at the centre of the bend were measured at the interface surface and at the outside surface via strain gauge rosettes (circumferential/skew/longitudinal). The measured strains on both surfaces were converted into longitudinal and circumferential stresses by using Hooke's law for isotropic plates, and using 7.45 kN.mm^{-2} tensile modulus and 0.3 Poisson's ratio for CSM laminates.

The circumferential and the longitudinal stress distribution under in-plane mode of bending are presented in Figs. 7.7 and 7.8 respectively. The circumferential and the longitudinal stress distribution under out-of-plane mode of bending are shown in Figs. 7.9 and 7.10 respectively. The figures present the experimentally measured stress distribution for all three bends S012, S014 and S016, compared with theoretical stress distribution for an unlined CSM bend of the same laminate construction using average CSM thickness of 5.45mm to formulate the pipe factor (λ).

The experimental/theoretical comparison of stress distribution and peaks could be summarised as follows:

- (a) Minimal stress scatter measured experimentally between the three bends on either surfaces and under both types of bending as demonstrated by the experimental results shown in Figs. 7.7 to 7.10. Such close comparability between the bends is mainly attributed to minimal thickness variations among the three bend fittings.
- (b) The measured in-plane longitudinal stress as shown from Fig. 7.7 follow reasonably the theoretical stress distribution predicted and the peaks are comparable particularly on the outside surface. Whilst the longitudinal stresses at the PVC-CSM interface compare

favourably with the mid-thickness theoretical distribution interpreted from the inside and the outside theoretical stress distribution.

- (c) The experimentally measured out-of-plane longitudinal stresses as presented in Fig. 7.9, although following a similar pattern of stress distribution as theory predicts, peak stresses are approximately 65% lower than theoretically predicted.
- (d) The experimental outside circumferential stresses for both the in-plane (Fig. 7.8) and under out-of-plane (Fig. 7.10) modes of bending have a far lower peak than predicted for an unlined bend, although stresses follow a similar pattern. It is expected to have a lower circumferential peak in a lined bend due to the enhancement of the circumferential flexural resistance brought about by the presence of the weaker UPVC liner.

The stress intensification factors (SIF) are obtained by the direct division of the experimentally measured stresses by the maximum stress induced in a straight pipe of similar construction undergoing the same bending moment. Such simple-beam stress could be predicted as a function of both the PVC and the CSM layers dimensions and mechanical properties, as already demonstrated for the straight pipes in article 7.3, via the use of Eq. (7.4). The SIF is obtained as the following via the use of Eq. (7.7) at any surface or layer, e.g. on the outside.

$$(SIF)_{\text{outside}} = \frac{E_{\text{CSM}}}{1-\nu_{\text{CSM}}^2} [\epsilon_{\text{circ.}} + \nu_{\text{CSM}} \epsilon_{\text{long.}}] \quad (7.7)$$

$$(CSM), \text{ circ.} \quad \frac{[E_{\text{CSM}} \cdot (r_i + t_{\text{PVC}} + t_{\text{CSM}})]}{\Sigma EI}$$

and $\Sigma EI = \Sigma EI_{(B)e}$ of Table 7.3.

Similarly, the SIF at the interface could be predicted.

Assuming that compatibility requirement is satisfied at the PVC/CSM interface as shown in Fig. 7.6, the strain on the inside surface of the PVC could be obtained by linear extrapolation of the measured outside

and PVC/CSM interface strains to the inner surface along the thickness axis. This is demonstrated in Fig. 7.11 where the inside circumferential strain at $\theta = 80^\circ$ of bend S016 under in-plane bending (opening) is obtained, to be

$$\begin{aligned} (\epsilon_{\text{circ}})_{\text{outside, CSM}} &= - 2.5 \text{ microstrain per (N) end load} \end{aligned}$$

$$\begin{aligned} (\epsilon_{\text{circ}})_{\text{PVC/CSM interface}} &= + 1.5 \text{ microstrain per (N) end load} \end{aligned}$$

$$\therefore \text{extrapolated inside } (\epsilon_{\text{circ}})_{\text{inside, PVC}} = 4.3 \text{ microstrain per (N) end load}$$

Similarly, the inside circumferential and longitudinal strains at all positions could be obtained.

From the extrapolated inside strains, the inside SIF are obtained via Hooke's law using a tensile modulus of 3 kN/mm² and 0.35 Poisson's ratio for the PVC in Eq. (7.7).

The experimentally measured outside SIF and the extrapolated inside SIFs are presented in Table 7.7 compared with theoretical SIF for an unlined bend using BS806⁽¹²³⁾ specifications and theory presented in App. II.

It is of practical interest to compare the maximum experimentally measured longitudinal and circumferential peak SIF with those of unlined bends of 100mm nominal bore, 1.8 kg/m² glass content of Set I bends already presented in Ch. 6. The average test results are presented in Table 7.8 for both the in-plane and out-of-plane mode of bending. The comparison, disregarding dimensional difference of bore (102 mm for unlined and 114mm for the lined), show that the introduction

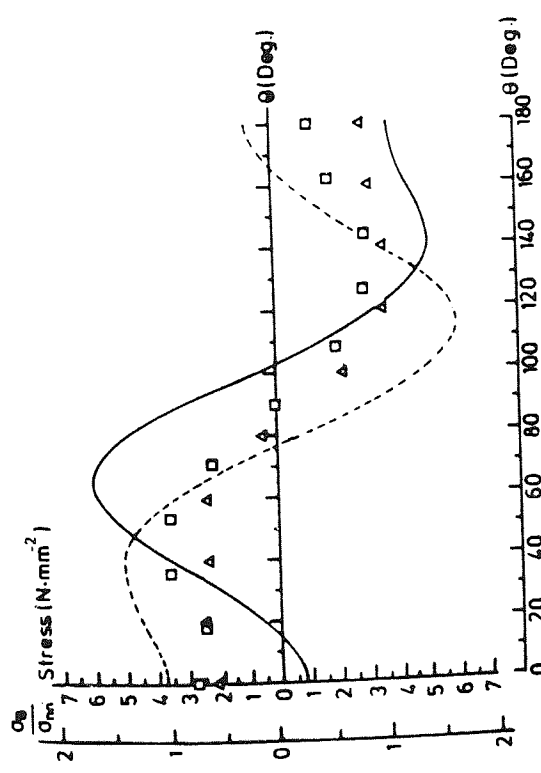


Figure (7.7a) Inside (interface) longitudinal stress distribution measured on smooth CSM/PVC lined S012, S014 and S016 bends under 2.37×10^5 N.mm in-plane bending moment (opening)

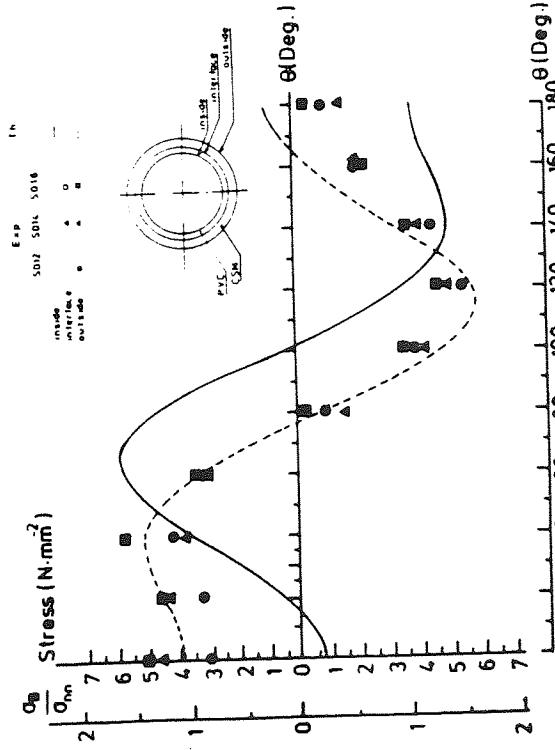


Figure (7.7b) Outside longitudinal stress distribution measured on smooth CSM/PVC lined S012, S014 and S016 bends under 2.37×10^5 N.mm in-plane bending moment (opening)

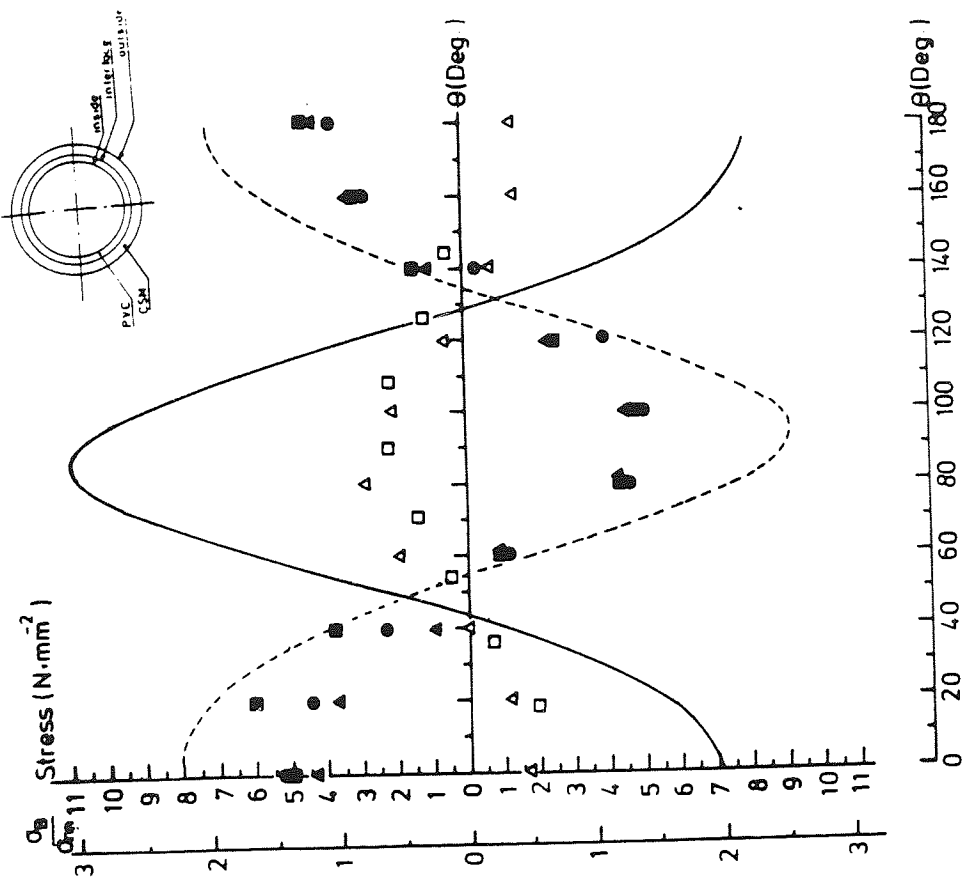
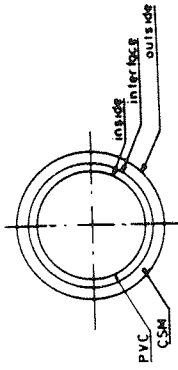


Figure (7.8) Circumferential stress distribution measured on smooth CSM/PVC lined S012, S014 and S016 bends under 2.37×10^5 N.mm in-plane bending moment (opening)

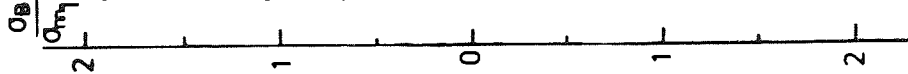
Exp Th

S012 S014 S016

inside
interface
outside



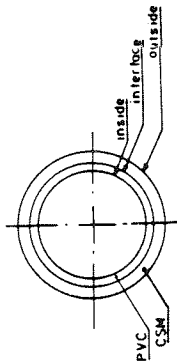
$\frac{\sigma_B}{\sigma_{m10}}$ Stress ($N \cdot mm^{-2}$)



Exp Th

S012 S014 S016

inside
interface
outside



$\frac{\sigma_B}{\sigma_{m10}}$ Stress ($N \cdot mm^{-2}$)

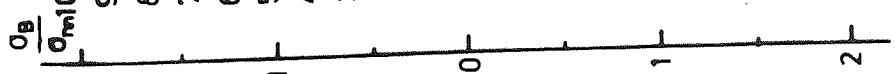


Figure (7.9a) Inside (interface) longitudinal stress distribution measured on smooth CSM/PVC lined S014 and S016 bends under 1.80×10^5 N mm out-of-plane bending

Figure(7.9b) Outside longitudinal stress distribution measured on smooth CSM PVC lined S014 and S016 bends under 1.80×10^5 N mm out-of-plane bending

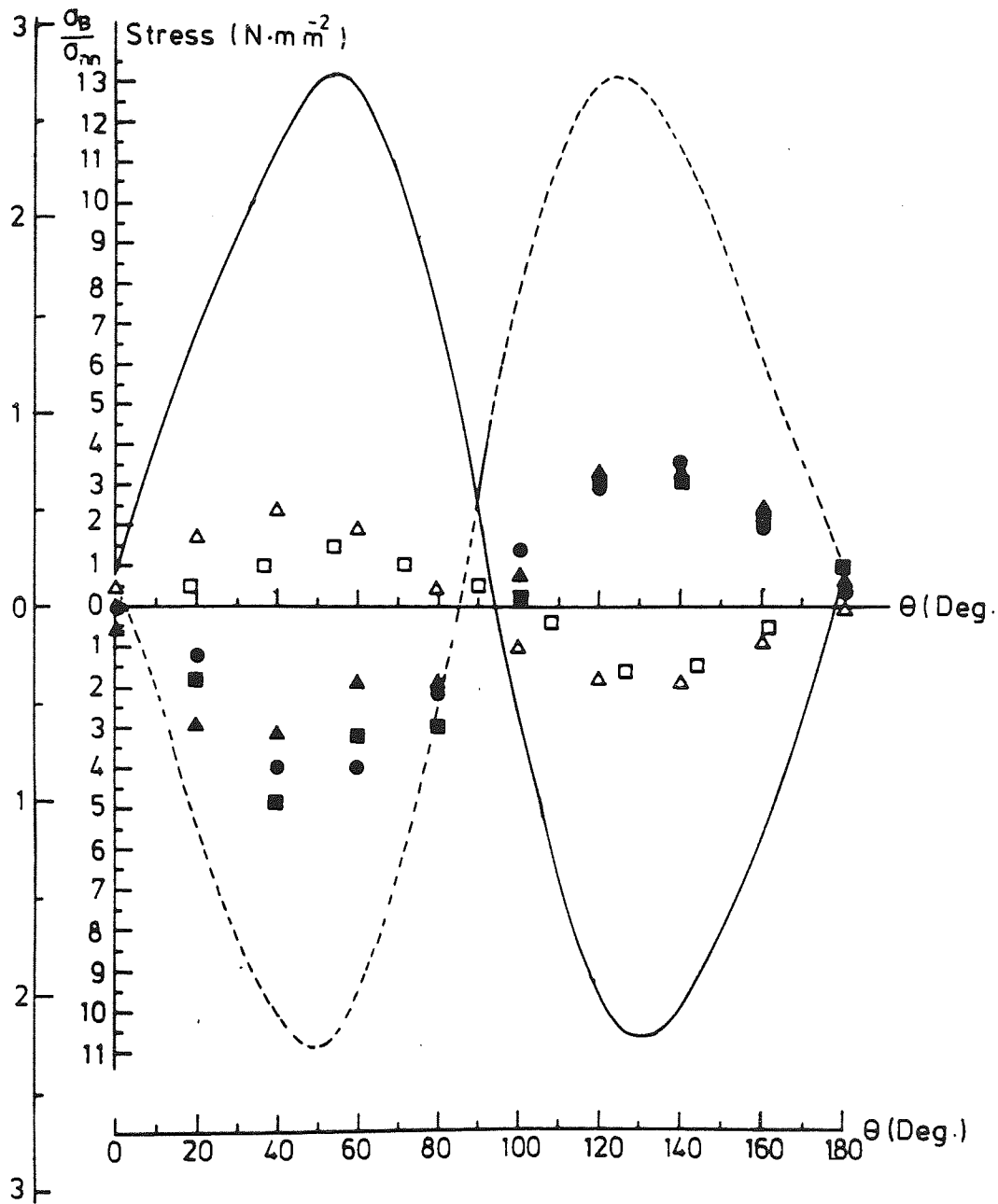


Figure (7.10) Circumferential stress distribution measured on smooth CSM/PVC lined S012, S014 and S016 bends under $1.80 \times 10^5 \text{ N}\cdot\text{mm}$ out-of-plane bending

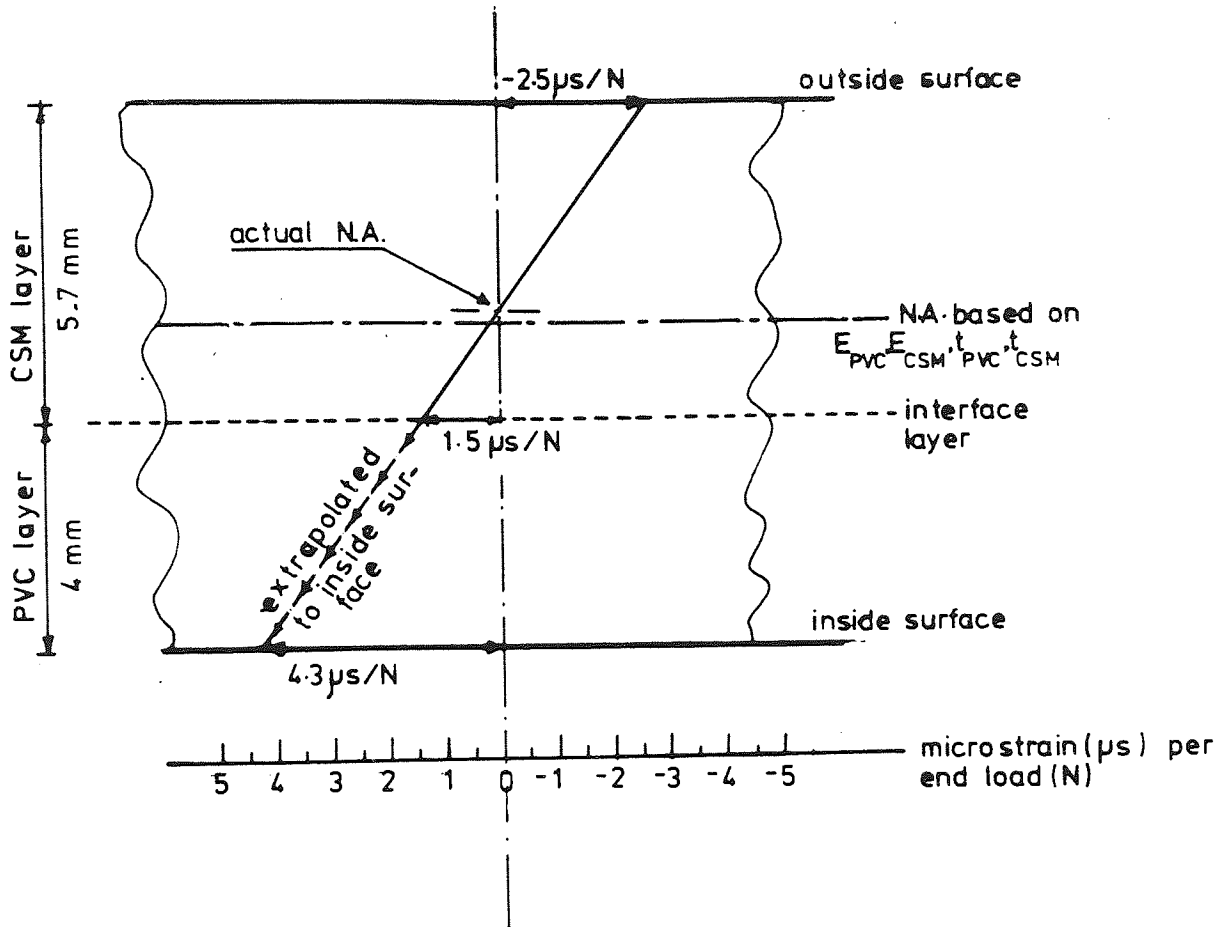


Figure (7.11) Prediction of strains on the inside surfaces (i.e. PVC), by extrapolating measured strains on the interface layer (i.e. PVC/CSM) and on the outside surface (i.e. CSM), for bend S016 under in-plane bending moment (opening)

TABLE 7.7a - Maximum Inside and Outside Longitudinal and Circumferential SIF's Experimentally Determined for Smooth CSM/PVC Lined Bends

| Bend Number | λ_e^* | In-plane SIF | | | | Out-of-plane SIF | | | |
|-------------|---------------|--------------|---------|-----------------|---------|------------------|---------|-----------------|---------|
| | | Longitudinal | | Circumferential | | Longitudinal | | Circumferential | |
| | | Inside | Outside | Inside | Outside | Inside | Outside | Inside | Outside |
| S012 | 0.509 | - | 1.50 | - | 1.39 | - | 1.15 | - | 0.95 |
| S014 | 0.509 | 0.97 | 0.61 | 1.59 | 1.33 | 0.74 | 1.35 | 1.04 | 1.01 |
| S016 | 0.509 | 0.97 | 1.33 | 1.89 | 1.25 | 0.72 | 1.05 | 1.22 | 0.84 |

TABLE 7.7b - Theoretical Comparison of the Experimental SIF's presented in Table 7.7a

| In-plane SIF | | Out-of-plane SIF | |
|--------------|-----------------|------------------|-----------------|
| Longitudinal | Circumferential | Longitudinal | Circumferential |
| BS 806 | BS 806 | BS 806 | BS 806 |
| Theory | Theory | Theory | Theory |
| 1.65 | 2.9 | 2.2 | 2.8 |
| 1.66 | 3.02 | 2.02 | 2.78 |

$$\lambda = 0.509$$

TABLE 7.8 - Experimental Comparison of Bend Specifications of the Same Nominal Glass Content and Nominal Dimensions but with (L) and Without (UL) of a uPVC Liner

| K _i | | In-plane | | | | Out-of-plane | | | | | |
|----------------|------|------------------|------|---------------------|------|----------------|------|------------------|------|---------------------|------|
| | | Longitudinal SIF | | Circumferential SIF | | K _O | | Longitudinal SIF | | Circumferential SIF | |
| UL* | L** | UL | L | UL | L | UL | L | UL | L | UL | L |
| 1.85 | 1.69 | 1.74 | 1.48 | 2.21 | 1.77 | 3.27 | 2.00 | 2.14 | 1.18 | 2.78 | 1.14 |

* Average experimental results of Set I of smooth CSM Bends presented in Table (6.10) to Table (6.15) of Chapter 6.

** Average experimental results of smooth CSM/PVC lined bends.

of the PVC liner, for those particular small diameter bends, has far more influence in reducing the out-of-plane flexibility factors and SIFs than those under in-plane bending mode of loading.

7.4.3 Failure test results of bend S016

Bend S016 was taken to failure under in-plane mode of bending (opening). Strain measurements at the centre of the bend and free end-deflection were measured as a function of the end-load to failure.

The end-deflection up to failure was measured using a dial gauge. Fig. 7.12 shows a reasonable linear function of end-load vs end-deflection.

Total failure was recorded at load 2460 N where the load cell started to give lower readings of load for continuous end-deflection. The bend was then brought to complete failure as shown in Figs. 7.13a,b.

Prior to failure, there was no visual signs of resin cracking on the outside surface. Audible noises started at approximately 2040 N end load, and severe cracking noises were heard at load 2340 N accompanied by laminate whitening occurring at about 100mm from the centre of the bend towards the free tangent at the failure position shown in Fig. 7.13b. It is believed that such whitening occurred due to delamination of the CSM layer from the PVC liner.

The bend was cut later for further investigations. Inside; longitudinal cracks were shown to have been developed on the PVC liner at an angular positions of $\theta = 90^\circ$ and $\theta = 270^\circ$ as shown in Fig. 7.14a,b. These cracks were located at the same position of the final failure shown in Fig. 7.13a. Referring back to Fig. 7.8, it could be seen that the peak circumferential flexural stress occurs, at position $\theta = 90^\circ$, and it is believed to have initiated the longitudinal cracks. The cracks are shown to be brittle, with no signs of yielding were observed.

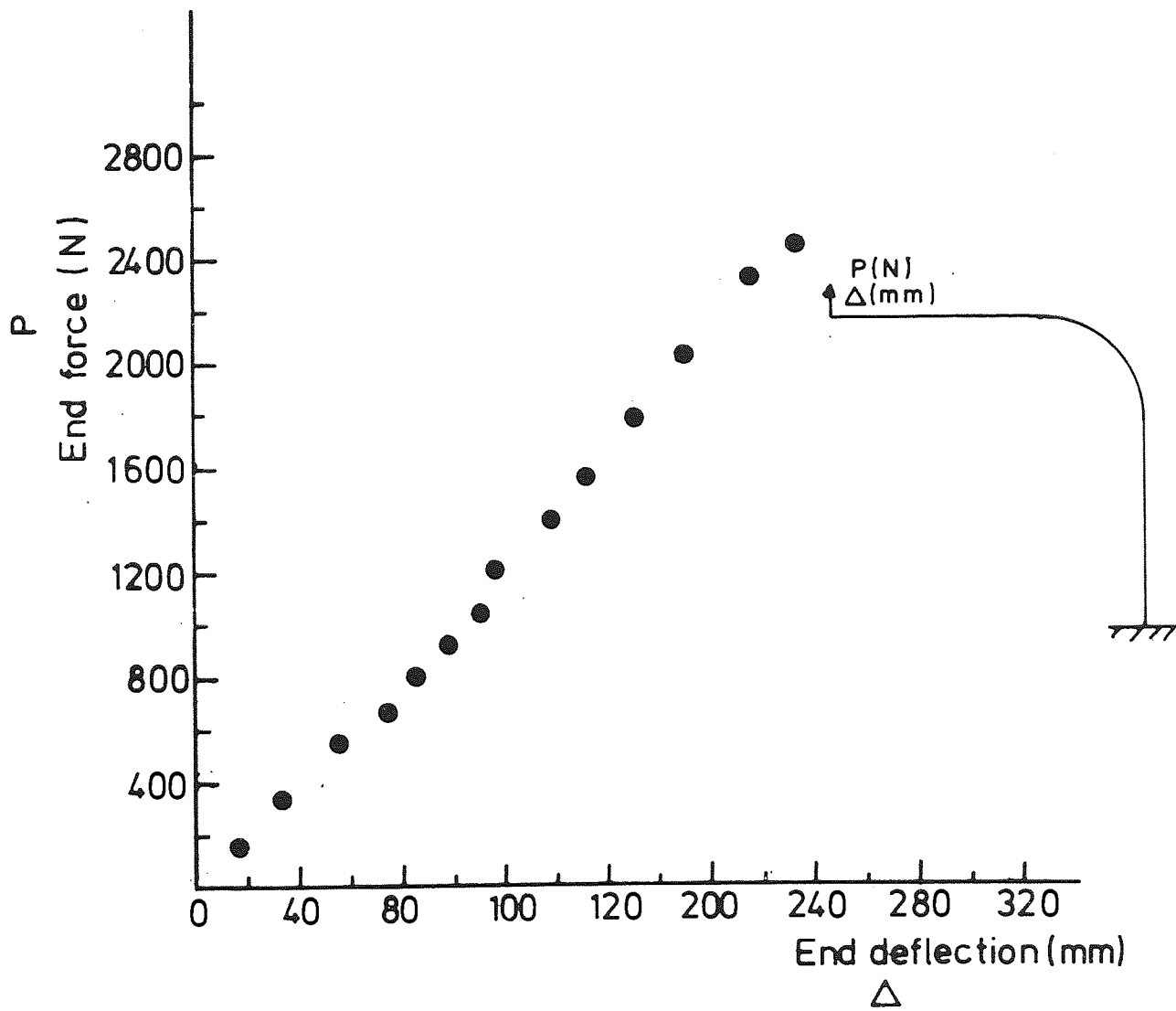


Figure (7.12) End-deflection versus end-load to failure of bend S016 under in-plane (opening) mode of loading

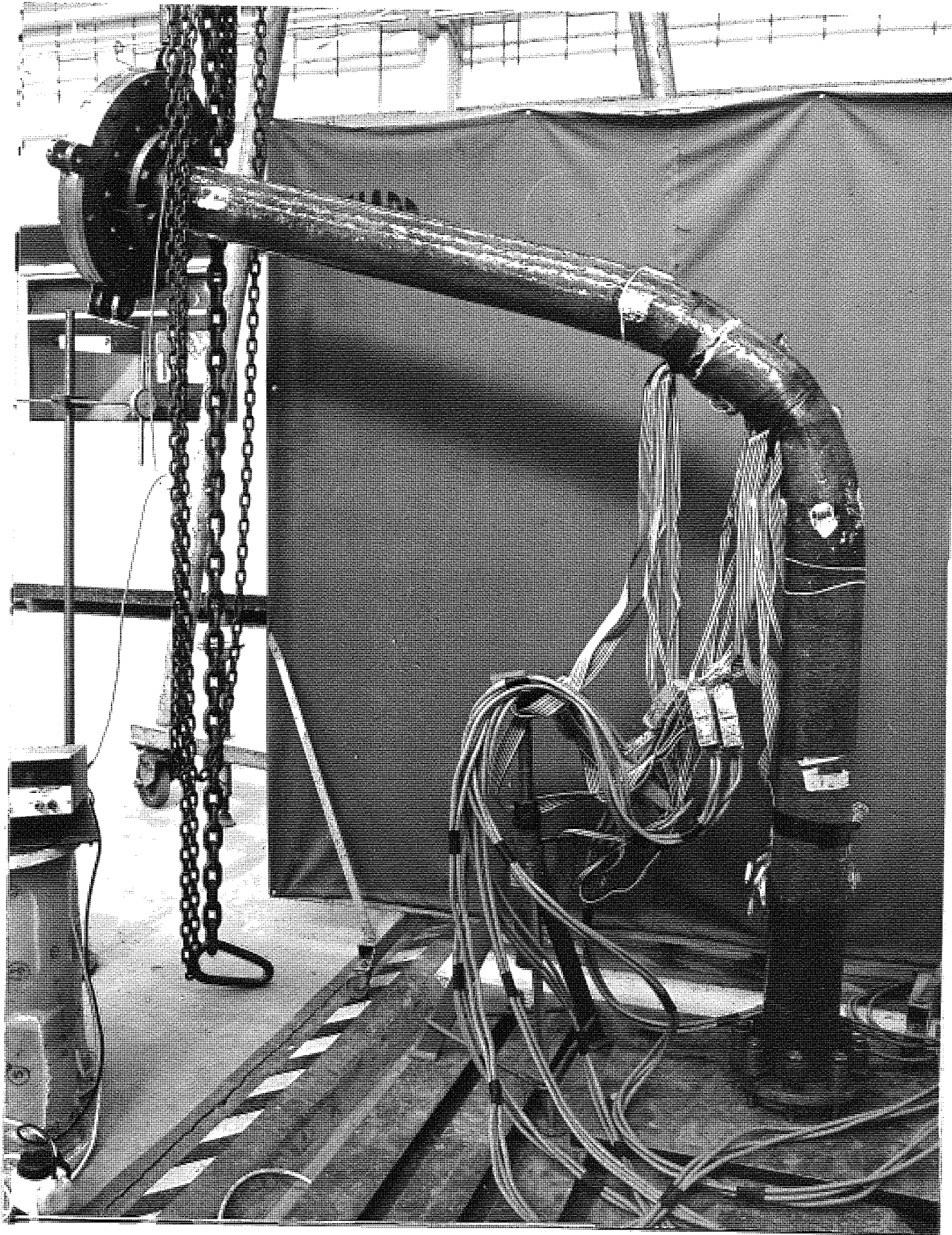


Figure (7.13a) Bend S016 taken to failure under in-plane loading (opening)

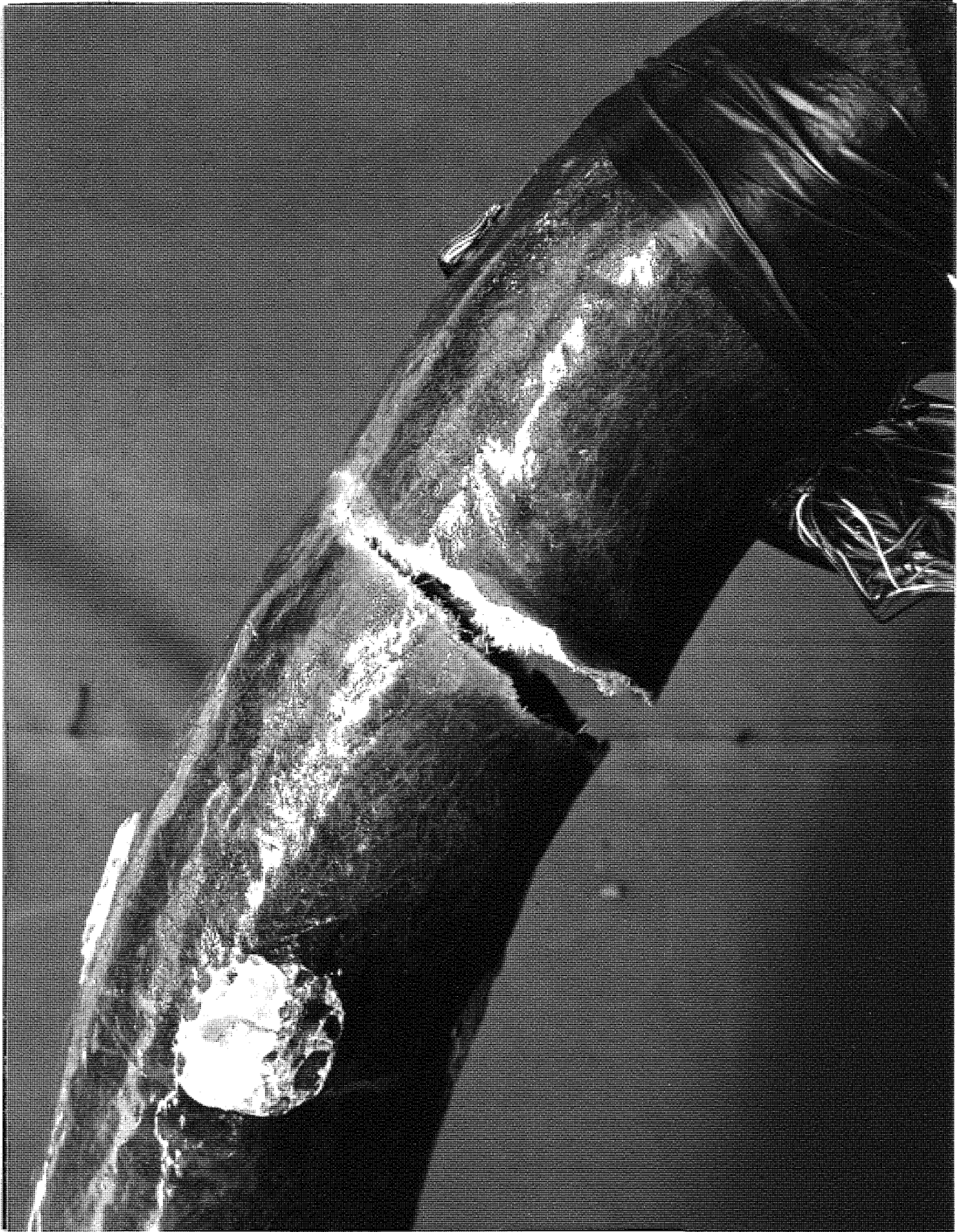


Figure (7.13b) Total failure of bend S016 as in Figure (7.13a)



Figure (7.14a) Brittle failure observed on PVC liner at $\theta = 90^\circ$ of bend S016 under in-plane (opening) mode of loading

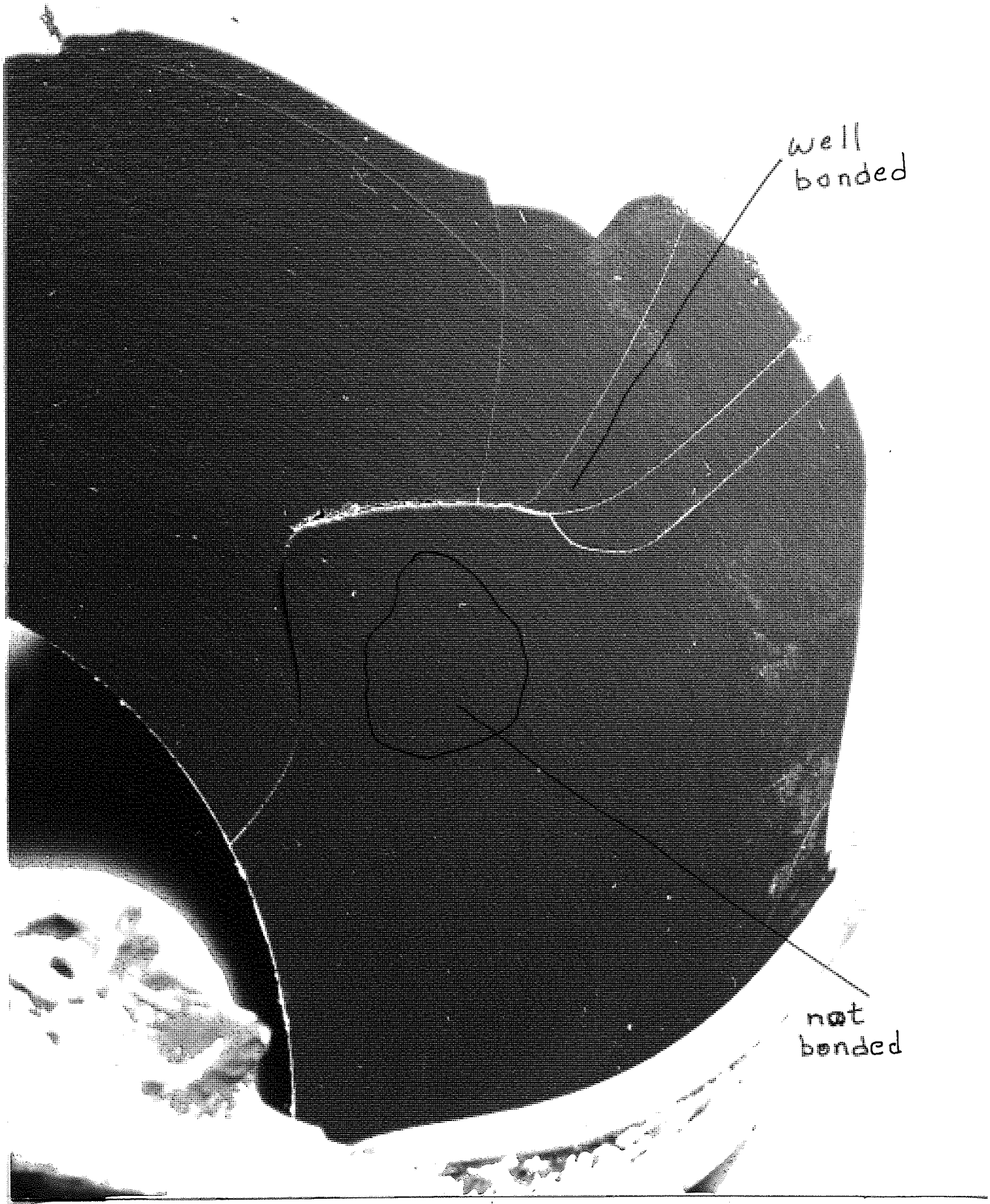


Figure (7.14b) Brittle failure observed on PVC Liner at $\theta = 270^\circ$ of bend S016 under in-plane (opening) mode of loading

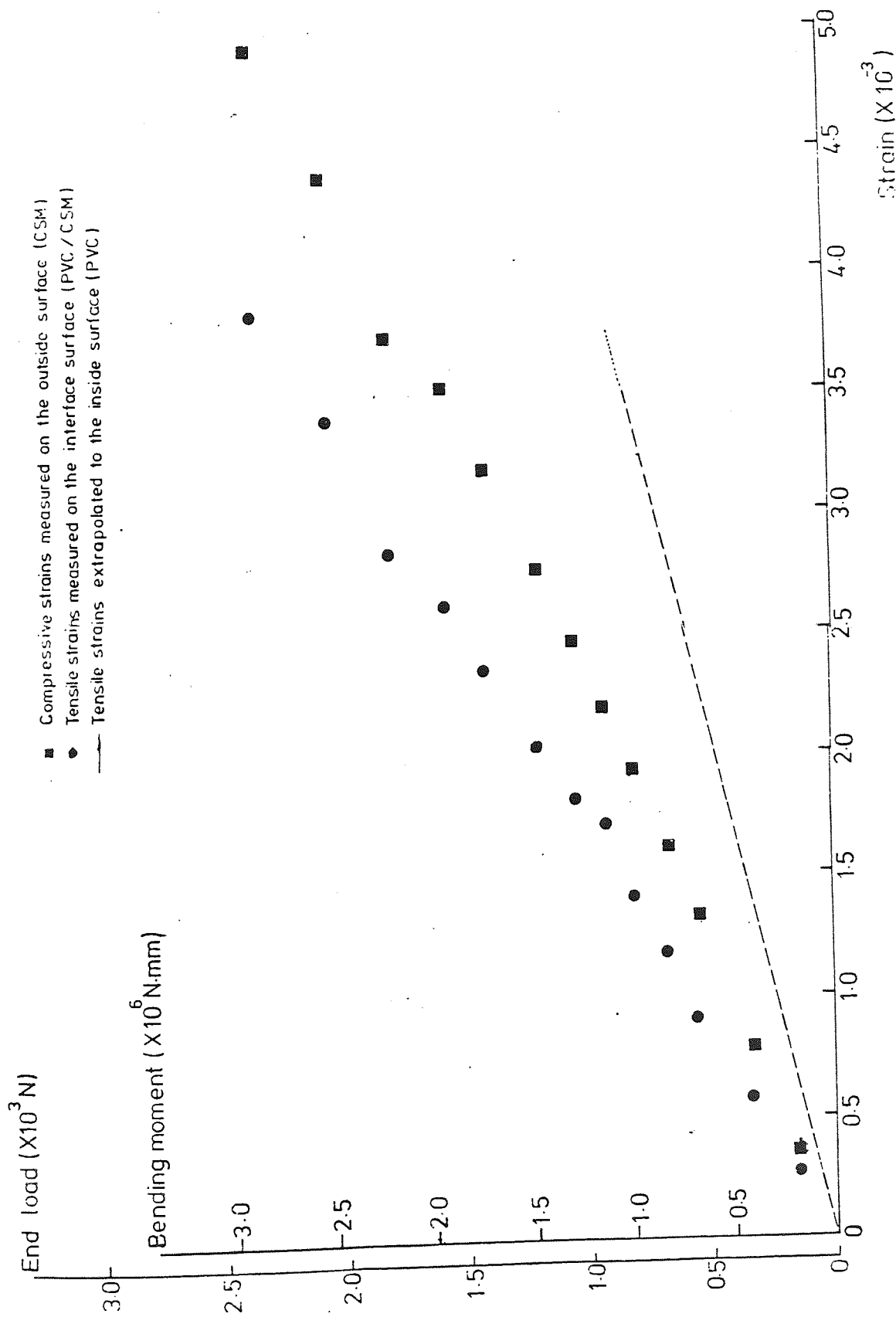


Figure (7.15) Measured strains versus end-load to failure of bend S016 under in-plane (opening) mode of loading

TABLE 7.9 - In-plane Bending Moments Experienced by Bend S016 to Failure

| | 2×10^{-3} strain | Total failure | 1/10 failure |
|--|---------------------------|---------------|--------------|
| End load (N) | 480 | 2460 | 250 |
| Bending moment (N mm) $\times 10^6$ | 0.58 | 2.99 | 0.3 |

TABLE 7.10 - Probable mechanisms of Crack Initiation and Propagation in Bend S016 under in-plane/opening Mode of Bending

MECHANISM A

I Crack initiation caused by inside maximum tensile circumferential strains at ± 90 from intrados as indicated by failure shown in Figure (14). Here, brittle failure of the PVC could not be explained.

II Crack propagation from inside PVC cracks to interface PVC/CSM surface causing delamination, i.e. separation of PVC from CSM at around load 2340 N.

III Failure of the CSM laminate by a tensile longitudinal stress initiated at the intrados leading to a circumferential crack as shown in Figure (13).

MECHANISM B

Peeling at interface due to interlaminar shear stresses and transverse tensile loading. This is believed to have been started at the originally unbonded PVC/CSM area shown in Figure (14b). This phase here is a crack propagation rather than crack initiation.

Through-thickness crack propagation from the delaminated interface (I above) towards both the inside surface (PVC) and the outside surface (CSM). At this phase the brittle failure could be explained to be a direct cause of the embrittlement of the resin.

The PVC liner acts on its own leading to the circumferential cracks initiated as shown in Figure (14).

Total failure of the bend due to CSM failure as in Figure (13).

Random inspection of the PVC/CSM interface layer, the PVC surface showed a 20mm diameter area which has not been bonded to the CSM.

Using the extrapolation technique described in Fig. 7.11, the maximum inside circumferential strain could be estimated up to failure as shown in Fig. 7.15. The magnitude of the bending moment corresponding to 0.2% maximum strain is found to be approximately twice the bending moment corresponding to 1/10th of the load to failure. The bending moment magnitudes are listed in Table 7.9.

It is envisaged that two possible mechanisms of failure initiation and crack propagation could have occurred; these are explained in Table 7.10. The two mechanisms indicate the role of the interlaminar shear stresses in either starting failure (mechanism B) or accelerating the rate to failure (mechanism A) via delamination.

7.5 Flexural Behaviour of Mitred CSM/PVC Lined Bends

7.5.1 Introductory remarks

The three sets of Group II in Table 7.1 constituting six mitred bends were investigated under in-plane mode of bending and under out-of-plane mode of bending.

The geometrical lay-out of the bend is shown in Fig. 7.16 which is made of three and a half segments constituting a mitre angle of 12.85° for all the tested bends. Strains were measured at position located at the bend centre and the segment-edge.

Fig. 7.17a shows a general view of the bend-tangent structure where CSM overlaps are observed in the circumferential direction around the mitred segments and in the longitudinal direction along the tangents. The thickening of the CSM overlaps are clearly shown from the bend longitudinal cross-section presented in Fig. 7.17b, where particular thickening is observed on the intrados. The cracks shown in Fig. 7.17b

- "A" Strain gauges on the inside & outside surfaces
- "B" Strain gauges on the inside surface

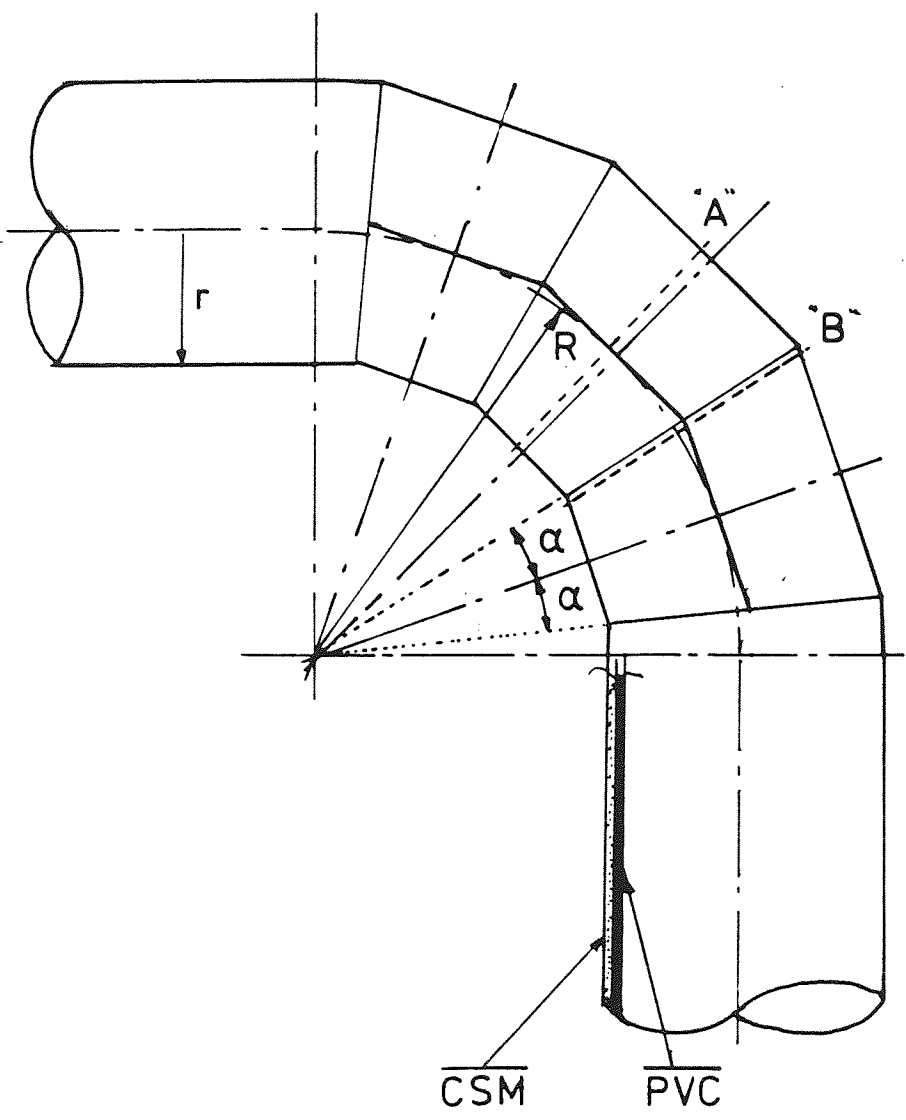


Figure (7.16) Three and half segments mitred, PVC lined, GRP bend

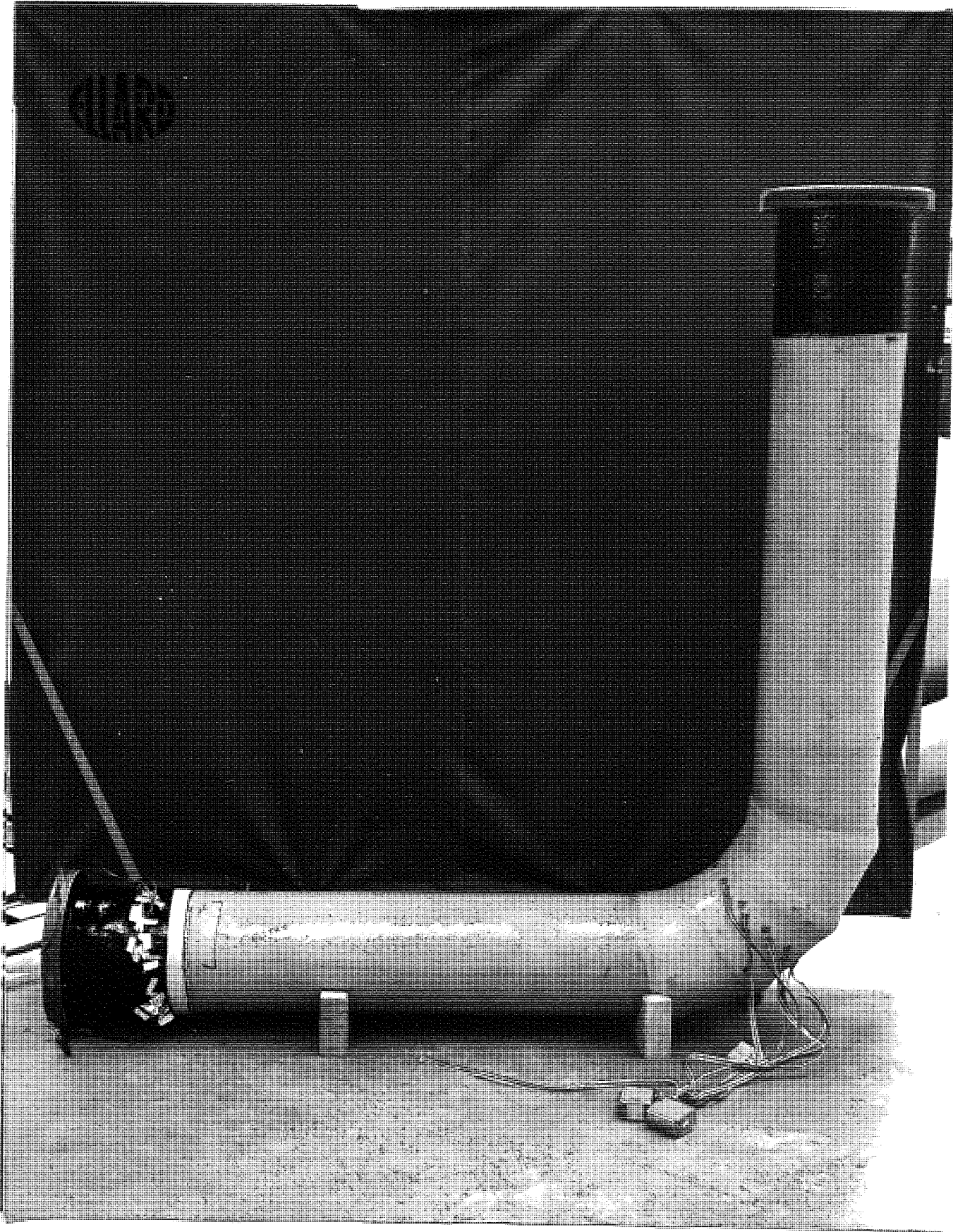


Figure (7.17a) General layout of 8 inches nominal bore PVC lined mitred GRP bend (S034)



Figure (7.17b) Section through bend S034

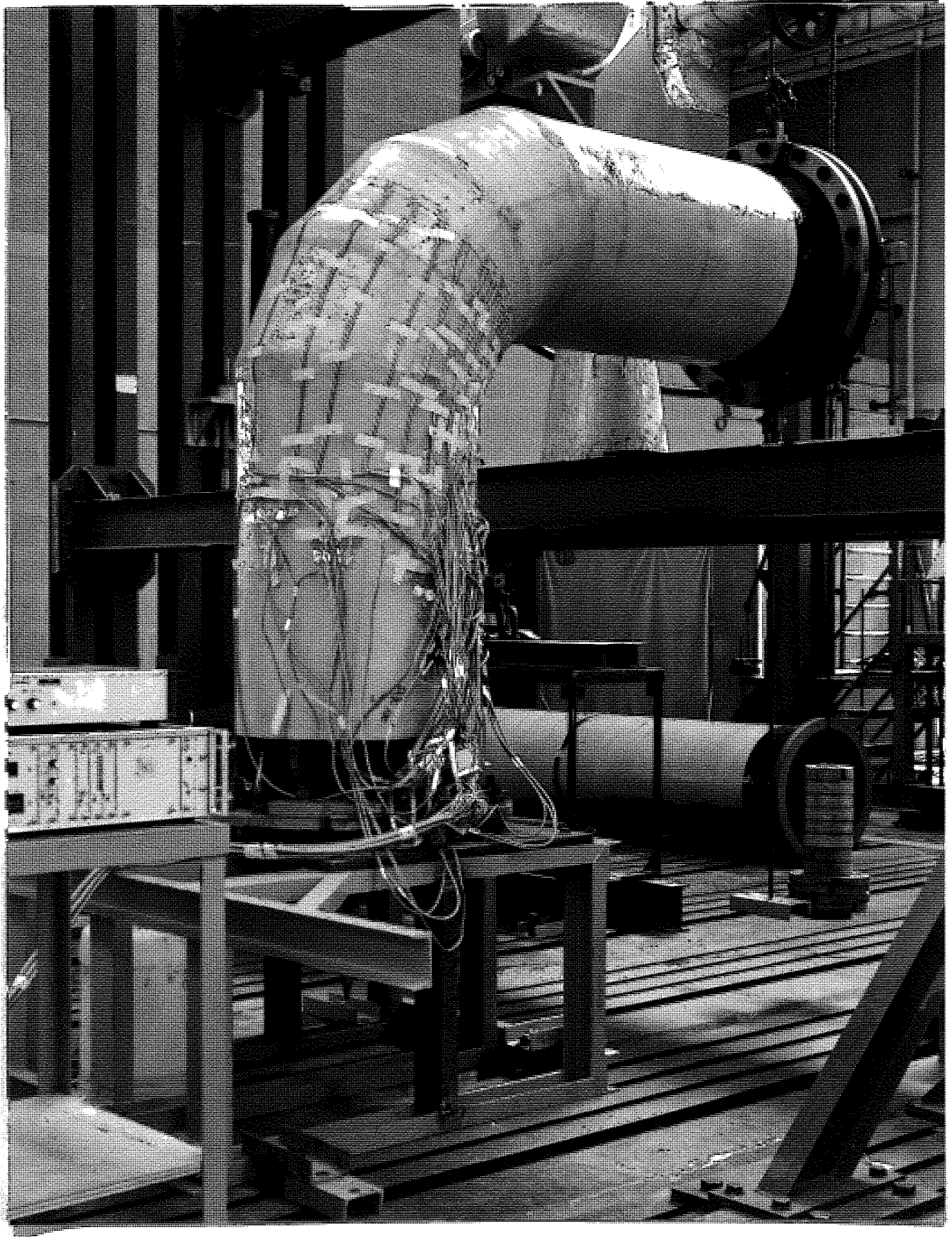


Figure (7.17c) General layout of testing 24 inches nominal bore mitred bend

are of bend S034 taken to failure under in-plane bending (opening), and are discussed later.

The bends' dimensions and laminate mechanical properties are tabulated in Table 7.4 based on the thicknesses measured by hand after cutting bend samples S034 and S036 which correspond to 200mm and 250mm nominal bores respectively. As for the 600mm nominal bore bends (S060 and S061), the thickness was obtained from measurement of the outside bend perimeters and the bore diameter.

The results of the testing are presented as in-plane and out-of-plane flexibility factors and stress intensification factors. A combined in-plane/out-of-plane loading was carried out on bend S060 and the results are compared and discussed with results obtained from individual modes of loading.

Diametral changes of the segment centre and at the segment-edge were measured under in-plane and out-of-plane bending for the 600mm bore bends using a pinned-dial gauge frame structure shown in Fig. 7.18. Using the same device, diametral reduction of bend S060 along tangent-bend direction was measured under in-plane bending (closing).

7.5.2 Ovality measurements

Diametral ovality was measured for two bends S060 and S061 under in-plane bending (closing) and under out-of-plane bending. The measurements were taken at the centre of the bend (segment-centre) for both bends, and at the segment edge adjacent to the fixed tangent for bend S060. Also for bend S060 diametral reduction of the vertical diameter (i.e. $\theta = 0^\circ/180^\circ$) was measured along the tangent-bend structure under in-plane closing. Twenty-four diametral points were measured with some difficulty especially on the segment-edge due to outside surface irregularities. The accuracy of the dial gauge used in

the instrument shown in Fig. 7.18 was 0.002 inches. No attempts were made to measure initial ovality of the bends, although diameter measurements were taken on bend S033 revealing 217 mm at $0^\circ/180^\circ$ position against 213 mm at $90^\circ/270^\circ$ position, and for bend S037 the $0^\circ/180^\circ$ position was measured to be 266mm against 257mm at $90^\circ/270^\circ$ position.

The experimental ovality measurements for bend S060 under in-plane bending and under out-of-plane bending are shown in Figs. 7.19 and 7.20 respectively. The results are presented as a function of the mean bending moment applied at that particular centre line position on the bend. Similarly, for bend S061 the diametral deformation are presented in Figs. 7.21 and 7.22 under in-plane bending moment and under out-of-plane bending moment respectively.

The absolute maximum peak values of the diametral deformation under in-plane mode of bending are located at $90^\circ/270^\circ$ position as shown from Figs. 7.19 and 7.21, approaching zero deformation at positions $50^\circ/230^\circ$ and $125^\circ/305^\circ$ indicating zero bending moment, and minimising at positions $15^\circ/195^\circ$ and $170^\circ/300^\circ$ positions. The maximum-minimum peaks for in-plane mode of bending is summarised in Table 7.11 for both the bend centre (mid-segment) and the segment-edge based on the diametral deformation presented in Figs. 7.19 and 7.21.

Similarly, for the out-of-plane mode of bending, the maximum-minimum diametral deformation peaks are summarised in Table 7.12 based on the distribution presented in Figs. 7.20 and 7.22.

Comparable magnitude of diametral change is measured on the mid-segment and on the segment-edge. The measured strain at the same positions as presented later reveal that circumferential strains measured at the edge could be up to 30% higher than that measured on the segment-centre for both type of in-plane and out-of-plane bending. This

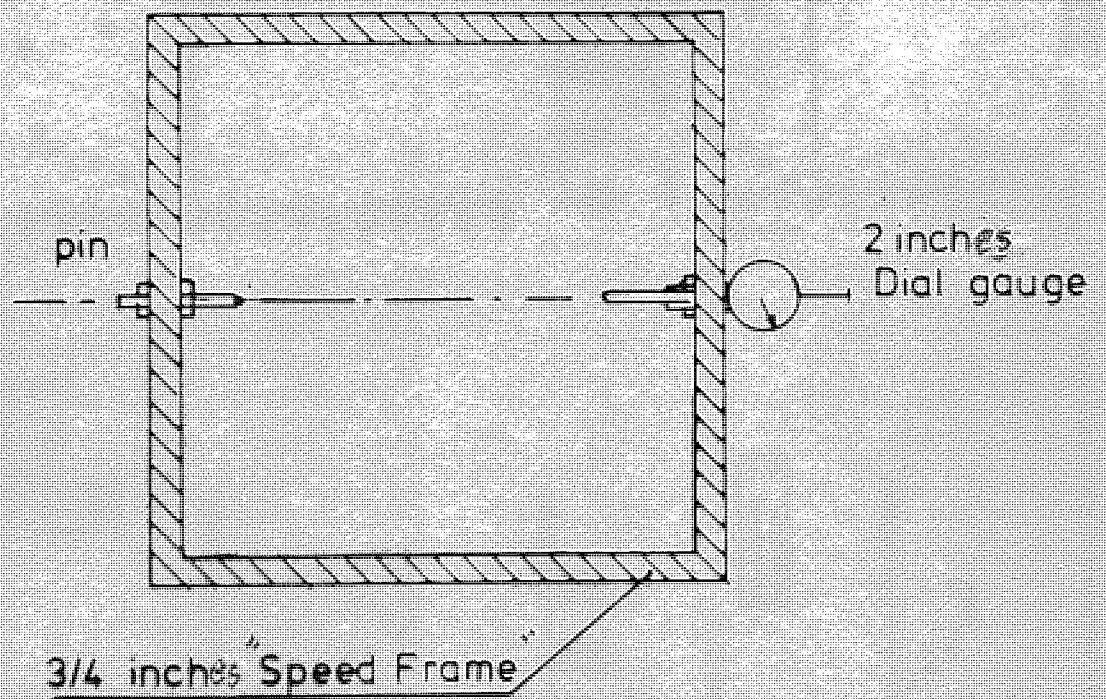


Figure (7.18) Device for measuring bend ovalization

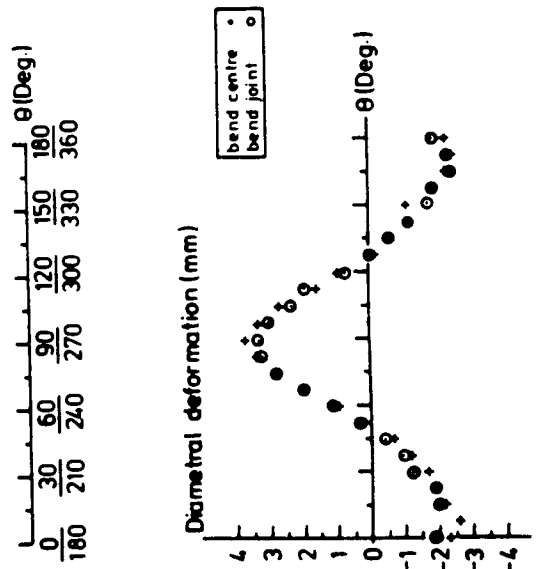
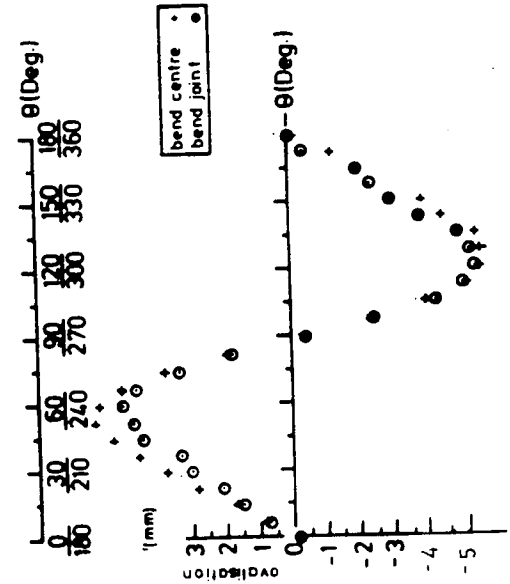
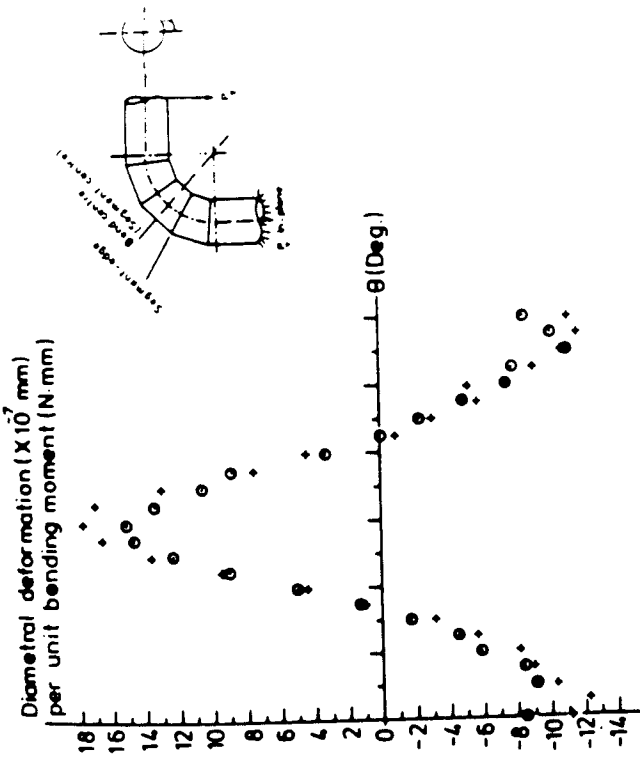
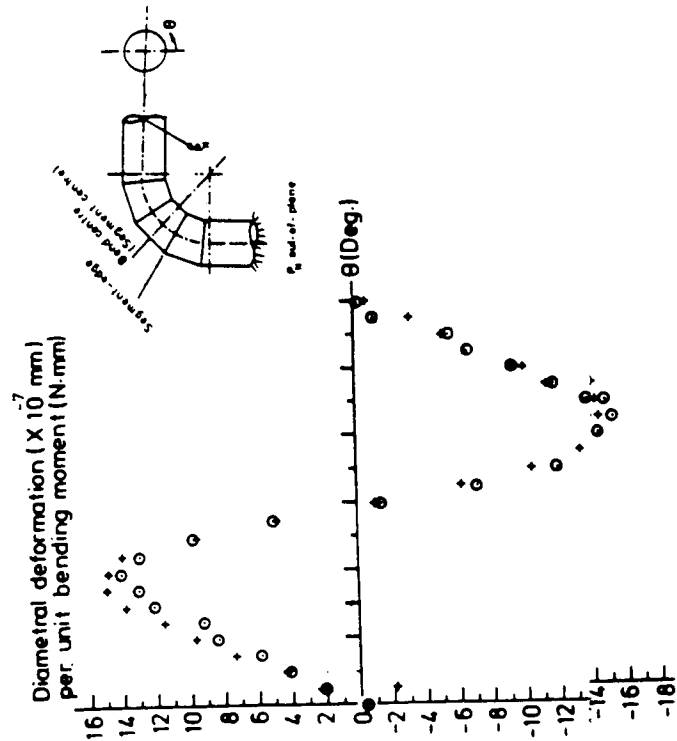


Figure (7.19) Diametral ovalization measured on bend S060 under 1454N 'in-plane/closing' end-load

Figure (7.20) Diametral ovalization measured on bend S060 under 3243N out-of-plane end-load

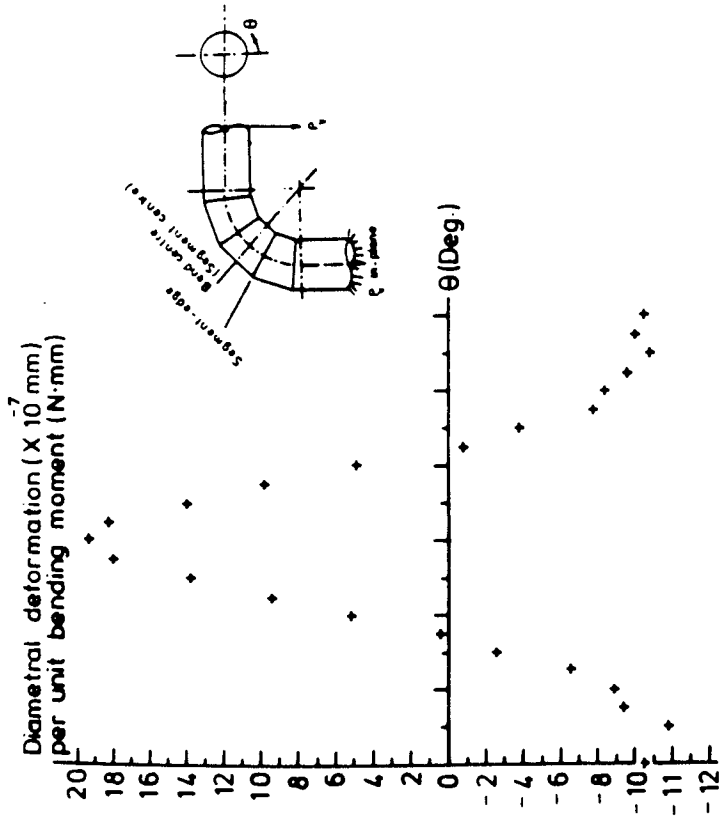


Figure (7.21) Diametral ovalization measured on bend S061 under 1454N 'in-plane/closing' end-load

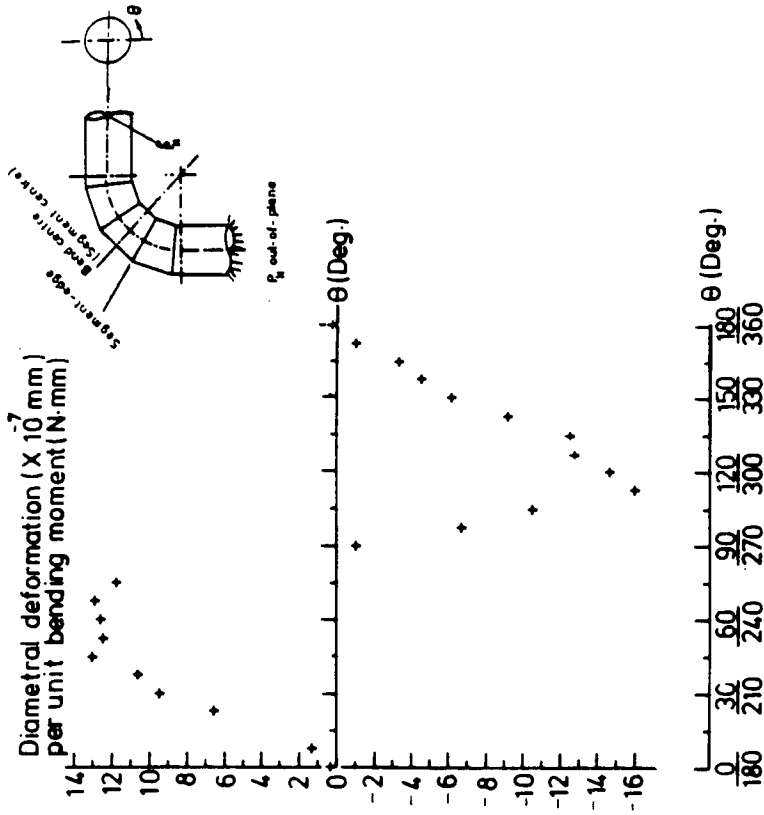


Figure (7.22) Diametral ovalization measured on bend S061 under 1454N 'out-of-plane' end-load

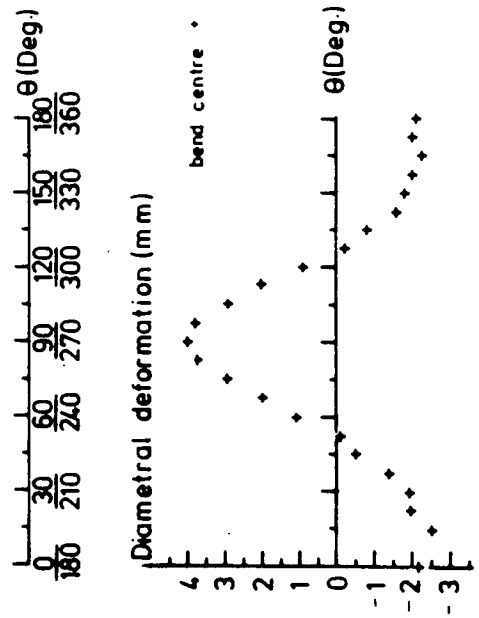


Figure (7.21) Diametral ovalization measured on bend S061 under 1454N 'in-plane/closing' end-load

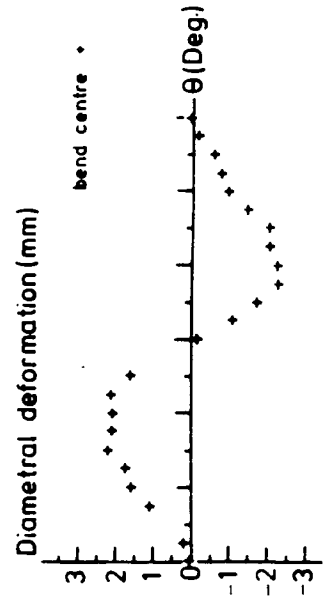


Figure (7.22) Diametral ovalization measured on bend S061 under 1454N 'out-of-plane' end-load

TABLE 7.11 - Diametral Ovalization of 600 mm nominal bore mitred CSM/PVC lined Bends under in-plane/
Closing Mode of Bending

| Bend S060* | | | Bend S061* | | |
|----------------------------|--|----------------------------|--|----------------------------|--|
| Bend Centre (mid-segment) | | Segment-edge | | Bend Centre (mid-segment) | |
| Angular position (Degrees) | Diametral deformation per unit B.M. (x 10 ⁻³ mm/N.mm) | Angular position (Degrees) | Diametral deformation per unit B.M. (x 10 ⁻³ mm/N.mm) | Angular position (Degrees) | Diametral deformation per unit B.M. (x 10 ⁻³ mm/N.mm) |
| 0°/180° | -11.2 | 0°/180° | - 8.6 | 0°/180° | -10.6 |
| 15°/195° | -12.3 | 30°/210° | - 9.2 | 30°/210° | -11.8 |
| 50°/230° | 0 | 50°/230° | 0 | 50°/230° | 0 |
| 90°/270° | +17.7 | 86°/266° | +14.4 | 90°/270° | +19.2 |
| 125°/305° | 0 | 128°/308° | 0 | 125°/305° | 0 |
| 173°/353° | -11.8 | 165°/345° | -11.0 | 165°/345° | -10.8 |

* positive means increase in diameter.

** B.M. = bending moment

TABLE 7.12 - Diametral Ovalization of 600 mm nominal bore mitred CSM/PVC lined Bends under out-of-plane
Mode of Bending

| Bend S060* | | | Bend S061* | | |
|----------------------------|--|----------------------------|--|----------------------------|--|
| Bend Centre (mid-segment) | | Segment-edge | | Bend Centre (mid-segment) | |
| Angular position (Degrees) | Diametral deformation per unit B.M. (x 10 ⁻³ mm/N.mm) | Angular position (Degrees) | Diametral deformation per unit B.M. (x 10 ⁻³ mm/N.mm) | Angular position (Degrees) | Diametral deformation per unit B.M. (x 10 ⁻³ mm/N.mm) |
| 0°/180° | - 0.60 | 0°/180° | - 0.30 | 0°/180° | + 0.30 |
| 56°/236° | +15.00 | 60°/240° | +14.0 | 60°/240° | +13.0 |
| 90°/270° | 0 | 90°/270° | 0 | 87°/267° | 0 |
| 120°/300° | -14.50 | 120°/300° | -15.3 | 113°/293° | -16.1 |

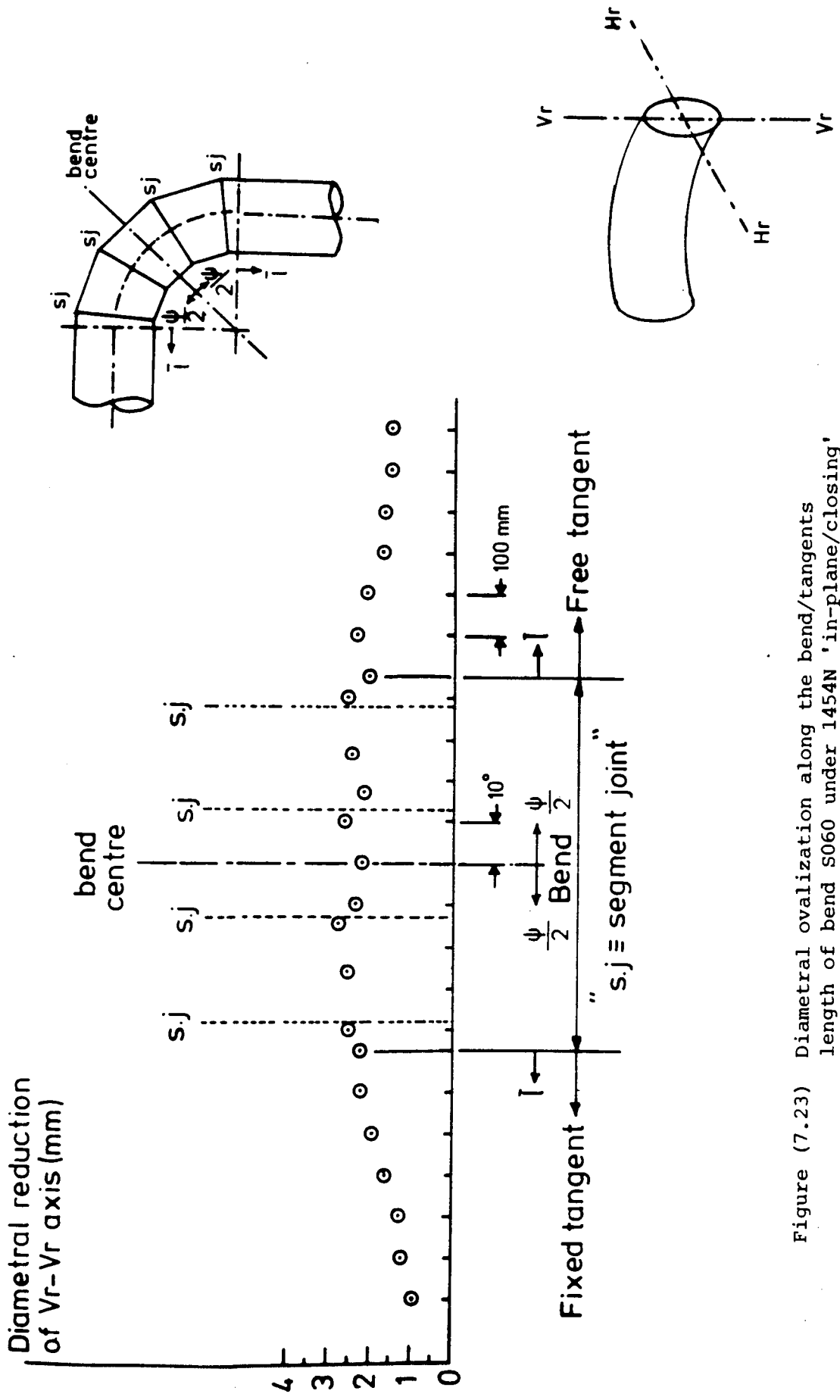


Figure (7.23) Diametral ovalization along the bend/tangents length of bend S060 under 1454N 'in-plane/closing' end-load

has been explained by the fact that forces and moments satisfying compatibility at the edge are of short decay lengths⁽¹⁷¹⁾, and hence would constitute a negligible contribution to the overall constant-flattening strain energy of the bend. Thus, it is not necessarily implied that the strain at the segment-edge should be identical to that of the segment-centre based on the similarities of diametral change in both positions⁽¹⁶⁶⁾.

Fig. 7.23 shows the diametral reduction at position $0^\circ/180^\circ$ (i.e. vertical diameter) of bend S060 measured over the bend and the tangents. The flattening experienced by the bend as a whole is approximately constant; decaying on the tangents. Naturally, the ovalization of the tangent would tend to increase its flexibility from unity; usually assumed for straight pipes. Again it could be shown that the segment-centre deformations and the segment-edge deformations are comparable in magnitudes.

7.5.3 In-plane and out-of-plane flexibility factors

With the knowledge of the measured free end-deflections, along with the bend dimensions and mechanical properties (Table 7.4), the in-plane and the out-of-plane flexibility factors are determined by using Eq. (I.6) and (I.18) of App. I respectively.

The bend is assumed to be of a smooth curvature with the bend radius running tangent to the centre line of the three and a half segments constituting the mitre bend as shown in Fig. 7.16. Such an assumption would imply that all the segments would contribute equally to the angular rotation of the bend, i.e., uniform flexibility throughout the bend component.

The straight tangents are assumed to have unity flexibility factor, although diametral measurements as shown in Fig. 7.23 suggest that this

is not the case due to ovalization of the tangents. Nevertheless, it would be equally assumed that what is lost on the flexibility of the bend due to tangent restraint might be compensated by the extra flexibility of the tangent.

For the calculation of the flexibility factor, the PVC stiffness contribution has been included in the overall pipe rigidity representing the bend (similar to Eq. (7.5b), using a tensile modulus of 7450 N/mm² and a Poisson's ratio of 0.30 for the CSM and a tensile modulus of 3000 N/mm² and a Poisson's ratio of 0.35 for the PVC liner.

Similar to the out-of-plane flexibility analysis of smooth bends, it is also assumed that any torsional moment on the bend does not contribute to the ovalization, i.e. not flexibility dependent, and the bend torsional contribution to the end-deflection is calculated using bend torsional rigidity of $\Sigma GJ_{(B)e}$.

The experimentally determined flexibility factors are compared with theoretical predictions for unlined bends. This is a common practice used in ICI⁽⁵⁾ code of practice. The theoretical flexibility factors are presented using:

(a) Smooth bend analysis

Such a procedure is adopted by ICI code of practice⁽⁵⁾, where the bend characteristics are as presented in BS806⁽¹²³⁾. According to Kitching⁽¹⁷⁰⁾, such a comparison would be only valid when the mitre angle is less than 9° and ratio of the pipe radius to the bend radius is less than 0.4. In the present investigation, all bends have 12.85° mitre angle and the radii ratios are of 0.33 and 0.50.

(b) Mitred bend analysis

(i) ANSI B.31⁽¹²⁴⁾ code of practice.

(ii) Kitching and Bond analysis⁽¹⁶⁸⁻¹⁷⁰⁾.

Their theoretical prediction covers the following range of bend parameters.

$$0.0125 < \lambda < 0.25$$

$$0.1 < r_m/R < 0.5$$

$$9.0^\circ < \alpha < 22.5^\circ$$

and their theoretical results were favourably compared with experimental results obtained from metallic bends under both in-plane⁽¹⁷¹⁾ and out-of-plane⁽¹⁷²⁾ modes of bending.

The experimentally measured in-plane and out-of-plane flexibility factors are presented in Table 7.13 together with their theoretical prediction based on that of a smooth bend theory and mitred bend theory. The experimental results are obtained, using the average effective rigidities, i.e. $\Sigma EI_{(B)e}$ and $\Sigma GJ_{(B)e}$ in Table 7.4. The results are also presented in a diagrammatical form as shown in Fig. 7.24.

Following a similar trend of results to the smooth bends, the mitred bends exhibited a higher out-of-plane flexibility factor in comparison with the in-plane flexibility factor. This discrepancy could be attributed to the thickness variability of the segmented bend and the tangents in contributing to the end-deflection, via their torsional deformation, which at the present analysis is based upon having an average uniform thickness together with an assumed circular section representing the bend-tangents specimens.

The comparison with theory as shown in Fig. 7.24 reveal that experimental results are bounded by the region enclosed by BS806⁽¹²³⁾ specification and ANSI B.31⁽¹²⁴⁾ specification. The best agreement is obtained by comparison with Kitching's⁽¹⁷⁰⁾ theoretical prediction.

TABLE 7.13 - In-plane and Out-of-plane Flexibility Factors experimentally determined for Mitred CSM/PVC Lined Bends

| Bend Number | Pipe factor λ_e^* | Experimental Results | | Theoretical Results | | |
|-------------|------------------------------|----------------------|--------------|-------------------------------|-----------------------------|---------------------------------|
| | | In-plane | Out-of-plane | Smooth Bend (123) BS806 | Mitre Bend (124) ANSI | Mitre Bend (170) Kitching |
| S033 | 0.177 | 6.40 | 9.55 | 9.32 | 6.43 | 8.84 |
| S034 | 0.177 | 6.03 | 9.71 | 9.32 | 6.43 | 8.84 |
| S036 | 0.087 | 11.1 | 15.6 | 18.92 | 11.62 | 15.93 |
| S037 | 0.087 | 11.73 | 16.09 | 18.97 | 11.62 | 15.93 |
| S060 | 0.061 | 22.30 | 28.14 | 27.5 | 15.85 | 23.19 |
| S061 | 0.061 | 24.16 | 25.96 | 27.5 | 15.85 | 23.19 |

* Based on the thickness of the CSM.

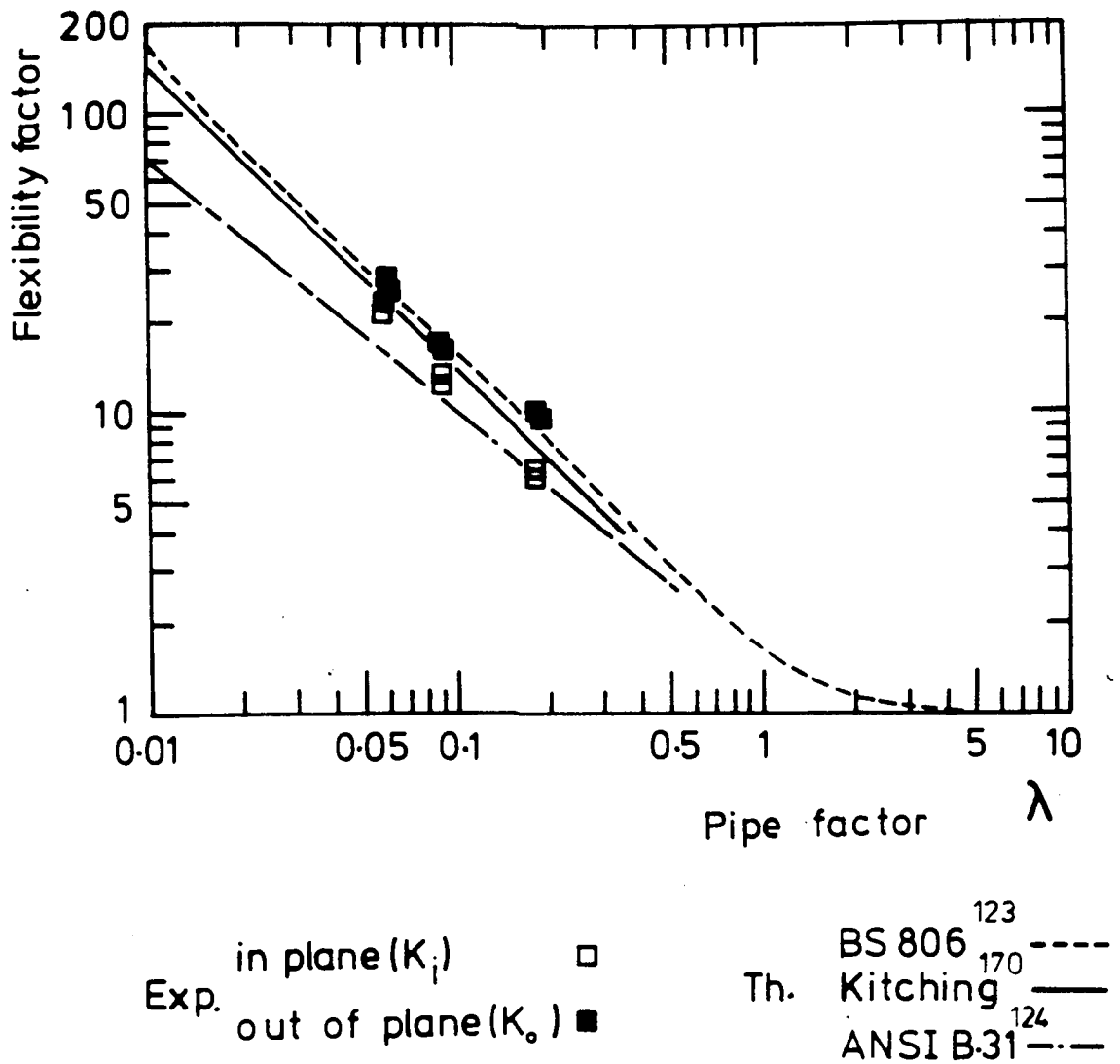


Figure (7.24) Experimentally determined in-plane and out-of-plane flexibility factors for CSM/PVC lined mitred bends

7.5.4 In-plane and out-of-plane bend strains and stresses

Under in-plane and out-of-plane bending moments, strains in the circumferential, skew and longitudinal directions were measured at the positions shown in Fig. 7.16. The experimental stresses were determined using Hooke's law for isotropic plates. The elastic moduli and Poisson's ratios for both the PVC and the CSM are listed in Table 7.4.

For in-plane loading, the bending moments at the different positions on the bend were determined from direct multiplication of the end force times the distance to the strain gauged positions, using the tangent-bend centre-line as the mean axis for the distance measured.

For the out-of-plane loading, the flexural moment is taken as the vector component at right-angle to the centre-line curvature lying in the plane of the bend at the strain gauged positions.

For both types of bending, the test results are presented as strain distribution and stress ratio distribution (σ_B/σ_{nn} , Eqs. (I.9) and (I.20) of App. I). The test results are also presented as stress intensification factors compared with theory⁽¹⁷⁰⁾ and standard specifications^(123,124).

Different pipe rigidities are used to calculate σ_{nn} for the bend-centre (segment-centre) and for the segment-edge. These are $\Sigma EI_{(B.c)e}$ and $\Sigma EI_{(B.j)e}$ respectively as presented in Table 7.4. These rigidities are based on the thickness measured at that particular position averaged with the thickness measured on the straight tangents.

Bend S060 was taken under a combined loading of in-plane/out-of-plane bending using equal end loadings. The measured strains are then discussed and compared with those obtained from both types of loading applied individually.

Bend S034 was later taken to failure under in-plane bending (opening mode), and the failure procedure is also discussed based on its load-deflection, and on the incrementally measured strains.

7.5.4.1 In-plane stress ratio distribution and stress intensification factors (SIF_i)

The experimentally measured strain distribution and the experimentally determined stress ratio distributions at the bend-centre (segment-centre) and the segment-edge are presented successively in Figs. 7.25 and 7.36 as a function of their angular position starting from the intrados and terminating at the extrados over the 180° of the bend parameter.

The common behaviour of all the bends regardless of their dimensions could be presented as the following.

- (a) The maximum strain, is the circumferential strain measured on the inside of the PVC liner situated at the segment-edge. Bends S036, S037 did not have strain gauges at that position.
- (b) The maximum experimental stress ratio is the circumferential one located on the inside of the PVC liner and positioned at the segment edge. See Figs. 7.26b, 7.28b, 7.34b and 7.36b.
- (c) The central segment of bend S033 was strain gauged at the joint nearer to the free tangent, whilst that for bend S034 was nearer to the fixed tangent. Measured circumferential strains are comparable in magnitude for both bends as shown in Figs. 7.25b and 7.27b. This observation is supported by the flattening deformation measurements taken bend S060 in Fig. 7.24 where the joints located on the central segment show similar level of ovality.
- (d) The maximum experimentally measured longitudinal strain, is always located on the outside (CSM) surface positioned at the bend-centre (segment-centre). This is not always the case with the experimentally measured longitudinal stress ratio where the maximum could be found on either the inside or the outside surface as will be presented later in Table 6.14. With reference to the

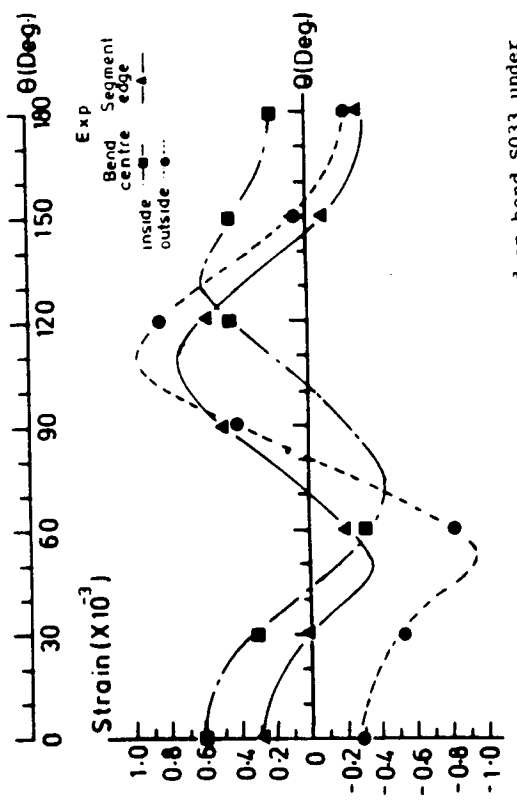
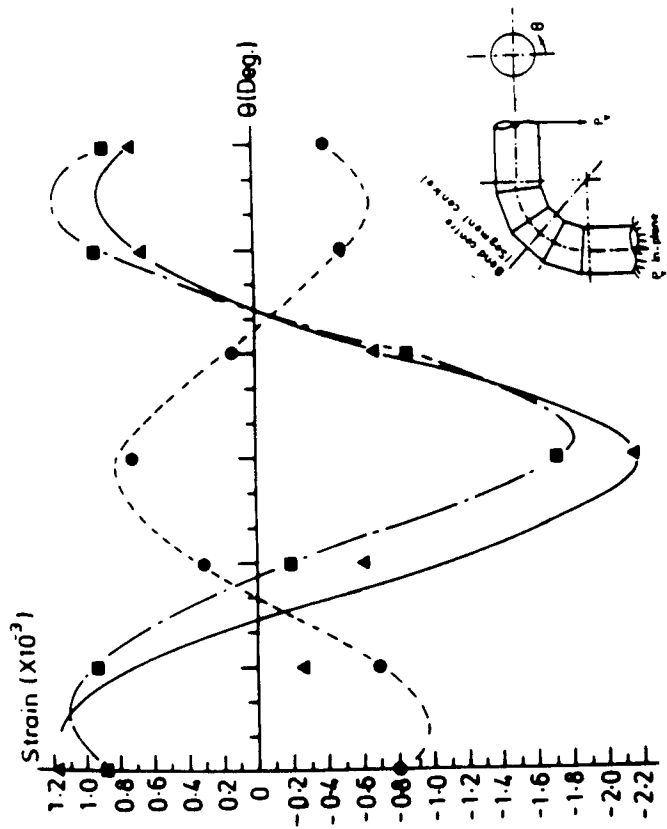


Figure (7.25) Strain distribution measured on bend S033 under in-plane/closing mode of loading. End load = 675N, $M_{B,C} = 8.21 \times 10^5$ N.mm, $M_{B,J} = 7.85 \times 10^5$ N.mm

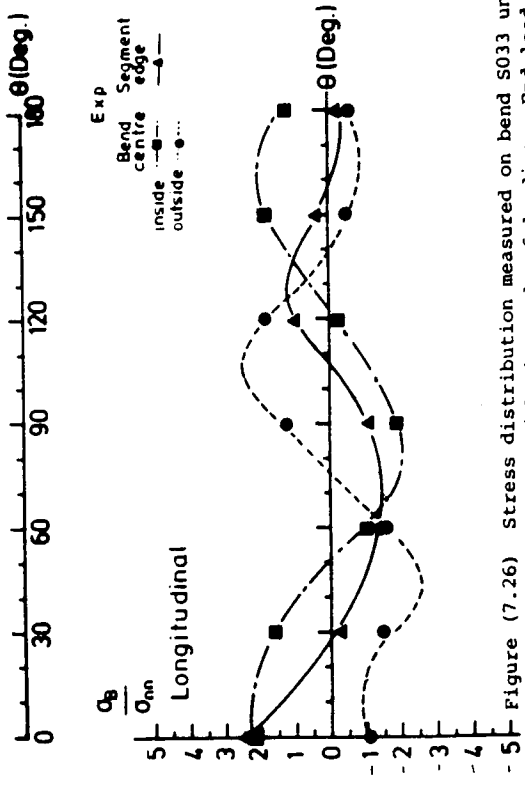
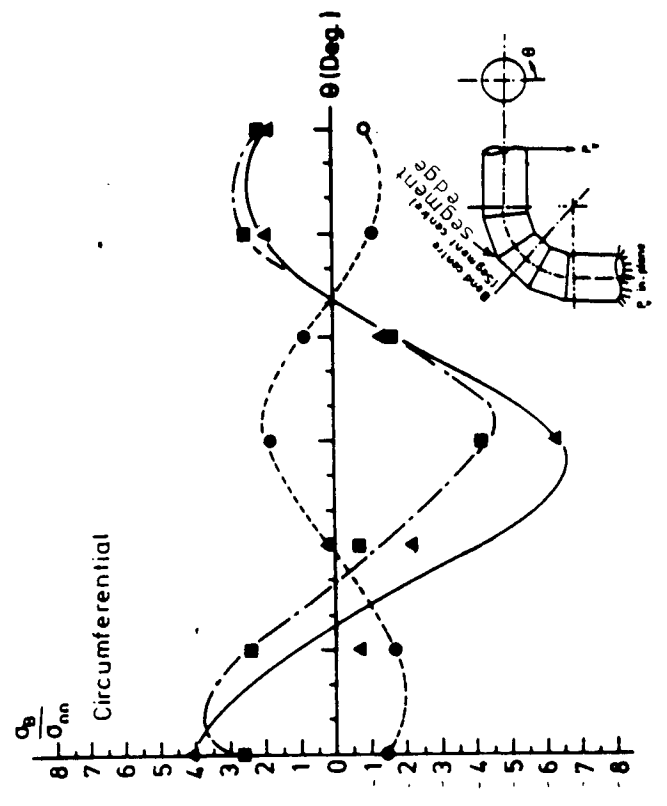


Figure (7.26) Stress distribution measured on bend S033 under in-plane/closing mode of loading. End load = 675N, $M_{B,C} = 8.21 \times 10^5$ N.mm, $M_{B,J} = 7.85 \times 10^5$ N.mm

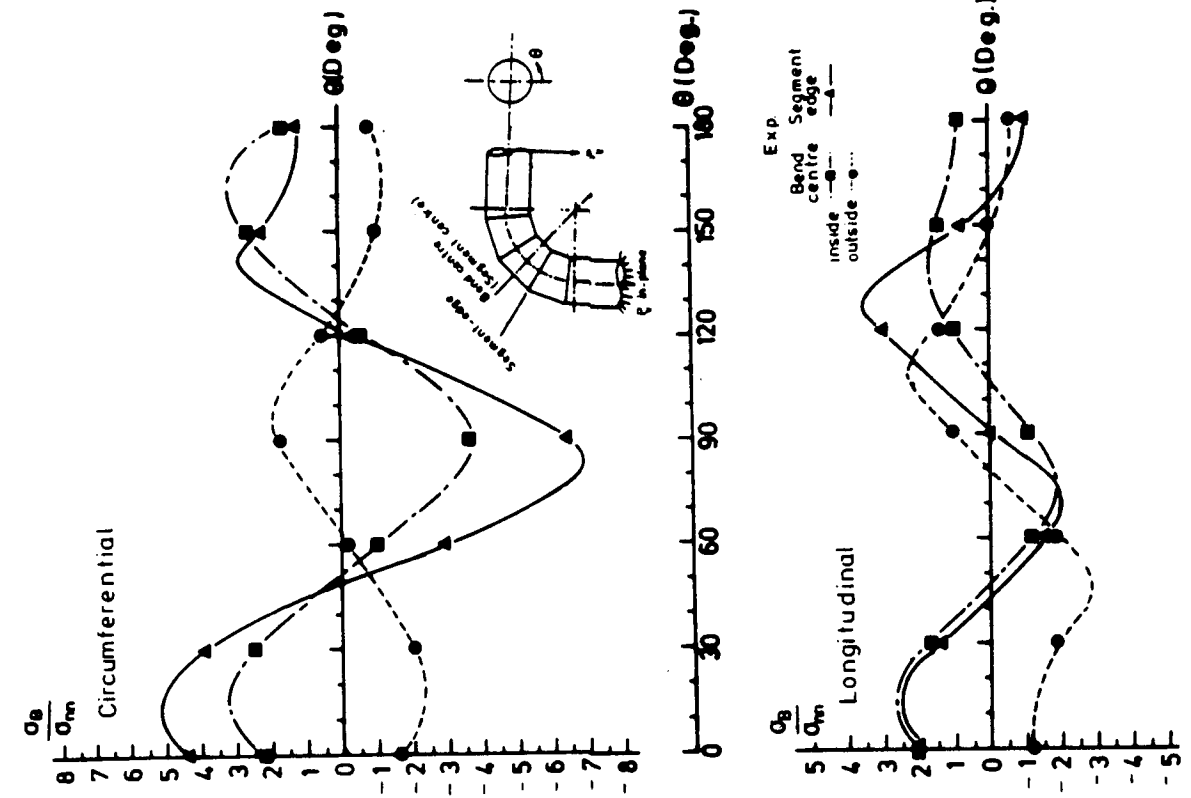


Figure (7.28) Stress distribution measured on bend S034 under in-plane/closing mode of loading. End load = 675N, $M_{B.C} = 8.21 \times 10^5 \text{ N.mm}$, $M_{B.J} = 8.49 \times 10^5 \text{ N.mm}$

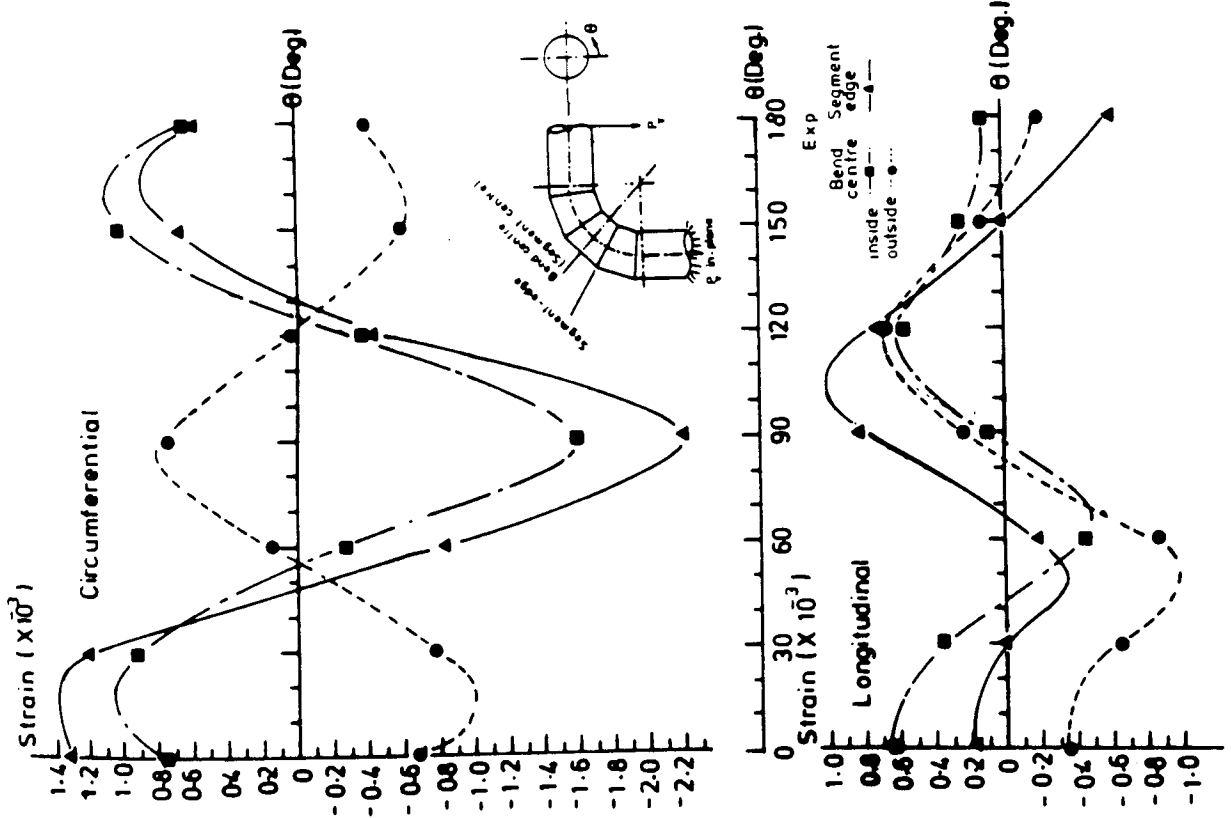


Figure (7.27) Strain distribution measured on bend S034 under in-plane/closing mode of loading. End load = 675N, $M_{B.C} = 8.21 \times 10^5 \text{ N.mm}$, $M_{B.J} = 8.49 \times 10^5 \text{ N.mm}$

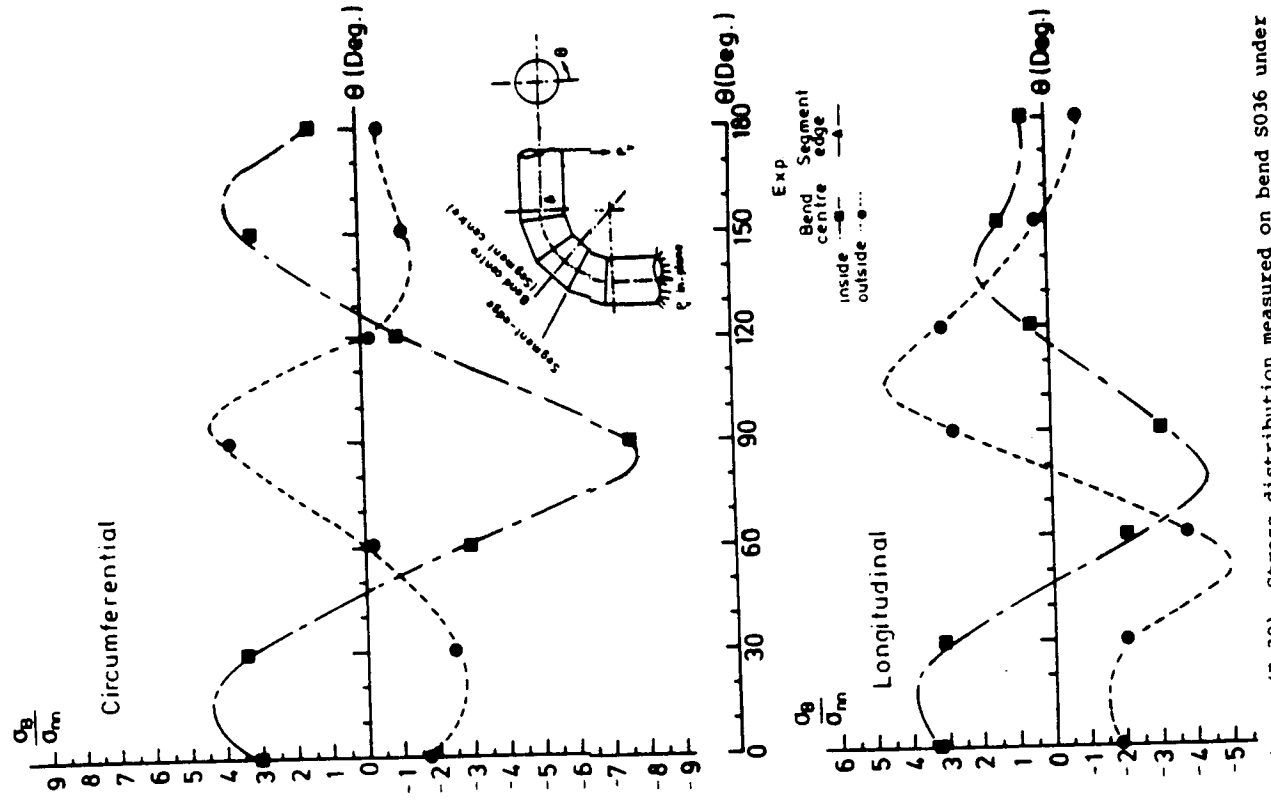


Figure (7.30) Stress distribution measured on bend S036 under in-plane/closing mode of loading. End load = 630N, $M_{B.C} = 7.18 \times 10^5 \text{ N.mm}$

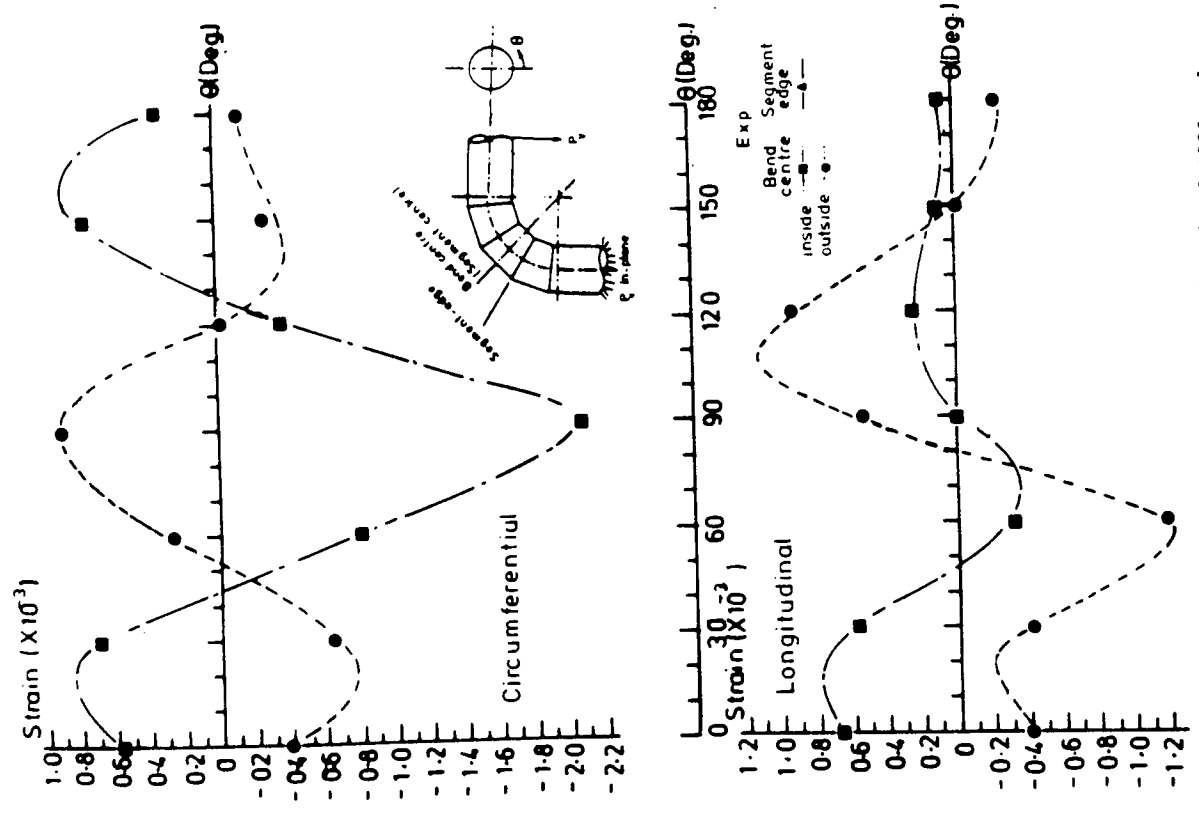


Figure (7.29) Strain distribution measured on bend S036 under in-plane/closing mode of loading. End load = 630N, $M_{B.C} = 7.18 \times 10^5 \text{ N.mm}$

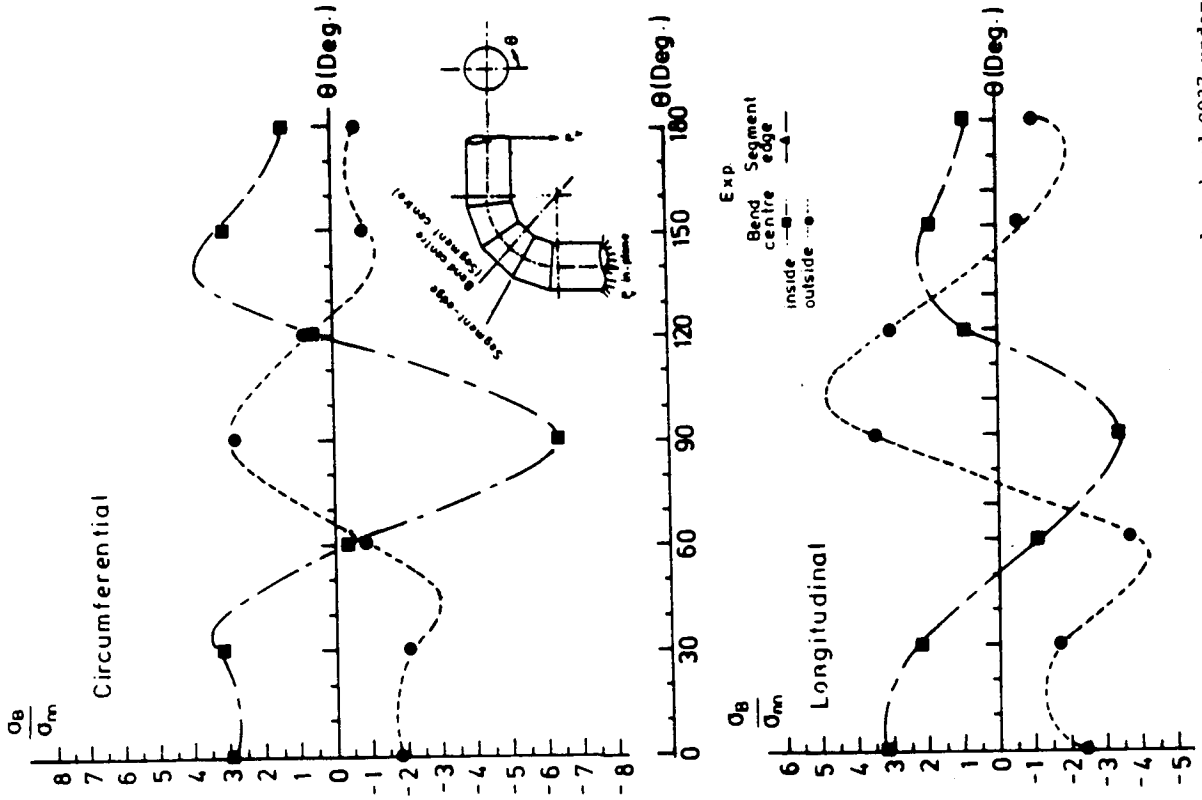


Figure (7.31) Strain distribution measured on bend S037 under in-plane/closing mode of loading. End load = 630N, $M_{B.C} = 7.18 \times 10^5 \text{ N.mm}$

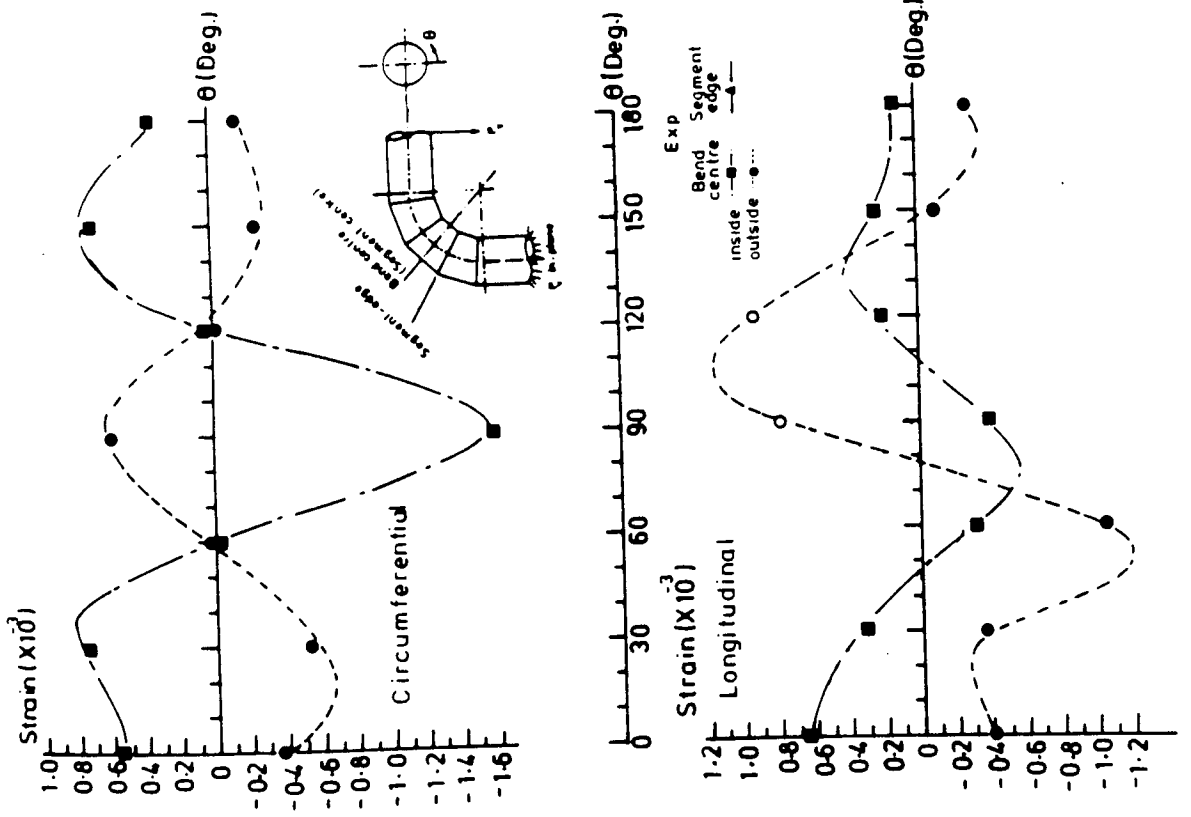


Figure (7.32) Stress distribution measured on bend S037 under in-plane/closing mode of loading. End load = 630N, $M_{B.C} = 7.18 \times 10^5 \text{ N.mm}$

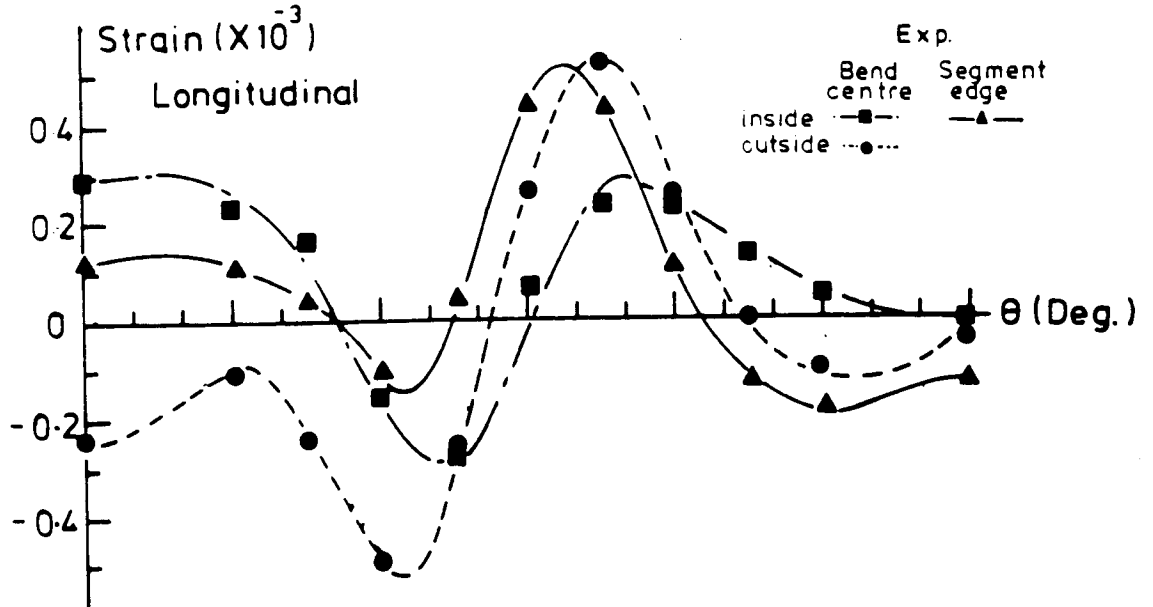
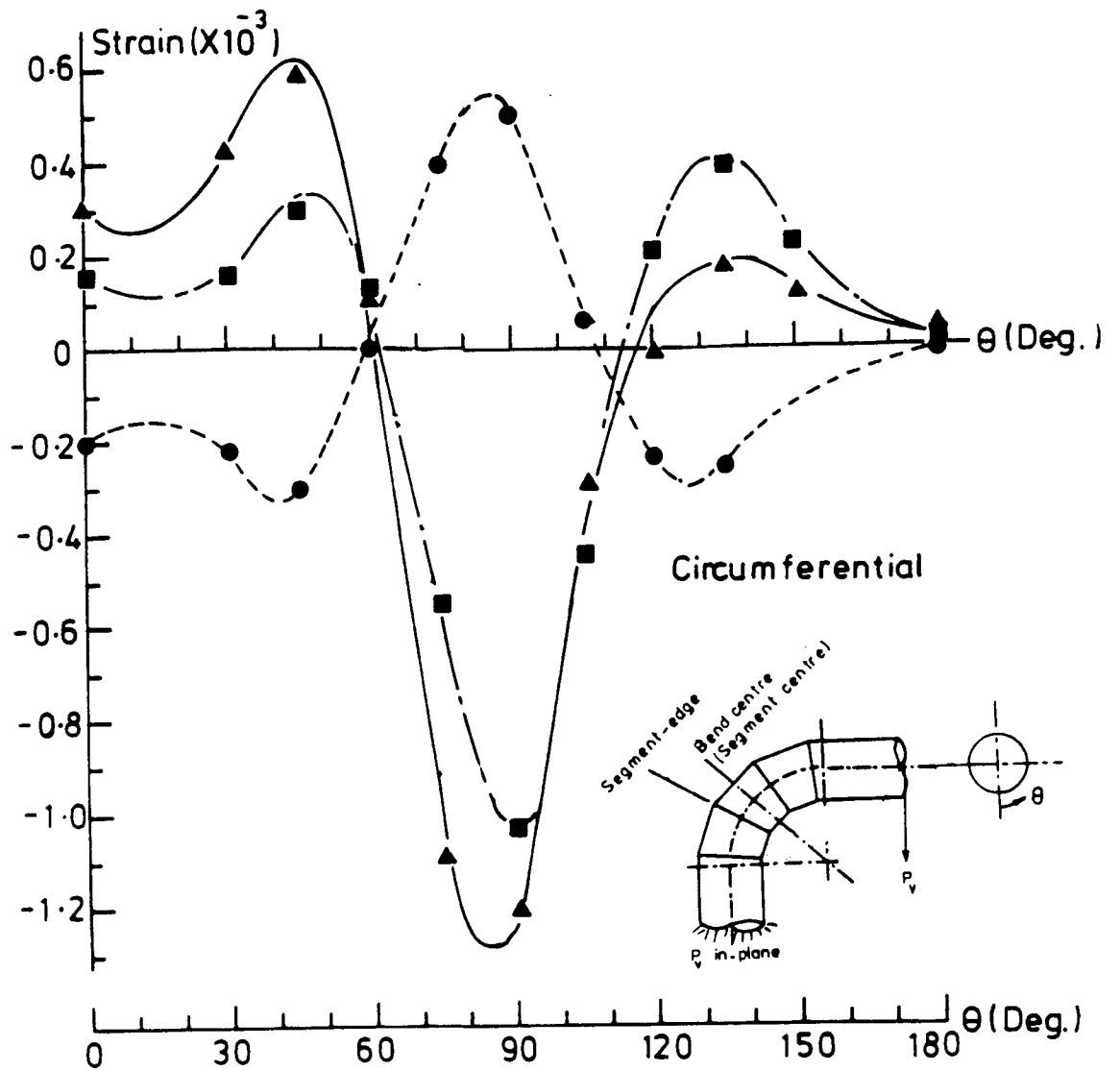


Figure (7.33) Strain distribution measured on bend S060 under in-plane/closing mode of loading. End load = 1454N, $M_{B.C} = 20.81 \times 10^5$ N.mm, $M_{B.J} = 22.06 \times 10^5$ N.mm

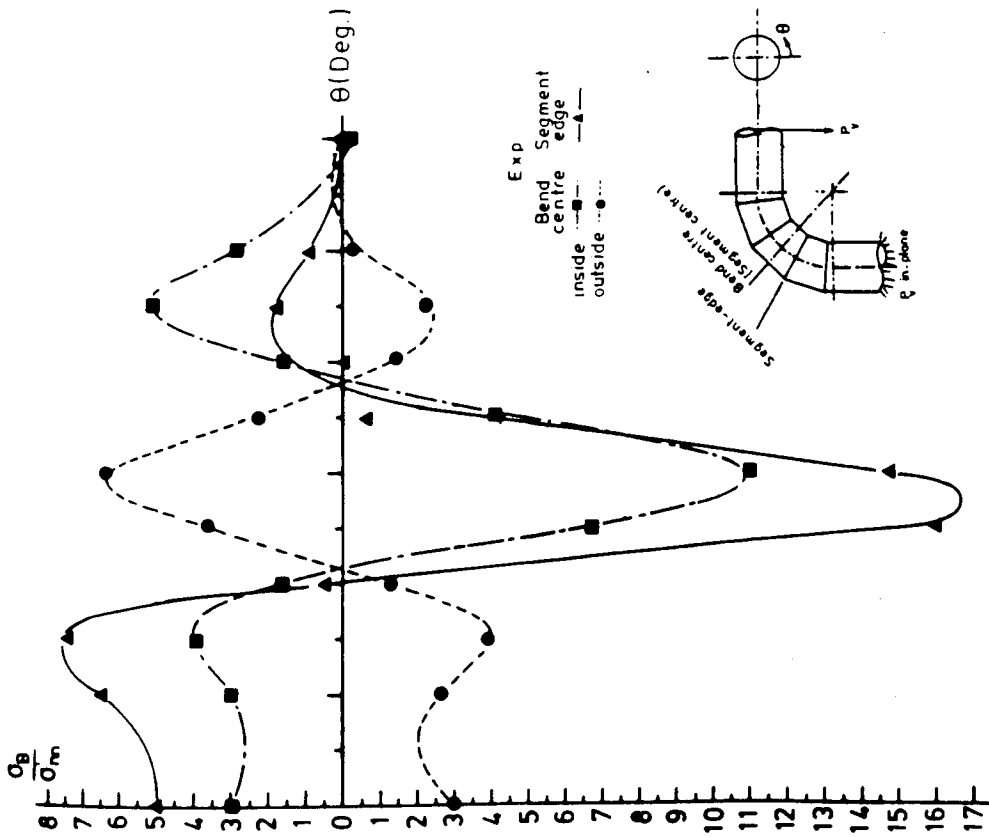


Figure (7.34a) Circumferential stress distribution measured on bend S060 under n-plane/closing mode of loading. End load = 1454N, $M_{B.C} = 20.81 \times 10^5 \text{ N.mm}$, $M_{B.J} = 22.06 \times 10^5 \text{ N.mm}$

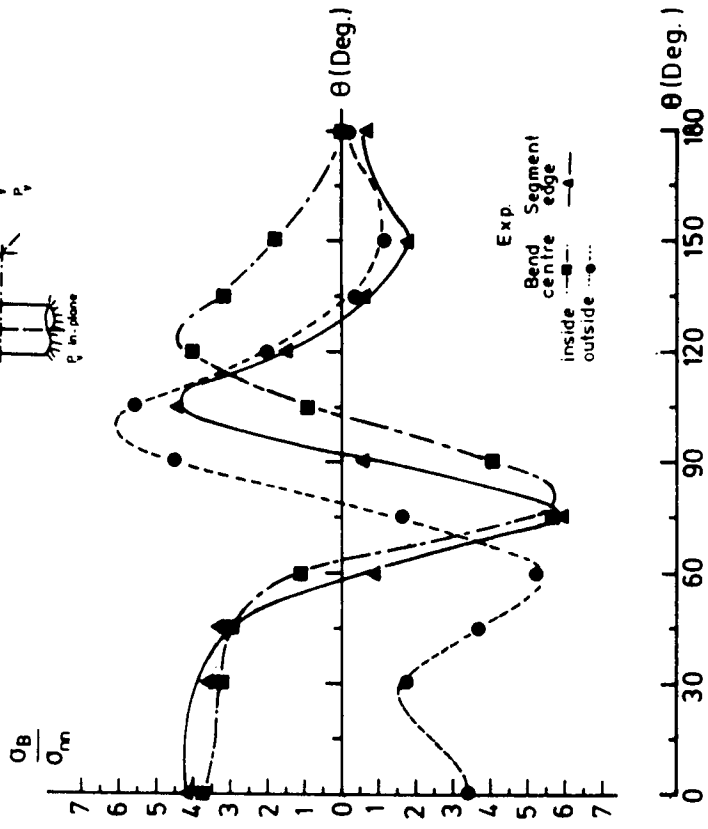


Figure (7.34b) Longitudinal stress distribution measured on bend S060 under in-plane/closing mode of loading. End load = 1454N, $M_{B.C} = 20.81 \times 10^5 \text{ N.mm}$, $M_{B.J} = 22.06 \times 10^5 \text{ N.mm}$

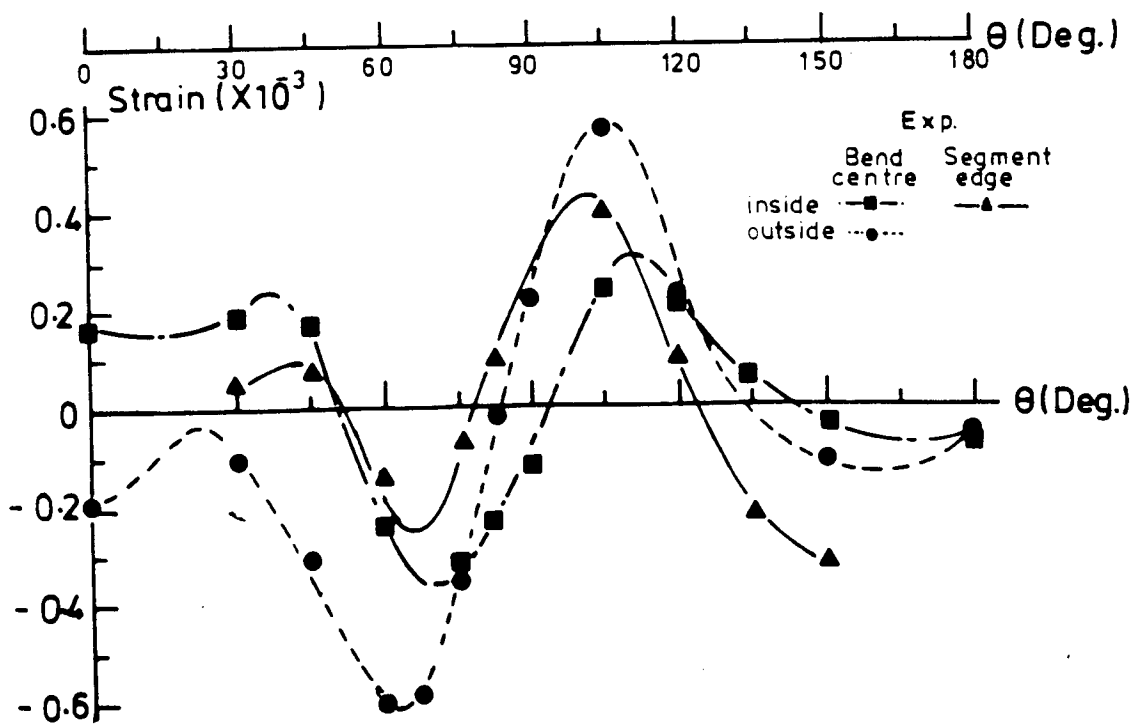
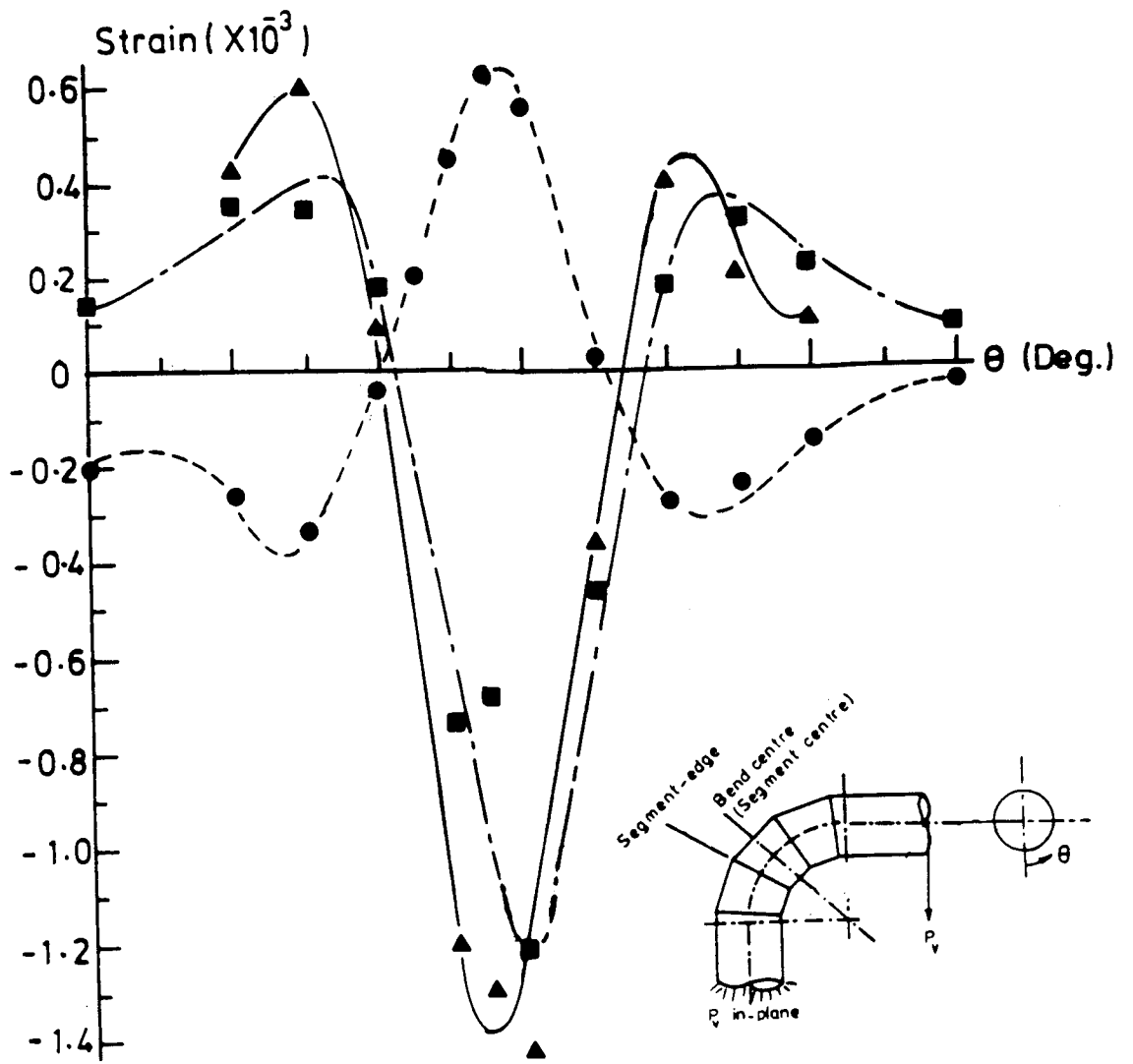


Figure (7.35) Strain distribution measured on bend S061 under in-plane/closing mode of loading. End load = 1454N, $M_{B.C} = 20.81 \times 10^5$ N.mm, $M_{B.J} = 22.06 \times 10^5$ N.mm

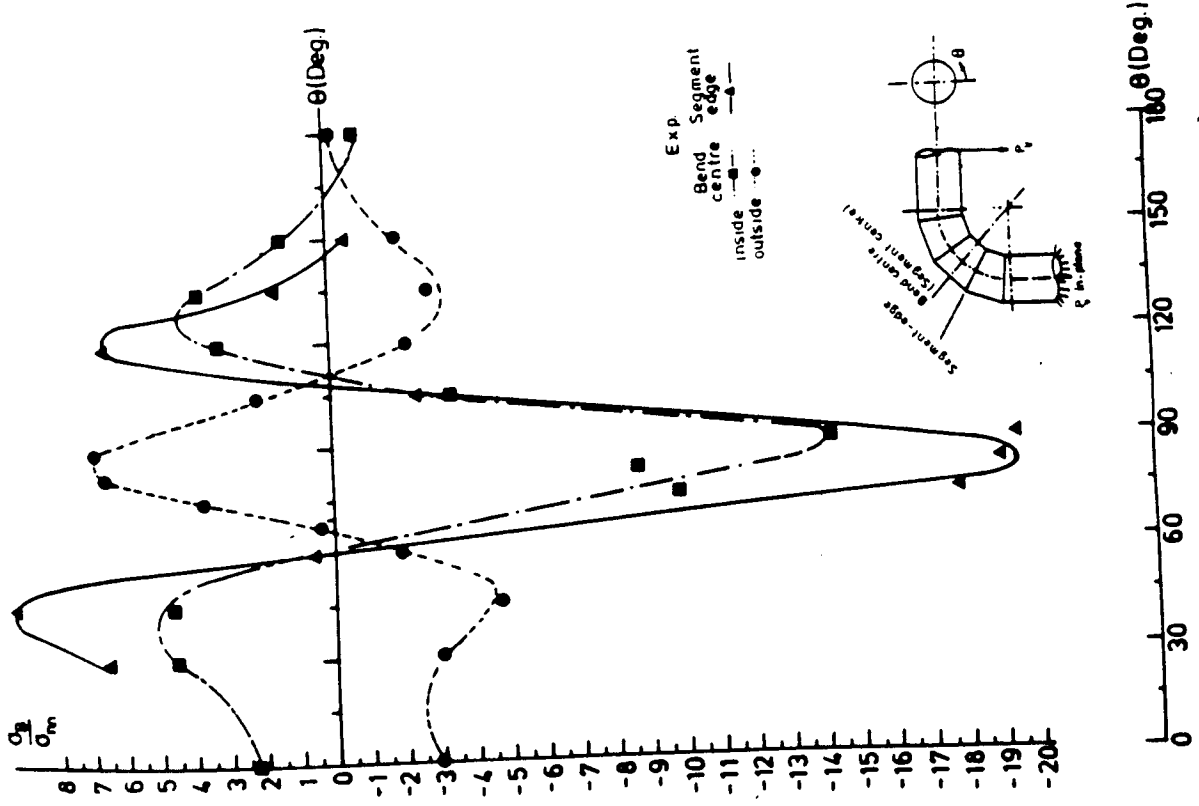


Figure (7.36a) Circumferential stress distribution measured on bend S061 under in-plane/closing mode of loading. End load = 1454N, $M_{B.C} = 20.8 \times 10^5$ N.mm, $M_{B.J} = 22.06 \times 10^5$ N.mm

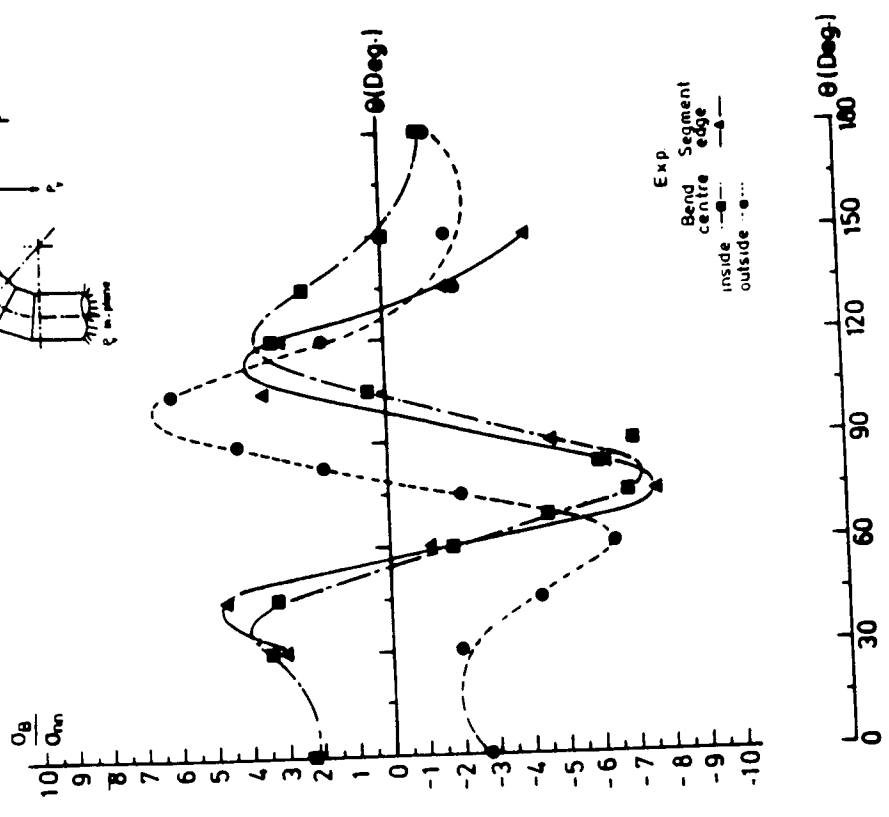


Figure (7.36b) Longitudinal stress distribution measured on bend S061 under in-plane/closing mode of loading. End load = 1454N, $M_{B.C} = 20.8 \times 10^5$ N.mm, $M_{B.J} = 22.06 \times 10^5$ N.mm

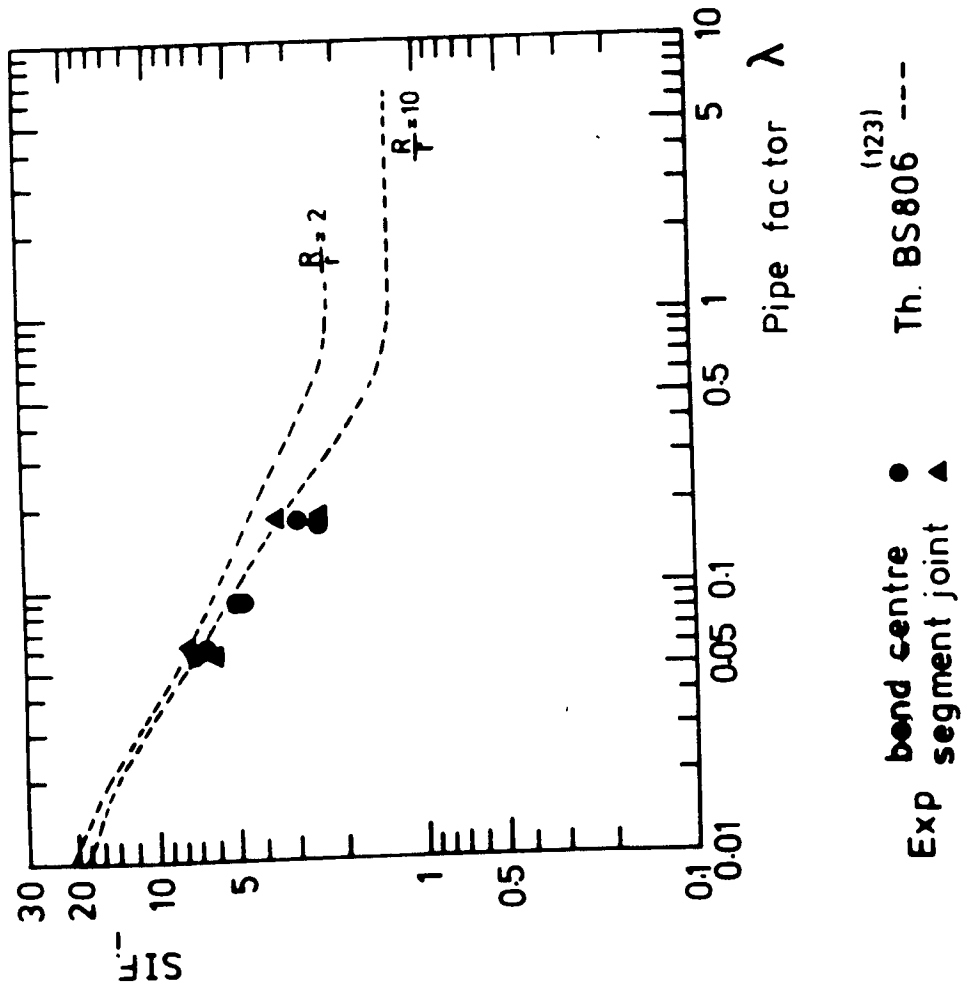


Figure (7.37) Maximum in-plane longitudinal stress intensification factors ($SIF_{i,L}$) of mitred CSM/PVC lined bends

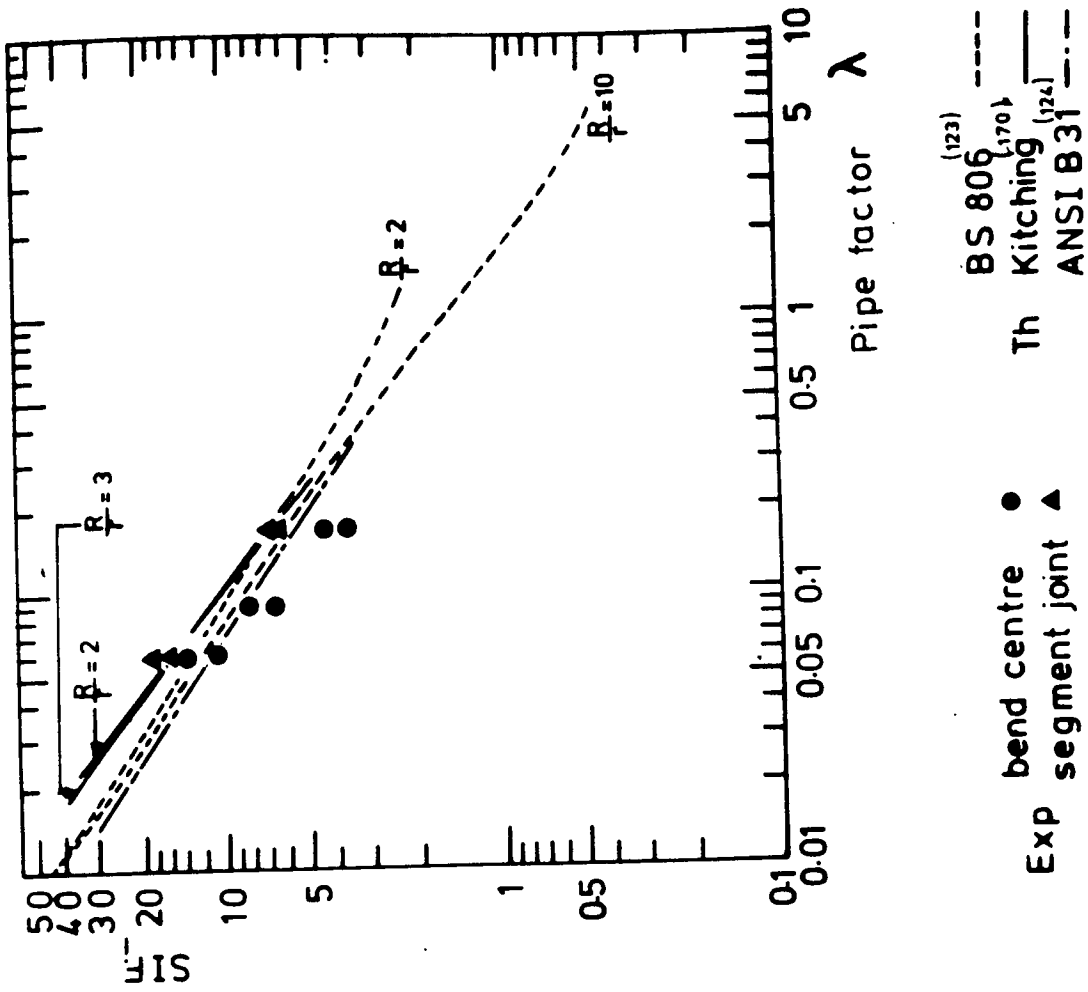


Figure (7.38) Maximum in-plane circumferential stress intensification factors of mitred CSM/PVC lined bends

TABLE 7.14 - In-plane Stress Intensification Factors (SIF) experimentally determined for Mitred CSM/PVC Lined Bends

| Bend No. | Bore (mm) | $\frac{r_i}{R}$ | λ_e | Experimental | | | | | | Theoretical | | | |
|----------|-----------|-----------------|-------------|-----------------------------|-----------------------------|-----------------------------|-----------------------------|-----------------------------|------------------------------|-----------------|--------------|------------------|-------------------|
| | | | | Segment-edge | | Segment-centre | | | | BS 806 (123) | | 2X (124) ANSI | (170) Kitching |
| | | | | Circumferential | Longitudinal | Circumferential | | Longitudinal | | Circumferential | Longitudinal | | |
| | | | | | | Inside | Outside | Inside | Outside | | | | |
| S033 | 195 | 1/3 | 0.177 | 6.5 $\theta = 85^\circ$ | 2.5 $\theta = 0^\circ$ | 4.5 $\theta = 95^\circ$ | 2.0 $\theta = 95^\circ$ | 2.5 $\theta = 45^\circ$ | 2.0 $\theta = 90^\circ$ | 6.3 | 3.7 | 5.71 | 6.91 |
| S034 | 195 | 1/3 | 0.177 | 6.9 $\theta = 85^\circ$ | 3.5 $\theta = 125^\circ$ | 3.7 $\theta = 90^\circ$ | 1.9 $\theta = 95^\circ$ | 2.5 $\theta = 25^\circ$ | 2.9 $\theta = 45^\circ$ | 6.3 | 3.7 | 5.71 | 6.91 |
| S036 | 244 | 1/2 | 0.087 | - | - | 8.2 $\theta = 85^\circ$ | 4.30 $\theta = 95^\circ$ | 4.4 $\theta = 75^\circ$ | 5.0 $\theta = 50^\circ$ | 10.5 | 6.3 | 9.17 | 11.71 |
| S037 | 244 | 1/2 | 0.087 | - | - | 6.50 $\theta = 90^\circ$ | 2.80 $\theta = 90^\circ$ | 3.4 $\theta = 90^\circ$ | 4.8 $\theta = 100^\circ$ | 10.5 | 6.3 | 9.17 | 11.71 |
| S060 | 589 | 1/2 | 0.061 | 16.5 $\theta = 80^\circ$ | 6.0 $\theta = 75^\circ$ | 11.0 $\theta = 90^\circ$ | 6.50 $\theta = 90^\circ$ | 6.0 $\theta = 80^\circ$ | 6.10 $\theta = 100^\circ$ | 13.0 | 7.7 | 11.62 | 15.91 |
| S061 | 589 | 1/2 | 0.061 | 19.0 $\theta = 83^\circ$ | 7.7 $\theta = 78^\circ$ | 14.0 $\theta = 90^\circ$ | 7.20 $\theta = 87^\circ$ | 7.40 $\theta = 80^\circ$ | 6.70 $\theta = 100^\circ$ | 13.0 | 7.7 | 11.62 | 15.91 |

theoretical work carried out by Kitching and Bond⁽¹⁷⁰⁾, the maximum longitudinal stress is located on the outside surface at the segment-edge position and it is approximately equal in magnitude to the maximum circumferential stress. All the bends investigated in the present programme do not have strain gauges located on the outside of the segment-edge position.

The maximum-minimum peak stress ratios (i.e. SIF) obtained for the different angular displacement of the bends on the inside and on the outside surfaces, are summarised in Table 7.14, and compared with theoretical prediction of unlined CSM bends using smooth and mitred bend theory and specifications. The maximum absolute SIF values obtained from Table 7.14 are presented diagrammatically in Figs. 7.37 and 7.38 for the longitudinal direction and the circumferential direction respectively.

7.5.4.2 Out-of-plane stress ratio distribution and stress intensification factors (SIF_o)

The experimentally measured strain distribution and the experimentally measured stress ratio distribution at the segment-centre and at the segment-edge are present successively in Figs. 7.39-7.50 as a function of their angular position starting from the intrados and terminating at the extrados over the 180° of the bend perimeter.

The strain/stress behaviour of all the bends could be described and presented as the following:

- (a) The maximum measured strains and stresses are located at an angular position of 50°-70° for all mitre bends in the circumferential direction situated at the segment-edge, as shown, e.g. in Figs. 7.39b and 7.40b for the 200mm nominal bore bends and in Figs. 7.49b and 7.50b for the 600mm nominal bore bends.

- (b) Circumferential strain and stress ratio distribution measured at the inside surface of the segment-edge show two peaks located at an angular positions of $\theta = 70^\circ$ and $\theta = 110^\circ$, e.g. Fig. 7.48b. For all the mitred bends tested, the absolute value of the peak situated nearer to the intrados (i.e. $\theta = 70^\circ$) is greater than the absolute value of the peak situated nearer to the extrados (i.e. $\theta = 110^\circ$). The corresponding peaks observed on the segment-centre have comparable magnitudes of their absolute values. Such pattern of peak stresses could be also observed on test results presented for metallic mitred bends^(166,174). In bend areas where such maximum local bending were to occur, radial stress will occur with accordance to theory of bending of thick curved beams⁽³⁰⁾.
- (c) The maximum longitudinal measured strain is located at the outside surface of the segment-centre, whilst the maximum longitudinal stress ratio can be either on the inside or the outside surface, and its value is comparable with BS806⁽¹²³⁾ prediction. With accordance to Kitching's work⁽¹⁷²⁾, the maximum longitudinal stress is located on the outside surface of the segment-edge and is comparable in value with the maximum circumferential stress. For all the bends tested, no strain gauges were situated at the outside surface of the segment-edge position.

The maximum-minimum longitudinal and circumferential stress ratio peaks (i.e. SIF) are summarised in Table 7.15 with their corresponding angular position. They are compared with BS806 specifications⁽¹²³⁾, ANSI B.31⁽¹²⁴⁾ specifications, and Kitching and Bond⁽¹⁷⁰⁾ theoretical predictions. The maximum experimental SIF are also presented diagrammatically as shown in Figs. 7.51 and 7.52 for the longitudinal and the circumferential directions respectively.

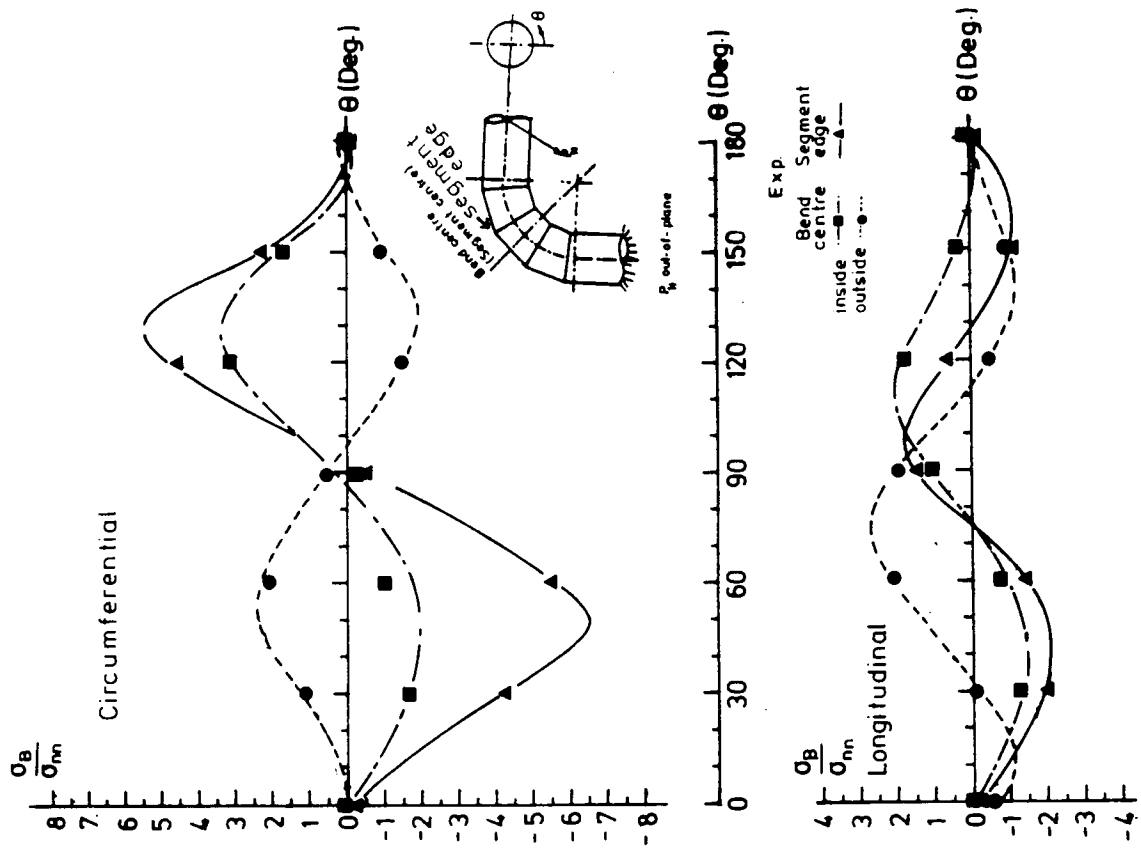


Figure (7.39) Strain distribution measured on bend S033 under out-of-plane mode of loading. End load = 675N, $M_{B,C} = 6.23 \times 10^5$ N.mm, $M_{B,J} = 6.81 \times 10^5$ N.mm

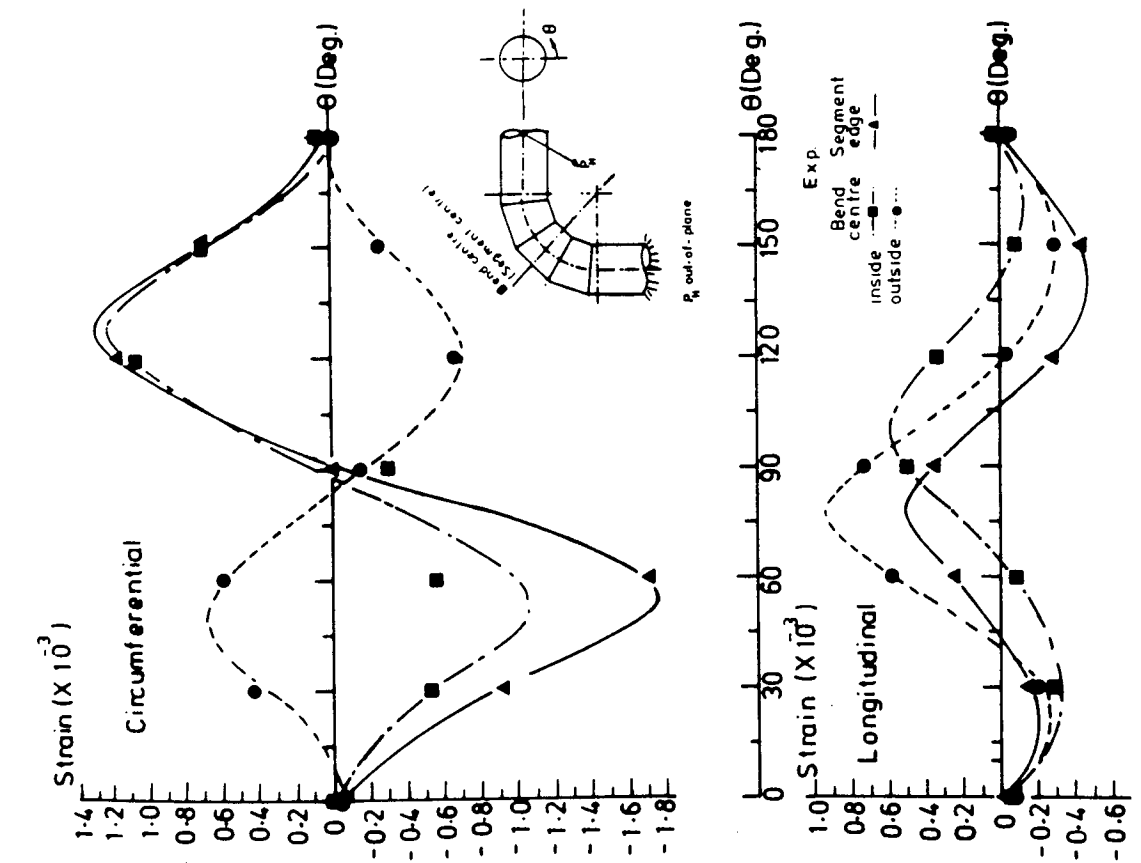


Figure (7.40) Stress distribution measured on bend S033 under out-of-plane mode of loading. End load = 675N, $M_{B,C} = 6.23 \times 10^5$ N.mm, $M_{B,J} = 6.81 \times 10^5$ N.mm

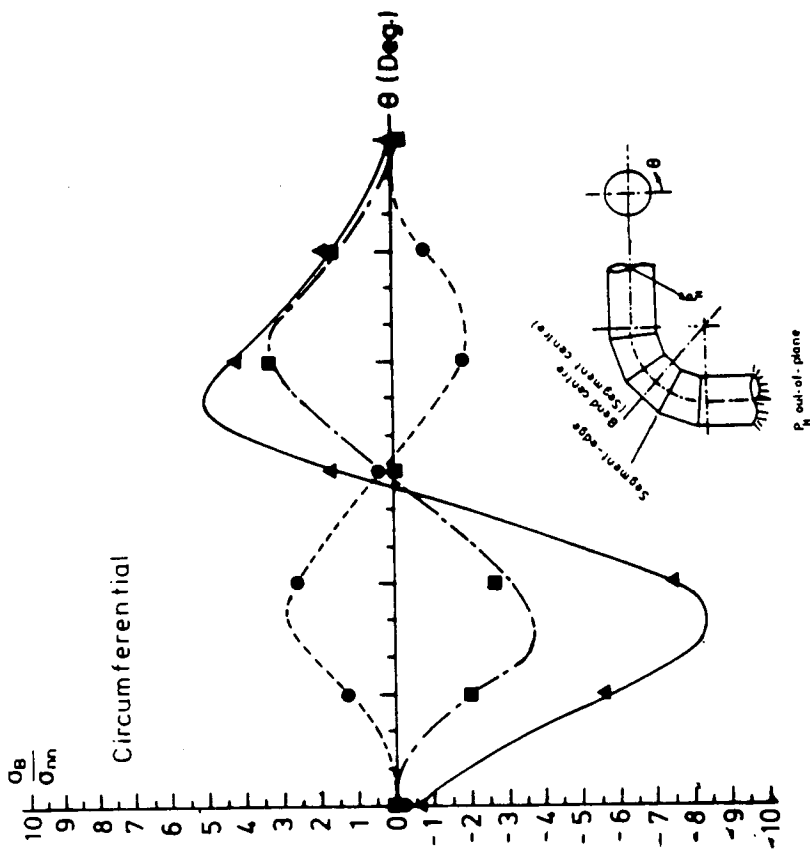


Figure (7.41) Strain distribution measured on bend S034 under out-of-plane mode of loading. End load = 675N, $M_{B.C} = 6.23 \times 10^5$ N.mm, $M_{B.J} = 5.33 \times 10^5$ N.mm

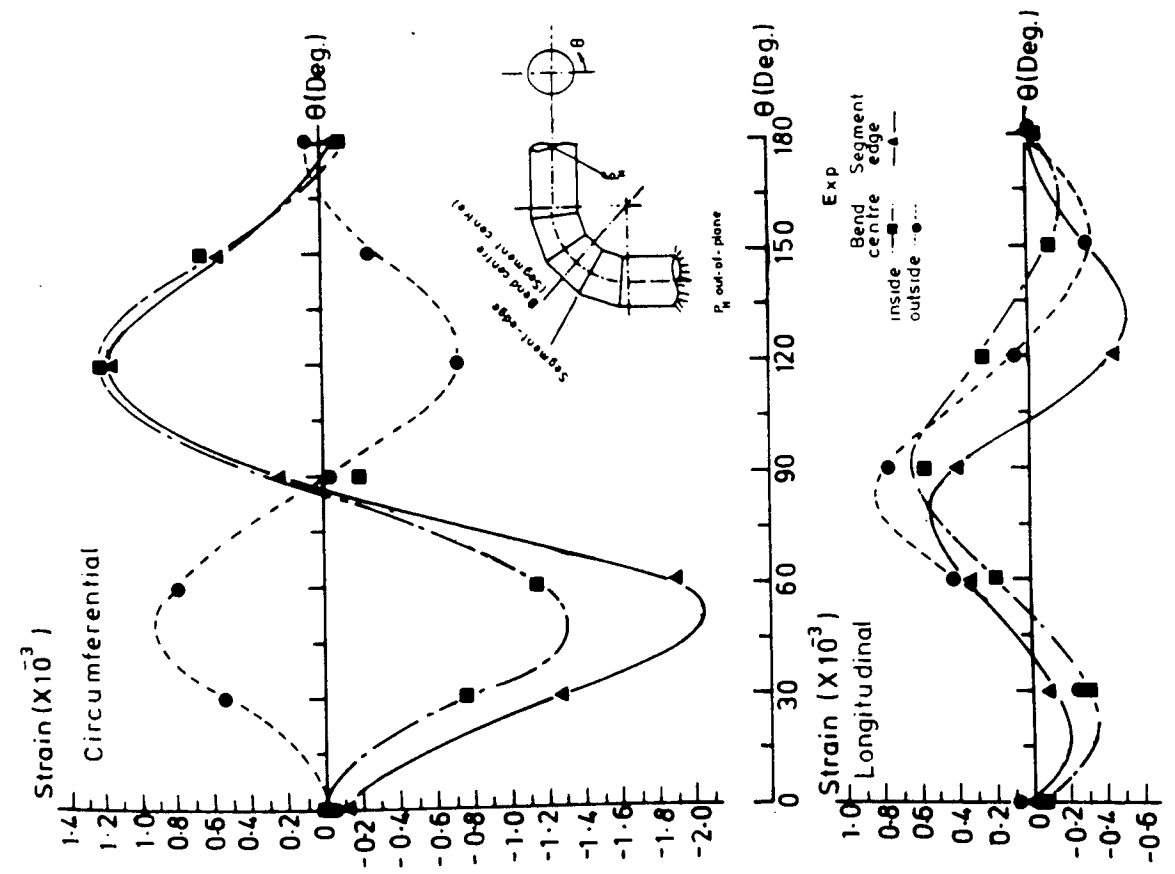


Figure (7.42) Stress distribution measured on bend S034 under out-of-plane mode of loading. End load = 675N, $M_{B.C} = 6.23 \times 10^5$ N.mm, $M_{B.J} = 5.33 \times 10^5$ N.mm

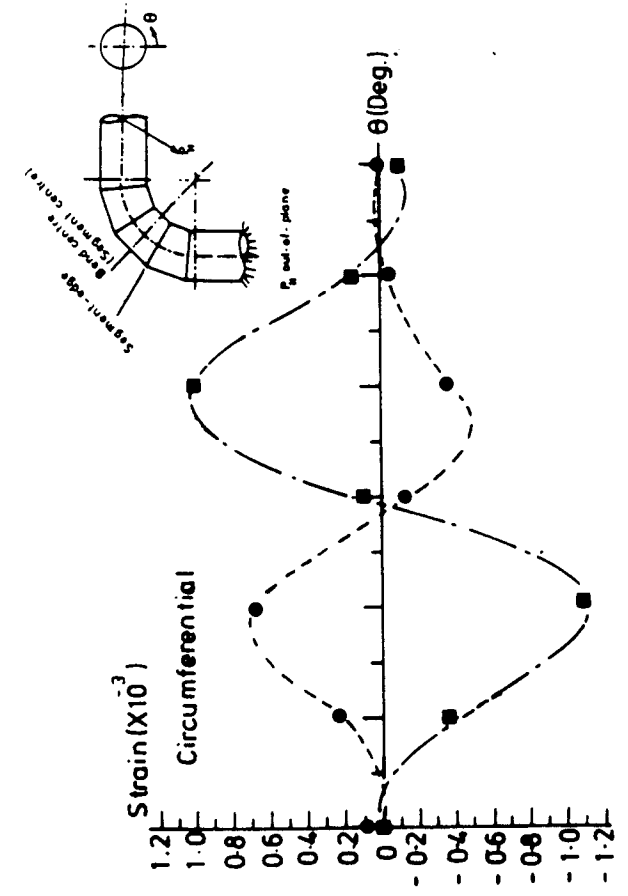


Figure (7.43) Strain distribution measured on bend S036 under out-of-plane mode of loading. End load = 630N, $M_{B.C} = 5.57 \times 10^5 \text{ N.mm}$

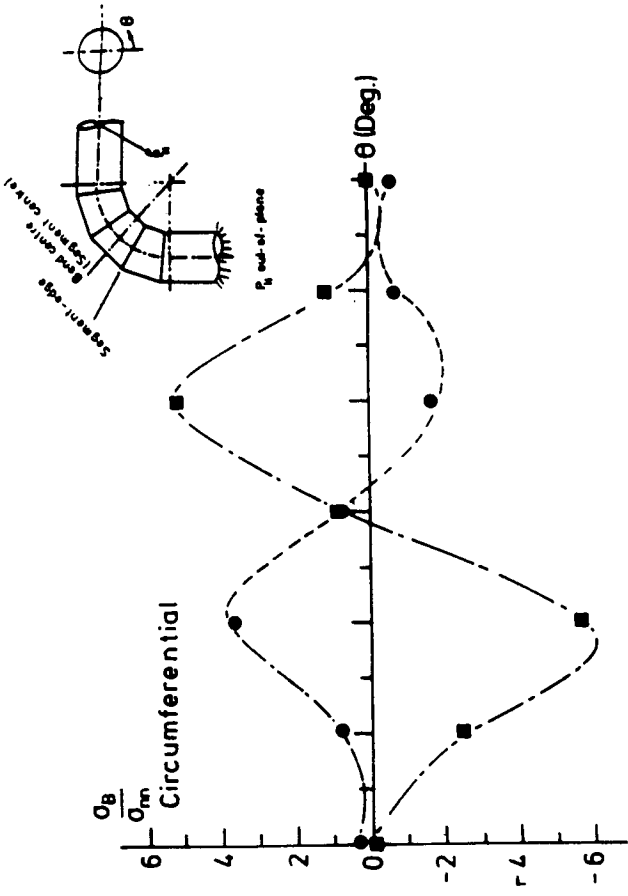


Figure (7.44) Stress distribution measured on bend S036 under out-of-plane mode of loading. End load = 630N, $M_{B.C} = 5.57 \times 10^5 \text{ N.mm}$

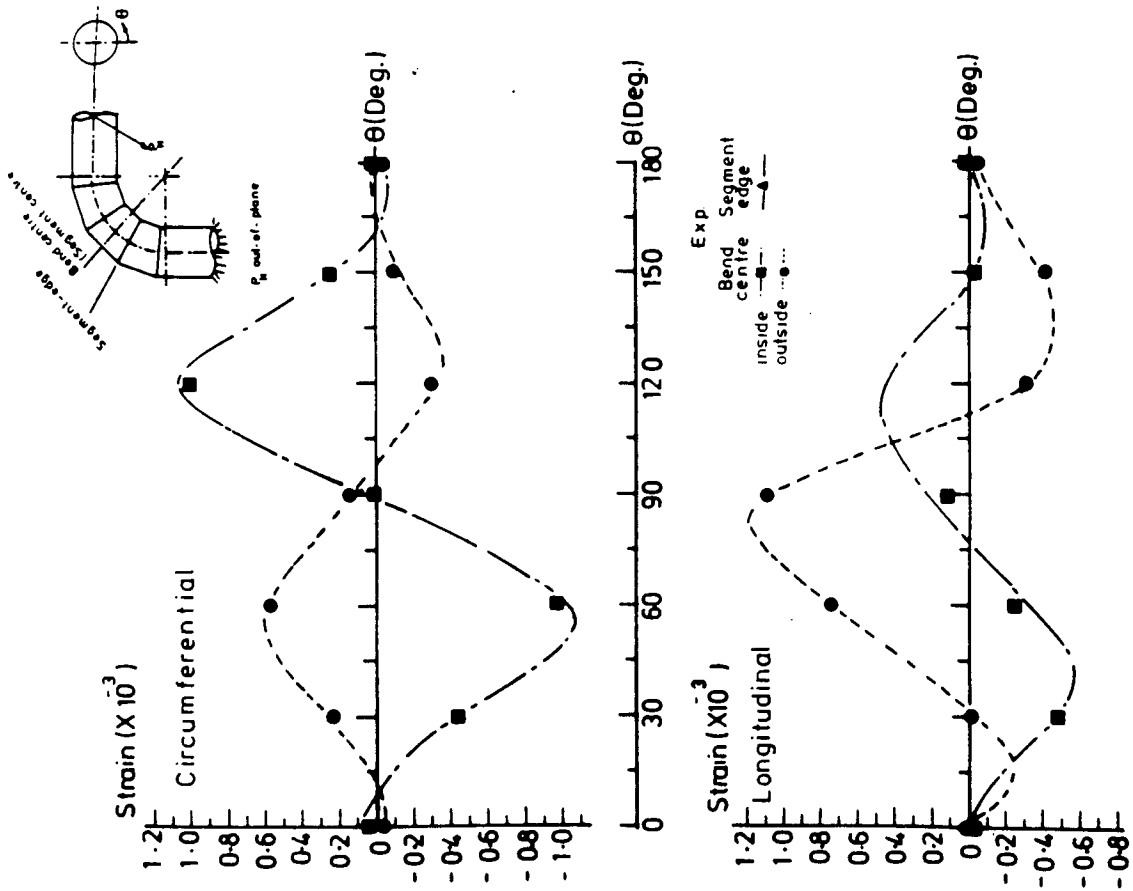


Figure (7.45) Strain distribution measured on bend S037 under out-of-plane mode of loading. End load = 630N, $M_{B,C} = 5.57 \times 10^5 \text{ N.mm}$

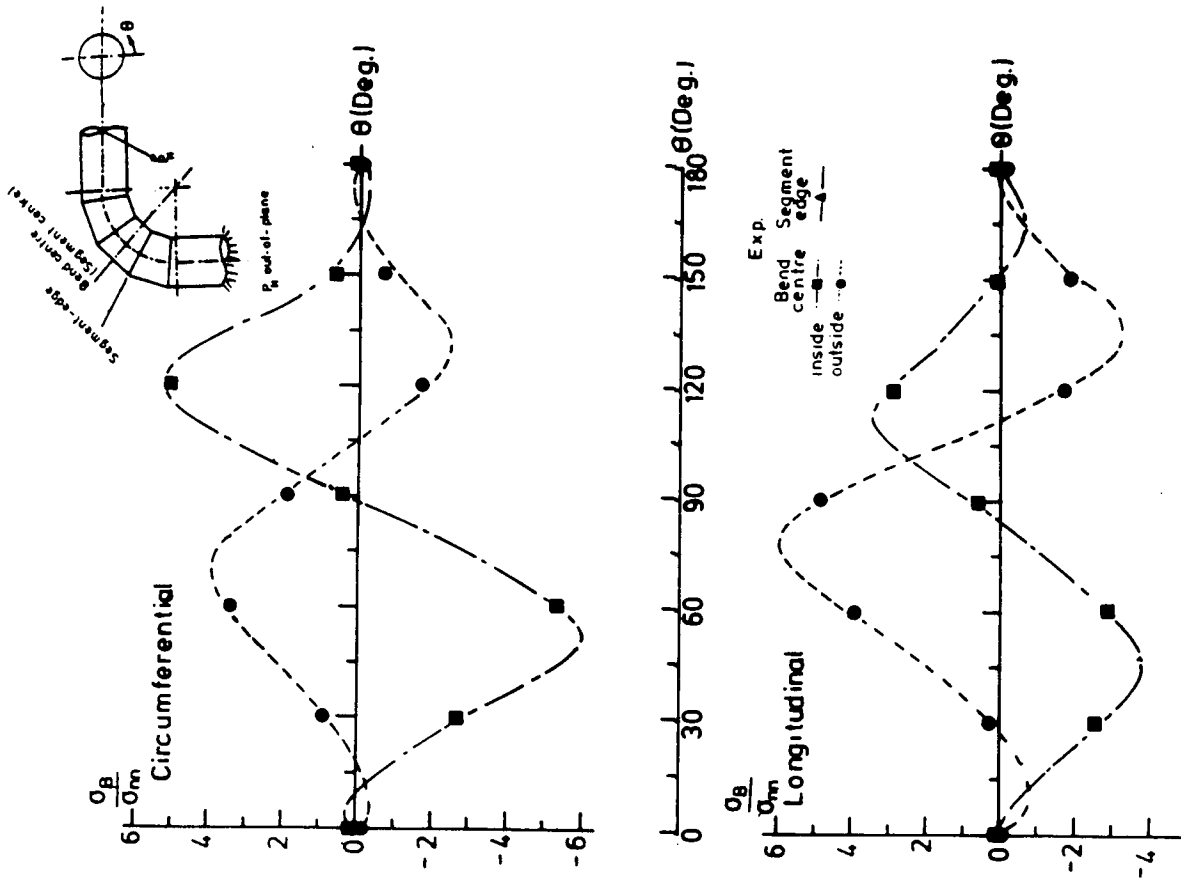


Figure (7.46) Stress distribution measured on bend S037 under out-of-plane mode of loading. End load = 630N, $M_{B,C} = 5.57 \times 10^5 \text{ N.mm}$

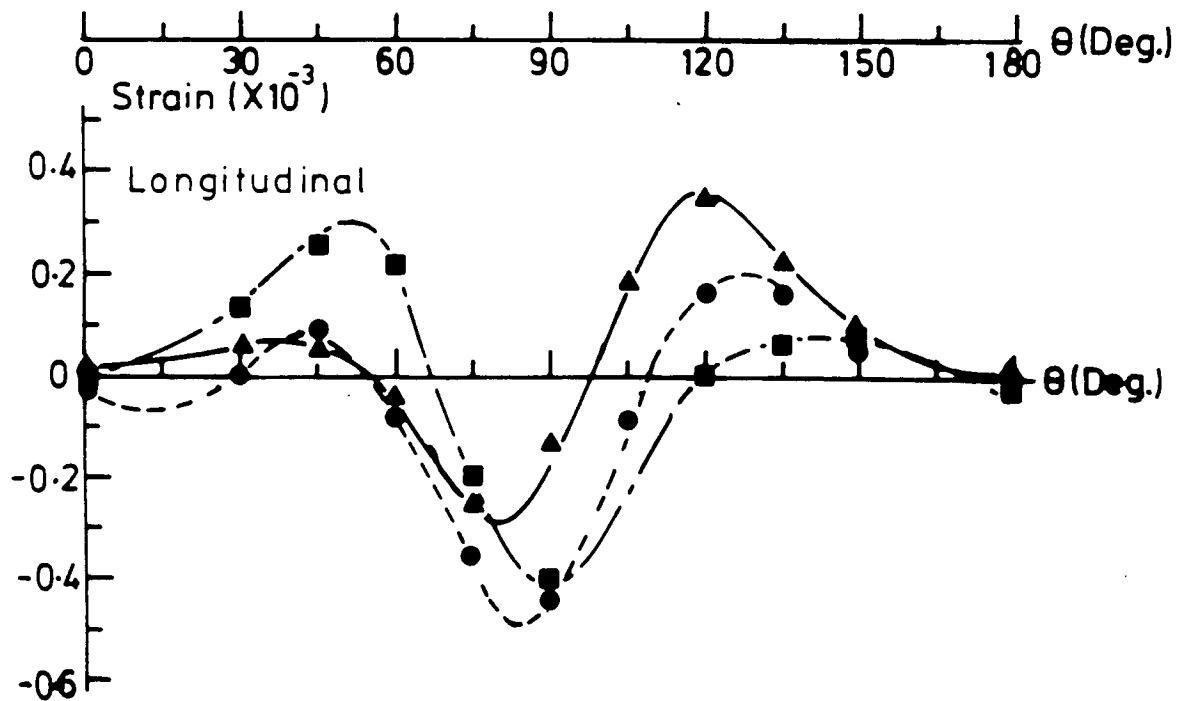
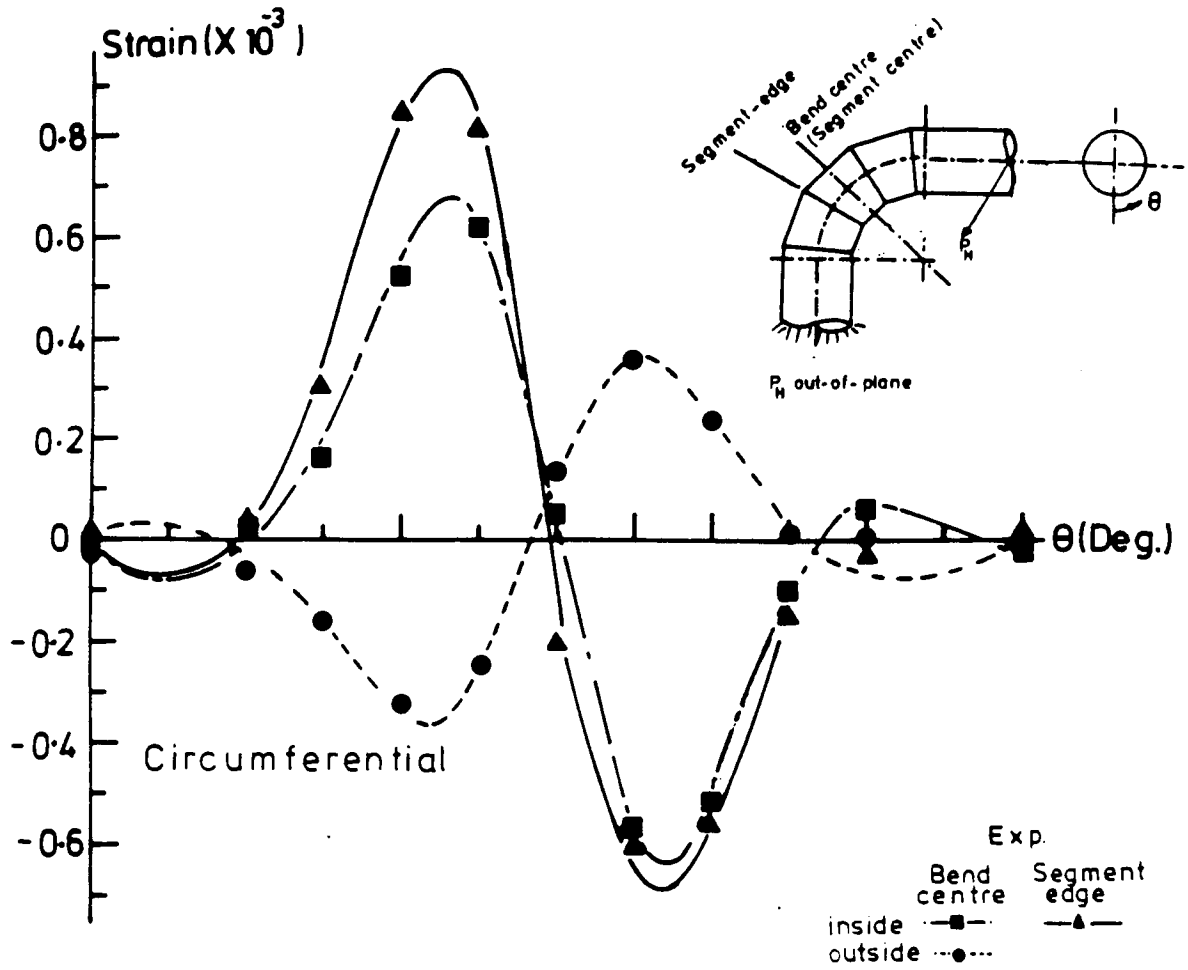


Figure (7.47) Strain distribution measured on bend S060 under out-of-plane mode of loading. End load = 1454 N, $M_{B.C} = 16.6 \times 10^5$ N.mm, $M_{B.J} = 15.2 \times 10^5$ N.mm

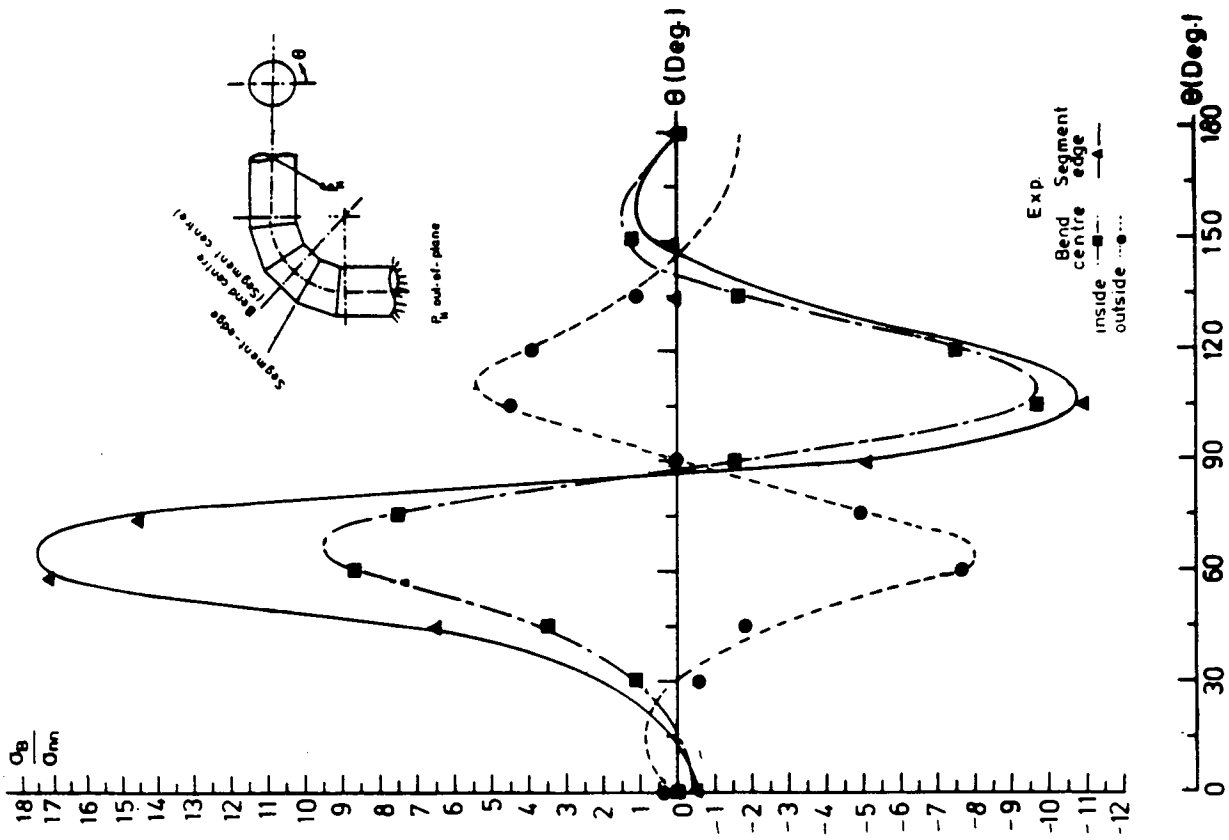


Figure (7.48b) Circumferential stress distribution measured on bend S060 under out-of-plane mode of loading. End load = 1454 N, $M_{B,C} = 16.6 \times 10^5$ N mm, $M_{B,J} = 15.2 \times 10^5$ N mm

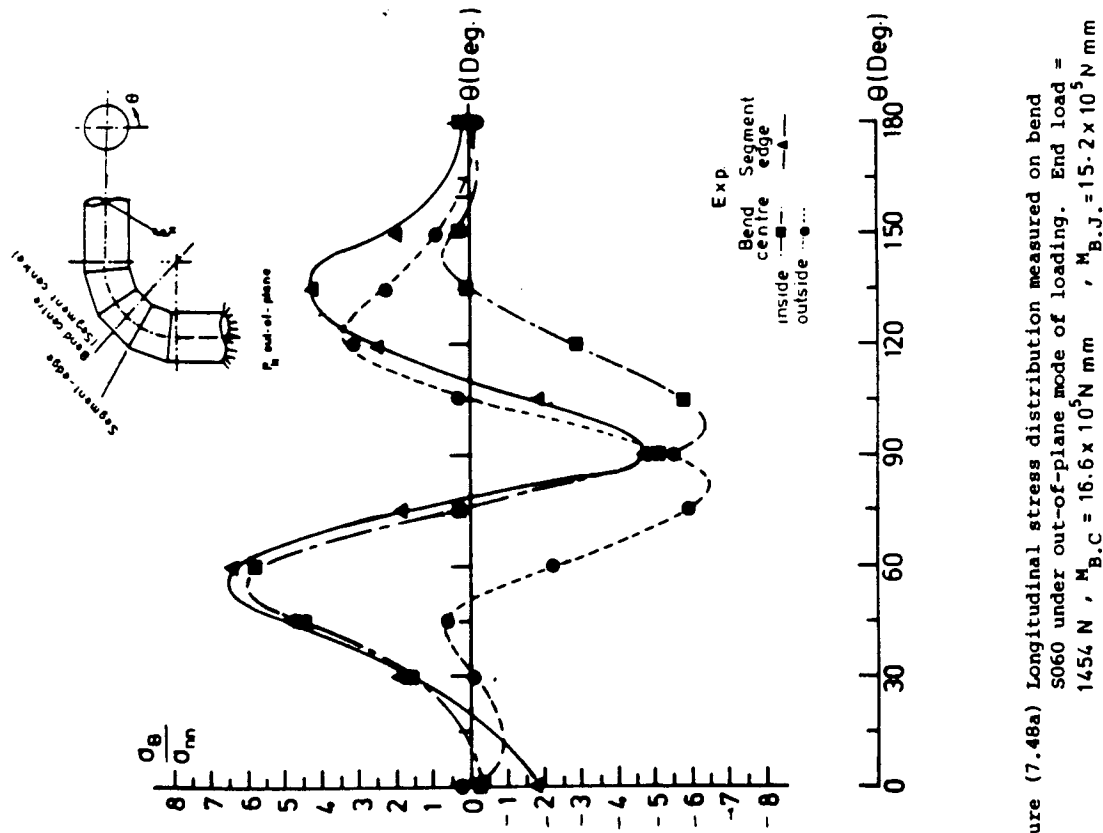


Figure (7.48a) Longitudinal stress distribution measured on bend S060 under out-of-plane mode of loading. End load = 1454 N, $M_{B,C} = 16.6 \times 10^5$ N mm, $M_{B,J} = 15.2 \times 10^5$ N mm

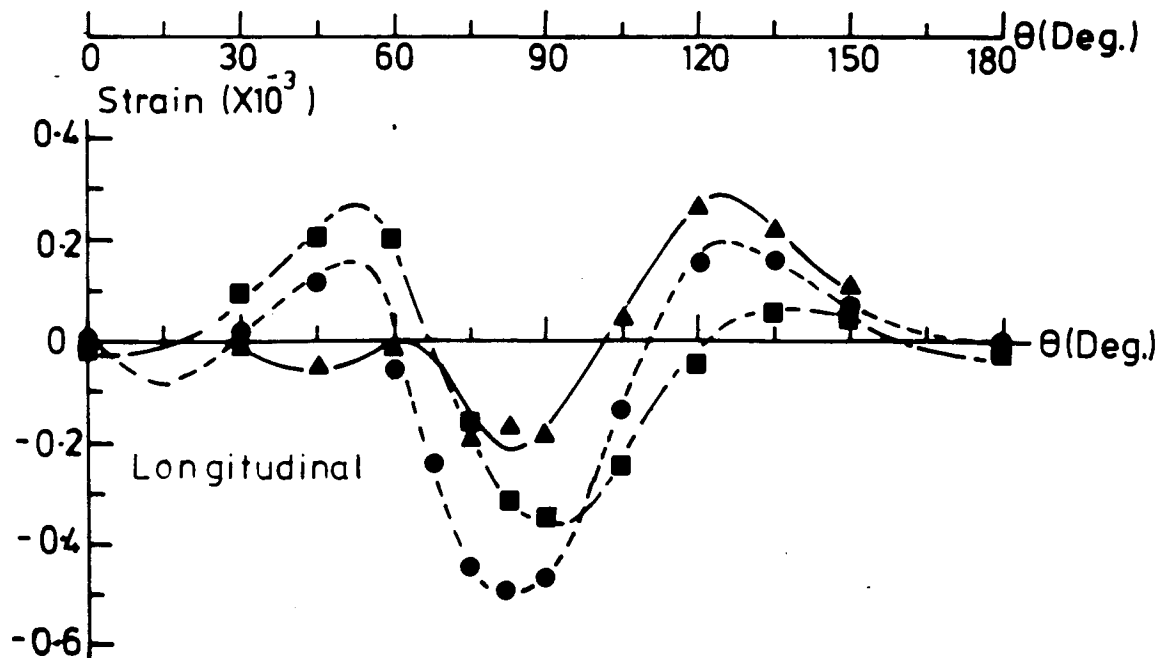
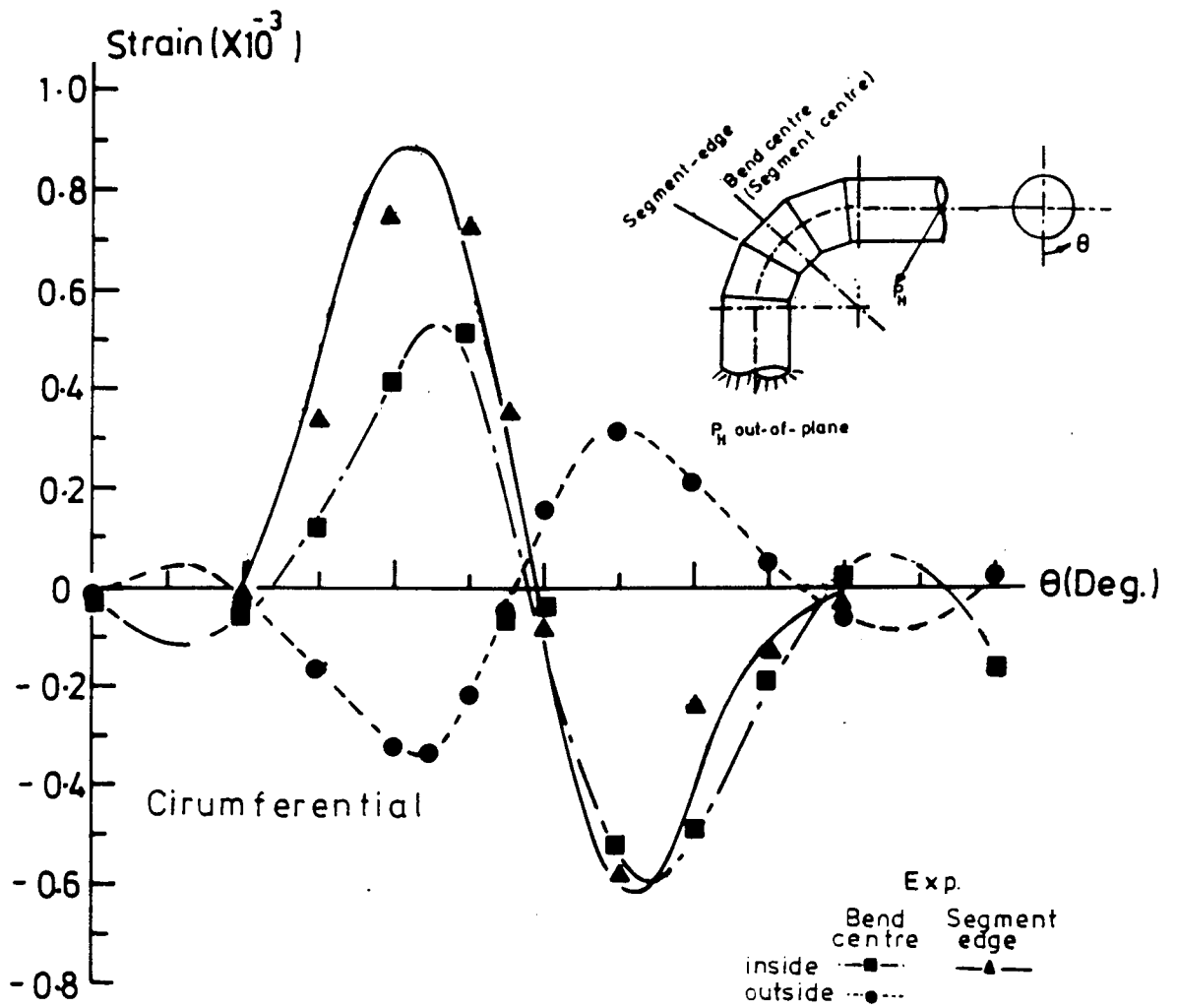


Figure (7.49) Strain distribution measured on bend S061 under out-of-plane mode of loading. End load = 1454 N
 $M_{B.C} = 16.6 \times 10^5$ N-mm , $M_{B.J} = 15.2 \times 10^5$ N-mm

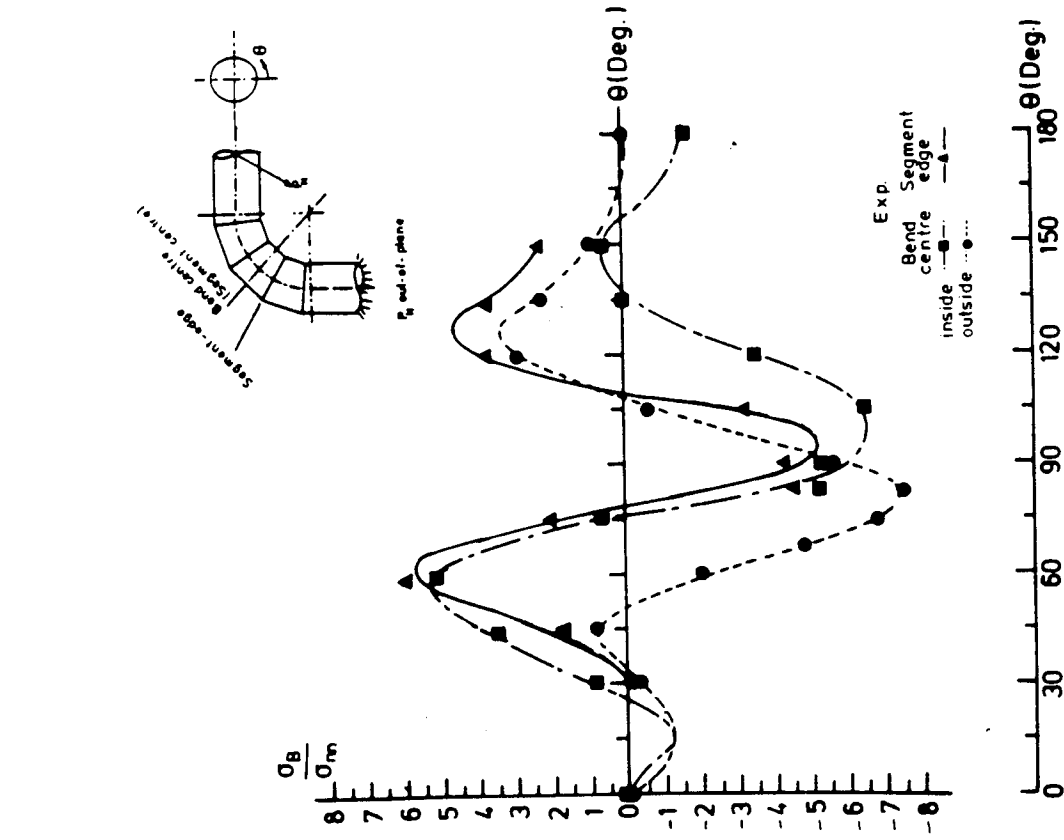


Figure (7.50a) Longitudinal stress distribution measured on bend S061 under out-of-plane mode of loading. End load = 1454 N, $M_{B.C} = 16.6 \times 10^3$ N mm, $M_{B.J} = 15.2 \times 10$ N mm

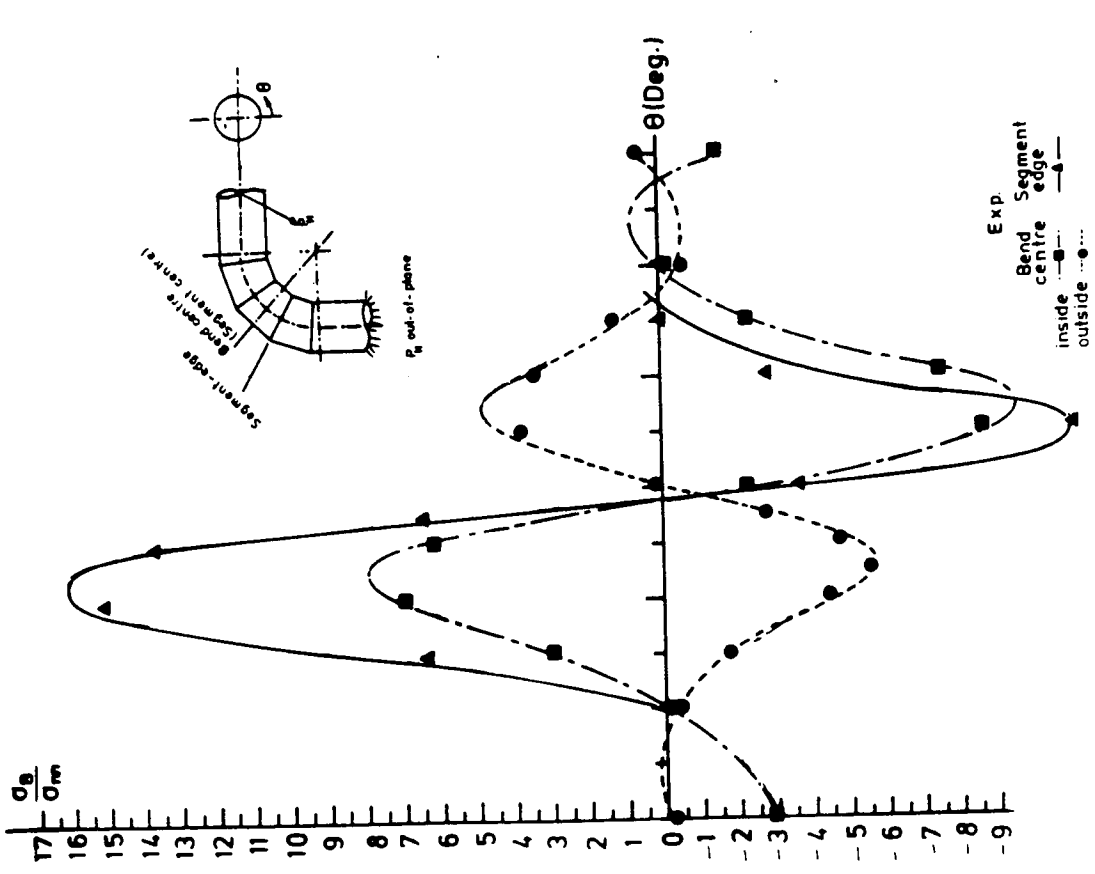


Figure (7.50b) Circumferential stress distribution measured on bend S061 under out-of-plane mode of loading. End load = 1454 N, $M_{B.C} = 16.6 \times 10^3$ N mm, $M_{B.J} = 15.2 \times 10^3$ N mm

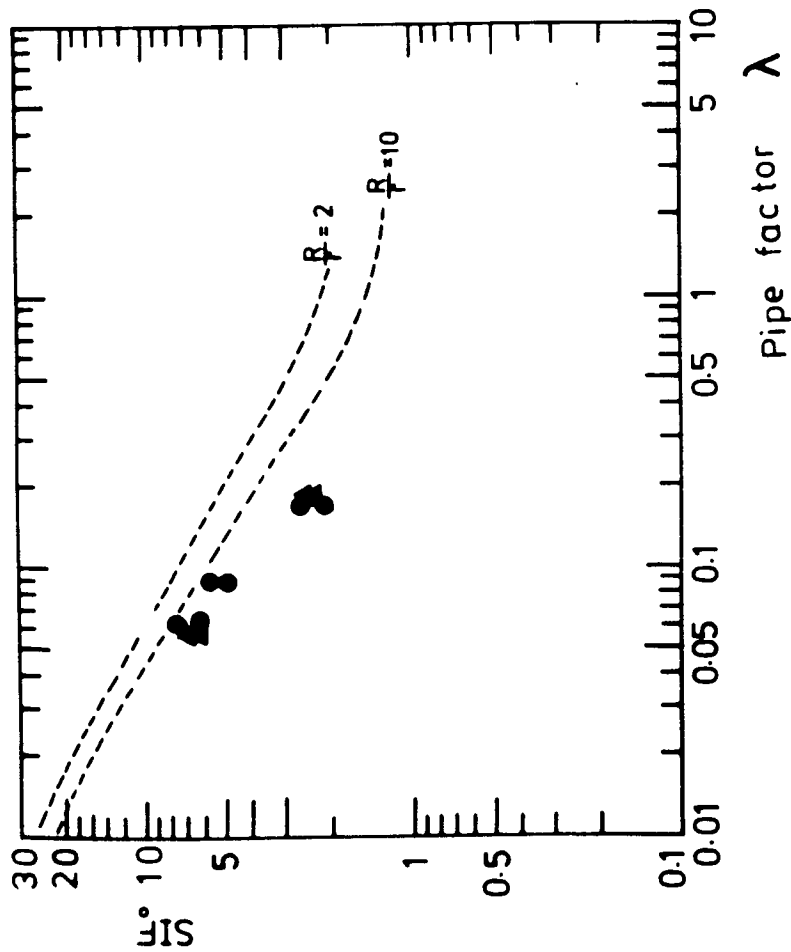


Figure (7.51)
 Maximum out-of-plane longitudinal stress
 intensification factors ($SIF_{0,L}$) of mitred CSM/PVC
 lined bends

Exp. bend centre \bullet Th BS 806 ---
 segment joint \blacktriangle (123)

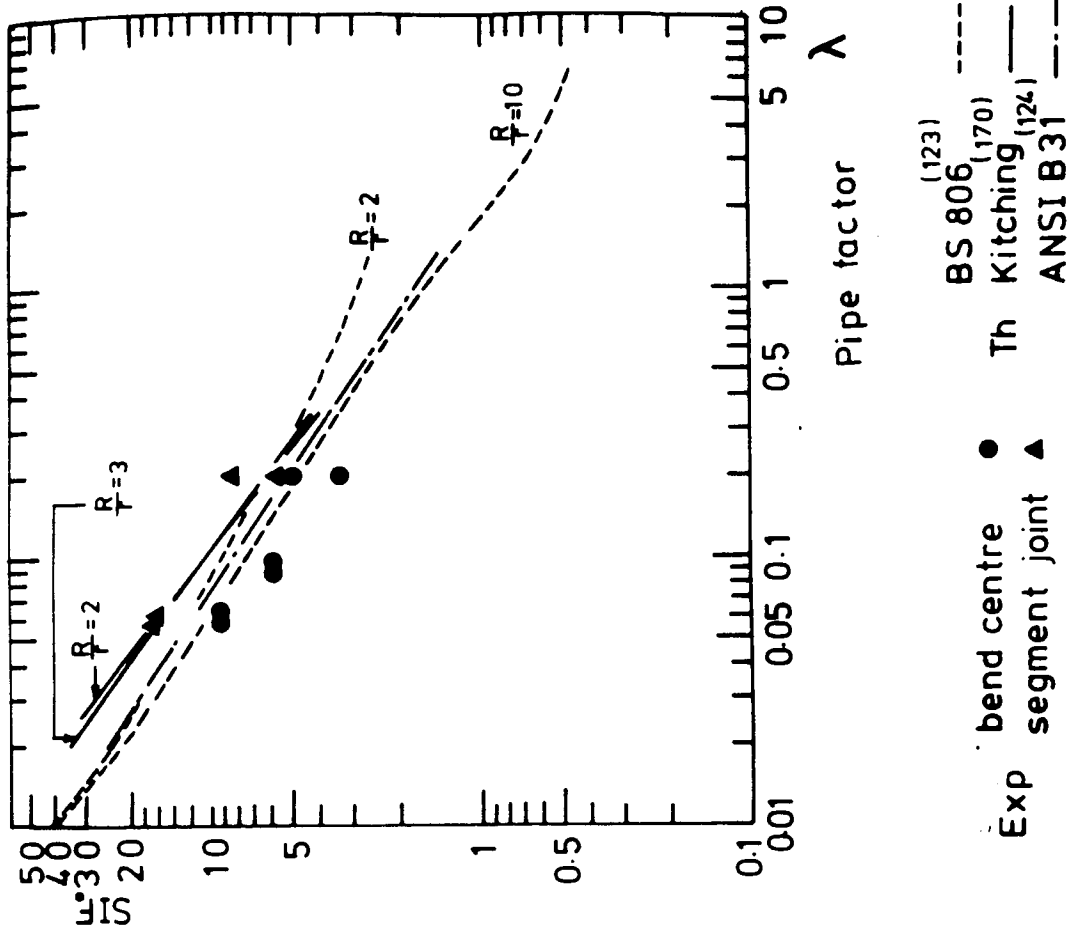


Figure (7.52)
 Maximum out-of-plane circumferential stress
 intensification factors ($SIF_{0,C}$) of mitred CSM/PVC
 lined bends

Exp. bend centre \bullet Th Kitching ---
 segment joint \blacktriangle (124) (123)
 BS 806 ---
 ANSI B 31 ---

TABLE 7.15 - Out-of-plane Stress Intensification Factors (SIF) experimentally determined for Mitred CSM/PVC Lined Bends

| Pipe No. | Bore (mm) | $\frac{f_i}{R}$ | λ_e | Experimental | | | | | | | | Theoretical | | | |
|----------|-----------|-----------------|-------------|--------------------------------|-------------------------------|-------------------------------|-------------------------------|-------------------------------|-------------------------------|-----------------|--------------|---------------|-----------------------|--|--|
| | | | | Segment-edge | | Segment-centre | | | | BS 806 (123) | | 2X ANSI (124) | BS 806 (170) Kitching | | |
| | | | | Circumferential | Longitudinal | Circumferential | | Longitudinal | | Circumferential | Longitudinal | | | | |
| | | | | | | Inside | Outside | Inside | Outside | | | | | | |
| S033 | 195 | 1/3 | 0.177 | -6.6, $\theta = 50^\circ$ | -2.3, $\theta = 40^\circ$ | -2.0, $\theta = 45^\circ$ | 2.3, $\theta = 50^\circ$ | 1.5, $\theta = 40^\circ$ | 2.6, $\theta = 75^\circ$ | 6.0 | 4.8 | 5.71 | 6.91 | | |
| | | | | -5.5, $\theta = 130^\circ$ | -1.8, $\theta = 100^\circ$ | -3.4, $\theta = 125^\circ$ | -2.0, $\theta = 130^\circ$ | 2.0, $\theta = 120^\circ$ | -1.2, $\theta = 140^\circ$ | | | | | | |
| | | | | -8.5, $\theta = 50^\circ$ | -2.3, $\theta = 35^\circ$ | -4.0, $\theta = 45^\circ$ | 2.8, $\theta = 50^\circ$ | -1.5, $\theta = 35^\circ$ | 2.2, $\theta = 75^\circ$ | | | | | | |
| S034 | 195 | 1/3 | 0.177 | -5.0, $\theta = 110^\circ$ | +2.5, $\theta = 100^\circ$ | -5.0, $\theta = 110^\circ$ | -2.0, $\theta = 130^\circ$ | 2.0, $\theta = 110^\circ$ | -1.4, $\phi = 150^\circ$ | 6.0 | 4.8 | 5.71 | 6.91 | | |
| | | | | -6.0, $\theta = 120^\circ$ | -6.0, $\theta = 120^\circ$ | 3.7, $\theta = 60^\circ$ | 4.0, $\theta = 65^\circ$ | -3.7, $\theta = 45^\circ$ | 5.8, $\theta = 80^\circ$ | | | | | | |
| | | | | -5.1, $\theta = 120^\circ$ | -5.1, $\theta = 120^\circ$ | -2.0, $\theta = 130^\circ$ | -2.5, $\theta = 130^\circ$ | 3.0, $\theta = 100^\circ$ | -2.3, $\theta = 140^\circ$ | | | | | | |
| S036 | 244 | 1/2 | 0.087 | - | - | - | - | - | - | 9.5 | 8.0 | 9.17 | 11.71 | | |
| | | | | - | - | - | - | - | - | | | | | | |
| | | | | - | - | - | - | - | - | | | | | | |
| S060 | 589 | 1/2 | 0.061 | 17.0, $\theta = 70^\circ$ | 6.5, $\theta = 60^\circ$ | 9.5, $\theta = 70^\circ$ | -82, $\theta = 65^\circ$ | 6.0, $\theta = 55^\circ$ | -6.5, $\theta = 85^\circ$ | 12.5 | 10.0 | 11.62 | 15.91 | | |
| | | | | -11.0, $\theta = 170^\circ$ | -4.7, $\theta = 95^\circ$ | -9.5, $\theta = 120^\circ$ | -5.4, $\theta = 120^\circ$ | -6.5, $\theta = 100^\circ$ | -3.4, $\theta = 120^\circ$ | | | | | | |
| | | | | - | - | - | - | - | - | | | | | | |
| S061 | 589 | 1/2 | 0.061 | 16.5, $\theta = 60^\circ$ | 6.0, $\theta = 65^\circ$ | 7.6, $\theta = 65^\circ$ | -5.5, $\theta = 65^\circ$ | 5.5, $\theta = 65^\circ$ | -7.5, $\theta = 80^\circ$ | 12.5 | 10.0 | 11.62 | 15.91 | | |
| | | | | -11.0, $\theta = 115^\circ$ | 4.2, $\theta = 95^\circ$ | 9.4, $\theta = 120^\circ$ | 4.5, $\theta = 120^\circ$ | -6.5, $\theta = 100^\circ$ | -3.2, $\theta = 135^\circ$ | | | | | | |
| | | | | - | - | - | - | - | - | | | | | | |

7.5.4.3 Combined in-plane (closing)/out-of-plane bending of bend

S060

Bend S060 (600mm nominal bore) was loaded under combined loading of in-plane bending (closing) and out-of-plane bending both applied at the same time. The measured strains on the inside surface at the segment-edge and on the inside/outside surfaces at the segment-centre are presented as a function of their angular position around the circumference in Fig. 7.53a,b,c for end loads of 1454 N being applied perpendicular to each other at the end of the free tangent.

Table 7.16 lists the experimentally measured circumferential strains obtained from the individually applied in-plane bending moment (Fig. 6.33) and the individually applied out-of-plane moment (Fig. 6.47), and their direct superimposed values are compared with circumferential strains obtained the combined IN/OUT mode of bending.

7.5.5 Failure test results of smooth bend S034

Bend S034 (200mm nominal bore) shown in Fig. 7.17a was taken to failure under in-plane mode of bending by opening the bend.

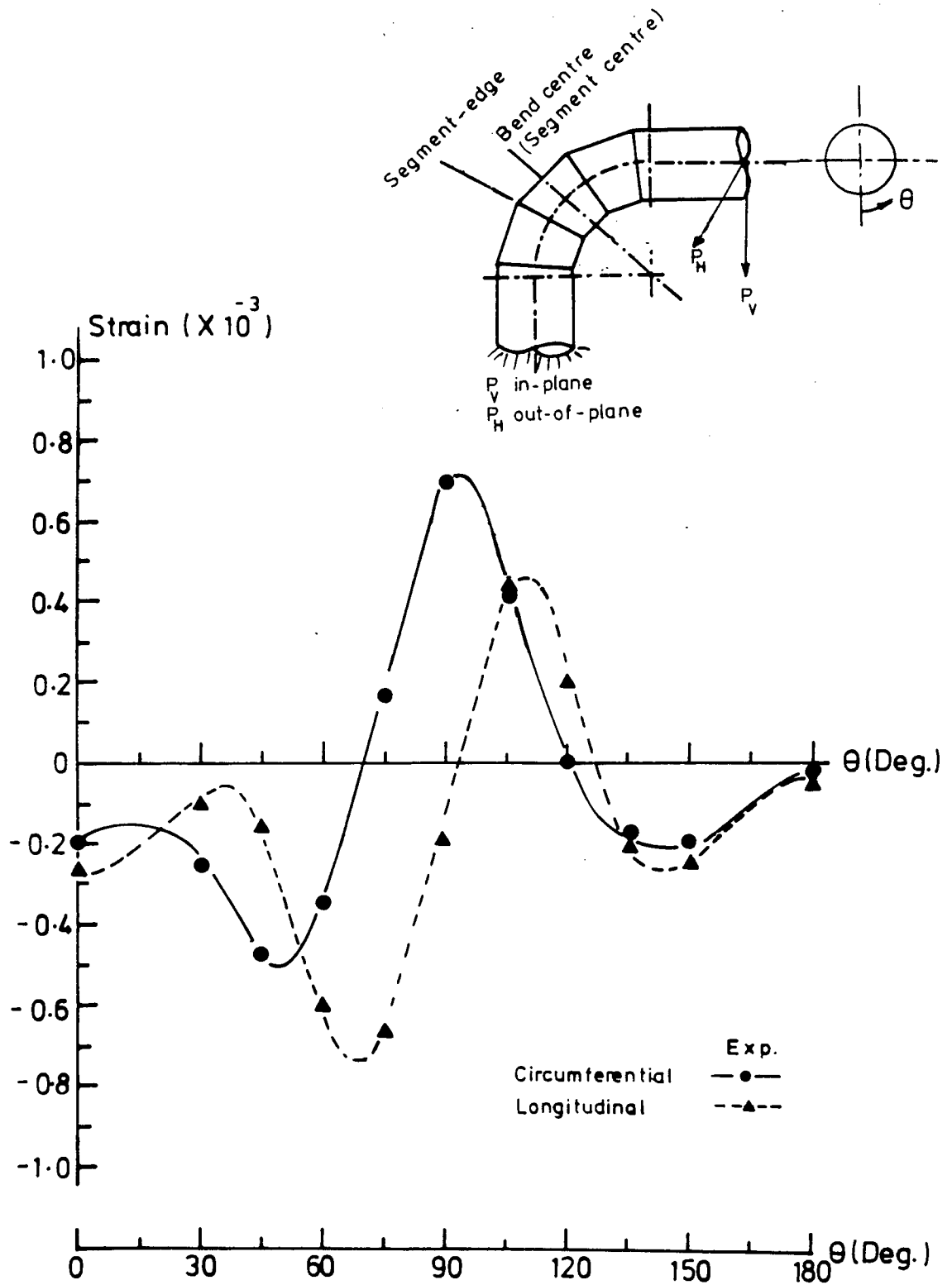
The stages of cracking and failure developments as outlined in Fig. 7.54 could be summarised as the following:

Stage A

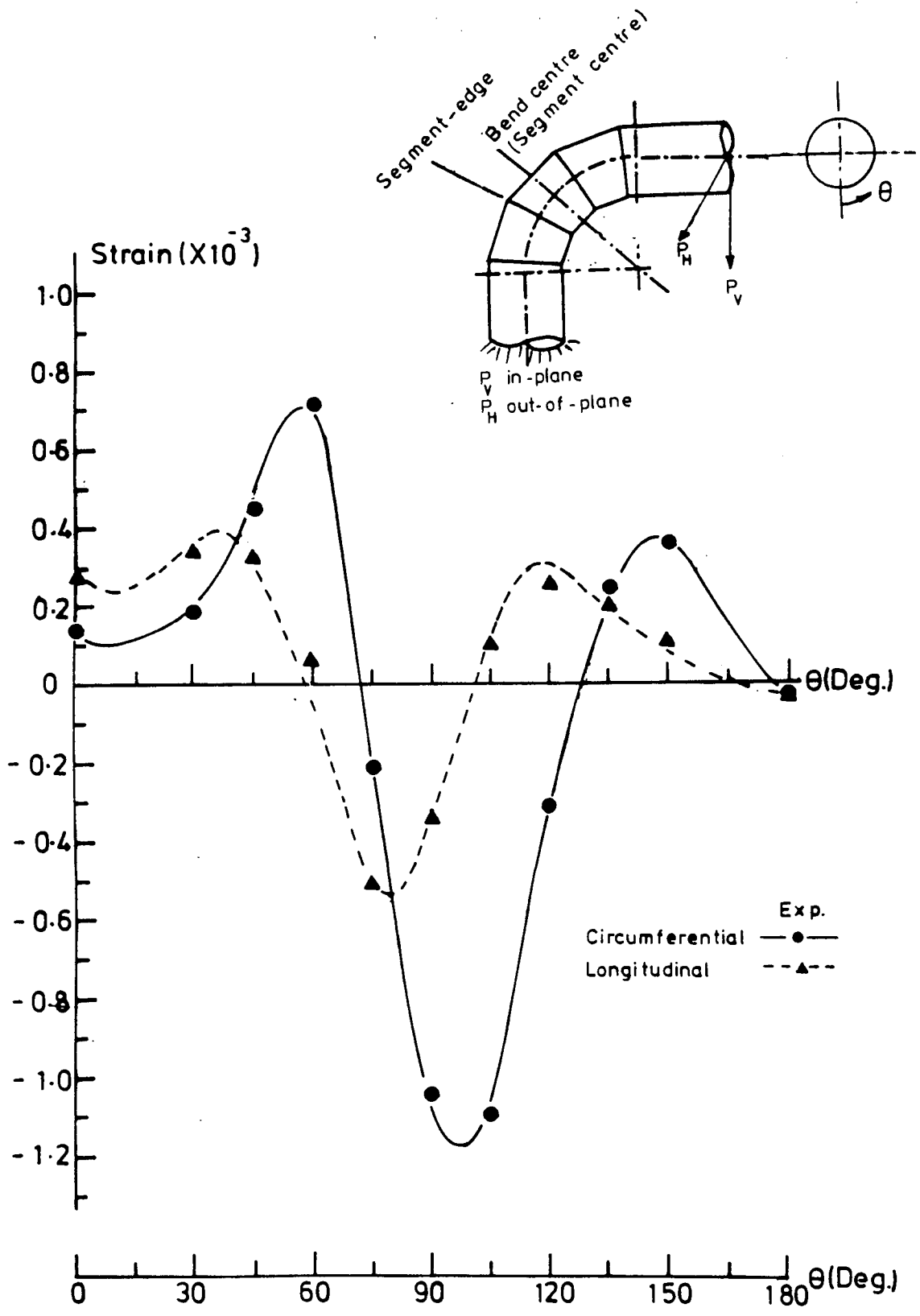
At approximately 3400 N end load, audible noises were heard.

Stage B

At load 7350 N, external cracks running longitudinally were observed at $\theta = 0^\circ$ - 30° angular position measured from the intrados as shown in Fig. 7.55. The cracks are running across the centre segment and extending towards the free tangent. Due to the longitudinal direction of the cracks, they are believed to be due to flexural circumferential stress. In fact, referring to the stress ratio



Figure(7.53a) Outside strain distribution measured at the segment centre (bend centre) of bend S060 under combined in-plane / out-of-plane bending, $P_V = 1454\text{N}$, $P_H = 1454\text{N}$



Figure(7 53b) Inside strain distribution measured at the segment-centre (bend centre) of bend S060 under combined in-plane / out-of-plane bending, $P_V = 1454\text{N}$, $P_H = 1454\text{N}$

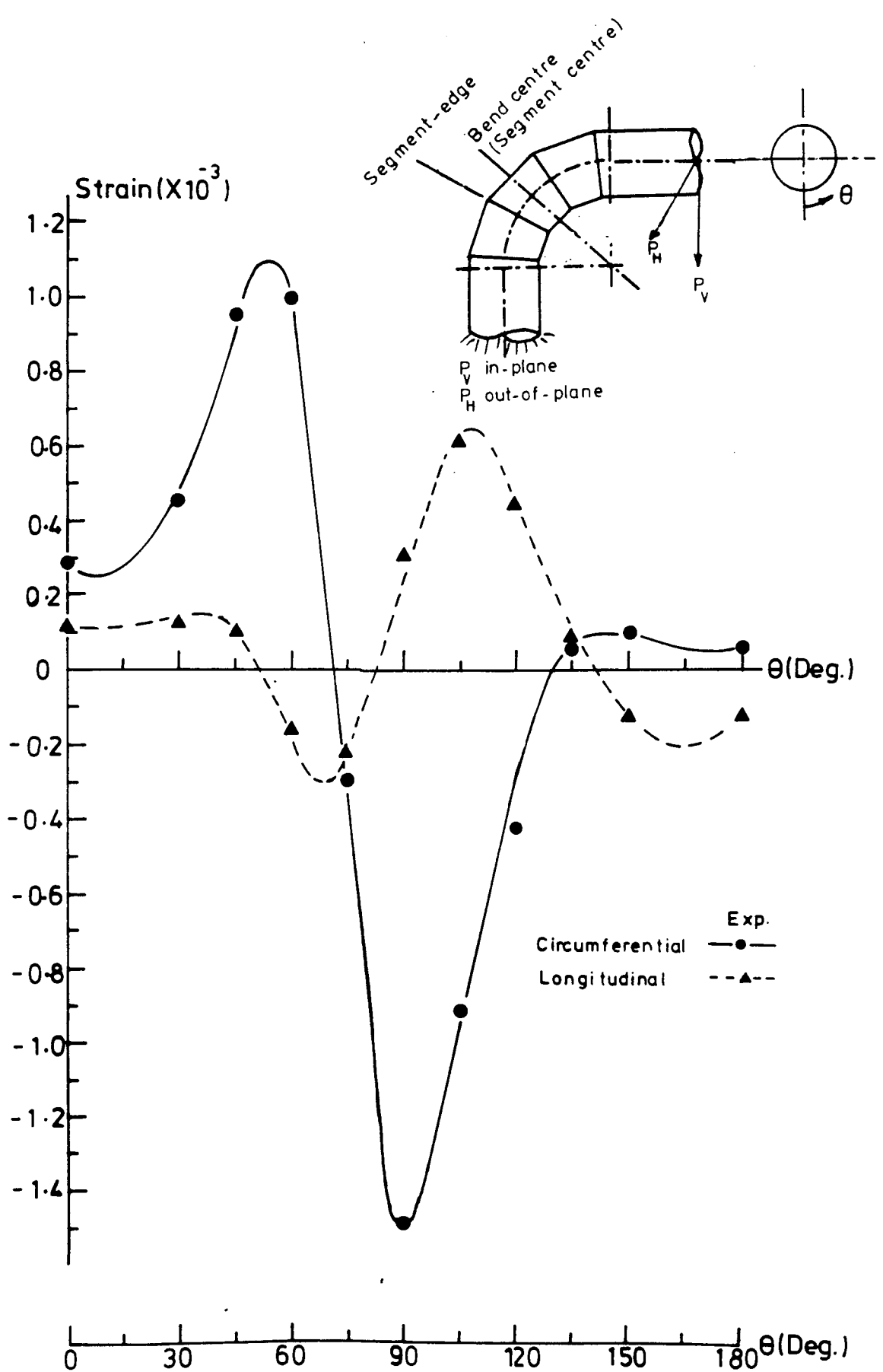


Figure (7 53c) Inside strain distribution measured at the segment edge of bend S060 under combined in-plane/ out-of-plane bending, $P_V = 1454\text{N}$, $P_H = 1454\text{N}$

TABLE 7.16 - Measured Strain Distribution on Bend S060 under Combined
In-plane/Out-of-plane Mode of Bending (units in
microstrain)

$P_V = 1454N$, $P_H = 1454N$

Segment-Centre Circumferential (Inside)

| Circum. Position (θ) | 0° | 30° | 45° | 60° | 75° | 90° | 105° | 120° | 135° | 150° | 180° |
|----------------------------------|-----|-----|-----|-----|-------|-------|-------|------|------|------|------|
| Measured in-plane (CL)* | 160 | 160 | 290 | 175 | - 560 | -1030 | - 470 | 220 | 400 | 160 | 0 |
| Measured out-of-plane | 0 | 30 | 160 | 515 | 610 | 40 | - 565 | -520 | -150 | 90 | 0 |
| Superimposed IN-OUT | 160 | 180 | 450 | 690 | 50 | - 990 | -1035 | -300 | 250 | 250 | 0 |
| Measured IN-OUT | 140 | 185 | 450 | 715 | - 210 | -1045 | -1090 | -310 | 255 | 315 | -20 |

Segment-Centre Circumferential (Outside)

| | | | | | | | | | | | |
|---------------------------|------|------|------|------|-------|-------|-----|------|------|------|---|
| Measured in-plane (CL) | -200 | -220 | -290 | 0 | 450 | 550 | 70 | -200 | -200 | -100 | 0 |
| Measured out-of-plane | 0 | - 35 | -165 | -300 | - 250 | 130 | 350 | 250 | 0 | 0 | 0 |
| Superimposed IN-OUT | -200 | -255 | -455 | -300 | - 200 | - 680 | 420 | 50 | -200 | -100 | 0 |
| Measured IN-OUT | -190 | -250 | -470 | -350 | 165 | 700 | 410 | 0 | -180 | -200 | 0 |

Segment-Edge Circumferential (Inside)

| | | | | | | | | | | | |
|---------------------------|-----|-----|-----|------|-------|-------|------|------|------|-----|-----|
| Measured in-plane (CL) | 300 | 410 | 580 | 100 | -1100 | -1200 | -275 | - 10 | 170 | 100 | -50 |
| Measured out-of-plane | 0 | 30 | 300 | 850 | 800 | - 200 | -500 | -500 | -100 | 0 | 0 |
| Superimposed IN-OUT | 300 | 440 | 880 | 950 | - 300 | -1400 | -775 | -500 | 70 | 130 | -50 |
| Measured IN-OUT | 300 | 460 | 950 | 1000 | - 290 | -1490 | -920 | -400 | 60 | 100 | 50 |

* CL = Closing

distribution in an opening mode of bending as shown in Fig. 7.56, it could be seen that the circumferential stress at an angular position of 20° - 30° (from the intrados) constitute a maximum positive peak, located on the outside surface.

Stage C

At loading corresponding to 7700 N, circumferential cracks on the tangent-bend joint were observed as shown in Fig. 7.57. The pattern of the cracks indicate that they were initiated due to a tensile longitudinal stress.

Stage D

Delamination in the form of local buckling, as shown in Fig. 7.58 was observed at load 9700 N just before the maximum load was released. The damaged area showed a distinctive whitening with a local (domed-shaped) contour being formed, which flattened again after releasing the load. The delaminated area was located at an angular position of -90° measured from the intrados, and with reference to Fig. 7.56, such an area is seen to experience a compressive circumferential stress occurring on the outside surface where local buckling has been observed. The delaminated area was located nearer to the segment-edge towards the fixed tangent.

The bend was later cut for inside crack observations. Two major cracks of brittle nature were observed at an angular position of $\pm 90^{\circ}$ displaced from the intrados. Fig. 7.17b shows the crack initiated at $+90^{\circ}$ angular position, and Fig. 7.59 shows the crack initiated at -90° angular position. A closer look at the crack in Fig. 7.59 is shown in Fig. 7.60. The cracks were both initiated at the segment-edge and running in the longitudinal direction with all segment edges having formed similar cracks.

The direction of the crack, its angular position (i.e. $\pm 90^{\circ}$) and its location at the segment edge, all indicate that they were initiated

due to an inside maximum circumferential stress, which coincide with the location of the maximum circumferential stress measured experimentally in the elastic region (Fig. 7.55b).

Maximum strain measurements located at 90° at the inside surface of the segment-edge are presented as a function of the end load in Fig. 7.61, where a typical GRP deformation is observed, having the PVC totally dominated by the behaviour of the GRP.

A non-linearity strain measured from Fig. 7.61 to be 0.62% strain corresponding to an end-load of 2700 N and a bending moment of 3.3 MN mm. This is lower by 20% than the end load of 3400 N when audible noises were heard (Stage A). A bending moment of 1.06 MN mm corresponds to a strain level of 0.2%.

The strain gauge ceased to function at 7000 N end load which corresponds to 2% strain. Hence, at 10^+ kN load, the total strain to failure would be higher than 2% corresponding to a failure of bending moment of 8.51^+ MN mm. The different observed stages of damage are presented in terms of their corresponding applied load, and compared with that of 0.2% strain and 1/10th of the failure load as listed in Table 7.17.

No signs of delamination between the PVC and the CSM were observed when random cuts were carried out on the laminate.

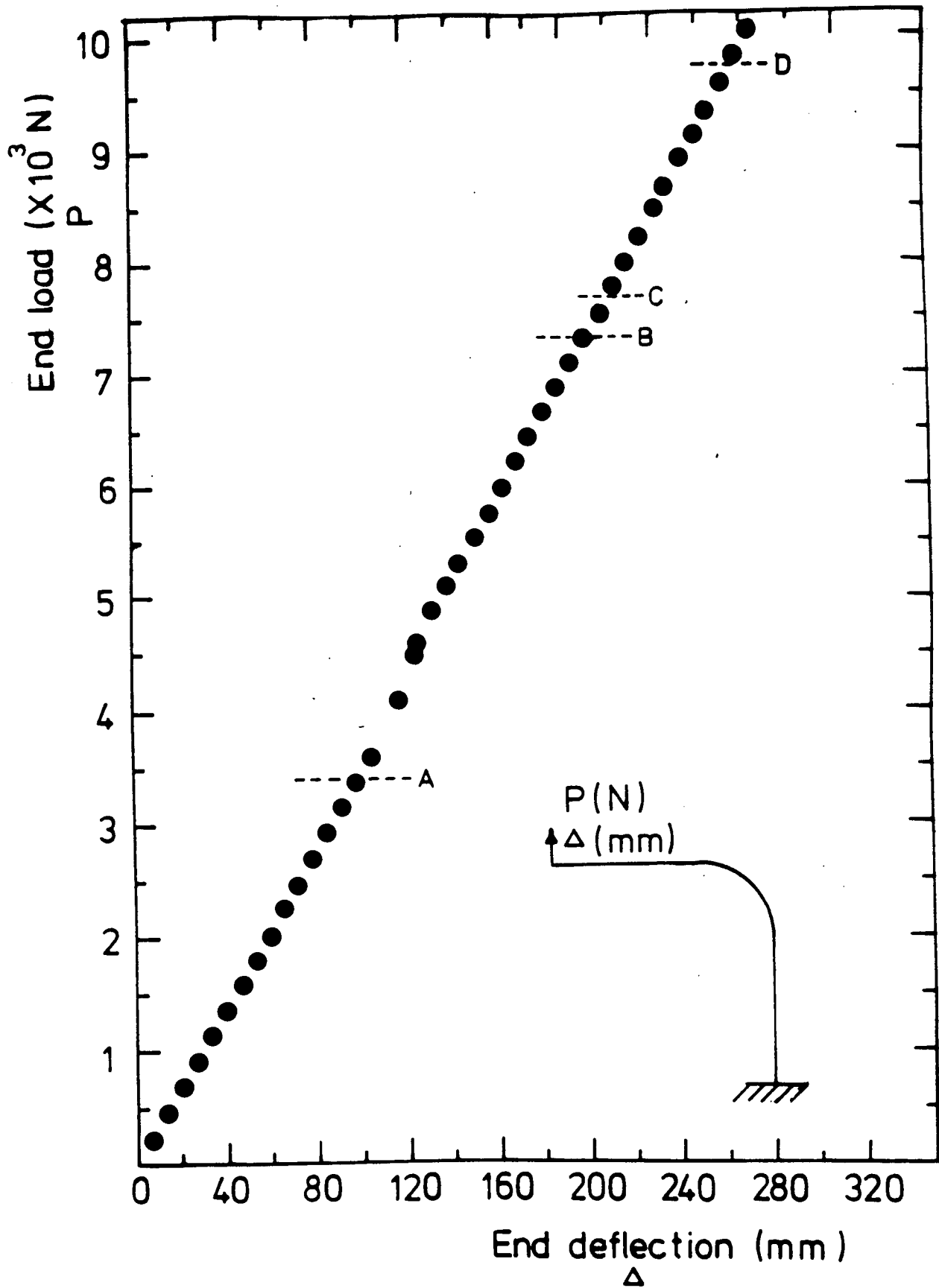


Figure (7.54) End-deflection versus end-load to failure of bend S034 under in-plane/opening mode of bending



Figure (7.55) Failure cracks shown on centre of bend S034 under in-plane/opening mode of loading

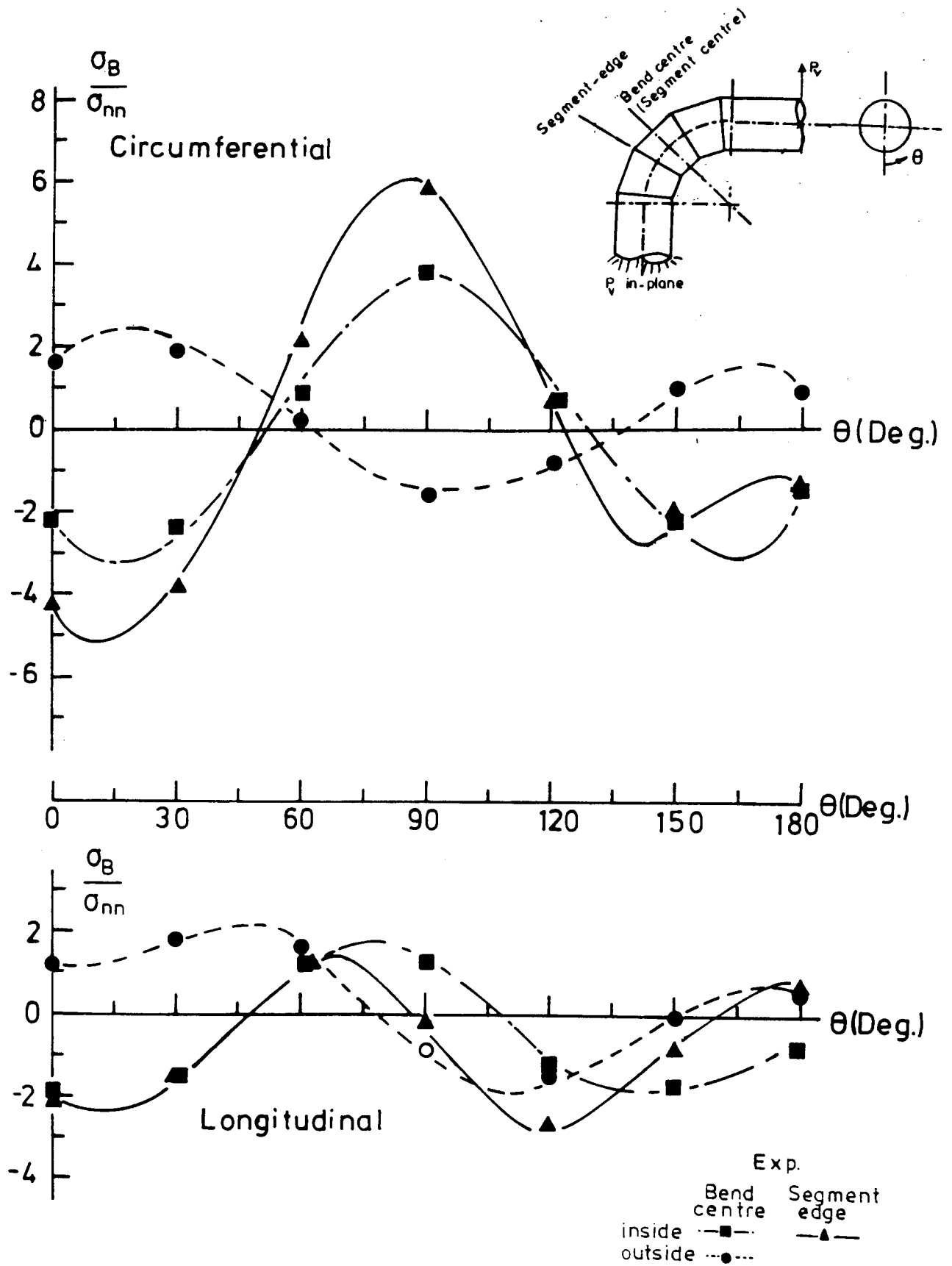


Figure (7.56) Stress distribution measured on bend S034 under in-plane/opening mode of bending. End load = 675N



Figure (7.57) Failure cracks of bend S034 shown on bend/tangent joint occurring at end load of 7700N under in-plane/opening mode of loading

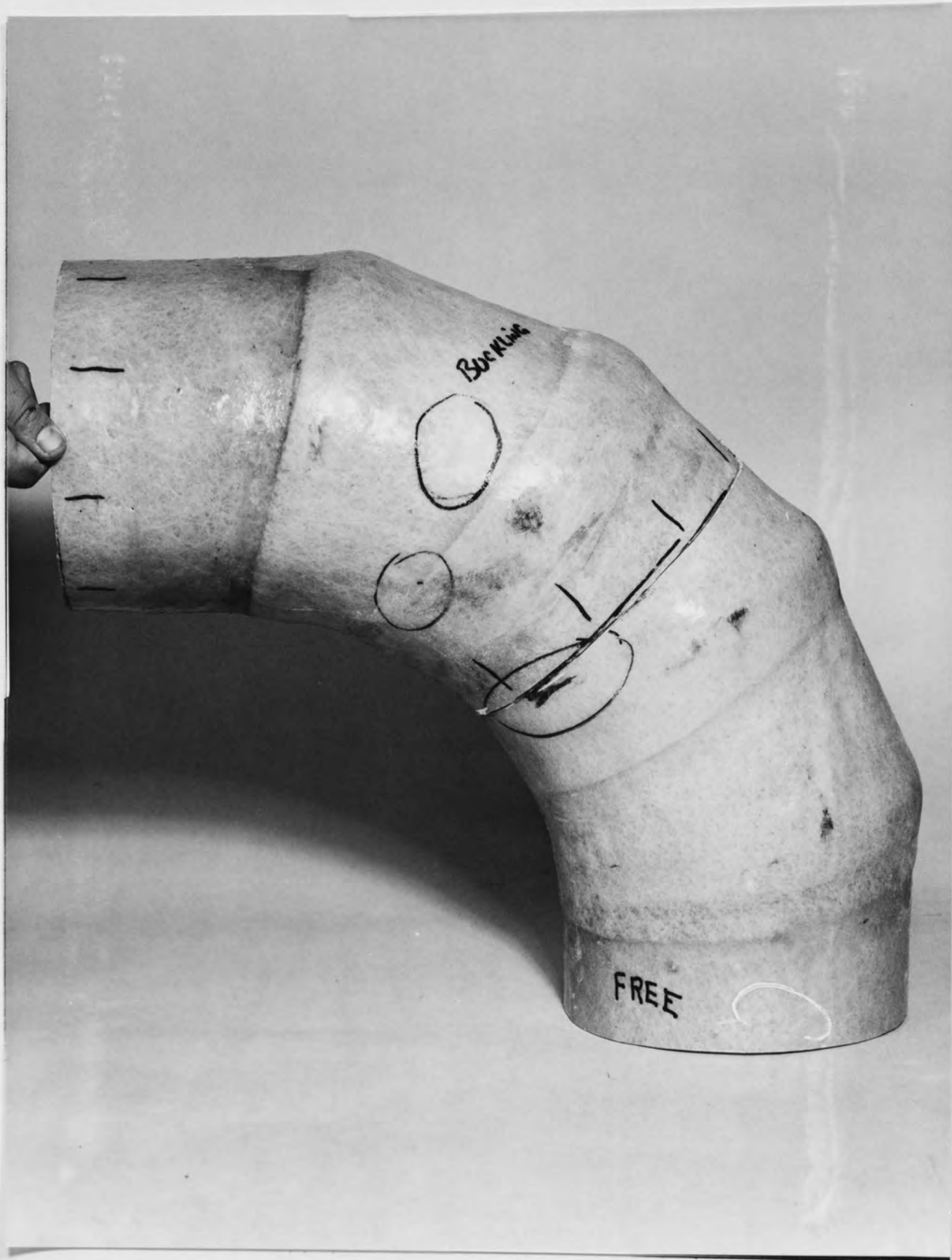


Figure (7.58) Failure in the form of local buckling (or delamination) observed on bend S034 at 9700N end load under in-plane/opening mode of bending

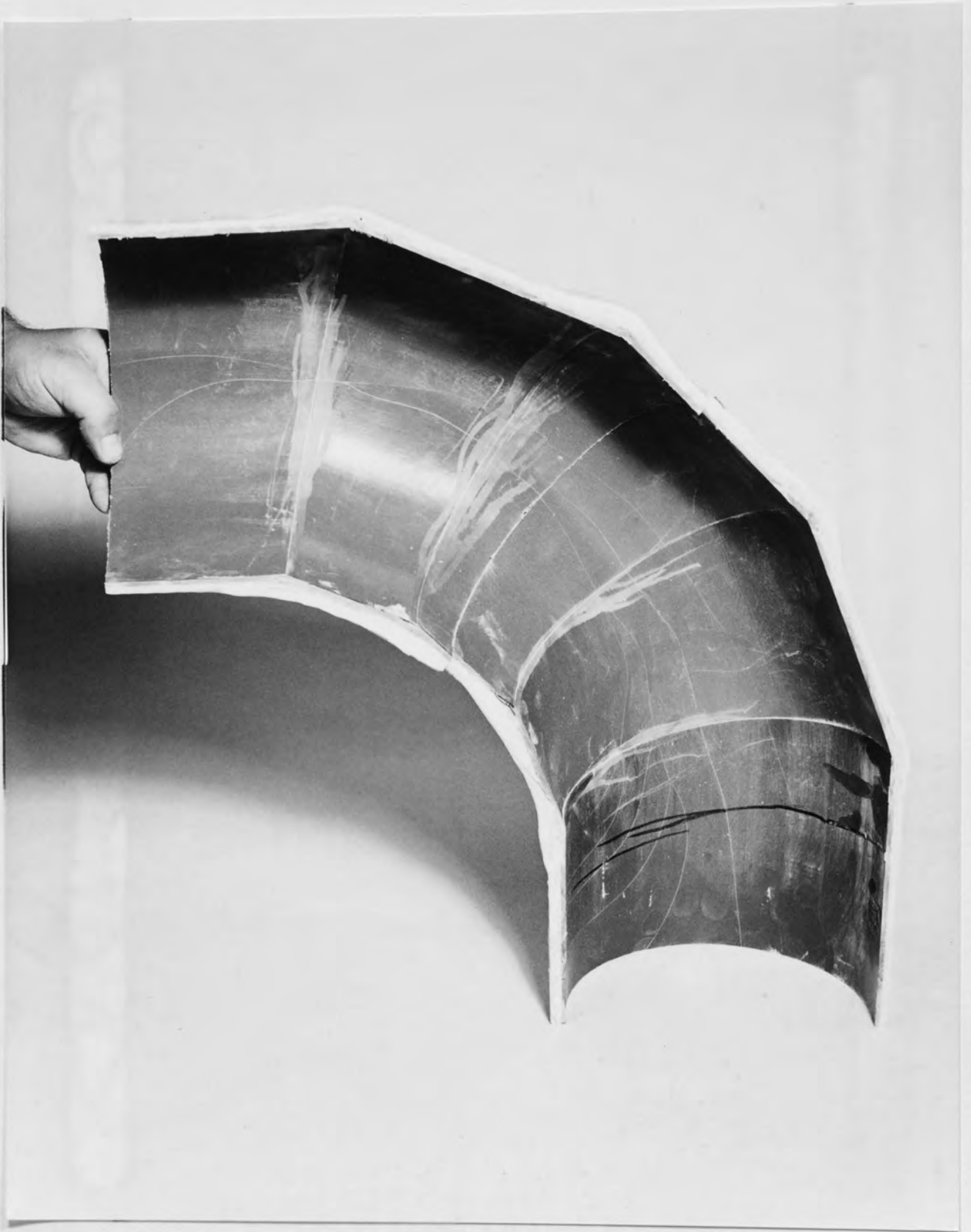
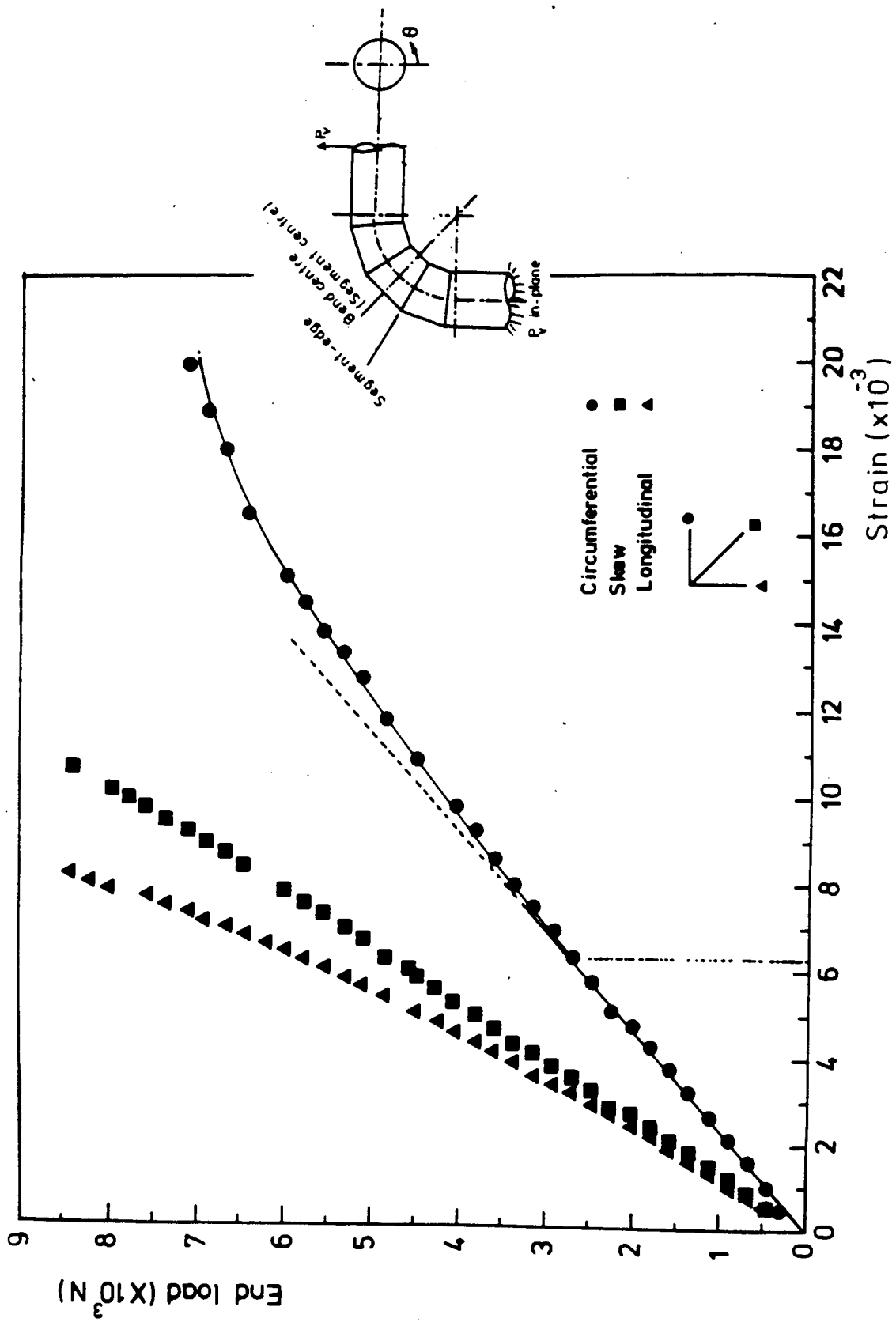


Figure (7.59) Longitudinal cracks initiated on the inside PVC surface of bend S034 under in-plane/opening type of loading



Figure (7.60) Magnification of the cracks shown in Figure (7.59) before



Figure(7.61) Strain to failure monitored on bend sample S034 at the segment edge (0=90) under in plane mode of bending (opening)

TABLE 7.17 Levels of end-loads corresponding to the different damage observed on bend S034 under in-plane bending (opening) to failure

| <u>Applied end-load (kN)</u> | <u>Stage of damage</u> |
|------------------------------|---|
| 0.9 | 0.2% strain |
| 2.7 | non-linearity strain (0.62%) |
| 3.4 | Stage A - audible noises |
| 7.4 | Stage B - outside longitudinal cracks |
| 7.7 | Stage C - outside circumferential cracks on the joint |
| 9.7 | Stage D - local delamination of outside surface |
| >10 | Total failure |
| > 1.0 | 1/10th failure |

CHAPTER EIGHT

FLEXURAL TESTING OF CSM/WR/UD CONSTRUCTED
STRAIGHT PIPES AND BENDS

CHAPTER EIGHT

FLEXURAL TESTING OF CSM/WR/UD CONSTRUCTED STRAIGHT PIPES, AND BENDS

8.1 Introduction

Twelve bends and five straights of in-plane orthotropic laminate construction have been tested under flexural and torsional testing. The types of reinforcements used for the construction of these pipe components are CSM combined with WR and circumferential UD and FW type of reinforcements. They were provided by different manufacturers from the UK and from abroad. They are defined as presented in Table 8.1 as nominally specified by the manufacturers and the details of the laminate construction, dimensions and mechanical properties are included as each set of pipe components results are presented.

8.2 Orthotropic CSM/WR/UD smooth bends of 2:1 circumferential to longitudinal extensibility ratio, Set I

8.2.1 Glass content, dimensions and mechanical properties

Samples were cut from the different parts of bend S039; after being tested; for glass content examination using burn-off tests⁽³³⁾. The glass content was examined at the intrados, extrados, straight tangents and at the joint. The results in terms of percentage glass content, glass mass per unit area, type of reinforcements and measured thicknesses of the samples are presented in Table 8.2. The maximum glass content per unit area is located on the bend intrados and at the joint. The variability of the thickness on the bend is of direct function of the glass mass where the thickness drops as it departs from the intrados towards the extrados. The minimum thickness and glass mass are located on the straight tangents and they are comparable to those on the extrados of the bend. Although different glass mass,

TABLE 8.1 - Orthotropic Bends and Straights as specified by the Pipe Manufacturers

| Set | Component | Description |
|-------|---|--|
| I | (A) | |
| | S039) | 200 mm nominal bore smooth bend, $1\frac{1}{2}D$ bend radius, construction: 4.8 kg/m ² CSM/WR/UD reinforcements with 2:1 circumferential to longitudinal extensibility ratio. |
| | S040) | |
| | S041 | |
| | (B) | |
| | S045) | 250 mm nominal bore smooth bend, 1D bend radius construction: 4.8 kg/m ² CSM/WR/UD reininforcements with 2:1 circumferential to longitudinal axial extensibility ratio. |
| S046) | | |
| S047 | 3000 mm long straight pipe same construction as S045/046. | |
| II | S042) | 200 mm nominal bore smooth bend, $1\frac{1}{2}D$ bend radius, construction: 4.8 kg/m ² CSM/WR/ with 1:1 circumferential to longitudinal extensibility ratio. |
| | S043) | |
| | S044 | 3000 mm long straight, same construction as S042/043. |
| III | S048) | 100 mm nominal bore smooth bends, 1D bend radius construction: woven rovings for the bends and filament windings for the tangent straights. |
| | S049) | |
| | S050) | |
| IV | S028) | 250 mm nominal bore smooth bends, 2D bend radius construction: 65% volume WR for bends and 75% volume F.W. tangents. |
| | S029) | |
| | S030) | |
| | S031) | 3000 mm straights of similar construction to the tangents of S028/029/030. |
| | S032) | |

* moduli ratio is defined as extensibility ratio by UK manufacturers and users with reference to BS 4994.

TABLE 8.2 - Glass Mass of the Constituent Layers measured from the Different Parts of Orthotropic Bend S039

| Position of Sample | Sample area mm ² | Sample weight g | Sample thickness mm | Total Glass Mass | | Individual Layers, inside to outside | | | | | | | |
|--------------------------------|-----------------------------|-----------------|---------------------|--------------------------------------|-------|--------------------------------------|----------------------------|---------------------------|---------------------------|----------------------------|----------------------------|---------|----------|
| | | | | Mg/m ⁻² kg/m ² | Mg % | 'C' * mass kg/m ² | CSM mass kg/m ² | WR mass kg/m ² | UD mass kg/m ² | CSM mass kg/m ² | 'C' mass kg/m ² | | |
| Free tangent | 1300 | 17.35 | 9.82 | 5.97 | 44.9 | 1.2×10^{-2} | 1.22 | 1.48 | 2.81 | 0.39 | 1.2×10^{-2} | | |
| Fixed tangent | 820 | 11.02 | 9.20 | 6.53 | 48.4 | - | 1.28 | 1.57 | 3.28 | 0.39 | - | | |
| Intrados bend centre | 1560 | 32.63 | 16.75 | 10.24 | 48.93 | - | 2.01 | 2.11 | 5.46 | 0.64 | - | | |
| -90° from Intrados bend centre | 1455 | 23.91 | 11.30 | 7.99 | 48.62 | - | 1.85 | 1.30 | 4.06 | 0.76 | - | | |
| Extrados bend centre | 1630 | 12.50 | 10.67 | 7.65 | 48.10 | - | 1.79 | 1.16 | 3.90 | 0.79 | - | | |
| Joint tangent bend | 995 | 22.53 | 16.65 | 8.58 | 37.9 | CSM 2.49 | WR 1.12 | CSM 1.06 | WR 0.88 | CSM 0.85 | WR 0.49 | UD 0.66 | CSM 1.04 |

* 'C' = 'C' glass veil

per unit area are measured on the different parts, the percentage glass content does not differ except at the joint; this is due to the proportional absorption capability of each layer when impregnated by the resin. At the joint, where a relatively large mass of CSM is measured, the percentage glass content drops due to high resin impregnation by the CSM. Contrary to the recommendations specified and suggested for the construction of GRP vessels and tanks⁽³⁾, no CSM reinforcements were used to act as an interlayer between the WR and the UD reinforcements. This is envisaged to lead to lower bonding strength between the successive layers.

Directional deviation of the circumferential UD filaments from the circumferential direction was up to 15° which would account for stiffness reduction of around 30%, with negligible increase in the longitudinal stiffness (see Fig. 3.4 of Ch. 3). As for the WR reinforcements, directional variation of around 5° was observed.

Mechanical properties in both the circumferential and the longitudinal directions were obtained from tensile testing of longitudinal strips and rings using the opposite-point flexural loading⁽¹¹⁶⁾. Both types of samples were cut from the actual pipe.

Five rings were tested under opposite-load flexural test, with one ring strain gauged on the inside and the outside as presented in Table 8.3a. One ring was cut from the joint area, three from the straights and one from the bend. The average modulus obtained is 11.3 kN.mm⁻² excluding the joint modulus due to the different laminate construction. The different moduli of 10.2 kN.mm⁻² obtained on the inside and 15.6 kN.mm⁻² obtained on the outside, indicate a shift of the neutral axis from the centroidal axis towards the outside. This is expected when the glass reinforcements sequence is considered. Failure starts with a crack initiated on the outside surface where the load is

applied followed by an inside gel coat crack at 90° from the applied load propagating to the mid-thickness splitting the laminate. Final failure occurs by total breakage of the ring at the position of the applied load. The strength values presented in Table 8.3a are the flexural strength.

Two longitudinal strips, having their ends adhered to aluminium plates using cold cured epoxy resin, were tested under tension. One sample was monitored via strain gauges affixed on both surfaces of the sample and the second was monitored under loading using an optical extensometer. The average modulus of 6.2 kN.mm^{-2} obtained from Table 8.3b is 50% lower than the circumferential modulus, having 1.88:1 circumferential to longitudinal elastic anisotropy. No tensile strength values are obtained due to failure of the epoxy.

The measured Poisson's ratios vary between 0.11-0.24 as obtained from the longitudinal tests and 0.25-0.33 as obtained from the ring tests. Theoretically for an anisotropic laminate⁽⁴⁹⁾ the Poisson's ratios are related to the circumferential and the longitudinal moduli, as follows

$$\frac{\nu_{LC}}{E_L} = \frac{\nu_{CL}}{E_C}; \quad \frac{(E_C)_{av}}{(E_L)_{av_{exp}}} = 1.88, \quad \frac{(\nu_{CL})_{av}}{(\nu_{LC})_{av_{exp}}} = 1.76 \quad (8.1)$$

The above longitudinal and circumferential moduli could be theoretically predicted based on the mass per unit area of the constituent reinforcements. Such prediction could be carried out by Eq. (8.2) as follows:

$$(E)_{\text{laminate}} \cdot t_{\text{total}} = E_{\text{CSM}} \cdot M_{\text{CSM}} \cdot t_{\text{CSM}} + E_{\text{WR}} \cdot M_{\text{WR}} \cdot t_{\text{WR}} + E_{\text{UD}} \cdot M_{\text{UD}} \cdot t_{\text{UD}} \quad (8.2)$$

TABLE 8.3a - Circumferential Mechanical Properties obtained from Ring Specimens cut from Bend S039

| Specimen Number | t mm | W mm | 2r _i mm | E _v N.mm ⁻² | E _{strain} (N.mm ⁻²) | | | | ν _{LC} | | σ _f (N.mm ⁻²) |
|-----------------|---------|---------|-----------------------|--------------------------------------|--|---------|-------------------|------------------|-----------------|---------|---|
| | | | | | Inside | | Outside θ = 0° | θ = 0° Inside | θ = 90° | | |
| | | | | | θ = 0° | θ = 90° | | | Inside | Outside | |
| 1 (ST.) | 9 | 28.0 | 202 | 9050 | 10400 | 9900 | 15600 | 0.25 | 0.30 | 0.34 | - |
| 2 (ST.) | 9.79 | 26.2 | 202 | 9570 | - | - | - | - | - | - | 250 |
| 3 (ST.) | 9.71 | 25.3 | 202 | 11630 | - | - | - | - | - | - | 230 |
| 4 (Joint) | 14.50 | 26.1 | 202 | 7120 | - | - | - | - | - | - | 182 |
| 5 (Bend) | 12.53 | 26.0 | 202 | 8320 | - | - | - | - | - | - | 270 |
| Average | | | | 9640 | 10150 | 12900 | 15600 | 0.275 | 0.34 | | |
| Average | | | | | 11260 | | | | 0.308 | | |

TABLE 8.3b - Longitudinal Mechanical Properties obtained from
Tensile Specimens cut from Bend S039

| Specimen Number | t mm | W mm | E _{inside} N/mm ² | E _{outside} N/mm ² | v _{inside} (CL) | v _{outside} (CL) |
|----------------------|------|------|---------------------------------------|--|--------------------------|---------------------------|
| 1 (St.) ⁺ | 10.0 | 20.0 | 4500 | 6550 | 0.24 | 0.11 |
| 2 (St.) [*] | 9.20 | 15 | 6800 | | - | - |
| Average | | | 6160 | | 0.175 | |

+ strain gauged specimen

* tested via optical extensometer

from Table (8.2) - Specimen 1

$$M_{g,\text{total}} = 5.97 \text{ kg/m}^2$$

$$M_{\text{CSM}} = 1.61 \text{ kg/m}^2$$

$$M_{\text{WR}} = 1.48 \text{ kg/m}^2$$

$$M_{\text{UD}} = 2.81 \text{ kg/m}^2$$

and using the rule of mixture, $E_g = 73 \text{ kN.mm}^{-2}$, $E_r = 2.45 \text{ kN.mm}^{-2}$ (61)

$$E_{\text{CSM}} = 7.0 \text{ kN.mm}^{-2} \text{ (for 33\% glass mass, 20\% by volume)}$$

$$E_{\text{WR}} = 13.7 \text{ kN.mm}^{-2} \text{ (for 50\% glass mass, 33\% by volume)}$$

$$E_{\text{UD}} = 33 \text{ kN/mm}^{-2} \text{ (for 60\% glass mass, 43\% by volume)}$$

$$= 23 \text{ kN.mm}^{-2} \text{ when corrected to } 15^\circ \text{ shift from the}$$

circumferential direction

from BS.4994 (3)

$$t'_{\text{CSM}} = 2.2 \text{ mm per kg/m}^{-2} \text{ (33\% glass mass)}$$

$$t'_{\text{WR}} = 1.1 \text{ mm per kg.m}^{-2} \text{ (50\% glass mass)}$$

$$t'_{\text{UD}} = 0.85 \text{ mm per kg.m}^{-2} \text{ (60\% glass mass)}$$

substituting back in Eq. (8.2) above, with $t_{\text{total}} = 9.82 \text{ mm}$ as measured by hand, hence

$$(E_c)_{\text{predicted}} = 10.4 \text{ kN.mm}^{-2}, \text{ compared against } 11.3 \text{ kN.mm}^{-2} \\ \text{experimentally obtained}$$

Similarly for the longitudinal direction assuming zero contribution from the UD transverse direction.

$$(E_L)_{\text{predicted}} = 4.8 \text{ kN.mm}^{-2}$$

which is 20% lower than the experimentally determined longitudinal modulus of 6.2 kN.mm^{-2} (Table 8.3b).

The measured dimensions and mechanical properties are presented in Table 8.4 for bends S039, S040, S045 and S046.

8.2.2 Straight pipes test results

8.2.2.1 Cantilever test results

Straight pipe S041 (defined in Tables 8.1 and 8.4) of 200mm nominal bore was tested as a cantilever, as described in Ch. 5. Strain distribution were measured around 180° of the circumference from strain gauges affixed at the centre of the pipe. The experimental strains are compared against theoretical strains using the dimensions presented in Table 8.4 along with the experimentally determined longitudinal modulus of 6.2 kN.mm^{-2} . Both theoretical and experimental strain distribution are shown in Fig. 8.1 under end load of 660 N, where the results are reasonably comparable.

8.2.2 Torsion test results

Straight pipe S041 was tested under torsional moment. The results in terms of the inside and outside in-plane shear strains are presented graphically in Fig. 8.2 as a function of their angular position under torsional moment of 1.04 MN mm. The results are also tabulated in Table 8.5 where the directions of the experimentally determined principal strains are presented as measured from the longitudinal direction. Using the average of the measured shear strains from the inside surface and the outside surface, the corresponding shear moduli could be obtained via Eq. (8.3).

$$G_{\text{exp}} = \frac{Tr}{J \cdot \gamma_{\text{exp}}} \quad (8.3)$$

TABLE 8.4 - Dimensions and Mechanical Properties of Set I
Orthotropic Pipe Component, 2:1 Circumferential to
Longitudinal Extensibility

| | Set (IA) S039, S040 | Set (IB) S045, S046 |
|----------------------------|---------------------------------------|---------------------------------------|
| t_n (mm) | $1.3 \times 4.8_* = 6.24$ | 6.24 * |
| t_{St} | 9.67/10.5 | 9.00/14.00 * |
| t_B | 12.50 | 14.10 |
| t_j | 14.50 | 14.75 |
| t_e | 11.09 | 11.55 * |
| $2r_i$ (mm) | 202 | 253/250 |
| I_n (mm ⁴) | 2.21×10^7 | 4.12×10^7 |
| I_{St} | $3.60 \times 10^7 / 3.96 \times 10^7$ | $6.36 \times 10^7 / 10.1 \times 10^7$ |
| I_B | 4.85×10^7 | 1.055×10^7 |
| I_j | 5.78×10^7 | 11.12×10^7 |
| I_e | 4.21×10^7 | 8.40×10^7 |
| R/r_i | 3 | 2 |
| E_C (N/mm ²) | 11259 | 11259 |
| ν_{CL} | 0.30 | 0.30 |
| E_L (N/mm ²) | 6160 | 6160 |
| ν_{LC} | 0.17 | 0.17 |
| G_{LC} | 2710 | 2710 |
| λ_n | 0.176 | 0.095 |
| λ_{St} | 0.263 | 0.143 |
| λ_{Bend} | 0.331 | 0.181 |
| λ_e | 0.298 | 0.163 |

* Measured on the 3000 mm straight pipe

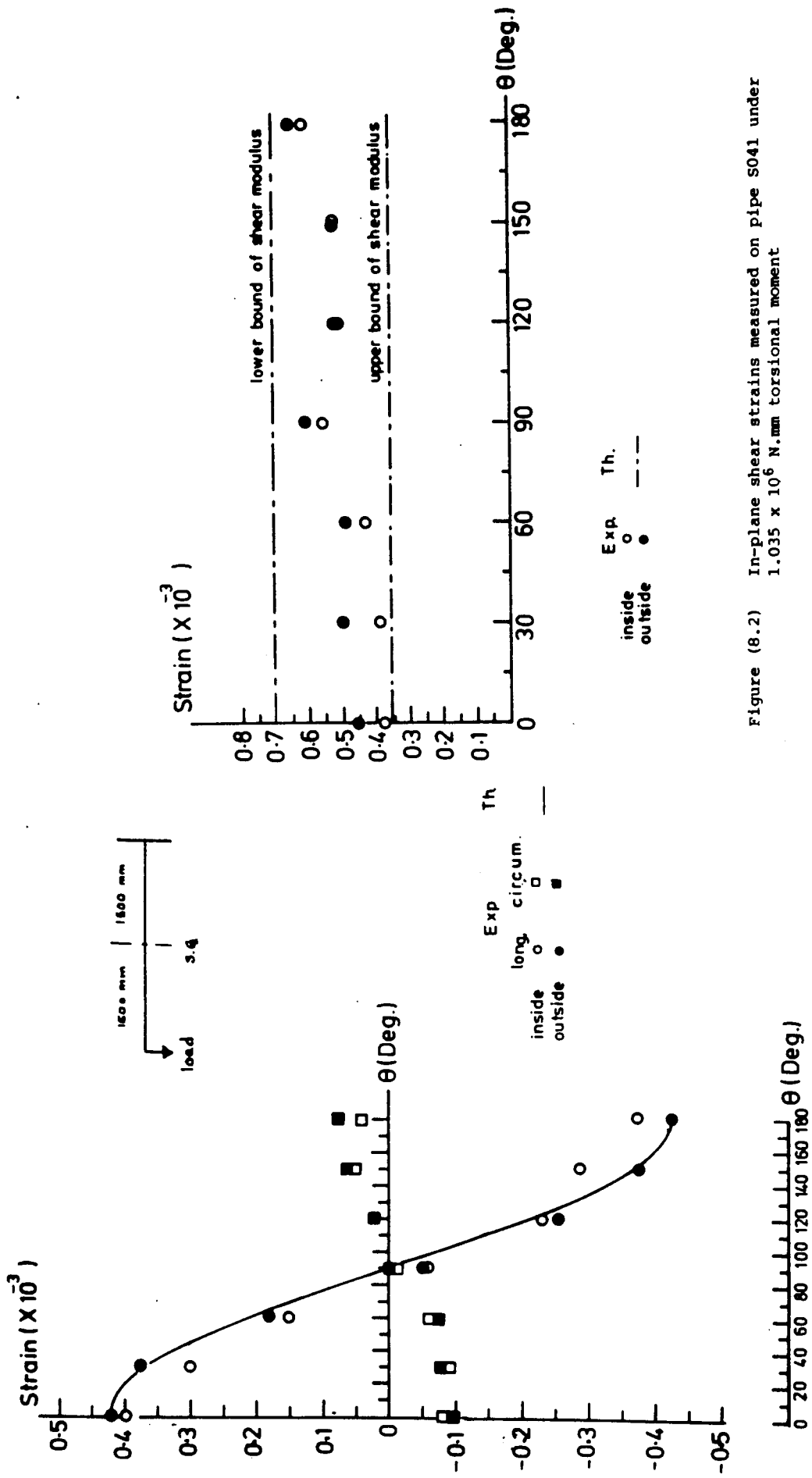


Figure (8.1) Strain distribution measured at the centre of pipe S041 under 660N cantilever end loading

Figure (8.2) In-plane shear strains measured on pipe S041 under 1.035×10^6 N.mm torsional moment

TABLE 8.5 - Shear Strains measured around 180° of a Straight Pipe Circumference (Pipe S041 of Table (8.1)) under 1.0345×10^6 N.mm torsional moment (Fig. 8.2)

| Angular Position θ (Deg.) | Inside surface | | | Outside surface | | |
|--|---------------------------------------|--------------------------------|-------------------|---------------------------------------|--------------------------------|-------------------|
| | $\epsilon_{45} \times 10^{-6}$ strain | $\gamma \times 10^{-6}$ strain | β_1^* (Deg) | $\epsilon_{45} \times 10^{-6}$ strain | $\gamma \times 10^{-6}$ strain | β_1^* (Deg) |
| 0 | -210 | 380 | -41 | -251 | 460 | +43 |
| 30 | -230 | 390 | -42 | -217 | 500 | 45 |
| 60 | -230 | 430 | -42 | -264 | 490 | -42 |
| 90 | -310 | 565 | -43 | -301 | 610 | 45 |
| 120 | -265 | 520 | +44 | -245 | 530 | 43 |
| 180 | -300 | 620 | -44 | -320 | 660 | +43 |
| Average | | 490 \pm 85 | | | 540 \pm 65 | |
| Exp. Shear Modulus (N.mm ⁻²) | 2700 | | | 2720 | | |
| Th. shear Modulus (N.mm ⁻²) | 1970-3880 | | | 1970-3880 | | |

β_1 is measured from the longitudinal direction

The in-plane shear modulus could be predicted on similar basis to that of the Young modulus by the knowledge of the glass mass per unit area of the constituent layers of glass reinforcement, e.g. using sample No. 1 of Table 8.2, the shear modulus could be predicted as follows:

$$\Sigma GJ = (GJ)_{CSM} + (GJ)_{WR} + (GJ)_{UD} + (GJ)_{CSM} \quad (8.4)$$

$$G_{\text{laminates}} t_{\text{total}} = (G_{CSM} \cdot M_{CSM} \cdot t'_{CSM} + G_{WR} \cdot M_{WR} \cdot t'_{WR} + G_{UD} \cdot M_{UD} \cdot t'_{UD})$$

- from Table (8.2) M_{CSM} , M_{WR} and M_{UD} are obtained
- from BS.4994, similar to article 8.2.1, t'_{CSM} , t'_{WR} , t'_{UD} are obtained
- $G_{CSM} = 2.8 \text{ kN.mm}^{-2}$ from article (6.3) of Ch. 6
- $G_{WR} = 3.0 \text{ kN.mm}^{-2}$ from (51)
- G_{UD} , this would have an upper and a lower bounds with accordance to theoretical work by Tsia (31).

$$(G_{UD}) \text{ lower bound} = G_r \frac{(1+v_g) G_g + v_r G_r}{(1+v_g) G_r + v_r G_g}$$

$$(G_{UD}) \text{ upper bound} = G_g \frac{(1+v_g) G_r + v_g G_g}{(1+v_r) G_g + v_g G_r}$$

where $G_g = \frac{E_g}{2(1+v_g)}$, $E_g = 73 \text{ kN.mm}^{-2}$; $v_g = 0.21$

$$G_r = \frac{E_r}{2(1+v_r)}$$
, $E_r = 2.45 \text{ kN.mm}^{-2}$, $v_r = 0.35$

∴ for glass mass percentage of 60% by mass (53% by volume) for the UD laminates, the in-plane shear modulus would be in the range of:

$$(G_{UD}) \text{ lower bound} = 2.5 \text{ kN.mm}^{-2}$$

$$(G_{UD}) \text{ upper bound} = 10.8 \text{ kN.mm}^{-2}$$

substituting back into Eq. (8.4), hence, the predicted in-plane shear modulus of total laminate is:

$$[G_{\text{laminate}}]_{\text{lower bound}} = 2.0 \text{ kN.mm}^{-2}$$

$$[G_{\text{laminate}}]_{\text{upper bound}} = 3.9 \text{ kN.mm}^{-2}$$

compares with 2.71 kN.mm^{-2} obtained experimentally (see Table 8.5).

8.2.3 Flexural behaviour of smooth bends

Four fully instrumented inside/outside bends, two of 200mm and the other two of 250mm nominal bores joined to two "one meter" straight tangents terminated with flanges, have been experimentally investigated under flexural loadings. The bends (S039, S040, S045, S046) of Table (8.1), were tested under in-plane bending, out-of-plane bending and bend S045 was also tested under combined in-plane/out-of-plane bending.

The experimental results describing the behaviour of the bends are presented as experimental flexibility factors and experimental stress intensification factors for both the in-plane and the out-of-plane modes of bending. The experimental results are compared with standard predictions such as BS.806⁽¹²³⁾ and smooth isotropic bend theory (App. II).

For GRP bends constructed from laminates having in-plane anisotropy (e.g. 2:1 extensibility ratio), the isotropic bend theory was modified from first principles of strain energy formulation. This is accomplished by substituting for the circumferential and the longitudinal stresses as in Eqs. (8.5a,b):

$$\sigma_L = \frac{E_L}{1 - \nu_{Lc} \nu_{cL}} [\epsilon_L + \nu_{cL} \epsilon_c] \quad (8.5a)$$

$$\sigma_c = \frac{E_c}{1 - \nu_{Lc} \nu_{cL}} [\epsilon_c + \nu_{Lc} \epsilon_L] \quad (8.5b)$$

and the theoretical analysis is presented in App. III.

The results of the smooth-orthotropic analysis predicts that for a bend laminate having a circumferential to longitudinal moduli ratio of two, the flexibility factor and the longitudinal SIF would be reduced, and the circumferential SIF would be slightly increased (see Fig. 4.3 of Ch. 4).

8.2.3.1 In-plane and out-of-plane flexibility factors

The experimentally determined flexibility factors are obtained by using Eqs. (I.6) and (I.18) of App. I for in-plane and out-of-plane bending respectively, where Δ/P is obtained from the best fit straight line of the measured end-deflection (Δ) recorded under the incremental application of the end load (P). The longitudinal modulus of 6.2 kN.mm^{-2} and the in-plane shear modulus of 2.7 kN.mm^{-2} together with the average effective thickness (t_e) are used to formulate the bend flexural and torsional rigidities respectively as listed in Table 8.4.

The flexibility analysis assumes that all tangents to have unity flexibility factor; the bend to have a uniform flexibility factor, and under out-of-plane bending, the torsional component of bending does not contribute to bend ovality.

The experimentally measured in-plane and out-of-plane flexibility factors are tabulated in column v of Table 8.6a and graphically in Fig. 8.3. These are determined using the average effective section second moment of area of the bend (i.e. I_e of Table 8.4). The experimental results are compared with theoretical prediction of smooth-isotropic bends (App. II), smooth-orthotropic bends (App. III) and BS.806,⁽¹²³⁾ as presented in Table 8.6b.

The consequences of using nominal thickness (as specified by BS.4994) would lead to the underestimation of the experimental results as shown in column ii for both types of flexibilities.

TABLE 8.6a - Experimental In-plane and Out-of-plane Flexibility Factors of Bends of Set I (see Table 8.1)

| Column Number | Experimental in-plane flexibility factor (K_i) | | | | Experimental out-of-plane flexibility factor (K_o) | | | | v | | | |
|---------------|--|-------------------------|--------------------------|-------------------------|--|---------------------------|----------------------------------|-------------------------|--------------------------|-------------------------|---------------------------------|---------------------------|
| | i | ii | iii | iv | i | ii | iii | iv | | | | |
| Bend Number | $\Delta/P \times 10^{-5}$ (mm/N) | Nominal thickness K_i | Straight thickness K_i | ST/Bend thickness K_i | Effective thickness λ_e | Effective thickness K_i | $\Delta/P \times 10^{-5}$ (mm/N) | Nominal thickness K_o | Straight thickness K_o | ST/Bend thickness K_o | Effective thickness λ_e | Effective thickness K_o |
| S039 | 1.714 | 0.344 | 2.42 | 3.89 | 0.298 | 3.34 | 2.52 | 0.02 | 5.35 | 8.38 | 0.298 | 7.68 |
| S040 | 1.580 | 0.100 | 2.02 | 3.25 | 0.298 | 2.87 | 2.46 | -0.17 | 5.03 | 7.91 | 0.298 | 7.32 |
| S045 | 1.08 | 1.46 | 4.19 | 6.95 | 0.163 | 6.69 | 1.40 | 1.70 | 9.53 | 13.09 | 0.163 | 15 |
| S046 | 1.04 | 1.27 | 3.90 | 6.47 | 0.163 | 6.31 | 1.59 | 3.41 | 12.23 | 16.79 | 0.163 | 18.46 |

TABLE 8.6b - Theoretical in-plane and Out-of-plane Flexibility Factors of Bends of Set I (see Table 8.1)

| Bend Number | $2r_i$ | R/r_i | λ_e | Theory-smooth bends | | BS 806 (123) |
|-------------|--------|---------|-------------|---------------------|------------------------|--------------|
| | | | | Isotropic (App. II) | Orthotropic (App. III) | |
| S039 | 202 | 3 | 0.298 | 5.49 | 3.87 | 5.5 |
| S040 | 202 | 3 | 0.298 | 5.49 | 3.87 | 5.5 |
| S045 | 253 | 2 | 0.163 | 10.03 | 7.25 | 10 |
| S046 | 253 | 2 | 0.163 | 10.03 | 7.25 | 10 |

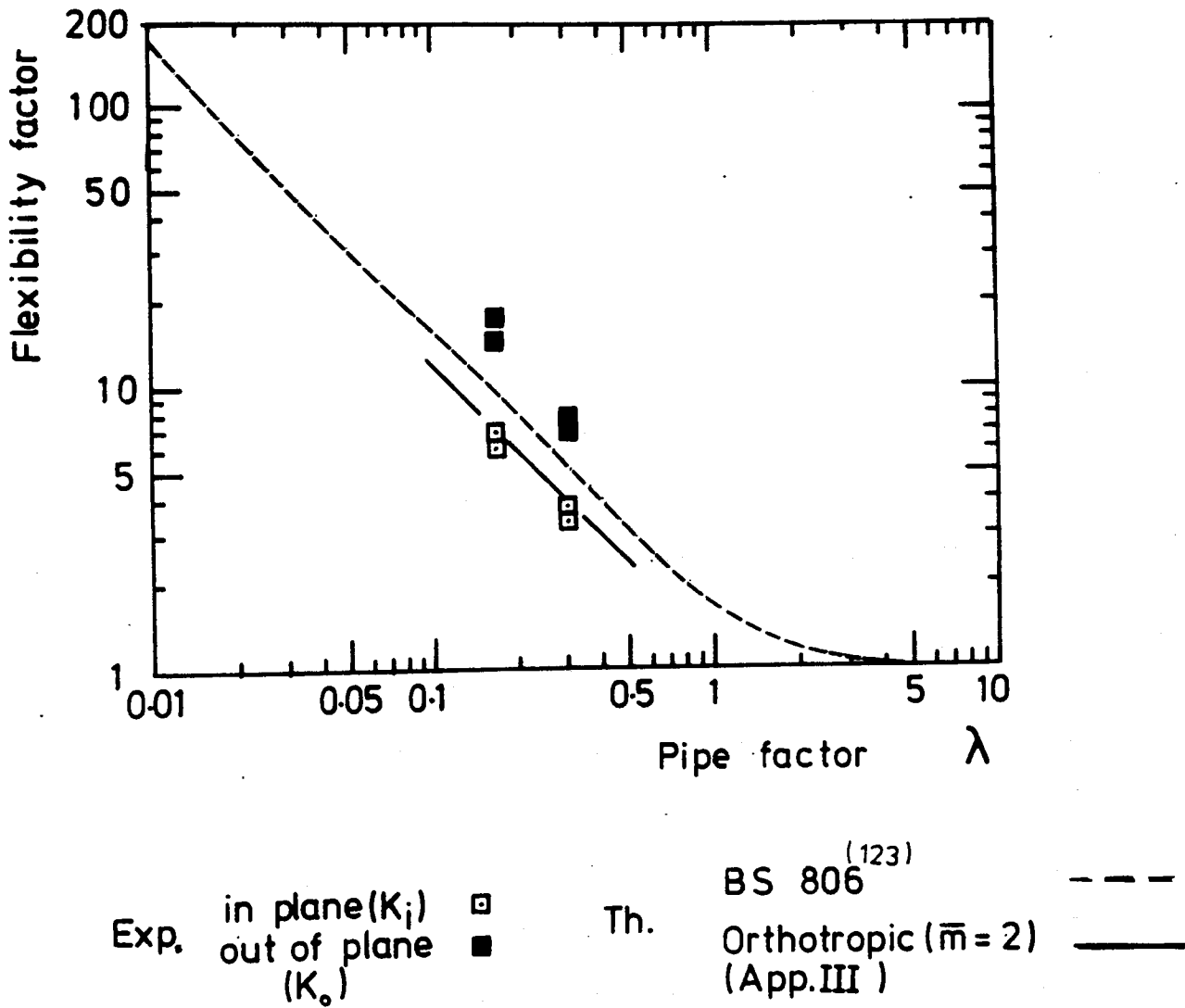


Figure (8.3) Experimentally determined in-plane and out-of-plane flexibility factors for orthotropic S039, S040, S045, S046 bends

The experimentally determined in-plane flexibility factors are favourably compared with the smooth-orthotropic prediction theory taking the 2:1 extensibility ratio into consideration, and those are about 40% lower than BS.806 specification (Fig. 8.3) and smooth-isotropic bend prediction (see Table 8.6b).

The experimentally determined out-of-plane flexibility factors follow a similar pattern for all the bends tested in Chs. 6 and 7, whereby they are higher than their corresponding experimentally determined in-plane flexibilities. This is thought to be attributed to the weaker "joint" torsional rigidity in comparison to the rest of the bend body.

In actual piping systems, the flexibility of the system is favourable, not only to minimise anchor loads on the attached vessels, but also to reduce cost, e.g. less numbers of expansion bellows. With the variability of flexibility factors shown by the present bends from in-plane bending to out-of-plane bending, it is justifiable from a design point of view, to use the minimum value of the flexibility factor i.e. in-plane values, hence estimating conservative anchor loads.

8.2.3.2 In-plane and out-of-plane stress ratio distribution and stress intensification factors (SIF)

At the same time as the end-deflections were recorded under the incremental application of the end load, strain measurements in the circumferential, skew, and the longitudinal directions were recorded from strain gauge rosettes situated at the centre of the bend. Experimental stresses are obtained using the stress/strain relation of Eq. (8.5).

The test results are presented as stress ratio distribution and stress intensification factors as calculated by Eqs. (I.9) and (I.20) of App. I for in-plane bending and out-of-plane bending respectively.

(i) In-plane stress results of bends S039, S040, S045 and S046

The experimentally measured strain and stress ratio distributions are presented in Figs. 8.4 and 8.5 for bends S039 and S040 under 1.79 MN mm in-plane bending, and in Figs. 8.6 and 8.7 for bends S045 and S046 under 2.22 MN mm in-plane bending. The theoretical stress distributions are based on the analysis presented in App. III for orthotropic smooth bends, together with that presented in App. II for smooth isotropic bends. For both the experimental and the theoretical results, the average effective thickness (t_e) is used to formulate σ_n and λ_e .

The following summary of comparison between experimental results and smooth-orthotropic prediction of bend theory would be relevant to describe the actual bend behaviour.

- (a) Measured strains versus increment of applied bending moment formed a reasonable linear relationship.
- (b) Comparison of the measured strains and stress ratios between the bends of similar construction showed minimal scatter.
- (c) The experimentally measured circumferential and longitudinal stress ratios follow a similar pattern of distribution with theory.
- (d) Figs. 8.4b and 8.7b show that the inside experimental circumferential stress ratios are favourably compared with theory, whilst on the outside they are marginally lower. This could be attributed to the higher anisotropy of the outside surface brought about by the presence of the UD reinforcements nearer to outside surface (Table 8.2).
- (e) The experimentally measured longitudinal stress ratios show a higher flexural bending stress nearer to the intrados ($\theta = 0^\circ$) than theory predicts (Figs. 8.5 and 8.7a). This discrepancy has been previously observed on the CSM bends presented in Chapter 6, and it is believed to be due to the extra thickening present at the intrados (Table 8.2).

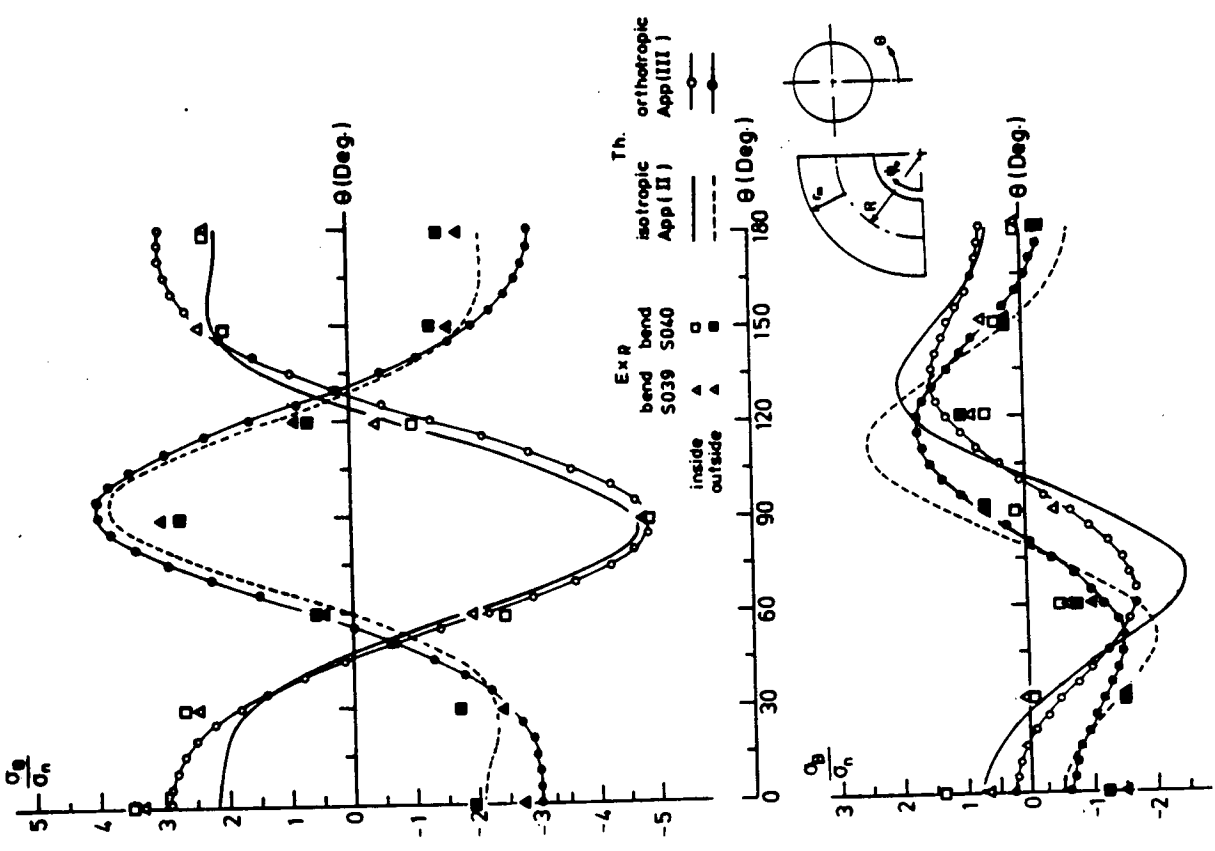


Figure (8.5) Stress distribution measured on bends S039 and S040 under 1.79×10^6 N.mm in-plane/closing bending moment

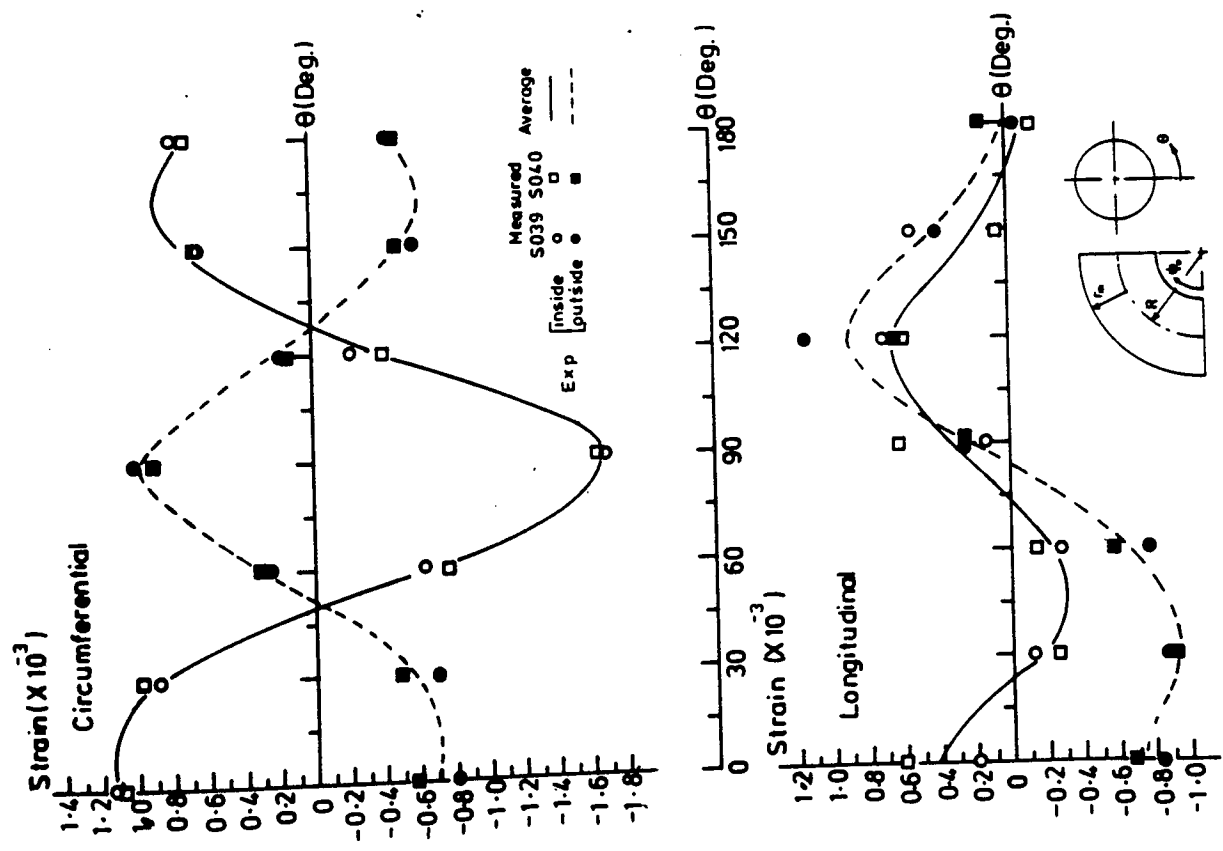


Figure (8.4) Strain distribution measured on bends S039 and S040 under 1.79×10^6 N.mm in-plane/closing bending moment

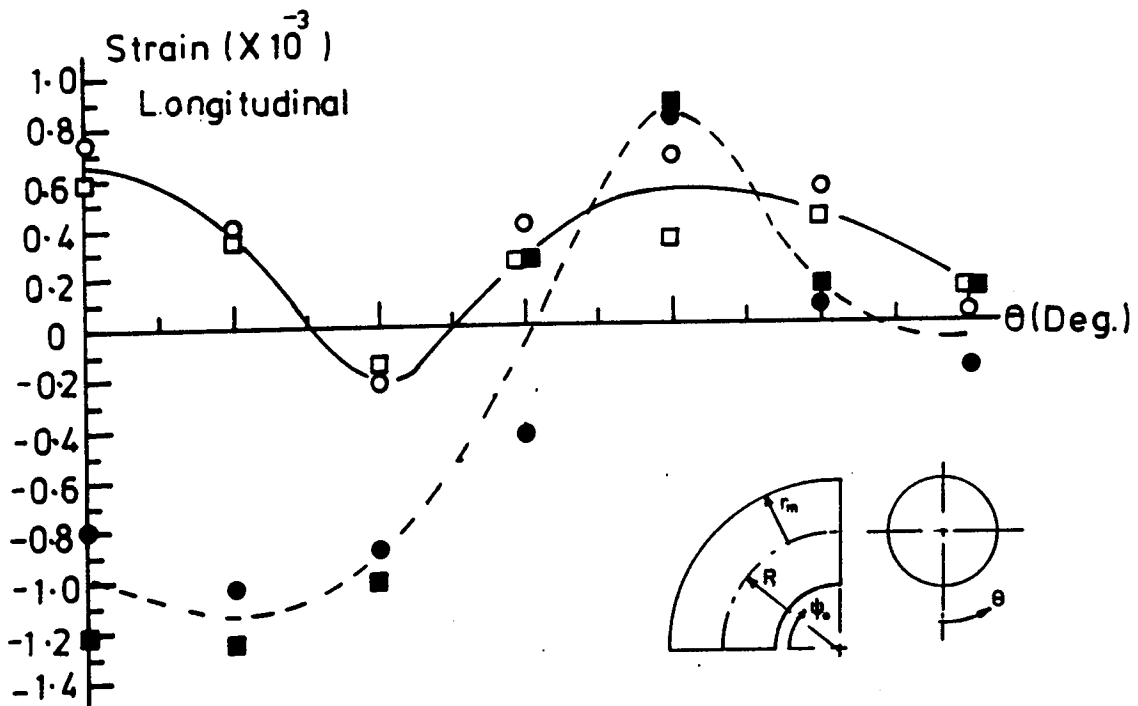
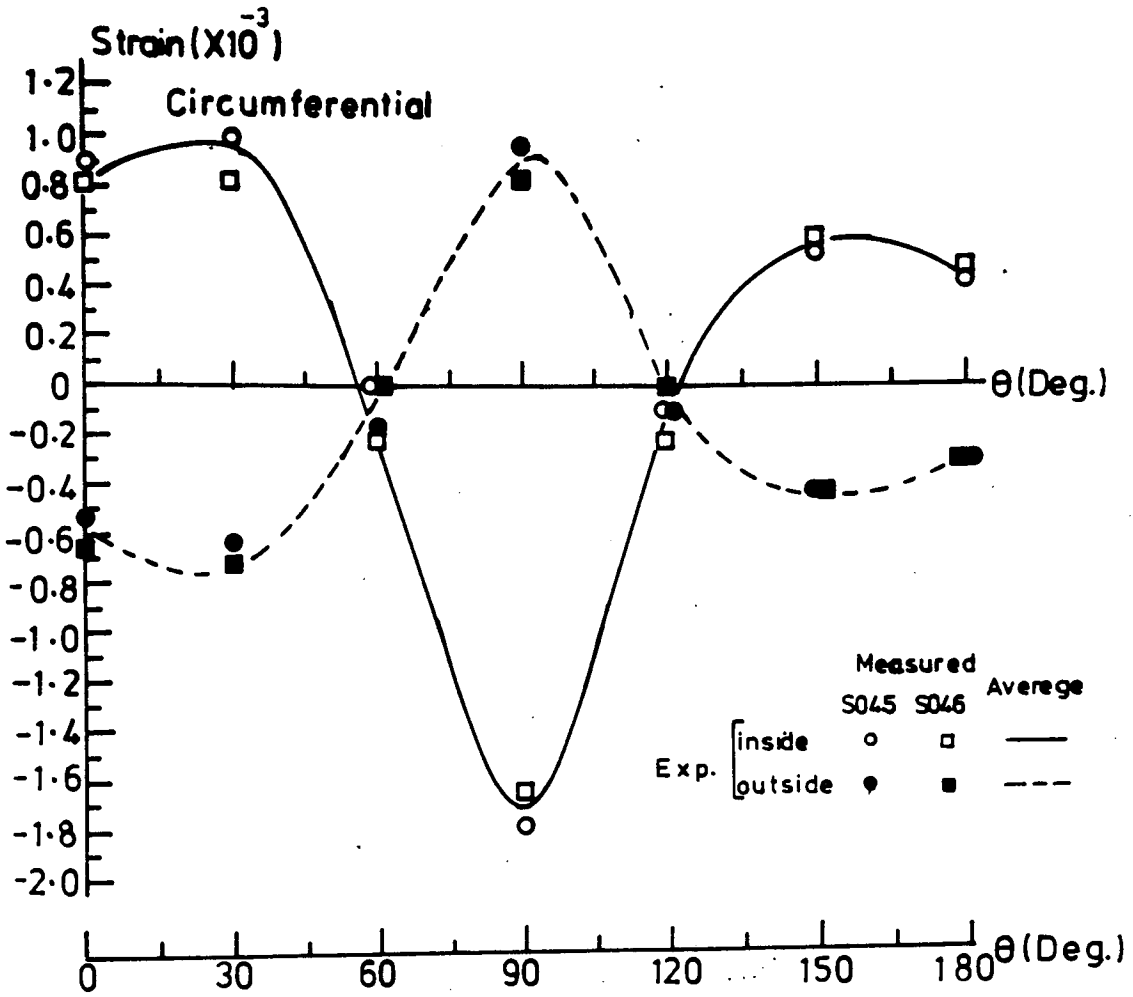


Figure (8.6) Strain distribution measured on bends S045 and S046 under 2.22×10^6 N.mm in-plane/closing bending moment

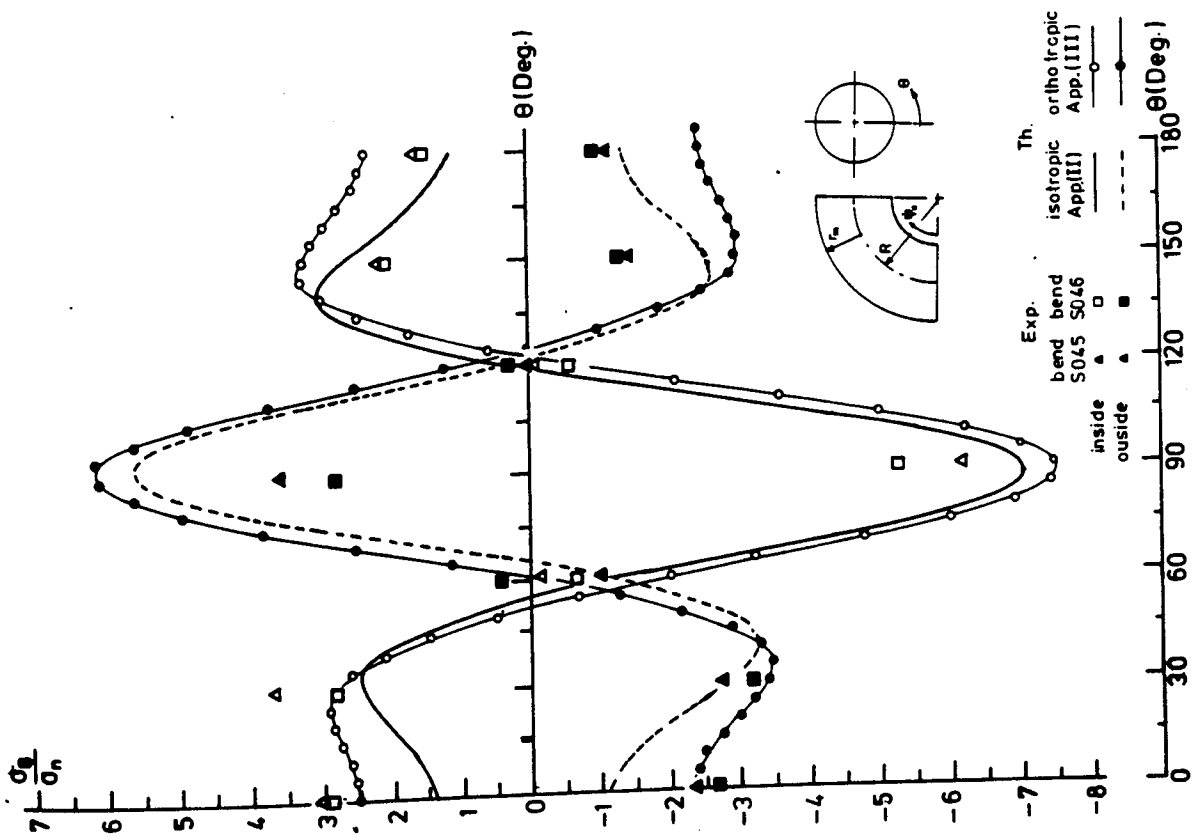


Figure (9.7a) Circumferential stress distribution measured on bands S045 and S046 under 2.22×10^6 N mm in-plane/closing bending moment.

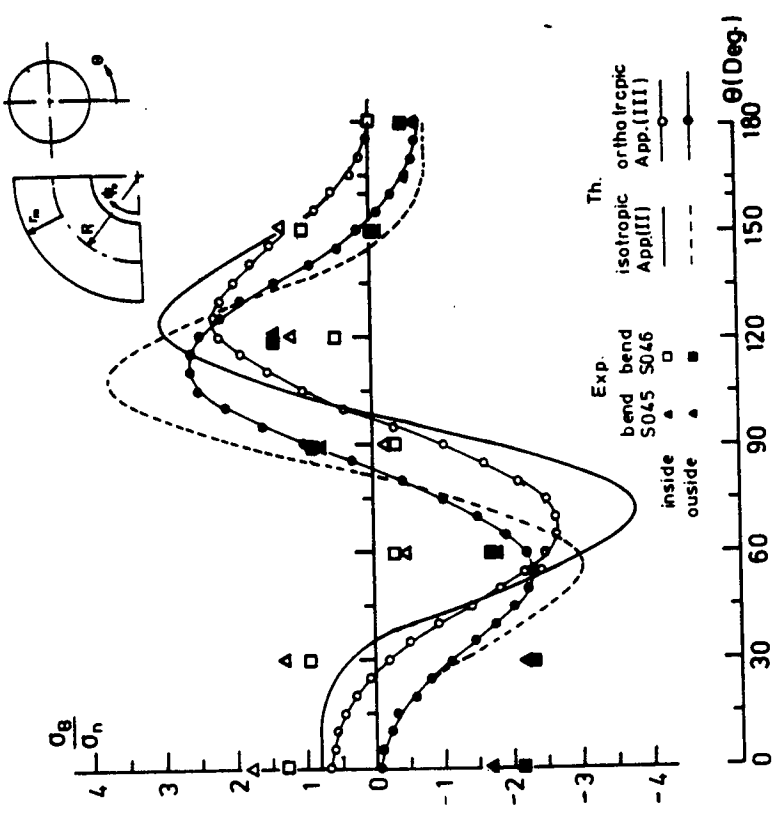


Figure (9.7b) Longitudinal stress distribution measured on bands S045 and S046 under 2.22×10^6 N mm in-plane/closing bending moment.

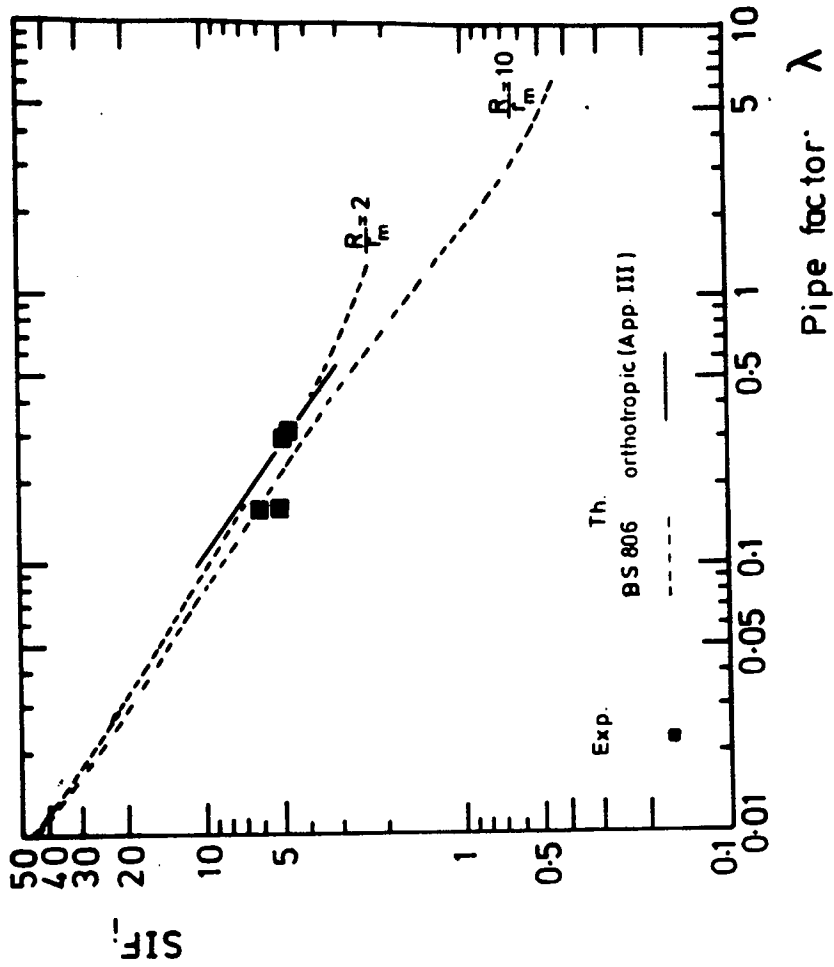


Figure (8-8a)
 Maximum in-plane longitudinal stress intensification factors (SIF_L) of orthotropic S039, S040, S045 and S046 bends

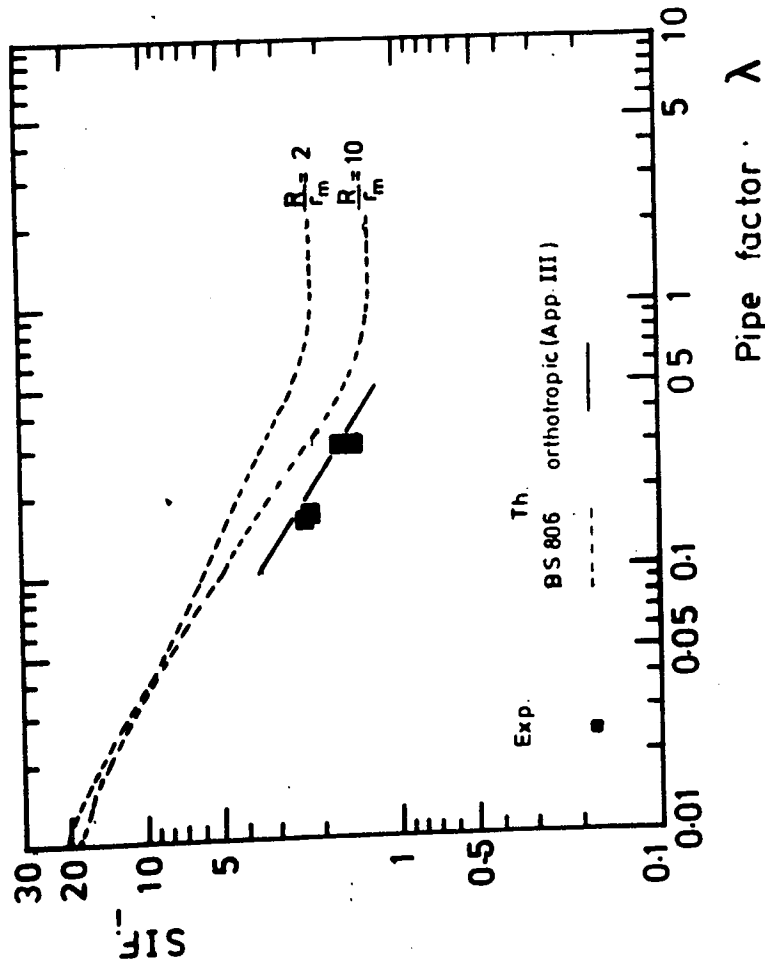


Figure (8-8b)
 Maximum in-plane circumferential stress intensification factors (SIF_C) of orthotropic S039, S040, S045 and S046 bends

TABLE 8.7 - Experimentally determined In-plane SIF. for Orthotropic Bends of 2:1 Extensibility Ratio of Set No. I (see Table 8.1 i.e. Bends S039, S040, S045, and S046)

| Bend Number | λ_e | Experimental SIF | | | | | | Theoretical SIF | | | | | |
|-------------|-------------|-----------------------------|-----------------------------|-----------------------------|----------------------------|--------------|---------|-----------------|---------|------------------------|---------|--|--|
| | | Longitudinal | | Circumferential | | BS 806 (123) | | Smooth Bend | | Orthotropic (App. III) | | | |
| | | Inside | Outside | Inside | Outside | long | circum. | long | circum. | long | circum. | | |
| S039 | 0.298 | 0.9 $\theta = 120^\circ$ | -1.5 $\theta = 0^\circ$ | -4.7 $\theta = 90^\circ$ | 3.0 $\theta = 90^\circ$ | 2.5 | 4.5 | 2.5 | 4.6 | 1.7 | 4.8 | | |
| | | 1.7 $\theta = 120^\circ$ | | | | | | | | | | | |
| S040 | 0.298 | 1.4 $\theta = 0^\circ$ | -1.5 $\theta = 30^\circ$ | -4.8 $\theta = 90^\circ$ | 2.7 $\theta = 90^\circ$ | 2.5 | 4.5 | 2.5 | 4.6 | 1.7 | 4.8 | | |
| | | 0.7 $\theta = 120^\circ$ | | | | | | | | | | | |
| S045 | 0.163 | 1.7 $\theta = 0^\circ$ | -2.2 $\theta = 30^\circ$ | -6.1 $\theta = 90^\circ$ | 3.6 $\theta = 90^\circ$ | 4.5 | 7.0 | 3.7 | 7.1 | 2.65 | 7.45 | | |
| | | 1.5 $\theta = 120^\circ$ | | | | | | | | | | | |
| S046 | 0.163 | 1.25 $\theta = 0^\circ$ | -2.3 $\theta = 30^\circ$ | -5.3 $\theta = 90^\circ$ | 2.8 $\theta = 90^\circ$ | 4.5 | 7.0 | 3.7 | 7.1 | 2.65 | 7.45 | | |
| | | 1.0 $\theta = 135^\circ$ | | | | | | | | | | | |

(f) Strains and stresses measured under in-plane closing and in-plane opening modes of bending form a mirror image when plotted as a function of the angular position.

(g) The directions of the principal stresses deviate only few degrees from the longitudinal or the circumferential axes.

The maximum/minimum experimentally measured stress ratio peaks (i.e. SIF) are summarised in Table 8.7 as a function of their angular position and graphically presented in Fig. 8.8a,b where they are compared with theoretical prediction as specified by smooth isotropic bend theory (App. II), smooth-orthotropic bend theory (App. III) and BS806⁽¹²³⁾.

(ii) Out-of-plane stress results of bends S039, S040, S045 and S046

The experimentally measured strain and stress ratio distributions are presented in Figs. 8.9 and 8.10 for bends S039 and S040 under 1.25 MN mm out-of-plane bending, and in Figs. 8.11 and 8.12 for bends S045 and S046 under 1.32 MN mm out-of-plane bending moment. The theoretical stress ratio distributions are based on the analysis presented in App. II and App. III for isotropic and orthotropic smooth bends respectively.

The strain and the stress ratio distributions could be described as follows:

- (a) The experimentally measured inside longitudinal strains and stress ratios are lower than those on the outside surface for all the tested bends as shown in Figs. 8.8-8.11. The outside stress ratios show a better pattern of distribution with smooth-orthotropic theory predictions.
- (b) The experimentally measured circumferential stress ratios follow a similar pattern to smooth-orthotropic theoretical predictions, with comparable peak magnitude. The maximum circumferential stress

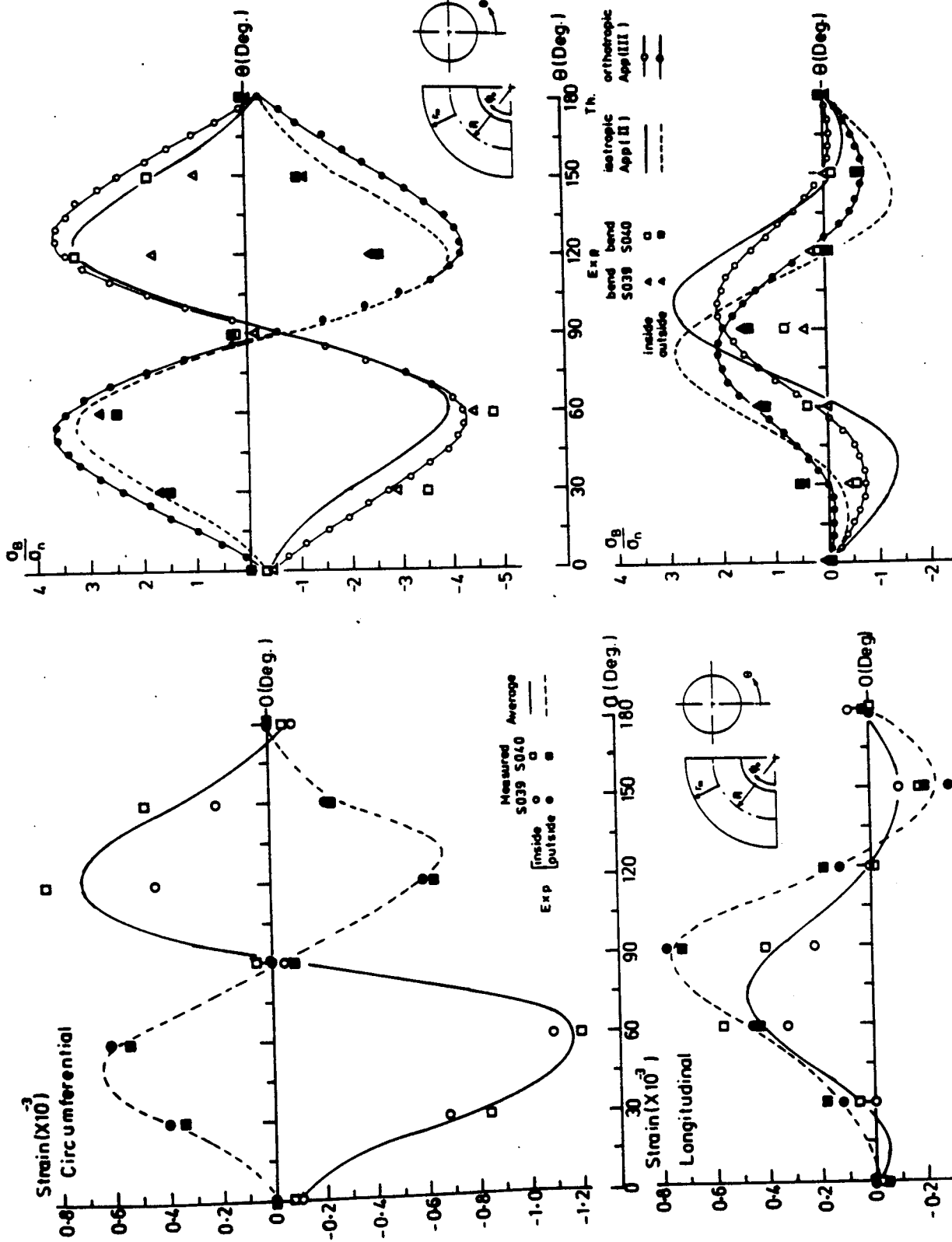


Figure (8.9) Strain distribution measured on bends S039 and S040 under 1.25×10^6 N.mm out-of-plane bending moment

Figure (8.10) Stress distribution measured on bends S039 and S040 under 1.25×10^6 N.mm out-of-plane bending moment

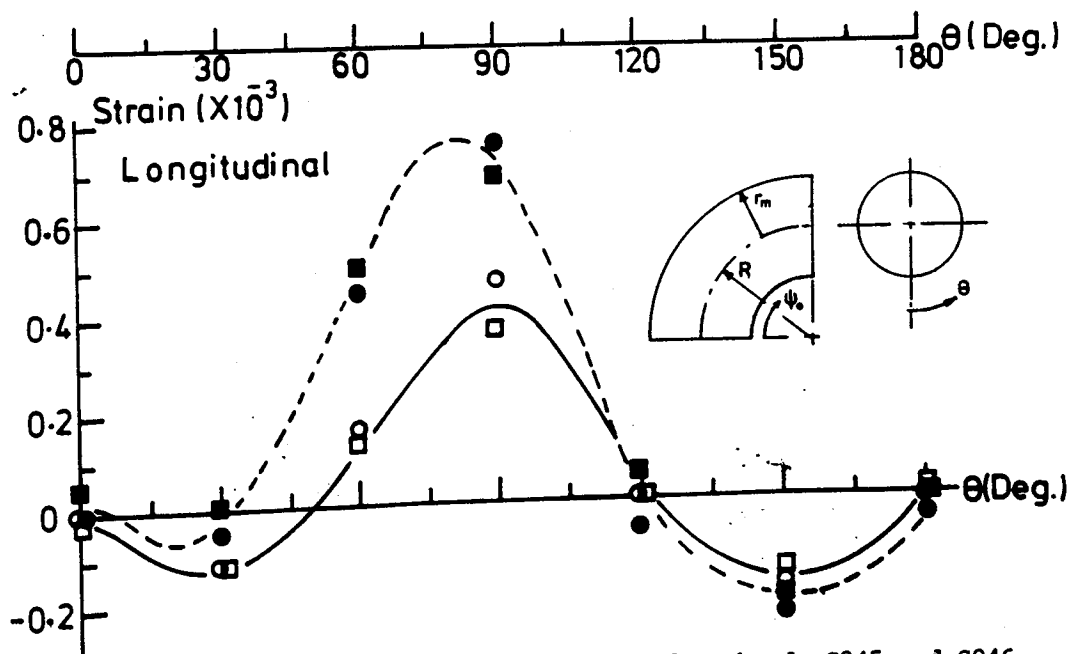
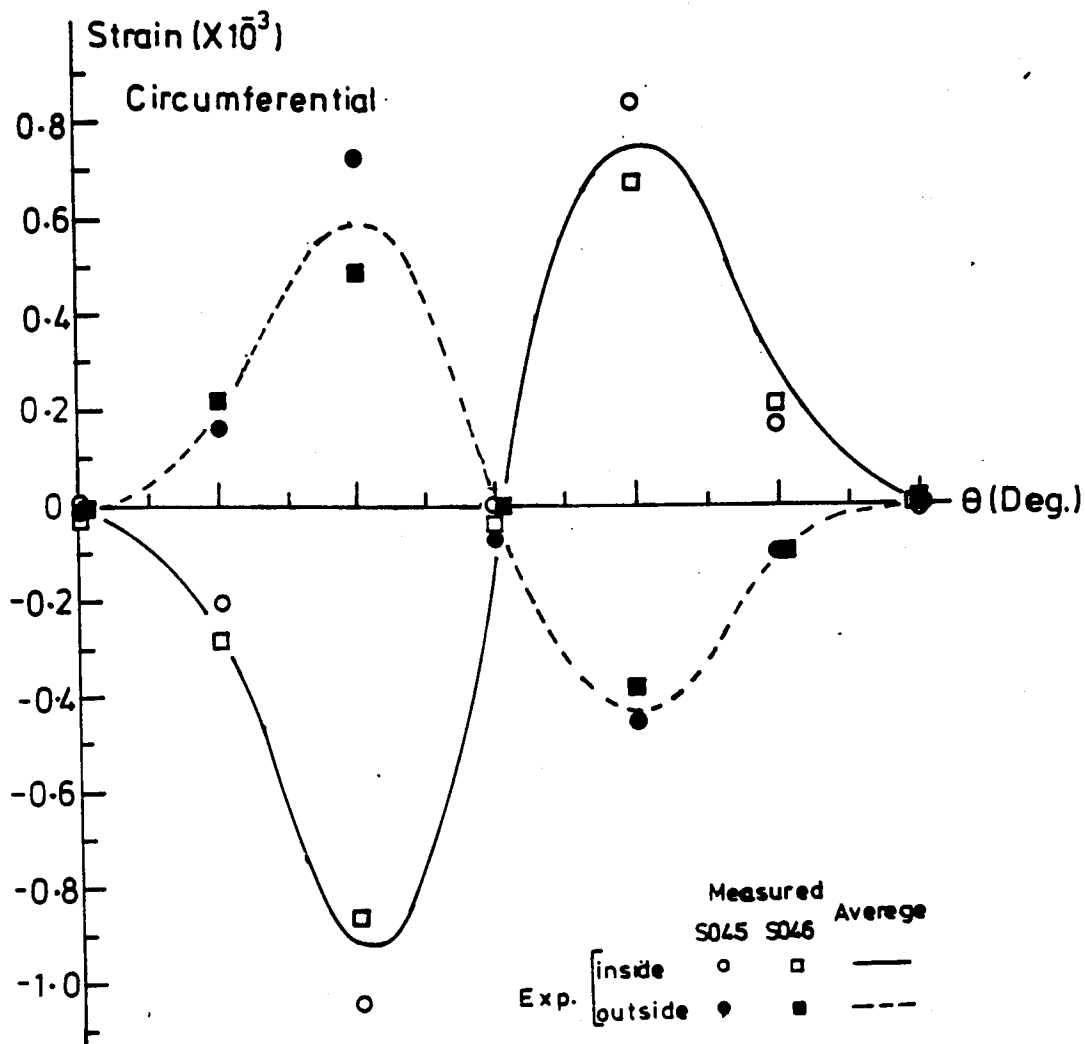


Figure (8.11) Strain distribution measured on bends S045 and S046 under 1.32×10^6 N.mm out-of-plane bending moment

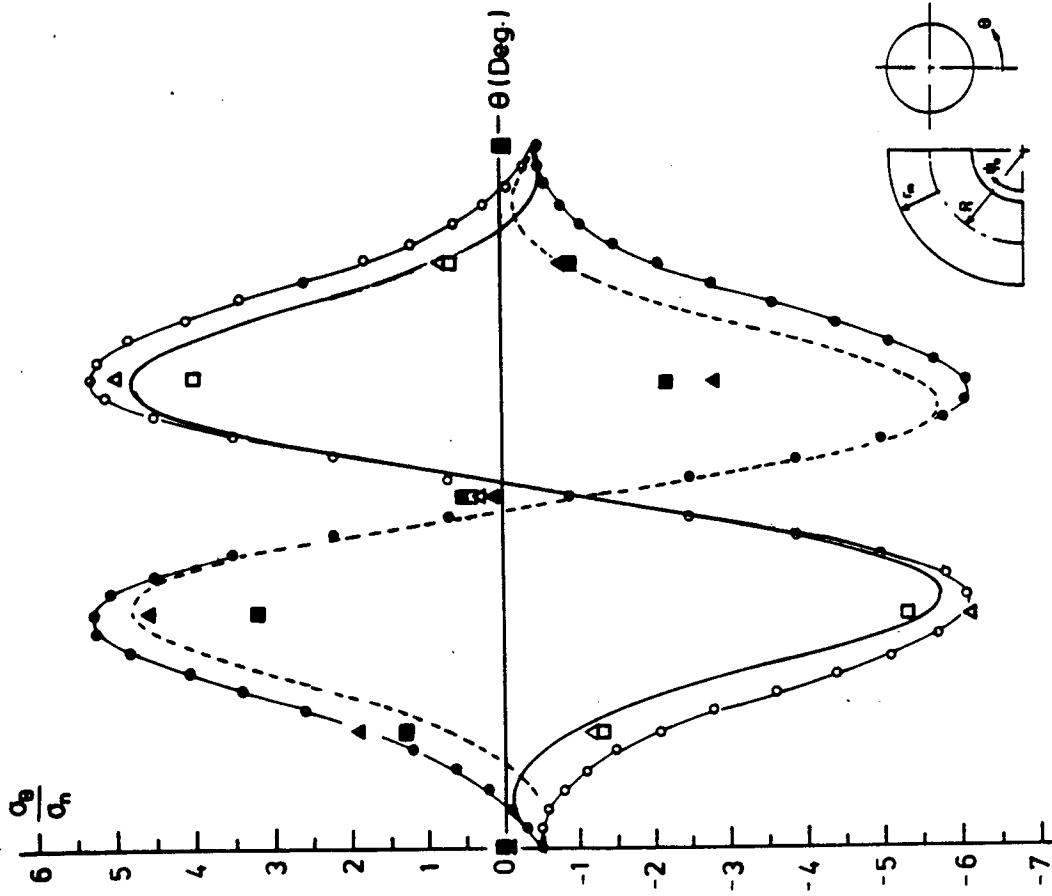


Figure (8.12b) Circumferential stress distribution measured on bends S045 and S046 under 1.32×10^6 N mm out-of-plane bending moment.

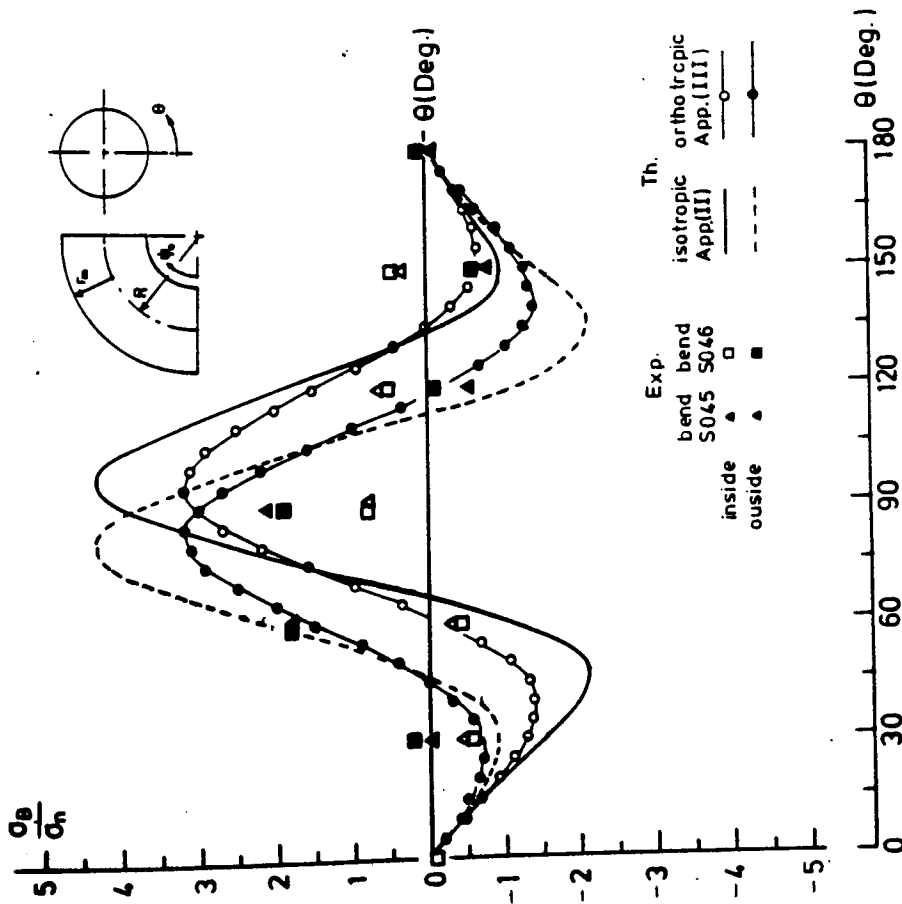


Figure (8.12a) Longitudinal stress distribution measured on bends S045 and S-46 under 1.32×10^6 N mm out-of-plane bending moment.

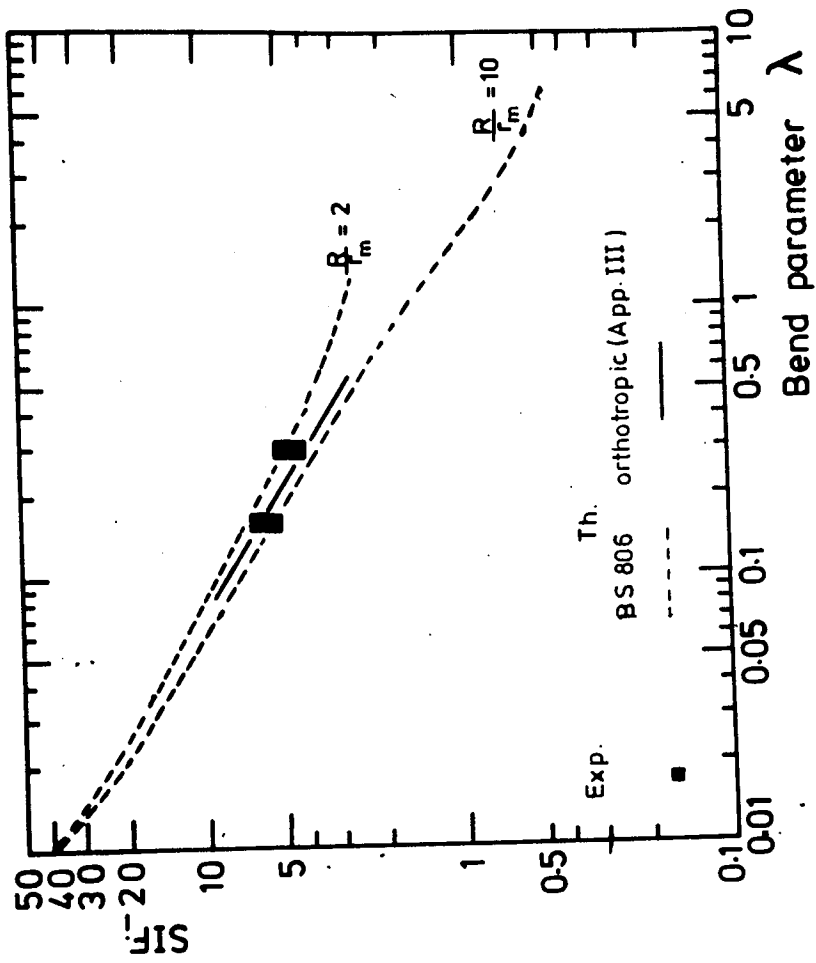


Figure (8.13b)

Maximum out-of-plane circumferential stress intensification factors (SIF_{QC}) of orthotropic S039, S040, S045 and S046 bends

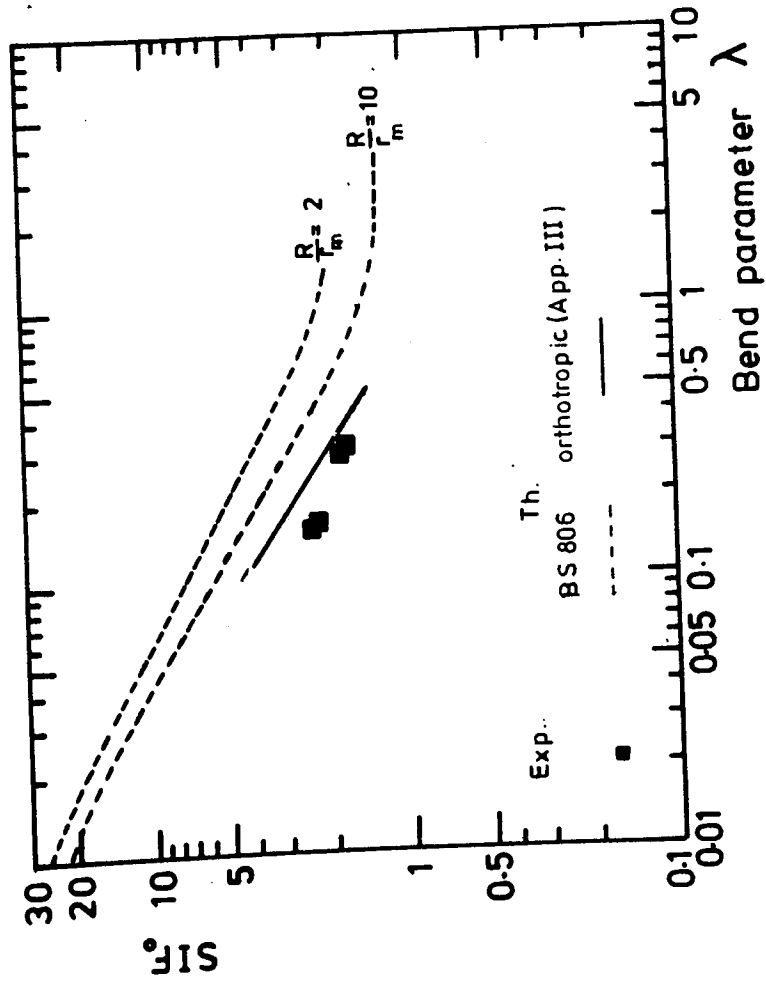


Figure (8.13a)

Maximum out-of-plane longitudinal stress intensification factors (SIF_{QL}) of orthotropic S039, S040, S045 and S046 bends

TABLE 8.8 - Experimentally determined Out-of-plane SIF for Orthotropic Bends of 2:1 Extensibility Ratio of Set No. I (see Table 8.1 i.e. Bends S039, S040, S045, and S046)

| Bend Number | λ_e | Experimental SIF | | | | Theoretical SIF | | | | | | | |
|-------------|-------------|------------------|---------------------|----------------------|---------------------|----------------------|---------------------|----------------------|---------|------------------------|---------|-----|-----|
| | | Longitudinal | | Circumferential | | BS 806 | | Smooth Bend | | Orthotropic (App. III) | | | |
| | | Inside | Outside | Inside | Outside | long | circum. | long | circum. | long | circum. | | |
| S039 | 0.298 | 0.4 | $\theta = 90^\circ$ | -4.4 | $\theta = 60^\circ$ | 2.9 | $\theta = 50^\circ$ | 3.5 | 4.5 | 2.9 | 3.9 | 2.1 | 4.2 |
| | | | 1.75 | $\theta = 80^\circ$ | 1.8 | $\theta = 120^\circ$ | -2.4 | $\theta = 120^\circ$ | | | | | |
| S040 | 0.298 | 0.9 | $\theta = 80^\circ$ | -4.9 | $\theta = 50^\circ$ | -2.6 | $\theta = 50^\circ$ | 3.5 | 4.5 | 2.9 | 3.9 | 2.1 | 4.2 |
| | | | 1.75 | $\theta = 80^\circ$ | 3.5 | $\theta = 125^\circ$ | -2.6 | $\theta = 120^\circ$ | | | | | |
| S045 | 0.163 | 2.25 | $\theta = 75^\circ$ | -6.1 | $\theta = 60^\circ$ | 4.5 | $\theta = 60^\circ$ | 5.5 | 7.0 | 4.25 | 5.75 | 3.2 | 6.1 |
| | | | 1.2 | $\theta = 105^\circ$ | 5.0 | $\theta = 120^\circ$ | 3.25 | $\theta = 120^\circ$ | | | | | |
| S046 | 0.163 | 2.25 | $\theta = 75^\circ$ | -5.3 | $\theta = 60^\circ$ | 3.25 | $\theta = 60^\circ$ | 5.5 | 7.0 | 4.2 | 5.75 | 3.2 | 6.1 |
| | | | 1.2 | $\theta = 105^\circ$ | 4.0 | $\theta = 120^\circ$ | -2.2 | $\theta = 120^\circ$ | | | | | |

ratio is located on the inside surface for all the bends tested, and located at an angular position of $\theta = 50^\circ$ - 60° .

- (c) Minimal or negligible longitudinal and circumferential stress ratios occur at both the intrados ($\theta = 0^\circ$) and the extrados ($\theta = 180^\circ$).
- (d) Due to the torsional component of bending, the principal stress do not lie in the principle longitudinal and circumferential axes of the bend.

The maximum-minimum experimental stress ratios are summarised in Table 8.8 together with their theoretical comparison to BS806⁽¹²³⁾, smooth-isotropic (App. II) and smooth-orthotropic (App. III) predictions, and are graphically presented in Fig. 8.13a,b.

8.2.3.3 Combined in-plane (closing)/out-of-plane bending of bend S045

Bend S045 (250mm nominal bore) of Table 8.1 was loaded under combined in-plane (closing)/out-of-plane bending. End loads up to 1.75 kN were applied perpendicularly to each other at the end of the free tangent simulating a total force of $\sqrt{2} \cdot p$ inclined 45° from the plane of the bend. All strains and deflections showed a reasonable linear relationship with the applied load.

The experimentally measured strains under the combined loading are compared with the superposition of the strains measured individually under in-plane and the out-of-plane tests reported in article 8.2.3.2. They are presented in both the circumferential and the longitudinal directions on both the inside and the outside surfaces in Table 8.9.

The superimposed strains compare accurately with those measured under the combined bending mode. This indicates the validity of predicting bend strains and stresses under combined loading from stress factors obtained from individual testing.

TABLE 8.9 - Results of Experimentally measured Strains under combined In-plane/Out-of-plane Bending Moment of 2.21×10^6 N.mm applied at 45° to the plane of Bend S045 (1500 N in-plane and out-of-plane loads)

| Angular Position (Deg.) | 0 | 30 | 60 | 90 | 120 | 150 | 180 |
|---|------|------|-------|-------|------|------|------|
| <u>Inside long. ($\times 10^{-6}$ strain)</u> | | | | | | | |
| In-plane | 570 | 310 | - 180 | 310 | 520 | 420 | 30 |
| Out-of-plane | 0 | -120 | 100 | 460 | 0 | -320 | 0 |
| In/Out superimposed | 570 | +190 | - 30 | 770 | 520 | 100 | 30 |
| In/Out measured | 580 | 180 | - | 740 | 520 | 130 | 70 |
| <u>Outside long. ($\times 10^{-6}$ strain)</u> | | | | | | | |
| In-plane | -600 | -800 | - 700 | 340 | 670 | 50 | -180 |
| Out-of-plane | 0 | - 40 | 440 | 750 | - 70 | -260 | 50 |
| In/Out superimposed | -600 | -840 | - 260 | 1090 | 600 | -210 | -130 |
| In/Out measured | -620 | -840 | - 270 | 1080 | 560 | -200 | -130 |
| <u>Inside circum. ($\times 10^{-6}$ strain)</u> | | | | | | | |
| In-plane | 690 | 760 | 0 | -1400 | - 70 | 420 | 340 |
| Out-of-plane | 0 | -320 | -1050 | 0 | 850 | 170 | 0 |
| In/Out superimposed | 690 | 440 | -1050 | -1400 | 780 | 590 | 340 |
| In/Out measured | 680 | 430 | -1080 | -1390 | 770 | 590 | 310 |
| <u>Outside circum. ($\times 10^{-6}$ strain)</u> | | | | | | | |
| In-plane | -420 | -500 | - 150 | 700 | - 70 | -320 | -230 |
| Out-of-plane | 0 | 160 | 730 | - 70 | -460 | -100 | 0 |
| In/Out superimposed | -420 | -340 | 580 | 680 | -530 | -420 | -230 |
| In/Out measured | -450 | -330 | 560 | 690 | -520 | -410 | -250 |

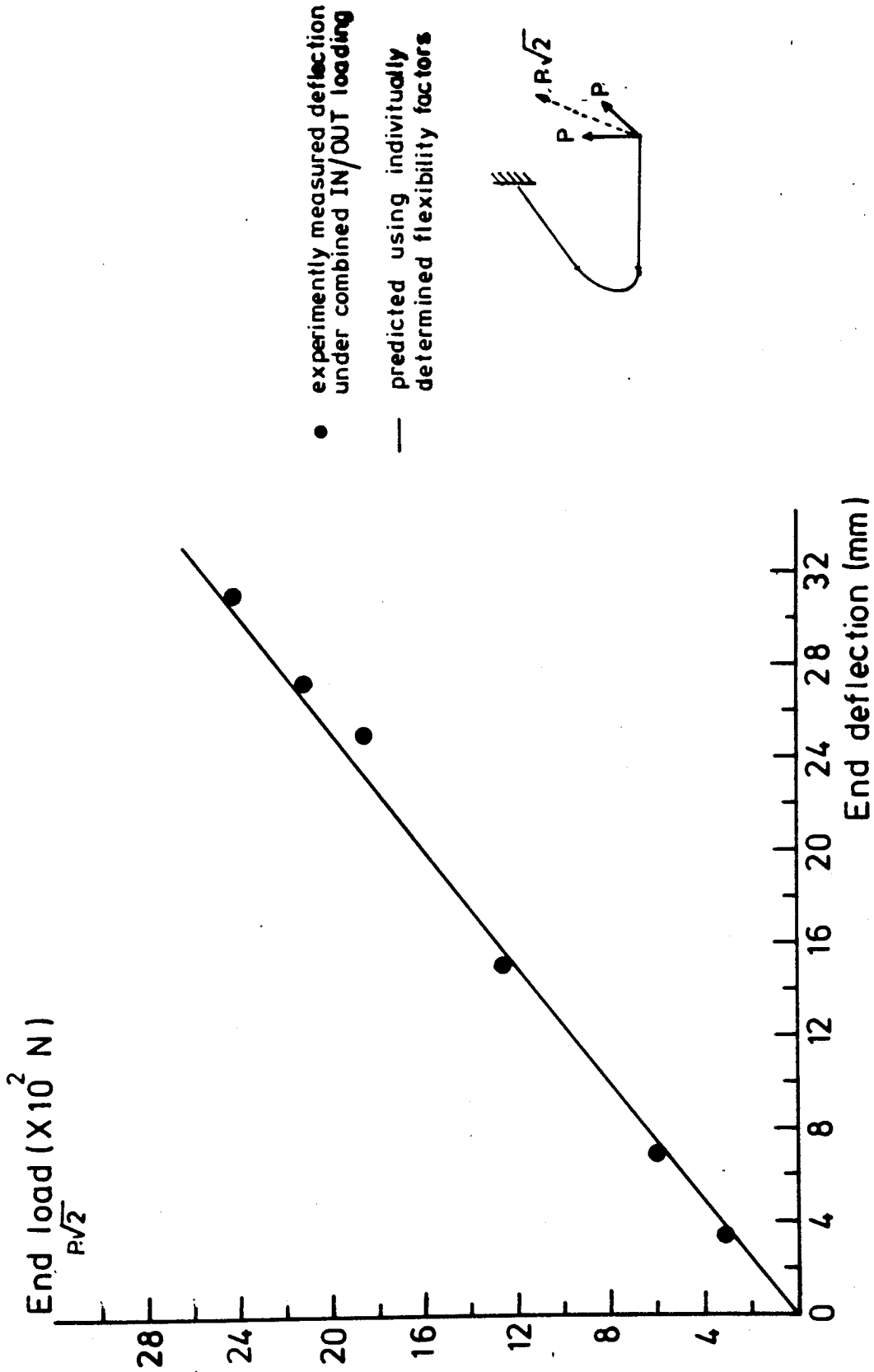


Figure (8.14) End-deflection versus end-load of bend S045 under combined in/out loading

The experimentally measured end-deflections under the combined loading is compared in Fig. 8.14 with the resultant deflection $\Delta_{IN/OUT}$ calculated by Eq. (8.6):

$$\Delta_{IN/OUT} = [\Delta_{IN}^2 + \Delta_{OUT}^2]^{\frac{1}{2}} \quad (8.6)$$

Δ_{IN} is calculated using K_1 of Table 8.6a, EI of Table 8.4 and Eq. (I.6) of App. I. Δ_{OUT} is calculated using K_0 of Table 8.6a, EI and GJ of Table 8.4 and Eq. (I.18) of App. I.

8.3 Orthotropic CSM/WR straight pipes and smooth bends of 1:1

circumferential to longitudinal extensibility ratio, sets II, III and IV

8.3.1 Glass content, dimensions and mechanical properties

In-plane and out-of-plane flexural test results of bend sets II, III and IV of Table 8.1 are presented as flexibility factors and longitudinal and circumferential SIF..

The bend fittings and tangents of Set II are constructed from CSM/WR reinforcements. Whilst for Sets III and IV, the bend fittings are constructed from WR reinforcements and the tangents are constructed from FW reinforcements. Thus, the common factor among all bend fittings is 1:1 longitudinal to circumferential extensibility ratio. Flexibility and stress test results are compared with the prediction of isotropic bend theory presented in App. II and BS806⁽¹²³⁾ specifications.

Burn-off⁽³³⁾ test results are presented in Tables 8.10a,b for both types of bends. They are presented in the form of glass mass percentage, glass mass per unit area and thickness measured at the different parts of the bend/tangent structure. Similar to the previous burn-off test results, the intrados is found to be the thickest amongst the bend perimeter, where the maximum value of glass mass per unit area

is also located. The directional young moduli were obtained by testing rings and longitudinal strips⁽¹¹⁶⁾ cut from the bends, and are presented in Tables 8.11 and 8.12 together with the measured Poisson's ratios.

The dimensions and the mechanical properties representing the straights and the bends are summarised in Tables 8.13 and 8.14 for all bend Sets II, III and IV.

8.3.2 Straight pipes test results

8.3.2.1 Cantilever test results

Cantilever test results, in the form of strain distribution around 180° of the circumference of straight pipes S044 and S031, are presented in Figs. 8.15 and 8.16 respectively, compared with the prediction of simple beam theory. For pipe S031, the elastic constants are predicted using Tsia analysis summarised in App. V, using $\bar{c} = 0.20$.

8.3.2.2 Torsion test results

Test results in the form of in-plane shear distribution around 180° of the circumference of straight pipes S044 and S032 are presented in Figs. 8.17 and 8.18 respectively.

Based on the average shear strain values of Fig. 8.17, pipe S044 would have 2.5 kN.mm^{-2} in-plane shear modulus, compared with 2.8 kN.mm^{-2} theoretically predicted shear modulus using similar analysis to Eq. (8.4).

Using Tsia analysis (App. V), pipe S032 would have a theoretical in-plane shear modulus varying between 10.6 kN.mm^{-2} (using $\bar{c} = 0$) up to 13.1 kN.mm^{-2} (using $\bar{c} = 1.0$). This compares with 13.4 kN.mm^{-2} experimentally measured.

TABLE 8.10a - Glass Mass of the Constituent Layers measured from the Different Parts of Orthotropic Bend S043

| Position of Sample | Sample area mm ² | Sample weight g | Sample thickness mm | Total Glass Mass | | Individual Layers, inside to outside | | | | | | | | | |
|--------------------------------|-----------------------------|-----------------|---------------------|-------------------|------|--------------------------------------|------------------------|------------------------|------------------------|------------------------|------------------------|------------------------|------------------------|------------------------|------------------------|
| | | | | Mg/m ² | Mg % | 'C' | CSM | WR | Weave | WR | Weave | WR | Weave | WR | CSM |
| | | | | | | mass kg/m ² | mass kg/m ² | mass kg/m ² | mass kg/m ² | mass kg/m ² | mass kg/m ² | mass kg/m ² | mass kg/m ² | mass kg/m ² | mass kg/m ² |
| Free tangent | 1610 | 26.15 | 10.81 | 7.55 | 46.5 | * | 1.60 | 2.74 | 0.09 | 2.60 | 0.06 | - | 0.44 | | |
| Fixed tangent | 1640 | 22.38 | 9.52 | 6.02 | 44 | * | 1.40 | 2.14 | 0.08 | 1.85 | 0.08 | - | 0.49 | | |
| Intrados bend centre | 1290 | 26.91 | 14.24 | 9.77 | 46.9 | * | 2.62 | 3.98 | 0.28 | 2.26 | 0.17 | - | 0.44 | | |
| +90° from Intrados bend centre | 1490 | 22.37 | 10.48 | 7.05 | 46.9 | * | 1.42 | 3.06 | 0.23 | 1.62 | 0.13 | - | 0.58 | | |
| Extrados bend centre | 1590 | 22.19 | 9.4 | 6.59 | 47.2 | * | 1.45 | 3.18 | 0.23 | 1.20 | 0.08 | - | 0.43 | | |
| Joint Flange | 740 | 15.75 | 15.68 | 7.76 | 36.4 | CSM 1.91 | WR 0.53 | CSM 1.1 | WR 0.47 | CSM 0.79 | WR 1.05 | W 0.12 | WR 1.1 | CSM 0.1 | W 0.54 |

* 'C' veil is present.

TABLE 8.10b - Glass Content Construction of Bends S028 and S050 (see Table 8.1) obtained from Burn-off Tests

| Bend No. | Position on Bend | Area mm ² | Thickness mm | Total Mass | | GSM + C weave kg/m ² | WR | | | | FW | | |
|----------|--|----------------------|------------------------|-----------------------|------------------------|---------------------------------|-------------------------------------|--------------------------|------------------------|---------------------|---------------|--|-------------|
| | | | | Mg kg/m ² | Mg % | | Individual layers inside to outside | | | Individual layers | | | |
| | | | | | | | Fine kg/m ² | Coarse kg/m ² | Fine kg/m ² | φ from longitudinal | No. of layers | Average mass per layer kg/m ² | |
| S028 | Straight | 1900 | 5.12 | 6.47 | 69.2 | - | - | - | - | ± 55 | 11 | 0.588 | |
| | Straight | 2580 | 5.35 | 6.72 | 69.93 | - | - | - | - | ± 55 | 12 | 0.59 | |
| | Bend: (1) Intrados (2) ± 90 Intrados (3) Extrados | 2740 2100 2730 | 16.75 10.67 8.42 | 14.78 9.22 7.33 | 57.2 57.1 56.6 | 0.18 0.11 - | 1.33 0.89 0.83 | 13.23 8.20 6.48 | - - - | - - - | - - - | - - - | - - - |
| S050 | Straight | - | 5.0 | - | - | - | - | - | - | ± 55 | - | - | |
| | Straight | - | 5.0 | - | - | - | - | - | - | ± 55 | - | - | |
| | Bend: (1) Intrados (2) ± 90 Intrados (3) Extrados | 1250 2210 2380 | 12.25 7.67 6.79 | 7.70 5.10 3.94 | 44.07 45.30 42.5 | 2.90 1.56 1.47 | 1.84 1.11 0.89 | 1.10 1.27 0.83 | 1.86 1.16 0.83 | - - - | - - - | - - - | - - - |

TABLE 8.11a - Mechanical properties obtained from Ring Specimens for Set No. II (see Table 8.1)

| Sp. No. | t (mm) | W (mm) | r _i (mm) | E _H ⁻² (N.mm ⁻²) | E _V ⁻² (N.mm ⁻²) | Strain gauged ring | | | | σ _f ⁺ (N.mm ⁻²) | |
|-----------|-----------|-----------|------------------------|---|---|------------------------|--------|---------|--------|--|-----|
| | | | | | | E (N/mm ²) | | ν | | | |
| | | | | | | outside | | inside | | | |
| | | | | | | θ = 0 | θ = 90 | outside | inside | | |
| 1 (St.) | 9.87 | 27.65 | 101 | - | 6140 | 6140 | 9000 | 0.19 | 0.28 | 0.27 | - |
| 2 (St.) | 9.98 | 25.8 | 101 | 7820 | 8190 | - | - | - | - | - | 235 |
| 3 (Joint) | 15.74 | 25.25 | 101 | 7900 | 6870 | - | - | - | - | - | 210 |
| 4 (Bend) | 10.48 | 25.23 | 101 | 8910 | 7750 | - | - | - | - | - | 190 |
| Average | | | | | | 7700 | | 0.24 | | | |

TABLE 8.11b - Mechanical Properties obtained from Longitudinal Specimens for Set No. II (see Table 8.1)

| t (mm) | W (mm) | E _{inside} (N.mm ⁻²) | E _{outside} (N.mm ⁻²) | ν _{inside} | ν _{outside} | σ _f ⁺⁺ (N.mm ⁻²) |
|-----------|-----------|--|---|---------------------|----------------------|---|
| 9.6 | 18.25 | 8060 | 13970 | 0.30 | 0.20 | 148 |
| 9.2 | 19.01 | 9100 | | - | - | 137 |

* obtained via optical extensometer monitoring

+ flexural strength

++ tensile strength

TABLE 8.12 - Mechanical Properties of Bends of Set III and Set IV
(see Table 8.1)

| Bend No. | t (mm) | W (mm) | E (N.mm ⁻²) | σ_f (N.mm ⁻²) | Rule of Mixture E, (N.mm ⁻²) |
|-------------------|-----------|-----------|----------------------------|-------------------------------------|---|
| S050 (Set III) | 8.84 | 16.29 | 8500 | 157 | 10000 |
| | 8.95 | 12.90 | 7800 | 205 | |
| | 7.50 | 16.00 | 9000 | 173 | |
| Average | | | 8430 | | |
| S029* (Set IV) | 16.1 | 29.4 | 13200 | - | 18000 |
| | 16.1 | 29.4 | 12700 | - | |
| | 11.40 | 29.3 | 11560 | - | |
| Average | | | 12500 | | |

* Compression modulus of 14000 N.mm⁻² obtained by NEL.

TABLE 8.13 - Dimensions and Mechanical Properties of Set II,
Table 8.1 of Pipe Components of Circumferential to
Longitudinal Extensibility of 1:1

| | |
|----------------------------------|---------------------------------------|
| Thickness (mm) | |
| t_n | $1.3 \times 4.8 = 6.24$ |
| $t_{St.}$ | 9.93/11.1 |
| t_{Bend} | 12.45 |
| t_{joint} | 15.00 |
| t_e | 11.19 |
| $2r_i$ (mm) | 202 |
| Second moment of area (mm^4) | |
| I_n | 2.21×10^7 |
| $I_{St.}$ | $3.71 \times 10^7 / 4.22 \times 10^7$ |
| I_{Bend} | 4.82×10^7 |
| I_{Joint} | 6.02×10^7 |
| I_e | 4.26×10^7 |
| R/r_i | 3 |
| E_L ($N.mm^{-2}$) | 9000 |
| E_C | |
| ν | 0.25 |
| G_{LC} ($N.mm^{-2}$) | 2480 |
| Pipe factor | |
| λ_n | 0.176 |
| $\lambda_{St.}$ | 0.27 |
| λ_B | 0.33 |
| λ_e | 0.300 |

TABLE 8.14 - Dimensions and Mechanical Properties of WR Bends/F.W.
Tangents of Set III and Set IV (see Table 8.1)

| | Set No. III | Set No. IV | | |
|--------------------------------|-------------------------------|-----------------------|--------------------|--------------------|
| | Bends S048 S049 S050 | Bends S028 S030 | Bends S029 | Average |
| <u>Thickness (mm):</u> | | | | |
| t_n | 5 | 5 | 5 | 5 |
| $t_{min, Bend}$ | 6.65 | - | - | - |
| $t_{max, Bend}$ | 16.0 | - | - | - |
| $t_{av, Bend}$ | 8.9 | 13.5 | 11.46 | 12.48 |
| $t_{St,}$ | 5.3 | 5.2 | | |
| <u>Radii:</u> | | | | |
| r_i (mm) | 51 | 125 | 125 | 125 |
| R (mm) | 127 | 500 | 500 | 500 |
| R/r_i | 2.5 | 4.0 | 4.0 | 4.0 |
| <u>Second moment of area</u> | | | | |
| I_n (mm ⁴) | 2.4×10^6 | 3.26×10^7 | 3.26×10^7 | 3.26×10^7 |
| I_{min} (mm ⁴) | 3.35×10^6 | - | - | - |
| I_{max} (mm ⁴) | - | - | - | - |
| I_{av} (mm ⁴) | 4.76×10^6 | 9.7×10^7 | 8.04×10^7 | 8.87×10^7 |
| $I_{St.}$ | 2.4×10^6 | 3.26×10^7 | 3.26×10^7 | 3.26×10^7 |
| λ_n | 0.222 | 0.15 | 0.15 | 0.15 |
| λ_{min} | 0.29 | - | - | - |
| λ_{max} | - | - | - | - |
| λ_{av} | 0.37 | 0.38 | 0.34 | 0.36 |
| Tangent length (mm) | 1000 | 500/450* | 500 | |
| <u>Bends:</u> | | | | |
| E_L (N.mm ⁻²) | 9000 | | | 12500 |
| E_C (N.mm ⁻²) | | | | |
| G_{LC} (N.mm ⁻²) | 3100 | | | 3100 |
| <u>Straight:</u> | | | | |
| E_C (N.mm ²) | 22000 | | | 22000 |
| E_L (N.mm ²) | 13700 | | | 13700 |
| G_{LC} (N.mm ²) | 11000 | | | 11000 |

* 450 mm for fixed tangent of Bend S030.

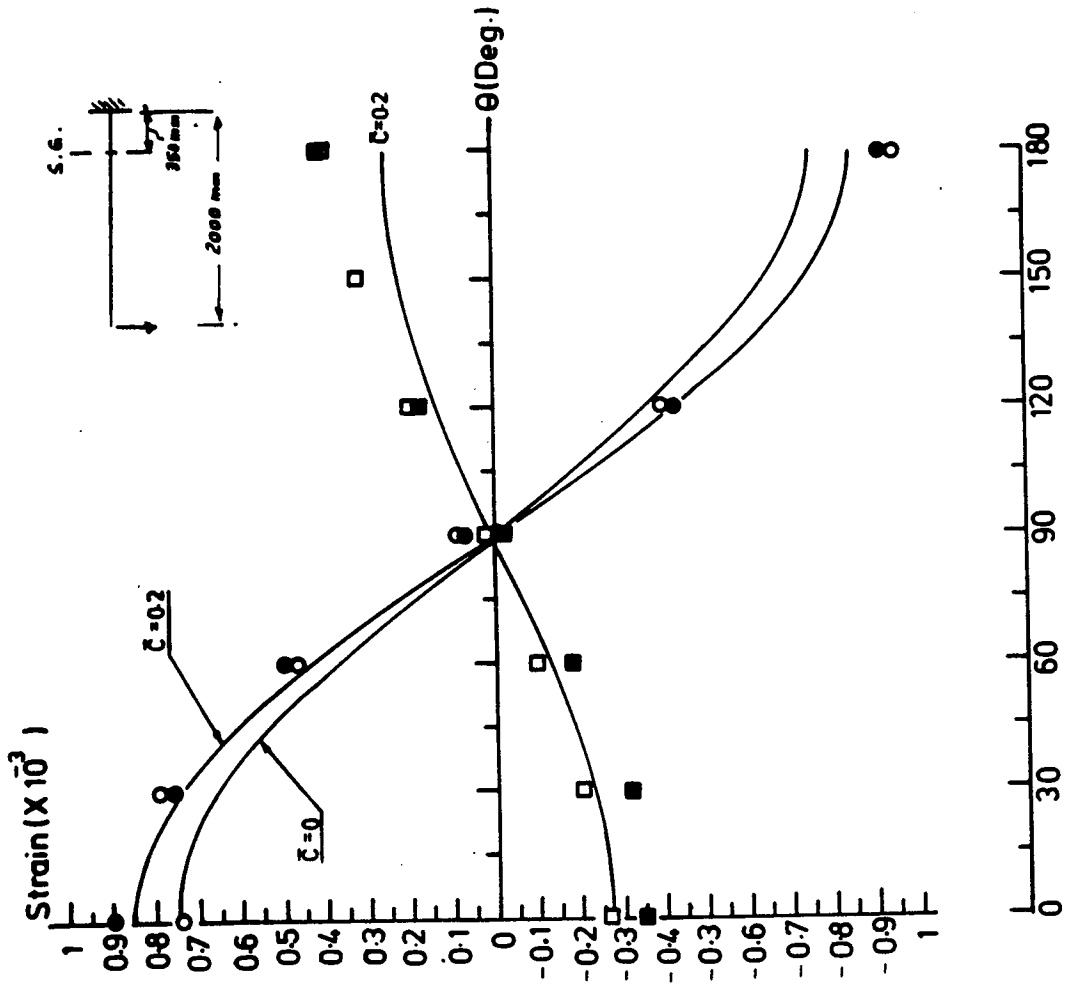


Figure (8.15) Strain distribution measured at the centre of pipe S044 under 714N cantilever end load

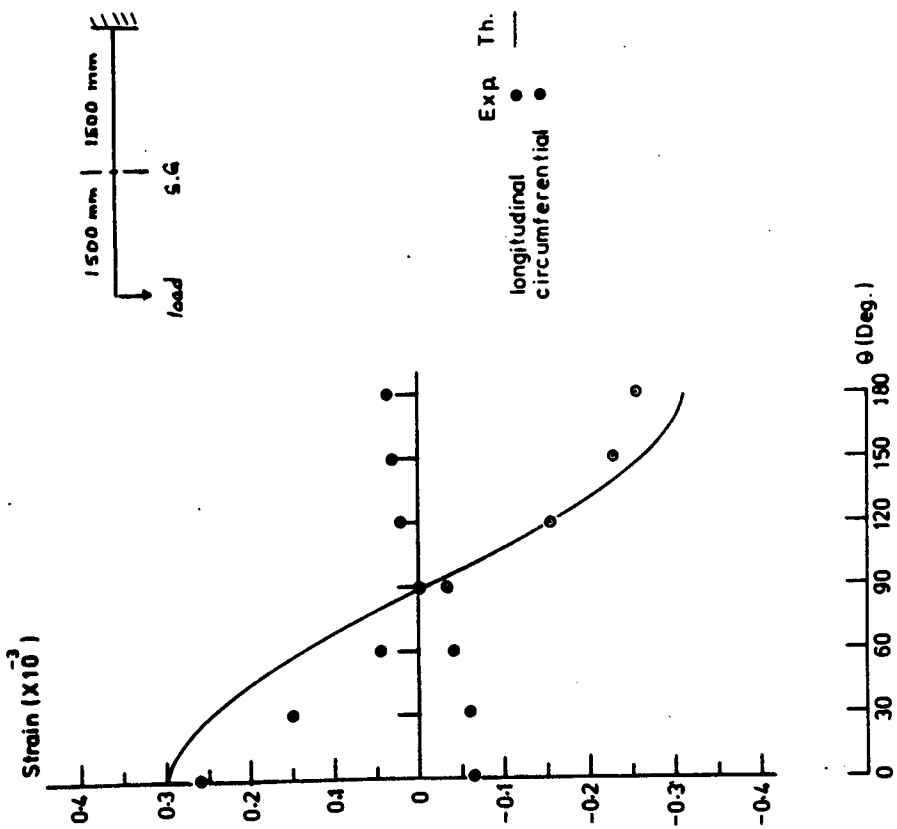


Figure (8.16) Strain distribution measured on pipe S032 under 1875N cantilever end loading

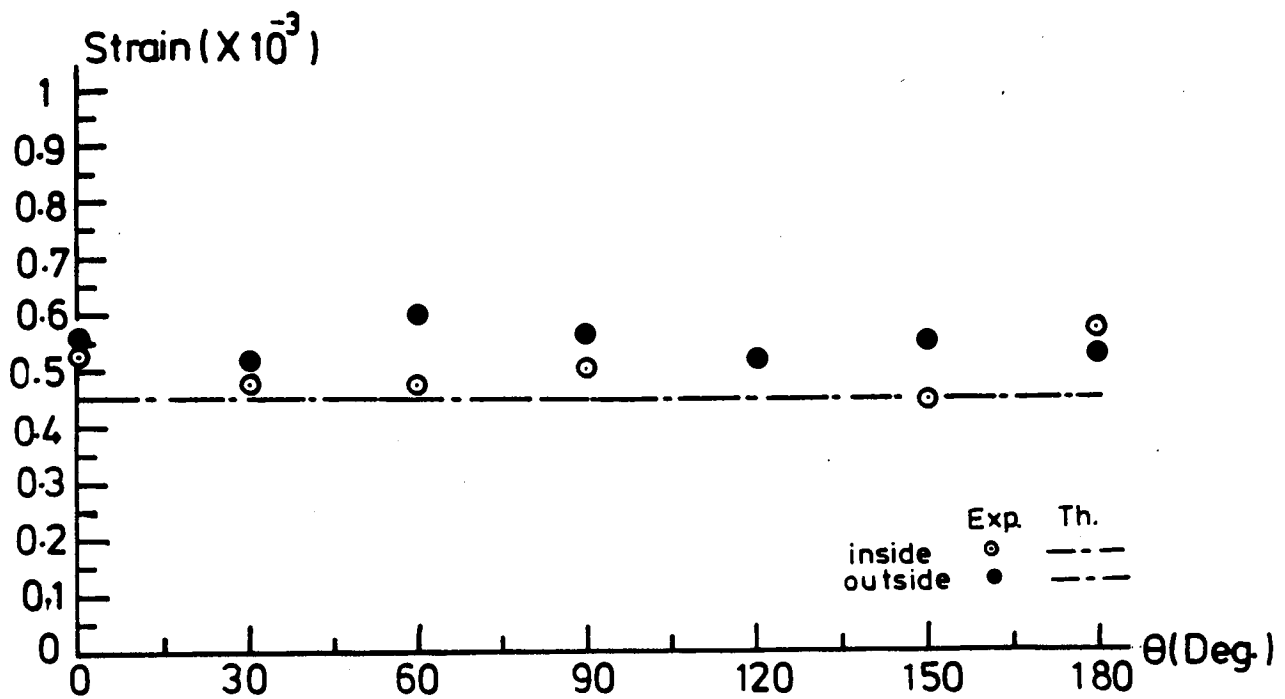


Figure (8.17) In-plane shear distribution measured on pipe S044 under 1.035×10^6 N mm torsional moment

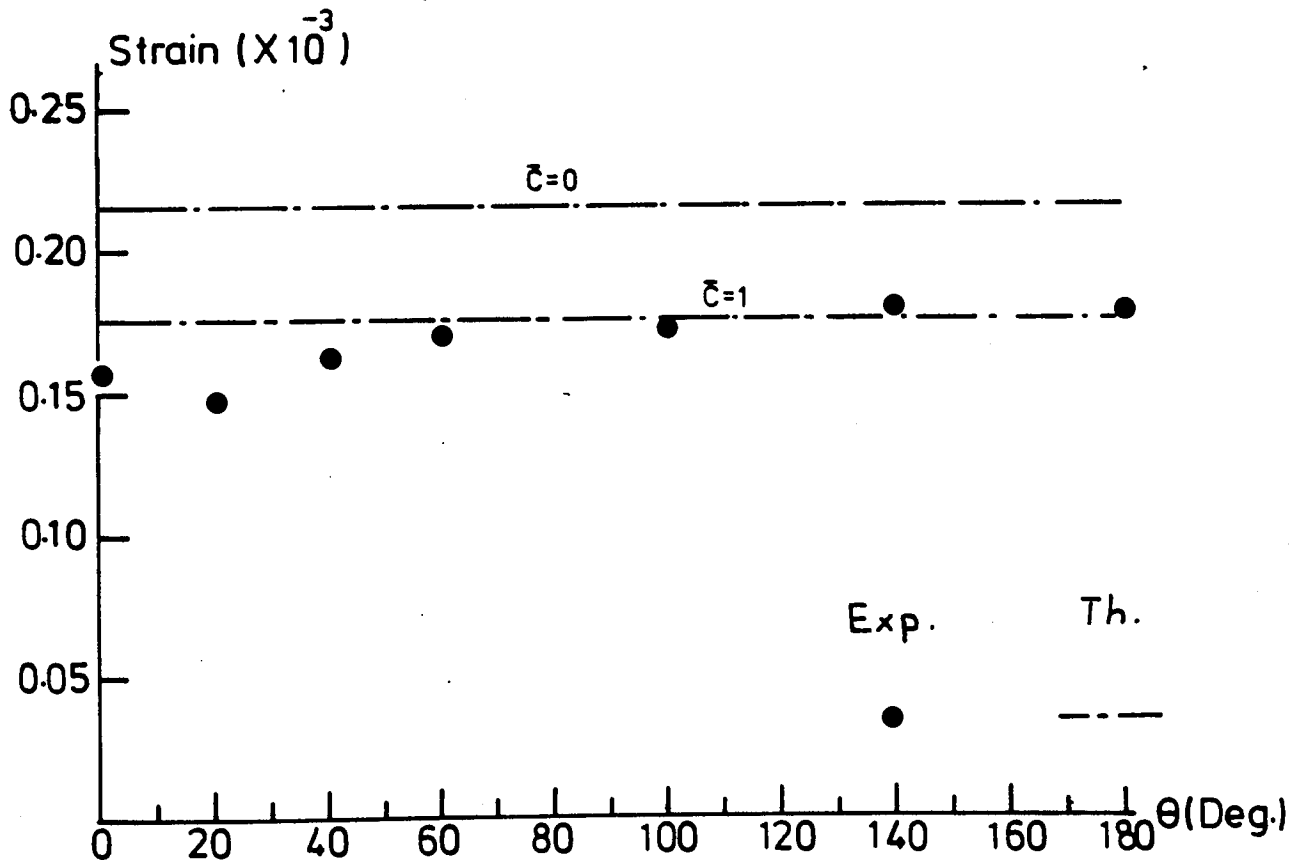


Figure (8.18) In-plane shear strain distribution of pipe S031 under 1.16×10^6 N mm torsional moment

8.3.3 Flexural behaviour of smooth bends

8.3.3.1 In-plane and out-of-plane flexibility factors

For bends S042 and S043, Eq. (I.6) of App. I is used to determine the in-plane flexibility factor (K_i), and Eq. (I.18) of App. I is used for the determination of the out-of-plane flexibility factor (K_o). For the purpose of calculations, the flexural rigidity and the torsional rigidity are calculated using E and G_{LC} in Table 8.13 together with the average effective thickness (t_e).

For bends S048, S049, S050, S028, S029 and S030, Eq. (I.7) of App. I is used for the determination of K_i , and Eq. (I.19) of App. I is used for the determination of K_o . For the flexibility calculations, the flexural rigidity and the torsional rigidity, i.e. EI and GJ , are used differently for the bend fitting (WR) and for the tangents (FW). The dimensions and the mechanical properties for both the tangents and the bend fittings are already presented in Table 8.14.

The experimentally determined K_i and K_o are shown in Fig. 8.19 compared with BS806⁽¹²³⁾ specifications. The experimental results show large scatter, with the out-of-plane flexibility factors being higher than the in-plane flexibility factors, except for the 100 mm nominal bore bends (S048, S049 and S050), where ill-conditioning of the results is apparent. In general the in-plane flexibility factors are in better agreement with BS806 specifications. The higher value of the out-of-plane flexibilities is attributed to the possible incompleteness of modelling the torsional deformations, which is believed to be associated with the over-estimation of the magnitude of the in-plane shear modulus, particularly at the joints.

Ovality measurements taken at the centre of the bend S050 are presented in Figs. 8.20 and 8.21 under in-plane and out-of-plane bending respectively. For both types of loadings, the experimental measurements

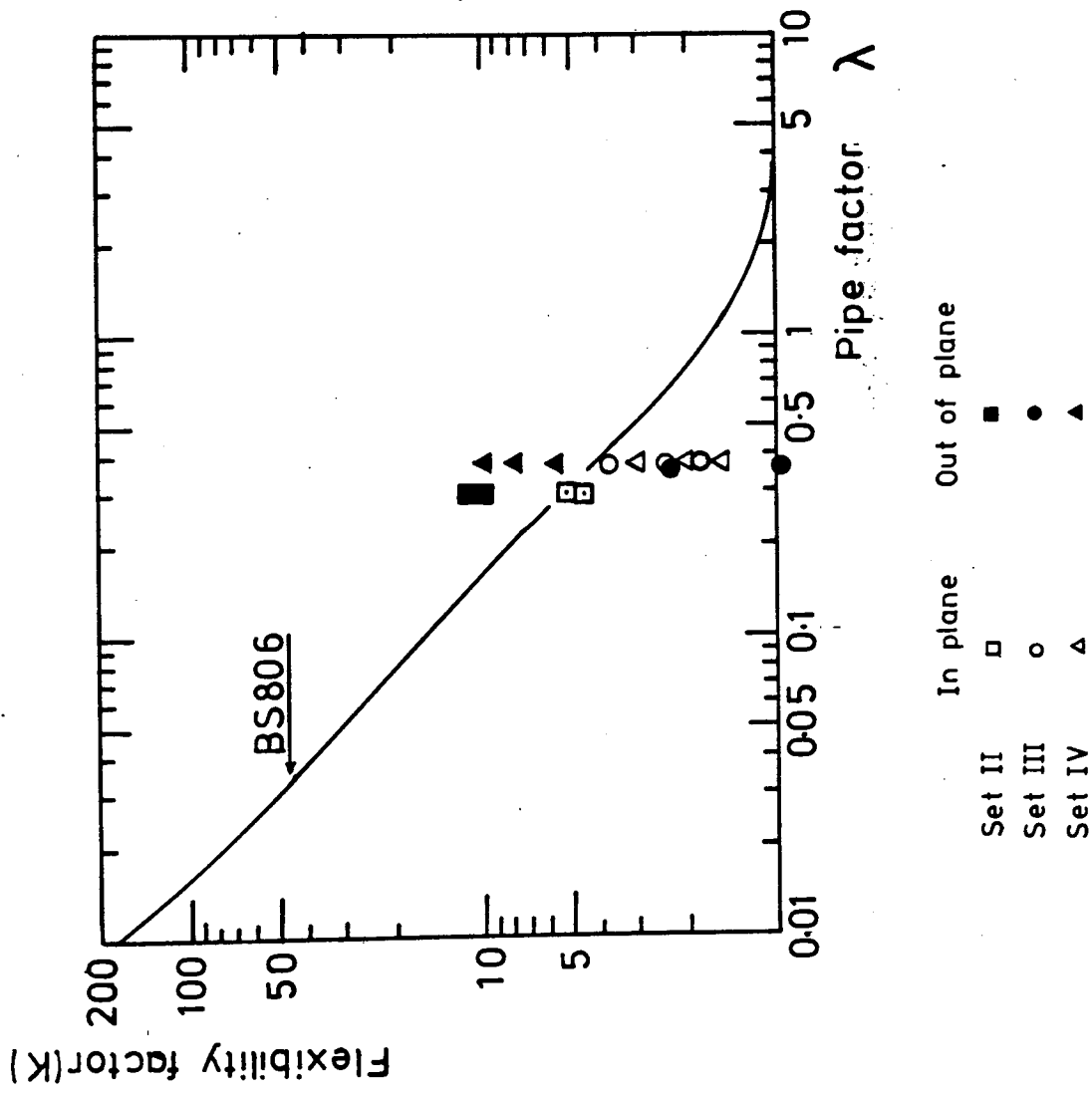


Figure (8.19) Experimentally determined In plane & Out of plane flexibility factors of WR(+CSM) bends

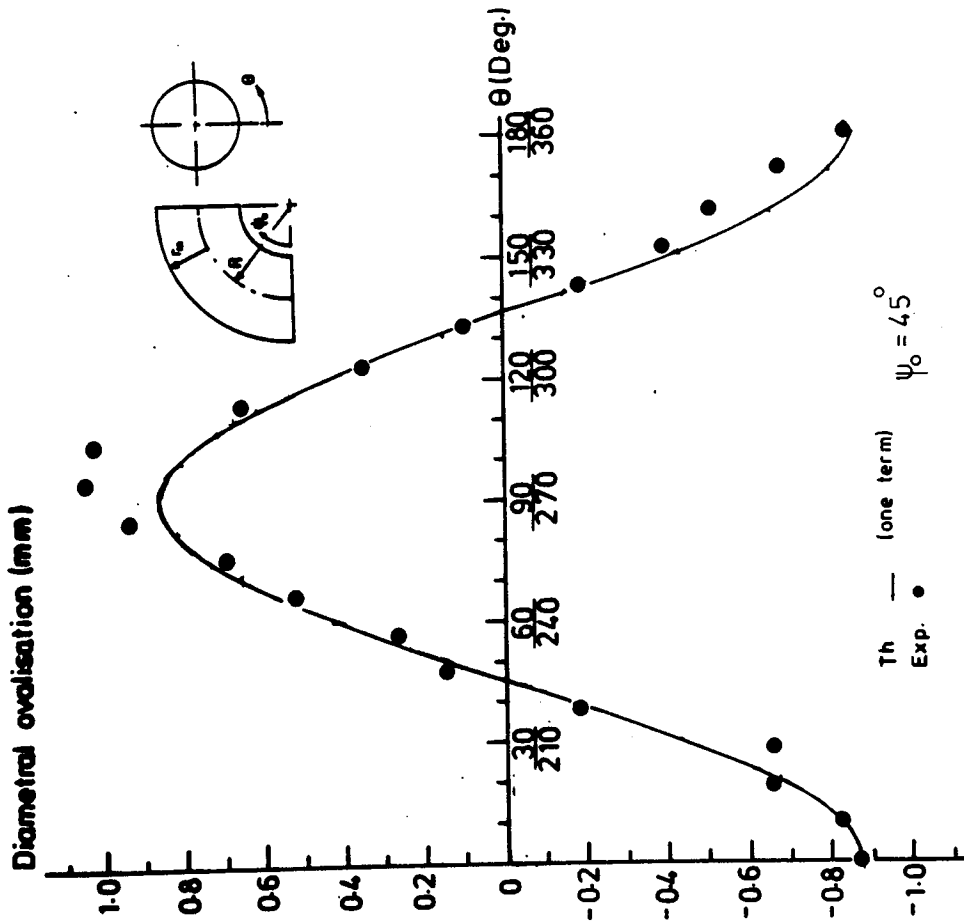


Figure (8.20) Diametral ovalization of bend S050 under 6.25×10^5 N mm in-plane/closing bending moment

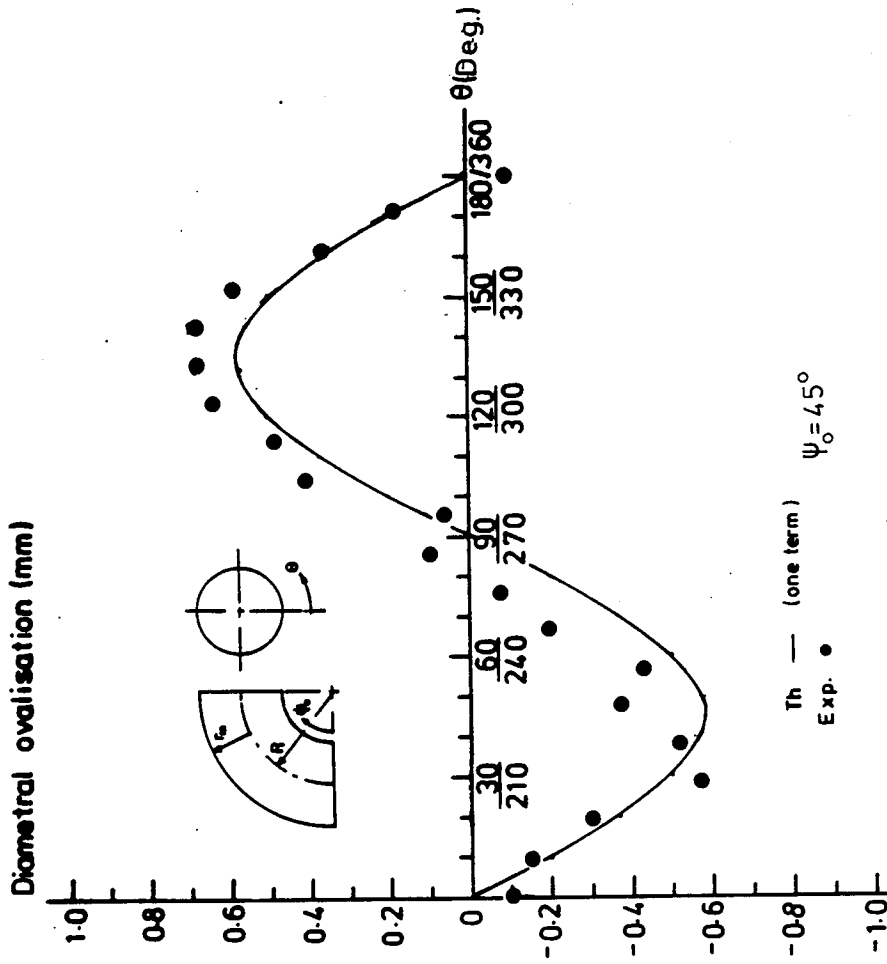


Figure (8.21) Diametral ovalization of bend S050 under 4.24×10^5 N mm out-of-plane bending moment

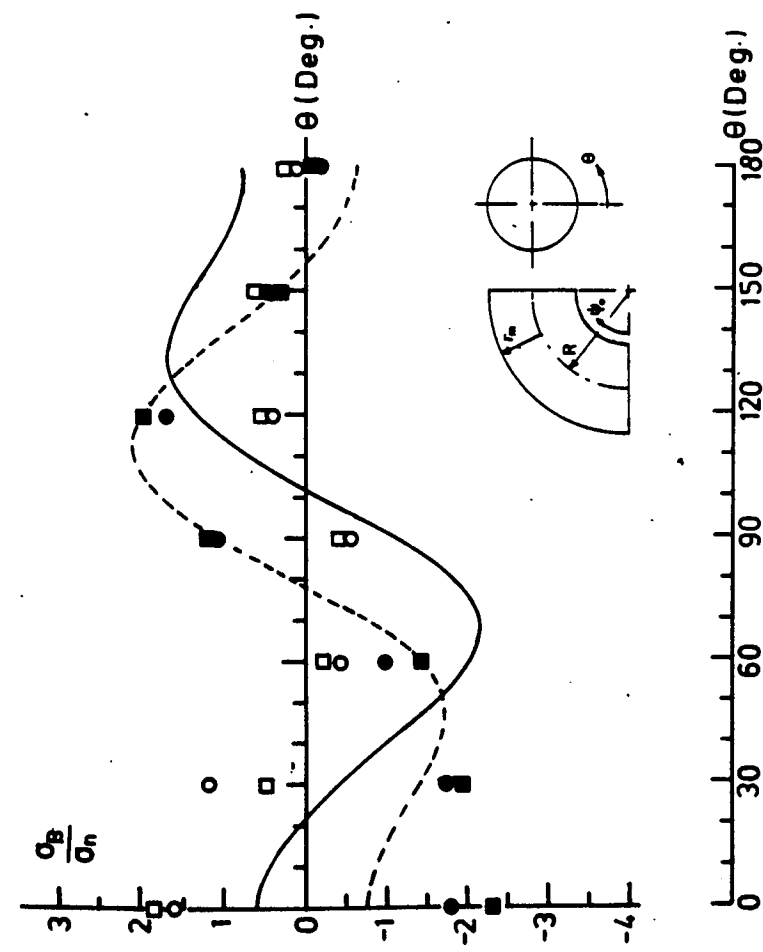
are compared with theoretical predictions using a flexibility factor of 4.1 estimated from BS806. The close agreement observed between experimentally measured ovalization and theoretically predicted, indicate that the bend fitting would have a similar magnitude of the maximum flexibility factors under in-plane and out-of-plane bending. It also indicates that the maximum flexibility factor approximately equals that specified by BS806.

8.3.3.2 In-plane and out-of-plane stress ratio distributions and stress intensification factors (SIF.)

Typical stress ratio (σ_B/σ_n) distributions are those measured at the centre of bends S048 and S049, and are shown in Figs. 22a,b under 0.41 kN mm in-plane bending, and in Figs. 8.23a,b under 0.41 kN mm out-of-plane bending; compared with theory of smooth isotropic bend theory (App. II).

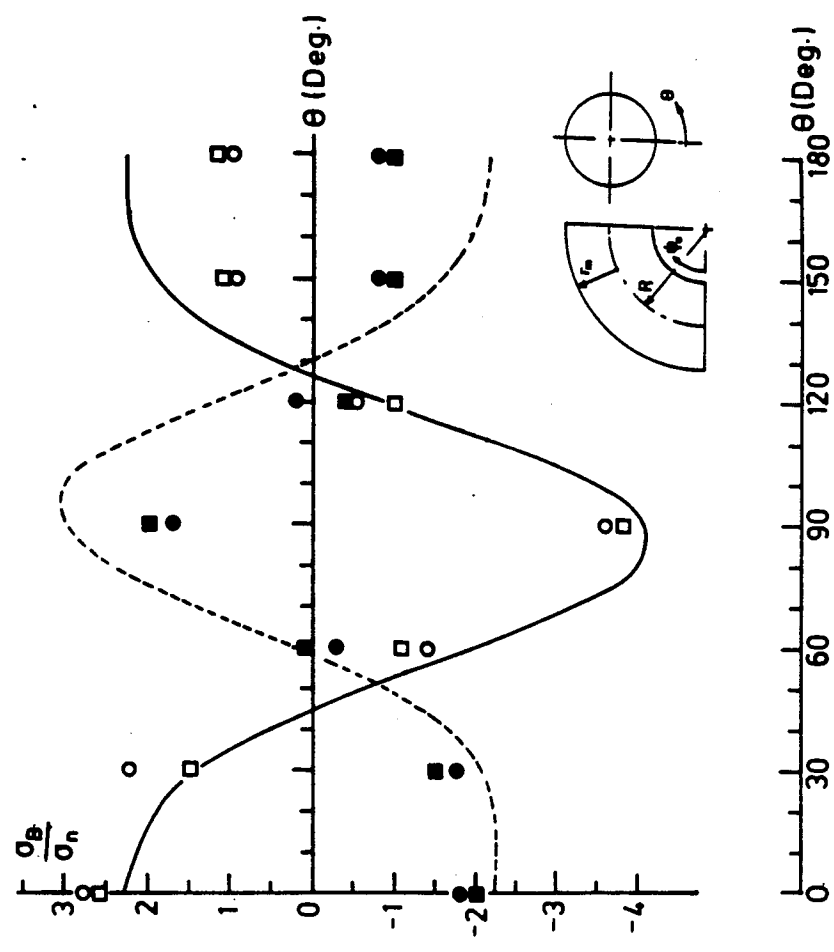
Comparable patterns of stress ratio distributions are observed between the experimental and the theoretical results, perhaps with some difference in peak magnitudes. The maximum/minimum peak stress ratios as a function of their angular positions, are listed in Table 8.15a,b for Set II (bends S042 and S043), Table 8.16a,b for Sets III and IV (bends S048, S049, S028, S029 and S030).

The experimental SIF results compared with BS806 specifications are shown in Figs. 8.24a,b for in-plane bending, and in Fig. 8.25a,b for out-of-plane bending. All experimental SIF are shown to be on average lower than BS806 specifications.



Exp Th
 S048 S049
 inside \circ \square —
 outside \bullet \blacksquare - - -

Figure (8.22a) Longitudinal stress distribution measured on bends S048 and S049 under 4.12×10^5 N mm in-plane/closing bending moment.



Exp Th
 S048 S049
 inside \circ \square —
 outside \bullet \blacksquare - - -

Figure (8.22b) Circumferential stress distribution measured on bends S048 and S049 under 4.12×10^5 N mm in-plane/closing bending moment.

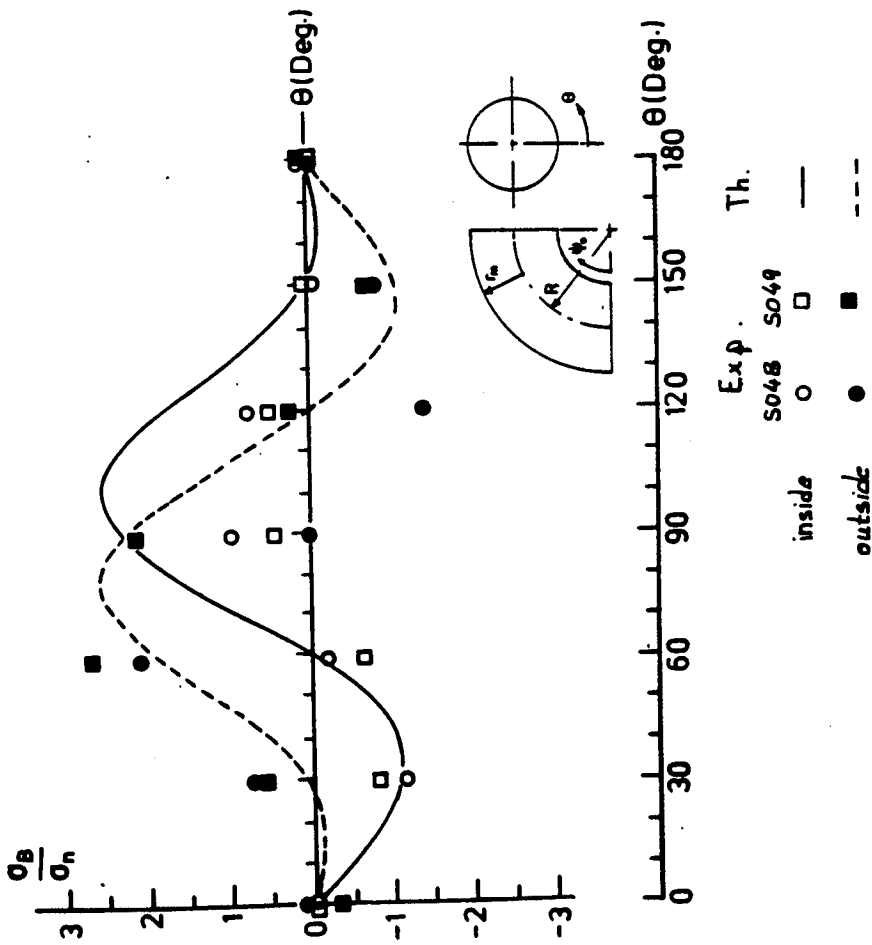


Figure (8.23a) Longitudinal stress distribution measured on bends S048 and S049 under 4.09×10^5 N mm out-of-plane bending moment.

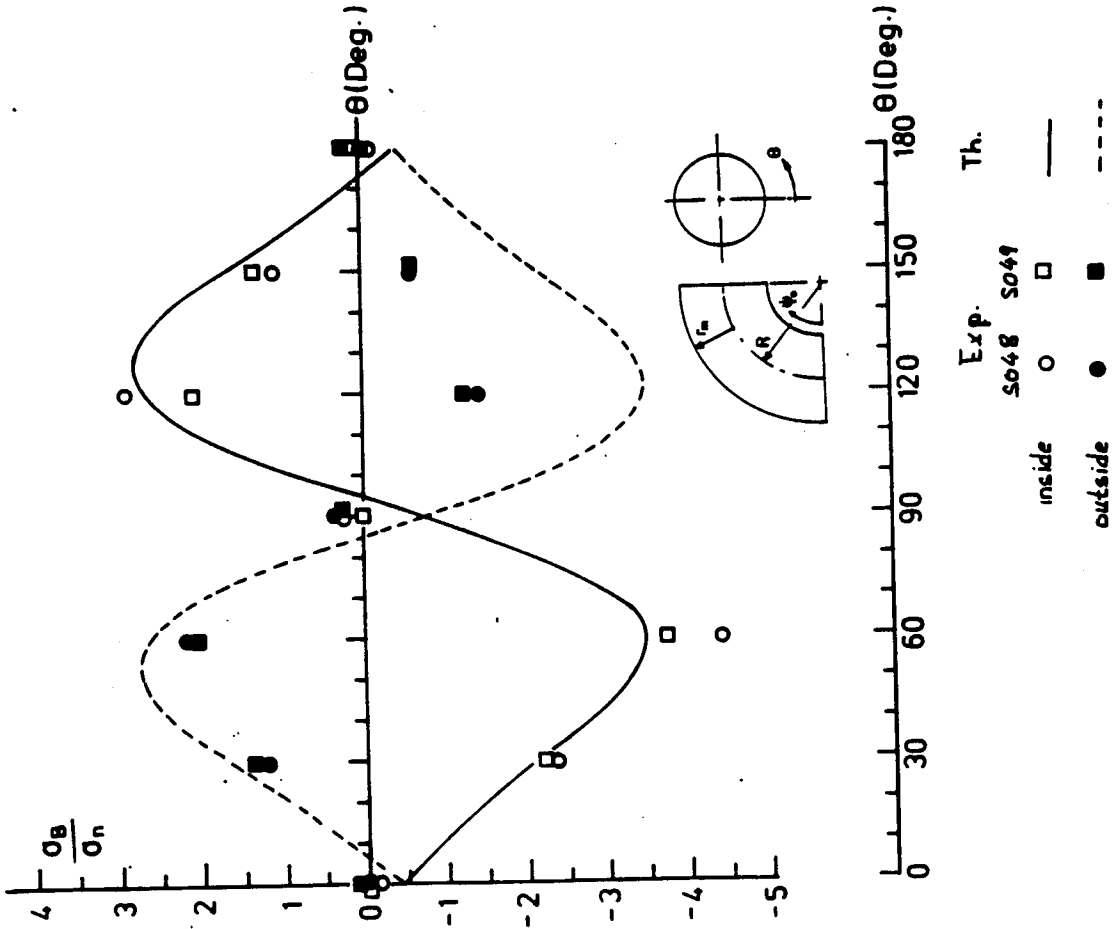


Figure (8.23b) Circumferential stress distribution measured on bends S048 and S049 under 4.09×10^5 N mm out-of-plane bending moment.

TABLE 8.15a - Experimentally determined In-plane Stress Intensification Factors (SIF) of Bends S042, S043 of CSM/WR Wall construction (see Table 8.1)

| Bend Number | λ_e | Experimental SIF | | | | Theoretical SIF | | | |
|-------------|-------------|--|--|---------------------------|--------------------------|-----------------|--------|-----------------------|--------|
| | | Longitudinal | | Circumferential | | BS 806 (123) | | Smooth Isotropic Bend | |
| | | Inside | Outside | Inside | Outside | Long | Circum | Long | Circum |
| S042 | 0.30 | 0.9, $\theta = 0$ 0.6, $\theta = 140^\circ$ | -1.8, $\theta = 50^\circ$ | -2.0, $\theta = 90^\circ$ | 1.7, $\theta = 90^\circ$ | 2.5 | 4.5 | 2.5 | 4.65 |
| S043 | 0.30 | -1.3, $\theta = 70^\circ$ 1.2, $\theta = 150^\circ$ | -2.0, $\theta = 50^\circ$ 2.5, $\theta = 110^\circ$ | -2.3, $\theta = 90^\circ$ | 2.2, $\theta = 90^\circ$ | 2.5 | 4.5 | 2.5 | 4.65 |

TABLE 8.15b - Experimentally determined Out-of-plane Stress Intensification Factors (SIF) of Bends S042, S043 of CSM/WR Wall construction (see Table 8.1)

| Bend Number | λ_e | Experimental SIF | | | | Theoretical SIF | | | |
|-------------|-------------|--------------------------|--------------------------|---|--|-----------------|--------|-----------------------|--------|
| | | Longitudinal | | Circumferential | | BS 806 (123) | | Smooth Isotropic Bend | |
| | | Inside | Outside | Inside | Outside | Long | Circum | Long | Circum |
| S042 | 0.30 | 1.4, $\theta = 90^\circ$ | 2.9, $\theta = 70^\circ$ | -2.6, $\theta = 50^\circ$ 1.4, $\theta = 120^\circ$ | 2.7, $\theta = 50^\circ$ -1.8, $\theta = 130^\circ$ | 3.5 | 4.5 | 2.90 | 3.9 |
| S043 | 0.30 | 1.2, $\theta = 90^\circ$ | 2.9, $\theta = 70^\circ$ | -3.8, $\theta = 60^\circ$ -3.0, $\theta = 120^\circ$ | 3.0, $\theta = 60^\circ$ -2.6, $\theta = 120^\circ$ | 3.5 | 4.5 | 2.90 | 3.9 |

TABLE 8.16a - In-plane Experimental Stress Intensification Factors for WR Bends/F.W. Tangents of Set III and IV

(see Table 8.1)

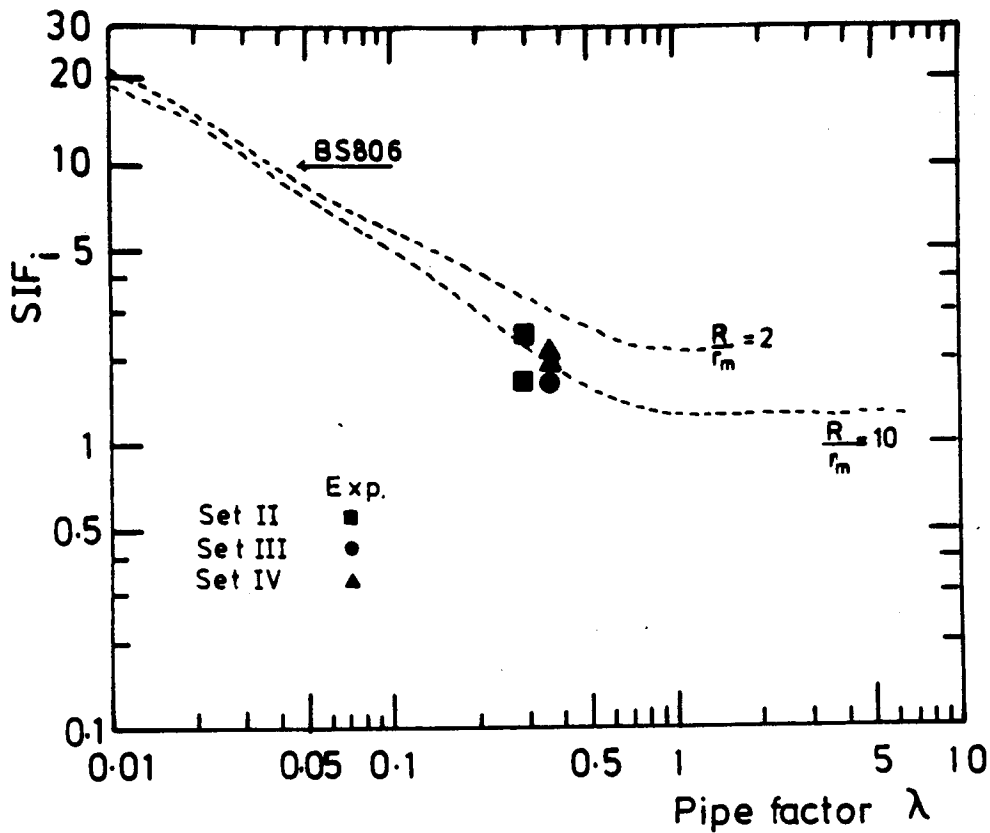
| Pipe No. | λ_{av} | R/r _i | Experimental | | | | | | Theoretical | | | | |
|----------|----------------|------------------|---|---|--------------------------|--------------------------|--------------|---------|-------------|--------------|-----|-----|------|
| | | | Longitudinal | | Circumferential | | BS 806 (123) | App. II | | 2X ANSI B.31 | | | |
| | | | Inside | Outside | Inside | Outside | | C* | L* | | C | L | |
| S028 | 0.362 | 4 | - | -1.5, $\theta = 50^\circ$ 1.7, $\theta = 120^\circ$ | - | 1.6, $\theta = 90^\circ$ | 3.9 | 2.1 | 3.9 | 2.1 | 3.9 | 2.1 | 3.54 |
| S029 | 0.362 | 4 | - | - 2.6, $\theta = 40^\circ$ 2.7, $\theta = 110^\circ$ | - | 3.6, $\theta = 90^\circ$ | 3.9 | 2.1 | 3.9 | 2.1 | 3.9 | 2.1 | 3.54 |
| S030 | 0.362 | 4 | -0.4, $\theta = 30^\circ$ 0.75, $\theta = 120^\circ$ | 1.7, $\theta = 45^\circ$ 1.6, $\theta = 110^\circ$ | 2.7, $\theta = 90^\circ$ | 1.7, $\theta = 90^\circ$ | 3.9 | 2.1 | 3.9 | 2.1 | 3.9 | 2.1 | 3.54 |
| S048 | 0.367 | 2.5 | -1.6, $\theta = 0^\circ$ 0.75, $\theta = 135^\circ$ | -1.75, $\theta = 0^\circ$ 2.0, $\theta = 100^\circ$ | 3.6, $\theta = 90^\circ$ | 1.7, $\theta = 90^\circ$ | 4.1 | 2.7 | 4.1 | 2.7 | 4.1 | 2.1 | 3.51 |
| S049 | 0.367 | 2.5 | 1.85, $\theta = 0^\circ$ 0.7, $\theta = 135^\circ$ | -2.3, $\theta = 0^\circ$ +2.0, $\theta = 110^\circ$ | 3.8, $\theta = 90^\circ$ | 2.0, $\theta = 90^\circ$ | 4.1 | 2.7 | 4.1 | 2.7 | 4.1 | 2.1 | 3.51 |

* C = Circumferential
L = Longitudinal

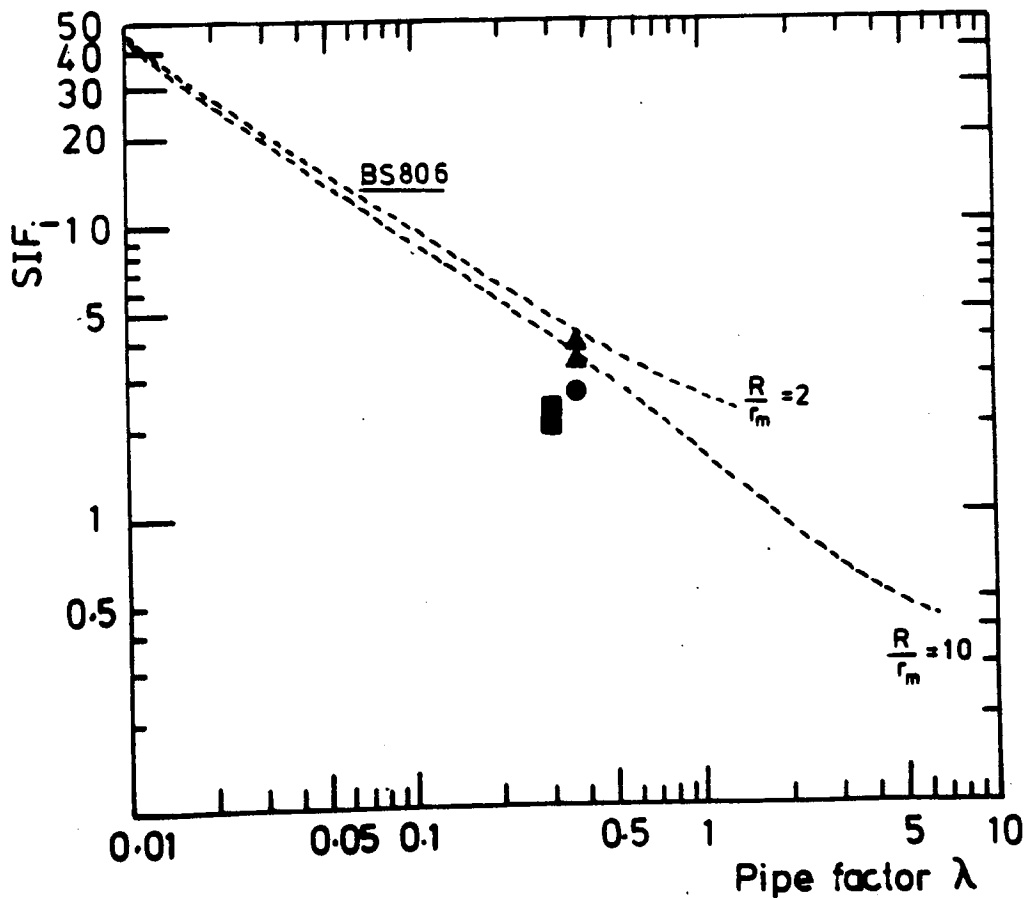
TABLE 8.16b - Out-of-plane Experimental Stress Intensification Factors for WR Bends/F.W. Tangents of Set III and IV
(see Table 8.1)

| Bend No. | λ_{av} | R/r _i | Experimental | | | | | | Theoretical | | | |
|----------|----------------|------------------|--|--------------------------|--|---|--------|-----|-------------|------|--------------|--|
| | | | Longitudinal | | Circumferential | | BS 806 | | Theory | | 2X ANSI B.31 | |
| | | | Inside | Outside | Inside | Outside | C* | L* | C | L | | |
| S028 | 0.362 | 4 | - | 2.2, $\theta = 80^\circ$ | - | 1.9, $\theta = 60^\circ$ -1.3, $\theta = 130^\circ$ | 3.8 | 2.8 | 3.5 | 2.55 | 2.95 | |
| S029 | 0.362 | 4 | - | 3.2, $\theta = 80^\circ$ | - | 3.2, $\theta = 60^\circ$ -2.0, $\theta = 120^\circ$ | 3.8 | 2.8 | 3.5 | 2.55 | 2.95 | |
| S030 | 0.362 | 4 | 1.0, $\theta = 90^\circ$ | 2.2, $\theta = 75^\circ$ | -1.8, $\theta = 50^\circ$ 1.7, $\theta = 120^\circ$ | 2.1, $\theta = 60^\circ$ 1.65, $\theta = 120^\circ$ | 3.8 | 2.8 | 3.5 | 2.55 | 2.95 | |
| S048 | 0.367 | 2.5 | -1.15, $\theta = 30^\circ$ 0.75, $\theta = 115^\circ$ | 2.1, $\theta = 60^\circ$ | -4.4, $\theta = 60^\circ$ 2.9, $\theta = 120^\circ$ | 2.2, $\theta = 60^\circ$ -1.4, $\theta = 120^\circ$ | 4.0 | 3.3 | 3.5 | 2.6 | 2.93 | |
| S049 | 0.367 | 2.5 | -0.8, $\theta = 30^\circ$ | 2.7, $\theta = 60^\circ$ | -3.7, $\theta = 60^\circ$ 2.1, $\theta = 120^\circ$ | 2.1, $\theta = 60^\circ$ -1.25, $\theta = 120^\circ$ | 4.0 | 3.3 | 3.5 | 2.6 | 2.93 | |

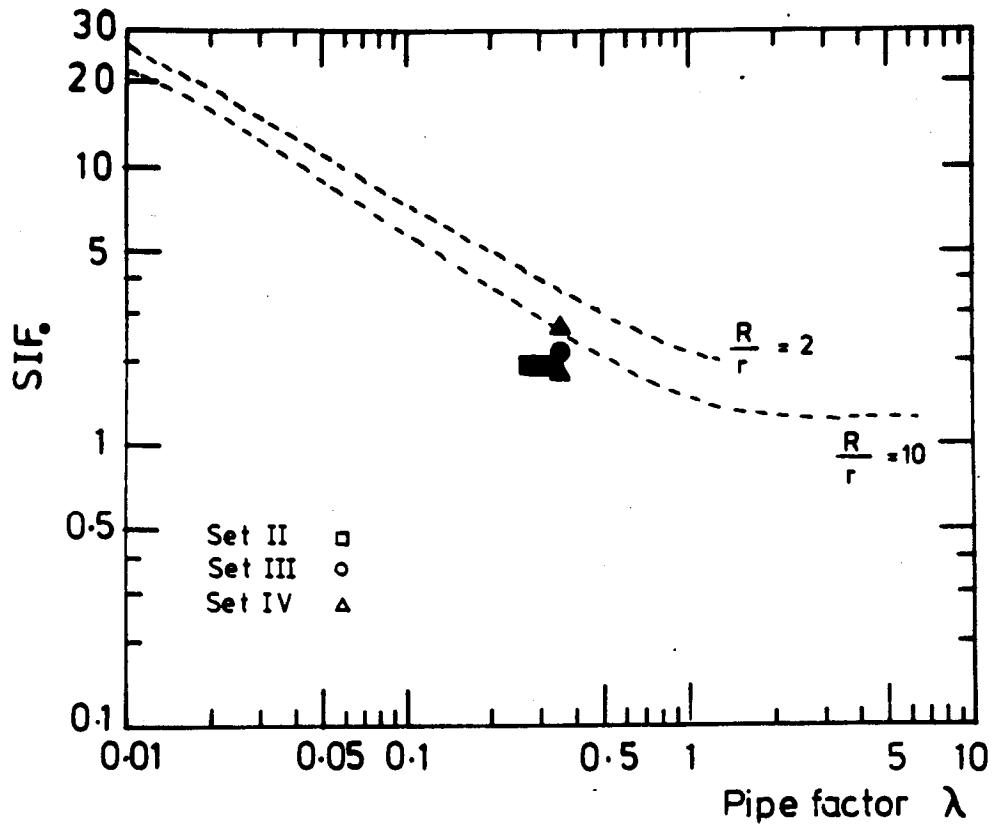
* C = Circumferential
L = Longitudinal



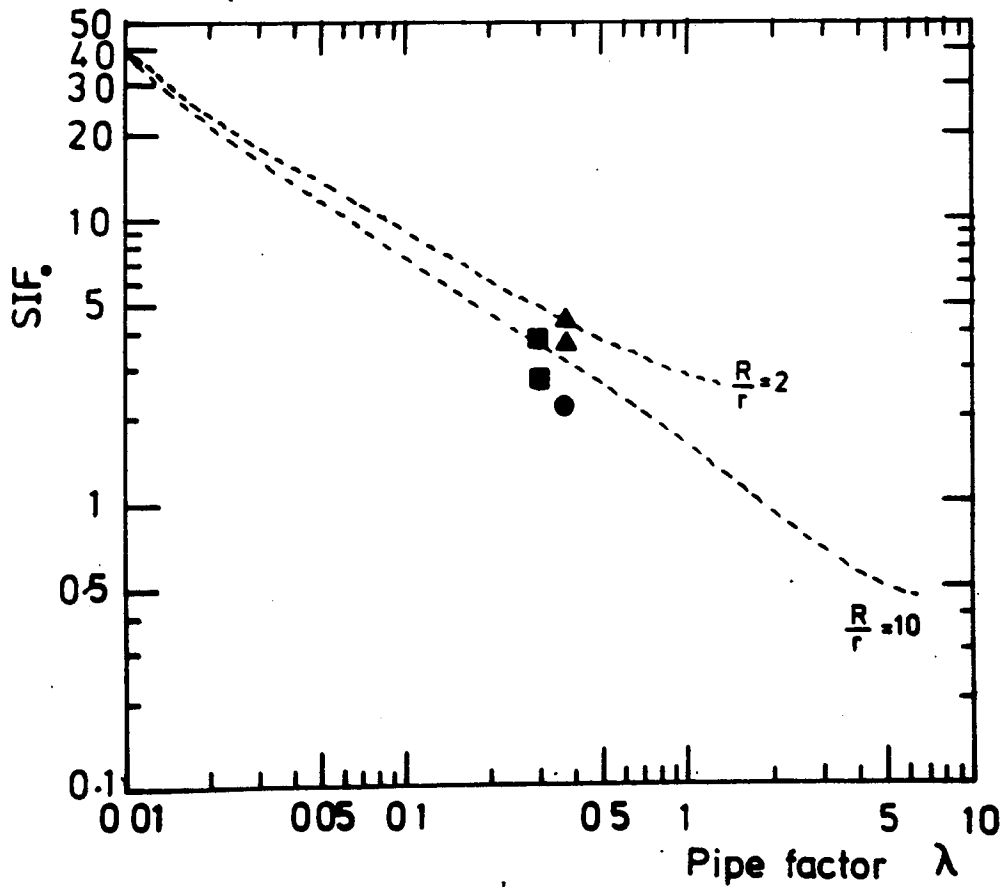
Figure(8.24 a)Maximum In-plane longitudinal stress intensification factors ($SIF_{i,L}$) of WR(+CSM) bends



Figure(8.24 b)Maximum In-plane circumferential stress intensification factors ($SIF_{i,C}$) of WR(+CSM) bends



Figure(8.25a)Maximum Out-of-plane longitudinal stress intensification factors ($SIF_{c,L}$) of WR(+CSM) bends



Figure(8.25b)Maximum Out-of-plane circumferential stress intensification factors ($SIF_{c,c}$) of WR(+CSM) bends

CHAPTER NINE

DISCUSSION OF RESULTS

DISCUSSION9.1 Discussion of Bend Theoretical Analysis

Reviews of experimental work carried out on metallic bends⁽¹³⁶⁾, have shown that von Karman's⁽¹³⁹⁾ theory with the exception of the approximate allowance of the circumferential membrane stresses introduced by Gross⁽¹⁵²⁾, gave results for the flexibility factors and the SIFs in a bend to be within $\pm 15\%$ over the range of pipe factor $1.5 > \lambda > 0.06$. It was further reported that allowable manufacturing tolerances as regard wall thickness, bend radius, pipe bore radius and variation in wall thickness around the circumference are such that they can lead to differences greater than $\pm 15\%$.

For the purpose of comparing experimental stress ratio distribution for smooth CSM bends, the author adopted the theoretical analysis reported by Dodge and Moore^(154,155). Their theoretical analysis included Gross modification of theory, and theoretical predictions were considered to be accurately compared with then existing experimental data⁽¹⁷⁹⁾. The analysis is presented in App. II, where theoretical stress ratio distribution and flexibility factors are numerically predicted using a computer programme written in BASIC. Four terms were used in the analysis to provide the required accuracy for bends having pipe factor up to $\lambda = 0.06$. The computer programme predicts theoretical results for both in-plane bending and out-of-plane bending, including the effect of internal pressure.

For the case of orthotropic bends constructed from laminates having a circumferential modulus greater than the longitudinal modulus, i.e. $m > 1$, the author rederived bend theory from first principles of energy considerations using a similar analysis to that of von Karman; and following the analytical procedure of Dodge and Moore⁽¹⁵⁴⁾. The

orthotropic bend analysis and its corresponding computer programme are presented in App. III.

In general, the quality of the theoretical results were found quite satisfactory and are considered adequate for the purpose of comparison with experimental results.

The accuracy of the theoretical analysis could be improved by taking odd terms, and increasing the number of terms. However, in practice, for bends manufactured by the hand lay-up process, a reasonable prediction of the bend dimensions is not possible until the bend is inspected in the finished form. As shown from the test results already presented, that the SIF could vary by up to 50% or more when actual thicknesses are considered from those determined for nominal dimensions. If however, manufacturing methods were to change to allow closer tolerances to be specified, then improvement in theoretical accuracy would be justified.

9.2 Discussion of Mechanical Properties and Geometrical Variations

9.2.1 Mechanical properties

Average values of the tensile modulus and strength of flat sheet coupons were found to be reasonably predicted using the rule of mixture. For CSM laminates, test results obtained from coupons tested in directions other than the longitudinal and the circumferential directions, supported the in-plane isotropy assumption. Flexural modulus measured by the three point bending tests was on average 35% lower than that measured under tension. Such difference in moduli results is due to the exclusion from the calculation of the interlaminar shear deformation in the three-point bending test. Flexural strength was on average 40% higher than the tensile strength due to the stress distribution pattern developed under each type of loading.

For dual laminates, tensile and flexural elastic deformations could be predicted using the theoretical model used for composite strips under loading. Flexural strengths of such laminates, could however, change considerably dependent on which side is experiencing tension.

The magnitude of the interlaminar shear strength of CSM laminates vary between 8 N/mm² obtained by the lap shear test⁽³⁾, up to values greater than 14 N/mm² obtained by the three point bending of short beams⁽³³⁾. The strength obtained by the lap shear test is believed to be underestimated due to edge stress concentration and the presence of peeling^(129,130).

The interlaminar shear strength for dual CSM/WR laminates obtained by the lap shear test was on average 12.4 N/mm². This is 33% higher than that obtained for the CSM laminates. Such a difference could be related to the comparatively higher flexural stiffness of the WR, which is believed to have provided a higher resistance to local peeling.

In-plane shear strength obtained by the punch test method was found to be 80 N/mm² for CSM laminates. This value is 25% higher than those reported in the literature, obtained from torsional tests of CSM pipes⁽⁴⁰⁾ and plates⁽⁷⁶⁾.

The average value of the tensile modulus obtained from testing longitudinal strips and rings cut from the pipes and bends are comparable with that of the flat sheet result, while tensile strength and strain to failure are lower in comparison. This is due to the higher occurrence of stress raisers such as voids and surface irregularities inherited in the finished product. The corresponding extensibility for CSM was calculated to be about 19.8 kN.mm⁻¹/kg.m⁻² which is 33% higher than specified by BS4994.

9.2.2 Pipes and bends geometrical variations

The maximum thickness measured on the bend fitting is located at the intrados, and it is 1.5-2.0 times higher than those measured at the bend extrados and at the straight pipe. Thickness measurements taken on the straight pipes could vary locally by 30%, and higher scatter being measured in the circumferential direction.

The thickness measured on the joint is slightly higher or equal to that measured at the bend intrados, with overlap lengths of 100-250mm. Lengths of joints for GRP pipes are calculated as a function of their pressure ratings⁽¹⁸⁹⁾, and under shell wall bending, the rigidity of the pipe wall can experience a different order of magnitude for the different pipe diameters. At the moment there is no reliable analysis available taking the joint longitudinal rigidity into account, except the superposition technique described in App. I, though in practice this may not be easy.

Both straight pipes and bends exhibit irregular outside surfaces, with the inside surface being smooth. However, inside surface irregularities have been observed due to surface imperfections of the mandrel used.

Increase of the laminate thickness was shown to be directly related to the increase of the glass mass per unit area, and for the purpose of formulating the pipe section modulus, the average effective thickness (t_e) was used in the calculations. Given considerations to the thickness variability exhibited by the laminates, it is very likely that under different types of loadings such as in-plane and out-of-plane bending, different values of the section modulus would resist the applied bending moment. Extensive thickness measurements taken on few bends have shown that in-plane section modulus of the tangent could differ by up to 7% in comparison to the out-of-plane section modulus,

and up to 10% on the bend fittings. The comparison was based on numerically integrating the second moment of the pipe cross-sectional area about two perpendicular diametral axes.

For all bends, glass mass per unit area and thickness measured could be as high as 2-2.5 times that which had been nominally specified⁽³⁾. The variations either in the form of glass mass per unit area or as thickness, could well be outside the limits specified by the standards in references (17-19).

9.3 Discussion of Straight Pipes and Bends Pressure Test Results

All the straight pipes were tested under closed-ended pressure test conditions. The inside circumferential surface strains were almost invariably higher than outside surface strains, implying that the specimen behaves as a thick walled pipe rather than as a thin walled pipe (Ch. 3). However, the unexpected scatter exhibited by the measured strains (see Fig. 3.8 of Ch. 3) made it difficult to reach firm conclusions. By using Hooke's law for isotropic homogeneous materials, assuming plane stress condition, the corresponding stresses exhibited similar scatter.

For a CSM pipe of a machined outside surface and of (r_m/t) ratio of 10, the difference between inside and outside circumferential stresses was observed to be smoother (see Fig. 3.12a of Ch. 3). Also negligible difference could be noticed between inside and outside circumferential stresses measured on pipes manufactured by the filament winding process ($r_m/t = 25$) and the centrifugal casting process ($r_m/t = 18$), see Fig. 3.14, where a uniform pipe-wall thickness is produced.

Based on the above observations of experimental results, it could be implied that the scatter of the pressure strain and stress test results, is of direct consequence of the irregular laminate thickness of

the pipes made by the hand lay-up process. The thick shell behaviour indicated by the strain measurements, is believed to be attributed to the low magnitude of the through-thickness modulus (E_{33}).

By representing the pressure experimental stresses as membrane and local bending rather than inside and outside, reasonable agreement was observed between the prediction of thin cylinder theory and membrane stresses (see Fig. 3.10b of Ch. 3).

For the smooth bends, the distribution of the membrane stresses was comparable with the prediction of thin torus shell theory (see Fig. 3.17b of Ch. 3). For the mitred bends, experimental strain distribution measured at the segment-centre and at the segment-edge were comparable with Owen and Emmerson⁽¹⁶⁷⁾ theoretical analysis (see Fig. 3.21a,b,c of Ch. 3), although however, maximum strains predicted by theory for the segment-edge were lower than experimentally measured; probably due to using larger value of the average thickness at that position.

The membrane stresses test results were then presented as pressure stress multiplier (PSM) for all the bends, with reasonable comparison in magnitude, but not in angular position.

No rational or empirical pattern could have been formulated to describe the experimental local bending stresses, either for the straight pipes or for the bends made by the hand lay-up process. These stresses were found in general to be of higher variability in the circumferential direction. The consequences of the presence of such local bending stresses is that interlaminar shear stresses will be induced in the pipe laminate. The maximum magnitude of such shear stresses is dependent upon the gradient of the bending stresses.

Failure patterns observed on CSM straight pipe and bend pressurised to failure, have shown delamination of the pipe wall laminate (see Figs. 3.22 and 3.23). Tensile strengths estimated at failure were on average 84 N/mm² for both pipe components.

9.4 Discussion of Flexural and Torsional Deformations of Straight

Pipes Test Results

Flexural stress distributions were found to be in good agreement in pattern and magnitude as predicted by the simple beam theory. The elastic constants of the CSM and the CSM/WR/UD laminates were obtained from coupon testing, and were reasonably compared with the prediction of the rule of mixture. For the FW pipes, the elastic constants were estimated using Tsia analysis (App. IV).

The presence of the flange joint was found to have increased the overall flexural rigidity of the pipe. Deflection measurements taken along a CSM pipe tested as a cantilever beam, were in reasonable agreement with deflection distribution predicted using the superposition technique, which incorporated the joint stiffening as presented in Fig. 6.8 of Ch. 6. Obviously, the consequence of ignoring such joint stiffening in a piping system, will underestimate the magnitude of anchor loads.

In-plane shear strains and stresses measured on GRP Pipes under torsion were reasonably predicted using the rule of mixture and Tsia analysis for CSM Pipes and orthotropic pipes respectively.

Experimental stress distribution measured under both flexural and torsional loadings did not exhibit the sever degree of scatter observed under pressure loading. The only physical fact that differentiate both type of loadings is the presence of the radial stress in the latter.

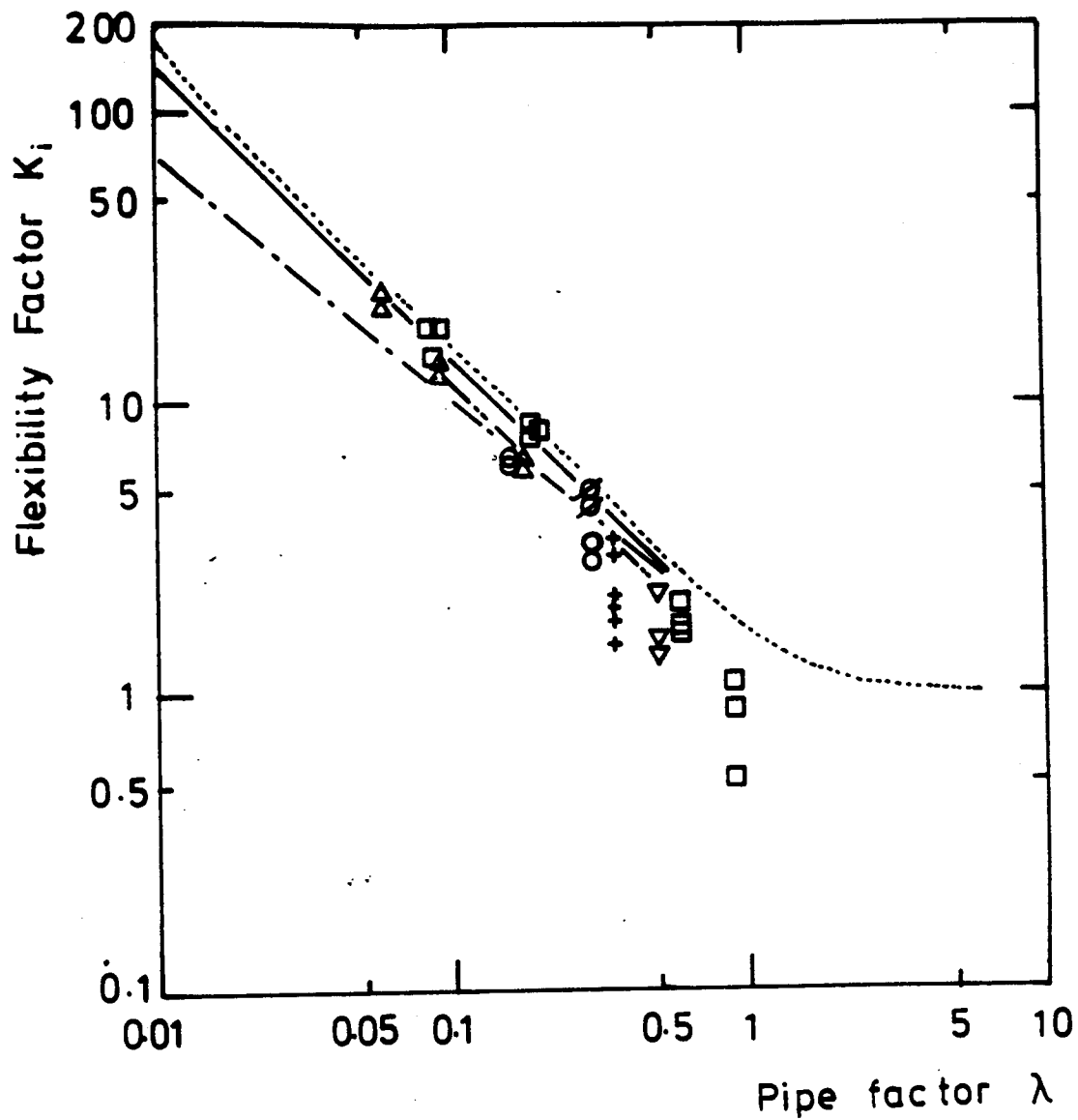
9.5 Discussion of Bends' Flexibility Factors Test Results

The major problem associated with deriving the flexibility factors is their dependence on the pipe stiffness used in the calculations. The variability of the thickness measured at the different parts of the bends, tangents, joints and flanges can only be approximately averaged,

and the material young's modulus and shear modulus can also vary, hence the accuracy of the flexibility factor is inevitably reduced. The representative flexibility factors of the bends were calculated on the basis of the average thickness measured on the tangents and the bend (t_e). Those were shown to be slightly lower than results based on the superposition technique (see Ch. 6 and App. I). As the pipe factor (λ) increases, particularly above 0.6, the reliability of the results are reduced, and could be largely overestimated by theory.

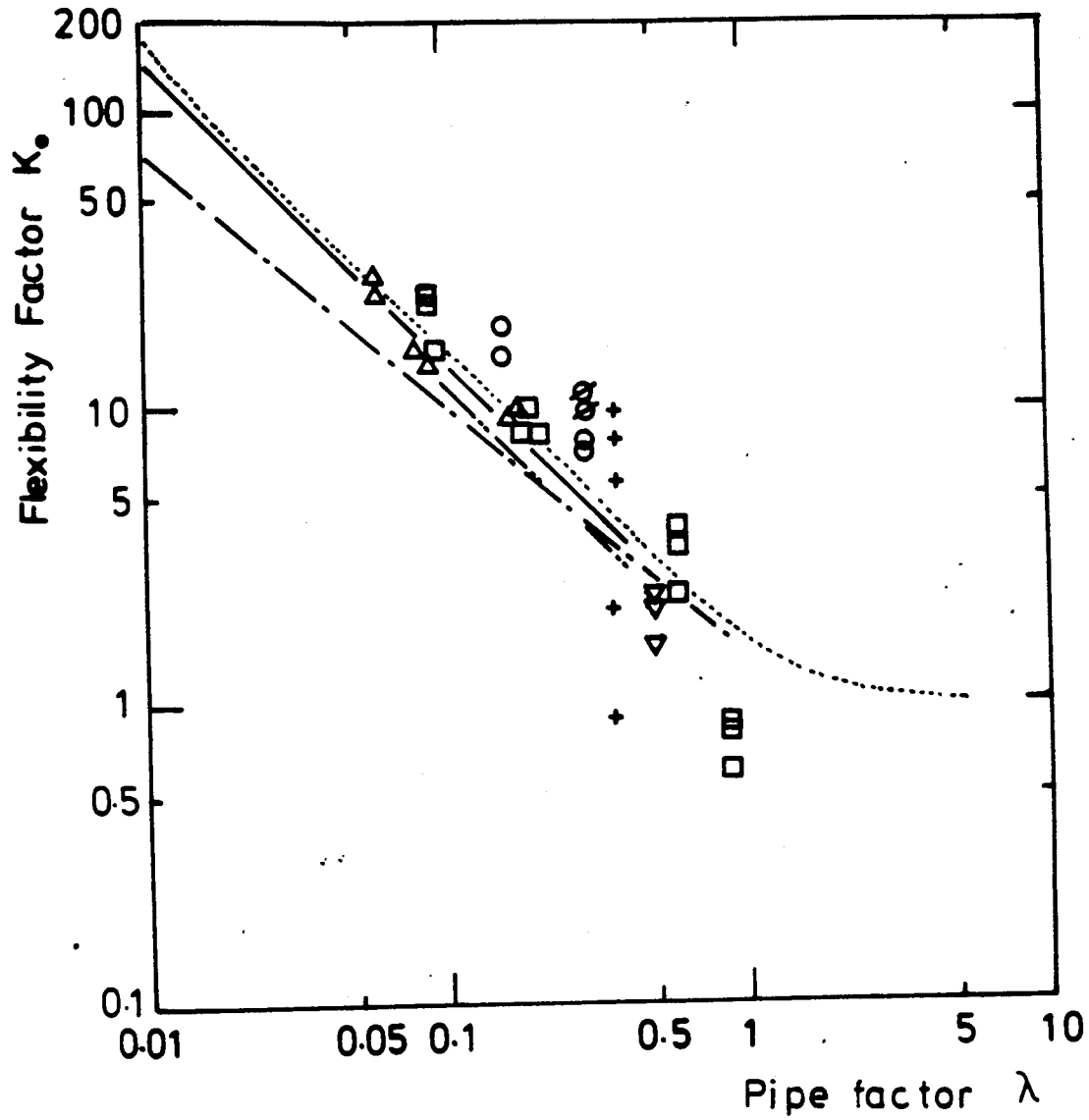
The experimentally determined flexibility factors for all the GRP Bends are plotted collectively for in-plane bending (K_i) in Fig. 9.1, and for out-of-plane bending (K_o) in Fig. 9.2. These are compared with BS806⁽¹²³⁾ and ANSI B31⁽¹²⁴⁾ specifications, Kitching and Bond's⁽¹⁷⁰⁾ prediction and orthotropic bend theory prediction for $\bar{m} = 2$. Although not comprehensive, the presentation does provide an overall look at the flexibility results determined for the different bend constructions.

From Figs. 9.1 and 9.2, it could be observed that experimental results obtained under in-plane bending tend to lie below the theoretical curves, whilst for out-of-plane bending the experimental results tend to lie above the theoretical curves. Referring to the analysis presented in App. I, it is shown that for K_i derivation; only the flexural rigidity (EI) is required, whilst for the purpose of calculating K_o both the flexural rigidity (EI) and the torsional rigidity (GJ) are needed to be considered, which would further reduce the accuracy of the latter. It is therefore believed that the experimentally determined K_i values are more accurate than those of K_o . Furthermore, for the purpose of design, a conservative estimate of anchor loads will be predicted by using the values of the experimentally determined in-plane flexibility factors (K_i).



- | Exp. | Th. |
|--|--|
| □ - Smooth, CSM Ch. 6 | BS 806 ⁽¹²³⁾ |
| △ - Mitred, PVC/CSM Ch. 7 | Kitching ⁽¹⁷⁰⁾ |
| ▽ - Smooth, PVC/CSM Ch. 7 | App(III) |
| ∅ - Smooth CSM/WR ext. 1:1 Ch. 8 | ANSI B31 ⁽¹²⁴⁾ |
| + - Smooth WR/FW ext. 1:1 Ch. 8 | |
| ○ - Smooth CSM/WR/UD ext. 2:1 Ch. 8 | |

Figure (9.1) In-plane Flexibility Factors



| Exp. | Th. |
|--|---------------------------|
| □ - Smooth, CSM Ch. 6 | BS 806 ⁽¹²³⁾ |
| △ - Mitred, PVC/CSM Ch. 7 | Kitching ⁽¹⁷⁰⁾ |
| ▽ - Smooth, PVC/CSM Ch. 7 | App(III) |
| ⊘ - Smooth CSM/WR ext. 1:1 Ch. 8 | ANSI B31 ⁽¹²⁴⁾ |
| + - Smooth WR/FW ext. 1:1 Ch. 8 | |
| ⊙ - Smooth CSM/WR/UD ext. 2:1 Ch. 8 | |

Figure (9.2) Out of plane Flexibility Factors

Theoretical flexibility factors are predicted based on the assumptions that the bend experiences constant flattening with no end restraint, and that such flattening is caused by the application of an external bending moment of constant magnitude. The GRP bends investigated in the program had tangent restraints, which forced flattening to be reduced as the tangents are approached as shown in Fig. 6.13 for smooth bend S006, and in Fig. 7.23 for mitred bend S060. Also due to the end loading system used, the bending moment varies along the bend radius. Based upon those, it could only be implied that the experimentally determined flexibility factors for the different GRP bends are of an average value.

Ovality measurements taken at the centre of few bends as in Figs. 6.13; 6.29; 7.23; 8.20 and 8.21, suggest that:

- (i) the maximum bend flexibility factor is located at the bend centre, where maximum ovality is measured;
- (ii) and the maximum in-plane and out-of-plane flexibility factors are of similar magnitude and are approximately equal to that specified by BS806. This is based on the reasonable agreement obtained between theoretically and experimentally measured change of diameter.

The above remarks tie up with experimental flexibility results discussed for metallic bends^(180,181). It was reported that for metallic bends having tangents of several pipe diameter in length, the distribution of the flexibility factor along the radius of the bend was suggested to follow a similar pattern to that experienced by the flattening measurements. Smith and Ford⁽¹⁸¹⁾ assumed that the variation to be symmetrical about the mid-section of the bend and may therefore be represented by a cosine function, and for 90° bends this could be in the form of

$$K_{\psi_0} = Z_1 K_{av} \cos n (\psi_0 - \pi/4) \quad (9.1)$$

where K_{ψ_0} is the flexibility factor at an angle ψ_0 (Fig. I.1c of App. I), K_{av} is the average flexibility factor of the bend fitting, n is an integer and Z_1 is a constant. $Z_1 = \pi \sqrt{2}/4$ for bend fittings welded to tangents ($n=1$), and $Z_1 = \pi/2$ for bend fittings welded directly to flanges ($n=2$). The reduction of the flattening to zero would imply a flexibility factor of unity, thus, $(K_{\psi_0} - 1)$ would be proportional to the measured change of diameter at angle ψ_0 . They also suggested that the maximum value of the flexibility factor could be assumed to be reasonably equated to the flexibility factor predicted by theory.

The average experimental in-plane flexibility factors for all smooth bends, of CSM construction (Ch. 6) and of CSM/WR construction (Ch. 8); in the range of $0.09 < \lambda < 0.6$, are on average 10-15% lower than BS806⁽¹²³⁾ prediction. Using ($n=1$) in Smith and Ford analysis, give average flexibility factor to be 90% of the maximum. Therefore, it could be argued that within acceptable experimental error, the criteria of Eq. (9.1) could be satisfactorily used for GRP bends having tangent lengths several times the pipe diameter.

For all the bends, a straight line was found to adequately describe the experimentally measured free end-deflection plotted versus end loads. This would imply that any change of the bend flexibility factor due to incremental ovality upon loading, could be assumed negligible.

Also, all the bends investigated in the present programme, were tested under in-plane closing and opening. The reported experimental flexibility factors were based on the lower value of the end deflection per unit end load measured among both tests. Deflection measurements taken on large diameter bends in particular, did not give conclusive evidence that a higher value of the flexibility factor (or a larger unit deflection), should be measured under closing mode of bending in

comparison to the opening mode. Results show that both deflections could be of similar magnitude, or in some cases deflections measured under closing could be higher than that under opening, and in other cases it is vice versa. In all, the deflection measurements were up to 8% different. The expectation of a higher flexibility factor under closing mode of bending, is brought about by the pattern of bend ovality as shown in Fig. 4.1 of Ch. 4.

9.5.1 Flexibility factors of smooth CSM Bends

For all bends having $0.09 \leq \lambda \leq 0.58$, the flexibility factors are considered reasonably covered by the previous discussion, where for the purpose of design, 85% of the values specified by BS806 is considered adequate. For bends of $\lambda = 0.90$, the experimental in-plane flexibility factors are approximately 50% of those specified by BS806. In this instance, the tangent/joint restraints are believed to be the main contributor to such stiffening, although however, it should be also mentioned that ill-conditioning as described in Ch. 6 could reflect some doubts on the flexibility results.

9.5.2 Flexibility factors of mitred CSM/PVC lined bends

The experimentally determined in-plane flexibility factors of three bend sets; with each set containing two bend samples, have shown results to be in agreement with Kitching and Bond's prediction⁽¹⁷⁰⁾ for $\lambda = 0.06$; and for bend of $\lambda = 0.163$ the agreement was better with ANSI B31⁽¹²⁴⁾ specification, and for $\lambda = 0.09$ test results lie in between Kitching and Bond's prediction and ANSI B31 specification as shown in Fig. 9.1.

Kitching and Bond theoretical results were in good agreement with flexibility factors obtained from testing metallic mitred bends, where manufacturing tolerances are not as high as for GRP bends. Based upon that, it could be argued that mitred GRP bends would be better

represented by Kitching and Bond theoretical results, although using ANSI B31 specifications would lead to a conservative estimate of anchor loads. This is only applicable for bends of $R/r_m < 3$. For $R/r_m > 10$ then Kitching and Bond analysis would be more conservative⁽¹⁷⁰⁾.

Experimentally determined out-of-plane flexibility factors were found to be higher than the in-plane flexibility factors. The difference on average was about 30% for $\lambda = 0.163$ being reduced to about 13% for $\lambda = 0.061$. Ovality measurements presented as diametral change per unit bending moment for both in-plane bending and out-of-plane bending as in Figs. 7.19 and 7.20, shown approximately to have similar peak magnitudes. Hence, give or take few per cent, it could be suggested that mitred bends would have similar flexibility factors under both types of bending. The difference of the in-plane and the out-of-plane flexibility test results are believed to be due to the incompleteness of the mathematical model in describing the actual torsional rigidities of the different segments of the bend.

9.5.3 Flexibility factors of smooth orthotropic bends

(a) Bends of circumferential to longitudinal extensibility ratio of 1:1

Experimentally determined in-plane flexibility factors for bends constructed of CSM/WR reinforced laminates (bends S042 and S043 of Ch. 8) were shown to follow similar trends to those of smooth CSM bends. They were on average to be 6% lower when compared with BS806 specification ($\lambda = 0.30$ in Fig. 8.19). Given the tangent restrains considerations, it could be argued that GRP bends constructed from bidirectional reinforced laminates would have similar flexibility factors to isotropic bends. This is providing the reinforcements lie in the principle axes of deformations, i.e. the longitudinal and the circumferential bend directions. Otherwise, the results could be affected as will be discussed later.

For bends having the bend fittings constructed from WR reinforcements and the tangents constructed from FW reinforcements, (bends S028, S029, S030 and S048, S049, S050 of Ch. 8), the experimentally determined flexibility factors were 58% and 52% of those specified by BS806. Although it is difficult to assess the reliability of these test results, it is thought however, that since the tangents have a circumferential modulus approximately twice to that of the bends, then higher end restraints are imposed on the bend ovality. Further, the joints and flanges used with such pipe systems could be considered stiffer than those used for the other pipe components. Ovality measured at the centre of bend S050 (100mm nominal bore) under in-plane bending and under out-of-plane bending were reasonably compared with theory, using flexibility factor specified by BS806 (see Figs. 8.20 and 8.21). In this instance, it could be argued that the dramatic reduction of the average flexibility factor mentioned above, is probably brought about by the relatively rapid reduction of ovality as it approaches the tangents. Whether discussing the results in the view of the bend fitting on its own, or in conjunction with such tangents, it will be in the practical interest to assume that these bends are approximately twice as stiff than theoretically predicted.

(b) Bends of circumferential to longitudinal modulus ratio of 2:1

By introducing additional UD reinforcements in the circumferential direction, the circumferential modulus was increased to twice that in the longitudinal direction as the case for bends S039, S040, S045 and S046 of Ch. 8. The theoretical analysis derived by the author and presented in App. III has shown that the theoretical flexibility factor for $\bar{m} = 2:1$; using one term in the analysis, could be predicted by using Eq. (9.2), as

$$K = \frac{10 + 12 \bar{m} \lambda^2}{1 + 12 \bar{m} \lambda^2} \quad (9.2)$$

Eq. (9.2) will predict flexibility factors lower than those predicted by the isotropic bend theory (see Fig. 4.3a of Ch. 4).

The experimentally determined in-plane flexibility factors were on average to be 80% and 94% of those predicted by orthotropic bend theory ($\bar{m} = 2$) for $\lambda = 0.30$ and 0.163 respectively (see Table 8.6 of Ch. 8). Given the considerations of the tangent restraints as reported by Smith and Ford⁽¹⁸¹⁾, then agreement between experimental and theoretical results would be considered adequate. The experimental results suggest that such bends will be approximately 60% of those specified by BS806⁽¹²³⁾.

The consequence of using such bends in a piping system, will be to increase the anchor loads in comparison with CSM bends of the same dimensions and pipe factor λ .

9.6 Discussion of Bend Stress Ratio Distribution and Stress Intensification Factors (SIF) Test Results

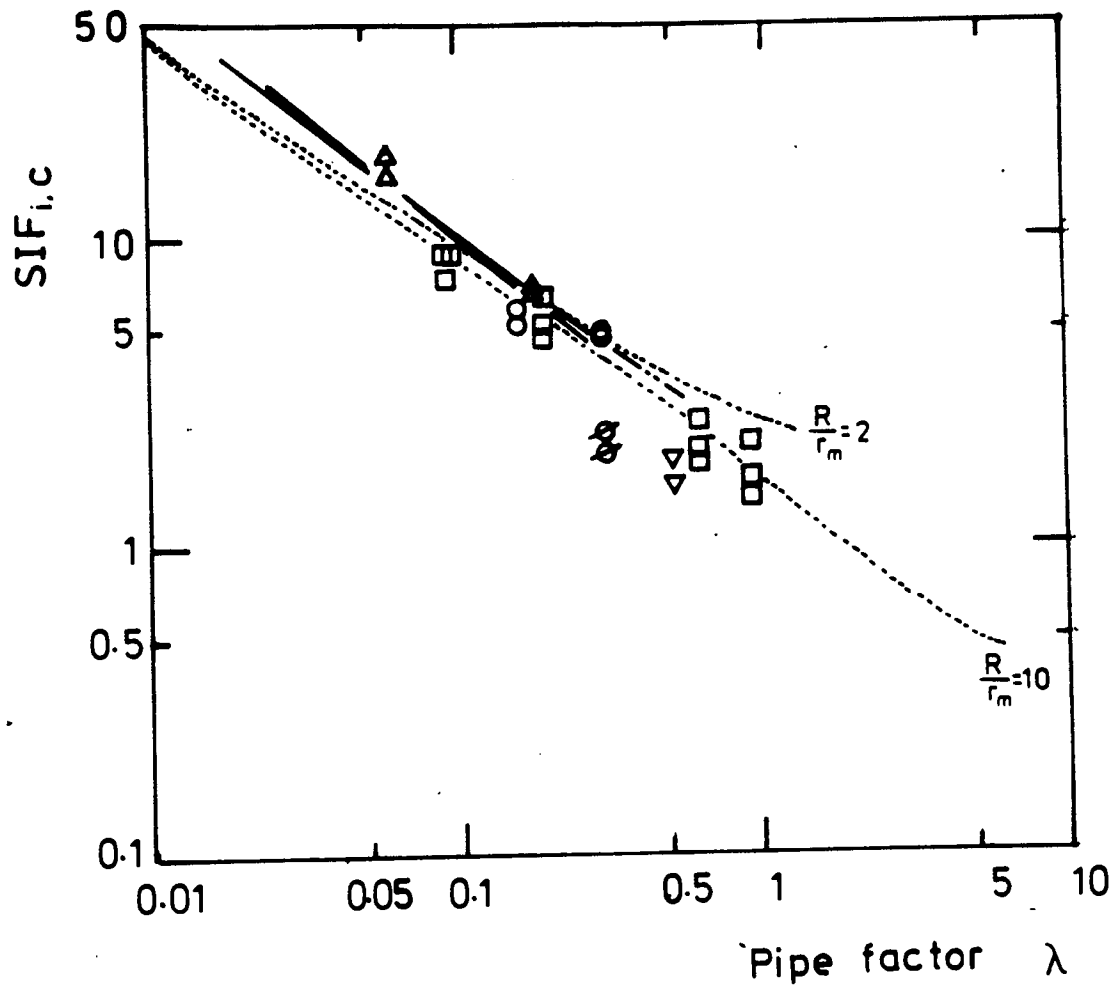
Since maximum ovality has shown to occur at the bend centre, then, the experimentally measured strains are the maximum measured on the bend.

The bend test results in the form of experimental stresses and stress ratio (bend stress/ σ_n) distribution, is believed to be more reliable than those of the experimentally determined flexibility factor. This conclusion is based on the fact that; since strains were directly measured on the bend, thus the end results in the form of SIF are independent of the deformations experienced by the tangents including the joint and flange effects.

It is for the above reasons, it is believed that the stress ratio experimental results are considered to be more valuable for the purpose of investigations and design considerations. The accuracy of these results is however, reduced by the approximate magnitudes of both the young's modulus, and the section modulus required for the purpose of calculation (App. I). Also, due to the finite length of the strain gauges (2-3mm), the experimentally measured strains are of average value over that length.

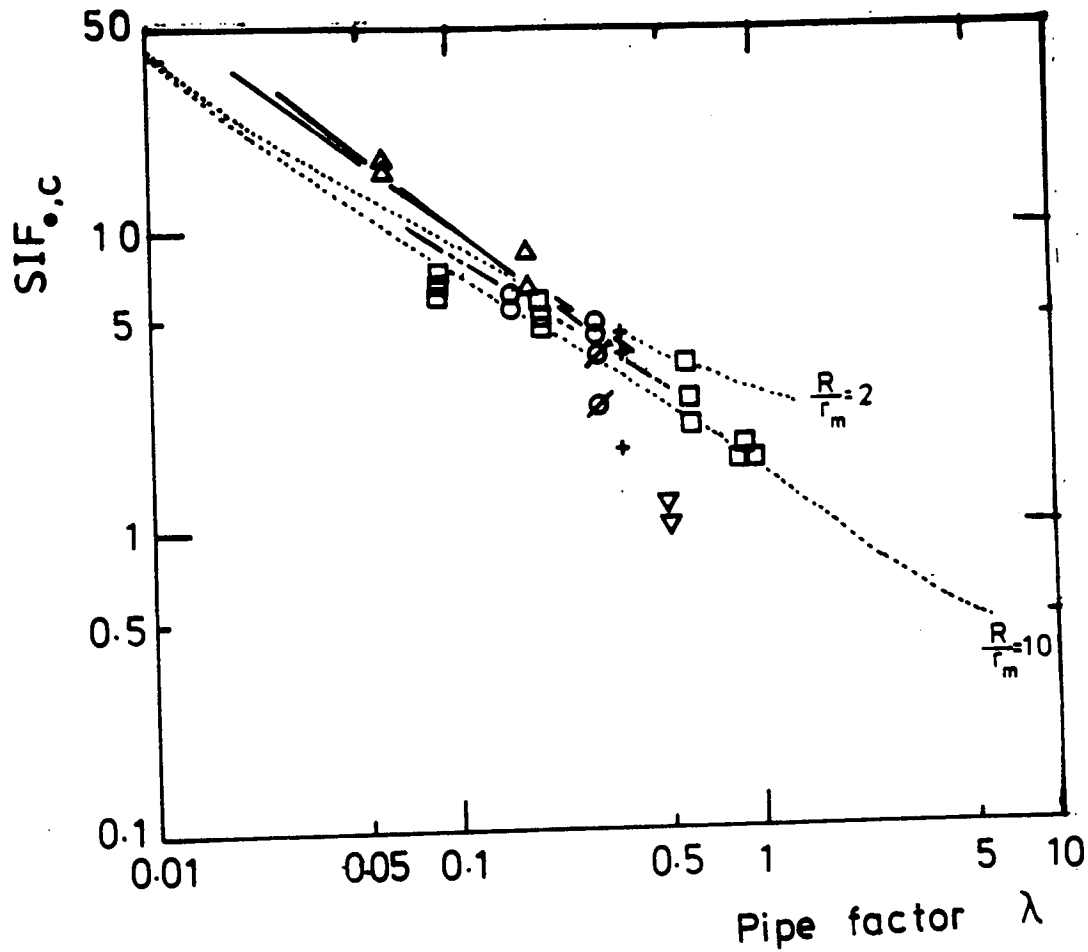
As with any experimental stress analysis, using strain gauges, the results must be considered as subject to errors due to positioning and instrumentation variations. It is difficult to position gauges accurately on the outside surface which is very uneven; this is particularly tedious at the intrados position where acute double curvature occurs. Gauging on the inside surface is very difficult, as the bend is curved and the pipe diameter seldom allows more than one hand to be used through one end. But, the precision with which gauges were placed was very good according to checks made after sectioning specimens following testing. Bearing in mind these difficulties, the general shapes of stress distribution justifies confidence in the quality of instrumentation.

In general, the maximum stress ratios were found in the circumferential direction for both in-plane and out-of-plane bending. The overall test results in the form of the circumferential SIF are presented in Figs. 9.3 and 9.4 for in-plane bending and out-of-plane bending respectively. These are presented along with BS806⁽¹²³⁾ specifications, ANSI B31⁽¹²⁴⁾ specifications, Kitching and Bond⁽¹⁷⁰⁾ prediction and the prediction of orthotropic bend theory for $\bar{m}=2$ (App. III). The maximum stress ratios represented by the SIF, are obtained at angular positions around $\theta = 90^\circ$ for in-plane bending, and at



- | Exp. | Th. |
|--|-------------------------------------|
| □ - Smooth, CSM Ch. 6 | BS 806 ⁽¹²³⁾ ----- |
| △ - Mitred, PVC/CSM Ch. 7 | Kitching ⁽¹⁷⁰⁾ _____ |
| ▽ - Smooth, PVC/CSM Ch. 7 | App(III) -.-.-.-.- |
| ⊙ - Smooth CSM/WR ext. 1:1 Ch. 8 | ANJI.B31 ⁽¹²⁴⁾ - - - - - |
| + - Smooth WR/FW ext. 1:1 Ch. 8 | |
| ◊ - Smooth CSM/WR/UD ext. 2:1 Ch. 8 | |

Figure (9.3) Maximum in-plane Stress Intensification Factors



- | Exp. | Th. |
|--|---------------------------------|
| □ - Smooth, CSM Ch. 6 | BS 806 ⁽¹²³⁾ ----- |
| △ - Mitred, PVC/CSM Ch. 7 | Kitching ⁽¹⁷⁰⁾ ----- |
| ▽ - Smooth, PVC/CSM Ch. 7 | App(III) ----- |
| ∅ - Smooth CSM/WR ext. 1:1 Ch. 8 | ANSI B31 ⁽¹²⁴⁾ ----- |
| + | |
| ∅ - Smooth WR/FW ext. 1:1 Ch. 8 | |
| ∅ - Smooth CSM/WR/UD ext. 2:1 Ch. 8 | |

Figure(9.4) Maximum out-of-plane Stress Intensification Factors

positions $\theta = 45-90$ for out-of-plane bending depending on values of λ , and are measured on the inside surface.

Experimental stress ratios measured on all smooth bends reasonably fit stress ratio distributions predicted by theory. The longitudinal stress ratios showed in general a better agreement with theoretical distributions than those measured in the circumferential directions. For in-plane bending, the longitudinal stress ratios showed a higher shell bending at the bend intrados than theory predicts (e.g. Fig. 6.21, 8.7b, and 8.22a). This is believed to be due to the local thickening present at the intrados, which would probably tend to enhance the flexural nature of stresses. Under out-of-plane bending both longitudinal and circumferential stress ratios are of negligible magnitude at both the intrados and the extrados.

The effect of R/r_m ratio exhibited by the different bends cannot be explicitly identified among the SIF results shown in Figs. 9.3 and 9.4. It is thought that the effect of such ratio (i.e. R/r_m) could be best identified from bends having similar pipe factors (λ) but of different R/r_m and t/r_m ratios, and in the case of GRP bends the pipe wall should be of similar laminate construction. In this instance, such a comparison could be based on limited test results of bends S048 and S049 (Set III) and bend S030 (Set IV); both of Ch. 8. They both have similar values of λ , but with different ratios of R/r_m , of 2.5 and 4.0 respectively. The experimentally measured SIF reveal that they are higher for $R/r_m = 2.5$ than for $R/r_m = 4.0$. Stress intensification factors specified by BS806⁽¹²³⁾ are a function of R/r_m ratio, whilst they are considered independent of such bend ratio for smooth bends specified by ANSI B31⁽¹²⁴⁾.

Strain distributions and stress ratio distributions measured on all bends, under in-plane closing and opening modes of bending, have shown to be a mirror image when plotted as a function of angular positions, e.g. see Figs. 7.28 and 7.56 of Ch. 7.

In order to check the application of superposition to combined in-plane and out-of-plane bending moments, tests were carried out on bend S060 (mitred bend, Fig. 7.53 and Table 7.16 of Ch. 7), and on bend S045 (smooth bend, Table 8.8 of Ch. 8), in which strains were measured while the bends were subjected to equal magnitudes of out-of-plane load (P_H) and in-plane load (P_V). The comparison between these tests and measurements taken under individually applied test are very good as presented in Tables 7.16 and 8.8.

9.6.1 Stress test results of smooth CSM bends

Due to the in-plane isotropy of the laminate and the smooth shape of the bend, the test results could be compared with BS806⁽¹²³⁾ with relatively high confidence. The SIF test results are in general reasonably compared with BS806 specifications as reported in Ch. 6, and as shown in Figs. 9.3 and 9.4. Strains per unit load measured on bends of the same nominal dimensions and glass content, have shown similar patterns of distribution, but also shown different levels of maximum strains. A typical presentation of such measurements is shown in Figs. 6.16 and 6.17 for in-plane bending, and in Figs. 6.32 and 6.33 for out-of-plane bending.

9.6.2 Stress test results of mitred CSM/PVC bends

Due to the complex nature of the analysis of mitred bends, it was not possible to develop a computer program which would have predicted theoretical stress ratio distribution. But the experimental results in the form of SIF were compared with theoretical results based on Kitching and Bond work⁽¹⁷⁰⁾. The theoretical work was reported to be

accurately compared with SIF of metallic bend as reported later by the same authors⁽¹⁷¹⁻¹⁷³⁾.

The maximum SIF results presented in Figs. 9.3 and 9.4 are those measured on the inside surface of the segment-edge. They are shown to be reasonable compared with Bond and Kitching's predictions. They are in general higher than twice the values specified by ANSI B31⁽¹²⁴⁾ (see Tables 7.14 and 7.15 of Ch. 7).

The circumferential inside strains measured at the segment-edge were always higher than those measured at the segment-centre. The difference of magnitude are on average to be 20% for in-plane bending (Figs. 7.27 and 7.35), and 35% under out-of-plane bending (Figs. 7.41 and 7.49). With reference to mitre bend theory⁽¹⁴⁸⁾, the segment-centre strains and their corresponding stress-ratios are considered to be directly related to constant flattening. This is reasonably shown to be the case as in the SIF results in Figs. 7.38 and 7.52. The higher level of strains and stress ratios at the segment-edge is brought about by rotation of the edge which necessitate the superposition of local stresses⁽¹⁴⁸⁾.

For the bends investigated, no strain gauges were positioned on the outside surface of the segment-edge. In this position, theory and previous experiments⁽¹⁷⁰⁾ suggested the longitudinal SIF to be of similar magnitude to the maximum circumferential SIF.

9.6.3 Stress test results of smooth orthotropic bends

(a) Bends of circumferential to longitudinal modulus ratio of 1:1

Longitudinal and circumferential stress ratios measured on such bends were found to be reasonable compared with the stress ratio distribution predicted using isotropic bend theory (App. II). Also, the experimental SIF compare reasonably with those specified by BS806⁽¹²³⁾ as shown in Figs. 8.24 and 8.25 of Ch. 8. Additional experimental

errors that would affect the accuracy of the test results, are the deviation of the fibre reinforcements from the longitudinal and the circumferential axes, which is inevitable in the lamination process. Such fibre disorientation would alter the modulus values used for conversion of strains into stresses. Also it may have further consequences for large difference of longitudinal and circumferential moduli as will be discussed below.

(b) Bends of circumferential to longitudinal modulus ratio of 2:1

Experimental stress ratios for bends S039, S040, S045 and S046 have shown that for bends of such in-plane anisotropy, the longitudinal SIF would be lower than predicted for isotropic smooth bends, whilst the circumferential SIFs would sustain similar magnitudes. It may be recalled that those bends also have lower flexibility factors.

The theoretical analysis for orthotropic bends of $\bar{m} > 1$ has been derived from first principles of strain energy considerations and represented as a computer programme written in BASIC and presented in App. III. Theoretical stress ratio distributions obtained for bends of $\bar{m}=2$ compared with isotropic bend theory are shown in Figs. 8.5 and 8.7 for in-plane bending, and in Figs. 8.10 and 8.12 for out-of-plane bending. Comparison of theoretical SIF ($\bar{m}=2$) and BS806 specifications are presented in Tables 8.7 & 8.8. The modified theoretical analysis supported by the experimental results, suggest that the longitudinal SIF are 45% and 55% lower than predicted by BS806 for in-plane bending and out-of-plane bending respectively. While for the experimental circumference SIF the difference could be considered negligible ($\sim 5\%$) in comparison.

In comparison with smooth CSM bends, the use of such orthotropic bends ($\bar{m}=2$) will inevitably lead to higher anchor loads, and at the same time the bend will experience similar levels of maximum stresses. Given

the considerations that such bends would suffer from relatively inferior chemical resistance due to the higher glass content, then it can only be implied; that their utilisation in the chemical plant piping systems should be carefully reviewed at the design stage.

9.7 Discussion of Bends Failure Test Results under In-Plane Bending

Test results for three GRP bends taken to failure under in-plane (opening) bending are summarised in Table 9.1. The following points prove to be relevant to the failure discussion.

- (a) All three bends appear to initiate failure due to maximum circumferential stress. This is shown in Figs. 6.48, 7.13 and 7.14, 7.59 and 7.60, where failure was initiated close to $\theta = 90^\circ$ and 270° positions running longitudinally along the bend radius.
- (b) For the two smooth bends, 1/10th of the failure bending moment is about one half of that measured at 0.2% maximum strain. In this instance, the design factor is taken on average to be 10. For the mitre bend, the level of both moments is comparable.
- (c) The design bending moment based upon; nominal dimensions, BS806⁽¹²³⁾ (SIF), BS4994⁽³⁾ (UTUS), and a design factor of 10, is seen to be less than the bending moment measured at 0.2% strain, or 1/10th of the bending moment at failure.
- (d) Using Gross theoretical analysis⁽¹⁵¹⁾, the interlaminar shear stress on failure for the smooth CSM bend, is calculated to be of similar magnitude to the interlaminar shear strength presented in Ch. 3, which is 30% higher than 7 N/mm² quoted by BS4994. For bends under external loading, the high rate of change of bending moment with distance around the circumference will lead to interlaminar shear stresses. This effect is likely to be pronounced in thick laminates. Failure test results reported by

Kitching⁽¹⁸⁵⁾ for smooth CSM bends, have suggested that ultimate bending moments calculated on the basis of the laminate tensile strength and the lap shear strength were of similar magnitudes under both in-plane and out-of-plane modes of bending.

- (e) For the mitre bend, the crack was initiated at the segment-edge, and although non-linearity was detected during incremental measurement of the maximum strain (see Fig. 7.61), the end-deflection versus load to failure (Fig. 7.54) showed a linear relationship. This is not expected, and it would imply that the bend would have the same flexibility up to failure.

For the purpose of design, it is not possible to draw general conclusions from three failure cases of bends of different construction. However, the remarks above do indicate the importance of checking shear stresses in the design stage. In this instance, the approximate analysis proposed by Gross⁽¹⁵¹⁾ and generalized by Dodge and Moore⁽¹⁵⁴⁾ is believed to be adequate for this purpose.

A stress component which is usually ignored in metallic pipe bend analysis, is the radial stress component induced under bending of curved beams. In the case of GRP it is commonly identified as the through thickness stress component, and it is usually ignored for thin GRP structures; using the plane stress assumption. The strength magnitude of WR laminates, measured perpendicular to the reinforcement is quoted to be 10 N/mm^2 ⁽⁶⁸⁾. For curved GRP structures such as bends, the presence of a through thickness tensile or compressive stress due to shell bending in the circumferential direction is inevitable. No bend analytical solution is available at the present time which predicts such stress component.

TABLE 9.1 Summary of bending moments, strains and interlaminar shear stress measured on three bends taken to failure under In-plane bending (opening)

| Type of Bend | Reference | λ | Bending moment, MN mm | | | Non-linearity strain (%) | Failure strain (%) | $\bar{\tau}^{-2}$ (N.mm ⁻²) | Design bending moments (MN mm) |
|---------------------------|---------------------|-----------|-----------------------|----------------|---------|--------------------------|--------------------|---|--------------------------------|
| | | | 0.2% strain | 1/10th failure | failure | | | | |
| Smooth CSM Bend | Ch. 6 Table 6.17 | 0.35 | 2.44 | 1.16 | 11.6 | - | >1 | 10 | 0.45 |
| Smooth CSM/PVC lined bend | Ch. 7 Table 7.9 | 0.51 | 0.58 | 0.30 | 2.99 | - | >1 | - | 0.1 |
| Mitred CSM/PVC lined bend | Ch. 7 Table 7.17 | 0.18 | 1.06 | >0.85 | >8.51 | 0.62 | >2 | - | 0.23 |

* Based on Design Factor of 10.

9.8 Design of GRP Bends

Two main requirements are needed, firstly is to predict the bend behaviour under load, and secondly, to identify the maximum acceptable limits for a design strain or for a design stress. The present program covers a wide spectrum of the first requirement, and as for the second; this will be discussed with reference to the type of load, reinforcements used, and previous experience in the field.

Variation in properties is a familiar problem faced by designers dealing with GRP structures especially those manufactured by the hand lay-up process. Taking CSM laminate as an example, BS3496⁽¹⁹⁾ specifies allowable glass content variation to be a maximum of 20%. Given also considerations to imperfections such as voids, then, it is for these reasons that design for GRP vessels and tanks using BS4994⁽³⁾, ASTM D3299⁽⁷²⁾ and also ICI standards for GRP pipes^(4,5,122), unit stresses and strains are limited well below the level reported for irreversible damage of 0.3% strain^(93,95).

The values of ultimate tensile unit strength and extensibility used in design calculations are set as the maximum acceptable properties, according to BS4994. Hence for CSM, the ultimate tensile unit stress is $200 \text{ N.mm}^{-1}/\text{kg.m}^{-2}$ and the extensibility is $12700 \text{ N.mm}^{-1}/\text{kg.m}^{-2}$, which in practice these values could be exceeded, but they are used to lead to low levels of design unit stress and strain.

For piping system flexibility analysis, using values of extensibility lower than actually exhibited by the pipe wall laminate will lead to underestimation of anchor loads, which may have dangerous consequences on both the pipes and on the attached GRP vessels. The

average value measured in this work for CSM extensibility was about $19.8 \text{ kN.mm}^{-1}/\text{kg.m}^{-2}$, i.e. 33% higher than specified by BS4994.

In BS4994, the design unit stress concept is used for the purpose of design, where the stresses lie in the plane of the laminate. For bends under flexural loading, the maximum strains and stresses occur at the inner and the outer surfaces of the bend wall. Hence it will be more logical to use modulus and tensile strength concept for the purpose of bend design rather than extensibility and ultimate tensile unit strength. For the former, the laminate thickness is required to be known for the purpose of stress analysis.

Alternatively, the concept of failure strain and design strain will be applicable to both membrane and flexural types of deformation. For the purpose of bend design, a biaxial strain to failure is required to be reasonably identified, and bend deformation will be in this case be presented as strain intensification factors ($\sigma_B/E(Mr/I)$). Maximum design strains reported in the literature for GRP structures are 0.1% as specified by ASTM D3299⁽⁷²⁾, 0.15% reported by Roberts^(109,110), and 0.2% specified by BS4994.

Once a design stress or a design strain is defined, then GRP tangent/bend elastic deformations are reasonably predicted based upon modified versions of BS806⁽¹²³⁾, orthotropic bend theory (App. III), Kitching and Bond's analysis⁽¹⁷⁰⁾, and ANSI B31⁽¹²⁴⁾.

CHAPTER TEN

CONCLUSIONS AND FUTURE WORK

CONCLUSIONS AND FUTURE WORK

10.1 Conclusions

1. The flexural behaviour of glass reinforced plastic (GRP) bends of tangent lengths of several pipe diameters, is satisfactorily described using bend theory.
2. Modified versions of the bend flexibility factors (K) and stress intensification factors (SIF), specified by standards used for metallic bends, can therefore be used.
3. Because of the high flexural stress gradient experienced by the bend in the circumferential direction, the interlaminar shear stresses could become significant.
4. Stress intensification factors based upon nominal thickness could be under estimated by approximately 50% compared with those based upon actual thickness. Likewise flexibility factors can also be underestimated.
5. Large differences in magnitude have been found between the average thickness, measured on the straight pipes and pipe bends, and those nominally specified in accordance with the nominal glass content. Also bends of so-called identical nominal construction were found to exhibit thickness variability.
6. The presence of butt-joints leads to an increase in flexural rigidity. It is believed that, if such extra rigidity is not taken into account, then the reactions at the anchors of a pipe lay-out

could be underestimated. Superposition techniques proved to give satisfactory correlations with measured deflections, but these techniques may prove to be too complex to be used in practice.

7. Because of flattening of the bend under flexural loading, a marginal length of the straight tangents will ovalize accordingly, thus leading to a bi-axial state of stress. In this instance, discontinuities such as butt-joints located in these margins, may experience an unfavourable pattern of loading. Kirk⁽⁴⁰⁾ reported that peel failures have been observed on butt-joints of GRP bends taken to failure under external loading.
8. The level of design extensibility (Ext.) and hence laminate modulus specified for CSM laminates, is low. This value is not suitable for use in flexibility calculations for pipes, since it could lead to underestimation of anchor reactions and hence higher bending moments in the pipeline.
9. Failure patterns observed on GRP bends lined with unplasticised polyvinyl chloride (uPVC), have indicated embrittlement of the uPVC. Thus failure strains for uPVC under these conditions are of a similar magnitude to those for GRP.
10. The design bending moment based upon; nominal dimensions, and a design factor of 10, is seen to be less than the bending moment measured at 0.2% strain, or 1/10th of the bending moment at failure. This has been shown to be the case for two bends under in-plane bending (opening) taken to failure.

11. The membrane strains and stresses, measured on GRP straight pipes and pipe bends under pressure loading, have been analysed using thin shell theory. This analysis is shown to give realistic values for and distribution of strains and stresses. However, significant local bending strains and stresses were found to arise in the pipe components. These are believed to arise because of thickness variations and surface irregularities exhibited within the pipe wall laminate. Under pressure loading of GRP pipes of uniform thickness, local bending stresses were shown to be of negligible magnitude.

As a consequence of local bending moments, interlaminar shear stresses are to be induced in the pipe wall component. This will further complicate the stress system in the pipe and possibly lead to premature failure. One straight pipe and one bend components taken to failure under pressure load have shown interlaminar shear failures.

10.2 Future Work

There is wide scope for further work on GRP pipe structures. It can be divided into four main areas; experimental, theoretical, manufacturing and design.

1. Experimental

Although the work carried out in this programme covers a wide range of laminate reinforcements and bend shapes, the number of bends representing particular pipe factors and specific laminate constructions cannot be considered sufficient for a proper statistical analysis. Further testing is required to obtain estimate of scatter.

Results presented here are based on the application of an end-load and measurement of the free end-deflection. Future experimental work should preferably include end bending moments, torsional loading, end-axial force, applied separately and in combination for better assessment of the bend flexibility factor. In this instance a nodal stiffness matrix can be constructed relating loads to displacements on the different positions of the bend. No tests have been carried out on the effect flanges being joined directly to the bend.

The ideal test would be on a network of GRP pipe fittings. It should be possible to pressurise the system with a high temperature fluid. This would provide a complete picture of GRP pipe deformation.

For all the above proposed work, test samples should be loaded to failure. Manufacturing and structural weakness is thereby more easily identified. Overlap joints are often a weak area.

2. Theoretical work

It is necessary to further develop bend theories to consider the laminate nature of GRP. In this instance, interlaminar shear stresses and through thickness stresses predictions should be included in the theoretical results. These can be conveniently represented by a stress intensification factor, i.e. as a correction factor to the maximum stress predicted by simple beam theory. Similarly under pressure loading, a modified analysis of thick shell theory should consider the relatively low magnitude of the through thickness modulus. It can be speculated that what might be considered a thin shell ($r_m/t > 10$) for metallic pipes is different for GRP Pipes.

Bend theory should also be extended to include deformations of bends constructed from multilayers, for example lined GRP Pipe components. The modified analysis will probably be more important for multilayer laminates containing different types of reinforcement, where stress discontinuities will arise through the laminate thickness.

3. Manufacturing techniques

There have been two main problems associated with the bends tested in this programme; firstly, the variable thickness and surface irregularity, and secondly, the low interlaminar strength.

The technique of automated manufacturing process used for GRP pipe may in the future be further developed to be as an alternative to the hand lay-up process, where tightly controlled laminate is produced. With the introduction onto the market of fibres and resins which are highly resistant to chemicals, chemical attack problems can be contained.

The availability of through thickness reinforcements (e.g. stitched fibres) may well increase structural integrity, yet at the same time will save material used for extra reinforcements.

4. Design

GRP bends under load induce complex stress patterns; biaxial if not triaxial. Design strains and stresses should take this into account for safety. Complete failure envelopes have not been found in the literature, although a partial failure envelope has been reported for CSM and fabric constructions, the data was determined at ambient temperature and future work at elevated temperatures and on the effects of chemicals would provide valuable information.

APPENDIX I

BEND / TANGENT DEFORMATION UNDER
EXTERNAL LOADING

APPENDIX I

BEND/TANGENT DEFORMATION UNDER EXTERNAL LOADING

I.1. Uniform thickness throughout the bend/tangent structure ^(131,143,163)

I.1.1 In-plane Bending

In-plane mode of bending is induced on the GRP bends by a force acting in the plane of the bend and applied at the flange of the free tangent as shown in Figure I.1a.

I.1.1.1 Determination of in-plane flexibility factor

The applied end load (p) versus the end deflection Δ_D could be inter-related using the bend dimensions and mechanical properties by (a) superposition technique or (b) energy technique assuming small deflection, i.e. δ/DAD' is very small.

(a) Superposition technique (Figure I.1b)

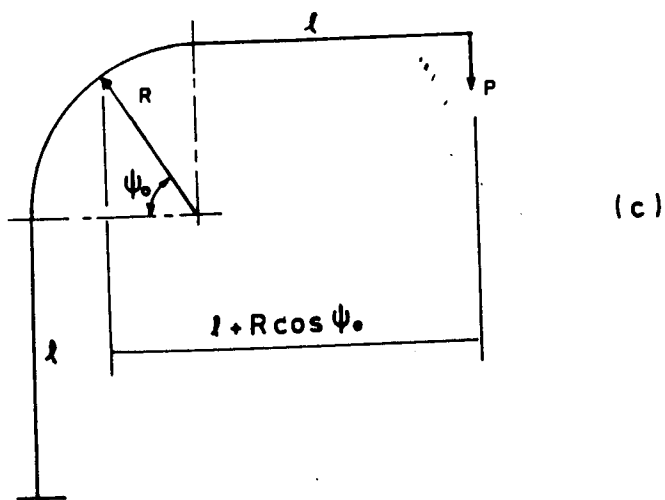
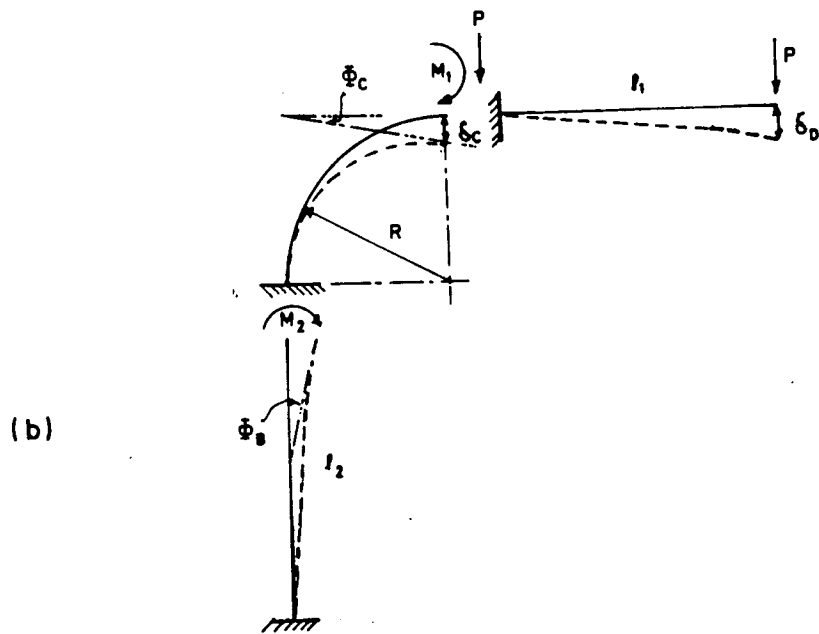
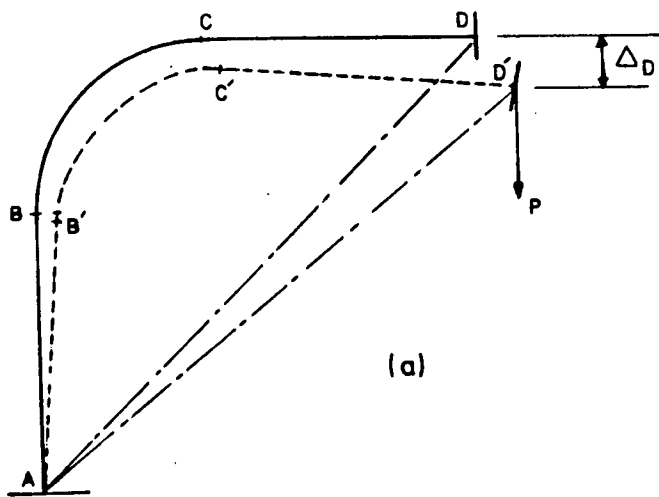
$$\Delta_D = \bar{\phi}_B (\ell_1 + R) + \bar{\phi}_C (\ell_1) + \delta_C + \delta_D \quad (I.1)$$

where

$$\begin{aligned} \bar{\phi}_B &= \text{slope at point (B) due to } M_2. \\ \bar{\phi}_C &= \text{slope at point (C) due to } P \text{ and } M_1. \\ \delta_C &= \text{deflection at point (C) due to } P \text{ and } M_1 \\ \delta_D &= \text{deflection at point (D) due to } P \end{aligned}$$

Now

$$\begin{aligned} \bar{\phi}_B &= \frac{M_2 \ell_2}{EI} = \frac{P(\ell_1 + R) \ell_2}{EI} \\ \bar{\phi}_C &= \frac{PR^2 + \frac{\pi}{2} M_1 R}{EI} = \frac{PR^2 + \frac{\pi}{2} P \ell_1 R}{EI} \end{aligned} \quad (I.2)$$



Figure(I.1) Diagrammatic representation of load-deflection of 90° Bend / Tangent structure under In-plane bending

introducing in-plane flexibility factor K_i to represent bend flexibility brought about by ovalization. Thus

$$\therefore \delta_C = PR \frac{R + \frac{\pi}{2} \ell_1}{EI} K_i \quad (I.3)$$

similarly

$$\begin{aligned} \delta_C &= \frac{\frac{\pi}{4} PR^3 + M_1 R^2}{EI} \\ &= PR^2 \frac{\frac{\pi}{4} R + \ell_1}{EI} K_i \end{aligned} \quad (I.4)$$

and

$$\delta_D = \frac{P \ell_1^3}{3EI} \quad (I.5)$$

substituting back in Eqs. I.2 and I.5 into Eq. I.1, hence

$$\begin{aligned} \Delta_D &= \frac{P(\ell_1 + R)^2 \ell_2}{EI} + K_i \frac{PR}{EI} \left[\ell_1^2 \frac{\pi}{2} + 2R\ell_1 + R^2 \frac{\pi}{4} \right] \\ &\quad + \frac{P \ell_1^3}{3EI} \end{aligned} \quad (I.6)$$

if the bend stiffness $(EI)_B$ is different from the straight stiffness $(EI)_{st}$, and, for equal tangent lengths (ℓ), then

$$\begin{aligned} \Delta_D &= \frac{P(\ell + R)^2 \ell}{(EI)_{st}} + K_i \frac{PR}{(EI)_B} \left[\ell^2 \frac{\pi}{2} + 2R\ell + R^2 \frac{\pi}{4} \right] \\ &\quad + \frac{P \ell^3}{3(EI)_{st}} \end{aligned} \quad (I.7)$$

In Eqs. I.6 and I.7, K_i is the only unknown.

(b) Energy method

$$\begin{aligned} \Delta_D = \frac{\partial U}{\partial P} &= \int_A^B \frac{M}{EI} \frac{\partial M}{\partial P} dS \\ &\quad + \int_B^C \frac{M}{EI} \frac{\partial M}{\partial P} dS \\ &\quad + \int_C^D \frac{M}{EI} \frac{\partial M}{\partial P} dS \end{aligned} \quad (I.8)$$

which provides exactly the same answer to superposition technique represented in equation I.6.

I.1.1.2 In-plane Stress intensification factor

The stress ratios and the stress intensification factors are obtained by dividing the bend stresses by the maximum stress predicted using simple beam theory, i.e.

- for smooth bends

$$\begin{aligned} \text{stress ratio} &= \frac{(\sigma_B)_\theta}{\sigma_{nn}} = \frac{(\sigma_B)_\theta}{M_i r_m / I} \\ \text{SIF} &= \frac{(\sigma_B)_{\max}}{M_i r_m / I} \end{aligned} \quad (\text{I.9})$$

- mitred bends

$$\begin{aligned} \text{stress ratio} &= \frac{(\sigma_B)_\theta}{\sigma_{nn}} = \frac{(\sigma_B)_\theta}{M_i y_i E_i / \Sigma EI} \\ \text{SIF} &= \frac{(\sigma_B)_{\max}}{\sigma_{nn}} \end{aligned}$$

The bend stresses measured at the bend centre where the strain gauges are located. The flexural bending moment acting on the bend is calculated to be (Figure I.1c)

$$M_i = P (l + R \cos \psi_o) \quad (\text{I.10a})$$

and at the centre of the bend, $\psi_o = 45^\circ$

$$M_i = P \left(l + \frac{R}{\sqrt{2}} \right) \quad (\text{I.10b})$$

I.1.2 Out-of-plane Bending

Out-of-plane mode of bending is introduced into the bend structure by applying a load perpendicular to the plane of the bend acting at the flange of the free tangent as shown in Figure I.2a.

I.1.2.1 Determination of Out-of-plane flexibility factor

Similar to the in-plane analysis, the end load and the measured end deflection are related; using the superposition method as a function of the mechanical characterization of the bend/tangent structure (Fig. I.2b) as follows:

$$\Delta_D = \delta_B + \bar{\Phi}_B \cdot R + \bar{\beta}_B (\ell_1 + R) + \delta_C + \bar{\Phi}_C \cdot \ell_1 + \delta_D \quad (\text{I.11})$$

where

$$\delta_B = \frac{Pl_2^3}{3EI} + \frac{M_2 \ell_2^2}{2EI} \quad (\text{I.12})$$

$$= \frac{Pl_2^3}{3EI} + \frac{PR \ell_2^2}{2EI}$$

$$\bar{\Phi}_B = \frac{Pl_2^2}{2EI} + \frac{M_2 \ell_2}{EI} \quad (\text{I.13})$$

$$= \frac{Pl_2^2}{2EI} + \frac{PR \ell_2}{EI}$$

$$\bar{\beta}_B = \frac{T \cdot \ell_2}{GJ} \quad (\text{I.14})$$

$$= \frac{P(\ell_1 + R) \ell_2}{GJ}$$

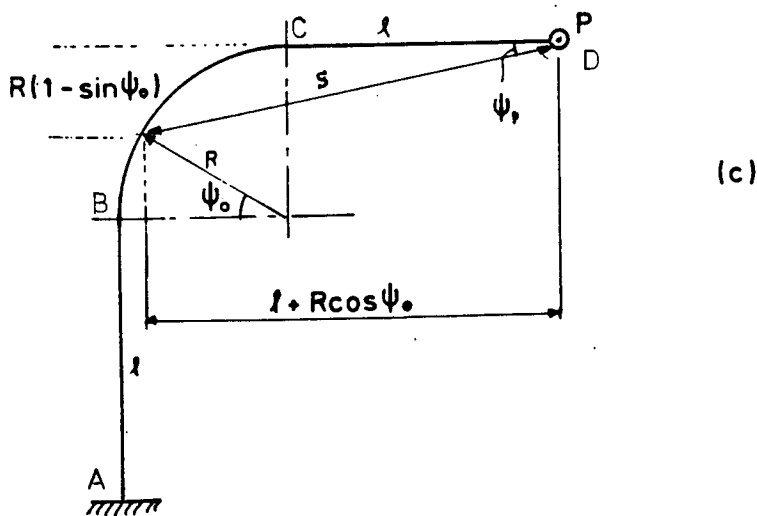
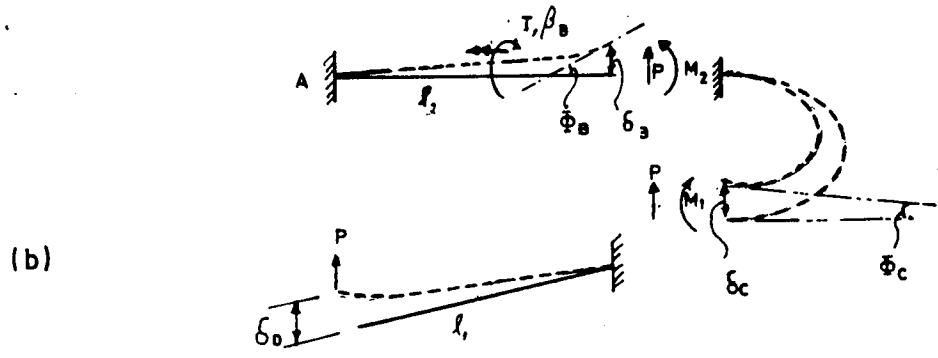
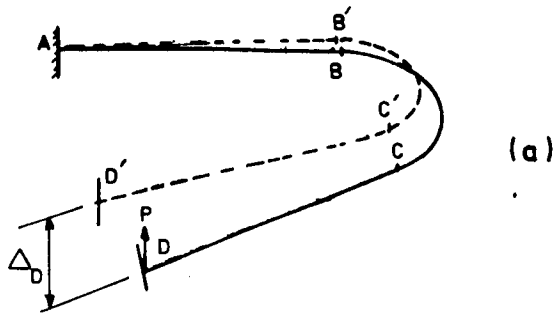
$$\delta_C = \frac{PR^2}{2} \left[\left(\frac{R\pi}{2} + \ell_2 \right) \left(\frac{K_O}{EI} + \frac{1}{GJ} \right) + 2R \frac{\frac{\pi}{2} - 2}{GJ} \right] \quad (\text{I.15})$$

$$\bar{\Phi}_C = PR \left[\left(\frac{K_O}{EI} + \frac{1}{GJ} \right) \cdot \left(\frac{R}{2} + \frac{\ell_2 \pi}{4} \right) \right] \quad (\text{I.16})$$

where K_O is the out-of-plane flexibility factor associated with the flexural rigidity (EI) only.

$$\text{and } \delta_D = \frac{Pl_2^3}{3EI} \quad (\text{I.17})$$

substituting Eqs. (I.12) to (I.17) back into Eq. (I.11), hence



Figure(I.2) Diagrammatic representation of load deflection of 90° Bend / Tangent structure under out-of-plane bending

$$\begin{aligned}
\Delta_D = & \frac{P}{EI} \left[\frac{l_2^3}{3} + l_2^2 R + l_2 R^2 \right] \\
& + \frac{P}{GJ} (l_1 + R)^2 l_2 \\
& + \frac{PR}{EI} K_o \left[l_2^2 \frac{\pi}{4} + l_2 R + R^2 \frac{\pi}{4} \right] \\
& + \frac{PR}{GJ} \left[l_2^2 \frac{\pi}{4} + l_2 R + \left(\frac{3\pi}{4} - 2 \right) R^2 \right] \\
& + \frac{P l_2^3}{3EI}
\end{aligned} \tag{I.18}$$

for $l_1 = l_2 = l$, and if the bend rigidity $(EI)_B$ is different from the straight rigidity $(EI)_{st}$, then equation I.18 would be:

$$\begin{aligned}
\Delta_D = & \frac{P}{(EI)_{St.}} \left[\frac{l^3}{3} + l^2 R + l R^2 \right] \\
& + \frac{P}{(GJ)_{St.}} (l + R)^2 l \\
& + \frac{PR}{(EI)_3} K_o \left[l^2 \frac{\pi}{4} + l R + R^2 \frac{\pi}{4} \right] \\
& + \frac{PR}{(GJ)_3} \left[l^2 \frac{\pi}{4} + l R + \left(\frac{3\pi}{4} - 2 \right) R^2 \right] \\
& + \frac{P l^3}{3(EI)_{St.}}
\end{aligned} \tag{I.19}$$

The only unknown in equation I.19 is K_o .

I.1.2.2 Out-of-plane Stress intensification factor

- for smooth bends

$$\text{stress ratio} = \frac{(\sigma_B)_\theta}{\sigma_n} = \frac{(\sigma_B)_\theta}{M_o r_m / I}$$

$$\text{SIF} = \frac{(\sigma_B)_{\max.}}{\sigma_n} \quad (\text{I.20})$$

- for mitred bends

$$\text{stress ratio} = \frac{(\sigma_B)_\theta}{\sigma_{nn}} = \frac{(\sigma_B)_\theta}{M_o y_i E_i / \Sigma EI}$$

$$\text{SIF} = \frac{(\sigma_B)_{\max.}}{\sigma_{nn}}$$

where M_o is derived with reference to Figure I.2c.

$$M = P \cdot S$$

$$M_o = \text{flexural bending moment} = M \cdot \sin(\psi_o + \psi_1)$$

$$T = \text{torsional moment} = M \cdot \cos(\psi_o + \psi_1)$$

$$M_o = P \cdot S (\sin \psi_o \cos \psi_1 + \cos \psi_o \sin \psi_1)$$

$$= P \cdot S \left(\sin \psi_o \frac{l_1 + R \cos \psi_1}{S} + \cos \psi_o \frac{R (1 - \sin \psi_o)}{S} \right)$$

$$= P [l_1 \sin \psi_o + R \cos \psi_o]$$

(I.21)

hence, at the centre of the bend $\psi_o = 45^\circ$,

$$M_o = \frac{P}{\sqrt{2}} (l + R)$$

For the mitred bends discussed in Chapter 7, bends S034, S060, S061 have gauges situated at the mitre-joint located at $\psi_0 = 32.14$, and bend S033 at mitre-joint located at $\psi_0 = 57.88^\circ$.

I.2 Non-Uniform Thickness of the Bend/Tangene Structure

Here the actual measured thickness of the butt joint, straight tangents and the bend fittings are taken into consideration in formulating the applied end load versus the measured end deflection for calculating the flexibility factor of the bend. Such non-uniform thickness is modelled as shown in Fig. I.3a. The technique used to formulate such a relation is the superposition technique.

I.2.1 Joint Effect on Straight Pipe Behaviour

I.2.1.1 Under bending moment (Fig. I.3a)

In general

$$EI \frac{d^2y}{dx^2} = -\bar{M} \quad (I.22)$$

For $0 \leq x \leq x_1$

$$(EI)_1 \frac{d^2y_1}{dx^2} = M \quad (I.23a)$$

$$(EI)_1 \frac{dy_1}{dx} = Mx + C_1 \quad (I.23b)$$

$$(EI)_1 y_1 = \frac{Mx^2}{2} + C_1 x + C_2 \quad (I.23c)$$

For $x_1 \leq x \leq x_2$

$$(EI)_2 \frac{d^2y_2}{dx^2} = M \quad (I.24a)$$

$$(EI)_2 \frac{dy_2}{dx} = Mx + C'_1 \quad (I.24b)$$

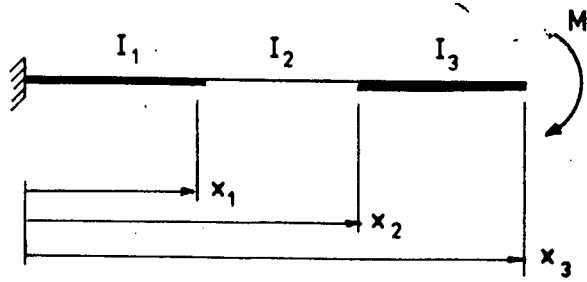
$$(EI)_2 y_2 = \frac{Mx^2}{2} + C'_1 x + C'_2 \quad (I.24c)$$

For $x_2 \leq x \leq x_3$

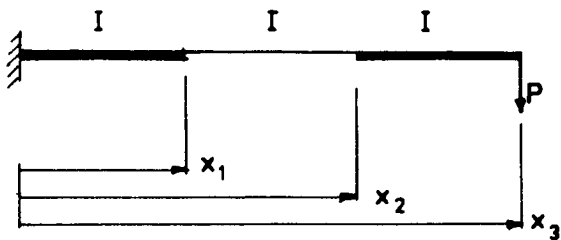
$$(EI)_3 \frac{d^2y_3}{x^2} = M \quad (I.25a)$$

$$(EI)_3 \frac{dy_3}{dx} = Mx + C''_1 \quad (I.25b)$$

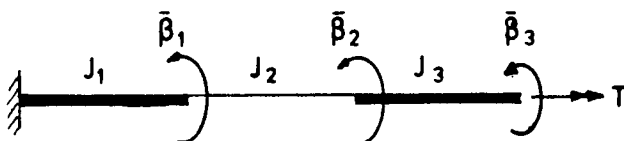
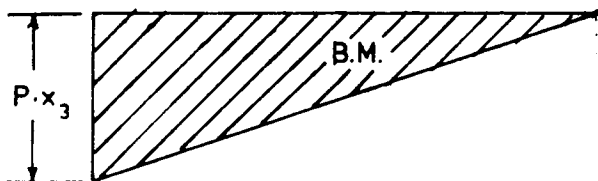
$$(EI)_3 y_3 = \frac{Mx^2}{2} + C''_1 x + C''_2 \quad (I.25c)$$



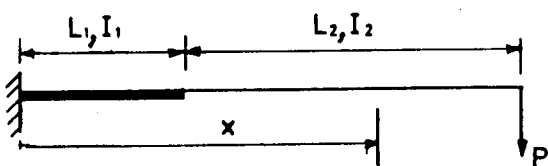
(a)



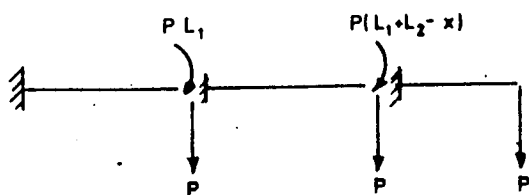
(b)



(c)



(d)



Figure(I.3) Flexural and Torsional bending of variable cross section beam

For comparability and B.C 's

$$y_1 = 0 \quad \text{at } x = 0 \quad (\text{I.26a})$$

$$dy_1/dx = 0 \quad \text{at } x = 0 \quad (\text{I.26b})$$

$$dy_1/dx = dy_2/dx \quad \text{at } x = x_1 \quad (\text{I.26c})$$

$$y_1 = y_2 \quad \text{at } x = x_1 \quad (\text{I.26d})$$

$$dy_1/dx = dy_2/dx \quad \text{at } x = x_2 \quad (\text{I.26e})$$

$$y_2 = y_3 \quad \text{at } x = x_2 \quad (\text{I.26f})$$

Eq. (I.26b) into (I.23b)

$$\therefore C_1 = 0$$

Eq. (I.26a) into (I.23c)

$$\therefore C_2 = 0$$

Eq. (I.26c) into (I.23b) and (I.24b), thus

$$C_1' = Mx_1 \left[\frac{I_2}{I_1} - 1 \right]$$

Eq. (I.26d) into Eq. (I.23c) and (I.24c), thus

$$C_2' = \frac{Mx_1^2}{2} \left[1 - \frac{I_2}{I_1} \right]$$

Eq. (I.26e) into Eqs. (I.24b) and (I.25b), thus

$$C_1'' = Mx_2 \left(\frac{I_3}{I_1} - 1 \right) + \frac{I_3}{I_2} (Mx_1) \left(\frac{I_2}{I_1} - 1 \right)$$

Eq. (I.26f) into Eqs (I.24c) and (I.25c), thus

$$C_2'' = \frac{Mx_2^2}{2} \left(1 - \frac{I_3}{I_2} \right) + \frac{Mx_1^2}{2} \frac{I_3}{I_2} \left(1 - \frac{I_2}{I_1} \right)$$

To find the slope ϕ_3 , and the end deflection Δ , (Fig. I.3a) use Eq. (I.25b) and (I.25c) and substitute for C_1'' & C_2'' as derived above, i.e.

$$\Phi_3 = \left[\frac{dy_3}{dx} \right]_{x=x_3} = \frac{1}{(EI)_3} [Mx_3 + C_1'']$$

$$\Phi_3 = \frac{M}{(EI)_3} \left[x_3 + x_2 \left(\frac{I_3}{I_2} - 1 \right) + \frac{I_3}{I_2} x_1 \left(\frac{I_2}{I_1} - 1 \right) \right] \quad (\text{I.27a})$$

and

$$\Delta_3 = \left[y_3 \right]_{x=x_3} = \frac{1}{(EI)_3} \left[\frac{Mx_3^2}{2} + C_1'' x_3 + C_2'' \right]$$

$$\begin{aligned} \Delta_3 = \frac{M}{(EI)_3} & \left[\frac{x_3^2}{2} + x_2 x_3 \left(\frac{I_3}{I_2} - 1 \right) \right. \\ & + \frac{I_3}{I_2} x_1 x_3 \left(\frac{I_2}{I_1} - 1 \right) \\ & \left. + \frac{x_2^2}{2} \left(1 - \frac{I_3}{I_2} \right) + \frac{I_3}{I_2} \frac{x_1^2}{2} \left(1 - \frac{I_2}{I_1} \right) \right] \quad (\text{I.27b}) \end{aligned}$$

I.2.1.2 Under end load (Fig. I.3b)

In general

$$EI \frac{d^2y}{dx^2} = -\bar{M}$$

for $0 \leq x \leq x_1$

$$(EI)_1 \frac{d^2y_1}{dx^2} = P(x_3 - x) \quad (\text{I.28a})$$

$$(EI)_1 \frac{dy_1}{dx} = P(xx_3 - \frac{x^2}{2} + C_1) \quad (\text{I.28b})$$

$$(EI)_1 y_1 = P\left(\frac{x^2}{2}x_3 - \frac{x^3}{6}\right) + C_1 x + C_2 \quad (\text{I.28c})$$

for $x_1 \leq x \leq x_2$

$$(EI)_2 \frac{d^2 y_2}{dx^2} = P(x_3 - x) \quad (I.29a)$$

$$(EI)_2 \frac{dy_2}{dx} = P\left(xx_3 - \frac{x^2}{2}\right) + C_1' \quad (I.29b)$$

$$(EI)_2 y_2 = P\left(\frac{x^2}{2} x_3 - \frac{x^3}{6}\right) + C_1' x + C_2' \quad (I.29c)$$

for $x_2 \leq x \leq x_3$

$$(EI)_3 \frac{d^2 y_3}{dx^2} = P(x_3 - x) \quad (I.30a)$$

$$(EI)_3 \frac{dy_3}{dx} = P\left(xx_3 - \frac{x^2}{2}\right) + C_1'' \quad (I.30b)$$

$$(EI)_3 y_3 = P\left(\frac{x^2}{2} x_3 - \frac{x^3}{6}\right) + C_1'' x + C_2'' \quad (I.30c)$$

Using the compatibility and boundary conditions equation to Eq.

(I.26a) to (I.26f), thus:

$$C_1' = P\left(x_1 x_3 - \frac{x_1^2}{2}\right) \left(\frac{I_2}{I_1} - 1\right)$$

$$C_2' = P\left(\frac{I_2}{I_1} - 1\right) \left(\frac{x_1^3}{3} - \frac{x_1^2}{2} x_3\right)$$

$$C_1'' = P\left[\left(x_2 x_3 - \frac{x_2^2}{2}\right) \left(\frac{I_3}{I_2} - 1\right) + \frac{I_3}{I_2} \left(x_1 x_3 - \frac{x_1^2}{2}\right) \left(\frac{I_2}{I_1} - 1\right)\right]$$

$$C_2'' = P\left[\left(\frac{I_3}{I_2} - 1\right) \left(\frac{x_2^3}{3} - \frac{x_2^2}{2} x_3\right) + \frac{I_3}{I_2} \left(\frac{I_2}{I_1} - 1\right) \left(\frac{x_1^3}{3} - \frac{x_1^2}{2} x_3\right)\right]$$

Hence the end slope ϕ_3 and the end deflection Δ_3 , are

$$\begin{aligned}
 [\Phi_3]_{x=x_3} &= \frac{P}{(EI)_3} \left[\frac{x_3^2}{2} + (x_2 x_3 - \frac{x_2^2}{2}) (\frac{I_3}{I_2} - 1) \right. \\
 &\quad \left. + \frac{I_3}{I_2} (x_1 x_3 - \frac{x_1^2}{2}) (\frac{I_2}{I_1} - 1) \right] \quad (I.31a)
 \end{aligned}$$

$$\begin{aligned}
 [\Delta_3]_{x=x_3} &= \frac{P}{(EI)_3} \left[\frac{x_3^3}{3} + (x_2 x_3^2 - \frac{x_2^2}{2} x_3) (\frac{I_3}{I_2} - 1) \right. \\
 &\quad \left. + \frac{I_3}{I_2} (x_1 x_3^2 - \frac{x_1^2}{2} x_3) (\frac{I_2}{I_1} - 1) \right. \\
 &\quad \left. + (\frac{I_3}{I_2} - 1) (\frac{x_2^3}{3} - \frac{x_2^2}{2} x_3) \right. \\
 &\quad \left. + \frac{I_3}{I_2} (\frac{I_2}{I_1} - 1) (\frac{x_1^3}{3} - \frac{x_1^2}{2} x_3) \right] \quad (I.31b)
 \end{aligned}$$

For a straight pipe which has one butt joint situated at the fixed end, then following the superposition technique, the deflection at any point along the pipe length is calculated under cantilever loading as follows (Fig. I.3d):

$$\begin{aligned}
 L_1 \leq x \leq (L_1 + L_2) \\
 [\Delta]_{x=x} &= \frac{P L_1^2 L_2}{2EI_1} + \frac{P L_1^3}{3EI_1} + \frac{P(x - L_1)^3}{3EI_2} \\
 &\quad + \frac{P(L_1 + L_2 - x)(x - L_1)}{2EI_2} \\
 &\quad + (x - L_1) \left[\frac{P L_1 L_2}{EI_1} + \frac{P L_1^2}{2EI_1} \right] \quad (I.32)
 \end{aligned}$$

Such a straight has been discussed in Ch. 6, undergoing a cantilever loading, where

$$\begin{aligned}
 r_i &= 51 \text{ mm} \\
 t_{st} &= 4.6 \text{ mm}, \quad I = 2.18 \times 10^6 \text{ mm}^4 \\
 t_{joint} &= 9.0 \text{ mm}, \quad I_{joint} = 4.83 \times 10^6 \text{ mm}^4 \\
 L_1 + L_2 &= 1340 \text{ mm} \\
 L_1 &= \text{joint length} = 180 \text{ mm} \\
 E &= 7450 \text{ N/mm}^2 \\
 P &= \text{end load} = 100\text{N}
 \end{aligned}$$

Hence, by using Eq. (I.32), the following deflection distribution along the length is obtained.

| x (mm) | 200 | 300 | 400 | 500 | 600 | 700 | 800 | 900 | 1000 | 1100 | 1200 | 1300 | 1340 |
|-------------------------------------|-----|-----|-----|-----|------|------|------|------|------|------|------|------|------|
| $\Delta (\cdot 10^{-3} \text{ mm})$ | 108 | 278 | 547 | 906 | 1346 | 1857 | 2429 | 3052 | 3719 | 4417 | 5139 | 5875 | 6170 |

which compares favourably with the experimentally measured deflections as shown in Fig. (6.8) of Ch. 6.

I.2.1.3 Torsional deformation (Fig. I.3c).

Formulating the nodal force/rotation matrix ⁽¹⁸⁴⁾

$$\begin{bmatrix} 0 \\ 0 \\ T \end{bmatrix} = \begin{bmatrix} (k_{22}^1 + k_{11}^2) & k_{12}^2 & 0 \\ k_{21}^2 & (k_{22}^2 + k_{11}^3) & k_{23}^3 \\ 0 & k_{32}^3 & k_{22}^3 \end{bmatrix} \begin{bmatrix} \bar{\beta}_1 \\ \bar{\beta}_2 \\ \bar{\beta}_3 \end{bmatrix}$$

where

$$[k]^e = \frac{GJ}{l_e} \begin{bmatrix} 1 & -1 \\ -1 & 1 \end{bmatrix}$$

where l_e = element length

determining the determinant $|K|$ and the cofactor matrix $[K]^C$, hence

$$\{\bar{\beta}\} = [K]^{-1} \{T\}$$

$$\begin{bmatrix} \bar{\beta}_1 \\ \bar{\beta}_2 \\ \bar{\beta}_3 \end{bmatrix} = \frac{1}{|K|} \begin{bmatrix} [k_{22}^3 (k_{22}^2 + k_{11}^3) - k_{32}^3 k_{32}^3] & [k_{21}^2 k_{22}^3] & [k_{21}^2 k_{32}^3] \\ [k_{21}^2 k_{22}^3] & [k_{22}^3 (k_{22}^1 + k_{11}^2)] & [k_{32}^3 (k_{22}^1 + k_{11}^2)] \\ [k_{21}^2 k_{32}^3] & [k_{32}^3 (k_{22}^1 + k_{11}^3)] & [(k_{22}^1 + k_{11}^2)(k_{22}^2 + k_{11}^3)] \end{bmatrix} \begin{bmatrix} 0 \\ 0 \\ T \end{bmatrix}$$

$$\bar{\beta}_1 = \frac{T (k_{22}^1 + k_{11}^2) (k_{22}^2 + k_{11}^3)}{|K|}$$

$$\bar{\beta}_2 = \frac{T (k_{22}^1 + k_{11}^2) (k_{22}^2 + k_{11}^3)}{(k_{22}^1 + k_{11}^2) [(k_{22}^2 + k_{11}^3) k_{22}^3 - k_{23}^3 k_{32}^3] - k_{12}^2 (k_{21}^2 k_{22}^3)}$$

where

$$k_{22}^1 = \frac{(GJ)_1}{x_1}, \quad k_{11}^2 = \frac{(GJ)_2}{(x_3 - x_1)}, \quad k_{22}^3 = \frac{(GJ)_2}{(x_2 - x_1)}$$

$$k_{11}^3 = \frac{(GJ)_3}{x_3 - x_2}, \quad k_{33}^3 = \frac{(GJ)_3}{x_3 - x_2}, \quad k_{12}^2 = \frac{(GJ)_2}{x_2 - x_1}$$

$$\bar{\beta}_3 = \frac{T [(GJ)_1(x_2 - x_1) + (GJ)_2 x_1] [(GJ)_2(x_3 - x_2) + (GJ)_3(x_2 - x_1)]}{(x_2 - x_1) \cdot (GJ)_1 \cdot (GJ)_2 \cdot (GJ)_3}$$

1.2.2 Joint effects on bend/tangent structure under in-plane mode of bending (Fig. I.4)

Using the superposition technique as already summarised in article I.1 along with formulae in article I.2.1 of this Appendix, the applied end load versus the measured end deflection are related as follows:

$$\Delta_D = \Phi_B (\lambda + R) + \Phi_C \lambda + \delta_C + \delta_D \quad (I.33)$$

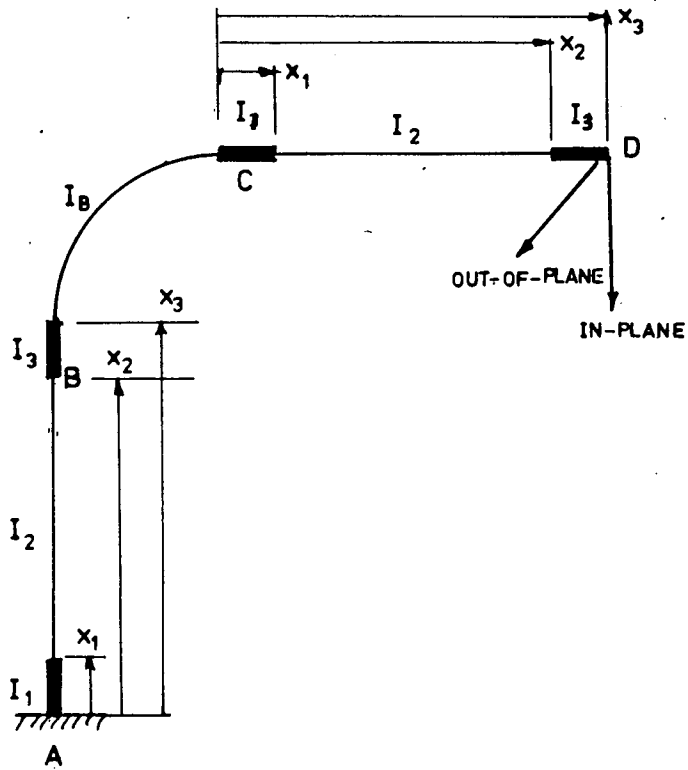
where

$$\left[\Phi_B \right]_{\substack{\text{fixed} \\ \text{tangent}}} = \frac{P(\lambda + R)}{(EI)_3} \left[x_3 + x_2 \left(\frac{I_3}{I_2} - 1 \right) + x_1 \frac{I_3}{I_2} \left(\frac{I_2}{I_1} - 1 \right) \right]$$

$$\left[\Phi_C \right]_{\text{Bend}} = PR \frac{R + \frac{\pi}{2} \lambda}{(EI)_B} K_i$$

$$\left[\delta_C \right]_{\text{Bend}} = PR^2 \frac{\frac{\pi}{4} R + \lambda}{(EI)_B} K_i$$

$$\begin{aligned} \left[\delta_D \right]_{\substack{\text{free} \\ \text{tangent}}} = & \frac{P}{(EI)_3} \left[\frac{x_3^3}{3} + (x_2 x_3^2 - \frac{x_2^2}{2} x_3) \left(\frac{I_3}{I_2} - 1 \right) \right. \\ & + \frac{I_3}{I_2} (x_1 x_3^2 - \frac{x_1^2}{2} x_3) \left(\frac{I_2}{I_1} - 1 \right) \\ & + \left(\frac{I_3}{I_2} - 1 \right) \left(\frac{x_2^3}{3} - \frac{x_2^2}{2} x_3 \right) \\ & \left. + \frac{I_3}{I_2} \left(\frac{I_2}{I_1} - 1 \right) \left(\frac{x_1^3}{3} - \frac{x_1^2}{2} x_3 \right) \right] \end{aligned}$$



Figure(I.4) GRP Bend/Tangent structure joined using overlap joints

I.2.3 Joint effects on bend/tangent structure under out-of-plane

mode of bending (Fig. I.4)

$$\Delta_D = \delta_B + \Phi_B R + \bar{\beta}_B (\ell + R) + \delta_C + \Phi_C \ell + \delta_D \quad (I.34)$$

where

$$\begin{aligned} \left. \delta_B \right|_{\substack{\text{fixed} \\ \text{tangent}}} &= \frac{P}{(EI)_3} \left[\frac{x_3^3}{3} + x_2 x_3 \left(x_3 - \frac{x_2}{2} \right) \left(\frac{I_3}{I_2} - 1 \right) \right. \\ &+ \frac{I_3}{I_2} x_1 x_3 \left(x_3 - \frac{x_1}{2} \right) \left(\frac{I_2}{I_1} - 1 \right) \\ &+ \left(\frac{I_3}{I_2} - 1 \right) \left(x_2^2 \right) \left(\frac{x_2}{3} - \frac{x_3}{2} \right) \\ &+ \left. \frac{I_3}{I_2} \left(\frac{I_2}{I_1} - 1 \right) \left(x_1^2 \right) \left(\frac{x_1}{3} - \frac{x_3}{2} \right) \right] \\ &+ \frac{PR}{(EI)_3} \left[\frac{x_3^2}{2} + x_2 x_3 \left(\frac{I_3}{I_2} - 1 \right) + x_1 x_3 \frac{I_3}{I_2} \left(\frac{I_2}{I_1} - 1 \right) \right. \\ &+ \left. \frac{x_2^2}{2} \left(1 - \frac{I_3}{I_2} \right) + \frac{I_3}{I_2} \frac{x_1^2}{2} \left(1 - \frac{I_2}{I_1} \right) \right] \end{aligned}$$

$$\begin{aligned} \left. \Phi_B \right|_{\substack{\text{fixed} \\ \text{tangent}}} &= \frac{P}{(EI)_3} \left[\frac{x_3^2}{2} + x_2 \left(x_3 - \frac{x_2}{2} \right) \left(\frac{I_3}{I_2} - 1 \right) \right. \\ &+ \left. \frac{I_3}{I_2} x_1 \left(x_3 - \frac{x_1}{2} \right) \left(\frac{I_2}{I_1} - 1 \right) \right] \\ &+ \frac{PR}{(EI)_3} \left[x_3 + x_2 \left(\frac{I_3}{I_2} - 1 \right) + x_1 \frac{I_3}{I_2} \left(\frac{I_2}{I_1} - 1 \right) \right] \end{aligned}$$

$$\left. \bar{\beta}_B \right|_{\substack{\text{fixed} \\ \text{tangent}}} = \frac{P(\ell + R) \left[(GJ)_1 (x_2 - x_1) + (GJ)_2 x_1 \right] \left[(GJ)_2 (x_3 x_2) + (GJ)_3 (x_2 - x_1) \right]}{(x_2 - x_1) \cdot (GJ)_1 (GJ)_2 (GJ)_3}$$

$$\left[\delta_C \right]_{\text{Bend}} = \frac{PR^2}{2} \left\{ \left(\frac{R\pi}{2} + \lambda \right) \left[\frac{K_o}{(EI)_B} + \frac{1}{(GJ)_B} \right] + 2R \frac{\frac{\pi}{2} - 2}{(GJ)_B} \right\}$$

$$\left[\Phi_C \right]_{\text{Bend}} = PR \left[\frac{K_o}{(EI)_B} + \frac{1}{(GJ)_B} \right] \left[\frac{R}{2} + \frac{\lambda \pi}{4} \right]$$

$$\begin{aligned} \left[\delta_D \right]_{\text{free tangent}} &= \frac{P}{(EI)} \left[\frac{x_3^3}{3} + x_2 x_3 \left(x_3 - \frac{x_2}{2} \right) \left(\frac{I_3}{I_2} - 1 \right) \right. \\ &\quad + \frac{I_3}{I_2} x_1 x_3 \left(x_3 - \frac{x_1}{2} \right) \left(\frac{I_2}{I_1} - 1 \right) \\ &\quad + \left(\frac{I_3}{I_2} - 1 \right) \left(x_2^2 \right) \left(\frac{x_2}{3} - \frac{x_3}{2} \right) \\ &\quad \left. + \frac{I_3}{I_2} \left(\frac{I_2}{I_1} - 1 \right) \left(x_1^2 \right) \left(\frac{x_1}{3} - \frac{x_3}{2} \right) \right] \end{aligned}$$

APPENDIX II

THEORY OF ISOTROPIC SMOOTH BEND

THEORY OF ISOTROPIC SMOOTH BEND

II.1 In-plane Bending Analysis

The analysis which is most frequently adopted for flexibility and stress calculations of smooth isotropic bends is that proposed by von Karman⁽¹³⁹⁾.

Consider a curved tube of angle ψ_0 and centre-line radius R which is bent by a bending moment M causing the end planes to rotate relatively through an angle of $\Delta\psi_0$ as shown in Fig. II.1a. Since both tensile forces at the extrados side and compressive forces at the intrados have resultants towards the neutral axis of the bend, the previously circular cross-section is flattened.

The circumferential flexural strains induced in a ring element of the bend is defined as a function of the radial deflection ω_r (Fig. II.1b) and at a distance z from the thickness centre (Fig. II.1c), as^(139,140).

$$\epsilon_C = \frac{z}{r_m^2} \left(\omega_r + \frac{d^2 \omega_r}{d\phi^2} \right) \quad (II.1)$$

From inextensibility⁽¹⁴⁰⁾ assumption, the radial deformation ω_r is related to the tangential deformation ω_t as

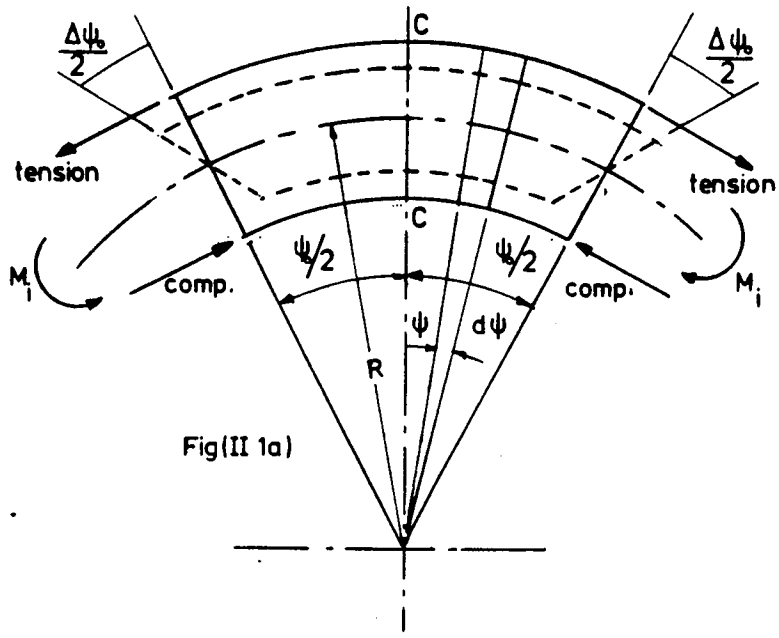
$$\omega_r = - \frac{d\omega_t}{d\phi} \quad (II.2)$$

At any point on the tube, at radius \bar{R} shown in Fig. (II.1b), let the change of radius \bar{R} due to bending⁽¹⁴⁸⁾ to be $d\bar{R}$ (Fig. (II.1c)).

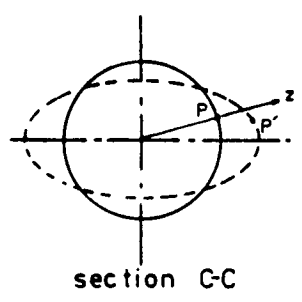
Longitudinal strains due to flattening is then⁽¹⁴⁸⁾:

$$\epsilon_L' = \frac{d\bar{R}}{\bar{R}} = \frac{\omega_t \cos \phi + \omega_r \sin \phi}{R + r_m \sin \phi} \quad (II.3a)$$

Due to simple bending of the tube through angle $\Delta\psi_0$ at the ends, longitudinal strain is⁽¹⁴⁸⁾

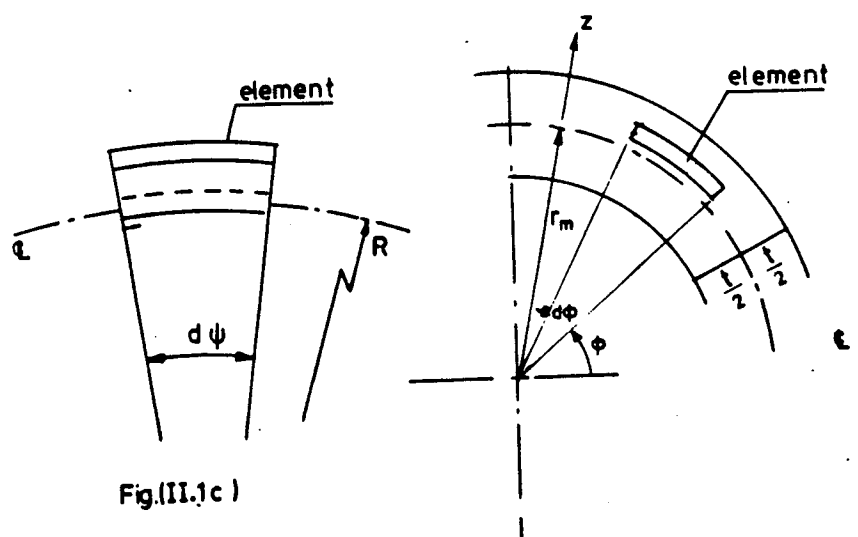
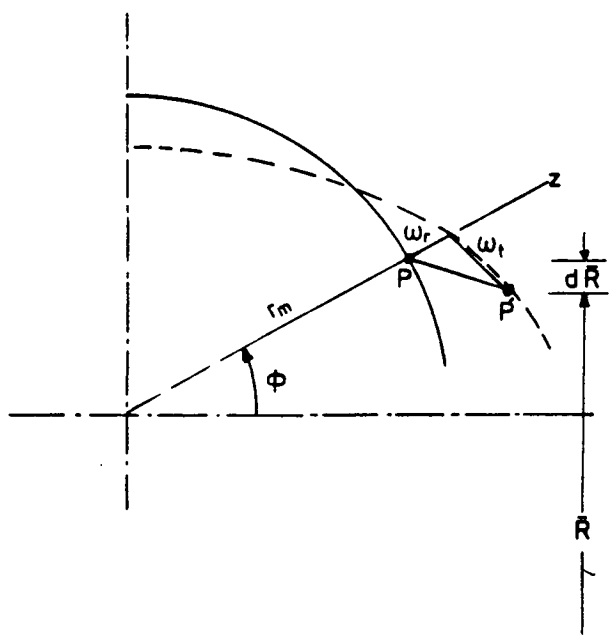


Fig(II 1a)



section C-C

Fig(II.1b)



Fig(II.1c)

Figure (II.1) Smooth bend under in plane bending

$$\begin{aligned}\epsilon_L'' &= \frac{r_m \sin \phi}{R} \cdot \frac{\Delta \psi_o}{\psi_o} \\ &= \frac{r_m \sin \phi}{R + r_m \sin \phi} \cdot \frac{\Delta \psi_o}{\psi_o}\end{aligned}\quad (\text{II.3b})$$

Total longitudinal strain ^(139,148)

$$\begin{aligned}\epsilon_L &= \epsilon_L' + \epsilon_L'' \\ &= \frac{1}{R + r_m \sin \phi} \left[\frac{\Delta \psi_o}{\psi_o} r_m \sin \phi + \omega_t \cos \phi + \omega_r \sin \phi \right]\end{aligned}\quad (\text{II.3c})$$

if it is assumed that $R > r_m$ ⁽¹³⁹⁾; then Eq. (II.3c) will be reduced to:

$$\epsilon_L = \frac{1}{R} \left[\frac{\Delta \psi_o}{\psi_o} r_m \sin \phi + \omega_t \cos \phi + \omega_r \sin \phi \right] \quad (\text{II.3d})$$

Assuming plane stress conditions ⁽¹³⁹⁾, the strain energy in the bend will be:

$$U_s = \frac{1}{2} \int_{\text{vol}} [\sigma_L \epsilon_L + \sigma_C \epsilon_C] d \text{Vol.} \quad (\text{II.4a})$$

using Hooke's law for isotropic homogeneous material;

$$\sigma_C = \frac{E}{(1-\nu^2)} [\epsilon_C + \nu \epsilon_L] \quad (\text{II.4b})$$

$$\sigma_L = \frac{E}{(1-\nu^2)} (\epsilon_C + \nu \epsilon_L) \quad (\text{II.4c})$$

then the bend total strain energy will be:

$$U_s = \int_{\text{Vol.}} \frac{E}{2(1-\nu^2)} [\epsilon_C^2 + \epsilon_L^2 + 2\nu \epsilon_L \epsilon_C] d. \text{Vol} \quad (\text{II.5a})$$

$$= U_1 + U_2 + U_3 \quad (\text{II.5b})$$

where

$$U_1 = \frac{E}{2(1-\nu^2)} \int_{-\frac{t}{2}}^{\frac{t}{2}} \int_0^{2\pi} \int_{-\frac{\psi_o}{2}}^{\frac{\psi_o}{2}} \epsilon_L^2 (Rd\psi) (rd\phi) dz \quad (\text{II.5c})$$

$$U_2 = \frac{E}{2(1-\nu^2)} \int_{-\frac{t}{2}}^{\frac{t}{2}} \int_0^{2\pi} \int_{-\frac{\psi_o}{2}}^{\frac{\psi_o}{2}} \epsilon_C^2 (Rd\psi) (rd\phi) dz \quad (\text{II.5d})$$

$$U_3 = 0 \quad (\text{II.5e})$$

Considering radial deformation symmetry about plane represented by $\phi = \pm 90$ (Fig. II.1a), von Karman approximated the tangential deformation, using a sinusoidal form, as^(139,148).

$$\omega_t = \sum_{n=1}^N C_n \sin 2\phi \quad (\text{II.6})$$

When internal pressure is considered⁽¹⁷⁹⁾, the additional work represented by the internal pressure p_i acting against the change in volume must be considered per unit length of the bend centre line, this is

$$U_p = P\Delta A \quad (\text{II.7a})$$

ΔA , the increase in area of the bend cross section is

$$\begin{aligned} \Delta A &= \frac{1}{2} \int_0^{2\pi} (r_m + \omega_r)^2 d\phi - \frac{1}{2} \int_0^{2\pi} r_m^2 d\phi \\ &= \frac{1}{2} \int_0^{2\pi} (2r_m \omega_r + \omega_r^2) d\phi \end{aligned} \quad (\text{II.7b})$$

Hence, the net energy stored in the bend will be:

$$U_T = U_s - U_p \quad (\text{II.8})$$

terms C_n of Eq. (II.6) are determined by the principle of least work, i.e. (139,179)

$$\frac{\partial (U_s - U_p)}{\partial C_n} = 0 \quad (\text{II.9})$$

by using one term C_1 in Eq. (II.6) and substituting back into Eq. (II.9), then

$$C_1 = - \left[\frac{3}{5 + 6\lambda^2 + 24\psi} \right] r_m \frac{\Delta\psi_0}{\psi_0} \quad (\text{II.10a})$$

and substituting for d_1 to be

$$d_1 = \frac{C_1}{r_m (\Delta\psi/\psi_0)} \quad (\text{II.10b})$$

where

$$\lambda = \frac{tR}{r_m^2}$$

and $\bar{\psi} = \frac{P_i R_2}{E r_m t}$

for zero internal pressure ($\bar{\psi} = 0$), and substituting c_1 into Eq. (II.8) the minimum energy stored in the bend will be (139)

$$(U_T)^*_{\min} = \frac{r_m^3 t E \pi R \psi_0}{2R^2 (1 - \nu^2)} \left(\frac{\Delta\psi_0}{\psi_0} \right)^2 \left[1 - \frac{9}{10+12\lambda^2} \right] \quad (\text{II.11})$$

The principle of virtual work gives bending moment M_i to be applied to produce $\Delta\psi_0$ as (148)

$$M_i = \frac{d(U_T)^*_{\min}}{d(\Delta\psi_0)} = \frac{\pi E r_m^3 t}{2R (1 - \nu^2)} \left(2 \frac{\Delta\psi_0}{\psi_0} \right) \left[1 - \frac{9}{10+12\lambda^2} \right]$$

$$= \frac{EI}{(1 - \nu^2)} \frac{\Delta\psi_0}{R\psi_0} \left[\frac{1+12\lambda^2}{10+12\lambda^2} \right] \quad (\text{II.12})$$

where $I = \pi r_m^3 t$.

If flattening is ignored, the result for simple bending, vis:

$$M_i = \frac{EI}{(1 - \nu^2)} \frac{\Delta\psi_0}{R\psi_0} \quad (\text{II.13})$$

If flattening is considered then,

$$\frac{\Delta\psi_0}{R\psi_0} = K_i \frac{M_i (1 - \nu^2)}{EI} \quad (\text{II.14a})$$

where

$$K_i = \frac{12 \lambda^2 + 10}{12 \lambda^2 + 1} \quad (\text{II.14b})$$

The longitudinal and the circumferential stress distribution will

be:

$$\left[\frac{\sigma_{L,i}}{M_i r_m / I} \right] = \frac{K}{1 - \nu^2} \left[\pm 3d_1 \nu \lambda \cos 2\phi + \left(1 + \frac{3d_1}{2} \right) \sin \phi - \frac{d_1}{2} \sin 3\phi \right] \quad (\text{II.15})$$

$$\left[\frac{\sigma_{C,i}}{M_i r_m / I} \right] = \frac{K}{1 - \nu^2} \left\{ \mp 3d_1 \lambda \cos 2\phi + \nu \left[\left(1 + \frac{3d_1}{2} \right) \sin \phi - \frac{d_1}{2} \sin 3\phi \right] \right\} \quad (\text{II.16})$$

Gross⁽¹⁵²⁾ experimental results obtained from in-plane testing of bends, showed that circumferential stresses measured on the inside surface were higher than those measured on the outside surface. He reasoned such deviation from von Karman theory to be caused by the presence of a circumferential membrane stress component assumed to be zero in the original theory⁽¹³⁶⁾. By superimposing such circumferential membrane stress on top of the circumferential flexural stresses predicted by Eq. (II.16), he found a better comparison between theoretical and experimental results. With reference to Fig. II.2, Gross modification of bend theory was achieved by assuming that the inward component of the mid-layer longitudinal stress (σ_L) must be balanced by a shear stress (τ) and a circumferential membrane stress (σ_{CC}) occurring in the bend wall. His end results for in-plane bending are as follows:

$$\tau \cos \phi + \sigma_{CC} \sin \phi = 0 \quad (\text{II.17})$$

and

$$\sigma_{CC} = - \frac{r_m}{R} \cos \phi \int_{\phi}^{\frac{\pi}{2}} \sigma_L d\phi \quad (\text{II.18})$$

where σ_L is the mid-plane stress predicted by Eq. (II.15).

Using one term in the trigonometric series, i.e. C_1 , in Eqs. (II.17) and (II.18), the circumferential membrane stress (σ_{CC}), and the shear stress (τ) are

$$\sigma_{CC} = - \frac{K_i M_i r_m^2}{IR} \cos \phi \left[\cos \phi \left(1 - \frac{9}{12 \lambda^2 + 10} \right) + \frac{\cos 3\phi}{12 \lambda^2 + 10} \right] \quad (\text{II.19})$$

and

$$\tau = - \frac{K_i M_i r_m^2}{IR} \sin \phi \left[\cos \phi \left(1 - \frac{9}{12 \lambda^2 + 10} \right) + \frac{\cos 3\phi}{12 \lambda^2 + 10} \right] \quad (\text{II.20})$$

For GRP bends, τ is defined as the interlaminar shear stress.

The total circumferential stresses occurring on the inside and the outside surface of the bend are obtained by direct addition of Eq. (II.19) to Eq. (II.16).

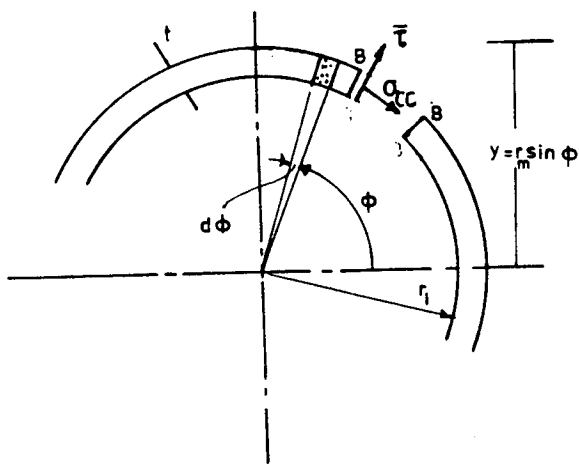
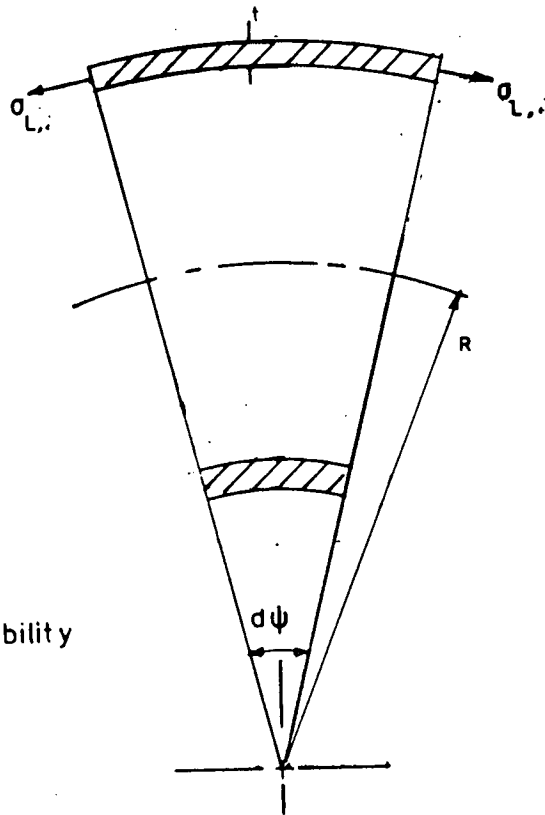


Figure (II.2)
Correction for extensibility



II.2 Out-of-plane bending analysis

Vigness^(143,144) used the same energy approach and predicted the bend flexibility factor and stresses under out-of-plane bending. In this case the tangential deformation ω_t is assumed to be

$$\omega_t = C_1 \cos 2 \phi \quad (\text{II.21})$$

and

$$d_1 = C_1/r \left(\frac{R}{\rho}\right)$$

where

ρ ⁽¹⁷⁹⁾ = radius of curvature, in a plane perpendicular to a plane containing bend radius, caused by an out-of-plane bending moment.

By using the same analysis in article II.1 and using one term in Eq. (II.21), the following results are given⁽¹⁴⁸⁾:

$$K_o = \frac{12 \lambda^2 + 10}{12 \lambda^2 + 1} = K_i$$

which is identical to the in-plane bending (Eq. I.14b), and the longitudinal and the circumferential stresses are⁽¹⁷⁹⁾:

$$\left[\frac{\sigma_L}{M_b r_m / I} \right] = \frac{K_o}{1 - \nu^2} \left[\pm 3 \nu \lambda d_1 \sin 2\phi + \left(1 + \frac{3d_1}{2}\right) \cos \phi - \frac{d_1}{2} \cos 3\phi \right] \quad (\text{II.22})$$

$$\left[\frac{\sigma_C}{M_b r_m / I} \right] = \frac{K_o}{1 - \nu^2} \left\{ \pm 3 \lambda d_1 \sin 2\phi + \nu \left[\left(1 + \frac{3d_1}{2}\right) \cos \phi - \frac{d_1}{2} \cos 3\phi \right] \right\} \quad (\text{II.23})$$

The membrane circumferential stress and the shear stress are similarly derived to that of Eqs. (II.17) and (II.18)⁽¹⁵⁴⁾. The total circumferential stresses at the inside and the outside surfaces of the bend are similarly obtained.

II.3 Generalized Solution (179,154,155)

Rodabaugh et al⁽¹⁷⁹⁾, generalized the von Karman theory, except for Gross modification, for both in-plane and out-of-plane bending. Dodge and Moore⁽¹⁵⁴⁾ later generalized Gross modification of theory for both in-plane and out-of-plane theory. Their results, including the effect of internal pressure combined with external loading, are given below.

Minimizing the total energy (U_T), a set of n equations for $n+1$ unknown values of c_n are obtained, i.e.:

$$\begin{aligned} \frac{\partial U_T}{\partial C_1} &= 0 = 3 r_m \eta + (5 + 6 \lambda_1^2 + 24 \bar{\psi}) C_1 - \frac{5}{2} C_2 \\ \frac{\partial U_T}{\partial C_2} &= 0 = -\frac{5}{2} C_1 + (17 + 600 \lambda_1^2 + 480 \bar{\psi}) C_2 - \frac{21}{2} C_3 \\ \frac{\partial U_T}{\partial C_n} &= 0 = C_{n-1} \frac{(2n-3)(2n+1)}{2} \\ &\quad + C_n \left\{ (4n^2+1) + (8n^3-2n)^2 \frac{\lambda_1^2}{6} \right. \\ &\quad \left. + [8n^2 (4n^2-1)] \bar{\psi} \right\} - C_{n+1} \frac{(2n-1)(2n+3)}{2} \end{aligned} \quad (\text{II.24})$$

where

$$\lambda_1 = \frac{\lambda}{\sqrt{1-\nu^2}} = \frac{tR/r_m^2}{\sqrt{1-\nu^2}}$$

with $C_{n+1} = 0$, the values of C_1, C_2, \dots, C_n are the solution to the set of equations, and η is the change of angle of the bend, $\eta = \Delta\psi_o/\psi_o$ (in-plane), $\eta = R/\rho$ (out-of-plane), and

$$d_n = C_n/rn$$

The flexibility factor is obtained from Eq. (II.14b) for in-plane and out-of-plane bending, where

$$K_o = \frac{1}{\left(1 + \frac{3}{2} d_1\right)} = K_i$$

The corresponding longitudinal and circumferential stresses of the bend are:

(i) In-plane bending

$$\left[\frac{\sigma_{L,i}}{M_i r_m / I} \right] = \frac{K}{(1 - \nu^2)} \left\{ \left(1 + \frac{3d_1}{2}\right) \sin \phi + \frac{1}{2} \sum_{n=1}^N d_n (1-2n) \right. \\ \left. + d_{n+1} (2n+3) \right\} \sin (2n+1) \phi \quad (II.25) \\ \pm \frac{\nu \lambda_1}{2} \sum_{n=1}^N d_n (2n-8n^3) \cos 2n \phi \}$$

$$\left[\frac{\sigma_{C,i}}{M_i r_m / I} \right] = \frac{K}{(1 - \nu^2)} \left\{ \pm \frac{\lambda_1}{2} \sum_{n=1}^N d_n (2n-8n^3) \cos 2n \phi \right. \\ \left. + \nu \left(1 + \frac{3d_1}{2}\right) \sin \phi \right. \\ \left. + \frac{\nu}{2} \left[\sum_{n=1}^N d_n (1-2n) \right. \right. \\ \left. \left. + d_{n+1} (2n+3) \right] \sin (2n+1) \phi \right\} \quad (II.26)$$

and the in-plane membrane circumferential stress to be

$$\frac{\sigma_{CC,i}}{M_i r_m / I} = \frac{K}{(1 - \nu^2)} \left\{ -\frac{r_m}{R} [D \cos \phi + \frac{1}{2} \sum_{n=1}^N \frac{A_n}{(2n+1)} \cos (2n+1) \phi] \right. \\ \left. \cos \phi \right\} \quad (II.27)$$

(ii) Out-of-plane bending

$$\left[\frac{\sigma_{L,o}}{M_o r_m / I} \right] = \frac{K}{(1 - \nu^2)} \left\{ \left(1 + \frac{3d_1}{2}\right) \cos \phi + \frac{1}{2} \sum_{n=1}^N [d_n (1-2n) \right. \\ \left. + d_{n+1} (2n+3)] \cos (2n+1) \phi \right. \\ \left. \pm \frac{\nu \lambda_1}{2} \sum_{n=1}^N d_n (8n^3-2n) \sin 2 \phi \right\} \quad (II.28)$$

$$\left[\frac{\sigma_{C,o}}{M_o r_m / I} \right] = \frac{K}{(1 - \nu^2)} \left\{ \left(\pm \frac{\lambda_1}{2} \sum_{n=1}^N d_n (8n^3-2n) \sin 2n \phi \right. \right. \\ \left. \left. + \nu \left(1 + \frac{3d_1}{2}\right) \cos \phi \right. \right. \\ \left. \left. + \frac{\nu}{2} \sum_{n=1}^{\infty} [d_n (1-2n) + d_{n+1} (2n+3)] \cos (2n+1) \phi \right\} \quad (II.29)$$

and the out-of-plane membrane circumferential stress to be

$$\left[\frac{\sigma_{CC,o}}{M_o r_m / I} \right] = \frac{K}{(1 - \nu^2)} \left\{ \frac{r_m}{R} [D \sin \phi + \frac{1}{2} \sum_{n=1}^N \frac{A_n}{(2n+1)} \sin (2n+1) \phi] \right. \\ \left. \sin \phi \right\} \quad (II.30)$$

where

$$D = 1 + \frac{3}{2} d_1$$

$$A_n = (1-2n) d_n + (2n+3) d_{n+1}$$

$$B_n = (2n-8n^3) d_n$$

The generalized analysis presented in this Appendix has been represented as a computer programme written in BASIC and titled as 'Flexibility and Stress Intensification Factors of Smooth Isotropic Bends', using $N=4$. The listing of the programme is given below:

II.4 Computer programme

```

10 TEXT : HOME
15 PRINT "FLEXIBILITY & STRESS INTENSIFICATION FACTORS OF SMOOTH-ISOTROPIC
   C BENDS"
20 PRINT "=====
   ===== ": PRINT : PRINT
30 PRINT " AUTHOR : MAAN A.K. KANONA ": PRINT : PRINT
40 PRINT "*****
   ***** ": PRINT : PRINT
50 DEF FN A1(A2) = INT (A2 * 100 + .5) / INT (100 + .5)
100 REM *****
105 REM INPUT DATA
110 PRINT "GIVE ME INTERNAL RADIUS = ? ": INPUT RI
120 PRINT
130 PRINT "GIVE ME BEND RADIUS = ? ": INPUT BR
140 PRINT
150 PRINT "GIVE ME THICKNESS = ? ": INPUT T
160 PRINT
170 PRINT "GIVE ME POISSONS RATIO = ? ": INPUT NU
180 PRINT
190 PRINT "GIVE ME YOUNG MODULUS = ? ": INPUT MOD
200 PRINT
210 PRINT "GIVE ME INTERNAL PRESSURE = ? ": INPUT INP
220 PI = 3.141592654
230 RH = RI + T / 2
240 H = T * BR / RH / RH
250 LA = H / SQR (1 - NU * NU)
260 PHI = INP * BR * BR / MOD / RH / T
270 PRINT
280 PRINT
310 PRINT "=====
   ====="
320 N0 = 4
330 REM *****
   *****
335 REM SERIES IS OF 4 TERMS
340 A = 5 + 6 * LA ^ 2 + 24 * PHI
350 B = 17 + 600 * LA ^ 2 + 480 * PHI
360 C = 37 + 7350 * LA ^ 2 + 2520 * PHI
370 D = 65 + 42336 * LA ^ 2 + 8064 * PHI
380 E = 5 / 2
390 F = 21 / 2
400 G = 45 / 2
410 K = F / (C - (G ^ 2) / D)
420 H = E / (B - F * K)
430 C(1) = (- 1) * 3 / (A - E * H)
440 C(2) = H * C(1)
450 C(3) = K * C(2)
460 C(4) = C(3) * G / D
470 D1 = C(1)
480 D0 = 1 + 3 * D1 / 2
490 KK = 1 / D0
500 FF = KK / (1 - NU ^ 2)
510 REM *****
550 PRINT "PHI = ";PHI: PRINT : PRINT "LAMBDA = ";LA: PRINT : PRINT "H =
   ";H: PRINT
560 PRINT "FLEXIBILITY FACTOR = ";KK: PRINT : PRINT "=====
   ====="

```

```

1445 REM *****
1610 PRINT " GIVE ME INITIAL , FINAL & STEP OF ANGLE = ?.??.? ": INPUT T1,
T2,T3
1620 PRINT "=====
=====
1630 REM STRESS CALCULATIONS
1635 PRINT : PRINT : PRINT
1640 PRINT "IN-PLANE STRESS INTENFIFICATIO FACTOR": PRINT "=====
=====
1650 PRINT
1660 R = ((T2 - T1) / T3) + 1
1670 DIM S(R,5),X(R,5)
1680 PRINT "BETA A(OUT) A(IN) H(OUT) H(IN)"
1690 H = 0
1700 FOR BETA = T1 TO T2 STEP T3
1710 TH = BETA * PI / 180
1720 H = H + 1
1730 S1 = DD * SIN (TH)
1740 GOSUB 2450
1750 S1 = S1 + AS / 2
1760 BC = 0
1770 FOR I = 1 TO N0
1780 BC = BC + (2 * I - 8 * (I ^ 3)) * C(I) * ( COS (2 * I * TH))
1790 NEXT I
1800 S1 = (S1 + BC * NU * LA / 2) * FF
1810 S1 = FN A1(S1)
1820 S2 = (S1 - BC * NU * LA / 2) * FF
1830 S2 = FN A1(S2)
1840 PRINT
1850 S5 = DD * COS (TH)
1860 GOSUB 2550
1870 S5 = S5 + CA / 2
1880 S5 = S5 * COS (TH)
1890 S5 = S5 * (- 1) * PH / BR
1900 S5 = S5 * FF
1910 REM
1920 SJ = NU * DD * SIN (TH)
1930 SJ = SJ + NU * AS / 2
1940 S3 = FF * (SJ + BC * LA / 2) + S5
1950 S3 = FN A1(S3)
1960 S4 = FF * (SJ - BC * LA / 2) + S5
1970 S4 = FN A1(S4)
1980 PRINT
1990 PRINT BETA " ;S1 " ;S2" ;S3" ;S4
2000 S(H,1) = BETA:S(H,2) = S1:S(H,3) = S2:S(H,4) = S3:S(H,5) = S4
2010 NEXT BETA
2020 PRINT : PRINT : PRINT : PRINT
2030 PRINT "OUT OF PLANE SIF ": PRINT "=====
=====": PRINT
2040 H = 0
2050 PRINT "BETA A(OUT) A(IN) H(OUT) H(IN)"
2060 PRINT
2070 FOR BETA = T1 TO T2 STEP T3
2080 H = H + 1
2090 TH = BETA * PI / 180
2100 XI = DD * COS (TH)
2110 GOSUB 2550
2120 XI = XI + AC / 2

```

```

2180 BS = 0
2190 FOR I = 1 TO N0
2200 BS = BS + (2 * I - 8 * (I ^ 3)) * C(I) * ( SIN (2 * I * TH))
2210 NEXT I
2220 X1 = FF * (XI + NU * LA * (- 1) * BS / 2)
2230 X1 = FN A1(X1)
2240 X2 = FF * (XI - NU * LA * (- 1) * BS / 2)
2250 X2 = FN A1(X2)
2260 PRINT
2270 REM
2280 X6 = DD * SIN (TH)
2290 GOSUB 2450
2300 X6 = X6 + SA / 2
2310 X6 = X6 * SIN (TH)
2320 X6 = X6 * FF * RH / BR
2330 XJ = NU * DD * COS (TH)
2340 XJ = XJ + NU * AC / 2
2350 X3 = FF * (XJ + LA * (- 1) * BS / 2) + X6
2360 X3 = FN A1(X3)
2370 X4 = FF * (XJ - LA * (- 1) * BS / 2) + X6
2380 X4 = FN A1(X4)
2390 X(M,1) = BETA:X(M,2) = X1:X(M,3) = X2:X(M,4) = X3:X(M,5) = X4
2400 PRINT
2410 PRINT BETA" ";X1" ";X2" ";X4" ";X3
2420 NEXT BETA
2430 PRINT
2440 END
2445 REM ***** SUB-ROUTINES *****
2450 AS = 0
2460 FOR I = 1 TO N0
2470 IF I = N0 THEN GOTO 2510
2480 AS = AS + ((1 - 2 * I) * C(I) + (2 * I + 3) * C(I + 1)) * ( SIN ((2 *
I + 1) * TH))
2490 SA = AS / (2 * I + 1)
2500 GOTO 2530
2510 AS = AS + ((1 - 2 * I) * C(I)) * ( SIN ((2 * I + 1) * TH))
2520 SA = AS / (2 * I + 1)
2530 NEXT I
2540 RETURN
2550 AC = 0
2560 FOR I = 1 TO N0
2570 IF I = N0 THEN GOTO 2610
2580 AC = AC + ((1 - 2 * I) * C(I) + (2 * I + 3) * C(I + 1)) * ( COS ((2 *
I + 1) * TH))
2590 CA = AC / (2 * I + 1)
2600 GOTO 2630
2610 AC = AC + ((1 - 2 * I) * C(I)) * ( COS ((2 * I + 1) * TH))
2620 CA = AC / (2 * I + 1)
2630 NEXT I
2640 RETURN

```

APPENDIX III

THEORY OF ORTHOTROPIC SMOOTH BEND

THEORY OF ORTHOTROPIC SMOOTH BEND

III.1 Theoretical Derivation

In the present programme, smooth GRP bends constructed from laminates having circumferential to longitudinal modulus ratio of 2 have been investigated under in-plane bending and under out-of-plane bending. The analysis for the isotropic bend theory presented in App. II was modified including such difference of circumferential and longitudinal moduli. Using the same strain energy method of analysis, the flexibility and stress distribution are predicted. This is achieved by replacing Eqs. (II.4b,c) of App. II by Eqs. (III.1a,b) for representing the stress/strain relation for orthotropic type of laminate, as

$$\sigma_C = \frac{E_C}{1 - \nu_{LC}\nu_{CL}} [\epsilon_C + \nu_{LC}\epsilon_L] \quad (III.1a)$$

$$\sigma_L = \frac{E_L}{1 - \nu_{LC}\nu_{CL}} [\epsilon_L + \nu_{CL}\epsilon_C] \quad (III.1b)$$

and from symmetry requirements of the compliance matrix, then:

$$\frac{\nu_{CL}}{E_C} = \frac{\nu_{LC}}{E_L} \quad (III.2)$$

$$\text{and } \bar{m} = \frac{E_C}{E_L} = \frac{\nu_{CL}}{\nu_{LC}}$$

The bend strain energy is obtained by substituting Eq. (III.1) into Eq. (III.3):

$$U_s = \frac{1}{2} \left[\int_{Vol} \sigma_L \epsilon_L d(Vol) + \int_{Vol} \sigma_C \epsilon_C d(Vol) \right] \quad (III.3a)$$

hence

$$U_s = \frac{E_L}{2(1 - \nu_{LC}\nu_{CL})} \int_{Vol} \epsilon_L^2 d(Vol) + \frac{E_C}{2(1 - \nu_{LC}\nu_{CL})} \int_{Vol} \epsilon_C^2 d(Vol) \quad (III.3b)$$

$$+ \frac{1}{2(1 - \nu_{LC}\nu_{CL})} \int_{Vol} \epsilon_L \epsilon_C (\epsilon_L \nu_{CL} + E_C \nu_{LC}) d(Vol) \quad (III.3c)$$

$$= U_1 + U_2 + U_3$$

Using similar mathematical expressions assumed for the tangential component of deformation, for the longitudinal and for the circumferential strains as in App. II, and carrying out similar procedure of solution, the following theoretical results are obtained using one term, i.e. $N=1$,

$$C_1 = - \left[\frac{3}{5+6\bar{m}\lambda^2 + 24\bar{\psi}} \right] r \frac{\Delta\psi_0}{\psi_0} \quad (\text{III.4})$$

For $\bar{\psi} = 0$, the flexibility and stress distribution are as follows:

Flexibility factor

$$K_m = \frac{10 + 12\bar{m}\lambda^2}{1 + 12\bar{m}\lambda^2} \quad (\text{III.5})$$

and stresses:

-in-plane bending stresses:

$$\left[\frac{\sigma_{L,i}}{M_i r_m / I} \right] = \frac{K_m}{1 - \nu_{LC} \nu_{CL}} \left\{ \pm 3d_1 \lambda \nu_{CL} \cos 2\phi + \left(1 + \frac{3d_1}{2}\right) \sin \phi - \frac{d_1}{2} \sin 3\phi \right\} \quad (\text{III.6})$$

$$\left[\frac{\sigma_{C,i}}{M_i r_m / I} \right] = \frac{\bar{m} K_m}{1 - \nu_{LC} \nu_{CL}} \left\{ \pm 3d_1 \cos 2\phi + \nu_{LC} \left[\left(1 + \frac{3d_1}{2}\right) \sin \phi - \frac{d_1}{2} \sin 3\phi \right] \right\} \quad (\text{III.7})$$

- out-of-plane stresses

$$\left[\frac{\sigma_{L,o}}{M_o r_m / I} \right] = \frac{K_m}{1 - \nu_{LC} \nu_{CL}} \left[\pm 3 \nu_{LC} \lambda \sin 2\phi + \left(1 + \frac{3d_1}{2}\right) \cos \phi - \frac{d_1}{2} \cos 3\phi \right] \quad (\text{III.8})$$

$$\left[\frac{\sigma_{C,o}}{M_i r_m / I} \right] = \frac{\bar{m} K_m}{1 - \nu_{LC} \nu_{CL}} \left[\pm 3\lambda \sin 2\phi + \nu_{LC} \left(1 + \frac{3d_1}{2}\right) \cos \phi \right] \quad (\text{III.9})$$

III.2 Generalized Solution

To solve for C_n , then

$$\frac{\partial U_T}{\partial C_1} = 3r\eta + (5 + 6\lambda_{\bar{m}}^2 + 24\bar{\psi}) C_1 - \frac{5}{2} C_2$$

$$\frac{\partial U_T}{\partial C_n} = -C_{n-1} \frac{(2n-3)(2n+1)}{2} +$$

$$\begin{aligned}
& + C_n \{ (4n^2+1) + (8n^3-2n)^2 \frac{\lambda}{6} \\
& + [8n^2 (4n^2-1) \psi] \quad \text{(III.10)} \\
& - C_{n+1} \frac{(2n-1)(2n+3)}{2}
\end{aligned}$$

where $\lambda_{\bar{m}} = \sqrt{\bar{m}}$. $\lambda_1 = \left[\frac{\bar{m}}{1-v^2} \right]^{\frac{1}{2}} \lambda$

flexibility factor

$$K_{\bar{m}} = \frac{1}{1 + \frac{3}{2} d_1} \quad \text{(III.11)}$$

where $d_1 = C_1/rn$

and for the stresses

in-plane stresses

$$\begin{aligned}
\left[\frac{\sigma_{L,i}}{M_i r_m / I} \right] = & F \left[D \sin \phi + \frac{1}{2} \sum_{n=1}^N A_n \sin (2n+1) \phi \right. \\
& \left. \pm \frac{v_{CL} \lambda_1}{2} \sum_{n=1}^N B_n \cos 2n \phi \right] \quad \text{(III.12)}
\end{aligned}$$

$$\begin{aligned}
\left[\frac{\sigma_{C,i}}{M_i r_m / I} \right] = & F \left[v_{LC} D \sin \phi + \frac{v_{LC}}{2} \sum_{n=1}^N A_n \sin (2n+1) \phi \right. \\
& \left. \pm \frac{\lambda_1}{2} \sum_{n=1}^N B_n \cos 2n \phi \right] \quad \text{(III.13)}
\end{aligned}$$

$$\begin{aligned}
\left[\frac{\sigma_{CC,i}}{M_i r_m / I} \right] = & F \left\{ -\frac{r_m}{R} \left[D \cos \phi + \frac{1}{2} \sum_{n=1}^N \frac{A_n}{(2n+1)} \cos (2n+1) \phi \right] \cos \phi \right\} \\
& \text{(III.14)}
\end{aligned}$$

out-of-plane stresses

$$\begin{aligned}
\left[\frac{\sigma_{L,o}}{M_o r_m / I} \right] = & F \left[D \cos \phi + \frac{1}{2} \sum_{n=1}^N A_n \cos (2n+1) \phi \right. \\
& \left. \pm \frac{v_{CL} \lambda_1}{2} \sum_{n=1}^N (-1) B_n \sin 2n \phi \right] \quad \text{(III.15)}
\end{aligned}$$

$$\begin{aligned}
\left[\frac{\sigma_{C,o}}{M_o r_m / I} \right] = & F \left[v_{LC} D \cos \phi + \frac{v_{LC}}{2} \sum_{n=1}^N A_n \cos (2n+1) \phi \right. \\
& \left. \pm \frac{\lambda_1}{2} \sum_{n=1}^N (-1) B_n \sin 2n \phi \right] \quad \text{(III.16)}
\end{aligned}$$

$$\left[\frac{\sigma_{CC,0}}{M_i r_m / I} \right] = F \left\{ -\frac{r}{R} [D \sin \phi + \frac{1}{2} \sum_{n=1}^N \frac{A_n}{(2n+1)} \sin (2n+1) \phi] \sin \phi \right\} \quad (\text{III.17})$$

where

$$F = K_{\bar{m}} / (1 - \nu_{LC} \nu_{CL})$$

$$D = 1 + (3/2) d_1$$

$$A_n = (1-2n) d_n + (2n+3) d_{n+1}$$

$$B = (2n - 8n^3) d_n$$

The generalized solution presented in this Appendix has been represented as a computer programme written in BASIC and titled as 'Flexibility and Stress Intensification Factors of Smooth - Orthotropic Bends', using N=4. The listing of the programme is given below:

III.3 Computer programme

```

10 TEXT : HOME
15 PRINT "FLEXIBILITY & STRESS INTENSIFICATION FACTORS OF SMOOTH-ORTHOTRO
PIC BENDS "
20 PRINT "=====
===== "
30 PRINT " AUTHOR MAAN A. K. KANONA ": PRINT : PRINT
40 PRINT "*****
***** ": PRINT : PRINT
50 DEF FN A1(A2) = INT (A2 * 100 + .5) / INT (100 + .5)
100 REM *****
105 REM INPUT DATA
110 PRINT "GIVE ME INTERNAL RADIUS = ?": INPUT RI
120 PRINT
130 PRINT "GIVE ME BEND RADIUS = ? ": INPUT BR
140 PRINT
150 PRINT "GIVE ME THICKNESS = ? ": INPUT T
160 PRINT
170 PRINT "GIVE ME POISSONS RATIOS NL & NC = ? ": INPUT NL,NC
180 PRINT
190 PRINT "GIVE ME YOUNG MODULI EC & EL = ?,? ": INPUT EC,EL
195 REM EC = CIRCUM. MODULUS EL = LONG. MODULUS :REM EC/EL=NC/NL
200 PRINT
210 PRINT "GIVE ME INTERNAL PRESSURE = ? ": INPUT INP
220 PI = 3.141592654
230 RM = RI + T / 2
240 H = T * BR / RM / RM
250 LA = ( SQR (NC / NL)) * H / SQR (1 - NL * NC)
255 AL = LA / SQR (NC / NL)
257 PRINT " BEND PARAMETER = ",AL
260 PHI = INP * BR * BR / EC / RM / T
270 PRINT
280 PRINT
310 PRINT "=====
===== "
320 N0 = 4
330 REM *****
*****
335 REM SERIES IS OF 4 TERMS
340 A = 5 + 6 * LA ^ 2 + 24 * PHI
350 B = 17 + 600 * LA ^ 2 + 480 * PHI
360 C = 37 + 7350 * LA ^ 2 + 2520 * PHI
370 D = 65 + 42336 * LA ^ 2 + 8064 * PHI
380 E = 5 / 2
390 F = 21 / 2
400 G = 45 / 2
410 K = F / (C - (G ^ 2) / D)
420 H = E / (B - F * K)
430 C(1) = (- 1) * 3 / (A - E * H)
440 C(2) = H * C(1)
450 C(3) = K * C(2)
460 C(4) = C(3) * G / D
470 D1 = C(1)
480 D0 = 1 + 3 * D1 / 2
490 KK = 1 / D0
500 FF = KK / (1 - NL * NC)
510 REM ***
*****
550 PRINT "PHI = ";PHI: PRINT : PRINT "LA=SOR = ";AL: PRINT : PRINT "H =
";H: PRINT
550 PRINT "FLEXIBILITY FACTOR = "JK: PRINT : PRINT "=====
===== "

```

```

1445 REM *****
1610 PRINT " GIVE ME INITIAL , FINAL & STEP OF ANGLE = ?,?,? ": INPUT T1,
T2,T3
1620 PRINT "=====
=====
1630 REM STRESS CALCULATIONS
1635 PRINT : PRINT : PRINT
1640 PRINT "IN-PLANE STRESS INTENFIFICATIO FACTOR": PRINT "=====
=====
1650 PRINT
1660 R = ((T2 - T1) / T3) + 1
1670 DIM S(R,5),X(R,5)
1680 PRINT "BETA A(OUT) A(IN) H(OUT) H(IN)"
1690 H = 0
1700 FOR BETA = T1 TO T2 STEP T3
1710 TH = BETA * PI / 180
1720 H = H + 1
1730 S1 = D0 * SIN (TH)
1730 GOSUB 2450
1800 S1 = S1 + AS / 2
1810 BC = 0
1820 FOR I = 1 TO NB
1830 BC = BC + (2 * I - 1 * (I ^ 3)) * C(I) * ( COS (2 * I * TH))
1840 NEXT I
1850 S1 = (S1 + BC * NC * AL / 2) * FF
1860 S1 = FN A1(S1)
1870 S2 = (S1 - SC * NC * AL / 2) * FF
1880 S2 = FN A1(S2)
1890 PRINT
1900 S5 = D0 * COS (TH)
1910 GOSUB 2550
1920 S5 = S5 + CA / 2
1930 S5 = S5 * COS (TH)
1940 S5 = S5 * (- 1) * RM / BR
1950 S5 = S5 * FF
1960 REM
1970 SJ = NL * D0 * SIN (TH)
1980 SJ = SJ + NL * AS / 2
1990 S3 = (NC / NL) * FF * (SJ + BC * AL / 2) + S5
2000 S3 = FN A1(S3)
2010 S4 = (NC / NL) * FF * (SJ - BC * AL / 2) + S5
2020 S4 = FN A1(S4)
2030 PRINT
2040 PRINT BETA " ;S1" " ;S2" " ;S3" " ;S4
2050 S(H,1) = BETA:S(H,2) = S1:S(H,3) = S2:S(H,4) = S3:S(H,5) = S4
2060 NEXT BETA
2070 PRINT : PRINT : PRINT : PRINT
2080 PRINT "OUT OF PLANE SIF ": PRINT "=====
=====": PRINT
2090 H = 0
2100 PRINT "BETA A(OUT) A(IN) H(OUT) H(IN)"
2110 PRINT
2120 FOR BETA = T1 TO T2 STEP T3
2130 H = H + 1
2140 TH = BETA * PI / 180
2150 X1 = D0 + COS (TH)
2160 GOSUB 2550
2170 X1 = X1 + AC / 2
2180 BS = 0

```

```

2190 FOR I = 1 TO N0
2200 BS = BS + (2 * I - 8 * (I ^ 3)) * C(I) * ( SIN (2 * I * TH))
2210 NEXT I
2220 X1 = FF * (X1 + NC * AL * (- 1) * BS / 2)
2230 X1 = FN A1(X1)
2240 X2 = FF * (X1 - NC * AL * (- 1) * BS / 2)
2250 X2 = FN A1(X2)
2260 PRINT
2270 REM
2280 X6 = DD * SIN (TH)
2290 GOSUB 2450
2300 X6 = X6 + SA / 2
2310 X6 = X6 * SIN (TH)
2320 X6 = X6 * FF * RH / BR
2330 XJ = NL * DD * COS (TH)
2340 XJ = XJ + NL * AC / 2
2350 X3 = (NC / NL) * FF * (XJ + AL * (- 1) * BS / 2) + X6
2360 X3 = FN A1(X3)
2370 X4 = (NC / NL) * FF * (XJ - AL * (- 1) * BS / 2) + X6
2380 X4 = FN A1(X4)
2390 X(H,1) = BETA:X(H,2) = X1:X(H,3) = X2:X(H,4) = X3:X(H,5) = X4
2400 PRINT
2410 PRINT BETA"      ";X1"      ";X2"      ";X4"      ";X3
2420 NEXT BETA
2430 PRINT
2440 END
2445 REM ***** SUB-ROUTINES*****
2450 AS = 0
2460 FOR I = 1 TO N0
2470 IF I = N0 THEN GOTO 2510
2480 AS = AS + ((1 - 2 * I) * C(I) + (2 * I + 3) * C(I + 1)) * ( SIN ((2 *
I + 1) * TH))
2490 SA = AS / (2 * I + 1)
2500 GOTO 2530
2510 AS = AS + ((1 - 2 * I) * C(I)) * ( SIN ((2 * I + 1) * TH))
2520 SA = AS / (2 * I + 1)
2530 NEXT I
2540 RETURN
2550 AC = 0
2560 FOR I = 1 TO N0
2570 IF I = N0 THEN GOTO 2610
2580 AC = AC + ((1 - 2 * I) * C(I) + (2 * I + 3) * C(I + 1)) * ( COS ((2 *
I + 1) * TH))
2590 CA = AC / (2 * I + 1)
2600 GOTO 2630
2610 AC = AC + ((1 - 2 * I) * C(I)) * ( COS ((2 * I + 1) * TH))
2620 CA = AC / (2 * I + 1)
2630 NEXT I
2640 RETURN

```

APPENDIX IV

PREDICTION OF STRAINS AND STRESSES

IN

THIN WALL STRAIGHT PIPES

AND

BENDS LOADED BY INTERNAL PRESSURE

APPENDIX IV

PREDICTION OF STRAINS AND STRESSES IN THIN WALL STRAIGHT PIPES AND BENDS LOADED BY INTERNAL PRESSURE

IV.1 Straight Pipes

For a straight pipe of closed-ended conditions loaded by internal pressure p_i , the stresses predicted in the wall of the pipe assuming thin shell of isotropic homogeneous material, are:

- stresses

$$\sigma_C = \frac{p_i r_m}{t} \quad (IV.1a)$$

$$\sigma_L = \frac{p_i r_m}{2t} \quad (IV.1b)$$

- strains

$$\epsilon_C = \frac{1}{E} [\sigma_C - \nu \sigma_L] \quad (IV.2a)$$

$$\epsilon_L = \frac{1}{E} [\sigma_L - \nu \sigma_C] \quad (IV.2b)$$

- for orthotropic thin pipe walls

$$\epsilon_C = \frac{1}{E_C} [\sigma_C - \nu_{CL} \sigma_L] \quad (IV.3a)$$

$$\epsilon_L = \frac{1}{E_L} [\sigma_L - \nu_{LC} \sigma_C] \quad (IV.3b)$$

IV.2 Smooth Bends

The stresses induced in a pressurized smooth tangent/bend structure are assumed to be similar⁽¹⁵¹⁾ to those predicted using thin torus shell analysis. The circumferential and the longitudinal stresses for a torus thin shell under internal pressure loading; with the aid of Fig. IV.1a, are:

$$\sigma_C = \frac{p_i r_m}{t} \left[\frac{R + (R - r_m \cos \theta)}{R - r_m \cos \theta} \right] \quad (IV.4a)$$

$$\sigma_L = \frac{p_i r_m}{2t} \quad (IV.4b)$$

and the strains are similarly predicted using Eq. (IV.2).

IV.3 Mitre Bends

For a mitred bend/tangent structure loaded by internal pressure, the stresses induced at the mitred joint (segment-edge) are predicted similarly using the analysis of a single mitred bend developed by Owen and Emmerson⁽¹⁶⁷⁾. With reference to Fig. IV.1b the membrane stresses superimposed on the flexural stress, i.e. total stress are predicted using Eqs. (IV.5a,b) as follows:

$$\sigma_L = \sigma_\xi \left[\begin{array}{l} \text{outside} \\ \text{inside} \end{array} \right] = \frac{p_i r_m}{2t} \left[1 \pm \frac{t}{r_m} \frac{k_2}{1 - \nu^2} \cos \theta \tan \alpha \right] \quad (\text{IV.5a})$$

$$\sigma_C = \sigma_\theta \left[\begin{array}{l} \text{outside} \\ \text{inside} \end{array} \right] = \frac{p_i r_m}{t} \left[1 + \frac{k_2 \cos \theta \tan \alpha}{2} \pm \frac{\nu}{2} \frac{t}{r_m} \frac{k_2}{1 - \nu^2} \cos \theta \right] \tan \alpha \quad (\text{IV.5b})$$

where $k_2 = \left[\frac{3r_m^2}{t^2} (1 - \nu^2) \right]^{1/4}$

The strains are predicted using Eq. (IV.2).

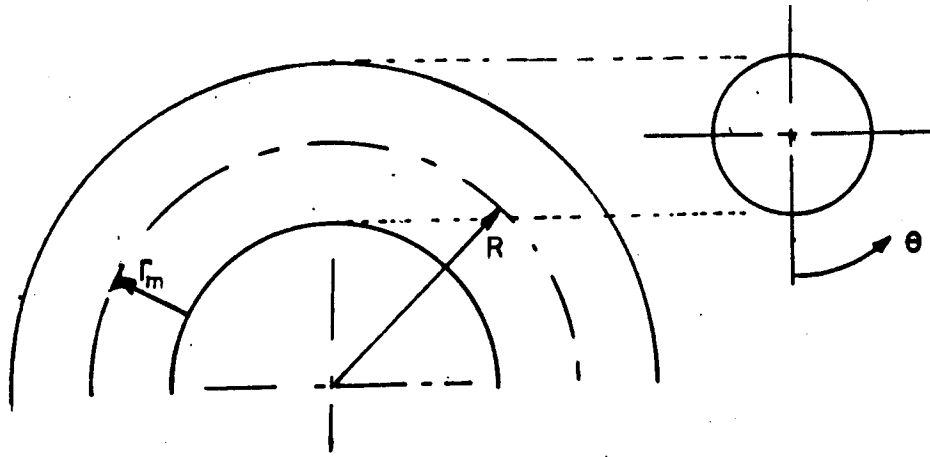


Figure (IV.1a) Torus shell

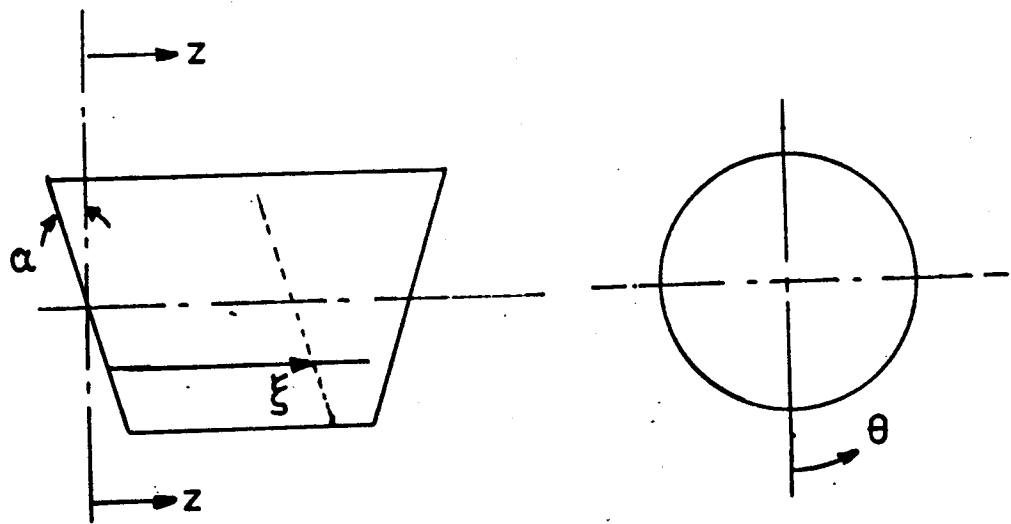


Figure (IV.1b) Axes of mitre joint

APPENDIX V

THEORETICAL DETERMINATION

OF THE

ELASTIC CONSTANTS OF A LAMINATE

APPENDIX V

THEORETICAL DETERMINATION OF THE ELASTIC CONSTANTS OF A LAMINATE

V.1 Elastic Constants Properties of Unidirectional Laminate (Fig. V.1)

(31)
 Micromechanical method reported by Tsia incorporate two factors in the analysis, these are:

- k : fibre misalignment factor; ≤ 1
- \bar{C} : continuity factor, varying from 0 to 1

The formulae used to predict the elastic constants are as follows:

V.1.1 Longitudinal modulus (in the fibre direction)

$$E_l = k [E_g V_g + (1 - V_g) E_r] \quad (V.1)$$

V.1.2 Transverse modulus (perpendicular to the fibre direction)

$$E_t = 2 [1 - v_r - V_g (v_g - v_r)] \left[(1 - \bar{C}) \frac{K_g (2K_r + G_r) - G_r (K_g - K_r) (1 - V_g)}{(2K_r + G_r) + 2 (K_g - K_r) (1 - V_g)} + \bar{C} \frac{K_f (2K_r + G_g) + G_g (K_r - K_g) (1 - V_g)}{(2K_r + G_g) - 2 (K_r - K_g) (1 - V_g)} \right] \quad (V.2)$$

where

$$K_g = E_g / 2 (1 - v_g)$$

$$K_r = E_r / 2 (1 - v_r)$$

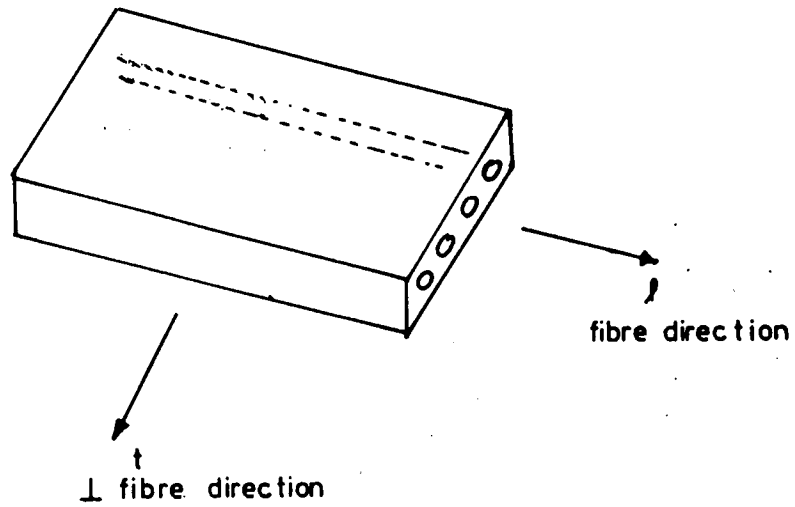
$$G_g = E_g / 2 (1 - v_g)$$

$$G_r = E_r / 2 (1 - v_r)$$

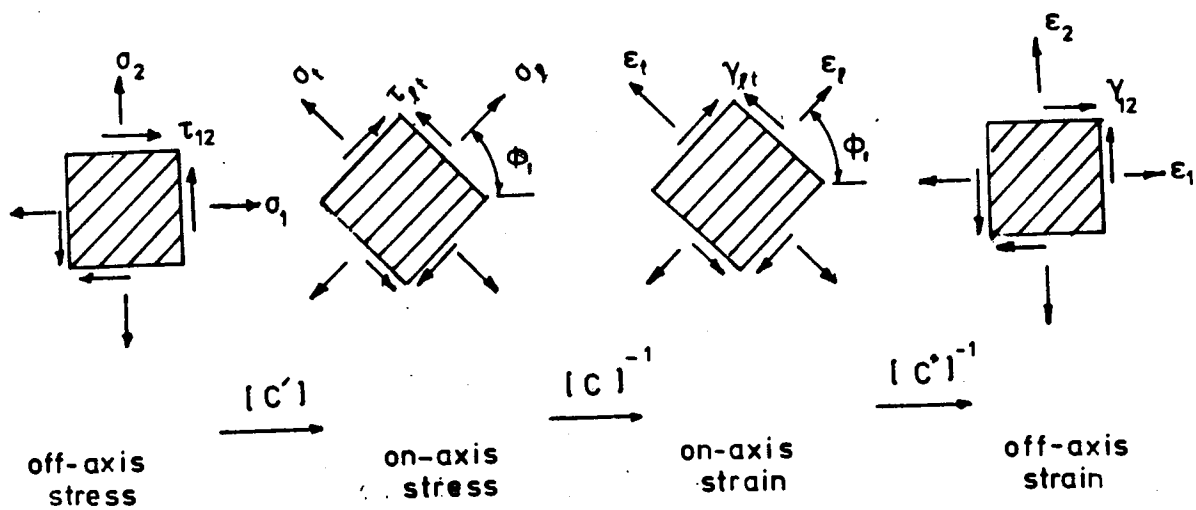
V.1.3 Poissons ratio

$$v_{lt} = (1 - \bar{C}) \frac{K_g v_g (2K_r + G_r) V_g + K_r v_r (2K_g + G_r) (1 - V_g)}{K_g (2K_r + G_r) - G_r (K_g - K_r) (1 - V_g)} + \bar{C} \frac{K_r v_r (2K_g + G_g) (1 - V_g) + K_g v_g (2K_r + G_r) V_g}{K_g (2K_r + G_g) + G_g (K_r - K_g) (1 - V_g)} \quad (V.3a)$$

$$v_{tl} = v_{lt} \frac{E_t}{E_l} \quad (V.3b)$$



Figure(V.1) UD composite model



Figure(V.2) Off axis stress/strain relationship

V.1.4 In-plane shear modulus

$$G_{lt} = (1 - \bar{C}) G_r \frac{2G_g - (G_g - G_r)(1 - \nu_g)}{2G_r + (G_g - G_r)(1 - \nu_g)} + \bar{C} G_g \frac{(G_g + G_r) - (G_g - G_r)(1 - \nu_g)}{(G_g + G_r) + (G_g - G_r)(1 - \nu_g)} \quad (V.4)$$

V.2 Off-axis Stress/Strain Relationship

For off-axis loading, the off-axis mechanical properties are dependent on the on-axis elastic constants and on the off-axis angle of loading. With the aid of Fig. V.2, the off-axis stress/strain relationship is obtained as follow ^(29,119) :

$$\begin{bmatrix} \sigma_1 \\ \sigma_2 \\ \tau_{12} \end{bmatrix} = [C']^{-1} [C] [C''] \begin{bmatrix} \epsilon_1 \\ \epsilon_2 \\ \gamma_{12} \end{bmatrix} \quad (V.5)$$

where

$$[C'] = \begin{bmatrix} m^2 & n^2 & 2mn \\ n^2 & m^2 & -2mn \\ -mn & mn & m^2 - n^2 \end{bmatrix}$$

$$[C] = \begin{bmatrix} E_l / (1 - \nu_{lt} \nu_{tl}) & \nu_{tl} E_l / (1 - \nu_{lt} \nu_{tl}) & 0 \\ \nu_{lt} E_t / (1 - \nu_{lt} \nu_{tl}) & E_t / (1 - \nu_{lt} \nu_{tl}) & 0 \\ 0 & 0 & G_{lt} \end{bmatrix}$$

$$[C''] = \begin{bmatrix} m^2 & n^2 & mn \\ n^2 & m^2 & -mn \\ -2mn & 2mn & m^2 - n^2 \end{bmatrix}$$

and

$$m = \cos \phi_1$$

$$n = \sin \phi_1$$

or the off-axis stress could be related to the off-axis strain as:

$$\begin{bmatrix} \sigma_1 \\ \sigma_2 \\ \tau_{12} \end{bmatrix} = \begin{bmatrix} Q_{11} & Q_{12} & Q_{16} \\ Q_{21} & Q_{22} & Q_{26} \\ Q_{61} & Q_{62} & Q_{66} \end{bmatrix} \begin{bmatrix} \epsilon_1 \\ \epsilon_2 \\ \gamma_{12} \end{bmatrix} \quad (V.7)$$

where

$$\Omega = 1 - \nu_{lt} \nu_{tl}$$

$$Q_{11} = \frac{1}{\Omega} [E_l \cos^4 \phi_1 + E_t \sin^4 \phi_1 + \sin^4 \phi_1 \cos^2 \phi_1 (2E_l \nu_{lt} + 4\Omega G_{lt})]$$

$$Q_{12} = \frac{1}{\Omega} [E_t \nu_{lt} (\cos^4 \phi_1 + \sin^4 \phi_1) + \sin^2 \phi_1 \cos^2 \phi_1 (E_t + E_l - 4\Omega G_{lt})]$$

$$Q_{16} = \frac{1}{\Omega} [\sin \phi_1 \cos^3 \phi_1 (E_l - \nu_{lt} E_t - 2\Omega G_{lt}) + \sin^3 \phi_1 \cos \phi_1 (\nu_{lt} E_t + 2\Omega G_{lt})]$$

$$Q_{21} = Q_{12}$$

$$Q_{22} = \frac{1}{\Omega} [E_t \cos^4 \phi_1 + E_l \sin^4 \phi_1 + \sin^2 \phi_1 \cos^2 \phi_1 (2 \nu_{lt} E_t + 4\Omega G_{lt})]$$

$$Q_{26} = \frac{1}{\Omega} [\sin \phi_1 \cos^3 \phi_1 (\nu_{lt} E_t - E_t + 2\Omega G_{lt}) + \sin^3 \phi_1 \cos \phi_1 (E_l - \nu_{lt} E_t - 2\Omega G_{lt})]$$

$$Q_{61} = Q_{16}$$

$$Q_{62} = Q_{26}$$

$$Q_{66} = \frac{1}{\Omega} [E_l + E_t - 2 \nu_{lt} E_t - 2\Omega G_{lt}) \sin^2 \phi_1 \cos^2 \phi_1 + \Omega G_{lt} (\sin^4 \phi_1 + \cos^4 \phi_1)]$$

V.3 Stress/Strain Relationship for Multi-layer Laminated Plate ⁽¹¹⁹⁾

V.3.1 General Consideration

Consider a plate element cut from a multi-layered laminate consisting of n distinct layers, loaded with edge forces N_x , N_y , N_{xy} and moments M_x , M_y , M_{xy} applied in a case of plane stress as shown in Fig.

V.3. The general relationship between the planar and flexural stresses and their corresponding strains is expressed as:

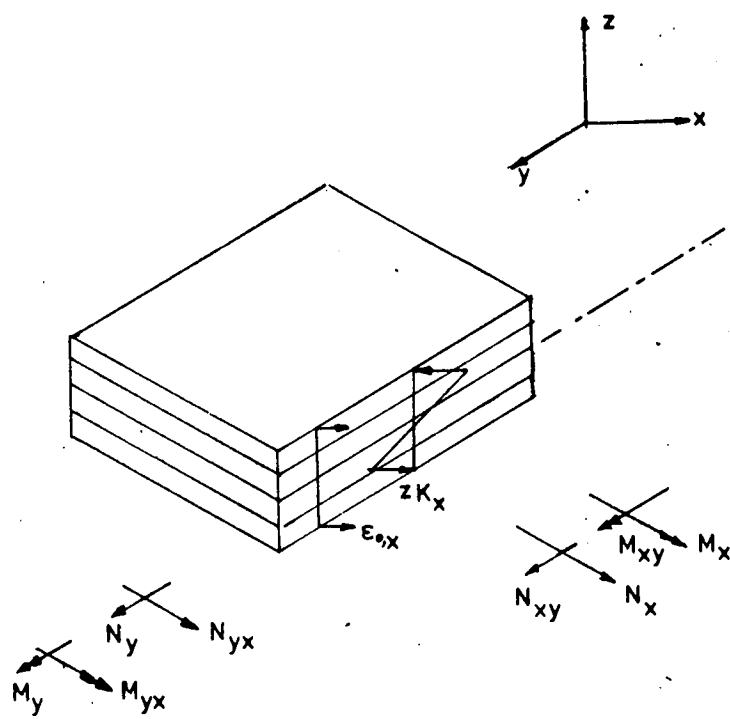
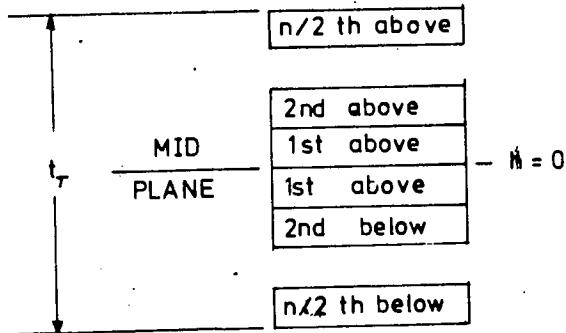


Figure (V.3) Forces and strains on multi layer laminate



| ply order | h | $h-(h-1)$ (A_{ij}) | $h^2-(h-1)^2$ (B_{ij}) | $h^3-(h-1)^3$ (D_{ij}) |
|-----------|-----|---------------------------|-------------------------------|-------------------------------|
| 6th above | 6 | 1 | 11 | 91 |
| 5th above | 5 | 1 | 9 | 61 |
| 4th above | 4 | 1 | 7 | 37 |
| 3rd above | 3 | 1 | 5 | 19 |
| 2nd above | 2 | 1 | 3 | 7 |
| 1st above | 1 | 1 | 1 | 1 |
| mid plane | | | | |
| 1st below | 0 | 1 | -1 | 1 |
| 2nd below | -1 | 1 | -3 | 7 |
| 3rd below | -2 | 1 | -5 | 19 |
| 4th below | -3 | 1 | 7 | 37 |
| 5th below | -4 | 1 | -9 | 61 |
| 6th below | -5 | 1 | 11 | 91 |

Figure (V.4) Nomenclature for laminate with even plies

$$\begin{bmatrix} N_x \\ N_y \\ N_{xy} \\ \dots \\ M_x \\ M_y \\ M_{xy} \end{bmatrix} = \begin{bmatrix} A_{11} & A_{12} & A_{16} & | & B_{11} & B_{12} & B_{16} \\ A_{21} & A_{22} & A_{26} & | & B_{21} & B_{22} & B_{26} \\ A_{61} & A_{62} & A_{66} & | & B_{61} & B_{62} & B_{66} \\ \dots & \dots & \dots & | & \dots & \dots & \dots \\ B_{11} & B_{12} & B_{16} & | & D_{11} & D_{12} & D_{16} \\ B_{21} & B_{22} & B_{26} & | & D_{21} & D_{22} & D_{26} \\ B_{61} & B_{62} & B_{66} & | & D_{61} & D_{62} & D_{66} \end{bmatrix} \begin{bmatrix} \epsilon_x \\ \epsilon_y \\ \gamma_{xy} \\ \dots \\ k_x \\ k_y \\ k_{xy} \end{bmatrix} \quad (V.8)$$

V.3.2 Stress/strain relationship for $\pm 55^\circ$ FW straight pipe,
(12 layers)

This special case of Eq. (V.8) is for straight pipes S031 and S032 (Ch. 8), of 5.1mm total thickness, made from Epoxy-glass fibre reinforcements.

In this case, the stacking sequence is shown in Fig. V.4, and the problem is treated as a special case by Tsia⁽²⁹⁾, by assuming that the layers of constant thickness, and A_{ij} , B_{ij} , D_{ij} of Eq. (V.8) are obtained as follows:

$$\begin{aligned}
 A_{ij} &= t_o \sum_{h=1-n/2}^{n/2} Q_{ij}^{(h)} [h - (h-1)] \\
 B_{ij} &= \frac{t_o^2}{2} \sum_{h=1-n/2}^{n/2} Q_{ij}^{(h)} [h^2 - (h-1)^2] \\
 D_{ij} &= \frac{t_o^3}{3} \sum_{h=1-n/2}^{n/2} Q_{ij}^{(h)} [h^3 - (h-1)^3]
 \end{aligned} \quad (V.9)$$

where

n = number of layers = 12

t_T = thickness of the laminate = 5.1 mm

t_o = thickness of individual layer = $t_T/n = 0.425$ mm

h = defines the order of each layer as shown in Fig. V.4.

$E_l, E_t, \nu_{lt}, \nu_{tl}, G_{lt}$ of each layer is calculated using Eqs. (V.1) to (V.4). The off-axis elastic constants Q_{ij} in Eq. (V.7) are then calculated. The mechanical constants are listed in Table V.1 using $\bar{C} = 0, \bar{C} = 0.2,$ and $\bar{C} = 1.0.$

For antisymmetric laminate of even number of layers with $\phi_1 = \pm 55^\circ,$ then ⁽²⁹⁾ :

$$\begin{aligned} B_{11} &= B_{22} = B_{12} = B_{66} = 0 \\ D_{16} &= D_{26} = A_{16} = A_{26} = 0 \end{aligned} \quad (V.10)$$

Eq. (V.9) is also simplified to:

$$\begin{aligned} A_{ij} &= t_T Q_{ij} \\ B_{ij} &= \frac{t_T^2}{24} Q_{ij} \\ D_{ij} &= \frac{t_T^3}{12} Q_{ij} \end{aligned} \quad (V.11)$$

By substituting back Eq. (V.10) and (V.11) into Eq. (V.9) and assuming only membrane strains to occur, then the laminate membrane unit forces and strains are related as follows:

$$\begin{bmatrix} N_x \\ N_y \\ N_{xy} \end{bmatrix} = \begin{bmatrix} A_{11} & A_{12} & 0 \\ A_{21} & A_{22} & 0 \\ 0 & 0 & A_{66} \end{bmatrix} \begin{bmatrix} \epsilon_x \\ \epsilon_y \\ \gamma_{xy} \end{bmatrix} \quad (V.12a)$$

or

$$\begin{bmatrix} N_x \\ N_y \\ N_{xy} \end{bmatrix} = t_T \begin{bmatrix} Q_{11} & Q_{12} & 0 \\ Q_{21} & Q_{22} & 0 \\ 0 & 0 & Q_{66} \end{bmatrix} \begin{bmatrix} \epsilon_x \\ \epsilon_y \\ \gamma_{xy} \end{bmatrix} \quad (V.12b)$$

For straight pipes S031 and S032, if the longitudinal axis is assumed to be in the direction of x-axis, and the circumferential axis in the direction of the y-axis, then:

TABLE V.1 Elastic constants of UD laminate

| Upper and Lower Bounds | ϕ , deg | E_l , N/mm ² | E_t , N/mm ² | G_{lt} , N/mm ² | ν_{lt} | ν_{tl} | Q_{11} | Q_{12} | Q_{16} | Q_{21} | Q_{22} | Q_{26} | Q_{61} | Q_{62} | Q_{66} |
|------------------------|--------------|---------------------------|---------------------------|------------------------------|------------|------------|----------|----------|----------|----------|----------|----------|----------|----------|----------|
| $\bar{C}=0$ | +55 | 40570 | 9700 | 4220 | 0.269 | 0.064 | 13810 | 9050 | 5050 | 9050 | 24560 | 9710 | 5050 | 9710 | 10610 |
| | -55 | | | | | | 13810 | 9050 | -5050 | 9050 | 24560 | -9710 | -5050 | -9710 | 10610 |
| $\bar{C}=0.2$ | +55 | 40570 | 11780 | 5810 | 0.262 | 0.076 | 16410 | 8420 | 4979 | 8420 | 26450 | 8820 | 4980 | 8820 | 11080 |
| | -55 | | | | | | 16410 | 8420 | -4979 | 8420 | 26450 | -8820 | -4980 | -8820 | 11080 |
| $\bar{C}=1.0$ | +55 | 40570 | 20100 | 12140 | 0.233 | 0.116 | 26660 | 5730 | 4610 | 5730 | 33860 | 5270 | 4610 | 5270 | 13060 |
| | -55 | | | | | | 26660 | 5730 | -4610 | 5730 | 33860 | -5270 | -4610 | -5270 | 13060 |

The results are based on the following resin and fibre properties:

$$E_r = 4000 \text{ N/mm}^2 \text{ (epoxy)}$$

$$E_g = 73000 \text{ N/mm}^2$$

$$\nu_r = 0.35$$

$$\nu_g = 0.21$$

glass content (by volume) = 53%

$$\begin{bmatrix} N_L \\ N_C \\ N_{LC} \end{bmatrix} = t_T \begin{bmatrix} Q_{11} & Q_{12} & Q_{16} \\ Q_{21} & Q_{22} & Q_{26} \\ 0 & 0 & Q_{66} \end{bmatrix} \begin{bmatrix} \epsilon_L \\ \epsilon_C \\ \gamma_{LC} \end{bmatrix} \quad (V.13)$$

- for longitudinal flexural bending of the straight pipe, then forces in Eq. (V.13) are defined as^(.3):

$$\begin{aligned} N_L &= \sigma_L \cdot t_T = \frac{M r_m}{I} t_T \\ N_C &= 0 \\ N_{LC} &= 0 \end{aligned} \quad (V.14a)$$

- for closed-ended pressure loading of the straight pipe, then the forces in Eq. (V.13) are defined as:

$$\begin{aligned} N_L &= \sigma_L \cdot t_T = p_i r_m / 2 \\ N_C &= \sigma_C \cdot t_T = p_i r_m \\ N_{LC} &= 0 \end{aligned} \quad (V.14b)$$

- and for torsional loading

$$\begin{aligned} N_L &= 0 \\ N_C &= 0 \\ N_{LC} &= \tau_{LC} \cdot t_T = \frac{T r_m}{J} t_T \end{aligned} \quad (V.14c)$$

Eq. (V.13) can be shown to be further represented as a function of the longitudinal and the circumferential elastic constants of the pipe laminate in conjunction with Eqs. (V.14a,b,c) as follows:

$$\begin{bmatrix} \sigma_L \\ \sigma_C \\ \tau_{LC} \end{bmatrix} = \begin{bmatrix} \frac{E_L}{(1 - \nu_{LC}\nu_{CL})} & \frac{\nu_{CL} E_L}{(1 - \nu_{LC}\nu_{CL})} & 0 \\ \frac{\nu_{LC} E_C}{(1 - \nu_{LC}\nu_{CL})} & \frac{E_C}{(1 - \nu_{LC}\nu_{CL})} & 0 \\ 0 & 0 & G_{LC} \end{bmatrix} \begin{bmatrix} \epsilon_L \\ \epsilon_C \\ \gamma_{LC} \end{bmatrix} \quad (V.15)$$

Hence, the stress/strain relation as a function of the longitudinal and the circumferential stiffness factors, and the elastic constants of the laminate as a function in the longitudinal and the circumferential directions are presented by substituting the values of Q_{ij} in Table V.1 into Eq. (V.13) and using Eq. (V.15), as follows:

(i) $\bar{C} = 0$

$$\begin{bmatrix} \sigma_L \\ \sigma_C \\ \tau_{LC} \end{bmatrix} = \begin{bmatrix} 13810 & 9050 & 0 \\ 9050 & 24560 & 0 \\ 0 & 0 & 10610 \end{bmatrix} \begin{bmatrix} \epsilon_L \\ \epsilon_C \\ \gamma_{LC} \end{bmatrix} \quad (V.16a)$$

and

$$\begin{aligned} E_L &= 10430 \text{ N/mm}^2 & E_C &= 18640 \text{ N/mm}^2 \\ \nu_{LC} &= 0.368 & \nu_{CL} &= 0.655 \end{aligned}$$

(ii) $\bar{C} = 0$

$$\begin{bmatrix} \sigma_L \\ \sigma_C \\ \tau_{LC} \end{bmatrix} = \begin{bmatrix} 16410 & 8420 & 0 \\ 84200 & 26450 & 0 \\ 0 & 0 & 11080 \end{bmatrix} \begin{bmatrix} \epsilon_L \\ \epsilon_C \\ \gamma_{LC} \end{bmatrix} \quad (V.16b)$$

and

$$\begin{aligned} E_L &= 13730 \text{ N/mm}^2 & E_C &= 22140 \text{ N/mm}^2 \\ \nu_{LC} &= 0.318 & \nu_{CL} &= 0.513 \end{aligned}$$

(iii) $\bar{C} = 1$

$$\begin{bmatrix} \sigma_L \\ \sigma_C \\ \tau_{LC} \end{bmatrix} = \begin{bmatrix} 26660 & 5730 & 0 \\ 5730 & 33860 & 0 \\ 0 & 0 & 13060 \end{bmatrix} \begin{bmatrix} \epsilon_L \\ \epsilon_C \\ \gamma_{LC} \end{bmatrix}$$

and

(V.16c)

$$E_L = 25690 \text{ N/mm}^2$$

$$E_C = 32630 \text{ N/mm}^2$$

$$\nu_{LC} = 0.169$$

$$\nu_{CL} = 0.215$$

APPENDIX VI

RADIAL DEFORMATION IN A THIN CYLINDRICAL SHELL

AT THE EDGE

RADIAL DEFORMATIONS IN A THIN CYLINDRICAL SHELL LOAD AT THE EDGE (168)

(Fig VI.1)

For a semi-infinite cylinder, the radial deformation which is assumed to vary sinusoidally around the circumference at any section:

$$\begin{aligned} \omega/r_m = \cos n \phi [e^{-\alpha_1 x/r} \{B_1 \cos (\zeta_1 x/r) + B_3 \sin (\zeta_1 x/r)\} \\ + e^{-\alpha_2 x/r} \{B_2 \cos (\zeta_2 x/r) + B_4 \sin (\zeta_2 x/r)\}] \end{aligned} \quad (\text{VI.1})$$

where:

n = number of harmonic

B_1 to B_4 = constants depending upon the boundary conditions
and

$$\begin{aligned} \alpha_1 = \frac{k + \Lambda}{2} \quad \alpha_2 = \frac{k - \Lambda}{2} \\ \zeta_1 = \frac{\Lambda}{k} \alpha_1 \quad \zeta_2 = \frac{\Lambda}{k} \alpha_2 \end{aligned} \quad (\text{IV.2})$$

$$\Lambda = \left\{ 3(1 - \nu^2) \right\}^{1/4} \left(\frac{r_m}{t} \right)^{1/2}, \quad k = \left[2n^2 + (4n^4 + \Lambda^4)^{1/2} \right]^{1/2}$$

The total deformation at any position will thus correspond to the superposing of two separate deformations, one corresponding to α_1 and the other α_2 .

- α_1 gives a short decay length along a generator of the cylinder
- α_2 gives a relatively long decay length for small values of n .

The decay lengths x_1 and x_2 corresponding to α_1 and α_2 are:

$$x_1 = \frac{\pi r_m}{\alpha_1} \quad x_2 = \frac{\pi r_m}{\alpha_2} \quad (\text{VI.3})$$

For the straight CSM Pipes investigated in Ch. 6, the long decay component has been calculated using $n = 2$ to check the effect of the applied load under four-point bending in the strains measured at mid-section of the pipes.

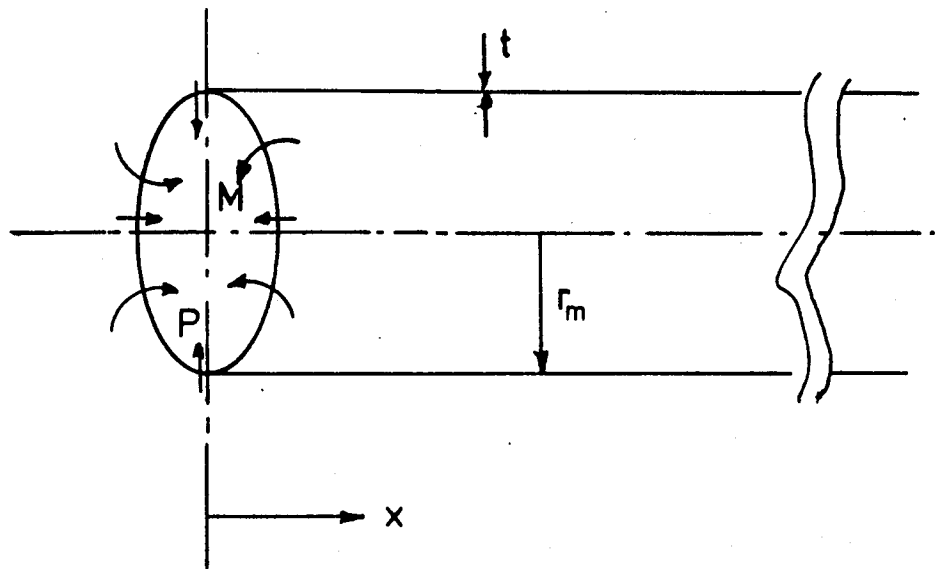


Figure (VI 1) Edge loading of a thin cylinder

REFERENCES

- 1 Designing with Plastics, Unit 12, T351, Materials under Stress, Open University Press.
- 2 Crystic Resin in Process Engineering, Case Histories, Scott Bader Publication.
- 3 BS 4994, 'Specifications for Vessels and Tanks in Reinforced Plastics, 1973.
- 4 B202B, Specification for the Fabrication of PVC lined GRP Pipe Systems, ICI, 1978.
- 5 B201B, Specification for the Fabrication of GRP Pipe Systems, ICI, 1978.
- 6 Crystic Monograph, Polyester Handbook, Scott Bader Publication.
- 7 L.T. Butt and D.C. Wright, Use of Polymers in Chemical Plant Construction, Applied Science Publication, 1980.
- 8 I.M. Daniel and T. Liber, Lamination Residual Strains and Stresses in Hybrid Laminates, Composite Materials - Testing and Design, 4th Conf., STP 617, May 1976, pp. 330-341.
- 9 PS15-69, NBS Voluntary Product Standard, Custom contact - Molded GRP Chemical Resistant Process Equipment, 1969.
- 10 M. Brich-Kisberyi, D. Harrison, R. Pinzeli, D.M. Eyre, G.P. Marshall, 'The Effect of Post-cure on Environmental Stress Corrosion of Vinyl Ester Laminate and Gel Coat Layers,' 12th Conf., BPF Publication, 1980, pp. 215-225.
- 11 L.S. Norwood and A.F. Millman, 'The Influence of Resin System on the Mechanical Performance of Glass Fibre Reinforced Polyesters', 3rd Int. Conf. on Composites Materials, Paris, Vol. 2, pp. 26-29, Aug. 1980, pp. 26-29.
- 12 Eric S.W. Kong, 'Sub Tg - Annealing Studies of Advanced Epoxy Matrix Graphite - Fibre Reinforced Composite', J. Appl. Phys., 52 (10), Oct. 1981, pp. 5921-5925.
- 13 D.C. Wright, 'The Effect of Cure History on the Creep Properties of Various Cold Curing Polyester Resins and Glass Laminates', PRI Conference, Paper No. 11, Feb. 1976, pp. 1-16.
- 14 D.J. Steel, 'Effects of Environmental Conditioning on the Interface Stresses arising from the Shrinkage of Polyester Resins in Glass Ring Cells', MEXE, Technical Note, No. 8/68, November 1968.
- 15 K. Phillips and M.G. Bader, 'Evaluation of the Effect of the State of Cure of the Matrix on the Properties of Glass-fibre Epoxy Resin Laminates', 3rd Int. Conf. on Composites Material, Vol. 1, Paris, Aug. 1980, pp. 875-884.

- 16 George Lubin, 'Handbook of Fibreglass and Advanced Plastic Composite', Van Nostrand Reinhold Company, 1969.
- 17 BS 3691, 'Glass fibre Rovings for the Reinforcement of Polyester and Epoxide Resin System', 1969.
- 18 BS 4749, 'Woven Glass-fibre Rovings Fabrics for the Reinforcements of Polyester Resin Systems', 1964.
- 19 BS 3469, 'E Glass-fibre Chopped Strand Mat for the Reinforcement of Polyester Resin System', 1973.
- 20 Structural Plastics Design Manual, Phase 1; Chapter 1-4, U.S. Department of Transportation FHWA-TS-79-203.
- 21 J.A. Raymond, 'Effect of Resin Content on the Mechanical Properties of Glass Reinforced Polyester Laminates', Reinforced Plastics Congress, Brighton, 1974, pp. 61-73.
- 22 J.A. Raymond, 'The Practical Significance of Resin Content and Properties in Laminate Behaviour', BPF; 8th Int. Reinforced Plastic Conf., Brighton, 1972, pp. 85-93.
- 23 C. Zebwen, W.S. Smith, M.W. Wardle, 'Test Methods for Fibre Tensile Strength Composite Flexural Modulus and Properties of Fabric-reinforced Laminate', Composite Material Testing and Design, ASTM STP 674, 1979, pp. 228-262.
- 24 Private communication with D.C. Wright, Head of the Plastics Division, RAPRA.
- 25 G.P. Marshall and J.G. Williams, 'The Analysis of Practical Failures of Plastic Pipelines', BPF; 3rd Int. Plastic Pipe Symposium, Sept. 1974, pp. 4:5:1-:9.
- 26 G.M. Gale and K.A. Scott, 'Failure of Rigid PVC Pipes reinforced by Wrapping with Glass-fibre Resin', RAPRA Member's Report, Oct. 1965.
- 27 W.E. Cowely, N.P. Dent, and R.H. Harris, 'The Brittle Failure of UPVC lined Glass Reinforced Plastics Pipelines', Chemistry and Industry, No. 3, June 1978, pp. 365-366.
- 28 R.D. Currie, 'Manufacture, Testing and Installation of Centrifugally Cast Pipes', Pipe Conf., Paper No. 12, June 1980.
- 29 S.W. Tsai and H.T. Hahn 'Introduction to Composite Materials', Technomic Publishing Company, 1980, Westport, Connecticut 06880.
- 30 S. Timoshenko and J.N. Goodier, 'Theory of Elasticity', 2nd Edition, McGraw-Hill Book Co.
- 31 W. Tsai, 'Structural Behaviour of Composite Materials', NASA Report No. NAS 7-215, Philco Corp., Newport Beach, California, July 1964.
- 32 Lee R. Calcote, 'The Analysis of Laminated Composite Structures', Van Nostrand Reinhold Co. Publication.

- 33 BS 2782, 'Methods of Testing Plastics', 1970.
- 34 S. Torp., 'Aspects of Continuous Filament Wound GRP Pipe', Pipe Conf., Paper No. 7, June 1980.
- 35 Engineering Materials: An Introduction, 6 Composite Materials, T252 Unit 6, The Open University Technology, A Second Level Course.
- 36 FIBERCAST Manual, Fibercast Pipes (GB) Ltd.
- 37 G. Menges and H.J. Roskothen, 'The Deformation and Failure Characteristics of Glass Mat Laminates with Special Reference to the Effect of Shear', *Kunststoffe*, Vol. 60, Dec. 1970, pp 1009-1014.
- 38 R.M. Ogorkiewicz and A.A.M. Sayigh, 'Torsional Stiffness of Plastic Tubes Reinforced with Glass Fibres', *J. of Strain Analysis*, Vol. 6, No. 4, 1971, pp. 226-230.
- 39 R.M. Christensen, 'Asymptotic Modulus Results for Composites containing Randomly Oriented Fibres', *Int. J. Solids Structures*, Vol. 12, 1976, pp. 537-544.
- 40 C.J. Kirk, 'Effect of Geometric Design Parameters on the Flexural behaviour of Glass Reinforced Plastic Pipe Intersection', Ph.D Thesis, UMIST, Mech. Eng. Dept., 1980.
- 41 D.C. Wright, 'Flexibility and Stress Intensification Factors for GRP Bend and Related System', RAPRA Confidential Report.
- 42 J.A. Kies, 'Maximum Strains in the Resin of Fibreglass Composite', Ballistic Branch - Mechanics Division, U.S. Naval Research Lab. Report 5752, March 1962, AD 274560.
- 43 J.A. Kies, 'Composite Strength as Related to the Properties of Glass Filaments and Resins', *J. Plastic Inst.*, Oct. 1965, pp. 145-152.
- 44 N.J. Pagano and J.M. Whitney, 'Geometric Design of Composites Cylindrical Characterization Specimens', *J. Composite Material*, Vol. 4, July 1970, p. 360.
- 45 M. Holmes and Q.J. AL. Khayalt, 'Structural Properties of GRP', *Composites*, Vol. 6, No. 4, July 1975, pp. 157-165.
- 46 Lawrence J. Broutman and Richard H. Krock, 'Modern Composite Materials', Addison-Wesley Publishing Company, 1967.
- 47 J.H. Greenwood, 'German Work on GRP Design', *Composite*, July 1977, pp. 175-184.
- 48 Dipl. Ing. alfred Puck, 'The Stresses and Strains in GRP Multi-layer Composite Component',:
 Part I, *Kunststoffe*, Vol. 57 (April 1967) pp. 284-293
 Part II, *Kunststoffe*, Vol. 57 (July 1967) pp. 573-582
 Part III, *Kunststoffe*, Vol. 57 (Dec. 1967) pp. 965-973

- 49 A.F. Johnson, 'Engineering Design - Properties of GRP', A Joint BPF, NPL Project 1978.
- 50 Marvin Knight, 'Three Dimensional Elastic Moduli of Graphite/Epoxy Composite', J. Comp. Material, Vol. 16, March 1982, p. 153.
- 51 Gibbs and Cox Inc., 'Marine Design Manual for Fibreglass Reinforced Plastics,' McGraw-Hill Book Company, 1960.
- 52 J.H. Sinclair and C.C. Chamis, 'Fracture Modes in Off-Axis Fibre Composites', Polymer Composites, Vol. 2, No. 1, Jan. 1981, pp.45-52.
- 53 H. Krenchel, 'Fibre Reinforcement', Akademish Forlag, Copenhagen, 1964.
- 54 R.M. Christensen and F.M. Waals, 'Effective Stiffness of Randomly Oriented Fibre Composite', J. Composite Material, Vol. 6, Oct. 1972, pp. 518-532.
- 55 J.K. Lees, 'A Study of the Tensile Modulus of Short Fibre Reinforced Plastics', Poly. Eng. and Sci., Vol. 8, No. 3, July 1968, pp. 186-194.
- 56 M. Knight and H.J. Hahn, 'Strength and Elastic Modulus of a Randomly Distributed Short Fibre Composite', J. Composite Materials, Vol. 9, No. 1, Jan. 1975, pp. 77-90.
- 57 H.T. Hahn, 'On Approximation of Strength of Random Fibre Composite', J. Composite Materials Vol. 9, No. 4, Oct. 1975, p. 316-326.
- 58 J.K. Lees, 'A Study of the Tensile Strength of Short Fibre Reinforced Plastics', Poly. Eng. and Sci., July 1969, Vol. 8, No. 2, pp. 195-201.
- 59 S.K. Gogger and R.J. Broutman, 'Strength Properties of Random Fibre Mat Composite', SDP 29th Annual Conf., Paper 17-E.
- 60 M.J. Owen and R.G. Rose, 'Polyester Flexibility versus Fatigue Behaviour of RP', J. Modern Plastics, Nov. 1970, Vol. 47, No. 11, pp. 130-138.
- 61 Atlac Polyester Resin, Fabricator's Notebook, ICI Americas Inc., Wilmington, Delaware, 19897.
- 62 ASTM D3846, 'In-plane Shear Strength of Reinforced Plastics'.
- 63 M. Doostson and P. Grant, 'Bonded Joints in Aircraft Structures', 6th Granfield Conf., PRI, Plastics Design Engng., 6-8 Jan. 1975.
- 64 C.T. Herakovich, 'On the Relationship between Engineering Properties and Delamination of Composite Material', J. Composite Material, Vol. 15, July 1981, pp. 336-348.
- 65 J.S. Han and J. Koutsky, 'Interlaminar Fracture Energy of Glass Fibre Reinforced Polyester Composite', J. Composite Material, Vol. 15, July 1981, p. 371.

- 66 Engineering Sciences Data, Structures; Vol. 14, Laminated Composites.
- 67 M.J. Owen, D.J. Rice, J.R. Griffiths and M.S. FOUND, 'Biaxial Static and Fatigue Strength of Glass Mat and Fabric Reinforced Polyester Resins', SPF, 35th Annual Conf., 1980, Section 23-E.
- 68 M.G. Bader and C.M. Tyson, 'The Mechanical Properties of Cross-reinforced GRP Laminates', Paper No. 12, RPG 4th Conf., Feb. 1975, University of Surrey.
- 69 PD 6480, 'Explanatory Supplement fo BS 4994', British Standard Institution, 1977.
- 70 P.T. Moore, 'Unit Strength and Extensibility - A New Design Concept of Glass-fibre Reinforced Plastics', Reinforced Plastics Congress, 1974, Brighton, pp. 85-90.
- 71 K.V. Gotham and M.J. Hitch, 'Factors Affecting Fatigue Resistance in Rigid UPVC Pipe Compositions, The British Poly. J., Vol. 10, March 1978, pp. 47-52.
- 72 ASTM D3299, 'Filament-wound Glass-fibre Reinforced Polyester Chemical Resistant Tanks'.
- 73 S.K. Gagger and L.J. Broutman, 'Effect of Matrix Ductility and Interface Treatment on Mechanical Properties of Glassfibre Mat Composite', Poly. Eng. and Sci., Aug. 1976, Vol. 16, No. 8, Aug. 1976, pp. 537-543.
- 74 P.K. Mallick and L.J. Broutman, 'The Influence of the Interface on the Fracture - Toughness of Low Aspect Ratio Fibre Composite', SPI 29th Annual Conf., 1974, Section 13-B.
- 75 G.A. Cooper and A. Kelly, 'Role of the Interface in the Fracture of Fibre-Composite Materials', ASTM STP 452, p. 90.
- 76 M.J. Owen and D.J. Rice, 'Biaxial Strength Behaviour of Glass Fabric - Reinforced Polyester Resin', Composites, Vol. 12, No. 1, Jan. 1980, pp. 33-37.
- 77 B. Spencer and D. Hull, 'Effect of Winding Angle on the Failure of Filament Wound Pipes', Composites, Oct. 1978, pp. 263-271.
- 78 D. Hull, M.J. Legg and B. Spencer, 'Failure of Glass/Polyester Filament Wound Pipes', Composites, Jan. 1978, pp. 17-24.
- 79 G.C. Eckold, D. Leadbetter, P.D. Soden, P.R. Griggs, 'Lamination Theory in the Prediction of Failure Envelopes for Filament Wound Materials subjected to Biaxial Loading', Composites, Oct. 1978, pp. 243-246.
- 80 P.D. Soden, D. Leadbetter, P.R. Griggs, G.C. Eckold, 'The Strength of a Filament Wound Composite under Biaxial Loading', Composites, Oct. 1978, pp. 247-250.
- 81 M.J. Owen and R. Dukes, 'Failure of Glass-reinforced Plastics under Single and Repeated Loading', J. of Strain Analysis, Vol. 2, No. 4, 1967, pp. 272-279.

- 82 T.R. Smith and M.J. Owen, 'The Progressive Nature of Fatigue Damage in Glass Reinforced Plastics', Proceedings of the 6th Int. Reinforced Plastic Conf., BPF, Nov. 1968, Paper No. 27.
- 83 J. Malmo, 'Surface Cracking of RP By Repeated Bending', 36th Annual SPI, Feb. 1981, Paper No. 19A.
- 84 R. Dodds, 'Transverse Fibre Debonding in Reinforced Thermosetts - A Review', Part 1, RAPRA Members' Journal, May/June 1976, pp. 49-56.
- 85 John Outwater, 'On the Flexural Failure of Cloth Reinforced Laminate', SPI, 14th Annual Conf. Section 6E.
- 86 K.J. Pascoe, 'Failure of Woven Glass-fibre Polyester Composite under Biaxial Stressing', Cambridge University, Eng. Dept.
- 87 A. Puck and W. Schneider, 'On Failure Mechanisms and Failure Criteria of Filament-Wound Glassfibre/Resin Composite', Plastic and Polymer, Feb. 1969, pp. 33-43.
- 88 W.G. Gottenberg, R.C. Allen, W.V. Breitigam, and C.T. Dickenson, 'Modes of Failure of Hydrostatically Overstressed Reinforced Plastic Pipe', 34th Annual Technical Conf., 1979, Section 13C.
- 89 M.J. Owen and M.S. FOUNd, 'Static and Fatigue Failure of Glass Fibre Reinforced Polyester Resins under Complex Stress Conditions', Faraday Special Discussion of the Chemical Society, No. 2, 1972, pp. 79-89.
- 90 ISO, Recommendation; R1167, 'Plastic Pipes for the Transport of Fluids - Determination of the Resistance to Internal Pressure', 1st Edition, 1970.
- 91 H Mieras, 'Irreversible Creep of Filament Wound Glass-Reinforced Resin Pipes', Plastic & Polymers, April 1973, pp. 84-89.
- 92 D. Hull, K.S. Chao, M.J. Legg, M. Lisenburg, and B. Spencer, 'Profile - ICI - Implex Terephthalic Polyester Resin', Dept. of Metallurgy and Material Science, University of Liverpool.
- 93 G.B. Greatorex, A.S. Tooth, 'The stresses induced in reinforced plastic matrix pipes by saddle supports', J. of Strain Analysis, Vol. 17, No. 3, July 1982, pp. 147-55.
- 94 A.H. Puppo and H.A. Evenson, 'Strength of Anisotropic Materials under Combined Stresses', AIAA Paper, No. 71-368, 1971, pp. 1-9.
- 95 M.J. Owen, 'Designing against Fatigue in Glass Reinforced Plastics', I. Mech. Eng. Conf. Pub. 1977-9, Paper No. C223/77, pp. 1-5.
- 96 J.W. Dally and L.J. Broutman, 'Frequency Effects on the Fatigue of Glass Reinforced Plastics', J. Composite Materials, Vol. 1, 1967, pp. 424-443.
- 97 M.J. Owen and J.R. SMith, 'Some Fatigue Properties of Chopped Strand Mat/Polyester - Resin Laminate', Plastic and Polymer, Feb. 1968, pp. 33-44.

- 98 G.D. Sims and D.G. Gladman, 'Effect of Test Conditions on the Fatigue Strength of a Glass-Fabric Laminate; Part A Frequency', *Plastics and Rubber: Materials and Applications*, May 1978, pp. 41-48.
- 99 M.J. Owen and R.J. Howe, 'The Accumulation of Damage in Glass Reinforced Plastics under Tensile and Fatigue Loading', *J. Phys. D. Appl. Phys.*, Vol. 5, 1972, pp. 1637-1649.
- 100 Joshio Tanimoto and Sado Amijima, 'Progressive Nature of Fatigue Damage of Glassfibre Reinforced Plastics', *J. Composite Material*, Vol. 9, Oct. 1979, pp. 380-390.
- 101 L.J. Broutman and S. Sahu, 'Progressive Damage of Glass Reinforced Plastics during Fatigue', *SPI, 24th Conf.*, 1969, Section 11D.
- 102 M.J. Owen, J.R. Smith and R. Dukes, 'Failure of Glass-reinforced Plastics with Special Reference to Fatigue', *Plastics and Polymers*, June 1969, pp. 227-233.
- 103 D.W. Van Krevelen and P.J. Hoftyzer, 'Properties of Polymers, Their Estimation with Chemical Structure', 2nd Edition, Elsevier Scientific Publishing Company, Amsterdam - Oxford - New York, 1976.
- 104 R.G. Davies and C.L. Magee, 'The Effect of Strain-rate upon the Tensile Deformation of Material', *J. of Eng. Material and Tech.*, April 1975, pp. 151-155.
- 105 R.G. Davies and C.L. Magee, 'The Effect of Strain Rate upon the Bending Behaviour of Materials', *J. of Eng. Mat. and Tech.*, Jan. 1977, pp. 47-51.
- 106 D.C. Wright, 'The Intiation and Growth of Micro-damage in Plastics', *RAPRA Member's Journal*, June 1974, pp. 153-161.
- 107 L. Nicolaes, G. Guerra, C. Migliaresi, L. Nicodemo, and A.J. Di Benedetto, 'Viscoelastic Behaviour of Glass-reinforced Epoxy Resin', *Polymer Composite*, July 1981, Vol. 2, No. 13, pp. 116-120.
- 108 Prof. Dr. Ing. Menges and Dip. Ing. H. Brintrup, 'Long Term Behaviour of RRC Laminate at Temperature Changes and Simultaneous Mechanical Load', *SDI, 29th Conf.*, 1974, Section 21D.
- 109 R.C. Roberts, 'Design, Strain and Failure Mechanism of GRP in a Chemical Environment', *The Reinforced Plastic Congress, 1978, BPF*, Paper No. 19, pp. 145-151.
- 110 R.C. Roberts, 'FRP Fatigue and Long Term Static Stress Failure Mechanism in Chemical Environment', 1979, *National Association of Corrosion Engineers*, pp. 103-106.
- 111 H. Hojo, K. Tsuda and M. Koyamo, 'Corrosion Behaviour of Glass Fibre Composite and Vinyl Ester Resin in Chemical Environments', *3rd Int. Conf. in Organic Coatings Sci. and Tech., Proceedings*, Vol. 1, Technomic Publication, 1977, pp. 221-234.

- 112 K.B. Lyons and N.G. Phillips, 'Creep-rupture and Damage Mechanisms in Glass-reinforced Plastics', *Composites*, Vol. 12, No. 3, Oct. 1981, pp. 265-271.
- 113 G. Maron and L.J. Broutman, 'Moisture Penetration into Composites under External Stress', *Polymer Composites*, July 1982, Vol. 2, No. 3, pp. 132-136.
- 114 A. M. Otto and W.H. Piret, 'Improvement of Long Term Properties of GRP Laminates exposed to Urban Heating Water (100-140°C) by using impermeable liners in Suitable Thickness', BPF Pub. 53/12, The 12th Reinforced Plastic Congress, 1980.
- 115 ASTM D3262, 'Specification for Reinforced Plastic Mortar Sewer Pipe', 1981.
- 116 BS 5480, 'Pipes and Fittings for use for Water Supply and Sewerage', 1977, British Standards Institution.
- 117 M.J. Owen and J.R. Griffiths, 'Internal Reinforcement Joints in GRP Under Static and Fatigue Loading', *Composites*, April 1979, Vol. 10, No. 2, pp. 89-94.
- 118 J.H. Faupel and F.E. Fisher, 'Engineering Design', 2nd Edition, A. Wiley Interscience Publication, 1981.
- 119 W.S. Carswell, 'Structures in Reinforced Composites', Paper No. 33 of *Composites Structures* edited by I.H. Marshall, Applied Science Publishers, pp. 484-495.
- 120 ASTM C581, 'Test for Chemical Resistance of Thermosetting Resins used in Glass Fibre Reinforced Structures'.
- 121 Statistical Theory, Ch. 6, User's Handbook of TI55.II Texas Instrument Calculator.
- 122 B220, 'The Flexibility and Stress Analysis of GRP and PVC/GRP Pipework including the Effects of Supporting and Internal Pressure', ICI Engineering Specifications, Dec. 1978.
- 123 BS806, 'Specification for Ferrous Pipes and Piping Installations for and in connection with Land Boilers', British Standard Institution, 1975.
- 124 ANSI B31.3-1976, American National Standard, Chemical Plant and Petroleum Refinery Piping, Appendix D.
- 125 T.J. Fowler and E. Gray, 'Development of an Acoustic Emission Test for FRP Equipment', ASCE Conf. Boston, April 1979.
- 126 BS 5500, 'Fusion Welded Pressure Vessels', British Standards Institution, 1976.
- 127 D.C. Barton and P.D. Soden, 'Short-term in-plane stiffness and strength properties of CSM reinforced polyester laminates', *Composites*, 13(1), 1982, pp. 66-78.

- 128 D.C. Barton and P.D. Soden, 'Stiffness and strength properties of asymmetric glass reinforced polyester laminates', *Composites*, Vol. 13, No. 2, April 1982, pp. 180-201.
- 129 M.F. Markham, D. Dawson, 'Interlaminar Shear Strength of Fibre-reinforced Composites', *Composites*, Vol. 6, No. 4, July 1975, pp. 173-176.
- 130 F.L. Matthews, P.F. Kilty and E.W. Godwin, 'Load-carrying Joints in Fibre Reinforced Plastics', *Plastics and Rubber Processing and Applications*, Vol. 2, No. 1, 1982, pp. 19-25.
- 131 S. Timoshenko, 'Strength of Materials', Part 1, 3rd Edition, Van Nostrand Reinhold.
- 132 S. Crocker, 'Piping Handbook', McGraw Hill, NY, 1945.
- 133 D. Fowle, 'The Design and Use of Reinforced Plastics Piping Systems in Chemical Plant', *Chemistry and Industry*, No. 11, June 1978, pp. 361-365.
- 134 Mark's Standard Handbook for Mechanical Engineers', 'Piping Flexural Stresses caused by Expansion or Movement of Supports', Ch. 5, 7th Edition, Baumeister, 1967.
- 135 BS 3351, 'Piping Systems for Petroleum Refineries and Petrochemical Plants', British Standard Institution, 1971.
- 136 H. Ford, 'Advanced Mechanics of Materials', John Wiley and Son Inc, New York, (NY, 1963).
- 137 'Design of Piping Systems', The M.W. Kellogg Company, John Wiley (1956).
- 138 A. Bantlin, 'Formänderung und Beanspruchung Federnder Ausgleichohre', *Z, VDI*, Vol. 54 (1910), pp. 213-219.
- 139 Th. von Karman, 'Über die Formänderung Dünnwandiger Rohre, Insbesondere Federnder Ausgleichrohre', *Z, VDI*, Vol. 55 (1911), pp. 1889-1895, RAPRA Translation.
- 140 J.P. Den Hartog, 'Advanced Strength of Materials', McGraw-Hill Book Company (1952).
- 141 W. Hovgaard, 'The Elastic Deformation of Pipe Bends', *J. of Mathematics and Physics*, M.I.T., Vol. 6, 1926, pp. 69-118.
- 142 W. Hovgaard, 'Deformation of Plane Pipes', *J. of Mathematics and Physics*, M.I.T., Vol. 7, 1927-1928, pp. 198-238.
- 143 I. Vigness, 'Elastic Properties of Curved Tubes', *Trans., ASME*, 1943, Vol. 65, pp. 105.
- 144 T.E. Pardue and I. Vigness, 'Properties of Thin-walled Curved Tubes of Short-Bend Radius', 1951, *Trans. ASME*, Vol. 73, pp. 77.
- 145 L. Beskin, 'Bending of Curved Thin Tubes', *J. of Applied Mechanics*, *Transaction of ASME*, Vol. 12, 1945, pp. A1-A7.

- 146 A.R.C. Markl and K.Y. Louisville, 'Fatigue Tests of Piping Components', Transaction of ASME, Vol. 74, 1952, pp. 287-303.
- 147 R.T. Smith, 'Theoretical Analysis of the Stresses in Pipe Bends subjected to Out-of-plane Bending', J. Mech. Eng. Sci., Vol. 9, No. 2, 1967, pp. 115.
- 148 S.S. Gill, 'The Stress Analysis of Pressure Vessels and Pressure Vessel Components', Vol. 3, Pergamon Press, 1970.
- 149 C.E. Turner and Prof. H. Ford, 'Examination of the Theories for Calculating the Stress in Pipe Bends subjected to In-plane Bending', Proc. Instn. Mech. Engrs., Vol. 171, pp. 513-525.
- 150 R.A. Clark and E. Reissner, 'Bending of Curved Tube', Advances in Applied Mechanics, Academic Press Inc., 1951, pp. 93.
- 151 N. Gross and H. Ford, 'The Flexibility of Short-radius Pipe-bend', Proc. Institution of Mechanical Engineers, Vol. 1(B), 1952-1953, pp. 480-509.
- 152 N. Gross, 'Experiments on Short-Radius Pipe Bends', Proc. Institution of Mechanical Engineers, Vol. 1 (B), 1952-1953, pp. 465-479.
- 153 P.G. Kafka and M.B. Dunn, 'Stiffness of Curved Circular Tubes with Internal Pressure', J. of App. Mechanics, Transaction of ASME, Vol. 78, 1956, pp. 247-254.
- 154 W.G. Dodge and S.E. Moore, 'Stress Indices and Flexibility Factors for Moment Loadings on Elbow and Curved Pipes', ORNL-3658 (March 1972), OAK RIDGE National Laboratory, Oak Ridge Tennessee 37830, USA.
- 155 W.G. Dodge and S.E. Moore, 'ELBOW: A Fortran Program for the Calculation of Stresses, Stress Indices and Flexibility Factors for elbows and Curved Pipe', Contract No. W-7405-Eng-26, April 1973, OAK RIDGE National Laboratory.
- 156 N. Jones, 'In-plane Bending of a Short-radius Curved Pipe Bend', J. of Eng. for Industry, Transaction of the ASME, May 1967, pp. 271-277.
- 157 J. Imamasa and K. Uragami 'Experimental Study of Flexibility and Stresses of Welding Elbows with End Effect', 2nd International Conf. on Pressure Vessel Technology, Part 1, DESIGN and ANALYSIS, Nov. 1974, pp. 417-426.
- 158 A.L. Tan, 'GRP Pipes and Piping Components', SERC/PED Mechanical Engineering Department Report, August 1979, UMIST.
- 159 R. Dodds and M. Kanona, 'Performance of GRP Pipe Bends Progress Report No. 2', RAPRA Confidential Report, CTR 5131, Sept. 1979, submitted to the Management Committee of the GRP Piping Design Code Project.

- 160 M. Kanona, 'GRP Piping Design Code Project', RAPRA Confidential Report, CTR 5872, August 1980, submitted to the Management Committee of the GRP Piping Design Code Project.
- 161 M. Kanona, 'RAPRA Report on GRP Bends', Bulletin RAPRA/13395, 14.9.81/PAA, submitted to the Management Committee of the GRP Piping Design Code Project.
- 162 M. Kanona, 'Stress Intensification Factors and Flexibility Factors for GRP Pipe Bends', RAPRA Confidential Report, CTR 7868, Nov. 1982, submitted to the Management Committee of the GRP Piping Design Code Project.
- 163 R. Raymond and W. Young, 'Formulas for Stress and Strain', 5th Edition, McGraw-Hill Kogakusha Ltd., pp. 454.
- 164 A. Van der Neut, 'Bending at the Oblique End Section of Cylindrical Shells', Proc. of the Symposium on the Theory of the Elastic Shells, Delft; 24-28; August 1959, edited by W.T. Koiter.
- 165 A.E. Green and W.C. Emmerson, 'Stresses in a Pipe with a Discontinuous Bend', J. Mech. Phys. Solids, 1961, Vol. 9, pp. 91-104,
- 166 P.H. Lane and R.T. Rose, 'Experiments on Fabricated Pipe Bends', British Welding Journal, 1961, June, Vol. 8, No. 6, pp. 323-334.
- 167 B. Owen and W.C. Emmerson, 'Elastic Stresses in Single Mitred Bends', J. Mech. Eng. Science, Vol. 5, No. 4, 1963, pp. 303-324.
- 168 R. Kitching, 'Mitre Bends subjected to In-plane Bending Moments', Int. J. Mech. Sci., Pergamon Press Ltd., 1965, Vol. 7, pp. 551-575.
- 169 R. Kitching, 'In-plane Bending of a 180° Mitred Pipe Bends', Int. J. Mech. Sci., Pergamon Press Ltd., 1965, Vol. 7, pp. 721-736.
- 170 R. Kitching and M.P. Bond, 'Flexibility and Stress Factors for Mitred Bends under In-plane Bending', Int. J. Mech. Sci., Pergamon Press, 1970, Vol. 12, pp. 267-285.
- 171 M.P. Bond and R. Kitching, 'Computation of Stresses and Flexibilities for Multi-mitred Pipe Bends under In-plane Bending', J. of Strain Analysis, Vol. 6, No. 2, 1971, pp. 77-88.
- 172 M.P. Bond and R. Kitching, 'Stress and Flexibility Factors for Multi-mitred Bends subjected to Out-of-plane Bending', J. of Strain Analysis, Vol. 6, No. 4, 1971, pp. 213-225.
- 173 M.P. Bond and R. Kitching, 'Stress and Flexibility Factors for Multi-mitred Pipe Bends subjected to Internal Pressure Combined with External Loadings', J. of Strain Analysis, Vol. 7, No. 2, 1972, pp. 97-108.
- 174 N. Jones and R. Kitching, 'An Experimental Investigation of a Right-angled Single Unreinforced Mitred-bend subjected to Various Bending Moments', J. of Strain Analysis, Vol. 1, No. 3, pp. 248-263.

- 175 N. Jones and R. Kitching, 'A Theoretical Study of In-plane Bending of a Single Unreinforced Mitred-Bend', J. of Strain Analysis, Vol. 1, No. 3, 1966, pp. 264-276.
- 176 R. Kitching and W.J. Thompson, 'In-plane bending of single unreinforced mited pipe bends', J. of Strain Analysis, Vol. 5, No. 1, 1970, pp. 14-24.
- 177 M.V. Murthy, 'Stresses in a mitred pipe joint under uniform internal pressure', Int. J. Mech. Sci, Pergamon Press Ltd., Vol. 6, 1964, pp. 361-370.
- 178 A. John Ingen Housz, 'GRP mitred pipe bend', Senior Scientific Officer, Technological University of Twente, Enschede, Netherland.
- 179 E.C. Rodabaugh and H.H. George; Louisville; K.Y., 'Effect of Internal Pressure on Flexibility and Stress Intensification Factors of Curved Pipe or Welding Elbows', Trans. ASME 79, 1957, pp. 939-940.
- 180 Smuth R.T. and Hugh Ford, 'Experimental Study of the flexibility of a full-scale two-dimensional stream pipeline', J. of Mechanical Engineering Science, Vol. 4, No. 3, 1962, pp. 270-285.
- 181 Smith^{R.T.} and Hugh Ford, 'Experiments on pipelines and pipe bends subjected to three-dimensional loading', J. of Mechanical Engineering Science, Vol. 9, No. 2, 1967, pp. 124-137.
- 182 'Draft Standard Specification for Reinforced Plastics Pipes and Fittings for Process Plant', British Standards Institution, Oct. 1976, sub-committee PLC/9/5 - Reinforced Plastics Pipes.
- 183 RAPRA Stressing Frame Specifications, Drawing Nos. 137.01-137.06, 1977.
- 184 M. Kanona, 'Vibration of torsional systems', M. Sc. Thesis, Oct. 1978, Dept. of Mech. Eng., Aston University in Birmingham.
- 185 R. Kitching, 'Test to Failure of GRP Pipes and Components', Discussion Meeting, 2nd Feb. 1984, The Institution of Mechanical Engineers, Process Industries Division.
- 186 F.J. Lockett, 'Effect of Fabrication on Deformation of CSM Pressure Pipe', Draft NPL Report Number DMA (D) 160, IN CONFIDENCE, Jan. 1979.
- 187 M.J. Owen, 'Static and Fatigue Strength of Glass Chopped Strand', Short fibre reinforced composite material, STP 772, 1982, pp. 64-84.
- 188 D.J. Fowle, 'The fabrication of GRP pipes and piping components for chemical process plant', Inst. Ch. Engrs. N.W. Branch, 1980, No. 1, pp. 2.1-2.12.

© MAAN KANONA 1985